



Deliverable 6.9.

**Modelling of a generic geological disposal:
evaluation of various approaches to model gas
transport through geological disposal systems.**

Task 4. Final technical report

Work Package **GAS**

This project has received funding from the European Union's Horizon 2020 research and innovation programme under grant agreement N°847593



Document information

Project Acronym	EURAD
Project Title	European Joint Programme on Radioactive Waste Management
Project Type	European Joint Programme (EJP)
EC grant agreement No.	847593
Project starting / end date	1st June 2019 – 30 May 2024
Work Package No.	6
Work Package Title	Mechanistic understanding of gas transport in clay materials
Work Package Acronym	EURAD-GAS
Deliverable No.	6.9
Deliverable Title	Modelling of a generic geological disposal: evaluation of various approaches to model gas transport through geological disposal systems. Task 4. Final technical report
Lead Beneficiary	Andra
Contractual Delivery Date	29/02/2024
Actual Delivery Date	22/05/2024
Type	Report
Dissemination level	PU
Editors	Jacques WENDLING (Andra), Simon NORRIS (NWS) and Magdalena DYMITROWSKA (IRSN)

To be cited as:

Wendling J., Norris S. and Dymitrowska M. (editors) (2024). Modelling of a generic geological disposal: evaluation of various approaches to model gas transport through geological disposal systems. EURAD-GAS: Work Package Gas (Mechanical understanding of gas transport in clay-based materials) of the HORIZON 2020 project EURAD. EC Grant agreement no: 847593. Task 4. Final technical report. Deliverable 6.9 (D6.9).

Disclaimer

All information in this document is provided "as is" and no guarantee or warranty is given that the information is fit for any particular purpose. The user, therefore, uses the information at its sole risk and liability. For the avoidance of all doubts, the European Commission or the individual Colleges of EURAD (and their participating members) has no liability in respect of this document, which is merely representing the authors' view.

Acknowledgement

This document is a deliverable of the European Joint Programme on Radioactive Waste Management (EURAD). EURAD has received funding from the European Union's Horizon 2020 research and innovation programme under grant agreement No 847593.

Status of deliverable		
	By	Date
Delivered (Lead Beneficiary)	Andra	11 March 2024
Verified (WP Leader)	ONDRAF/NIRAS	11 March 2024
Reviewed (Reviewers)	Elke Jacobs (SCK CEN)	27 March 2024
	Jean Talandier (Andra)	27 March 2024
Approved (PMO)	Bharti Reddy (Nuclear waste Services, UK)	20 May 2024
Submitted to EC (Coordinator)	Andra (Coordinator)	22 May 2024

Executive Summary

Task 4 of EURAD-GAS work-package established in the framework of EURAD European Joint programme aimed at fulfilling the second high-level objective of the EURAD-GAS, which is to evaluate the gas transport regimes that can be active at the scale of a geological disposal system and their potential impact on repository performance. It was dedicated in particular to answer end-users' questions concerning:

- the effects of gas on the transport of soluble and volatile radionuclides;
- the consequences of gas-induced hydro-mechanical perturbations on barrier integrity and long-term performance of the disposal system.

The objective of Subtask 4.1 was to assemble phenomenological descriptions of gas transport and of its consequences on barriers integrity and radionuclide transport at repository relevant scales, in the form of storyboards. The first conceptualization phase has been completed by the definition of (i) a “generic repository” configuration and sets of properties and conditions on which Subtask 4.2 has tested various evaluation approaches and (ii) a proposal for a set of indicators, covering the range of needs of various end-users in Europe for disposal systems in clayey host rock, representative of the processes to be evaluated (transport of radionuclides, volatile and soluble, barrier integrity for instance).

This final report mainly focusses on the compilation of the work done in Task 4.2 during the EURAD-GAS project. As team involvement varied widely, depending on the team, available results are not at the same level of representation and or coupling.

After presentation of the work done by each of the involved teams (Chapters 2 to 9), Chapter 10 offers a global discussion on all of these results trying to determine common elements favouring good practices for a phenomenologically representative evaluation of maximum gas pressures in a repository and their possible impacts on the host rock integrity and/or radionuclide transport. Last chapter (Chapter 11) provides a synthesis of EURAD-GAS Task 4 achievements that is end-users and decision-makers oriented, building on the work done inside Task 4.1, and Task 4.2, including Chapter 10.

Table of content

Executive Summary.....	5
Table of content.....	7
List of figures	12
List of Tables	21
1. Introduction	23
2. Contribution of Aalto University	27
2.1 Introduction	27
2.2 Thebes numerical framework	27
2.2.1 Mass conservation of components	28
2.2.2 Mass conservation of solids	28
2.2.3 Mass conservation of water	28
2.2.4 Mass conservation of Hydrogen	31
2.2.5 Mass conservation of air	34
2.2.6 Heat conservation.....	36
2.2.7 Mechanical Balance.....	38
2.3 Verification	38
2.3.1 1D Thebes vs Comsol verification	38
2.4 Dissolved gas diffusion validation.....	41
2.5 THG coupled test: Landfill gas migration.	41
2.6 2D modelling of a deposition tunnel section from Zone B.....	43
2.7 Numerical details	43
2.8 Simulation results	46
2.9 Conclusion	50
2.10 References	51
3. Contribution of Andra.....	53
3.1 Generalities.....	53
3.2 The numerical model	54
3.2.1 The code used	54
3.2.2 The phenomenological processes taken into account	55
3.2.3 The initial and boundary conditions	56
3.2.4 The mesh.....	56
3.2.5 Waste A cells	59
3.2.6 Waste B cell.....	61
3.2.7 Waste C cell.....	62
3.2.8 Seals	65

3.3	Base case results	68
3.3.1	Pressures results	68
3.3.2	Flow results	70
3.3.3	Radionuclides results	72
3.4	Sensitivity analysis	74
3.4.1	Sensitivity analysis on model extension	74
3.4.2	Sensitivity on gas source terms	76
3.4.3	Sensitivities on parameters values for maximum gas pressure estimation	81
3.4.4	Sensitivities on parameters values for gaseous ¹⁴ C migration	84
3.4.5	Sensitivities on parameters values for soluble ¹²⁹ I migration	87
3.5	Discussion and synthesis	88
3.5.1	Model extension	88
3.5.2	Mesh design	88
3.5.3	Optimized design for maximum gas pressure reduction	88
3.5.4	Gaseous radionuclides transfer	88
3.5.5	Solute radionuclides transfer	89
3.6	Conclusion	89
3.7	References	90
3.8	Appendix: description of the numerical implementation of explicit gas entry pressure in Van-Genuchten/Mualem formulations	90
3.8.1	Capillary pressure:	90
3.8.2	Relative Permeability:	93
4.	Contribution of BGR	95
4.1	Model approach	95
4.2	Model set-up and numerical details	98
4.3	Simulation results	108
4.4	Summary and future work	113
4.5	References	114
5.	Contribution of IRSN	117
5.1	Model description	117
5.2	Numerical details	125
5.3	Simulation results	126
5.4	Conclusions and perspectives	134
5.5	References	135
6.	Contribution of EDF	137
6.1	Contributions of EDF	137
6.2	Model description	137
6.2.1	Physical model	137
6.2.2	Physical parameters	142

6.3	Numerical details	144
6.3.1	Geometry of the modelling domain.....	144
6.3.2	Mesh	145
6.3.3	Boundary conditions	147
6.3.4	Initial conditions	151
6.4	Simulation results	151
6.4.1	3D modelling case	151
6.4.2	2D modelling.....	157
6.5	Conclusions	177
6.6	References	178
7.	Contribution of LEI.....	179
7.1	Model description.....	179
7.1.1	Modelling tool.....	180
7.1.2	Deviations from specification	186
7.2	Numerical details	187
7.2.1	Initial and boundary conditions	187
7.3	Simulation results	189
7.3.1	Isothermal conditions.....	189
7.3.2	Impact of temperature.....	194
7.3.3	Impact of mechanical deformations.....	198
7.3.4	Impact on radionuclide transport	200
7.4	Conclusions	202
7.5	References	203
8.	Contribution of SCK CEN	205
8.1	Model description.....	205
8.1.1	Material properties	205
8.1.2	Initial and boundary conditions	209
8.1.3	Software and results indicators	211
8.2	EURAD GAS modelling results from Code_Bright.....	211
8.2.1	Comparisons between 1D-3D model results.....	213
8.2.2	3D THG modelling results	213
8.2.3	Impact of including gas production in galleries and shaft.....	223
8.2.4	Sensitivity of seal permeability	224
8.3	Development and verification of two-phase flow model in COMSOL.....	225
8.3.1	Exercise 1—1D HG problem	226
8.3.2	Exercise 2—2D-axisymmetric HG problem.....	226
8.3.3	Exercise 3—2D THG problem	227
8.4	Modelling results of the 2D-PS EURAD model from COMSOL	228

8.4.1	Description of the EURAD 2D-PS TH(M)g problem	228
8.4.2	Result comparisons between COMSOL and Code_Bright for the reference 2D-PS THG model	231
8.4.3	Sensitivity of the diffusion coefficient of dissolved hydrogen.....	232
8.4.4	VG Retention curve	233
8.4.5	Effect of porosity variation induced by the thermal expansion	234
8.4.6	Effect of including mechanical coupling.....	235
8.4.7	Effect of considering vapor	236
8.4.8	The final case of EURAD 2D-PS THMG	237
8.5	Results of component-scale models from COMSOL.....	239
8.5.1	Model at cell scale	240
8.5.2	shaft analysis	243
8.5.3	Computation time.....	245
8.6	Conclusions	246
9.	Contribution of University of Liège.....	249
9.1	2D Model description	249
9.2	Governing equations	251
9.2.1	Balance equations	251
9.2.2	Constitutive equations	252
9.3	Material properties	255
9.4	Features of numerical analysis.....	256
9.4.1	Mesh generation	256
9.4.2	Initial boundary conditions	256
9.4.3	Time varying boundary conditions	257
9.5	Simulation results	259
9.5.1	Effect of SWRC formulation.....	260
9.5.2	Effect of geometric features (consideration of top/bottom aquifers).....	272
9.5.3	Role of temperature (THMG v/s HMG-coupling scenarios).....	280
9.5.4	Effect of gas (H ₂) generation on simulation results (THMG v/s THM-coupling scenario)	286
9.6	Conclusion	292
9.7	References	293
9.8	Appendix I	293
10.	Discussion	299
10.1	Mechanical coupling	299
10.1.1	General comments	299
10.1.2	Dilatancy versus two-phase flow	300
10.2	Model extension.....	300
10.3	Mesh refinement.....	301

10.4	Uncertainty on the gas pressure results	301
10.5	Optimized design for maximum gas pressure reduction	303
10.6	Gaseous radionuclides transfer	303
10.7	Solute radionuclides transfer	303
11.	Synthesis	305
11.1	Proposal of a generic storyboard at repository scale	306
11.2	Generic repository model	308
11.3	Uncertainties associated to the complexity of the problem to be treated and inherent limitations of modelling tools	309
11.4	Assessment of the mechanical integrity of the host rock	311
11.5	Assessment of the impact of gas on the migration of radionuclides	311
11.6	Recommendations for a treatment of gas at the repository design stage	312
12.	ANNEX: milestone MS 61	315
12.1	Aim of the exercise	315
12.2	Geometry of the generic repository	315
12.3	Initial boundary conditions	320
12.4	Time varying conditions	320
12.5	Source terms	321
12.5.1	Thermal source terms	321
12.5.2	Gas source terms	322
12.5.3	Radionuclides source terms	324
12.6	Parameters values	324
12.7	Indicators	330
12.8	Position of output points and surfaces	331

List of figures

Figure 1-1 Schematic horizontal slice of the generic repository at repository depth	24
Figure 2-1 Idealization of soil matrix with phases and components.....	28
Figure 2-2 Generic verification test setup.....	39
Figure 2-3 Gas phase diffusion flow verification test at centre point: a) Hydrogen pressure, and b) Air pressure (Test specifications refer to Gupta et al., 2023)	40
Figure 2-4 Total gas pressure, verification test for advective coupled two gas flow at the centre. (Test specifications refer to Gupta et al., 2023).....	40
Figure 2-5 Diffusion of two dissolved gases - experiment setup (Gupta et al., 2023 adapted from Jacobs et al., 2017).....	41
Figure 2-6 Dissolved gas diffused concentrations, Methane in chamber-2 (more details in Gupta et al., 2023).....	41
Figure 2-7 1D landfill gas and heat flow (Nastev et al. 2001)	42
Figure 2-8 Total gas pressures from Thebes and (Nastev et al. 2001).....	42
Figure 2-9 2D tunnel section from the disposal Zone B (EURAD: Milestone 61 2021).	43
Figure 2-10 Repository simulation mesh.....	44
Figure 2-11 Heat flux at the canister boundary	44
Figure 2-12 Total gas pressures.....	46
Figure 2-13 Molar fraction of hydrogen in time.....	47
Figure 2-14 Gas pressure heads (relative to 1 atm) at around 1 000 years: a) Air pressure head (m), b) Total gas pressure head (m)	47
Figure 2-15 Air molar fraction in time	48
Figure 2-16 Molar fraction of water vapour in time.....	48
Figure 2-17 Temperature profile in time	49
Figure 2-18 Degree of saturation in time.....	49
Figure 2-19 Pore water pressures in time	50
Figure 3-1 Mesh zoning.	57
Figure 3-2 Galleries denomination and cell numbering.	57
Figure 3-3 Vertical extension of the model.	58
Figure 3-4 Dimensions of a gallery.	58
Figure 3-5 Dimensions of a waste A cell.....	59
Figure 3-6 Geometry approximation and alignment of waste A cell and its access gallery (EDZ not represented). 60	
Figure 3-7 zone A mesh. General view and overhead view of a cell (right).	60
Figure 3-8 Dimensions of a disposal gallery in Zone B.	61
Figure 3-9 Conceptualisation of the different materials explicitly represented in the waste B cell mesh. 61	
Figure 3-10 « Conform » transition between access gallery and waste B cell; unfavourable situation with distorted elements not implemented.	62
Figure 3-11 Transition at constant diameter between the access gallery and a cell B thanks to a layer of host rock mesh (in pink). The illustration assumes a radius of the gallery of 3m. With a backfill radius increased to 4m, the “backfill” – “aggregated EDZs & concrete liner” limit is aligned with the “EDZOut” – “Host rock” interface (radius 3.75 m) on the cell side by moving a few nodes of the mesh.	62
Figure 3-12: detail of the global mesh representing the galleries and the deposition cells implemented; Note the “super-cells” in zone C; only 12 cells in the mesh representing the whole 72 cells.	63
Figure 3-13 Dimensions of a waste C cell.	64
Figure 3-14 Conceptualisation of a waste C cell.....	64
Figure 3-15 Axisymmetric mesh. y = axis of the cell, x: radius from the centre of the cell. The scale ratio between x and y is not respected.	65

Figure 3-16	Schematic representation of a horizontal seal.	66
Figure 3-17	Schematic representation of a vertical seal.....	66
Figure 3-18	Mesh of a horizontal seal with a maximum discretization step of 5 meters. The side mesh layers of the covering and EDZ are hidden on one side to visualize the core.	67
Figure 3-19	Mesh of a vertical seal with a maximum discretization step of 5 meters. The side mesh layers of the covering and EDZ are hidden on one side to visualize the core.	67
Figure 3-20:	Evolution of maximum gas pressure in the 3 deposition zones of the generic repository	69
Figure 3-21:	Gas pressure distribution in the repository at maximum gas pressure	69
Figure 3-22:	Gaseous hydrogen fluxes along the gallery's axes	70
Figure 3-23:	Gas flux entering the shaft toward the upper aquifer	70
Figure 3-24:	Water fluxes along the galleries axes.....	71
Figure 3-25:	Radial fluxes compared to longitudinal water fluxes along the galleries axes	72
Figure 3-26:	14C fluxes at deposition zones (through zone seals) and shaft level	73
Figure 3-27:	129I fluxes at deposition zones (through zone seals) and shaft level.....	73
Figure 3-28:	representation of the models including only one zone; same global extension as the total generic repository model but host rock replace the other zones.....	74
Figure 3-29:	Evolution of gas pressure in zone B supposed alone, with or without shaft	75
Figure 3-30:	Evolution of gas pressure in zone C supposed alone, with or without shaft	76
Figure 3-31:	Gas pressure in zone B stand-alone model with a shaft for different gas source terms	77
Figure 3-32:	Gas pressure in zone C stand alone with a shaft model for different gas source terms	77
Figure 3-33:	Gaz pressure in zone B stand-alone model with and without shaft for different gas source terms	78
Figure 3-34:	Gas pressure in zone C stand alone model with and without shaft for different gas source terms.....	79
Figure 3-35:	129I fluxes at different locations in the global model for different gas source terms	80
Figure 3-36:	14C fluxes through the shaft in the global model for different gas source terms	81
Figure 3-37:	Sensitivity analysis on backfill porosity: gas pressure for zone B and C in the global model	82
Figure 3-38:	Sensitivity analysis on host rock permeability: gas pressure for zone B and C in the global model	82
Figure 3-39:	Sensitivity analysis on host rock gas entry pressure: gas pressure for zone B and C in the global model	83
Figure 3-40:	Sensitivity analysis on diffusion coefficient of dissolved hydrogen in the host rock water: gas pressure for zones B and C in the global model.....	83
Figure 3-41:	Sensitivity analysis on corrosion rate: gas pressure for zone B and C in the global model	84
Figure 3-42:	Sensitivity on gas entry pressure of the host rock: gaseous 14C flux at shaft.....	85
Figure 3-43:	Sensitivity on diffusion coefficient of dissolved hydrogen in the host rock water: gaseous 14C flux at shaft	86
Figure 3-44:	Sensitivity on corrosion rate: gaseous 14C flux at shaft	87
Figure 3-45:	Sensitivity on diffusion coefficient of dissolved hydrogen in the host rock water: dissolved 129I flux at shaft	87
Figure 3-46	Capillary pressure function of effective saturation for the van Genuchten and the two alternative formulations with gas entry pressure. The “formulation 1” corresponds to equation 3-1 while “formulation 2” corresponds to equation 3-2. $P_r = 1.47 \cdot 10^7$ Pa, $m = 0.375$, $n = 1.6$, $P_e = 5$ MPa (formulation 1 and formulation 2 only)	91
Figure 3-47	Different implementations of the capillary pressure curves for Host Rock (HR). $P_r = 1.47 \cdot 10^7$ Pa, $m = 0.375$, $n = 1.6$, $P_e = 4$ MPa (ICP=19 only). Blue: usual modified van Genuchten (ICP=17, without entry pressure, with linearization at high saturations). Orange & green: van Genuchten with entry pressure. Right: close-up on the linearization close to full saturation. Orange and green curves differ by the linearization threshold.....	93

Figure 3-48	Relative permeability curves for Host Rock (HR) with different implementations of the relative permeability law. $P_r = 1.47 \cdot 10^7$ Pa, $m = 0.375$, $n = 1.6$, $P_e = 4$ MPa (for analytical solution and IRP=16 only).	94
Figure 4-1	Conceptual approach for the safety assessment on repository scale.	99
Figure 4-2:	Overview of disposal zone C as defined in the generic repository exercise (Wendling, 2020). Location and approximate horizontal extent of the full 3D model are highlighted by the red box.	100
Figure 4-3:	Summary of the model set-up containing initial and boundary conditions as well as repository conditions during the ventilation and the deposition phase. The origin of the coordinate system lies in the centre of the repository, so that the top boundary has the vertical coordinate $z = 600$ m.	103
Figure 4-4:	Comparison of the thermal source term for HLW canisters from the generic repository exercise (per m of canister) and the curves discussed in our model. The results presented in this report are based on the blue curve, which is based on the data from the generic repository exercise (Wendling, 2020) in combination with heat output as defined in the RESUS project (Alfarra et al. 2020 and Maßmann et al. 2022), which uses a thermal source term physically based on radioactive decay as summarized in Table 4-2.	104
Figure 4-5:	Gas source terms applied to the deposition tunnel as well as access galleries and shaft.	106
Figure 4-6:	General view of the repository-scale 3D mesh (top) and details of the mesh (bottom).	107
Figure 4-7:	2D (top) and 3D (bottom) plot of the output points as defined in Wendling (2020). Additional points have been introduced to investigate possible effects of the model boundaries. The labelling of these points ends with an "a".	108
Figure 4-8:	Temperature over time at the defined output locations given in Figure 4-7.	109
Figure 4-9:	Contour plots of the temperature after 55 years (left) and ~450 years (right).	109
Figure 4-10:	Saturation over time at the defined output locations given in Figure 4-7.	110
Figure 4-11:	Contour plots of the saturation after ~4000 years (left) and ~40,000 years (right).	110
Figure 4-12:	Gas pressure over time at the defined output locations given in Figure 4-7.	111
Figure 4-13:	Contour plots of the gas pressure after ~4000 years (left) and ~40,000 years (right).	111
Figure 4-14:	Liquid pressure over time at the defined output locations given in Figure 4-7.	112
Figure 4-15:	Contour plots of the liquid pressure after ~450 years (left) and ~40,000 years (right).	112
Figure 4-16:	Contour plot of the liquid pressure after 1834 years, indicating the impact of the boundary condition.	113
Figure 5-1 – (a)	Schematic horizontal slice at generic repository depth. (b) Schematic vertical slice of a gallery.	118
Figure 5-2 –	3D view of the stand-alone module of 72 HLW cells with shaft embedded within the host rock layer (PetraSim preprocessing; Thunderhead engineering inc.).	118
Figure 5-3 – (a)	Schematic representation of a connection gallery seal. (b) Schematic representation of the shaft seal.	119
Figure 5-4–	Schematic representation of a deposition tunnel in disposal zone C (inspired by Andra HLW deposition micro-tunnel): a/ Cross section inside the waste cell; b/ Longitudinal side of the waste cell.	119
Figure 5-5 – (a)	Materials defining drift and shaft seals. (b) Materials defining the waste cell.	120
Figure 5-6 -	Vogel et al. (2001) model with non-zero $P_{c,e}$ in the VGM water retention curve.	122
Figure 5-7 –	Original (continuous lines) vs modified (dashed lines) MQ-model for the unsaturated tortuosity factor of the host rock, for liquid and gas phases.	124
Figure 5-8 – (a)	Vertical mesh along OXZ plane. (b) Lateral mesh along OXY plane.	125
Figure 5-9 –	Points P1-P19 where results of temperature, gas pressure and gas saturation vs time are plotted. Blue points are new points not specified in the benchmark. Points in the host rock: P18 (adjacent to BC) and P19.	126
Figure 5-10–	Temperature variation in time simulated by scenario#3 ($P_{c,e} \neq 0$) at elements points P1-P19. (a) Cells. (b) host rock. (c) Access drifts.	127
Figure 5-11 –	Simulated temperature profiles at slice plane $Z = 75$ m simulated by scenario#3 ($P_{c,e} \neq 0$). (a) Time $t = 100$ y. (b) Time $t = 929$ y.	128

Figure 5-12 – Time evolution of gas pressure (above) and gas saturation (below) at elements points P1-P12 and P12b, simulated by scenario S#3. (a,b) Cells (WASTE and buffer bentonite). (c,d) Access drifts (backfill).	129
Figure 5-13 – Time evolution of (a) gas pressure (b) gas saturation at elements points P18 and P19 in the host rock.	130
Figure 5-14– Simulated profiles of (a) pressure and (b) gas saturation at the slice plane $z = 75$ m simulated by scenario#3 ($P_{c,e} \neq 0$) at time 50 000 y.	131
Figure 5-15 – Time evolution of gas pressure (above) and gas saturation (below) at elements points P13-P17 simulated by scenario S#3. (a,b) Main drift seal. (c,d) Shaft seal.	132
Figure 5-16– Profiles of (a) pressure and (b) gas saturation at slice plane $X = 1232.86$ m, simulated by scenario#3 ($P_{c,e} \neq 0$) at time 50 000 y.	132
Figure 5-17– Time evolution of gas pressure (above) and gas saturation (below) at elements points P3, P5, and P19 simulated by scenarios S#2 ($P_{c,e} = 0$) and S#3 ($P_{c,e} \neq 0$). (a,b) Cell buffer; (c,d) Access drift; (e,f) host rock between modules.	133
Figure 5-18– Time evolution of gas pressure (above) and gas saturation (below) at elements points P13, P14, P16 and P17. (a,b) Main drift backfill and seal; (c,d) Shaft seal and concrete.	134
Figure 6-1: Prolongation of Van-Genuchten function when $S > \varepsilon$	139
Figure 6-2: Representation of the modelling domain in the zone C (horizontal plan)	144
Figure 6-3: scheme of the modeling geometry for 3D and 2D computations	145
Figure 6-4: 3D mesh of the considered cross section (general view and zooms)	146
Figure 6-5: 2D Mesh (zoom around the tunnel)	147
Figure 6-6: 3D boundary conditions for $T < 50$ years	148
Figure 6-7: 3D boundary conditions for $T \geq 50$ years	149
Figure 6-8: 2D boundary conditions (vertical section around a HLW C) $t \geq 50$ years	149
Figure 6-9: thermal source term per meter of canister	150
Figure 6-10: temperature isovalues	152
Figure 6-11: gas pressure isovalues	152
Figure 6-12: gas pressure isovalues (host rock only)	153
Figure 6-13: output points ($y = -600$ m) (C1, LT, MT, P, G1, G2)	154
Figure 6-14: temperature on output points (a) and on profile (b)	155
Figure 6-15: gas pressure on output points (a) and on profile (b)	155
Figure 6-16: saturation on output points (a) and on profile (b)	156
Figure 6-17: capillary pressure on output points (a) and on profile (b)	156
Figure 6-18: gas pressure evolution – comparison of 3D computations with or without thermal flow	157
Figure 6-19: temperature evolution - comparison between 3D and 2D computations	158
Figure 6-20: gas pressure evolution - comparison between 3D and 2D computations	159
Figure 6-21: capillary pressure evolution - comparison between 3D and 2D computations	159
Figure 6-22: liquid pressure evolution - comparison between 3D and 2D computations	160
Figure 6-23: gas pressure evolution in the cell	161
Figure 6-24: dynamic liquid viscosities used in the computations	162
Figure 6-25: temperature evolution (cases 1 & 2)	162
Figure 6-26: gas pressure evolution (cases 1 & 2)	163
Figure 6-27: capillary pressure evolution (cases 1 & 2)	163
Figure 6-28: liquid pressure evolution (cases 1 & 2)	163
Figure 6-29: gas pressure evolution (cases 2 & 3)	164
Figure 6-30: capillary pressure evolution (cases 2 & 3)	164
Figure 6-31: liquid pressure evolution (cases 2 & 3)	165
Figure 6-32: expressed gas pressure evolution (case 3)	165
Figure 6-33: expressed gas pressure evolution (cases 3&4)	166
Figure 6-34: capillary pressure evolution (cases 3&4)	166
Figure 6-35: liquid pressure evolution (cases 3 & 4)	167
Figure 6-36: saturation evolution (cases 3 & 4)	167

Figure 6-37: comparison of capillary pressure curves used for case 3 (VGE) and for case 5 (VGM with ULiège parameters).....	168
Figure 6-38: comparison of liquid relative permeabilities curves used for case 3 (VGE) and for case 5 (VGM with ULiège parameters).....	169
Figure 6-39: gas relative permeabilities curves (/fg) used for case 3 (VGE) and for case 5 (VGM with ULiège parameters).....	169
Figure 6-40: gas pressure evolution (cases 3 &5).....	170
Figure 6-41: expressed gas pressure evolution (cases 3 &5).....	170
Figure 6-42: capillary pressure evolution (cases 3 &5).....	171
Figure 6-43: liquid pressure evolution (cases 3 &5).....	171
Figure 6-44: saturation evolution (cases 3 &5).....	172
Figure 6-45: gas pressure evolution (cases 5 &6).....	173
Figure 6-46: liquid pressure evolution (cases 5 &6).....	173
Figure 6-47: Configuration BC2 considering only host rock.....	174
Figure 6-48: gas pressure evolution (cases 5 & 7).....	175
Figure 6-49: expressed gas pressure evolution (cases 5 & 7).....	175
Figure 6-50: capillary pressure evolution (cases 5 & 7).....	175
Figure 6-51: liquid pressure evolution (cases 5 & 7).....	176
Figure 6-52: temperature evolution (cases 5 & 7).....	176
Figure 7-1– Schematic view of generic repository concept [1]. Blue dotted lines show LEI modelling domains in EURAD-GAS activities.....	179
Figure 7-2 – Comparison of gas profiles at different times specified (solid lines) [2] and TH model formulation for hydrogen in COMSOL Mutliphysics (dotted lines with marker).....	182
Figure 7-3 – SCK CEN diffusion test scheme [3].....	183
Figure 7-4 – Modelling results of cumulative gas flux out of the system: solid line – results from [2], dotted lines with markers – model results in COMSOL Multiphysics.....	184
Figure 7-5 – Comparison of modelling results with measurements presented in [2].....	185
Figure 7-6 – Schematic representation of deposition tunnel in Zone B specified in [1] and in COMSOL Multiphysics model.....	187
Figure 7-7 – Boundary conditions for TH model.....	188
Figure 7-8 – Boundary conditions for M model.....	189
Figure 7-9 – Simulated evolution of relative permeability for liquid phase with and without H ₂ gas generation in the tunnel.....	190
Figure 7-10 – Liquid saturation distribution around the deposition tunnel: a) considering modified Van Genuchten-Mulaem model with explicit gas entry pressure, b) unmodified Van Genuchten-Mulaem model (zero gas entry pressure).....	191
Figure 7-11 – Simulated evolution of relative permeability at observation points: a) considering modified Van Genuchten-Mulaem model with explicit gas entry pressure, b) unmodified Van Genuchten-Mulaem model (zero gas entry pressure).....	192
Figure 7-12 – Modelled evolution of liquid pressure at observation points: a) considering modified Van Genuchten-Mulaem model with explicit gas entry pressure, b) unmodified Van Genuchten-Mulaem model (zero gas entry pressure).....	193
Figure 7-13 – Modelled evolution of gas pressure at observation points: a) considering modified Van Genuchten-Mulaem model with explicit gas entry pressure, b) unmodified Van Genuchten-Mulaem model (zero gas entry pressure).....	193
Figure 7-14 – Modelled temperature evolution at observations points.....	195
Figure 7-15 – Temperature distribution at different times (including time for ventilation).....	196
Figure 7-16 - Modelled evolution of liquid saturation evolution in observation points under: a) isothermal conditions, b) non-isothermal conditions.....	196
Figure 7-17 – Modelled evolution of relative permeability evolution in observation points under: a) isothermal conditions, b) non-isothermal conditions.....	197
Figure 7-18 – Modelled evolution of a) liquid and b) gas pressure at observation points.....	198

Figure 7-19 – Modelled evolution of relative permeability at observation points: a) without mechanical couplings, b) with mechanical couplings	198
Figure 7-20 – Modelled evolution of a) liquid and b) gas pressure at observation points.....	199
Figure 7-21 – Simulated distribution of liquid pressure a) without consideration mechanical processes (THG model) and b) considering mechanics related couplings (THMG model) (geometry not to scale)	200
Figure 7-22 – Boundary conditions for I-129 transport in Zone B	201
Figure 7-23 –Modelled I-129 concentration in observation points and further in host rock in Zone B under different boundary conditions	201
Figure 7-24 – Evolution of effective diffusivity of I-129 in different barriers	202
Figure 8-1 Geometry of the full 3D model of Zone B	206
Figure 8-2 details of the full 3D model of Zone B.....	206
Figure 8-3: retention curves used in Code_Bright compared with retention curves in problem specification	208
Figure 8-4: the thermal load and gas production rate in the 3D THG model for zone B.....	210
Figure 8-5: (left) 14 observation points and their coordinates (right) Schematic 12 surfaces (purple segments) for output of gas flux	211
Figure 8-6: Comparison of gas pressure and water saturation at the mid-section of the central disposal cell between 1D-3D models.....	213
Figure 8-7: Evolution of gas pressure, water pressure, temperature and water saturation at 14 OB points from 3D THG simulation	214
Figure 8-8: gas pressure(left) and water saturation(right) contour at ~2 000 years.....	215
Figure 8-9: Contour of gas pressure at the end of gas injection (1E5 years) unit: MPa.....	215
Figure 8-10: Section A-A and the location with the maximum gas pressure	215
Figure 8-11: gas pressure (left, unit: MPa) and water saturation (right) profile along A-A section (Y=500 m, z=0) at 1E5 years	215
Figure 8-12: contours of S_l and P_g at section A-A at 1E5 years.....	216
Figure 8-13: section at OB10 (X=90m) with materials from inner to outer are backfill, liner, inner_EDZ, outer_EDZ and host rock, respectively (left); contour of gas pressure (middle) and water saturation (right) at section OB10 at 1E5 years	216
Figure 8-14: gas pressure (top), gas flux (middle) and water saturation (bottom) profile along the central line of the access gallery at 1E5 years.....	217
Figure 8-15: gas pressure (top), gas flux rate(middle) and water saturation (bottom) profile along the shaft.....	218
Figure 8-16:evolution of P_g, P_w, T and S_l at seven points around the mid-point of the central disposal cell. The seven observation points locate along the red line marked in the uppermost graph.	219
Figure 8-17: integrated advective gas flux through the backfill at 12 surfaces	220
Figure 8-18: Vector of gas flux at 55 years(left), 2300 years (middle) and 1E5 years(right)	220
Figure 8-19: gas flux vector along access galleries: X=200-500m(left) x=700-1000m at 1E5 years..	220
Figure 8-20: gas flux rate along the central cell (X=550) at 1E5 years	221
Figure 8-21: gas flux at the mid-section (Y=500 m) of disposal cells at 1E5 years, with materials from inner to outer are backfill, liner, inner_EDZ, outer_EDZ and host rock, respectively.....	221
Figure 8-22: a horizontal cross section on the shaft at z=580m (left) the cross sectional view (middle) integration of advective gas flux through the shaft cross section (right)	222
Figure 8-23: advective gas flux through each material at section of one disposal cell (A-A) and one section at access gallery (section 6)	223
Figure 8-24: impact of including access gallery and shaft gas production on the gas pressure.....	224
Figure 8-25: Comparisons of gas pressure around seals between the base case and an alternative case with 100 times higher permeability for the seal bentonite.	224
Figure 8-26: Comparisons of gas flux at shaft section (Z=580m) between the base case and an alternative case with 100 times higher permeability for the seal bentonite.....	225
Figure 8-27:schematic diagrams for three verification exercises used in Yu et al. (2011).....	226

Figure 8-28: Result comparisons between COMSOL and Code_Bright for a 1D HG problem at two observation points (dots are from Code_Bright and lines are from COMSOL).	226
Figure 8-29: Result comparisons between COMSOL and Code_Bright for a 2D-axisymmetric HG problem at five observation points(dots are from Code_Bright and lines are from COMSOL).	227
Figure 8-30: Results comparison between COMSOL and Code_Bright for a 2D-axisymmetric THG problem (dots are from Code_Bright and lines are from COMSOL).	228
Figure 8-31: EURAD 2D-PS THG model geometry, mesh and observation points.	229
Figure 8-32: Thermal source term per meter of disposal cell in zone B (lasting from 50 years to 3000 years).....	229
Figure 8-33: Result comparisons between COMSOL and Code_Bright for the 2D-PS THG reference case (dots are for Code_Bright and lines for COMSOL).	232
Figure 8-34: impacts of various diffusion coefficients on the gas pressure at the backfill point (1.49,0)	233
Figure 8-35: comparisons between VG model in Table 8-4 (circles) and linearized VG model (solid lines)	234
Figure 8-36: impacts of thermal expansion on porosity variation	234
Figure 8-37: impact of thermal expansion on pore/gas pressure (circles are for the reference case, dotted lines are for case 1 and solid lines are for case 2).....	235
Figure 8-38: comparison of thermal-induced and stress-induced volumetric strain in THMG analysis	236
Figure 8-39: comparison between THMG and THG models (dots are for the reference THG model and solid lines are for THMG model).....	236
Figure 8-40: time evolution of the effective circumferential stresses from the THMG model	236
Figure 8-41: percentage of vapour pressure in the total gas pressure(left) and effect of vapour on the gas pressure(right).	237
Figure 8-42: Effects of vapour on the total dissolved and total gaseous H ₂ in the system	237
Figure 8-43: The final THMG case (solid lines) in Table 8-6 compared with the reference case in Table 8-4 (circles).....	239
Figure 8-44: result from Code_Bright for the 3D full model of zone B: (left) Pg profile along the gallery and shaft at 1E5 years (right) schematic illustration of gas flux in zone B at around 2000 years.....	240
Figure 8-45: 3D COMSOL model at cell-scale (left) and mesh (right)	240
Figure 8-46: contour of Pg and Sw at 1E5 years from 3D COMSOL model at cell scale	241
Figure 8-47: time evolution of Pg, Pw, Sw and T at cell points (dashed lines) and gallery points(solid lines) from 3D COMSOL cell model	242
Figure 8-48: Comparison between gaseous and diffusive gas	242
Figure 8-49: Schematic vertical slice of the generic repository and shaft structure	243
Figure 8-50: 3D COMSOL shaft model(left), mesh of shaft (middle) and zoomed view shaft exit (right)	244
Figure 8-51: Evolution of gas pressure (left) and water saturation degree (right) at the mid-section of the shaft from the 3D COMSOL shaft model. The six observation points are located at x= 2, 4.5, 5.5, 6.75, 10, 25 m, Y=0 and Z=300m. Dots on the Pg curves marks the period when Sw >99%.	244
Figure 8-52: contour of gas pressure and water saturation degree at the shaft exit at 1E5 years.	245
Figure 8-53: (left) comparison between the total gas production rate and integration of the advective gas flux over different materials at the shaft exit (right) total gas mass produced in the shaft compared to total advective gas at the shaft top surface.	245
Figure 8-54: comparison of time step between cell model and shaft model	246
Figure 8-55: comparison of saturation degree between cell model and shaft model.....	246
Figure 9-1 Model dimensions and geometric features of 2D plane strain model.....	250
Figure 9-2 Finite element mesh (T = top aquifer, B = bottom aquifer; In Zone B: 1 = outer EDZ, 2 = inner EDZ, 3 = concrete liner, 4 = cementitious backfill, 5 = concrete buffer; In Zone C: 6 = outer EDZ, 7 = inner EDZ, 8 = steel liner, 9 = air void).....	256
Figure 9-3 Initial boundary conditions for 2D PS analysis (Not at scale).	257

Figure 9-4 Setting up of initial boundary conditions, (a) pore water pressure, (b) vertical stress, and (c) temperature along the Y-direction or the depth.....	258
Figure 9-5 (a), (b) Initiation of tunnel excavation process using theory of deconfinement, and (c), (d) implementation of dewatering process in Zone C and ventilation process in Zone B.....	258
Figure 9-6 Gas (hydrogen) and thermal source term for Zone B and Zone C.	259
Figure 9-7 Observation points in Zone B.....	259
Figure 9-8 Observation points in Zone C.	260
Figure 9-9 Comparison of an idealized van Genuchten water retention model with the specified water retention formulations considering the gas entry pressure with ϵ equals to 0.01.....	262
Figure 9-10 Evolution of temperature in Zone B (Case 1 v/s Case 2).	263
Figure 9-11 Evolution of temperature in Zone C (Case1 v/s Case 2).	264
Figure 9-12 Evolution of pore water pressure in Zone B (Case 1 v/s Case 2).....	265
Figure 9-13 Evolution of pore water pressure in Zone C (Case 1 v/s Case 2).	266
Figure 9-14 Evolution of gas (H ₂) pressure in Zone B (Case 1 v/s Case 2).....	267
Figure 9-15 Evolution of gas (H ₂) pressure in Zone C (Case 1 v/s Case 2).....	268
Figure 9-16 Evolution of water saturation in Zone B (Case 1 v/s Case 2).	269
Figure 9-17 Evolution of water saturation in Zone C (Case 1 v/s Case 2).	270
Figure 9-18 Evolution of effective vertical stress in Zone B (Case 1 v/s Case 2).	271
Figure 9-19 Evolution of effective vertical stress in Zone C (Case 1 v/s Case 2).	271
Figure 9-20 Evolution of temperature in Zone B (Case 2 v/s Case 3).	273
Figure 9-21 Evolution of temperature in Zone C (Case 2 v/s Case 3).	274
Figure 9-22 Evolution of pore water pressure in Zone B (Case 2 v/s Case 3).....	275
Figure 9-23 Evolution of pore water pressure in Zone C (Case 2 v/s Case 3).	276
Figure 9-24 Evolution of gas pressure (H ₂) in Zone B (Case 2 v/s Case 3).....	277
Figure 9-25 Evolution of gas pressure (H ₂) in Zone C (Case 2 v/s Case 3).....	277
Figure 9-26 Evolution of water saturation in Zone B (Case 2 v/s Case 3).	278
Figure 9-27 Evolution of water saturation in Zone C (Case 2 v/s Case 3).	278
Figure 9-28 Evolution of effective vertical stress in Zone B (Case 2 v/s Case 3).	279
Figure 9-29 Evolution of effective vertical stress in Zone C (Case 2 v/s Case 3).	279
Figure 9-30 Evolution of pore water pressure in Zone B (THMG v/s HMG-coupling scenario).	281
Figure 9-31 Evolution of pore water pressure in Zone C (THMG v/s HMG-coupling scenario).....	281
Figure 9-32 Evolution of gas pressure in Zone B (THMG v/s HMG-coupling scenarios).....	282
Figure 9-33 Evolution of water saturation in Zone B (THMG v/s HMG coupling scenarios).	283
Figure 9-34 Evolution of gas pressure in Zone C (THMG v/s HMG case).	284
Figure 9-35 Evolution of water saturation in Zone C (THMG v/s HMG case).	285
Figure 9-36 Evolution of effective vertical stress for case 3 and 4 (THMG v/s HMG coupling scenarios).	285
Figure 9-37 Evolution of effective vertical stress in Zone C (THMG v/s HMG case).	286
Figure 9-38 Evolution of temperature in Zone C (THMG v/s THM-coupling scenarios).	287
Figure 9-39 Temperature evolution in Zone C (THMG v/s THM-coupling scenario).	288
Figure 9-40 Evolution of gas pressure in Zone B (THMG v/s THM-coupling scenarios).	289
Figure 9-41 Pore water pressure evolution in Zone C (THMG v/s THM-coupling scenario).	290
Figure 9-42 Evolution of water saturation in Zone B (THMG v/s THM-coupling scenarios).	290
Figure 9-43 Evolution of water saturation in Zone C (THMG v/s THM-coupling scenario).	291
Figure 9-44 Effective vertical stress in Zone B (THMG v/s THM-coupling scenarios).	291
Figure 9-45 Effective vertical stress in Zone C (THMG v/s THM-coupling scenario).....	292
Figure 10-1: Example for zone B of reduction of differences between two models after discussions between ULiège and SCK CEN modelling teams; initial differences were mainly linked to different compressibility formulations	302
Figure 11-1: schematic representation of the main elements driving the storyboard at repository scale	308
Figure 11-2: Generic repository: schematic representation at main repository depth	309
Figure -12-1 Schematic vertical slice of the generic repository.....	316

Figure 12-2 - Schematic horizontal slice at generic repository depth	316
Figure 12-3 - Schematic vertical slice of a gallery	317
Figure 12-4 - Schematic representation of deposition tunnel in disposal zone A	317
Figure 12-5 - Schematic representation of a deposition tunnel in disposal zone B	318
Figure 12-6 - Schematic representation of a deposition tunnel in disposal zone C	318
Figure 12-7 - Schematic representation of a connection gallery seal	319
Figure 12-8 - Schematic representation of the shaft seal	319
Figure 12-9 - Schematic vertical slice of the generic repository with boundary and initial conditions	320
Figure 12-10 - Thermal source term per meter of canister/overpack.....	321
Figure 12-11 - Schematic representation of the gas source terms emplacements in the repository ..	323
Figure 12-12 - Schematic horizontal slice at repository depth positioning the 47 points (purple circles) for output values	331
Figure 12-13 - Schematic horizontal slice at repository depth positioning the 33 surfaces (purple segments) for output values	332

List of Tables

Table 2-1 Parameters values for gas component to calculate mixture viscosity (White 2006).....	31
Table 2-2 Common material properties for the whole modelled domain.....	45
Table 2-3 Material specific model properties (EURAD: Milestone 61 2021).....	45
Table 4-1 Material and fluid parameters used for the TH2M simulation. Parameters which are not directly taken from the specification in the generic repository exercise are marked in grey.	101
Table 4-2: Parameters for the thermal source term equation based on radioactive decay	104
Table 6-1 Materials parameters values. Parameters who differ from Milestone 61 are highlighted in grey	142
Table 6-2 fluid properties.....	143
Table 6-3: linear liquid thermal dilatation αl	143
Table 6-4: 3D Mesh repartition	146
Table 6-5: Mesh repartition.....	147
Table 6-6: ULiège parameters used for capillary pressure (case 5)	168
Table 6-7: ULiège parameters used for relative permeabilities (case 5).....	168
Table 6-8: mechanical parameters for reference case and case 6	173
Table 6-9: cases for sensitive analysis in 2D.	177
Table 7-1 – Parameters used in modelling diffusive flux of dissolved gas.....	182
Table 7-2 – Parameters used in modelling diffusive flux of dissolved He and CH ₄	183
Table 7-3 – Time dependent heat flux specified in deposition tunnel model	188
Table 7-4 – Observation points for the analysis.	189
Table 7-5 – Parameters considered in nonisothermal analysis.	195
Table 8-1 Material properties.....	207
Table 8-2: time varying conditions considered in the simulation	209
Table 8-3: the step-by-step scheme	212
Table 8-4: Material properties used in the 2D PS THG model (the reference case)	231
Table 8-5: mechanical parameters used in the THMG model.....	235
Table 8-6: Material properties used in the 2D-PS THMG model (the final case).....	238
Table 9-1 Features of time-varying boundary conditions (Note: σ_v ; σ_h is vertical or horizontal stresses, p_w is pore water pressure, T_z is temperature along the depth, RH is relative humidity, and s_t is total suction).	257
Table 9-2 Application of specified SWRC formulation in Zone B.	260
Table 9-3 Case1 and case 2 for investigating the effect of SWRC formulation.	261
Table 9-4 Parameters for an idealized classical van Genuchten SWRC.	261
Table 9-5 Case 2 and case 3 for investigating the effect of geometry.	272
Table 9-6 Case 3 and case 4 for investigating the effect of temperature.	280
Table 9-7 Case 3 and case 5 for investigating the effect of gas pressure on simulation results.	286
Table 12-1 – Parameters values	325

1. Introduction

Task 4 of EURAD-GAS work-package established in the framework of EURAD European joint programme aims at fulfilling the evaluation of gas transport regimes that can be active at the scale of a geological disposal system and their potential impact on repository performance. It is dedicated in particular to end-users questions concerning:

- the effects of the presence of gas and its transport on the transfer of soluble and volatile radionuclides;
- the consequences of gas-induced hydro-mechanical perturbations on barrier integrity and long-term performance.

Task 4 is mainly end-users oriented. Based on the input from tasks 2 and 3 of EURAD-GAS work-package and relevant input from other WPs in the EURAD project, the objective of subtask 4.1 is to assemble phenomenological descriptions of gas transport and its likely consequences on barrier integrity and radionuclide transfer at repository relevant scales, in the form of storyboards. These storyboards were established by the end-users involved in the sub-task 4.1 at an early stage of the project and published in a report associated to the milestone MS60 of EURAD-GAS. Storyboards are also resumed in the 1st state-of-the-art of the WP (Levasseur et al. 2021) and are therefore not included in this report.

This conceptualization phase has been completed by the definition of (i) a “generic repository” configuration and sets of properties and conditions on which sub-task 4.2 has tested various evaluation approaches and (ii) a proposal for a set of indicators, covering the range of needs of various end-users in Europe for clay-based host rock repository, representative of the processes to be evaluated (transfer of radionuclides, volatile and soluble, barrier integrity for instance). All these elements are described in a report associated to the milestone MS61 of EURAD-GAS and reported in Annex (chapter 12).

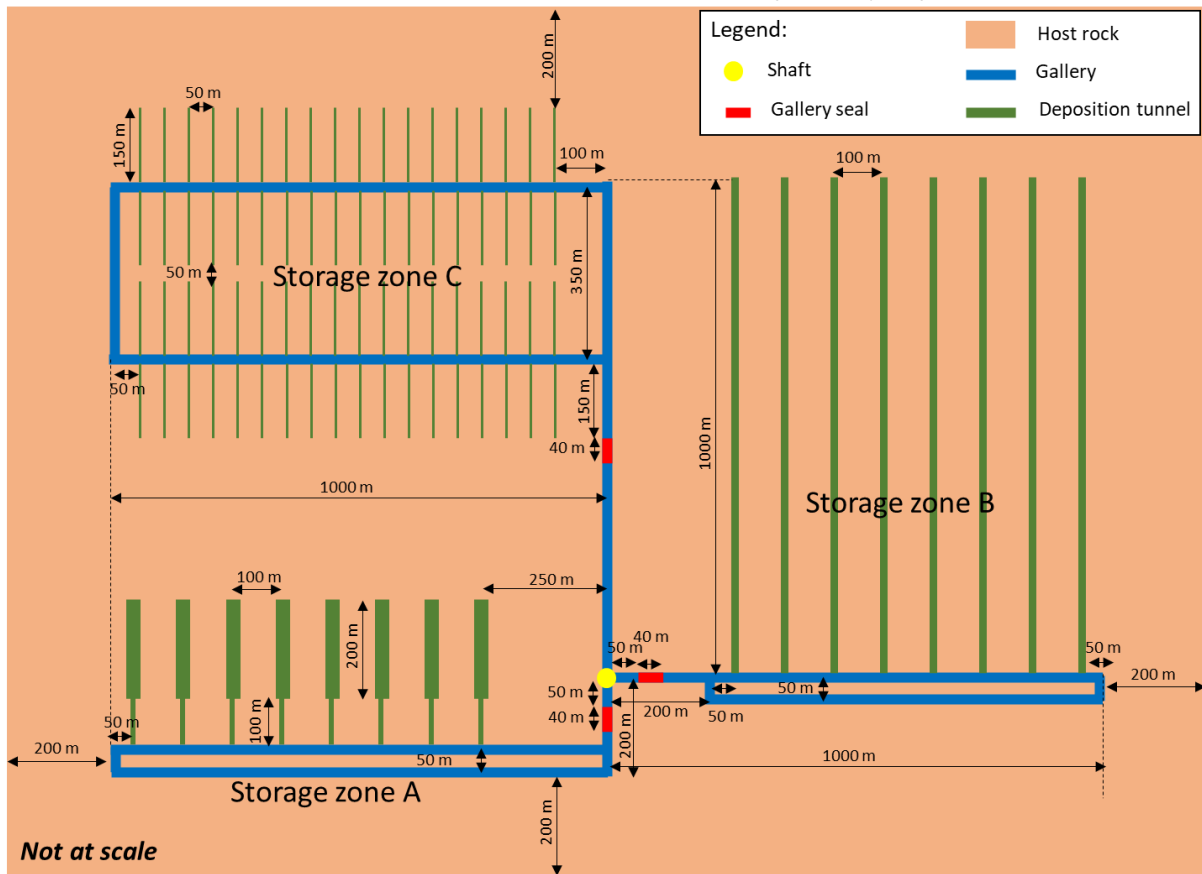


Figure 1-1 Schematic horizontal slice of the generic repository at repository depth¹

Figure 1-1 represents a global sketch of this generic repository layout. The “generic repository” includes, in part, highly simplified and generic elements of disposal concepts from several European countries for a repository in clay host rock. However, in order to ease the meshing and to reduce the calculation time, geometrical representations have been simplified compared to the original complexity of these concepts. Following the same idea, the processes and associated parameters are (i) representative of the global comprehension of the hydraulic-gas transient (in orders of magnitude for the parameters values) but (ii) somehow generic to have the same values in all the “generic repository” although specific national concept are built on specific material and host rock.

The resulting conceptualisations of gas transport and of its possible consequences for typical repository configurations in clayey host rocks has been passed on to subtask 4.2, which has developed different approaches and tools (e.g. numerical modelling) that can be used for evaluating the effect of gas on repository performance.

More precisely, sub-task 4.2 has assessed different approaches, building on the storyboards, the definition of the “generic repository” and sets of properties and conditions, indicators and scenarios proposed in subtask 4.1, to numerically describe disposal system behaviour in response to gas accumulation and pressure build-up. These assessments have compared:

¹ In some figures, the word “storage” is mistakenly used instead of “disposal”. According to the IAEA Nuclear Safety and Security Glossary (2022), “the term disposal implies that retrieval is not intended and would require deliberate action to regain access to the waste; it does not mean that retrieval is not possible”.

- the use of coupled high-resolution models taking into account the full complexity at repository scale of gas related process understanding towards total system performance;
- the application of traceable, component-based model upscaling techniques, i.e. establishing detailed models of components, accounting for the complexity of the mechanistic understanding embodied in the process level models, then simplifying the representation of the components in the total system performance models.

To assess the relevancy of these different levels of complexity, several modelling teams (Aalto University, Andra, BGR, IRSN, EDF, LEI, SCK CEN, U Liège) have applied various numerical approaches to the “generic repository” configuration with different sets of properties and conditions.

The main objective of subtask 4.2 is not to perform a formal performance assessment or a code benchmarking exercise, but to highlight the inherent strengths and limitations of each approach and assessing its suitability in different contexts depending on which system is being evaluated (host rock/design) or what is the quality of available data/what is the magnitude of uncertainties. The analysis of the results of numerical evaluations will focus on gas-oriented indicators, developed in cooperation with subtask 4.1, related to volatile and soluble radionuclides transfer and barrier integrity, which are of direct relevance to performance assessment.

This final report is the compilation of the work done in task 4.2 during the EURAD-GAS project. Each team has not done the same amount of work and thus, depending on the team, available results are not at the same level of representation and or coupling.

After presentation of the work done by each of the involved teams (chapters 2 to 9), Chapter 10 offers a global discussion on all of these results trying to determine common elements favouring good practices for a phenomenologically representative evaluation of maximum gas pressures in a repository and their possible impacts on the host rock integrity and/or radionuclide transfers. Last chapter (chapter 11) provides a synthesis for end-users of EURAD-GAS task 4, building on the work done inside task 4.1, and task 4.2, including chapter 10.

2. Contribution of Aalto University

2.1 Introduction

The present study is a part of the European Joint Program on Radioactive Waste Management (EURAD): WP6 Gas that focuses on the Engineered Barrier System (EBS), where corrosion of metal structures (canisters or steel liner) under anaerobic conditions can generate hydrogen gas. The gas accumulation can adversely affect the integrity of an Engineered Barrier System (EBS). EURAD sub-task 4.2 is defined to examine the hydrogen gas transport at the scale of a conceptual geological disposal system and its potential impact on repository performance.

To ensure successful gas modelling in a thermally active waste repository, we developed a novel numerical framework that accounts for a mixture of three gases: 2 inert incondensable gases and vapour. The framework is an extension of a Thermo-hydro-mechanical (THM) coupled finite element code Thebes (Abed and Sołowski 2017, 2018). The present work modifies Thebe's classical 3 components (air, water and soil) and 3 phase (gas, liquid and solid) system by adding an additional gas component. Moreover, the enhancements incorporate EURAD (EURAD: Milestone 61 2021) specifications for water retention and gaseous advective and diffusive flow behaviour and gas mixing laws. Note, although the latest developments in Thebes address any 2 inert, incondensable gases along with vapours (implicitly), the present work shows the derivation of the governing equation considering hydrogen (gas-1) and air (gas-2). This is to remain consistent with the ultimate aim of simulating hydrogen gas, entrapped air and vapour in the nuclear waste repository.

The verification of the new Thebes framework employs a series of simplified 2D (1x1 m² geometry) test case simulations in Thebes and COMSOL (V6.1). These trial cases focus on individual gas flow mechanisms, type of loading condition or gas mixture composition. Additionally, the scientific collaboration between Aalto and SCK CEN through the EURAD mobility program, further aids in partially validating the Thebes framework. During the research visit, Thebes reproduce a multi-gas dissolve diffusion experiment (methane and helium) on Boom Clay by Jacobs et al. (2017). Gupta et al. (2023) present some of these verification tests and dissolve diffusion experiment replication. Finally, Thebes simulates an advanced verification test that accounts for methane, carbon dioxide and vapours in landfill refuse subjected to heat and constant water infiltration. Due to space constraints, the report only consists of a summary of these verification tests and some results (See section 3).

The report, however, details an investigation of a hydrogen gas flow along with entrapped air and vapour in the 2D section of a deposition tunnel containing high-level waste (HLW) from Zone B. The analysis considers thermal, hydraulic and gas (THG) coupled repository conditions. The results estimate total gas, hydrogen, entrapped air, vapour and water flow and pressures for 1 000 years of the repository time. Further, it shows the influence of coupled mechanisms on the gas flow and overall repository behaviour.

2.2 Thebes numerical framework

The FEM code Thebes, traditionally a three-component system: a) air, b) soil (including salts), and c) water in 3 phases (gas, liquid and solids), is capable of modelling unsaturated soil in thermal-hydraulic and mechanical conditions (Abed and Sołowski 2017, 2018). An extension to the code to include hydrogen gas (see Figure 2-1) requires defining new physical relations, heat and mass conservation equations. The following section mainly discusses the influence of the hydrogen gas component in a numerical framework of Thebes. More elaborated information on other component derivations is available from Abed and Sołowski (2017).

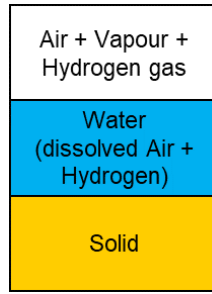


Figure 2-1 Idealization of soil matrix with phases and components.

2.2.1 Mass conservation of components

The soil component's mass balance derivation in Thebes follows a compositional method (Panday and Corapcioglu 1989). Equation (1) illustrates a general form of the mass balance expression for any component in phase i .

$$\underbrace{\frac{\partial(\phi^i \rho^i \omega_k^i)}{\partial t}}_{\text{storage}} + \underbrace{\nabla \cdot (\phi^i \rho^i \omega_k^i \mathbf{v}^i)}_{\text{advection}} + \underbrace{\nabla \cdot \mathbf{j}_k^i}_{\text{non-advection}} = \underbrace{Q_k^i}_{\text{source}} \quad 1$$

, where symbol: ϕ^i is the volume fraction, ρ^i is the density, ω_k^i is the mass fraction of component k , \mathbf{v}^i is the velocity vector, \mathbf{j}_k^i is the non-advective flux vector of component k . The diffusive flux follows a fundamental principle. Lastly, Q_k^i is the source/sink term of component k and in the absence of any external sink term follows the rule $\sum Q_k^i = 0$ (i : solid, liquid, gas and k : soil, water, air, hydrogen) .

2.2.2 Mass conservation of solids

According to Eq. (1), the mass conservation of solid leads to Eq. (2) for the rate of change in porosity (Abed and Sołowski 2017). The expression signifies the dependency of porosity on volumetric deformation and bulk material expansion while ignoring the contribution of solid grain compression.

$$\frac{\partial n}{\partial t} = (1 - n) \left(\frac{\partial \varepsilon_v}{\partial t} - \beta_{st} \frac{\partial T}{\partial t} \right) \quad 2$$

, where n is the soil porosity, ε_v is the volumetric strain and β_{st} is the coefficient for thermal expansion of solids.

2.2.3 Mass conservation of water

The mass balance of the water component in Thebes is hydraulic and total gas pressure-dependent (Eq. 3). Therefore, the expression remains unchanged (Abed and Sołowski 2017), accounting for hydrogen gas implicitly through total gas pressure head hg .

$$\begin{aligned}
& [n(\rho_w^l - \rho_w^g) \frac{\partial S^l}{\partial T} - (1-n)(S^l \rho_w^l + S^g \rho_w^g) \beta_{sT} - nS^l \beta_{wT} \rho_w^l + nS^g \frac{\rho_w^g}{T^2} (4974 + g \frac{M_w \psi}{R})] \frac{\partial T}{\partial t} \\
& + [nS^l \beta_{wp} g \rho_w^{l^2} + nS^g \frac{\rho_w^g g M_w}{RT} - n(\rho_w^l - \rho_w^g) \frac{\partial S^l}{\partial \psi}] \frac{\partial h_w}{\partial t} + [n(\rho_w^l - \rho_w^g) \frac{\partial S^l}{\partial \psi} - nS^g \frac{\rho_w^g g M_w}{RT}] \frac{\partial h_g}{\partial t} \\
& + (S^l \rho_w^l + S^g \rho_w^g) \frac{\partial \mathcal{E}_v}{\partial t} + \nabla \cdot (\rho_w^l q^l) + \nabla \cdot (\rho_w^g q^g) + \nabla \cdot j_w^g = 0
\end{aligned} \tag{3}$$

, where ρ_w^l and ρ_w^g is the water and vapour density. S^l and S^g are the degree of saturation for liquid and gas, respectively. β_{sT} and β_{wT} are the coefficients of thermal expansion in solids and water respectively. β_{wp} is the coefficient of water compressibility, T is the temperature, M_w is the molar mass of vapour and R is the universal gas constant. q^l and q^g are the water and vapour fluxes respectively. h_w and h_g are the water head and total gas pressure head, respectively. ψ is the matric suction head and j_w^g represents vapour diffusion.

The water retention governing equation follows EURAD specification (EURAD: Milestone 61 2021).

$$\begin{aligned}
P_c = & \frac{1}{\alpha} \left((S_e^* S_e)^{\frac{-1}{m}} - 1 \right)^{\frac{1}{n}}, \text{ if } S_e \leq 1 - \varepsilon \\
& \frac{1}{\alpha} \left((S_e^* S_e)^{\frac{-1}{m}} - 1 \right)^{\frac{1}{n}} \cdot \frac{(1 - S_e)}{\varepsilon}, \text{ if } 1 - \varepsilon < S_e < 1 \\
& 0, \text{ if } S_e = 1
\end{aligned} \tag{4}$$

, where $S_e = \frac{S - S_{res}}{S_{sat} - S_{res}}$ and P_c is a capillary or matric suction pressure. $Se^* = ((1 + (\alpha p_e)^n)^{-m}$, where

P_e is a gas entry pressure. Notice the above expression is isothermal therefore the $\frac{\partial S^l}{\partial T}$ associated terms are neglected in eq.3.

In Thebes, both the liquid density (Eq. 5, Diersch and Kolditz 2002) and vapour density (Eq. 6, Rutqvist et al. 2001) is temperature dependent function. Additionally, the vapour density is dependent on relative humidity (Rutqvist et al. 2001) through Eq. (7).

$$\rho_w^l = \rho_{w0}^l e^{\beta_{wp}(\rho_w - \rho_{w0}) - \beta_{wT}(T - T_0)} \tag{5}$$

, where ρ_{w0}^l is the water density and reference state water density, respectively. β_{wp} and β_{wT} are the coefficient of water compressibility and thermal expansion, respectively.

$$\rho_{w0}^g = 10^{-3} e^{19.891 - \frac{4974.0}{T}} \tag{6}$$

where ρ_{w0}^g is the saturated vapour density.

$$\rho_w^g = RH \rho_{w0}^g, \text{ } RH = e^{\frac{-g M_w \psi}{RT}} \tag{7}$$

, where RH is the relative humidity which is a suction (ψ) and temperature (T) dependent expression.

Further, the rate of change of water density (Eq. 8) and vapour density (Eq.9), respectively, are (Abed and Sołowski 2017):

$$\frac{\partial \rho_w^l}{\partial t} = -\beta_{wT} \rho_w^l \frac{\partial T}{\partial t} + \beta_{wp} g \rho_w^l \frac{\partial h_w}{\partial t} \quad 8$$

$$\frac{\partial \rho_w^g}{\partial t} = \frac{\rho_w^g}{T^2} (4974.0 + \frac{gM_w \psi}{R}) \frac{\partial T}{\partial t} + \frac{\rho_w^g g M_w}{RT} (\frac{\partial h_w}{\partial t} - \frac{\partial h_g}{\partial t}) \quad 9$$

Thebes uses (Philip and Vries 1957) expression for the vapour diffusion (j_w^g), Eq. (10).

$$j_w^g = -D_{vw} \nabla h_w + D_{vw} \nabla h_g - D_{vt} \nabla T \quad 10$$

The symbol D_{vw} and D_{vt} represents the diffusion coefficient due to suction variation and temperature variation, respectively. These coefficients are a function of the effective diffusion coefficient $D_{g(vapour)}^g$, which is the product of Millington's quirk correction factor (EURAD: Milestone 61 2021) and effective binary molecular diffusion coefficients as per gas mixing law (Bird et al. 1960).

Next, the bulk fluid flow is governed by Darcy's law (Darcy 1856), Eq. (11):

$$q^i = -K_i (\nabla h_i + 1) \quad 11$$

, where i is the gas or liquid phase, h_i represents the total pressure head and K_i is the hydraulic conductivity that is dependent on degree of saturation (Eq. 12) and fluid (gas and water) viscosity.

$$K_i = K_{ri} K_{i_sat} \quad 12$$

$$K_{rw} = \sqrt{Se} \cdot \left[\frac{1 - (1 - (S_e^* S_e)^{1/m})^m}{1 - (1 - S_e^{*1/m})^m} \right]^2, \quad (1 \text{ if } S_e = 1)$$

$$K_{rg} = f_g \sqrt{1 - Se} \cdot \left[\frac{(1 - S_e^{*1/m})^m - (1 - (S_e^* S_e)^{1/m})^m}{(1 - S_e^{*1/m})^m - 1} \right]^2, \quad (0 \text{ if } S_e = 1)$$

, where K_{i_sat} is the saturated hydraulic conductivity of the phase and K_{ri} is saturation-dependent relative permeability. K_{rw} and K_{rg} are relative permeability of water and gas phase.

The new framework also utilises a temperature-dependent expression of individual component viscosity (Sutherland 1893), Eq. 13) in Eq. (14) to evaluate total gas mixture viscosity (Herning and Zipperer 1936). Table 2-1 shows the reference values for air, vapour, and hydrogen.

$$\frac{\mu}{\mu_0} = \left(\frac{T}{T_0} \right)^{3/2} \frac{T_0 + S_\mu}{T + S_\mu} \quad 13$$

, where μ_0 and T_0 is the reference viscosity of the gas and temperature, S_μ is the Sutherland's constant.

Table 2-1 Parameters values for gas component to calculate mixture viscosity (White 2006).

Gas	μ_0 (Pa.s)	T_0 (K)	S_μ (K)
Air	1.716·10 ⁻⁵	273	111
Vapour	0.0000112	350	1064
Hydrogen	8.411e-6	273	97

$$\mu^g = \frac{\sum_{i=1}^N x_i \mu_i \sqrt{M_i}}{\sum_{i=1}^N x_i \sqrt{M_i}} \quad 14$$

, where for gas component the symbols x_i , μ_i and M_i represents the molar fraction, viscosity, and molar mass, respectively.

2.2.4 Mass conservation of Hydrogen

The hydrogen gas is present only in gas and liquid phases implying that the expression for hydrogen mass balance (Eq. 15) is the sum of gas and liquid phase storage, advection, and diffusion terms.

$$\frac{\partial(\phi^l \rho^l \omega_H^l)}{\partial t} + \nabla \cdot (\phi^l \rho^l \omega_H^l \mathbf{v}^l) + \nabla \cdot \mathbf{J}_H^l + \frac{\partial(\phi^g \rho^g \omega_H^g)}{\partial t} + \nabla \cdot (\phi^g \rho^g \omega_H^g \mathbf{v}^g) + \nabla \cdot \mathbf{J}_H^g = 0 \quad 15$$

, where subscript H represents the hydrogen component, ρ^l and ρ^g is the density of liquid and gas, respectively. ω_H^l and ω_H^g is the mass fraction of hydrogen in liquid and gas, respectively. \mathbf{v} is a velocity vector of gas component.

Expanding the storage terms of both liquid and gas phases gives:

$$\begin{aligned} \phi^l \rho^l \omega_H^l &= n H_H S^l \rho^l \left(\frac{\rho_H^l}{\rho^l} \right) = n H_H S^l \rho_H^l \\ \phi^g \rho^g \omega_H^g &= n S^g \rho_H^g \end{aligned} \quad 16$$

Where n is the porosity H_H is Henry's volumetric coefficient of solubility for hydrogen (Abed and Sołowski 2017).

Further, Eq. (17) shows the formula for the velocity vector for both the liquid and gas phases. The expression also accounts for slow solid matrix movement (\mathbf{v}^s) and its relationship with infinitesimal volumetric strain ε_v (Abed and Sołowski 2017).

$$v^l = \frac{q^l}{nS^l} + v^s \quad (\text{where } \nabla \cdot v^s = \frac{\partial \varepsilon_v}{\partial t}) \quad 17$$

$$v^g = \frac{q^g}{nS^g} + v^s$$

Further, diffusion of hydrogen gas for i th phase (gas or liquid) is according to Fick's Law of diffusion (Fick 1855):

$$J_H^i = D_{e-H}^i \nabla C_H^i \quad 18$$

, where C_H^i is the hydrogen gas concentration and D_{e-H}^i is the effective diffusion of hydrogen after Millington's quirk tortuosity factor (EURAD: Milestone 61 2021). In case of gas phase diffusion, similar to vapour, the effective diffusion coefficient additionally depends on molar fraction and mass as per Bird et al. (1960).

The dissolved hydrogen concentration is derived using the ideal gas law and Henry's solubility coefficient H_{c-H} (EURAD: Milestone 61 2021), Eq. 19) as per Eq. (20). The expression is only valid when the concentrations of dissolved hydrogen gas and the air remains negligible to that of water.

$$H_{c-H} = \frac{x_H}{P_H} \quad 19$$

, where x is a molar fraction, x_H is a molar fraction of dissolved hydrogen in water and P_H is a partial hydrogen gas pressure.

$$n_H^l = x_H \cdot n_w^l \quad 20$$

, where n_H, n_w is number of hydrogen moles and water moles, respectively.

Using Eq. (19) in Eq. (20), we have:

$$n_H^l = P_H H_{c-H} n_w^l \quad 21$$

Now number of moles of water as per ideal gas law can be calculated as:

$$n_w^l = \frac{\rho_w^l}{M_w} nS^l \quad 22$$

, where n is porosity

Subsequently, Eq. (21) can be written as:

$$n_H^l = (\rho_w^l g h_H) H_{c-H} \left(\frac{\rho_w^l}{M_w} nS^l \right) \quad 23$$

Where Hydrogen gas head h_H is normalized against water density.

Finally, by converting molar concentration (see Eq. 23) to mass concentration and substituting in Eq. (18), diffusive dissolved hydrogen mass flux is:

$$J_H^l = D_{e-H}^l \frac{M_H \rho_w^2 g n S^l H_{c-H}}{M_w} \nabla h_H \quad 24$$

Similarly, for the hydrogen flux in gas phase (J_H^g) we derive the mass concentration (m_H^g) based on ideal gas law as follows:

$$m_H^g = \frac{P_H n S^g}{RT} \quad (\text{where, } P_H = \rho_w^l g h_H) \quad 25$$

Therefore, the mass flux of hydrogen gas in the gas phase (J_H^g) is:

$$J_H^g = D_{e-H}^g \frac{M_H \rho_w^l g n S^g}{RT} \nabla h_H \quad 26$$

Next, the expansion of storage terms in Eq.(14), requires the differential of volumetric solubility coefficient H_H ((J Vaunat, C jommi 1997), Eq. 27), degree of saturation S^l ((Abed and Sołowski 2017), Eq.28) and hydrogen gas density ρ_H (Eq. 29).

$$H_H = H_{c-H} \rho_w^l \frac{RT}{M_w} \quad 27$$

$$\begin{aligned} \frac{\partial H_H}{\partial t} &= \frac{\partial H_H}{\partial \rho_w^l} \frac{\partial \rho_w^l}{\partial P_w} \frac{\partial P_w}{\partial h_w} \frac{\partial h_w}{\partial t} + \frac{\partial H_H}{\partial T} \frac{\partial T}{\partial t} \\ \frac{\partial H_H}{\partial t} &= g \rho_w^l \beta_{wp} H_H \frac{\partial h_w}{\partial t} + \left(\frac{1}{T} - \beta_{wT} \right) H_H \frac{\partial T}{\partial t} \end{aligned}$$

$$\begin{aligned} \frac{\partial S^l}{\partial t} &= \frac{\partial S^l}{\partial \psi} \frac{\partial \psi}{\partial h_g} \frac{\partial h_g}{\partial t} + \frac{\partial S^l}{\partial \psi} \frac{\partial \psi}{\partial h_w} \frac{\partial h_w}{\partial t} \\ &= \frac{\partial S^l}{\partial \psi} \left(\frac{\partial h_g}{\partial t} - \frac{\partial h_w}{\partial t} \right) \end{aligned} \quad 28$$

, where $\psi = h_g - h_w$ and $h_g = h_{vapour} + h_{hydrogen} + h_{air}$

According to the ideal gas law, the hydrogen density expression in both liquid and gas is:

$$\rho_H = \frac{P_H M_H}{RT} = \frac{\rho_w^l g h_H M_H}{RT} \quad 29$$

Note in the above expression, hydrogen gas pressure head (h_H) refers to an equivalent water pressure head. It further implies that the hydrogen density variation in time (see Eq. 30) is a function of water density, temperature, and hydrogen head h_H .

$$\frac{\partial \rho_H}{\partial t} = \frac{\partial \rho_H}{\partial \rho_w'} \frac{\partial \rho_w'}{\partial t} + \frac{\partial \rho_H}{\partial T} \frac{\partial T}{\partial t} + \frac{\partial \rho_H}{\partial h_H} \frac{\partial h_H}{\partial t} \quad 30$$

Expanding the above equation and utilizing the rate of water density change expression (see Eq. 8) gives the following formula:

$$\frac{\partial \rho_H}{\partial t} = -(\beta_{wT} \rho_H + \frac{\rho_H}{T}) \frac{\partial T}{\partial t} + \beta_{wp} g \rho_w' \rho_H \frac{\partial h_w}{\partial t} + \frac{\rho_w' g M_H}{RT} \frac{\partial h_H}{\partial t} \quad 31$$

By substituting expressions for rate of change in porosity (Eq. 2), velocity vector (Eq.17), diffusion expression (Eq. 24 and 26), rate of volumetric solubility coefficient (Eq.27), rate of change in saturation (Eq.28) and rate of hydrogen density change (Eq.31) in Eq. (15), the full formulation of hydrogen mass balance is as follows:

$$\begin{aligned} & \left[(1-n)\beta_{sT} \rho_H H_H S^l + (1-n)\beta_{sT} \rho_H S^s - \beta_{wT} \rho_H (2nH_H S^l + nS^s) - nS^s \frac{\rho_H}{T} \right] \frac{\partial T}{\partial t} \\ & + \left[nS^l \rho_H \frac{\partial H_H}{\partial h_w} + (1-H_H)n\rho_H \frac{\partial S^l}{\partial \psi} + n(H_H S^l + S^s)\beta_{wp} g \rho_w' \rho_H \right] \frac{\partial h_w}{\partial t} \\ & + \left[n\rho_H (H_H - 1) \frac{\partial S^l}{\partial \psi} \right] \frac{\partial h_g}{\partial t} + \left[n(H_H S^l + S^s) \frac{\rho_w' g M_H}{RT} \right] \frac{\partial h_H}{\partial t} \\ & + \nabla \cdot (H_H \rho_H q^l) + \nabla \cdot (\rho_H q^s) + \nabla \cdot \left(D_{e-H}^l \frac{M_H \rho_w^2 g n S^l H_{c-H}}{M_w} \nabla h_H \right) + \nabla \cdot \left(D_{e-H}^s \frac{M_H \rho_w g n (1-S^l)}{RT} \nabla h_H \right) \\ & + \rho_H (S^l H_H + S^s) \frac{\partial \varepsilon_v}{\partial t} = 0 \end{aligned} \quad 32$$

2.2.5 Mass conservation of air

The expression for the mass balance of air (Eq. 33) is extended in Thebes by updating the definition of diffusive flux and air density, to incorporate the influence of the hydrogen component.

$$\frac{\partial(\phi^l \rho^l \omega_a^l)}{\partial t} + \nabla \cdot (\phi^l \rho^l \omega_a^l v^l) + \nabla \cdot J_a^l + \frac{\partial(\phi^s \rho^s \omega_a^s)}{\partial t} + \nabla \cdot (\phi^s \rho^s \omega_a^s v^s) + \nabla \cdot J_a^s = 0 \quad 33$$

, where the subscript "a" symbolizes the air component.

Thebes, assumes air as a dilute solute in the water. Therefore, the diffusion expression (J_a^l) below, is similar to that of the hydrogen component.

$$J_a^l = D_{e-a}^l \frac{M_a \rho_w^2 g n S^l H_{c-a}}{M_w} \nabla h_a \quad 34$$

, where D_{e-a}^l is the effective air dissolve diffusion coefficient that includes Millington's quirk tortuosity factor (EURAD: Milestone 61 2021). M_a is a molar mass of air and H_{c-a} is Henry's solubility coefficient for air.

Whereas, the air diffusion in the gas phase (J_a^g) is in eq.(35). Here, the effective air diffusion coefficient (D_{e-a}^g) is as per the mixing law that depends on the molar fraction (Bird et al. 1960) and Millington's quirk tortuosity factor (EURAD: Milestone 61 2021).

$$J_a^g = D_{e-a}^g \frac{M_a \rho_w^l g n S^g}{RT} \nabla h_a \quad 35$$

Furthermore, Thebes accounts for air density implicitly by considering ideal gas laws and evaluating air partial pressure from total gas pressure. Equation (36) shows the extension work by employing the contribution of partial pressure of hydrogen gas in air density evaluation.

$$P_g = P_H + P_V + P_a \quad (\text{where, } P_V = \frac{\rho_w^g RT}{M_w}, P_g = \rho_w^l g h_g, P_H = \rho_w^l g h_H) \quad 36$$

$$\Rightarrow P_a = P_g - (P_H + P_V)$$

Now,

$$\rho_a^g = \frac{M_a P_a}{RT}$$

$$\rho_a^g = \frac{M_a (\rho_w^l g h_g - \rho_w^l g h_H - \frac{\rho_w^g RT}{M_w})}{RT}$$

$$\rho_a^g = \frac{M_a \rho_w^l g (h_g - h_H)}{RT} - \frac{M_a \rho_w^g}{M_w}$$

Subsequently, Eq. (37) shows the formula for rate of change in air density as a function of total gas pressure head (h_g), hydrogen pressure head (h_H) and temperature (T).

$$\frac{\partial \rho_a^g}{\partial t} = \frac{\partial \rho_a^g}{\partial h_g} \frac{\partial h_g}{\partial t} + \frac{\partial \rho_a^g}{\partial h_H} \frac{\partial h_H}{\partial t} + \frac{\partial \rho_a^g}{\partial \rho_w^g} \frac{\partial \rho_w^g}{\partial t} \quad 37$$

$$\frac{\partial \rho_a^g}{\partial t} = \frac{M_a \rho_w^l g}{RT} \left(\frac{\partial h_g}{\partial t} - \frac{\partial h_H}{\partial t} \right) - \frac{M_a}{M_w} \left[\frac{\rho_w^g}{T^2} \left(4974.0 + \frac{g M_w \psi}{R} \right) \right] \frac{\partial T}{\partial t} - \frac{M_a}{M_w} \left[\frac{\rho_w^g g M_w}{RT} \left(\frac{\partial h_w}{\partial t} - \frac{\partial h_g}{\partial t} \right) \right]$$

$$\frac{\partial \rho_a^g}{\partial t} = \left(\frac{M_a \rho_w^l g}{RT} + \frac{M_a \rho_w^g g M_w}{RT} \right) \frac{\partial h_g}{\partial t} - \frac{M_a \rho_w^g g M_w}{M_w RT} \frac{\partial h_H}{\partial t} - \frac{M_a \rho_w^g}{M_w T^2} \left(4974.0 + \frac{g M_w \psi}{R} \right) \frac{\partial T}{\partial t} \dots$$

$$\dots - \frac{M_a \rho_w^l g}{RT} \frac{\partial h_H}{\partial t}$$

According to Eq. (34), (35) and (37), the Eq. (38) shows the full and updated formulation of the air mass balance extending on (Abed and Sołowski 2017).

$$\begin{aligned}
& \left[n\rho_a[H-1]\frac{\partial S^l}{\partial T} + n\rho_a S^l \frac{\partial H}{\partial T} - (1-n)\rho_a[S^s + H_H S^l]\beta_{st} \right] \frac{\partial T}{\partial t} \\
& - \left[n[S^s + H_H S^l] \frac{M_a \rho_w^g}{M_w T^2} \left(4974 + \frac{gM_w \psi}{R} \right) \right] \frac{\partial T}{\partial t} \\
& - \left[n[S^s + H_H S^l] \frac{M_a \rho_w^g g M_w}{M_w RT} + n\rho_a[H-1] \frac{\partial S^l}{\partial \psi} - n\rho_a S^l \frac{\partial H}{\partial h_w} \right] \frac{\partial h_w}{\partial t} \\
& + \left[n[S^s + H_H S^l] \left(\frac{M_a \rho_w^l g}{RT} + \frac{M_a \rho_w^g g M_w}{M_w RT} \right) + n\rho_a[H-1] \frac{\partial S^l}{\partial \psi} \right] \frac{\partial h_g}{\partial t} - \left[n[S^s + H_H S^l] \frac{M_a \rho_w^l g}{RT} \right] \frac{\partial h_H}{\partial t} \\
& + \nabla \cdot (H_H \rho_H q^l) + \nabla \cdot (\rho_H q^s) + \nabla \cdot J_a^l + \nabla \cdot J_a^g + \rho_H (S^l H_H + S^s) \frac{\partial \varepsilon_v}{\partial t} = 0
\end{aligned} \tag{38}$$

2.2.6 Heat conservation

The general enthalpy balance equation is given by ((Abed and Sołowski 2017):

$$\underbrace{\frac{\partial \Phi_h}{\partial t}}_{\text{heat storage}} + \underbrace{L Q_w^g}_{\text{Latent heat of vaporization}} + \underbrace{\nabla \cdot q_h}_{\text{heat from conduction/convection}} = 0 \tag{39}$$

, where Φ_h is the soil heat capacity, L is the latent heat of vaporization, Q_w^g is the rate of vapour production and q_h is the heat flux from conduction and convection.

The current implementation of heat conservation integrates the contribution of hydrogen gas by changing the storage term and heat flow term. However, the vapour production formulation (see Eq. 40) remains unchanged from the previous version of Thebes ((Abed and Sołowski 2017).

$$Q_w^g = -(1-n)S^s \rho_w^g \beta_{st} \frac{\partial T}{\partial t} + S^s \rho_w^g \frac{\partial \varepsilon_v}{\partial t} - n\rho_w^g \frac{\partial S^l}{\partial t} + nS^s \frac{\partial \rho_w^g}{\partial t} + \nabla \cdot (\rho_w^g q^s) + \nabla \cdot j_w^g \tag{40}$$

Addressing the formulation of the storage term, Eq. (41) shows the general form of heat capacity, where the symbol E_{Tk}^i represents the thermodynamic state function (Diersch and Kolditz 2002) for the internal energy of component k in phase i .

$$\Phi_h = \phi^i \rho^i \omega_k^i E_{Tk}^i \quad (\text{where, } E_{Tk}^i = c_k^i (T_k^i - T_{k0}^i)) \tag{41}$$

Where c_k^i is the specific heat capacity of component k in phase i . Note that the above expression assumes that the different components in the soil are in thermal equilibrium ((Abed and Sołowski 2017).

Expanding Eq. (41) with the assumption that the dissolved air and hydrogen gas in water have the same specific heat capacity as in dry pore air, gives the following expression:

$$\Phi_h = [(1-n)\rho^s c_s + n(H_a S^l + S^s) \rho_a c_a + n(H_H S^l + S^s) \rho_H c_H + nS^l \rho_w^l c_w^l + nS^s \rho_w^g c_w^g] (T - T_0) \tag{42}$$

Next, eq. (43) shows the general expression for total heat flux in Thebes (Abed and Sołowski 2017). It includes: i) the contribution of heat flow by soil bulk (see Eq. 44), ii) the convection of heat by liquid flow (q^l) and iii) the convection of heat by gas diffusion (j_k^g).

$$q_h = q^T + \rho^i \omega_k^i E_{Tk}^i q^i + E_{Tk}^i j_k^g \quad 43$$

$$q^T = -\lambda_T \nabla T \quad 44$$

, where λ_T is the thermal conductivity of the soil skeleton.

Expanding Eq. (43) and adding the contribution of the hydrogen gas component gives the following expression for heat flow:

$$q_h = -\lambda_T \nabla T + [(\rho_a c_a + \rho_w^g c_w^g + \rho_H c_H) q^g + (\rho_w^l c_w^l + H_a \rho_a c_a + H_H \rho_H c_H) q^l] (T - T_0) + [c_w^g j_w^g + c_H j_H^g + c_a j_a^g + c_H j_H^l + c_a j_a^l] (T - T_0) \quad 45$$

By using the Eq. (40), (42) and (43), and assuming a constant specific heat capacity for all the components, the final form of the heat conservation equation is:

$$\begin{aligned} & \left[A(1-n) + LS^g \rho_w^g \right] \frac{\partial \varepsilon_v}{\partial t} \quad 46 \\ & \left[-[A + B + L(1-n)S^g \rho_w^g] \beta_{sT} + (nC - Ln \rho_w^g) \frac{\partial S^l}{\partial T} + D \right. \\ & \quad - n(H_H S^l + S^g) c_H (T - T_0) \left(\beta_{wT} \rho_H + \frac{\rho_H}{T} \right) \\ & \quad - nS^l c_w^l \beta_{wT} \rho_w^l (T - T_0) + (LnS^g + nS^g c_w^g (T - T_0)) \left[\frac{\rho_w^g}{T^2} (4974.0 + \frac{gM_w \psi}{R}) \right] \frac{\partial T}{\partial t} \\ & \quad - nc_a (H_a S^l + S^g) (T - T_0) \frac{M_a \rho_w^g}{M_w T^2} \left(4974.0 + \frac{gM_w \psi}{R} \right) \\ & \quad \left. + n\rho_a c_a S^l (T - T_0) \frac{\partial H_a}{\partial T} + n\rho_H c_H S^l (T - T_0) \frac{\partial H_H}{\partial T} \right] \\ & + \left[- (nC - Ln \rho_w^g) \frac{\partial S^l}{\partial \psi} - n(H_a S^l + S^g) c_a (T - T_0) \left(\frac{M_a \rho_w^g g M_w}{M_w RT} \right) \right. \\ & \quad + nS^l c_w^l (T - T_0) \beta_{wp} g \rho_w^{l2} + n(H_H S^l + S^g) c_H (T - T_0) \beta_{wp} g \rho_w^l \rho_H \\ & \quad \left. + (nS^g c_w^g (T - T_0) + LnS^g) \frac{\rho_w^g g M_w}{RT} + n\rho_a c_a S^l (T - T_0) \frac{\partial H_a}{\partial h_w} + n\rho_H c_H S^l (T - T_0) \frac{\partial H_H}{\partial h_w} \right] \frac{\partial h_w}{\partial t} \\ & + \left[n(H_H S^l + S^g) c_H (T - T_0) \frac{\rho_w^l g M_H}{RT} - n(H_a S^l + S^g) c_a (T - T_0) \frac{M_a \rho_w^l g}{RT} \right] \frac{\partial h_H}{\partial t} \\ & + \left[(nC - Ln \rho_w^g) \frac{\partial S^l}{\partial \psi} + n(H_a S^l + S^g) c_a (T - T_0) \left(\frac{M_a \rho_w^l g}{RT} + \frac{M_a \rho_w^g g M_w}{M_w RT} \right) \right. \\ & \quad \left. - (nS^g c_w^g (T - T_0) + LnS^g) \frac{\rho_w^g g M_w}{RT} \right] \frac{\partial h_g}{\partial t} \\ & \nabla \cdot q_h + L \nabla \cdot (\rho_w^g q^g) + L \nabla \cdot j_w^g = 0 \end{aligned}$$

$$\begin{aligned}
A &= (1-n)(T-T_0)(-\rho^s c_s + (H_a S^l + S^s) \rho_a c_a + (H_H S^l + S^s) \rho_H c_H + S^l \rho_w^l c_w^l + S^s \rho_w^s c_w^s) \\
B &= (1-n) c_s \rho^s (T-T_0) \\
C &= [\rho_a c_a (H_a - 1) + \rho_H c_H (H_H - 1) + \rho_w^l c_w^l - \rho_w^s c_w^s] (T-T_0) \\
D &= (1-n) \rho^s c_s + n[(H_a S^l + S^s) \rho_a c_a + (H_H S^l + S^s) \rho_H c_H + S^l \rho_w^l c_w^l + S^s \rho_w^s c_w^s] \\
\frac{\partial H_a}{\partial T} &= \left(\frac{1}{T} - \beta_{wT}\right) H_a \\
\frac{\partial H_H}{\partial T} &= \left(\frac{1}{T} - \beta_{wT}\right) H_H \\
\frac{\partial H_a}{\partial h_w} &= g \rho_w^l \beta_{wp} H_a \\
\frac{\partial H_H}{\partial h_w} &= g \rho_w^l \beta_{wp} H_H \\
q_h &= -\lambda_T \nabla T + [(\rho_a c_a + \rho_w^s c_w^s + \rho_H c_H) q^s + (\rho_w^l c_w^l + H_a \rho_a c_a + H_H \rho_H c_H) q^l] (T-T_0) \\
&\quad + [c_w^s j_w^s + c_H (j_H^s + j_H^l) + c_a (J_a^s + J_a^l)] (T-T_0)
\end{aligned}$$

2.2.7 Mechanical Balance

Thebes uses a local static mechanical force balance expression as shown below (Abed and Sołowski 2017):

$$\nabla \cdot \sigma^{tot} + b = 0 \quad 47$$

, where σ^{tot} is the total stresses and b denotes the body forces typically being a result of bulk density (ρ^b). Constitutive models in use are a linear and non-linear elastic and modified version of the Barcelona Basic Model (BBM).

2.3 Verification

2.3.1 1D Thebes vs Comsol verification

The new conceptual framework of Thebes is initially verified by performing several benchmark tests using a simple 1D (1x1 m²) geometry (see Figure 2-2) and thereby comparing the results against Comsol and analytical solutions.

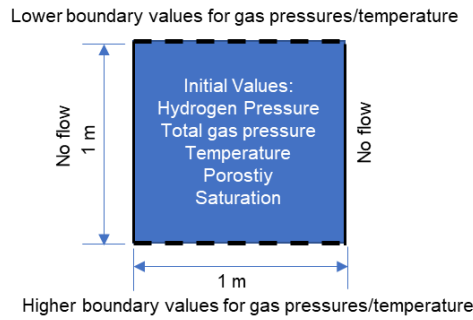


Figure 2-2 Generic verification test setup.

The test cases target specific flow mechanisms or coupling types because of coupling limitations in Comsol. All the test results give a good match between Thebes and Comsol simulation. Due to space constraints, we only discuss the summary of different test scenarios and their analysis method here:

i. Hydrogen-only diffusion/advection

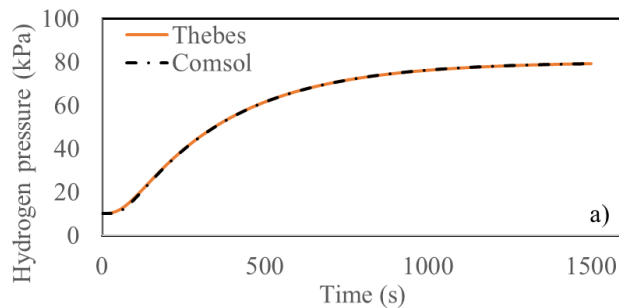
A test setup consists of a porous unsaturated material (constant 60% Sr) having unidirectional upward gas flow due to the difference between top and bottom pressure boundaries and closed vertical walls. We run two cases with the same setup a) Gas-phase diffusion-only flow, b) Gas-phase Darcian flow. In Comsol, the former case of diffusion type analysis uses "*Transport of diluted species in an unsaturated porous medium*", and the latter uses "*Darcy law in an unsaturated porous medium*".

ii. Hydrogen and Air diffusion/advection.

The verification test utilises a similar setup as in the previous case with additional upward air pressure at the hydrogen influx boundary. In Comsol however, coupling restrictions do not allow for a direct comparison. Hence, performing a diffusion analysis requires a semi-analytical approach by evaluating air pressure using the hydrogen gas pressure from the single gas diffusive flow simulation in Comsol (see, Figure 3). Equation (48) shows the expression to evaluate the air pressure values analytically. It is derived using the reduced form (diffusion only) of hydrogen and air mass balance (see Eq. 32 and 38). Performing the advective flow type test verification requires a simulation of total gas pressure in Comsol by treating hydrogen and air as one component (see, Figure 4).

$$h_{air} = -\frac{M_H}{M_a} h_H + c \quad 48$$

, where M_h and M_a are the molar masses of hydrogen and air respectively and c is the constant depending on the initial values.



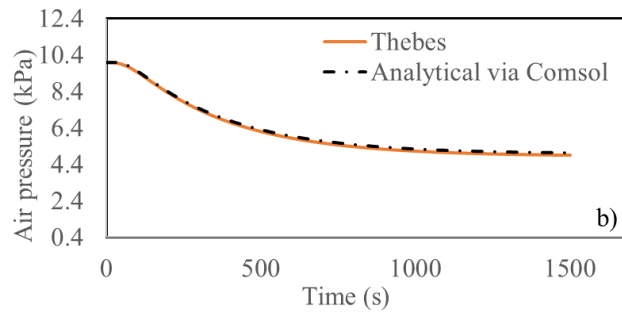


Figure 2-3 Gas phase diffusion flow verification test at centre point: a) Hydrogen pressure, and b) Air pressure (Test specifications refer to Gupta et al., 2023)

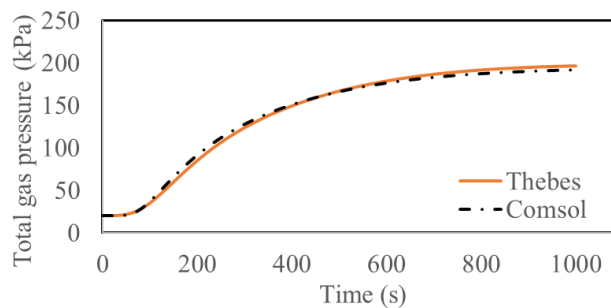


Figure 2-4 Total gas pressure, verification test for advective coupled two gas flow at the centre. (Test specifications refer to Gupta et al., 2023)

- iii. Hydrogen gas diffusive/advective flow and Heat transfer.
Due to extensive coupling in the heat balance expression in Thebes (see Eq. 46) and coupling limitations of Comsol, a verification test requires assuming an ideal case scenario where only the hydrogen gas flow and soil bulk provides thermal contribution. The test setup uses similar conditions as the case (i) for gas flow. Additionally, it consists of a constant temperature at the top and bottom boundaries creating an upward heat flow, whereas the vertical walls remain closed. Comsol only allows for advective flow type to couple with heat transfer physics. Hence performing a diffusion-based heat transfer analysis in Comsol requires adjusting the advection flow properties that simulate values like diffusive flux. The results show a close match between Comsol and Thebes simulation.
- iv. Hydrogen gas pressures and Mechanical coupling.
The verification work for this coupling utilises only an analytical solution. Equation (49) shows that analytically gas pressure is only dependent on volumetric strain and porosity changes and free from any initial set pressure gradients in the system. The equation is derived using the reduced coupled form of hydrogen mass balance (see Eq. 32). The test setup consists of the constant initial, top and bottom gas pressures with a closed vertical wall and confining mechanical pressure boundaries. The results show a good match in case of pressure build-ups in time at the midpoint of the domain.

$$h_H = e^{\frac{\varepsilon_v}{n} + c} \quad 49$$

, where ε_v is a total volumetric strain, n is the soil porosity and c is the constant depending on initial values.

2.4 Dissolved gas diffusion validation

To validate the dissolved gas diffusion, Thebes simulates Jacops et al. (2017) experiment that examines methane and helium diffusion in a fully saturated Boom Clay. Figure 2-5 shows the test setup containing a stainless steel diffusion cell enclosing a Boom Clay sample of 8 cm diameter, 3 cm height and 0.38 porosity. The two vessels are filled with half water and half gas on either side. Both vessels maintain a 10 bar pressure. To simulate the test, Thebes adapts 1D analysis with a 3 cm sample height and 200 elements. It maintains the loading conditions as aforementioned. Refer to Gupta et al., 2023 for more details on test parameters in Thebes.

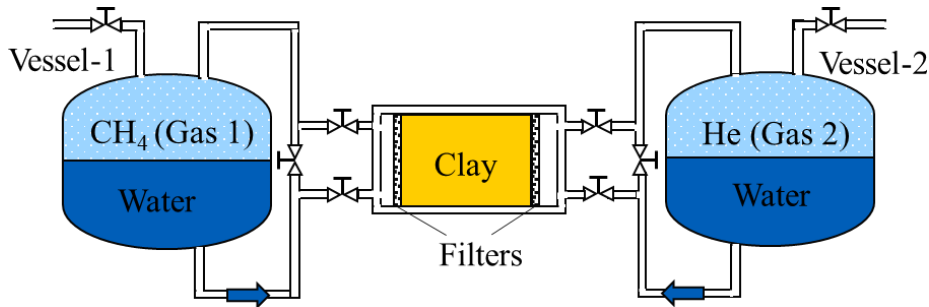


Figure 2-5 Diffusion of two dissolved gases - experiment setup (Gupta et al., 2023 adapted from Jacops et al., 2017)

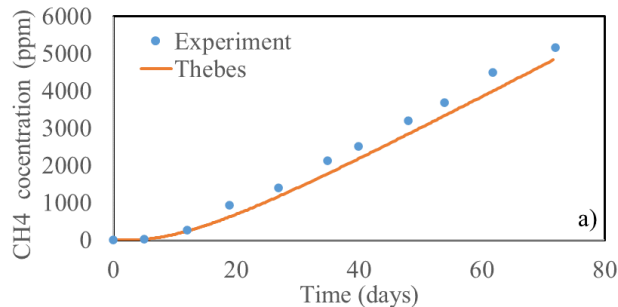


Figure 2-6 Dissolved gas diffused concentrations, Methane in chamber-2 (more details in Gupta et al., 2023)

2.5 THG coupled test: Landfill gas migration.

To further verify all the code modifications, Thebes replicates a highly coupled process of landfill gas migration under non-isothermal and constant water influx conditions. Nastev et al. (2001) performed the test by using its own built finite volume code Tough-LGM. Figure 2-7 shows the problem description, where the refuse of 40 m height due to bio-degradation produces a mixture of gases (methane 55% and carbon dioxide 45%) along with heat production of 40.2 kJ/mole. Constant water infiltration at the top boundary (401.6 mm/ year) represents average precipitation, and the bottom water table represents close boundaries for gas flow. To avoid full saturation at the top and maintain a gas outlet, maximum saturation is kept at 90%. Further, the landfill initially is at 1atm air pressure and maintains the same pressure/concentration at the top boundary. Other gas components are at zero concentration at the top. Initially, the landfill is at 40% saturation and 27°C temperature. The gas production is an exponentially decreasing function given by Eq.(50) and the test run time is 100 years. To simulate the test, Thebes utilizes 191 quadrilateral 4-noded elements for the present simulation. The material properties are kept according to Nastev et al. (2001).

$$\Omega = k_{gas} \Pi_0 e^{-k_{gas} t}$$

where, Ω is the total gas production rate at 1 atm pressure, k_{gas} is the overall kinetic rate constant at 0.055 per year and Π_0 is the initial gas production potential at 172 m³/ton (Nastev et al. 2001).

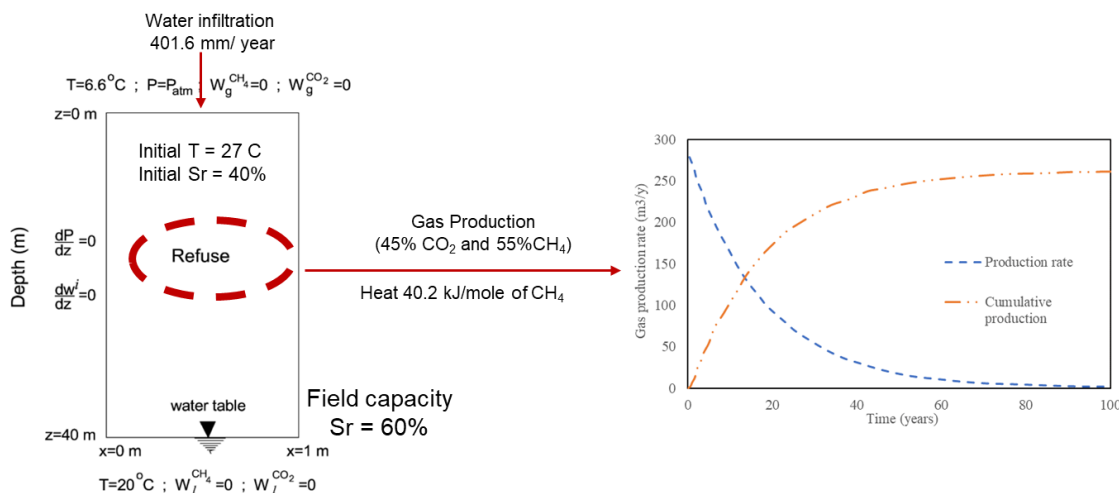


Figure 2-7 1D landfill gas and heat flow (Nastev et al. 2001)

Figure 2-8 shows the total gas pressure accumulation at different times along the landfill depth. The results indicate a good match between the original work and Thebes, with a maximum difference of 0.25 kPa in the 10-year profile. The initial pressure growth is driven mostly by methane and carbon dioxide driving air out at the very beginning of the simulation. However once the gas production rate slows, air diffuses back to the landfill from the top. This process initiates after approximately 40 years of simulation. The study also evaluates and compares the temperature, methane and air concentration profile, which shows a satisfactory match with the Nastev et al. (2001) simulation.

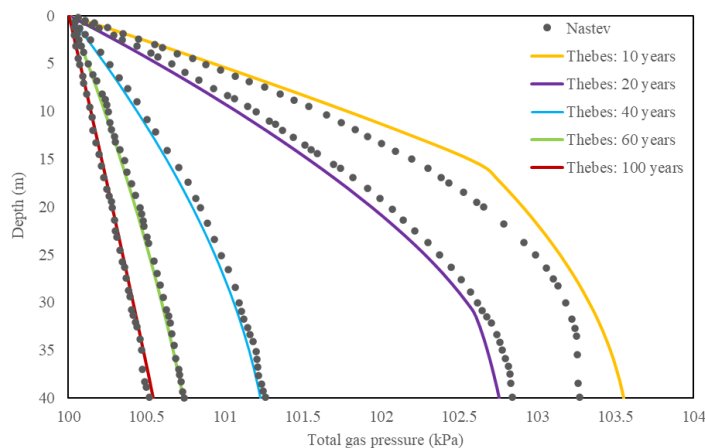


Figure 2-8 Total gas pressures from Thebes and (Nastev et al. 2001)

2.6 2D modelling of a deposition tunnel section from Zone B

In steps to achieve a complete Zone B (EURAD: Milestone 61 2021) repository model, this work presents a smaller study of modelling a single axisymmetric tunnel section (see Figure 2-9) in 2-D under a thermal-hydraulic and gas coupled environment. The multi-layer barrier system consists of a canister holding nuclear waste, layers of concrete, backfill, and inner/outer EDZ material enclosed in a rock mass (EURAD: Milestone 61 2021). The present modelling work of the high-level waste facility aims at understanding the process of hydrogen gas flow, desaturation/re-saturation cycle, the maximum gas pressure and temperature build-up during the first 1 500 years of repository life.

The current work does not account for mechanical coupling and gravitational flow. Further, the model considers only 21.25m of rock, instead of the given dimensions of 71.25 m, assuming that the far end of the rock will remain unaltered during the initial 1 500 years of simulation. The later section provides more details on modelling conditions, assumptions, and material properties.

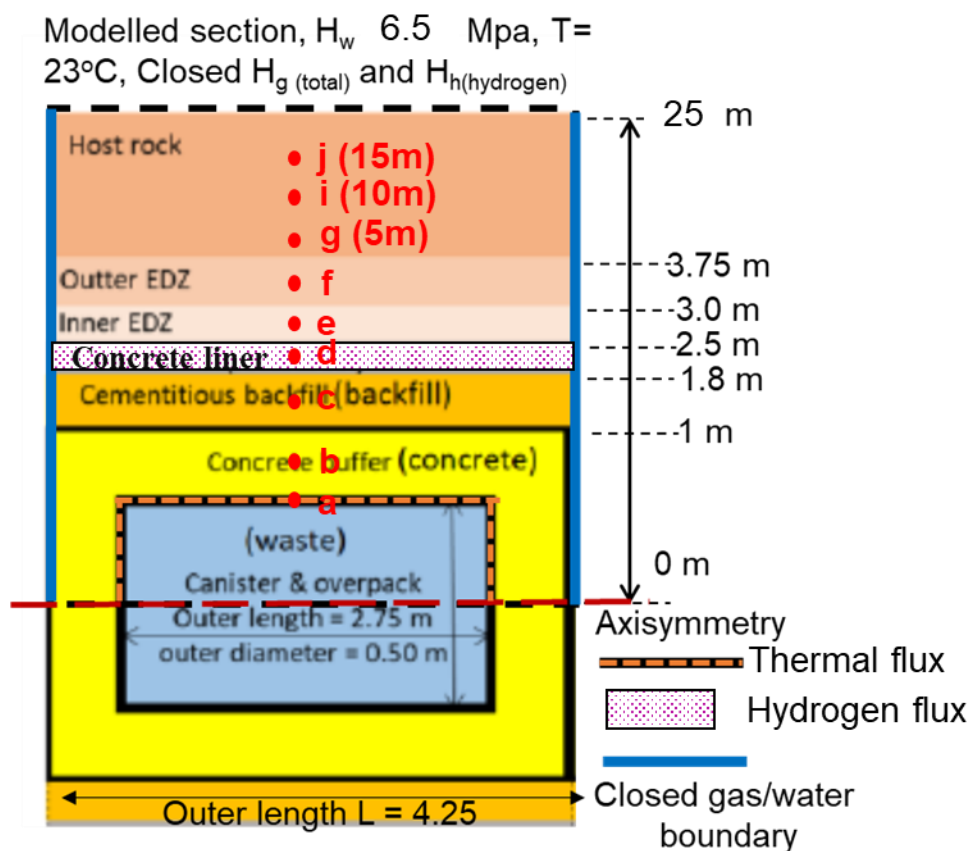


Figure 2-9 2D tunnel section from the disposal Zone B (EURAD: Milestone 61 2021).

2.7 Numerical details

Figure 2-9 shows the test setup (horizontally rotated) of the model that is 4.25 m in width and 25 m in length. The model consists of 5 150 four-noded quadrilateral finite elements with four integration points per element (see, Figure 2-10).

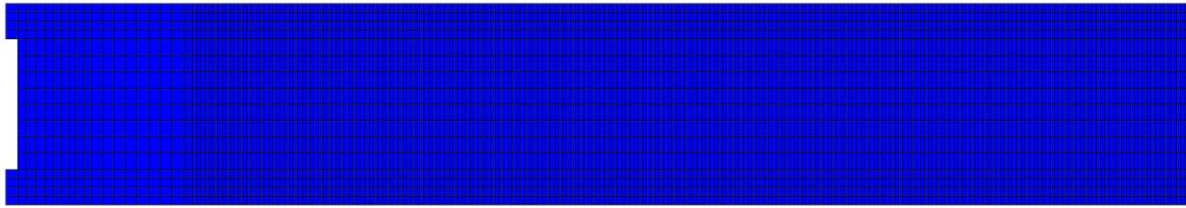


Figure 2-10 Repository simulation mesh

The simulation starts at $T = 50$ years, assuming instantaneous emplacement of the waste and closure of the whole repository (EURAD: Milestone 61 2021). Initially, the model assumes the repository's temperature at 23°C . The tunnel materials are at 80% saturation (Concrete, backfill, inner and outer EDZ), and the rock is at full saturation ($S_r = 100$). Due to differently assigned water retention properties of the materials (see Table 2-3), the saturation values correspond to distinct initial matric suction for each layer: a) concrete – 9.776MPa , b) backfill – 0.9776MPa , c) inner EDZ – 15.64MPa , d) outer EDZ – 16.57MPa , and e) Rock – 0MPa .

The hydraulic boundary at the top is 6.5MPa and the bottom is closed. The hydraulic pressure boundaries are proportional to the repository height (adjusted from the specification). Furthermore, in case of heat dissipation, the canister boundary is considered to be the heat source, whereas the top boundary maintains temperature of 23°C . Figure 2-11 shows the heat influx rate. Next, Thebes assumes a concrete liner as the source for hydrogen gas production. The gas flux rate due to anaerobic canister corrosion is given by EURAD (EURAD: Milestone 61 2021) as 0.25mol/y (per meter of zone B HLW cell) during the 100 000 years of the repository. The equivalent hydrogen mass flux per second from concrete liner is $1.59817\text{e-}11\text{Kg/m-s}$. The simulation further assumes top boundary closed for gases. The simulation exhibits 1D dimensional flow as such the vertical boundaries are closed for fluid (gas and liquid) and heat flow.

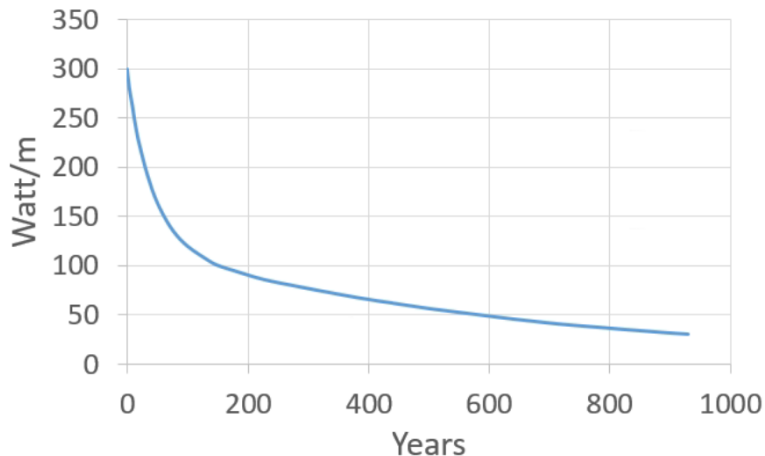


Figure 2-11 Heat flux at the canister boundary

Tables 2-2 and 2-3 show the common and specific material properties for the modelling, respectively. The gas phase diffusion uses Millington's quirk tortuosity factor (EURAD: Milestone 61 2021) and effective diffusion coefficient from gas mixing law by Bird et al. (1960) and Fuller et al. (1966). The model further uses standard constant specific heat parameter values.

Table 2-2 Common material properties for the whole modelled domain

Thermal properties		
Specific heat Water (c_w)	4180	J/kg/K
Specific heat vapour (c_v)	1900	J/kg/K
Specific heat air (c_a)	1006	J/kg/K
Specific heat hydrogen (c_h)	14307	J/kg/K
Latent Heat of vapourisation (L)	2.50E+06	J/kg
Thermal expansion of water (β_{wT})	3.43-4	[1/K]
Vapour diffusion ((Philip and Vries 1957)		
Thermal enhancement (f_{tv})	1	
Hydrogen diffusion (EURAD: Milestone 61 2021)		
Henry's constant Hydrogen (H_{c_H})	1.40E-10	1/Pa
Henry's Constant air (H_c)	1.00E-10	1/Pa
Dissolved Hydrogen diffusion coefficient (D_H^l)	5.00E-09	
Other constants		
Molar mass of air (M_a)	0.028013	kg/mol
Molar mass of water (M_w)	0.018016	kg/mol
Molar mass of hydrogen (M_h)	0.002016	kg/mol
R constant	8.3144	J/mol-K
Atmospheric pressure (P_{atm})	100	kPa
Initial water density (ρ_{w0}^l)	998.2	Kg/m3
Solid Material density for all layers (ρ_s)	2450	Kg/m3
Gravitational force (g)	9.806	
Full saturation (S_{sat})	1.0	
Residual saturation (S_{res})	0.0	

Table 2-3 Material specific model properties (EURAD: Milestone 61 2021).

	Concrete	Backfill	Inner EDZ	Outer EDZ	Rock
Porosity (n)	0.15	0.4	0.2	0.2	0.2
Void Ratio (e)	0.176471	0.666667	0.25	0.25	0.25
Water hydraulic conductivity (m/s) (K_{satw})	9.66E-09	9.66E-09	9.66E-09	9.66E-11	9.66E-13
Gas intrinsic permeability (m ²) (K_{intG})	1.00E-15	1.00E-15	1.00E-15	1.00E-16	1.00E-17
SWCC properties					
n_{sr}	1.5	1.50E+00	1.5	1.5	1.5
Pr (Pa)	10000000	1000000	1.60E+07	1.60E+07	1.60E+07
Gas entry pressure (Pa) (P_e)	0	0.00E+00	0.00E+00	1.70E+00	6.00E+06
Millington quirk					
a_{liq}	2	1.00E+00	1.50E+00	1.50E+00	1.50E+00

	Concrete	Backfill	Inner EDZ	Outer EDZ	Rock
b_{liq}	4	1.50E+01	1.00E+01	1.00E+01	1.00E+01
a_{gas}	0	3.00E+00	2.50E+00	2.50E+00	2.50E+00
b_{gas}	5	3.00E+00	2.50E+00	2.50E+00	2.50E+00
Thermal properties					
Bulk material conductivity (W/m/K) (λ_T)	2.30E+00	1.30E+00	1.70E+00	1.70E+00	1.70E+00
Solid specific heat (J/kg/K) (C_s)	9.00E+02	5.00E+02	7.20E+02	7.20E+02	7.20E+02
Thermal expansions of solids (1/K) (β_{sT})	2.00E-05	2.00E-05	4.00E-05	4.00E-05	4.00E-05

2.8 Simulation results

The simulation of the repository over 1500 years demonstrates that the total gas pressure reaches its peak at approximately 6.2 MPa in 450 years (refer to Figure 2-12). Furthermore, the gas pressure stabilizes once it exceeds the air entry values of the barrier material and progressively advances the saturation-unsaturation interface line resulting in the unsaturation of host rock at constant pressures. The moving saturation and unsaturation interface line is further evident from the rate of gas pressure accumulation, until rock at 5 m the pressure are built simultaneously, while it takes about 650 years for rock at 10 m to show any significant pressure accumulation.

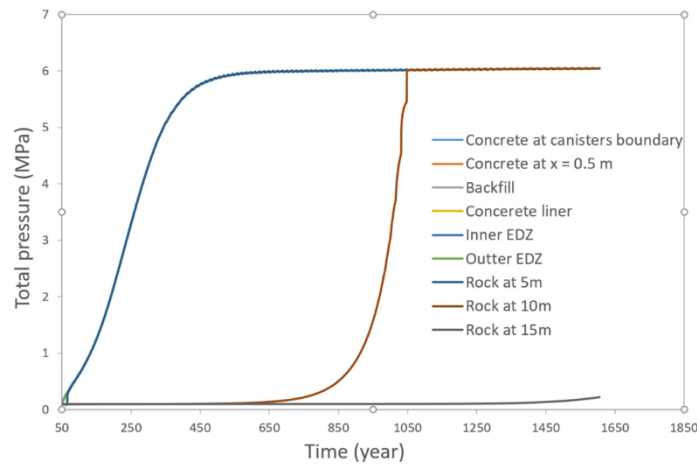


Figure 2-12 Total gas pressures

The hydrogen gas contribution along the tunnel materials (not including host rock) shows a rapid increase in time (see, Figure 2-13), closing 95% at around 230 years. Since these materials remain unsaturated, the advective gas flow quickly equalizes the pressures and hydrogen concentration. The host rock gradually becomes unsaturated in time, showing 80% molar contribution of hydrogen in the total gas at around 380 years for rock at 5 m. The same amount of hydrogen contribution takes a proportionally longer time to infiltrate further rock regions.

Note that the unusual increase in the percentage of hydrogen at a depth of 10 meters in the rock at around 1040 years is attributed to the accumulation of air pressure at the saturation-unsaturation interface line and its gradual migration. The findings demonstrate that, over time, the total gas pressure will displace most of the air at the saturation-unsaturation interface line, resulting in a peak air concentration (refer to Figure 2-14). As this interface line advances and creates an unsaturated zone within the rock, there will be a sudden surge in hydrogen pressure just behind it. Nevertheless, as the

interface line moves further away from the observed point, the molar fraction of hydrogen will eventually stabilize, ultimately reaching near 100%.

Moreover, the fact that air contributes 25% to the total gas pressure at the interface (see, Figure 2-14), highlights the importance of accounting for the entrapped air in the repository.

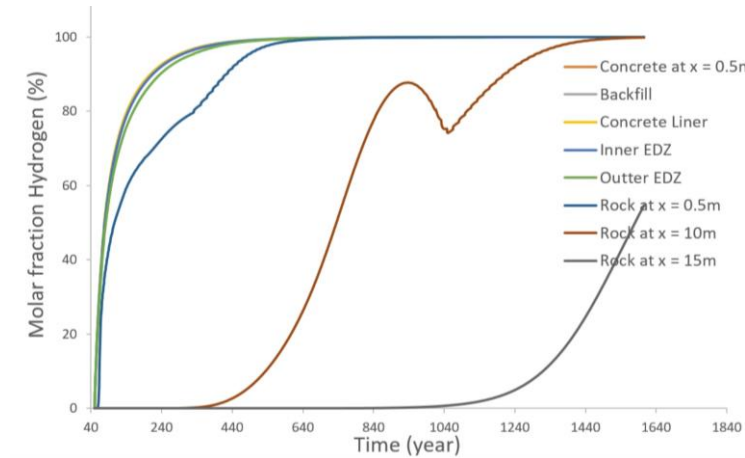


Figure 2-13 Molar fraction of hydrogen in time

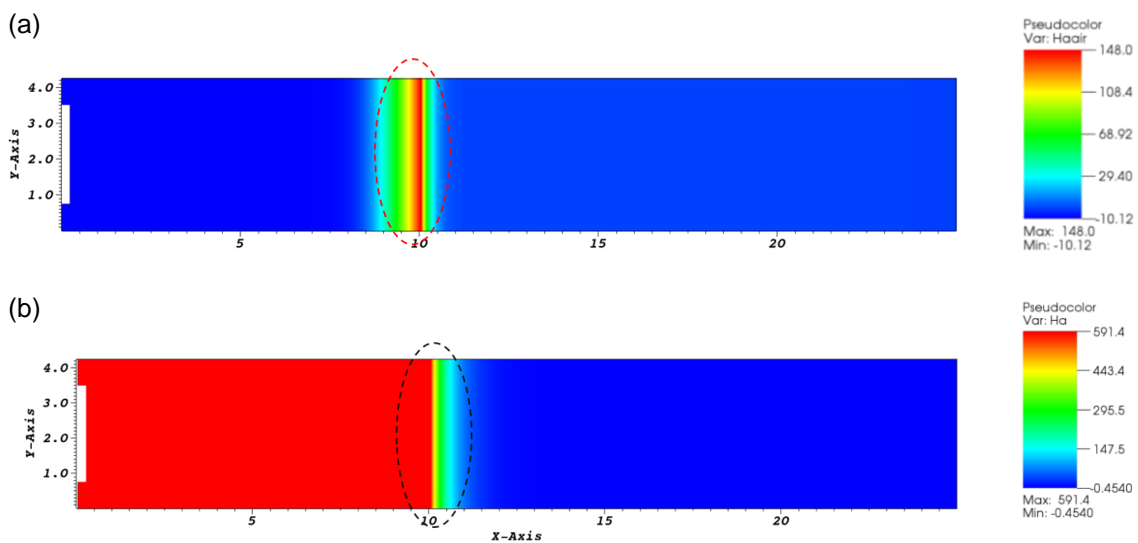


Figure 2-14 Gas pressure heads (relative to 1 atm) at around 1 000 years: a) Air pressure head (m), b) Total gas pressure head (m)

The air molar fraction profile shows an inverse behaviour to that of hydrogen. The air contribution along the tunnel material rapidly decreases from the initial 100%. However, it remains relevant even at 300 years with 5% contribution i.e., 0.23 MPa of total pressure. In the rock mass there is further a delay in reduction of air fraction, as it gradually becomes unsaturated.

This spike of air fraction at 10 m rock in about 1 000 years further indicates the phenomena of bulk air pressure moving and accumulating at the saturation interface. Overall long-term effects of entrapped air may not be large, but it plays an important role in desaturating the host rock.

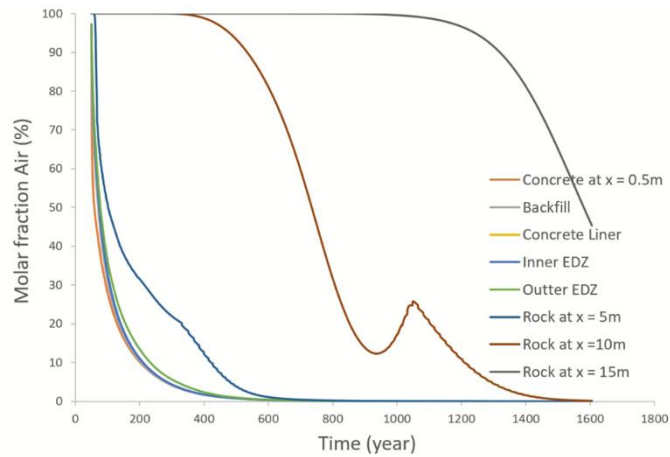


Figure 2-15 Air molar fraction in time

Figure 2-16 illustrates the temporal evolution of water vapour impact on the overall gas pressure. The spikes and patterns depicted in the figure indicate that water vapour behaviour closely mirrors the temperature profiles (refer to Figure 2-17). Furthermore, when considering the long-term perspective of the repository, the contribution of vapour appears to be minimal. Its influence is most prominent in proximity to the canister, peaking at a concentration of 45% (0.225 MPa in a total of 0.5 MPa gas pressure) within the first 60 years of the repository's existence. This percentage gradually decreases to 30% within a 0.05-meter distance from the canister boundary. Additionally, the water vapour fraction experiences a rapid decline over time and eventually becomes negligible after 240 years of simulation.

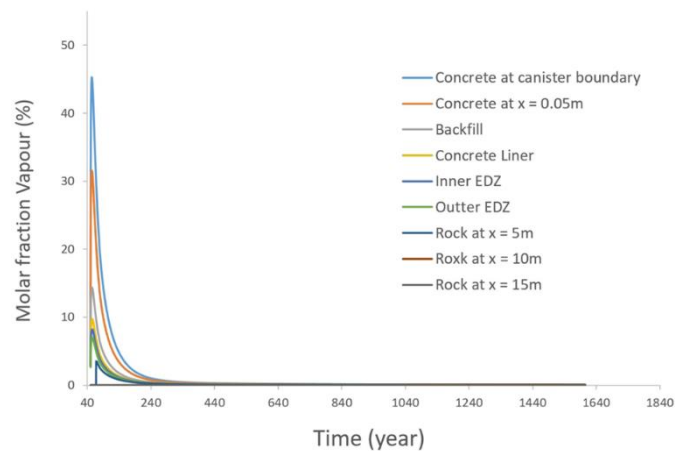


Figure 2-16 Molar fraction of water vapour in time

Figure 2-17 illustrates the evolution of the temperature profile over time. Initially, the findings indicate a swift increase in temperature, peaking at 97°C within the first 60 years of simulating the repository. Consequently, the temperature consistently remains below 100°C, affirming the acceptability of the thermal steady-state assumption in Thebes. Note, due to higher thermal conductivity the temperature trend is almost linear along the repository. Further, the results reveal that by the end of the simulation (1 500 years), the anticipated maximum repository temperature will drop below 30°C.

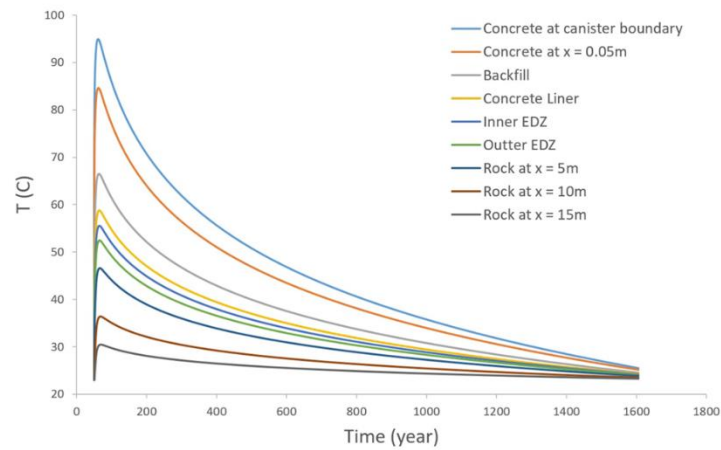


Figure 2-17 Temperature profile in time

The saturation profile depicted in Figure 2-18 indicates that the repository primarily remains nearly saturated throughout the simulation. Upon commencing the model, the tunnel material rapidly saturates, exceeding 99% saturation within the initial 100 years, except for the backfill. The initial decline in saturation in the backfill suggests that, due to its differing water retention properties and lower suction compared to the surrounding layers, water initially moves out of the backfill to saturate relatively drier zones. However, around 60 years into the simulation, water inflow from the rock gradually re-saturates the backfill, reaching up to 96% saturation. This higher degree of saturation further signifies a low risk of gas fracturing within the repository.

The water flow behaviour in the rocks becomes more evident through pore water pressure profiles, as shown in Figure 2-19. For rocks located at 10 and 15 meters, the initial increase in pore water pressure to 12 MPa is attributed to inflow from above. In contrast, in the case of rocks at 5 meters, the outflow of water to the tunnel materials exceeds the inflow, causing the initial pressure to drop close to 0. However, in the case of tunnel material, after an initial fluctuation observed in the saturation profile, the pore pressure increases with water influx. Ultimately, the repository reaches a steady state, with pore pressures aligning with saturation state pressures.

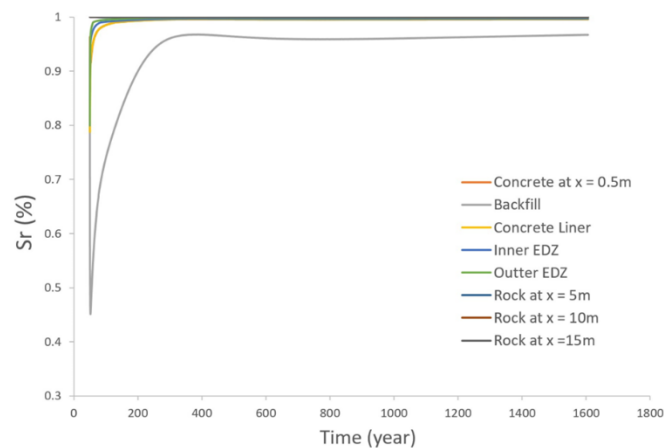


Figure 2-18 Degree of saturation in time

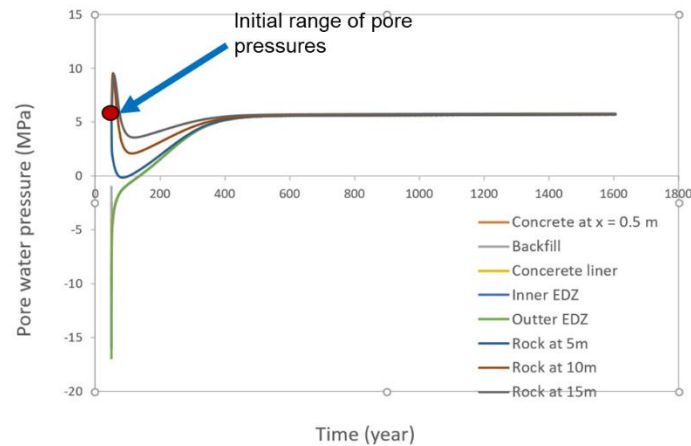


Figure 2-19 Pore water pressures in time

2.9 Conclusion

The report presents a new extension to the numerical framework of Thebes that enables the simulation of gas flow in a moist porous air medium. In a preliminary stage of analysis, the model proves capable of performing a full thermal-hydraulic and gas (THG) coupling for a 2D tunnel section of a high-level waste repository from disposal zone B.

The simulation predicts that the repository will reach a peak temperature of 97°C at 60 years and subsequently decrease to below 30°C after 1500 years. Additionally, the highest total gas pressure is approximately 6.2 MPa at 450 years. This excess pressure beyond the air entry value induces unsaturation in rocks while maintaining a constant peak value within the unsaturation zone. The analysis further indicates that hydrogen quickly becomes the dominant component of the total gas pressure within the repository, approaching 95% within 230 years. However, entrapped air plays a significant role and exhibits an intriguing phenomenon. Over time, the total gas pressure propels air toward the saturation/unsaturation interface, where it contributes up to 25% of the total gas pressure. On the other hand, water vapour exerts little long-term influence on the gas simulation. The highest contribution is around 45% in 60 years at the canister boundary, decreasing to a negligible value after 240 years. However, if the peak temperature is mispredicted and it would be more than 100 degrees Celsius, the water vapour contribution may become much more significant.

The report also emphasizes pore water flow within the repository, suggesting that, beyond the initial fluctuations, the repository maintains a high level of saturation, exceeding 95%. Considering the peak gas pressures, a high degree of saturation, and substantial in-situ stress, the likelihood of gas-induced fractures in the repository appears to be relatively low.

It is essential to note that while these results provide valuable insights into various couplings and critical processes within the repository, they are indicative and strongly reliant on the applied assumptions. In the future, our aim is to explore the impact of various assumptions and ultimately conduct a full thermal-hydraulic-mechanical and gas (THM-G) coupled analysis of the repository over a simulation period of 100 000 years.

2.10 References

- Abed AA, Sołowski WT (2017) A study on how to couple thermo-hydro-mechanical behaviour of unsaturated soils: Physical equations, numerical implementation and examples. *Comput Geotech* 92:132–155. <https://doi.org/10.1016/j.compgeo.2017.07.021>
- Abed AA, Sołowski WT (2018) Applications of the new thermo-hydro-mechanical-chemical coupled code “Thebes.” *Environmental Geotechnics* 7:3–16. <https://doi.org/10.1680/jenge.18.00083>
- Bird RB, Stewart WE, Lightfoot EN (1960) *Transport phenomena*. John Wiley & Sons, New York
- Darcy H (1856) *Les Fontaines Publiques de La Ville de Dijon*. Dalmont, Paris, France
- Diersch HJG, Kolditz O (2002) Variable-density flow and transport in porous media: Approaches and challenges. *Adv Water Resour* 25:899–944. [https://doi.org/10.1016/S0309-1708\(02\)00063-5](https://doi.org/10.1016/S0309-1708(02)00063-5)
- EURAD: Milestone 61 (2021) Technical Note defining a generic repository configuration, sets of parameters, conditions and relevant indicators
- Fick A (1855) Ueber Diffusion. *Annalen der Physik* 94:59–86
- Fuller EN, Schettler PD, Giddings JC (1966) A new method for prediction of binary gas-phase diffusion coefficients. *Ind Eng Chem* 58:18–27. <https://doi.org/10.1021/ie50677a007>
- Gupta A, Jacobs E, Abed A, Sołowski W (2023) Finite element modelling of multi-gas flow in expansive clay. In: 10th European Conference on Numerical Methods in Geotechnical. London
- J Vaunat, C jommi AAG (1997) Statergy for numerical analysis of the transition between saturated and unsaturated flow conditions. *Numerical Models in Geomechanics* 297–302
- Jacobs E, Aertsens M, Maes N, et al (2017) Interplay of molecular size and pore network geometry on the diffusion of dissolved gases and HTO in Boom Clay. *Applied Geochemistry* 76:182–195. <https://doi.org/10.1016/j.apgeochem.2016.11.022>
- Nastev M, Therrien R, Lefebvre R, Gelinas P (2001) Gas production and migration in landfills and geological materials
- Panday S, Corapcioglu MY (1989) Reservoir transport equations by compositional approach. *Transp Porous Media* 4:369–393. <https://doi.org/10.1007/BF00165780>
- Philip J, Vries D De (1957) Moisture movement in porous materials under temperature gradients. *Eos, Transactions American Geophysical Union* 38(2):222–232. <https://doi.org/https://doi.org/10.1029/TR038i002p00222>
- Sutherland W (1893) The viscosity of gases and molecular force. *Philosophical Magazine S. 5*:507–531
- White FM (2006) *Viscous Fluid Flow*, 3rd edn. McGraw-Hill

3. Contribution of Andra

(Jacques Wendling, Vincent Christaud)

3.1 Generalities

Concerning the estimation of pressures during the hydraulic-gas transient in the underground repositories, the data acquired by Andra on the Callovo-Oxfordian argillite and the EBS allowed the determination of physical, confirmed and consolidated models through 20 years of feedback via scientific articles in peer-reviewed journals as well as participation in international projects/congresses (notably European) allowing comparison with the academic world and our counterparts (notably NAGRA and ONDRAF/NIRAS).

These data made it possible to define the main elements of the physical conceptualization which are as follows:

- convective transfers based on an approach in equivalent porous media (no fractures) of the generalized Darcy type as for the PGZ (injection of gas in a borehole at metric scale) experiments carried out at the underground laboratory of Meuse/Haute-Marne this conceptualization allows a good reproduction of the kinetics and amplitudes of the phenomena.
- Other experiments show that the migration of dissolved hydrogen can be well reproduced by a generalized Fick type approach (taking into account the degree of water saturation) with regard to its diffusion, exchanges between phases can be managed via Henry's law.
- The presence of exothermic waste implies explicit coupling with thermal energy, the parameter values of which come from available data.
- The coupling with mechanics is done only via a compressibility coefficient (storage coefficient in hydraulics, inverse of the Biot modulus for mechanics). In the long term, this representation remains representative (i) as the delayed deformations of the argillite are very slow and do not involve pressurization of the fluids present in the galleries and (ii) as long as the gas pressures remain significantly lower than the minimum in-situ stress (i.e. gas pressures do not generate fracturing).
- No explicit coupling with chemistry is considered, however (i) the gas source terms, resulting mainly from a chemical process (corrosion), are considered in the evaluations but are imposed as input data and (ii) alkaline disturbance, the main chemical process developing at concrete/clay interfaces, is taken into account indirectly via sensitivity analyses on the permeability of these interfaces.

The uncertainties on the models (including the couplings, with mechanics and chemistry) and the values of the parameters are managed by sensitivity studies which make it possible to determine limits for the indicators of interest (the main one being the maximum gas pressure).

The gas migrates on the scale of the disposal system, it is necessary to represent the general network of the galleries and the connections between them as well as with the upper aquifer, via the surface-bottom connections, constituting the outlet for the gaseous hydrogen. As exchanges with the host rock are important for the dissolution of the gas, a good representation of the volumes, surfaces and lengths of the galleries is also necessary.

The gas source terms being distributed in all the excavations, localized consideration (reinforcement of supports in the galleries, lining/container in the deposition cells, etc.) is essential.

Explicit consideration of the contrasts in the properties of the different materials present in and around the repository (claystone, damaged zone, backfill, bentonite, concrete) allows for good distribution of flows within the excavations. In particular, a good representation of seals, the main localized fluid head losses for water and gas, is necessary.

Taking into account ventilation during the operation phase as well as exothermic waste allows a better assessment of pressure changes during the first thousand of years after closure.

The calculation code used for the numerical simulations of the hydraulic-gas transient is TOUGH2-MP, chosen by Andra after an analysis of the codes available on the market, internationally recognized as a reference code for two-phase flows in porous media and also used by many of our counterparts. This code allows the parallelization of calculations, it is therefore used on around a hundred CPU cores which represents an optimum in overall calculation time and makes it possible to reduce these times by more than a factor of ten compared to a non-parallelized code, thus increasing the number of simulations possible in sensitivity analyses.

The simulations considered the capabilities of the simulation tools, by the grouping of certain cells by macro-component (grouping of several cells in the mesh).

Andra's contribution to EURAD-GAS task 4.2 follows the precepts described above. It is described in the following chapters.

3.2 The numerical model

3.2.1 The code used

The description below is copied from TOUGH2-MP home page "<https://tough.lbl.gov/software/tough2-mp-software>". The version available at Andra is not the public version that can be uploaded from this home-page, some specific upgrades have been added.

TOUGH2-MP is a massively parallel version of TOUGH2. It was developed for running on distributed-memory parallel computers to solve large simulation problems that may not be solved by the standard, single-CPU **TOUGH2** code. **TOUGH2-MP** implements an efficient massively parallel scheme, while preserving the full capacity and flexibility of the original **TOUGH2** code. It uses the **METIS** software package for grid partitioning and **AZTEC** linear-equation solver. The standard **MPI** message-passing interface is adopted for communication among processors. The parallel code has been successfully applied from multi-core PCs to supercomputers on real field problems of multi-million-cell simulations for three-dimensional multiphase and multicomponent fluid and heat flow, as well as solute transport.

In performing a parallel simulation, the TOUGH2-MP code first subdivides a simulation domain, defined by an unstructured grid of a TOUGH2 mesh, into a number of subdomains using the partitioning algorithm from the **METIS** software package (special [installation instructions](#) for METIS Version 5 can be found in the [User Forum](#)). The parallel code then relies on the MPI (Message-Passing Interface) for its parallel implementation. Parallel simulations are run as multiple processes on a few or many processors simultaneously.

For a typical simulation with the fully implicit scheme and Newton iteration, such as in the TOUGH2 run, the most time-consuming steps of the execution consist of three parts:

- (1) updating thermophysical parameters,
- (2) assembling the Jacobian matrix, and
- (3) solving the linearized system of equations.

Consequently, one of the most important aims of a parallel simulation is to distribute computational time for these three parts. In addition, a parallel scheme must take into account domain decomposition, grid node/element reordering, data input and output optimizing, and efficient message exchange between processors. Each process/processor is in charge of one portion of the simulation domain for updating thermophysical properties, assembling mass and energy balance equations, solving linear equation systems, and performing other local computations. The local linear equation systems are solved in parallel by multiple processors with the [AZTEC](#) linear solver package. AZTEC includes a number of Krylov iterative methods, such as conjugate gradient (CG), generalized minimum residual (GMRES) and stabilized biconjugate gradient (BiCGSTAB). Although each processor solves the linearized equations of subdomains independently, the entire linear equation system is solved together by all processors collaboratively via communication between neighbouring processors during each Newton iteration step.

The numerical scheme of the TOUGH2 code is based on the integral finite-difference (IFD) method. In the TOUGH2 formulation, conservation equations, involving mass of air, water and chemical components as well as thermal energy, are discretized in space using the IFD method. Time is discretized fully implicitly using a first-order backward finite difference scheme. The resulting discrete finite-difference equations for mass and energy balances are nonlinear and solved simultaneously using the Newton/Raphson iterative scheme. All these numerical schemes are adopted by TOUGH2-MP. The parallel code also inherits all the process capabilities of the TOUGH2 code, including descriptions of the thermodynamics and thermophysical properties of the multiphase flow system.

TOUGH2-MP has been tested on IBM and CRAY supercomputers, Linux clusters, Macs, and multi-core PCs under different operating systems. The parallelization of TOUGH2 improves modeling capabilities significantly in terms of problem size and simulation time. The code demonstrates excellent scalability. Test examples show that a linear or super-linear speedup can be obtained on typical Linux clusters as well as on supercomputers. By using the parallel simulator, multi-million gridblock problems can be run on a typical Linux cluster with several tens to hundreds of processors to achieve ten to hundred times improvement in computational time or problem size. The growing availability of multi-core CPUs will make parallel processing on PCs far more attractive.

The current version of TOUGH2-MP includes the following modules: EOS1, EOS2, EOS3, EOS4, EOS5, EOS7, EOS7R, EOS8, EOS9, ECO2N, EWASG, T2R3D, TMVOC, and TOUGH+HYDRATE.

3.2.2 The phenomenological processes taken into account

The phenomenologies implemented in the model are:

- Generalized Fourier law for heat transfert
 - Saturation dependency taken into account
 - Water properties variable with temperature
- Generalized Darcy law for two-phase flow

- Retention curves and relative permeability curves are based on Van-Genuchten/Mualem formulations
- Generalized Fick law for two phase flow
 - Non saturated diffusion coefficient are based on Millington-Quirk formulation
- Henry's law for phase changes

Due to the use of Darcy law, a simple mechanical coupling is integrated in these equations under the form of a compressibility term noted specific storage by the hydraulicians.

Van-Genuchten/Mualem retention and relative permeability curves are adapted to take explicitly into account the gas entry pressure (see Section 3.8 for more details).

The values of the parameters in the base simulation are the one given in the specifications (milestone 61 of EURAD-GAS)

3.2.3 The initial and boundary conditions

For the base case, at repository level, the boundary conditions prescribed in the prescriptions are considered.

The operational phase is also considered according to the specifications.

The gas (hydrogen) and radionuclides (129I and 14C) source terms are implemented as specified.

3.2.4 The mesh

Andra decided to create a mesh reproducing the entire “generic repository”, namely the 3 disposal zones as well as the central zone containing the well towards the surface. As explained in the general chapter (Section 3.1), due to certain limitations of digital codes as well as calculation machines, this implies certain simplifications in the explicit consideration of certain geometric details in the mesh. Nevertheless, Andra's feedback on two-phase calculations during the gas hydraulic transient in underground waste storage facilities made it possible to determine which elements are necessary for a representativeness of the phenomena despite these limitations (Section 3.1).

Figure 3-1 and Figure 3-2 present the division into zones and the naming of the sub-areas of the global mesh.

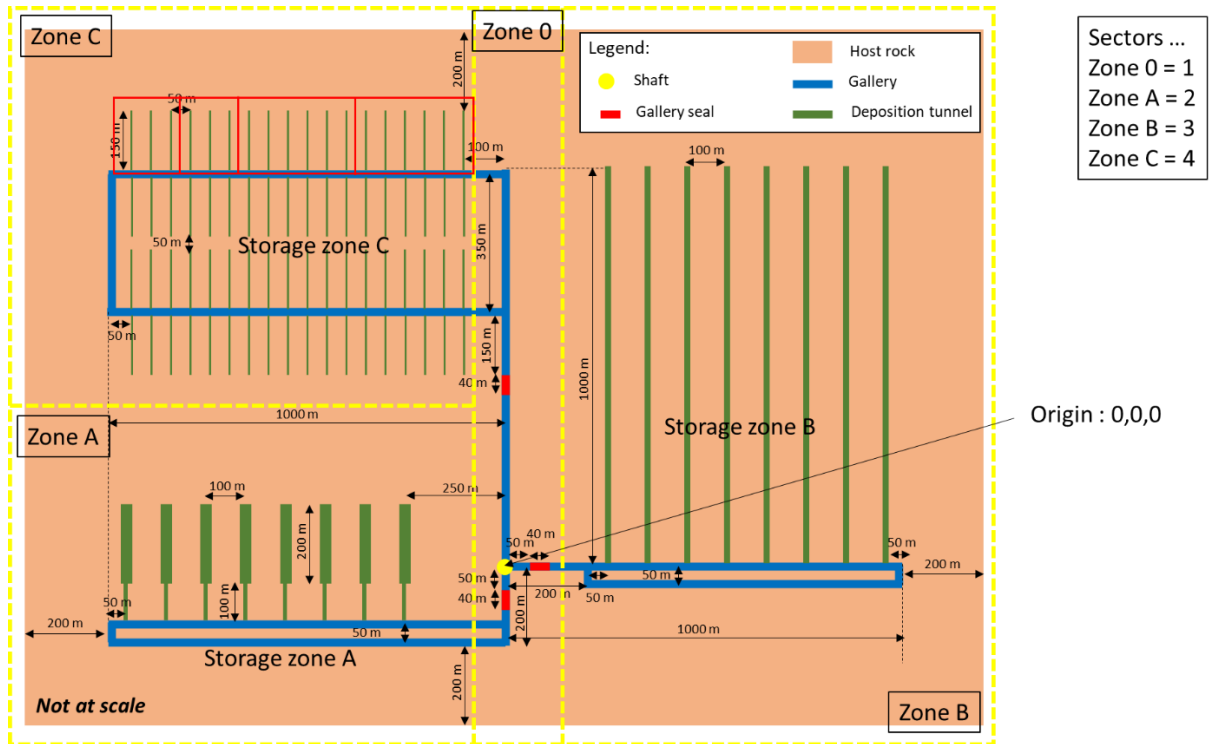


Figure 3-1 Mesh zoning.

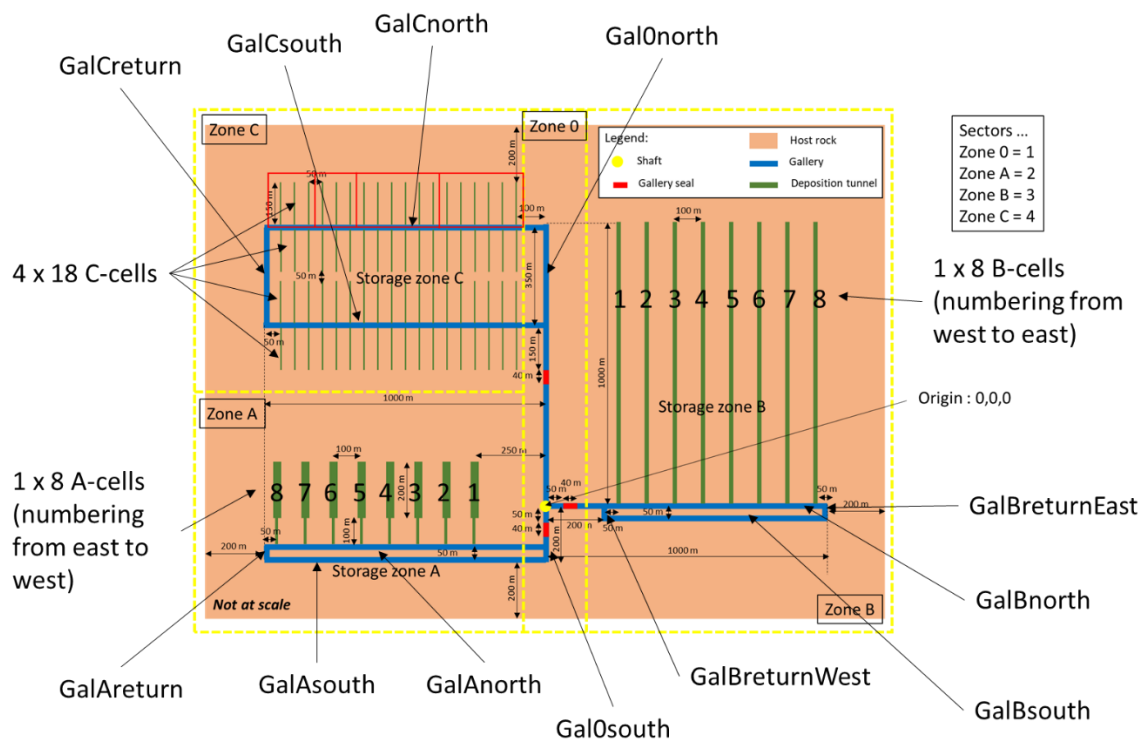


Figure 3-2 Galleries denomination and cell numbering.

The vertical boundaries of the model are the upper and lower limits of the host rock (Figure 3-3).

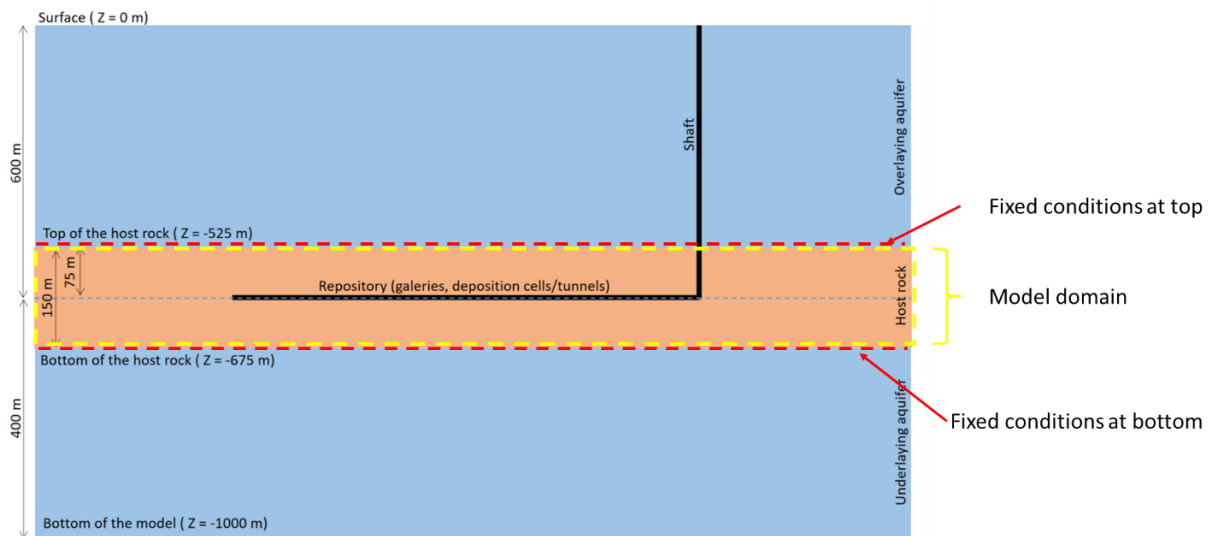


Figure 3-3 Vertical extension of the model.

3.2.4.1 Galleries

A “standard” gallery has an excavated radius of 5m, and a total diameter of 15m (Figure 3-4). These galleries are represented by a square section formed by a core (fill) and bolstered elements (aggregation of concrete and EDZs). The dimensions of these square sections are calculated to respect the volumes (valid for all galleries or cells approximated by square sections). We obtain:

- Square section of the core in embankment: 7.09 m (based on a radius of 4 m),
- Square section of the bolster elements (external dimension of the ZFD): 13.3 m (diameter: 15 m)

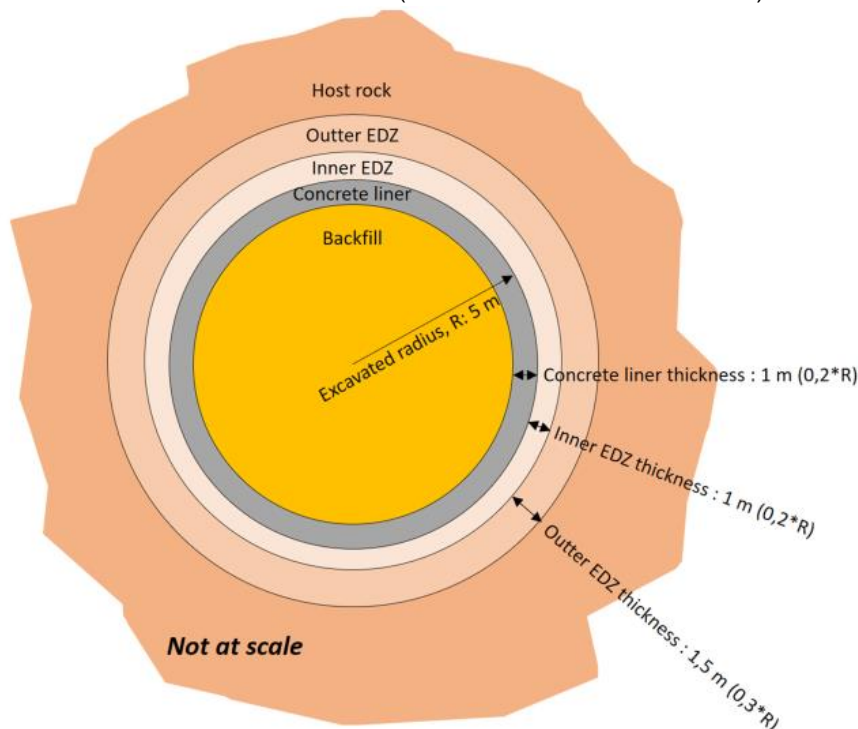


Figure 3-4 Dimensions of a gallery.

3.2.5 Waste A cells

A schematic representation of waste A is shown in Figure 3-5.

These are tunnels of fairly large diameter, in which waste is stacked. Around it, the voids are backfilled. The tunnel is consolidated by a concrete covering, and EDZs are present.

Andra's feedback shows that it is wise to represent the cell in 3D with tunnels approximated by square sections where a core is surrounded by several layers of "miter" elements which are more detailed than in access galleries.

The tunnel section of the A cells is larger than that of the access galleries, which involves specific treatment: a "standard" gallery is first created, then the detailed mesh of the cell is inserted and finally the dimensions are adapted.

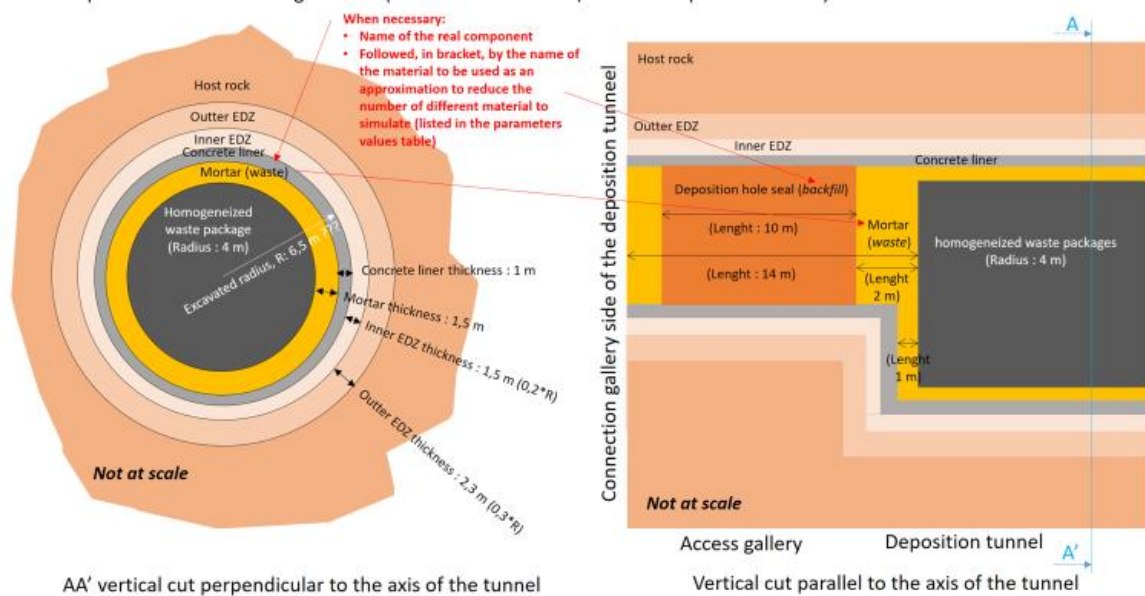


Figure 3-5 Dimensions of a waste A cell

To simplify the geometry, the center of the waste part is aligned with the center of the access gallery (Figure 3-6). The detailed part of the cell begins after sealing (Figure 3-7). For reasons of convenience, a transition element is added to the dead-end side of the cell.

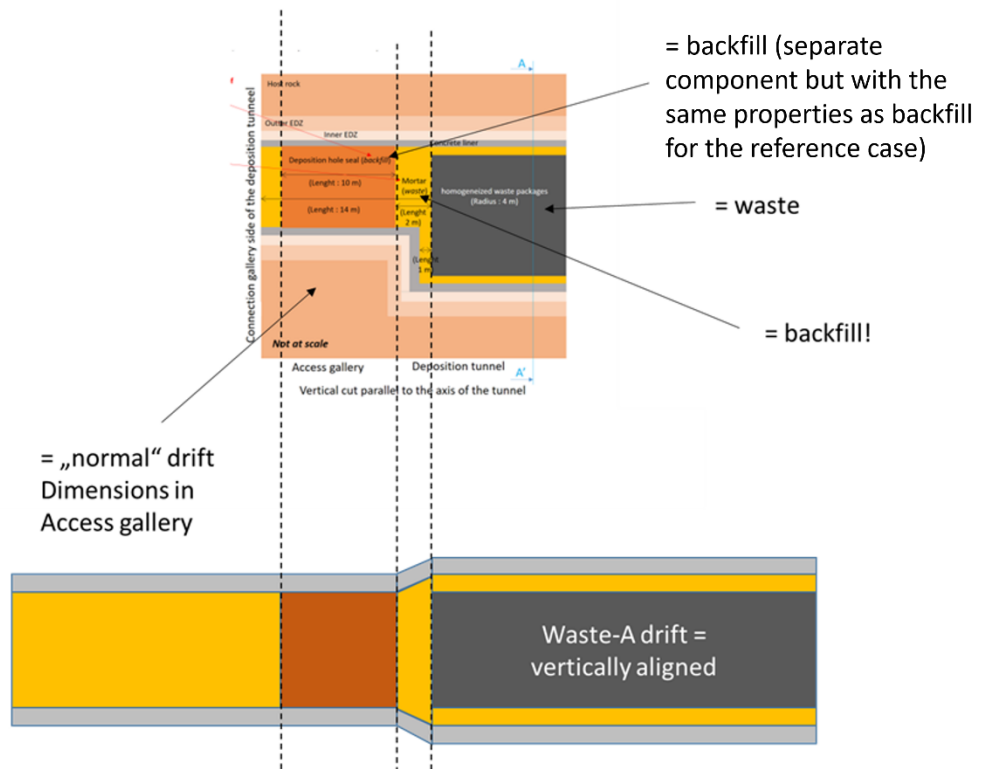


Figure 3-6 Geometry approximation and alignment of waste A cell and its access gallery (EDZ not represented).

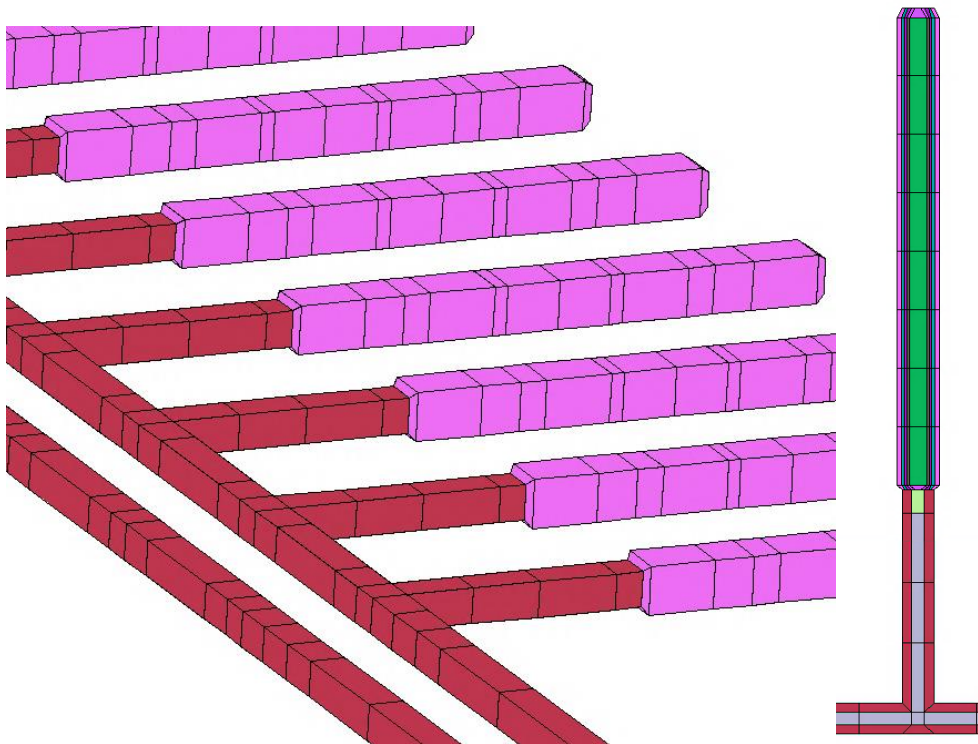


Figure 3-7 zone A mesh. General view and hoverhead view of a cell (right).

3.2.6 Waste B cell

A schematic representation of waste B is shown in Figure 3-8.

Given the relatively large diameter of these cells and the sufficiently large material thicknesses for the “concrete buffer”, the backfill, the covering and the EDZ, a 3D representation with an approximation by a square section was retained.

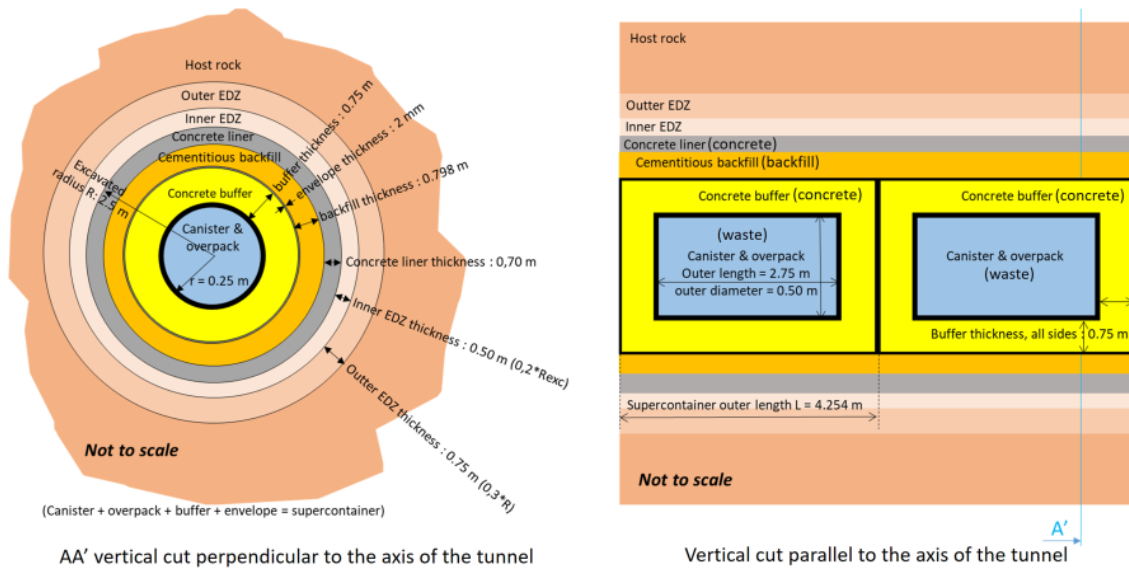


Figure 3-8 Dimensions of a disposal gallery in Zone B.

Figure 3-9 presents the materials explicitly represented in the level of conceptualization retained; the waste (container + over-container), the concrete “buffer” and the backfill are homogenized but the concrete lining of the tunnel and the EDZ are explicit.

The waste (container + over-container) is homogenized in the axial direction.

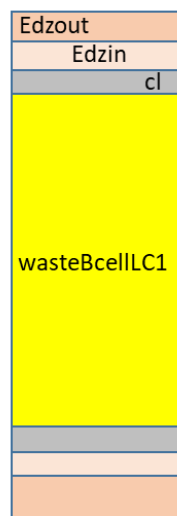


Figure 3-9 Conceptualisation of the different materials explicitly represented in the waste B cell mesh.

The diameter of cell B is significantly smaller than that of the access gallery (external radius of the ZFC: 3.75 m compared to 7.5 m). A change in diameter based on the exterior of the ZFC induces strongly distorted elements (Figure 3-10) as well as a significantly increased thickness of the first mesh layer of the host rock. To avoid this, it was decided to add a layer of host rock around cell B, whose “radial” extension corresponds to that of the ZFD of the access galleries. The assembly at the interface is non-compliant, as for all cells of this type (Figure 3-11).

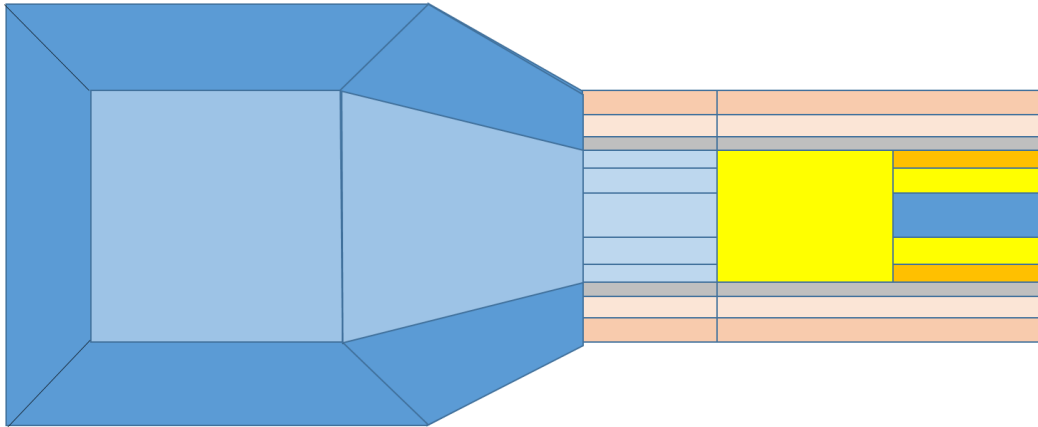


Figure 3-10 « Conform » transition between access gallery and waste B cell; unfavourable situation with distorted elements not implemented.

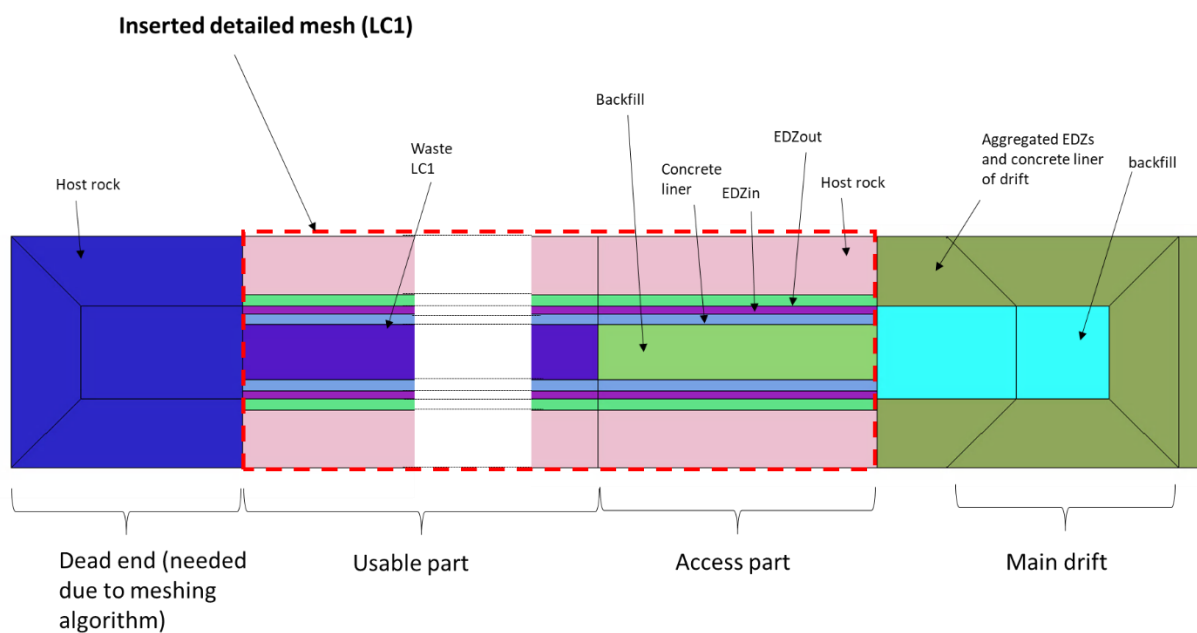


Figure 3-11 Transition at constant diameter between the access gallery and a cell B thanks to a layer of host rock mesh (in pink). The illustration assumes a radius of the gallery of 3m. With a backfill radius increased to 4m, the “backfill” – “aggregated EDZs & concrete liner” limit is aligned with the “EDZOut” – “Host rock” interface (radius 3.75 m) on the cell side by moving a few nodes of the mesh.

3.2.7 Waste C cell

In order to limit the number of elements in the mesh and to be able to represent all of the “generic repository”, it was decided to use “super-cells” which group together several cells supposed to have the same two-phase behaviour. In the repository configuration studied, there are 4 rows (from north to south) of 18 cells each. It was chosen to divide each row into three equal groups comprising 6 cells each which

form the super-cells (Figure 3-12). Thus, despite the grouping of 6 cells into one, it is still possible to distinguish edge effects and potentially different central behaviour.

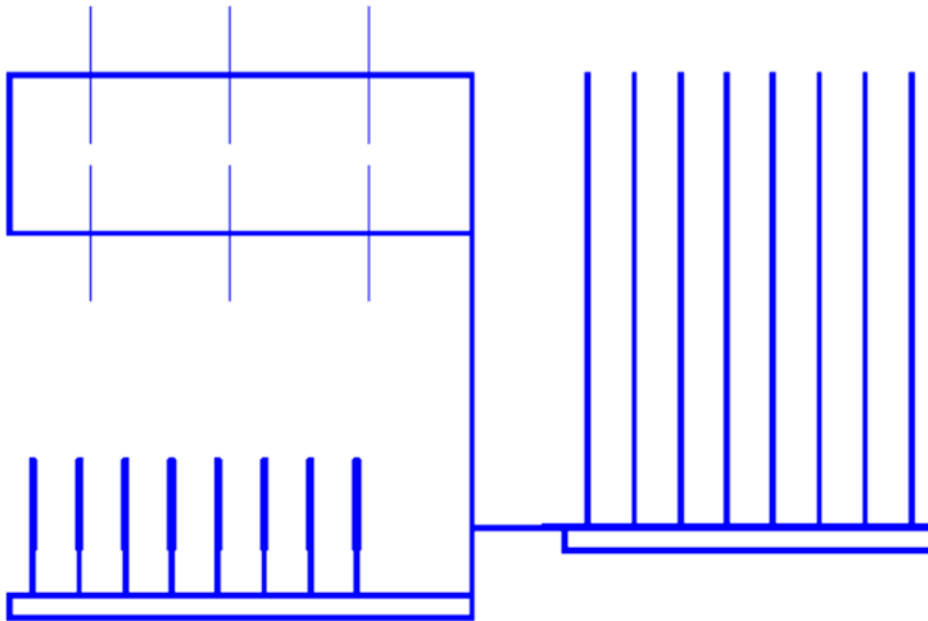


Figure 3-12: detail of the global mesh representing the galleries and the deposition cells implemented; Note the “super-cells” in zone C; only 12 cells in the mesh representing the whole 72 cells.

Note that this possibility of using “macro-components” (super-cells) is linked to the numerical formulation of the calculation code used, the TOUGH2-MP code, which is of finite volume type and whose structure of connections between elements is based only on distances between element centres and exchange surfaces. When constructing the mesh, the “macro-component” mesh is constructed separately and then the connections with the main mesh are adapted to reproduce the right distances and the right exchange surfaces.

A schematic representation of a waste C cell is presented in Figure 3-13. The proposed design is close (but not identical) to that of Cigéo’s HA cells.

Consequently, the conceptualization of axisymmetric 2-D super-cells implemented in the studies carried out for Cigéo is renewed. The definition of the level of conceptualization retained is presented in Figure 3-14 and the resulting mesh Figure 3-15.

By giving the waste hydraulic properties allowing good circulation of the gas linked to the presence of continuous voids at the scale of the cell (not explicitly represented in the mesh), we have a satisfactory homogenization of the circulation of the gas along the cell in the liner.

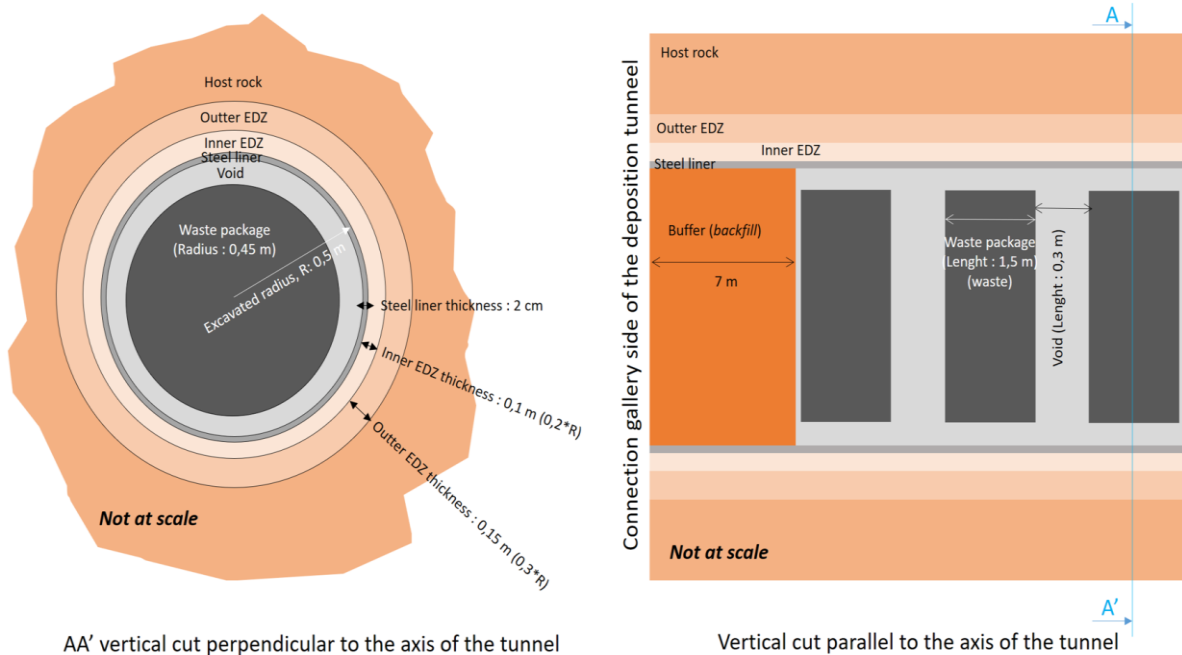


Figure 3-13 Dimensions of a waste C cell.

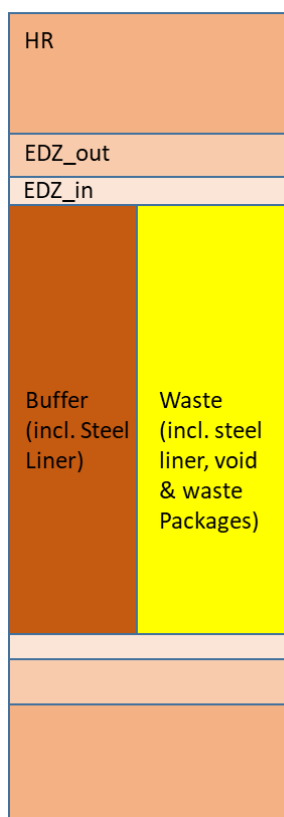


Figure 3-14 Conceptualisation of a waste C cell.

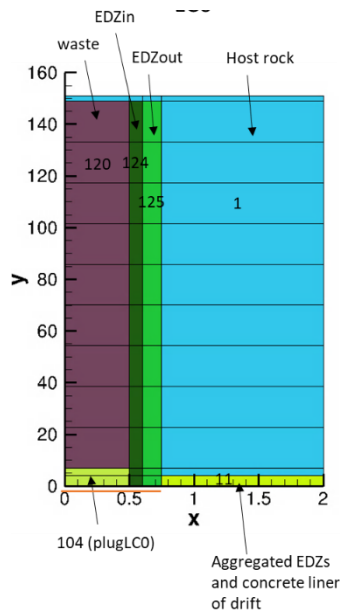


Figure 3-15 Axisymmetric mesh. y = axis of the cell, x : radius from the centre of the cell. The scale ratio between x and y is not respected.

3.2.8 Seals

There are horizontal seals, according to the diagram presented in Figure 3-16, and a vertical seal at the top of the well, according to the diagram presented in Figure 3-17.

The simplifications adopted for the horizontal seals consist of grouping the different grooves in the concrete into one. The discretization adopted imposes a maximum discretization step of 5 meters (Figure 3-18).

The design of the vertical seal is identical to the one of the horizontal seals with one nuance: given the available height and the position of the seal in contact with the roof of the host rock, the transition section towards the "ordinary" gallery is reduced to minimum (Figure 3-19).

Connection gallery seals (horizontal)

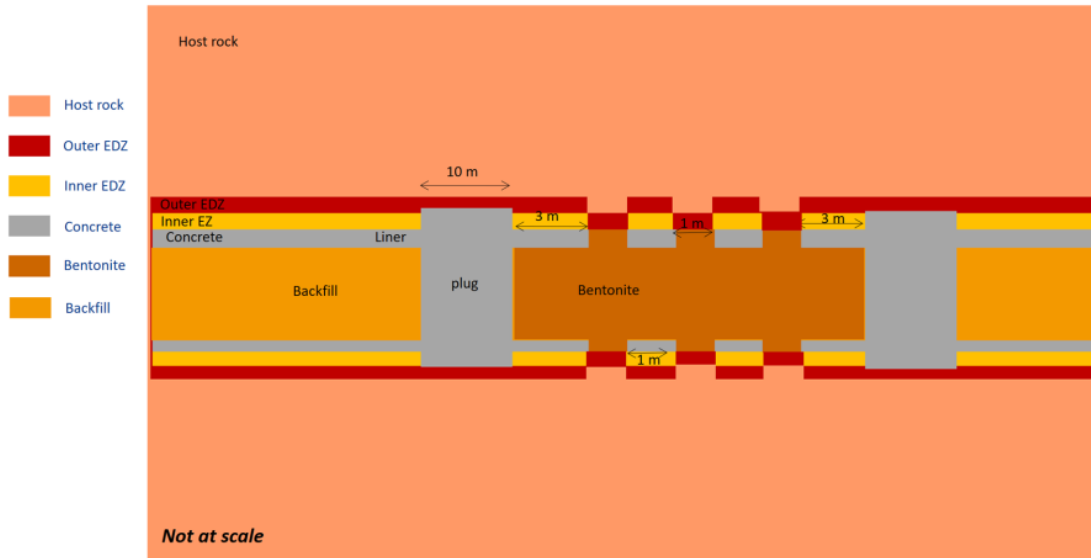


Figure 3-16 Schematic representation of a horizontal seal.

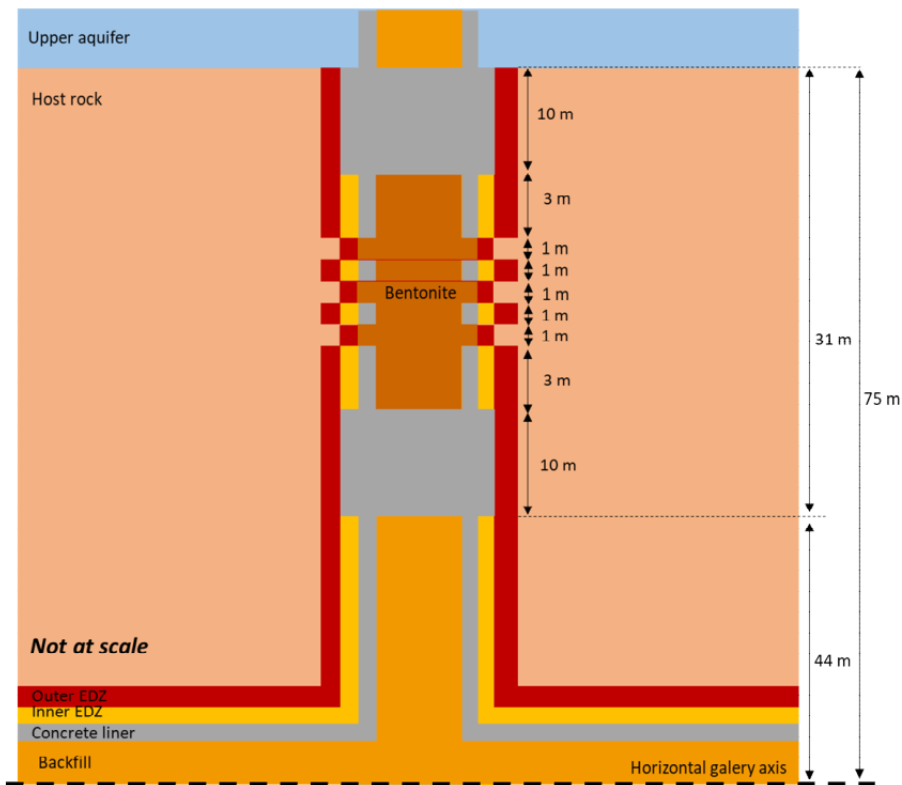


Figure 3-17 Schematic representation of a vertical seal.

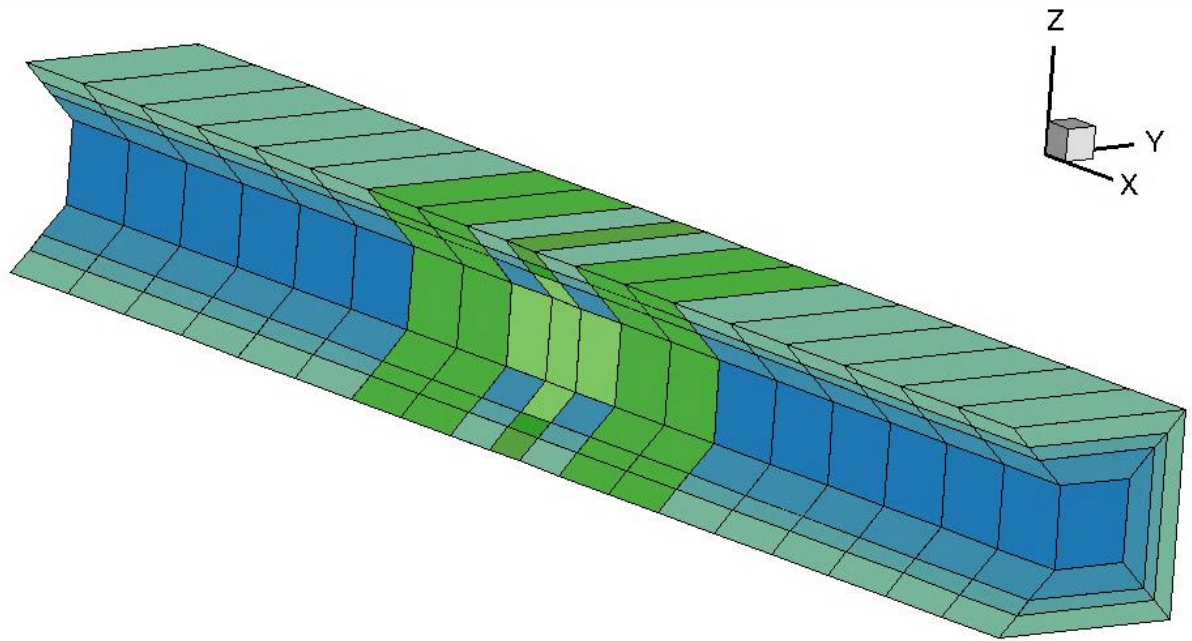


Figure 3-18 Mesh of a horizontal seal with a maximum discretization step of 5 meters. The side mesh layers of the covering and EDZ are hidden on one side to visualize the core.

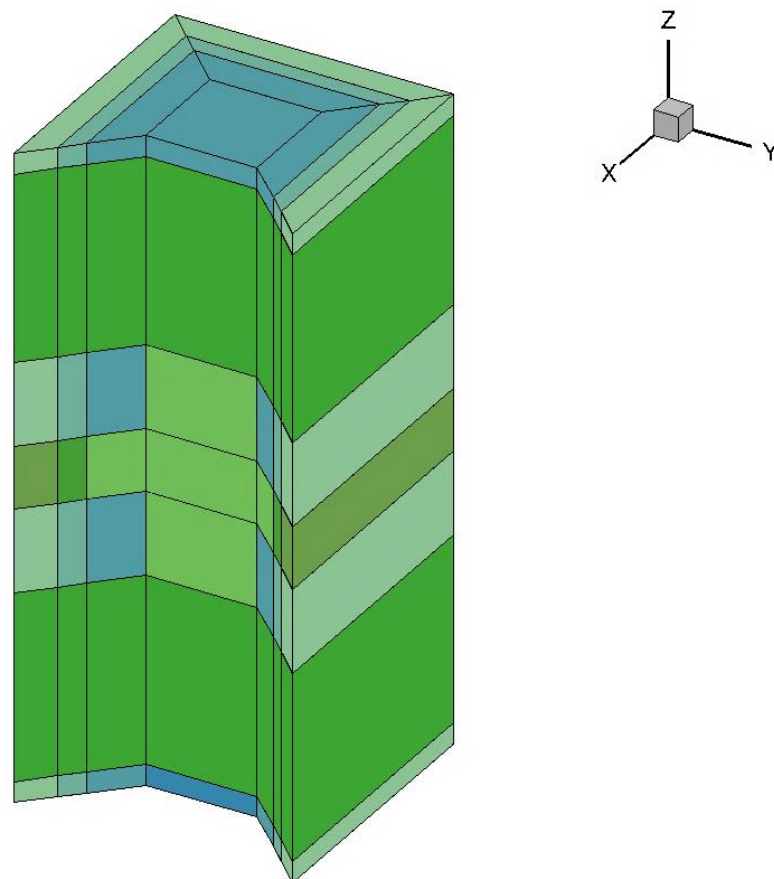


Figure 3-19 Mesh of a vertical seal with a maximum discretization step of 5 meters. The side mesh layers of the covering and EDZ are hidden on one side to visualize the core.

3.3 Base case results

For this base simulation, the entire generic repository was simulated. The descriptions and figures cover gas pressures, flows (gas and water) and the transfer of radionuclides (14C and 129I).

3.3.1 Pressures results

As the main result to be produced is the maximum gas pressure at repository level (to compare with gas pressure fracturing), Figure 3-20 is representing, at each time the maximum gas pressure in each of the three deposition zones. This means that the gas pressure values on the figure are not always positioned at the same location inside a zone but may be located at different points depending on time considered; this gives a rapid overview of the maximum gas pressure inside a deposition zone over time, and the maximum of the three curves is the maximum at repository scale.

In this base case, the maximum gas pressure at repository scale is present in zone A at several thousand years.

Concerning other specific behaviours:

- In zone C, the presence of an early gas pressure increase is representative high exothermal wastes (the other zones are not containing such HLW).
- After several 10 000 years the three zones have more or less the same gas pressure during several 10 000 years; there is an “equilibrium” between gas fluxes (see next sub-chapter) from one zone to the other through the gallery network and the seals.
- At around 100 000 years, gas pressure decreases due to the end of the gas fluxes (all the metal is corroded. This decrease is low; it takes several 100 000 years for the gas pressure to come down to the hydrostatic water pressure. After several 100 000 years the repository is completely resaturated.
 - The gas pressure decrease is very a low process as the remaining gas has to dissolve in the surrounding host rock water which is dissolved gas saturated. For new gas (H₂) molecule to dissolves it is necessary that already dissolved gas molecule move away from the dissolution zones (around galleries and deposition cells), and as the dissolved gas diffusion is low, this takes very long time.

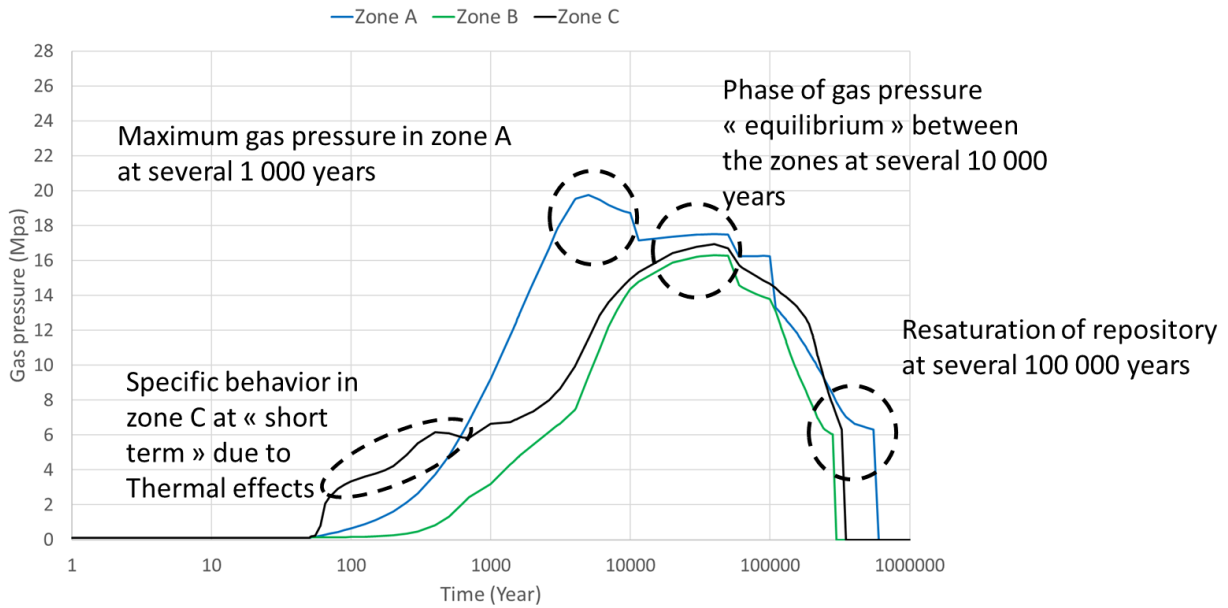


Figure 3-20: Evolution of maximum gas pressure in the 3 deposition zones of the generic repository

Focusing at the time of maximum gas pressure in the repository (Figure 3-21), shows that zone A is in overpressure compared to the other zones (which was already seen in the pressure evolution with time), but also that gas pressures are more or less constant at zone scale; This is mainly due to:

- “High” permeable backfill and EDZ continuous at zone scale implying homogenisation of pressure at this scale.
- “low” permeable seals between zones implying potential contrasts of pressures during transient periods (increase or decrease of pressure).

Figure 3-21 also shows that the gaseous hydrogen stays mainly in the excavation network; the host rock is hardly desaturated because of:

- A high gas entry pressure implying that gas preferentially stays in the galleries network.
- A much lower permeability than the EBS (especially backfill) implying that gas preferentially moves inside the galleries.

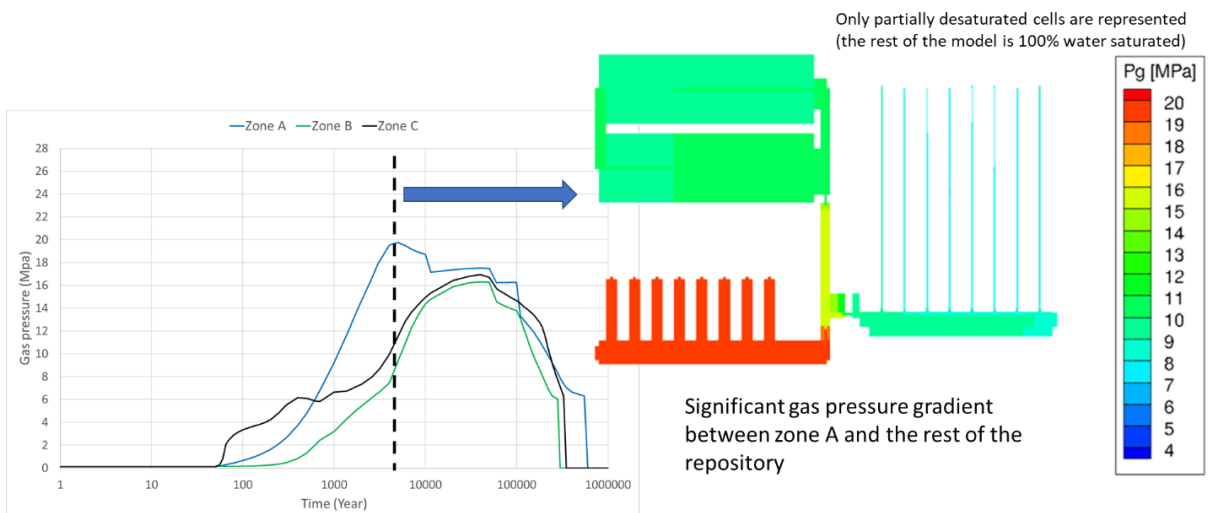


Figure 3-21: Gas pressure distribution in the repository at maximum gas pressure

3.3.2 Flow results

The gas overpressure of zone A compared to zone B and C implies gas fluxes from this zone toward the two others at around several thousand years after repository closure (Figure 3-22). At the same time part of the gas flux out of zone A is escaping the repository by the shaft. This becomes also the case after 10 000 years for zone B and C. Gas fluxes through the shaft toward the upper aquifer are lasting up to 100 000 years; they became null well before repository complete resaturation as gas pressure decreases and cannot overcome the overlaying aquifer pressure, additionned by the gas entry pressure in the seal core, anymore.

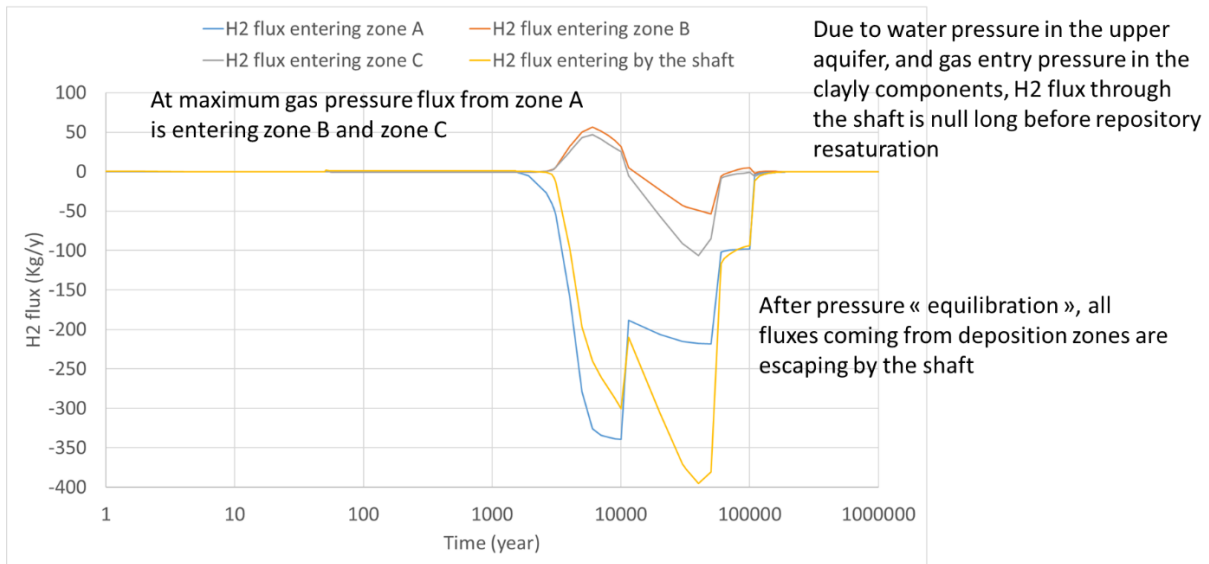


Figure 3-22: Gaseous hydrogen fluxes along the gallery's axes

On the total duration of the two-phase flow transient, the total gas flow escaping the repository by the shaft (Figure 3-23) represents 60% of the total production of the repository; this means that 40% of the gas produced in the repository has been dissolved and has moved under dissolved form toward the upper and underlying aquifers (or is still « trapped » in the host rock).



Figure 3-23: Gas flux entering the shaft toward the upper aquifer

Coming to water fluxes along the galleries (Figure 3-24), they are maximal just after repository closure around the seals; for the zone seals (at repository level) this is due to a reequilibrium between the capillary pressure inside the seal core which is much more important than in the surrounding backfill; seal bentonite core is sucking water from the backfill. Concerning the shaft seal the water fluxes are coming from the upper aquifer resaturating this seal.

After around 1 000 years, the seal cores are quite resaturated (water saturation around 90% - 95%) and the fluxes are less important and are representative of the increase of gas pressure in the deposition zones implying a longitudinal movement of water.

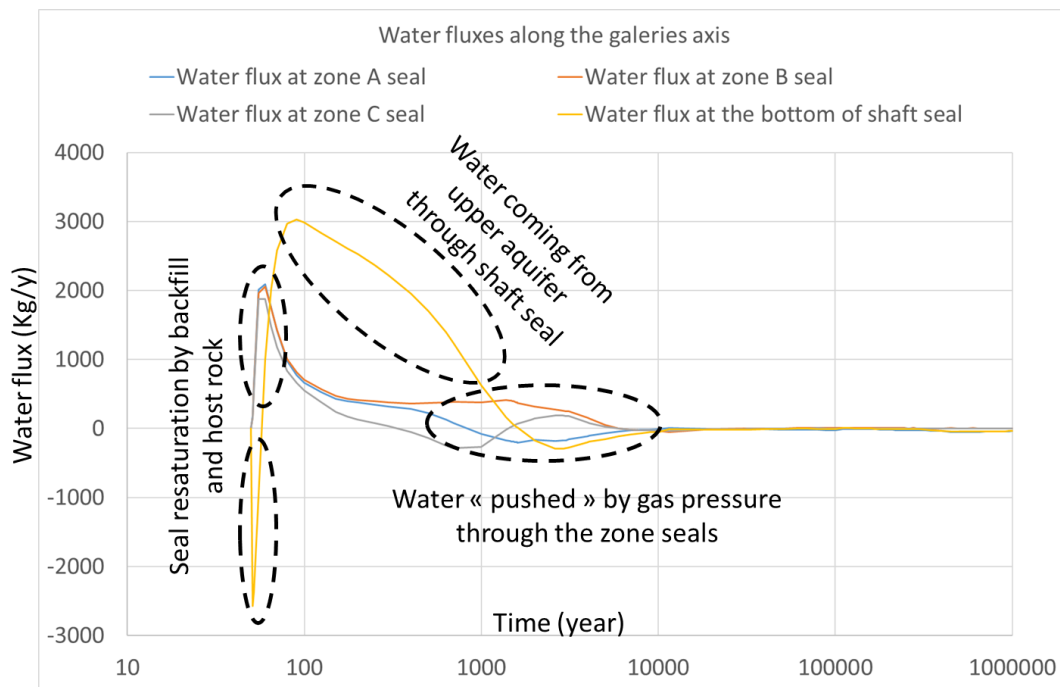


Figure 3-24: Water fluxes along the galleries axes

This “pushing” effect of the gas on the water along the galleries axes is real but is negligible compared to the other water fluxes in the repository (Figure 3-25). The total (at repository scale, over the whole length of the gallery’ network) water resaturation fluxes, coming radially from the host rock, is huge compared to longitudinal fluxes along the galleries; it is maximal just after repository closure and stays very significant for several 100 years. After this time the gas pressure increase inside the galleries and deposition cells implies a small desaturation of the repository; radial water fluxes become negatives. During the same period (from 1 000 years to 10 000 years) the longitudinal water fluxes linked to the pushing effect of gas on water are several orders of magnitude lower.

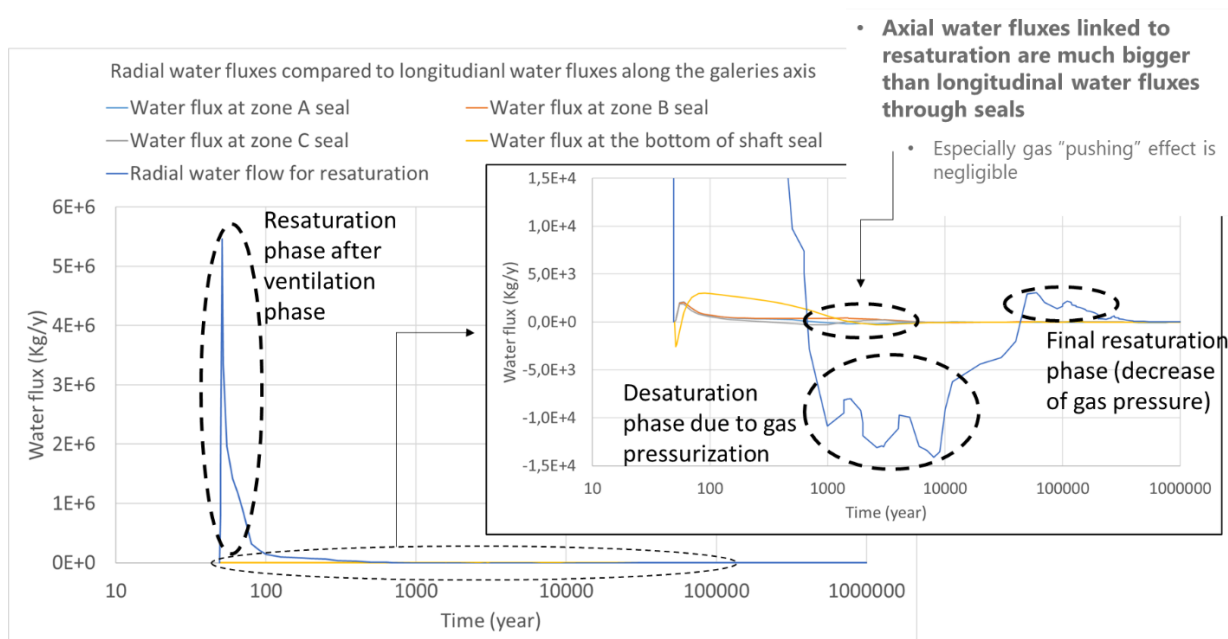


Figure 3-25: Radial fluxes compared to longitudinal water fluxes along the galleries axes

3.3.3 Radionuclides results

Rem: the values of ^{14}C and ^{129}I prescribed for zone A in the generic repository seem to be several orders of magnitude too high compared to values generally assumed for real repositories. Thus, the descriptions below should only be viewed as qualitative. For this reason, the sensitivity analysis described in the following chapters will be focused on zone B and C, not on zone A.

Zone A is the only one deposition zone containing ^{14}C . Due to its Henry coefficient, this radionuclide can be partially under gas form and partially dissolved. The generation rate of ^{14}C is much lower than the one of H_2 (generated by corrosion of the metal present in the repository), thus the gaseous part of ^{14}C is migrating along the bulk gas phase generated by H_2 , mainly by convection. ^{14}C is supposed to be 100% labile, which means that all the mass present in zone A is available for migration at repository closure. Due to the representative time for H_2 gas phase to build up and the $\frac{1}{2}$ life of ^{14}C , the maximum ^{14}C flux toward the shaft is around several 10 000 years (Figure 3-26). At this time a small part of this gaseous radionuclide is also migrating toward zone B and C, these zones being underpressured compared to zone A (convection) and containing no ^{14}C (diffusion). After 10 000 years ^{14}C fluxes are decreasing rapidly linked to the $\frac{1}{2}$ life of this radionuclides (around 5 000 years).

Note that if, in safety analyses for example, ^{14}C is supposed to migrate totally under dissolved form it will migrate much more slowly (than under gaseous form) toward the upper aquifer. Thus, under this assumption (water saturated flows) ^{14}C is not, or hardly, arriving at the upper aquifer.

Concerning ^{129}I , all the mass is dissolving in the surrounding water around the wastes (there is no ^{129}I under gaseous form). This means that it migrates at the same velocity as water, much more slowly than gas. The arrival at shaft begins after several 100 000 years and is maximum just before 1 000 000 years (Figure 3-27).

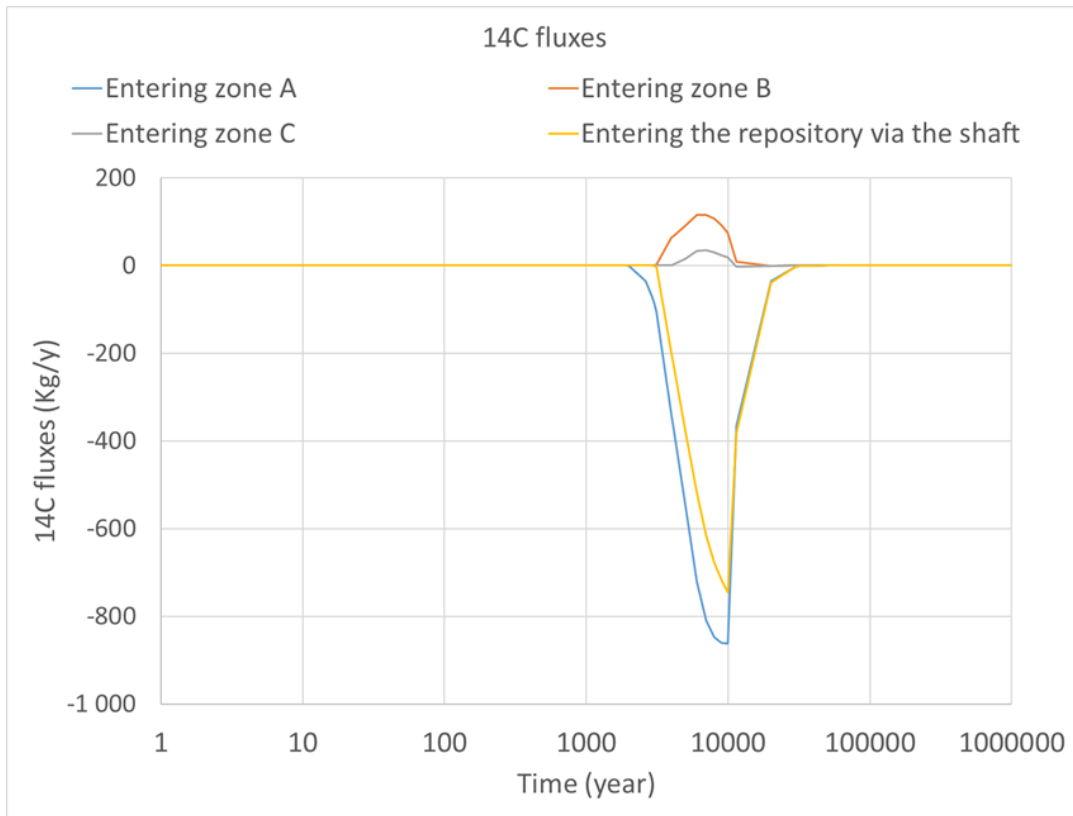


Figure 3-26: 14C fluxes at deposition zones (through zone seals) and shaft level

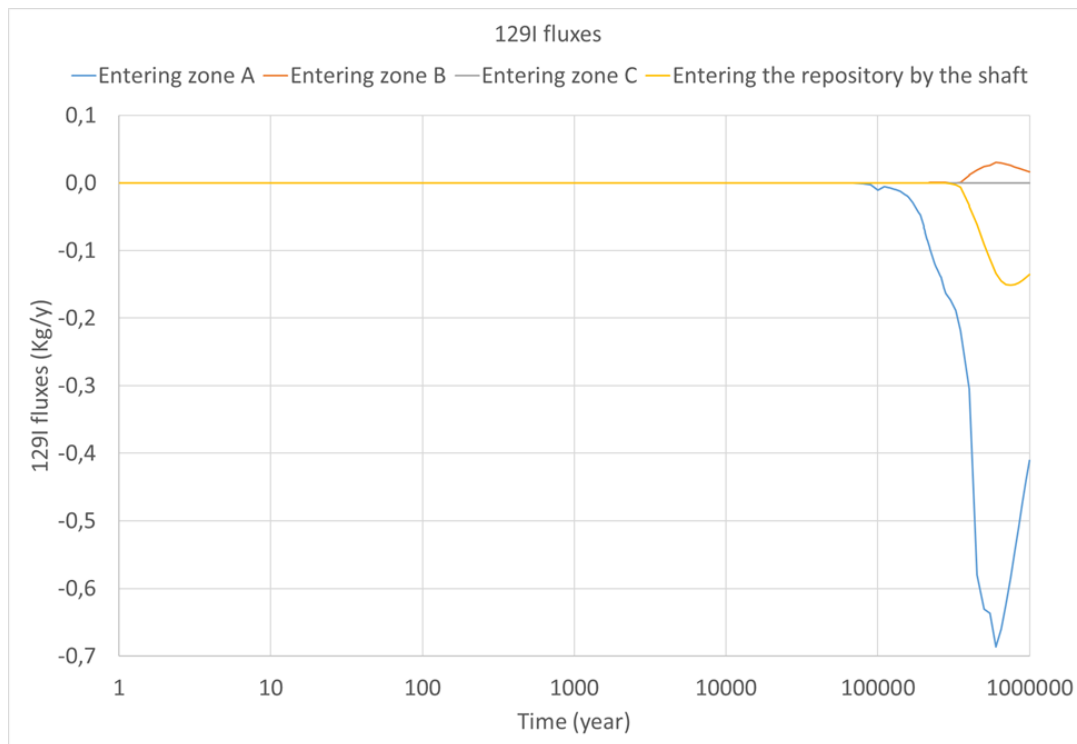


Figure 3-27: 129I fluxes at deposition zones (through zone seals) and shaft level

3.4 Sensitivity analysis

The main aims of EURAD-GAS concerning Task 4 being the evaluation at repository scale of gas pressure and its potential impact on host rock integrity and radionuclides migration, sensitivity analysis will focus only on these two estimations (i.e. there will be no water fluxes, gas fluxes or saturation description in this sensitivity analysis chapter).

As mentioned above, as some variables for zone A present in the specifications seems not coherent with “real repositories” (i.e. could lead to misleading conclusions), no specific sensitivity on this zone will be produced.

3.4.1 Sensitivity analysis on model extension

The base case is a model at full repository scale including all deposition zones (A, B and C) and the central zone integrating the shaft. The gas produced in the repository, whatever the production zone, is thus able to migrate at the whole repository scale and dissolve along the whole network of galleries, even in a deposition zone in which it was not produced (i.e. gas produced in zone A migrating partially toward zone B and C because zone A is overpressured compared to the two others), ending eventually in the upper aquifer by migrating through the shaft.

In this chapter models at zone scale will be produced for zone B and zone C. This is done by replacing all the materials in the excavations of the other zones by host rock material (Figure 3-28) and assuming no heat/gas/radionuclides production in the other zones. This “trick” enables to use the same mesh for all the calculations.

In addition to this, the “one zone” models were run assuming the availability of the shaft (possibility for gas and radionuclides to escape through the shaft) or not (the shaft is also replaced by host rock and gas and radionuclides cannot escape via this route; they can only dissolve and migrate under dissolved form toward the upper and under aquifers).

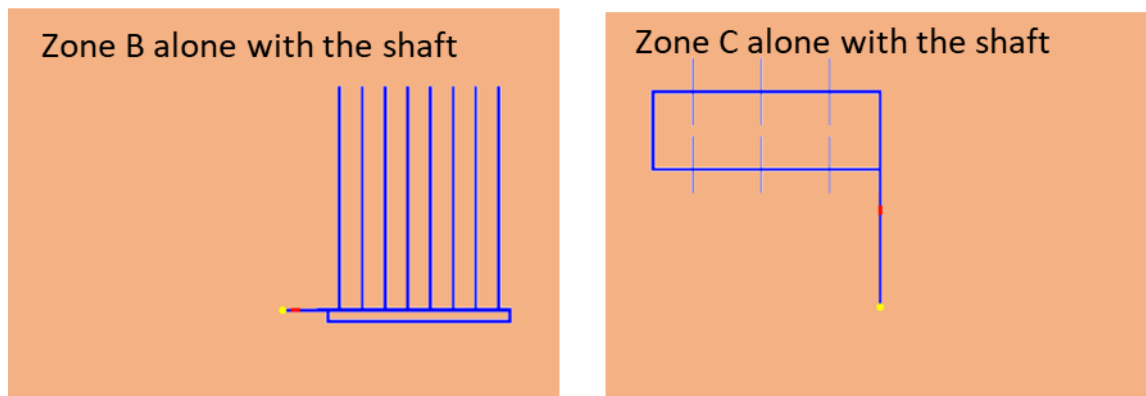


Figure 3-28: representation of the models including only one zone; same global extension as the total generic repository model but host rock replace the other zones

Figure 3-29 shows the maximum gas pressure evolution with time in zone B for the three simulations (total repository, stand-alone zone B with shaft, stand-alone zone B without shaft). Reducing the model extension has several implications:

- Only the gas generated in zone B is considered
 - There is no possibility for the gas to pass from one zone to another. In case of zone B this implies a lower initial increase of pressure as no gas can come from zone A as in the global model.
- In case of no shaft model, the hydrogen cannot escape the repository under gaseous form; it has to dissolve, this implies an increase of the maximum gas pressure

For zone B alone with a shaft the maximum gas pressure is thus lower than in the global model. But if no shaft is assumed, the maximum gas pressure is several MPa overestimated.

In terms of resaturation time, assuming no shaft increases significantly the end of the two-phase flow transient phase as all the gas produced in the zone has to dissolve before complete resaturation; no gas can flow out of the system.

For zone C the conclusions are exactly the same (Figure 3-30).

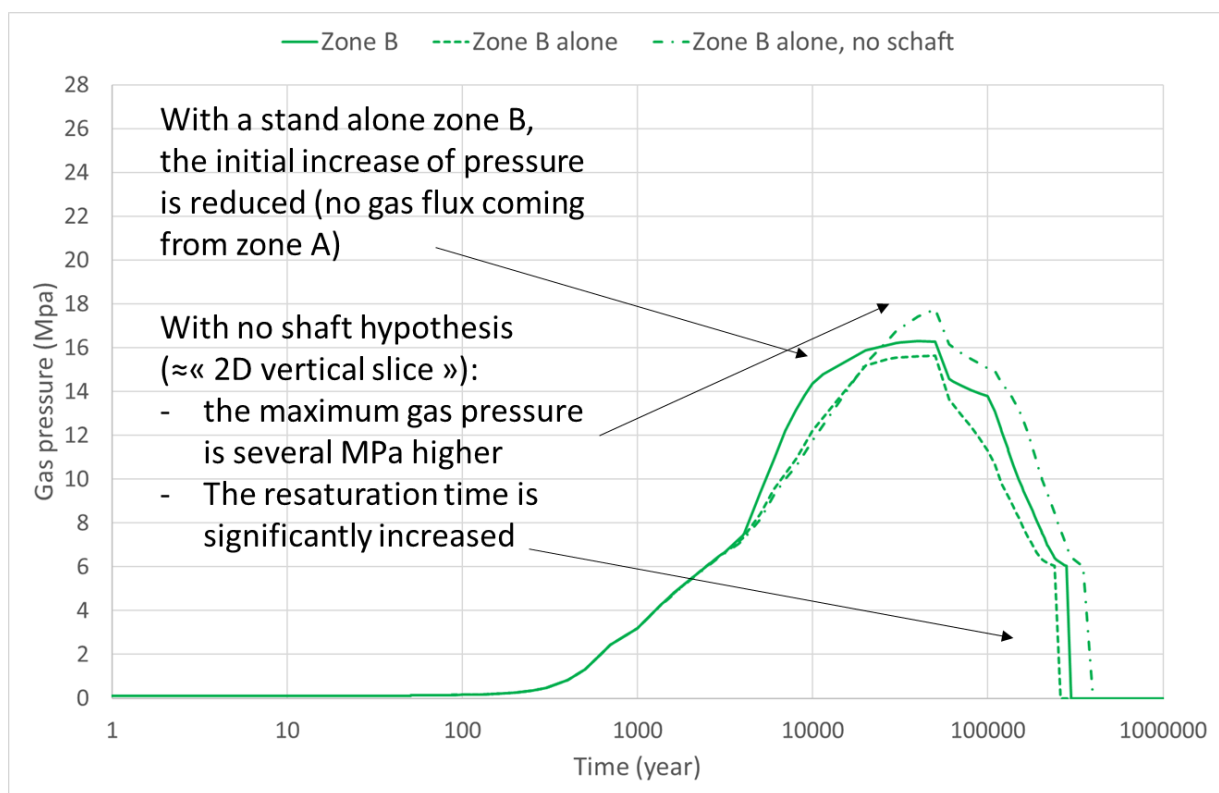


Figure 3-29: Evolution of gas pressure in zone B supposed alone, with or without shaft

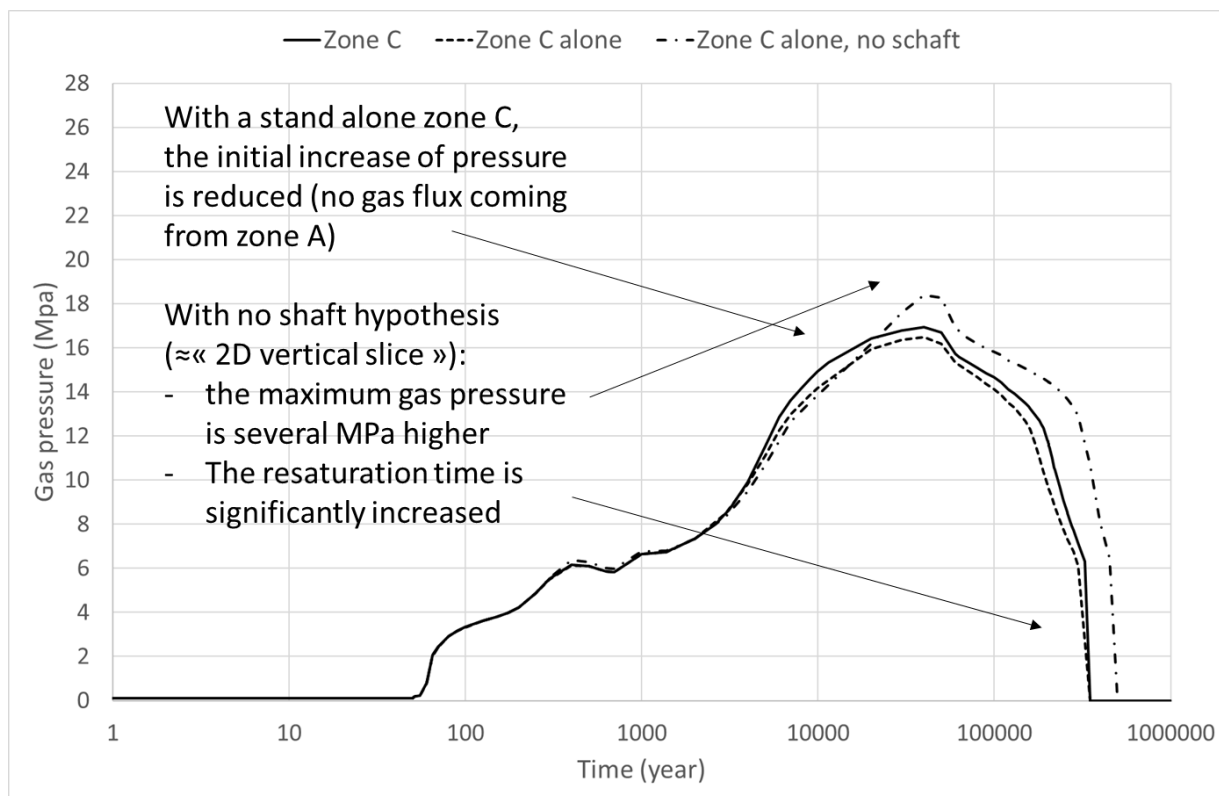


Figure 3-30: Evolution of gas pressure in zone C supposed alone, with or without shaft

3.4.2 Sensitivity on gas source terms

Several sensitivities considering a reduction of the gas source terms were done:

- On stand-alone zone C and zone B models, with and without shaft
- By reducing by a certain amount all the gas sources terms; a reduction factor of 2 (50% percent of the prescribed gas source terms for all terms and at each time step) and 4 (25% percent of the prescribed gas source terms for all terms and at each time step) were used

For stand-alone zone B model with a shaft results are presented in Figure 3-31. The maximum gas pressure is significantly reduced when the gas source terms are also reduced; for a reduction factor of 4 the reduction is very significant, but even with a reduction factor of 2 the reduction in estimated maximum gas pressure is of the order of one (or more) MPa.

The same results are valid for zone C stand-alone model with a shaft (Figure 3-32).

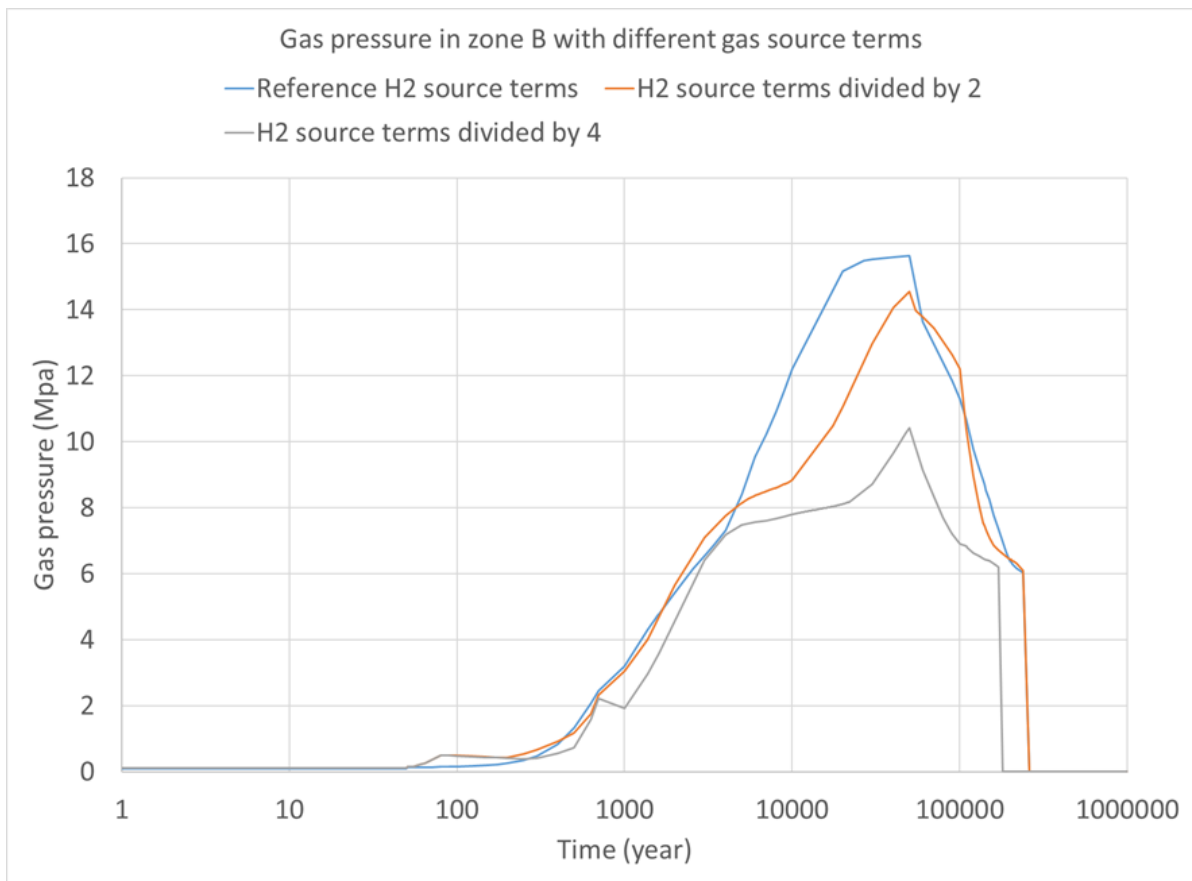


Figure 3-31: Gas pressure in zone B stand-alone model with a shaft for different gas source terms

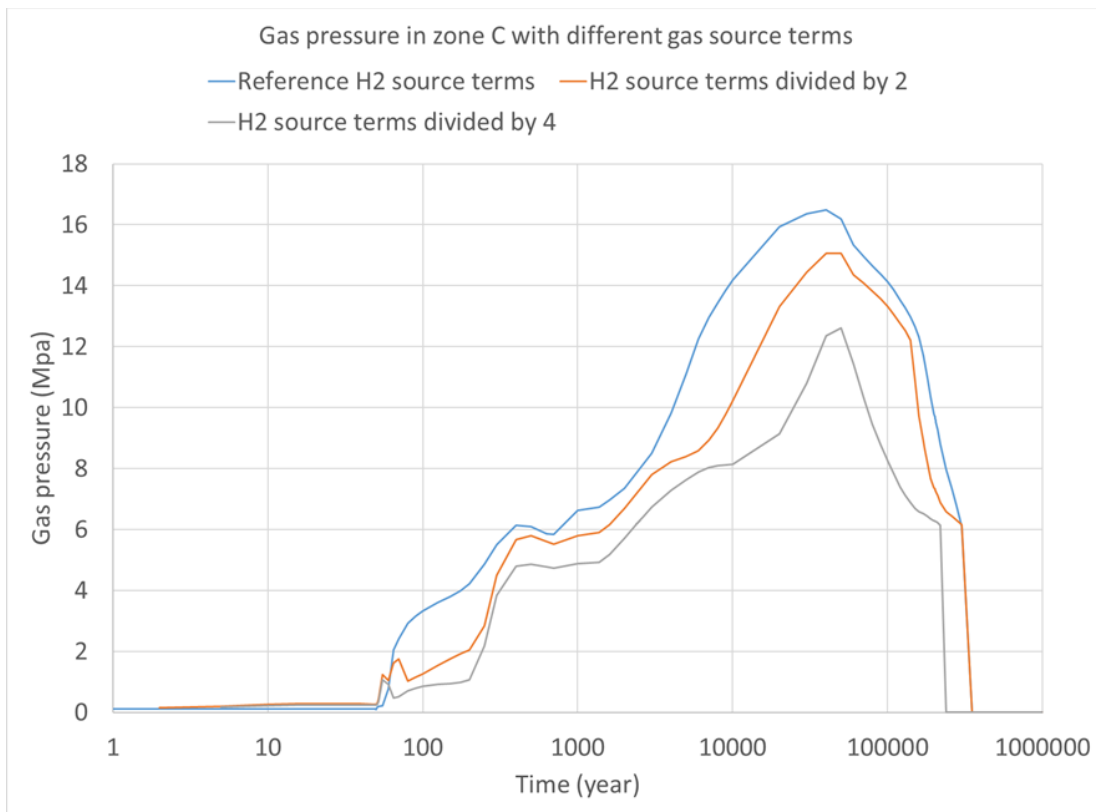


Figure 3-32: Gas pressure in zone C stand alone with a shaft model for different gas source terms

The same kind of simulations were done with models at zone scale but supposing no shaft (i.e. no escape route for gaseous hydrogen toward the upper aquifer). Figure 3-33 presents the results compared with the model assuming a shaft or zone B stand-alone model.

The global behaviour with or without shaft in terms of evolution with the gas source term is the same; the less important the gas source term, the less important the maximum gas pressure.

Something significant to notice is that for sufficiently low gas source terms, the estimated maximum gas pressure is very similar in the model with or without shaft. This is due to the fact that when the gas source term is low enough, all of the produced gas can dissolve inside the zone; due to the presence of the zone seal, acting as a bottleneck for gas migration, no (very few) gaseous hydrogen migrate through the seal toward the shaft.

A corollary is that if gaseous hydrogen does not pass through the shaft toward the upper aquifer, the gaseous ¹⁴C does not pass either.

The conclusions are the same for zone C stand-alone model (Figure 3-34).

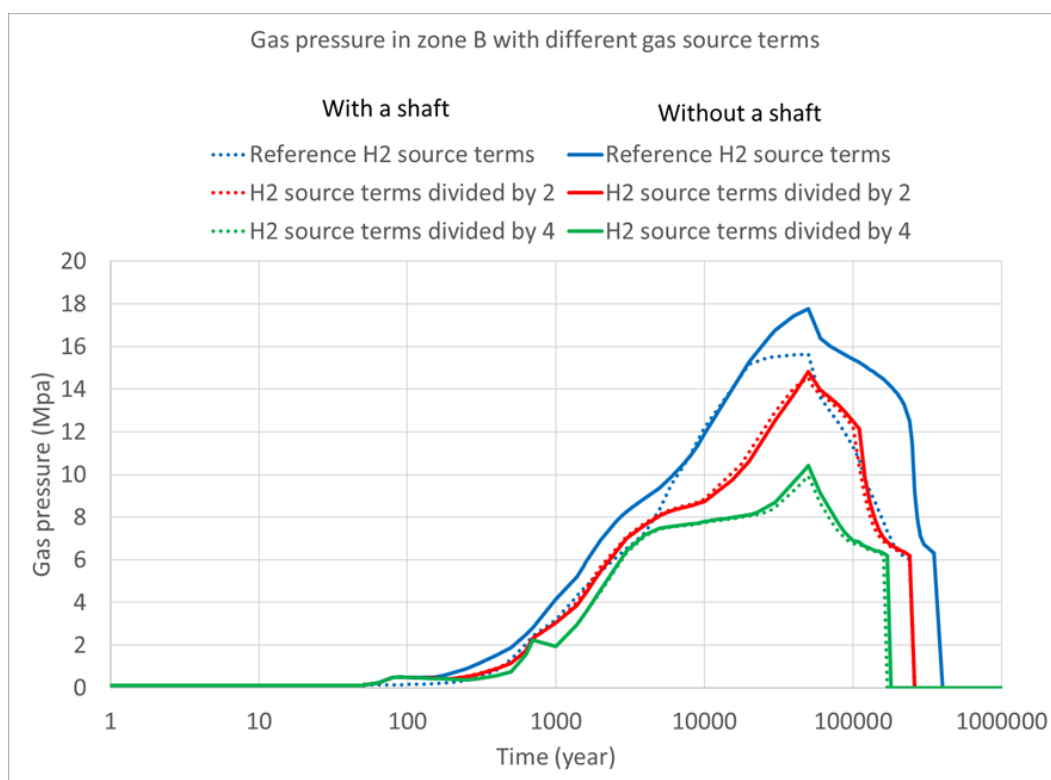


Figure 3-33: Gaz pressure in zone B stand-alone model with and without shaft for different gas source terms

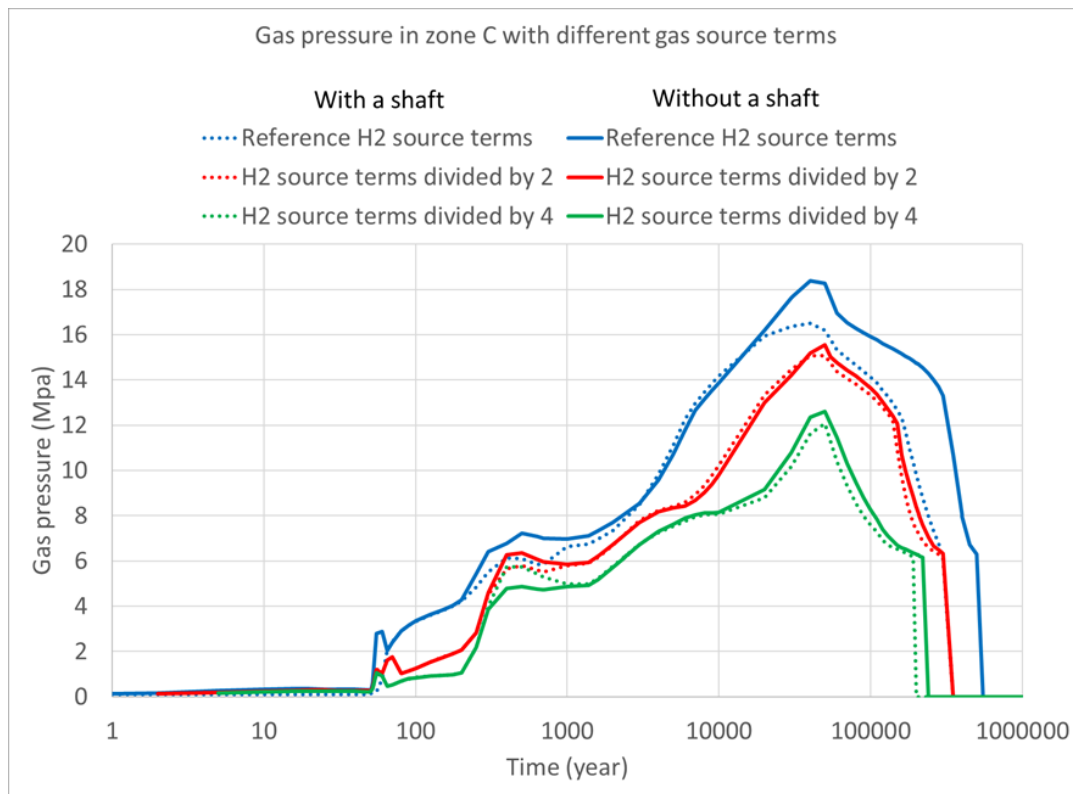


Figure 3-34: Gas pressure in zone C stand alone model with and without shaft for different gas source terms

A reduction of a factor 4 for the gas source terms was also applied on the global model (i.e. including zone A, B and C); as in zone A the gas source terms are significantly higher than in the other zones, this reduction factor is not enough to cancel out the gas flow through the shaft toward the upper aquifer; However, the reduction of the gas flow through the shaft is significant and only 15% of the total produced hydrogen (in the total model, including zone A, B and C) is passing under gaseous form toward the upper aquifer (in the total model with the prescribed gas source terms this was 60%); this means that 85% of the total produced hydrogen in the global repository is dissolving during the migration in the host rock waters. This reduction of the gaseous hydrogen toward the upper aquifer implies a similar reduction of the gaseous ^{14}C flow as well.

For this simulation (reduction of a factor 4 of the gas source terms in the global model), a comparison of the dissolved ^{129}I (^{129}I cannot migrate in gaseous form in the physicochemical environment of an underground repository in a clay host rock) flow toward the upper aquifer with prescribed gas source terms was done (Figure 3-35). This comparison shows that by reducing the gas source terms, thus increasing the over whole water saturation and reducing the total resaturation time of the repository, the dissolved ^{129}I fluxes toward the upper aquifer through the shaft are increasing and the first arrival time is decreasing.

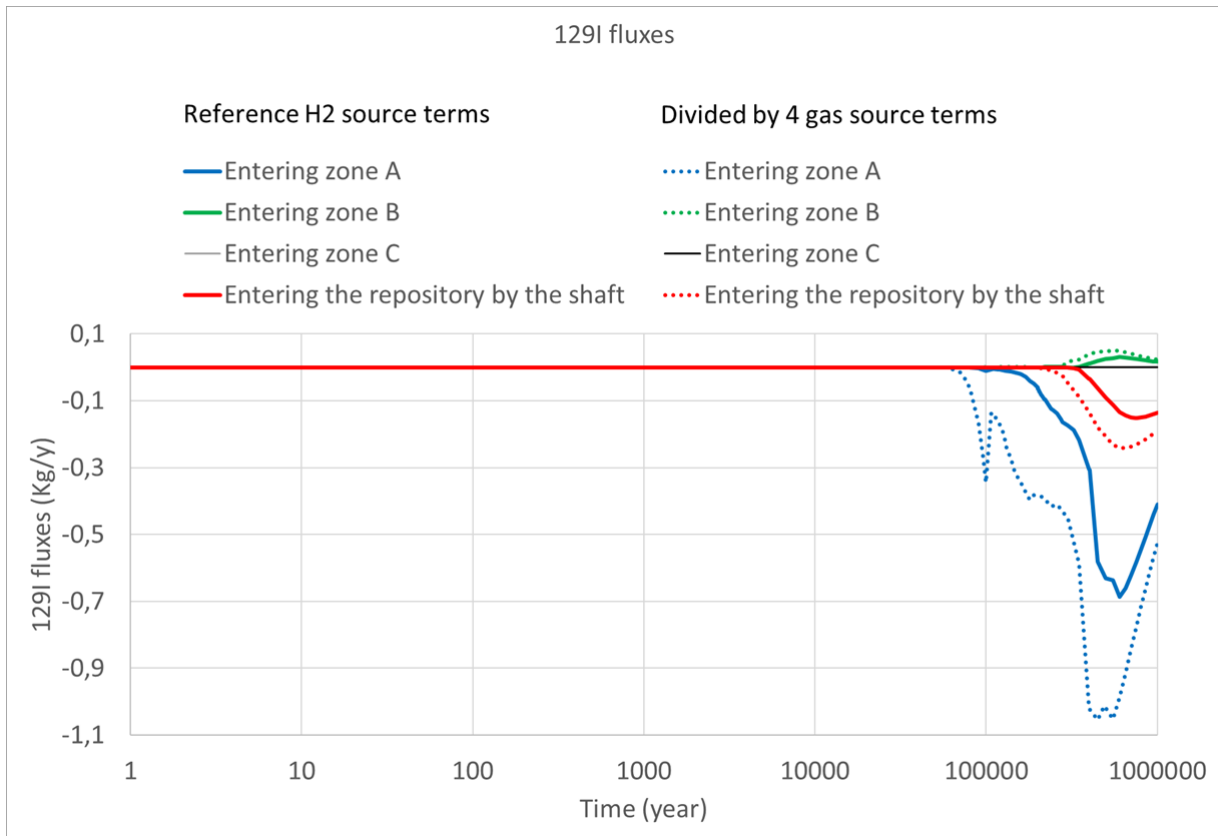


Figure 3-35: 129I fluxes at different locations in the global model for different gas source terms

Concerning the impact of the gas source terms on the migration of 14C, Figure 3-36 presents the fluxes at shaft for different values ranging from 25% to 120%. The impact is significant; the maximum flux being reduced from more than a factor 10 when passing from 120% to 20%. Note that in the tested range, this maximum flux is linearly linked to the reduction factor which could be interesting to evaluate rapidly the impact of a reduction factor on metal present in the repository linked to an optimization of the concept and flux of 14C arriving at the upper aquifer (everything been the same otherwise).

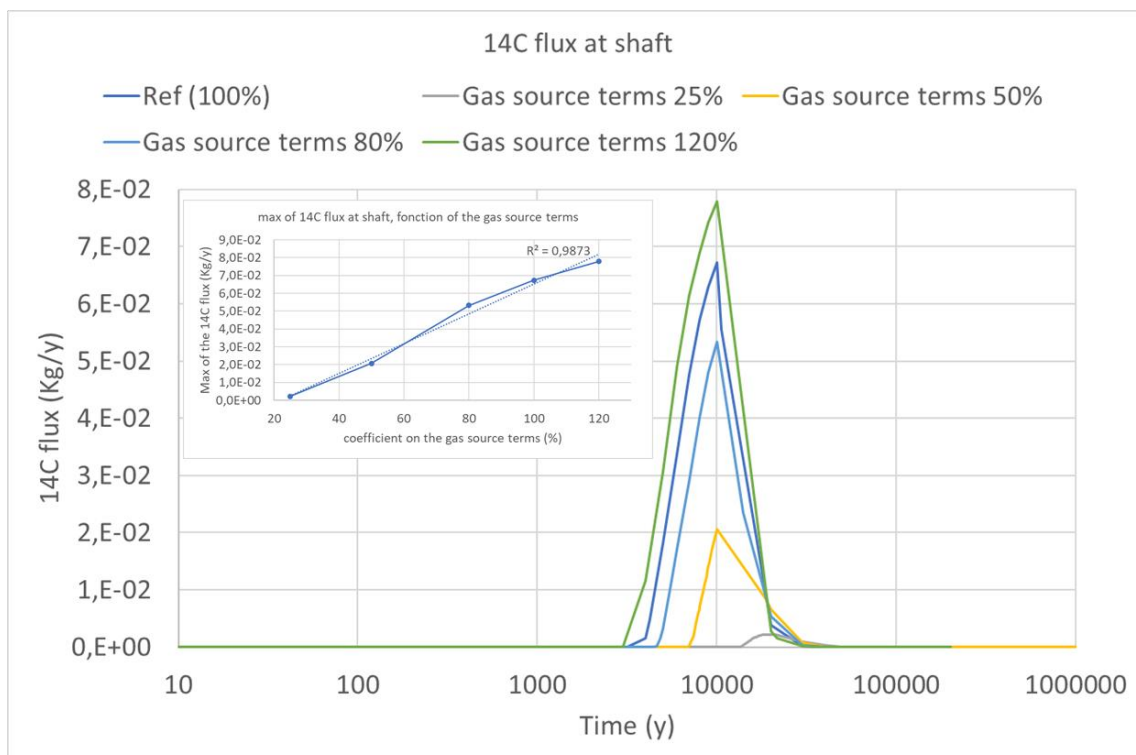


Figure 3-36: 14C fluxes through the shaft in the global model for different gas source terms

3.4.3 Sensitivities on parameters values for maximum gas pressure estimation

For these sensitivities simulations were done with the global model, but the results are presented only for zone B and C.

Rem: The sensitivities presented are monoparametric; the phenomena not being linear, the estimation of a multiparametric sensitivity cannot be deduced from the sum of the monoparametric effects

3.4.3.1 Backfill porosity

The prescribed porosity is 40%; 30% and 50% were tested; concerning gas pressures this sensitivity has not significant effect (Figure 3-37). This is due to the fact that the total porosity volume of backfill small compared to the total volume of gas generated; the storage of gas in the backfill porosity is a second order process.

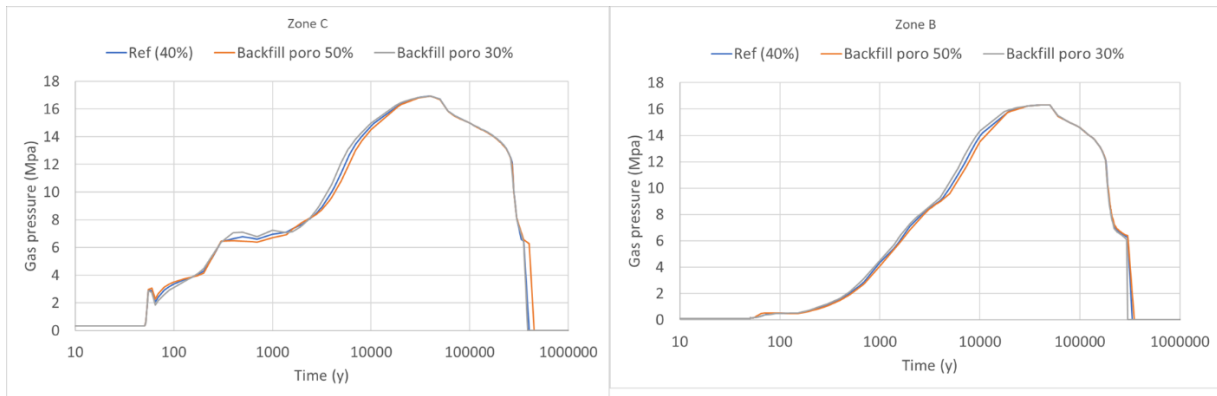


Figure 3-37: Sensitivity analysis on backfill porosity: gas pressure for zone B and C in the global model

3.4.3.2 Host rock permeability

The prescribed host rock intrinsic permeability is 10^{-20} m^2 ; 10^{-19} m^2 and 10^{-21} m^2 were tested (Figure 3-38).

For higher permeability the effect on maximum gas pressure is low, but if permeability is reduced the maximum gas pressure can increase significantly (several MPa).

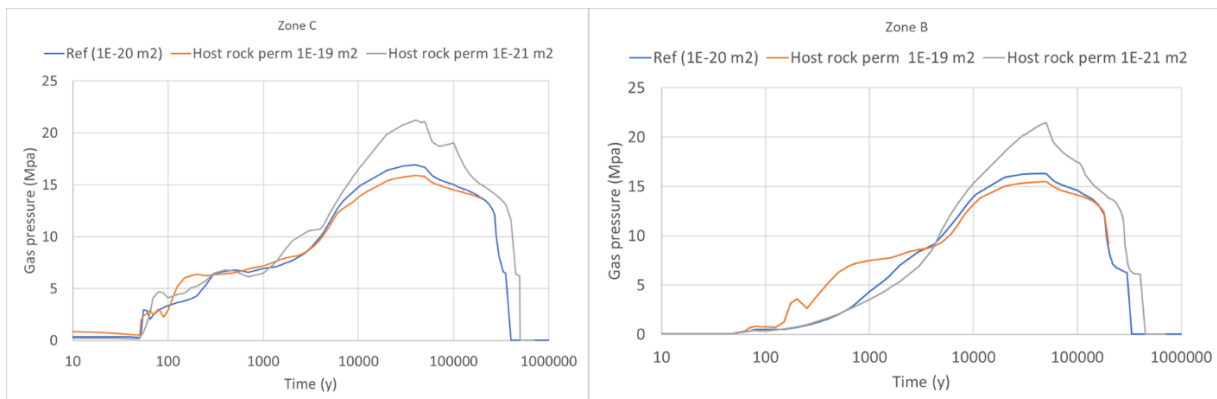


Figure 3-38: Sensitivity analysis on host rock permeability: gas pressure for zone B and C in the global model

3.4.3.3 Host rock gas entry pressure

This parameter is important in two-phase flow process as if capillary pressure stays under its value, not gas flow can initiate in a water saturated porous media, and as the host rock is water saturated its desaturation extension radially of the excavations is partly linked to this parameter.

Prescribed value is 6 MPa; 0 M/Pa and 12 MPa were tested (Figure 3-39). The influence on estimated maximum gas pressure in the deposition zones is very significant; several MPa at least. The reason is linked to the fact that the host rock is situated externally of the excavations and its surrounding EDZ, at a radial distance that is around 10 m from the galleries axes. Even if desaturation of the host rock occurred over only one meter, the affected volume is huge (more than 60 m^3 per m length of the galleries, passing to around $1\,000 \text{ m}^3$ if the desaturation affects 10 m of host rock). And even if the permeability of the host rock is low this can have a significant effect on gas migration along the galleries network as well as on the storage of gas.

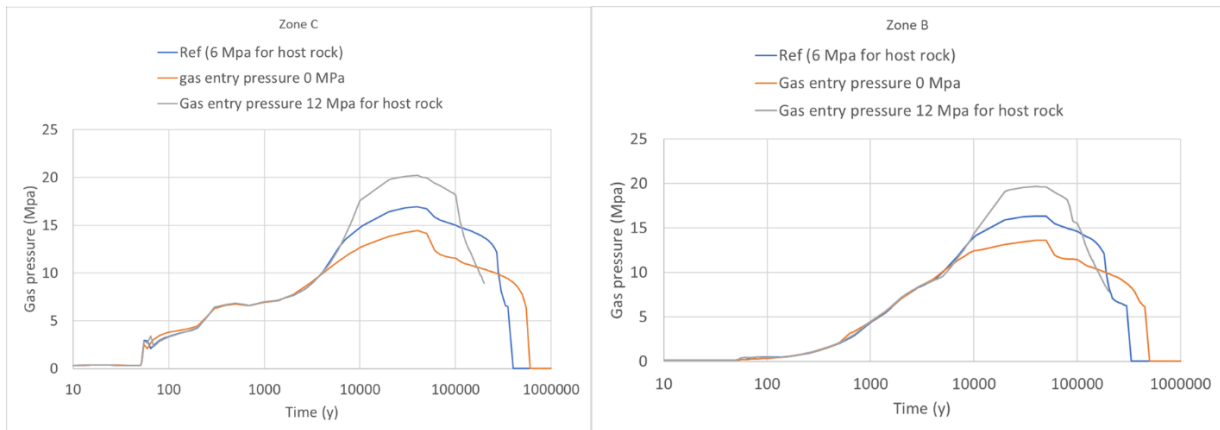


Figure 3-39: Sensitivity analysis on host rock gas entry pressure: gas pressure for zone B and C in the global model

3.4.3.4 Diffusion coefficient of dissolved hydrogen in the host rock

This parameter is important as during the migration of gaseous hydrogen toward the shaft it dissolves along the way and that the dissolved part is not negligible on the total migration process (for the prescribed value the percentage of dissolution for the total produced hydrogen is of 60%).

Values divided by five and multiplied by five compared to prescribed values were tested (Figure 3-40). The results are showing that the impact is significant on estimated maximum gas pressure, around 1 MPa, and very important on the total resaturation time of the repository (several 100 000 years and even more). The main reason being that when the diffusion coefficient of dissolved hydrogen in the host rock water is low, the possibility for dissolved hydrogen to migrate away from the excavations is reduced and as after several thousand years the host rock water near these excavations is already dissolved hydrogen saturated, for new hydrogen molecules to dissolve part of it has to migrate away from the galleries. The same process limit the dissolution of hydrogen on the long term increasing the total resaturation time.

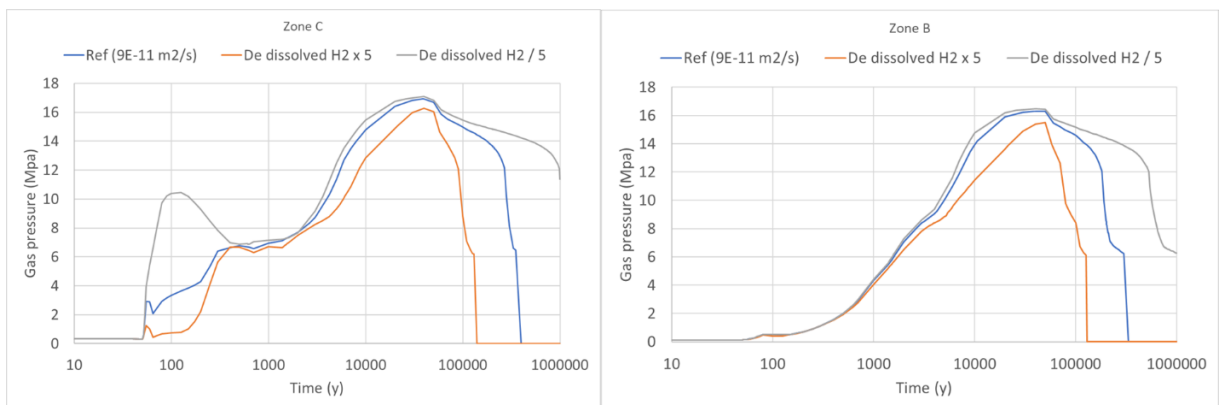


Figure 3-40: Sensitivity analysis on diffusion coefficient of dissolved hydrogen in the host rock water: gas pressure for zones B and C in the global model

3.4.3.5 Corrosion rate

As hydrogen flux is linearly related to the corrosion rate, and as this value is affected by a significant uncertainty (2 orders of magnitude in Andra's data base), testing the impact on gas pressure of this parameter seems important.

Prescribed value is 1 $\mu\text{m}/\text{y}$; tested values are 0,1 $\mu\text{m}/\text{y}$ and 10 $\mu\text{m}/\text{y}$. The results are presented in Figure 3-41.

The impact is very significant on both estimated maximum gas pressure (more than 10 MPa) and time of this maximum (several 100 000 years), the time being reduced when the corrosion rate is increased while the maximum being increased when corrosion rate is reduced.

This is essentially linked to the linearity between corrosion rate and hydrogen generation flux concerning maximum gas pressure. For to time of maximum the amount (more precisely the thickness) of the metallic elements is also of importance, this maximum being reached just before the end of the corrosion period (because no more metal is left to be corroded).

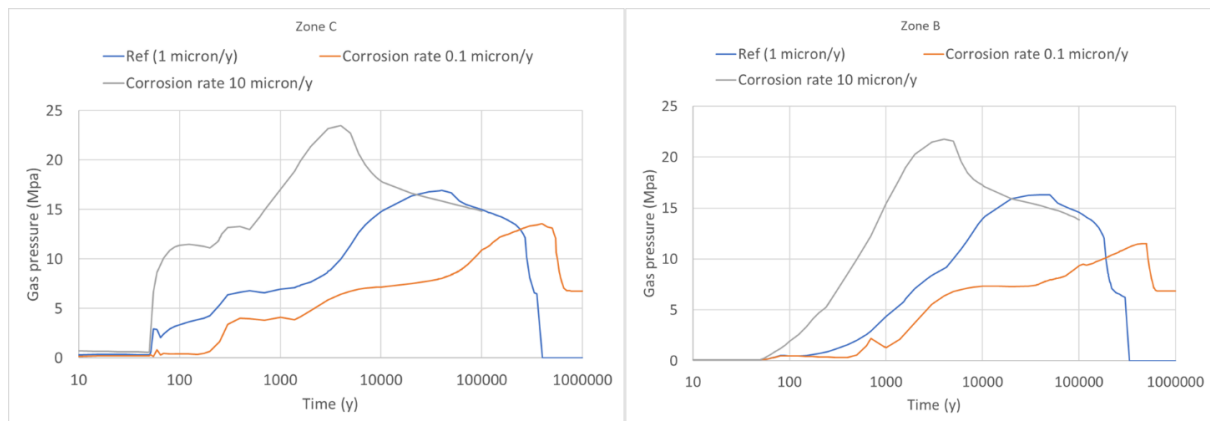


Figure 3-41: Sensitivity analysis on corrosion rate: gas pressure for zone B and C in the global model

3.4.4 Sensitivities on parameters values for gaseous ^{14}C migration

3.4.4.1 Host rock gas entry pressure

The results are presented Figure 3-42; they show that the flux of gaseous ^{14}C arriving at the shaft is not significantly impacted by this sensitivity.

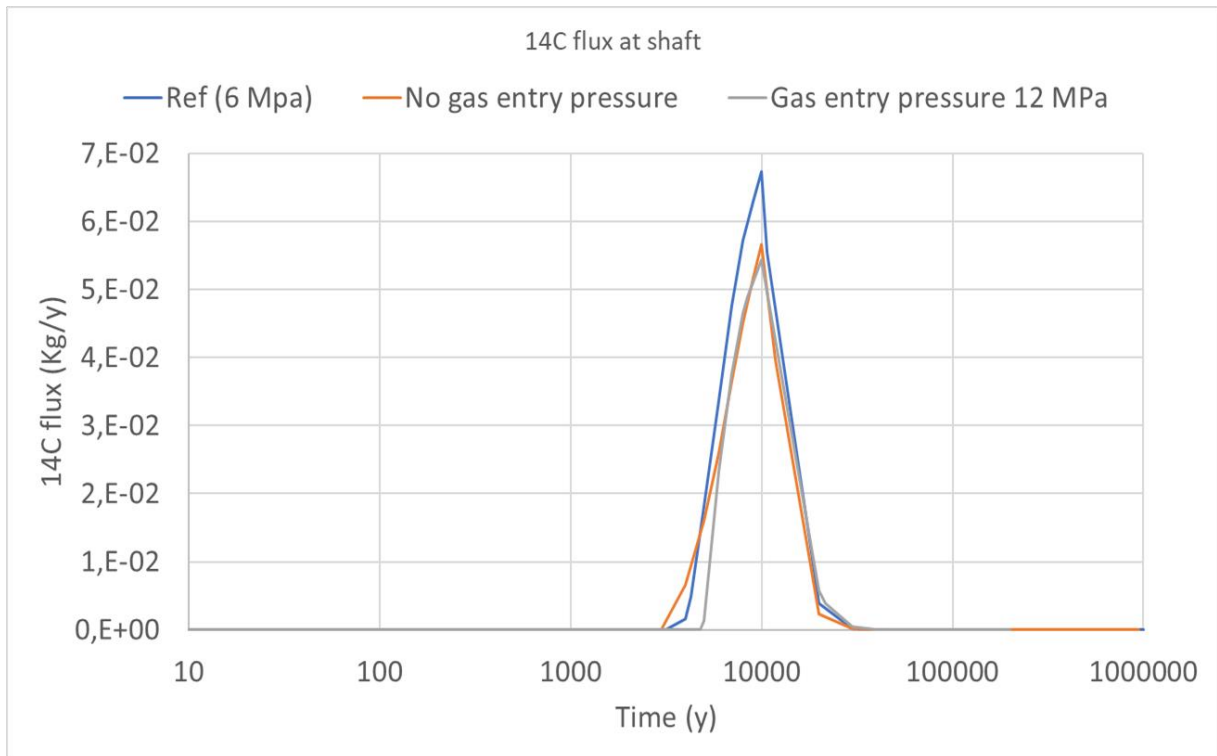


Figure 3-42: Sensitivity on gas entry pressure of the host rock: gaseous 14C flux at shaft

3.4.4.2 Diffusion coefficient of dissolved hydrogen in the host rock water

The results (Figure 3-43) show a significant impact of this sensitivity on 14C gaseous flux at shaft; the higher to diffusion coefficient, the higher the dissolution of gaseous hydrogen and thus the lower the flux of hydrogen arriving at the shaft. And as gaseous 14C migrates along the bulk gas phase generated by hydrogen, the lower the gaseous 14C flux at the shaft as well.

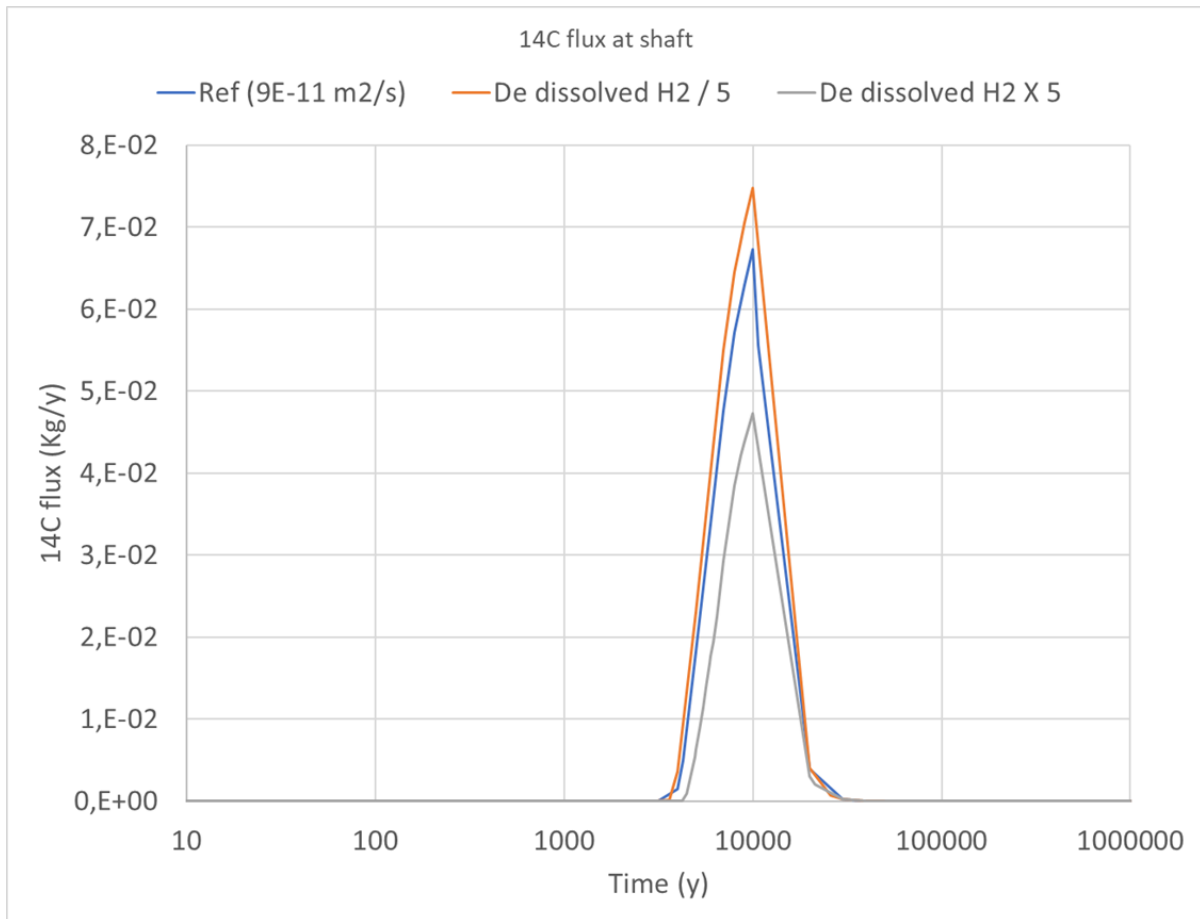


Figure 3-43: Sensitivity on diffusion coefficient of dissolved hydrogen in the host rock water: gaseous ¹⁴C flux at shaft

3.4.4.3 Corrosion rate

Figure 3-44 shows that the sensitivity of the corrosion rate on the gaseous ¹⁴C flux at the shaft is very important; several orders of magnitude (for a corrosion rate of only 0,1 μm/y, the flux is so low that it is not visible on the figure). The first arrival time is also significantly affected. This is due to the fact that gaseous ¹⁴C migrates along the bulk gas phase generated by gaseous hydrogen and that this gas phase is itself significantly affected by the corrosion rate.

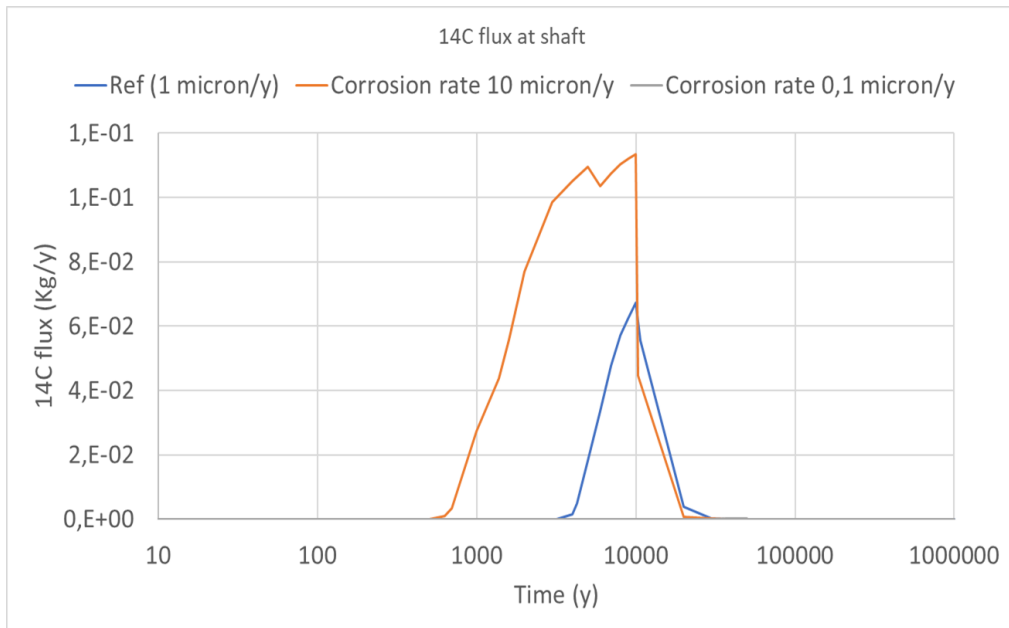


Figure 3-44: Sensitivity on corrosion rate: gaseous 14C flux at shaft

3.4.5 Sensitivities on parameters values for soluble 129I migration

Only one sensitivity is available for 129I migration: the one concerning the diffusion coefficient of dissolved hydrogen in the host rock water (Figure 3-45). This influence is very significant as well on time of first arrival and maximum as on maximum flux at shaft. Once again this is due to the fact that hydrogen gas phase is affected by the diffusion of dissolved hydrogen which pilots the dissolution of hydrogen when host rock water around the excavations is already dissolved hydrogen saturated (i.e. at long term, after several 1 000 years after closure).

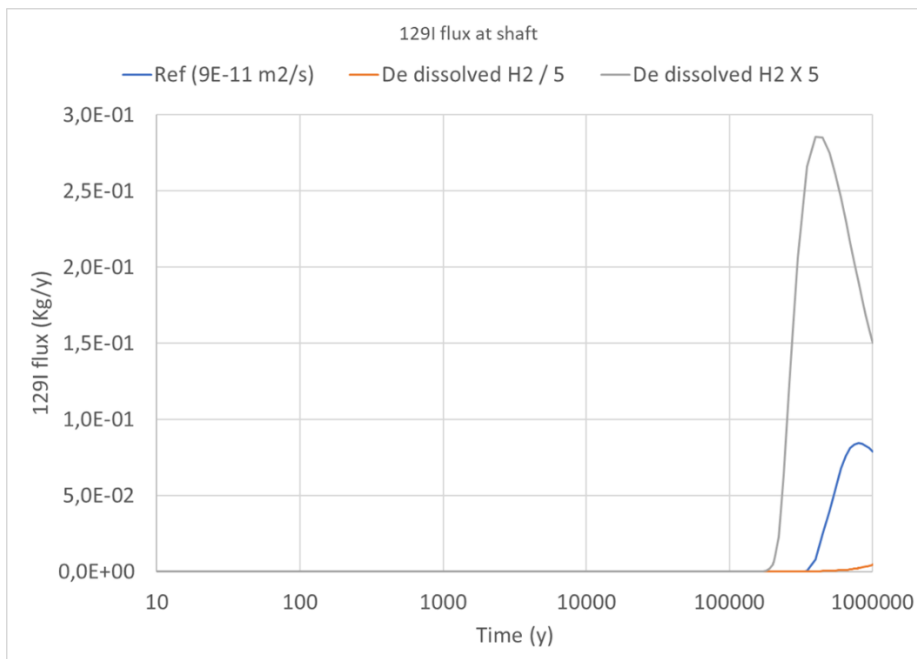


Figure 3-45: Sensitivity on diffusion coefficient of dissolved hydrogen in the host rock water: dissolved 129I flux at shaft

3.5 Discussion and synthesis

This part is dedicated to some discussions on elements of the sensitivity analysis that can be of interest for “end-users” as WMO’s or TSO’s. It tries to develop some general synthetic arguments (i.e. “good practices”) that could be used for specific repositories to avoid mis-estimations of maximum gas pressures and/or radionuclides transfer.

3.5.1 Model extension

The sensitivity analysis done on model extension (total repository, stand alone zones, with or without shaft) has shown that changing the extension of the model can lead to estimations of the maximum gas pressure that can either overestimate or underestimate the real value:

- If the restricted model does not include the zone producing the more hydrogen estimation can be underestimated
- If the restricted model does not include the path toward the shaft (or ramp) the estimation can be overestimated.

The only model that can give a reasonable estimation of the maximum gas pressure is a model integrating all the designed architecture of the repository to evaluate.

3.5.2 Mesh design

Concerning the mesh, the sensitivities have shown that even if the extension of the model covers the total extension of the repository, if all the paths from production zones of hydrogen (all the excavations; galleries as well as deposition zones) toward the upper aquifer via the shafts/ramps (for example the EDZ, but one can also think of the concrete lining) are not well represented in the mesh, this can lead to an overestimation of the estimated maximum gas pressure.

A reasonable estimation of the maximum gas pressure can only be achieved if all the materials representing a potential path for the gas toward the shafts/ramps is explicitly integrated in the mesh.

3.5.3 Optimized design for maximum gas pressure reduction

The sensitivity analysis has shown that assuming a certain architecture for a repository, it exists some ways to reduce the maximum gas pressure by optimizing the EBS two-phase flow characteristics. Increasing the permeability of the backfill is one of these. More generally **designing the EBS (backfill, concrete lining, seals etc.) to increase as much as possible the easiness of gas flow can help reducing significantly the maximum gas pressure estimated in a specific architecture for a given repository.**

Another way to reduce the gas pressure in a repository is to reduce, as much as possible, the amount of metal present in post-closure in the repository. One way to do this is to optimize the reinforcement of the concrete lining or even to replace it by non-metallic elements.

3.5.4 Gaseous radionuclides transfer

In the generic repository, the characteristic time for gaseous radionuclides to reach the shaft from the deposition zones is of several hundred years at minimal. From Andra’s experience this is true for real repositories as well.

This means that even under gaseous form all the radionuclides having a $\frac{1}{2}$ life of less than at least several tens of years will never reach the shaft with a significant flux (could be repository design dependant).

Another element is that gaseous radionuclides move much more rapidly toward the shaft than soluble one. Thus, **to have a good evaluation of the potential impact of radionuclides that can migrate at least partially under gaseous form, an evaluation considering two-phase flow at repository level is necessary.**

3.5.5 Solute radionuclides transfer

The sensitivity analysis made on gas source terms has shown that when these terms are reduced the time of first arrival (the maximum flux at shaft) is reduced (is increased). Thus, the less gas in the repository, the quicker the migration and the higher the flux of soluble radionuclides toward the shaft via the galleries network; **making soluble radionuclides migration evaluations under saturated conditions is conservative concerning arrival time and fluxes at shafts/ramps via the galleries network.**

3.6 Conclusion

Andra's contribution to EURAD-GAS task 4 has been to build a two-phase flow numerical model representing the whole generic repository designed for this exercise.

The code used was TOUGH2-MP, this code is used all around the world for nuclear repository evaluations and is well validated. Its numerical scheme is based on a finite volume formulation enabling the design of some complicated non-conforming sub-meshing which was used to reduce the number of cells in the global repository model especially in zone C. Some other simplifications were also considered in the inner part of the deposition cells and in the grouping of the concrete liner deposition zones in the seals.

The base simulation used all the elements described in the prescription for the two-phase flow model (no mechanical coupling was used), in terms of initial conditions (operational phase), boundary conditions (limited at the host rock), mass (hydrogen), heat and radionuclides generation fluxes.

The base results are described for evaluated gas pressure, gas flow and radionuclides fluxes.

Some sensitivities were done on several elements like:

- Model extension; zone models were build
- Gas source terms; reduction of these terms were used
- Physical parameters; permeabilities, diffusion coefficient, porosities ...

Results were presented in terms of maximum gas pressure as well as in terms of radionuclides migration.

The global analysis of these different results enabled the emergence of some "good practices" oriented toward "end-users" to ease the building of numerical two-phase flow modelling of a repository.

3.7 References

- [1] K. Pruess, C. Oldenburg and G. Moridis, TOUGH2 User's Guide, Version 2.0, Berkeley: Earth Sciences Division, Lawrence Berkeley National Laboratory, 1999.
- [2] M. Van Genuchten, "A closed-form equation for predicting the hydraulic conductivity of unsaturated soils," *Soil Science Society of America Journal*, pp. 892-898, 1980.
- [3] O. Ippisch, H.-J. Vogel and P. Bastian, "In the necessity of an entry pressure in the Mualem model," *Water Resources Research*, 2004.
- [4] T. Vogel and M. Cislérova, "On the reliability of unsaturated hydraulic conductivity calculated from the moisture retention curve", *Transp. In Por. Med.*, vol. 3, pp. 1-15, 1988.
- [5] T. Vogel, M. Van Genuchten and M. Cislérova, "Effect of the shape of the soil hydraulic functions near saturation on variably-saturated flow predictions," *Advances in Water Resources*, vol. 24, pp. 133-144, 2001.

3.8 Appendix: description of the numerical implementation of explicit gas entry pressure in Van-Genuchten/Mualem formulations

Rem: The formulations described below have been implemented in a specific version of TOUGH2-MP for Andra and are not present in the public version of this two-phase flow code.

In some materials, the possibility to explicitly take into account the gas entry pressure has been added. This necessitated to develop a new set of capillary pressure and relative permeability laws in TOUGH2-MP. Those laws, namely ICP=19 and IRP=16, which are derived from the modified van Genuchten laws, are specified in the following sub-sections (3.8.1 & 3.8.2) as follows:

3.8.1 Capillary pressure:

The model proposed by Van Genuchten [1] has been modified to introduce the gas entry pressure. The new formulation, from (Ippisch, Vogel, & Bastian, 2004) is as follows:

$$S_e = \frac{S_l - S_{lr}}{1 - S_{lr}}$$

$$\begin{cases} S_e = (1 + (\alpha(-p_c - p_e))^n)^{-m}, & \text{if } -p_c > p_e \\ S_e = 1, & \text{if } -p_c \leq p_e, \\ \text{with convention: } p_e \geq 0 \text{ and } p_c \leq 0 \end{cases} \quad 3-1$$

with, $m = 1 - 1/n$, and $\alpha = 1/P_r$

This formulation integrated in the Mualem model does not allow an analytical expression of the relative permeability. [4] and [5] propose, based on [3], a modified formulation (eq. 3-2) also taking into account the gas entry pressure and allowing an analytical formulation of the relative permeability curves.

$$S_e = \frac{S_l - S_{lr}}{1 - S_{lr}}$$

$$\begin{cases} S_e = \frac{1}{S_e^*} (1 + (-\alpha p_c)^n)^{-m}, & \text{if } -p_c > p_e \\ S_e = 1, & \text{if } -p_c \leq p_e, \\ \text{with convention: } p_e \geq 0 \text{ and } p_c \leq 0 \end{cases} \quad 3-2$$

With: $S_e^* = (1 + (\alpha p_e)^n)^{-m}$

$m = 1 - 1/n$, and $\alpha = 1/P_r$

The capillary pressure curves of both formulations, together with a standard van Genuchten formulation without entry pressure are presented in Figure 3-46.

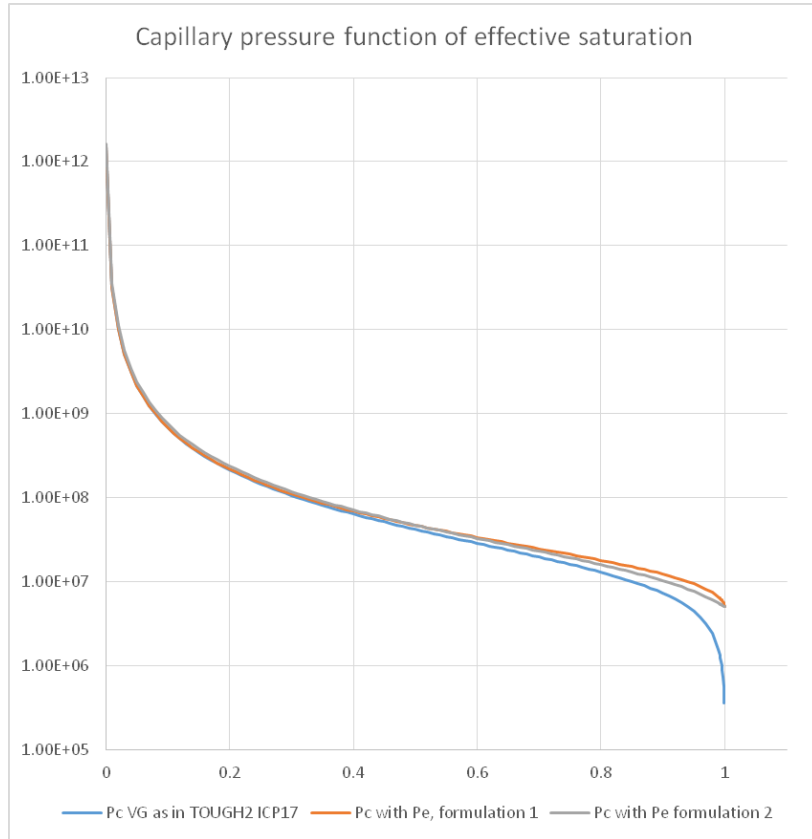


Figure 3-46 Capillary pressure function of effective saturation for the van Genuchten and the two alternative formulations with gas entry pressure. The “formulation 1” corresponds to equation 3-1 while “formulation 2” corresponds to equation 3-2. $P_r = 1.47 \cdot 10^7$ Pa, $m = 0.375$, $n = 1.6$, $P_e = 5$ MPa (formulation 1 and formulation 2 only)

In order to implement this law in TOUGH2-MP, equation 3-2 has to be expressed as a capillary pressure function of the effective saturation, which would give:

$$S_e = \frac{S_l - S_{lr}}{1 - S_{lr}}$$

$$\begin{cases} p_c = -\frac{1}{\alpha} \left((S_e^* S_e)^{\frac{1}{m}} - 1 \right)^{-\frac{1}{n}}, & \text{if } S_e < 1 \\ -p_c \leq p_e, & \text{if } S_e = 1 \end{cases}$$

3-3

With: $S_e^* = (1 + (\alpha p_e)^n)^{-m}$

$$m = 1 - 1/n, \text{ and } \alpha = 1/P_r$$

However, for implementation in TOUGH2-MP, the fuzzy condition $-p_c \leq p_e$, if $S_e = 1$ of equation 3-3 is not satisfying. Different options for setting up the value p_c for fully saturated porous media have been envisaged.

- Allowing $-p_c = p_e$ (or $p_c \neq 0$ in general) at $S_e = 1$ will lead to unphysical behaviour at the interface of two saturated porous media with different entry pressures (which should be in equilibrium) namely the appearance of a gas phase at water vapour pressure. This was indeed observed in a test simulation (in the material with the lower capillary pressure at $S_e = 1$).
- From the above it must be $p_c = 0$ at $S_e = 1$, as in 3-4 below. This however implies a discontinuity of the capillary pressure curve at $S_e = 1$. Numerical tests showed that this implementation was not allowing convergence of TOUGH2-MP simulations.

$$S_e = \frac{S_l - S_{lr}}{1 - S_{lr}}, \quad 3-4$$

$$p_c = \begin{cases} -\frac{1}{\alpha} \left((S_e^* S_e)^{\frac{1}{m}} - 1 \right)^{\frac{1}{n}}, & \text{if } S_e < 1 \\ 0, & \text{if } S_e = 1 \end{cases}$$

$$\text{With: } S_e^* = (1 + (\alpha p_e)^n)^{-m}$$

$$m = 1 - 1/n, \text{ and } \alpha = 1/P_r$$

- As a consequence, a linearization was applied for values close to full saturation (eq. 3-5):

$$S_e = \frac{S_l - S_{lr}}{1 - S_{lr}}, \quad 3-5$$

$$p_c = \begin{cases} -\frac{1}{\alpha} \left((S_e^* S_e)^{\frac{1}{m}} - 1 \right)^{\frac{1}{n}}, & \text{if } S_e \leq 1 - \varepsilon \\ -\frac{1}{\alpha} \left((S_e^* S_e)^{\frac{1}{m}} - 1 \right)^{\frac{1}{n}} \cdot \frac{1 - S_e}{\varepsilon}, & \text{if } (1 - \varepsilon) < S_e < 1 \\ 0, & \text{if } S_e = 1 \end{cases}$$

$$\text{With: } S_e^* = (1 + (\alpha p_e)^n)^{-m}$$

$$m = 1 - 1/n, \text{ and } \alpha = 1/P_r$$

This way of proceeding, which allows numerical convergence of simulations, is state of the art in TOUGH2. Indeed, the TRUST capillary pressure (ICP=3) which features an entry pressure is programmed this way, although it is not explicitly documented in [1].

The linearized implementation (eq. 3-5) must, however, be considered with care. Indeed, in the frequent situation of almost fully saturated materials, i.e. when $(1 - \varepsilon) < S_e < 1$, the computed capillary pressure is underestimated: it is below p_e while it should be greater than p_e according to the analytical formulation. This can allow some early gas entry in the porous material with an explicit gas entry pressure before this gas entry pressure is reached and initiate a desaturation that should not occur, with all its consequences. The best compromise between accuracy and numerical convergence is obtained² by selecting $\varepsilon \approx 10^{-3}$. The van Genuchten capillary pressure law with gas entry pressure as it has been implemented in TOUGH2-MP (ICP=19) is presented in Figure 3-47.

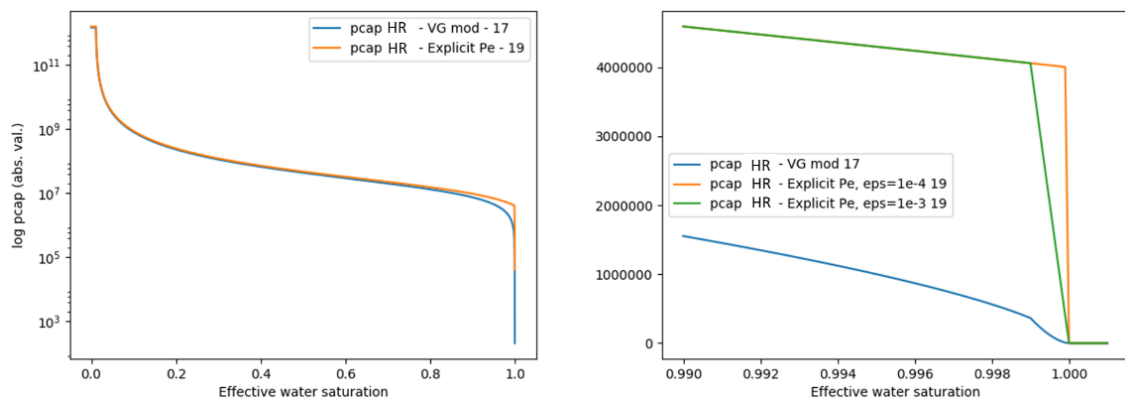


Figure 3-47 Different implementations of the capillary pressure curves for Host Rock (HR). $P_r = 1.47 \cdot 10^7$ Pa, $m = 0.375$, $n = 1.6$, $P_e = 4$ MPa (ICP=19 only). Blue: usual modified van Genuchten (ICP=17, without entry pressure, with linearization at high saturations). Orange & green: van Genuchten with entry pressure. Right: close-up on the linearization close to full saturation. Orange and green curves differ by the linearization threshold.

3.8.2 Relative Permeability:

From [5], relative permeability curves are adapted as follows to account for an explicit air entry pressure:

$$S_e = \frac{S_l - S_{lr}}{1 - S_{lr}}$$

$$k_{rw} = \begin{cases} \sqrt{S_e} \cdot \left[\frac{1 - (1 - (S_e^* S_e)^{1/m})^m}{1 - (1 - S_e^{*1/m})^m} \right]^2, & \text{if } S_e < 1 \\ 1, & \text{if } S_e = 1 \end{cases}$$

3-6

² A test simulation with epsilon = 1E-4 did not converge.

$$k_{rg} = \begin{cases} f_g \cdot \sqrt{1 - S_e} \cdot \left[\frac{(1 - S_e^{*1/m})^m - (1 - (S_e^* S_e)^{1/m})^m}{(1 - S_e^{*1/m})^m - 1} \right]^2, & \text{if } S_e < 1 \\ 0, & \text{if } S_e = 1 \end{cases}$$

With: $S_e^* = (1 + (\alpha p_e)^n)^{-m}$

$m = 1 - 1/n$, and $\alpha = 1/P_r$

The factor f_g in equation allows to increase the relative gas permeability in order to consider a specific intrinsic gas permeability.

Figure 3-48 below presents the gas and liquid relative permeability for the Host Rock as they have been implemented and applied in TOUGH2-MP. It allows to highlight differences between a classical modified van Genuchten (IRP=14), and the van Genuchten with air entry pressure (IRP=16; $P_e=4$ MPa). The analytical expression of the latter as in eq. 3-6 verifies the correct implementation in TOUGH2-MP.

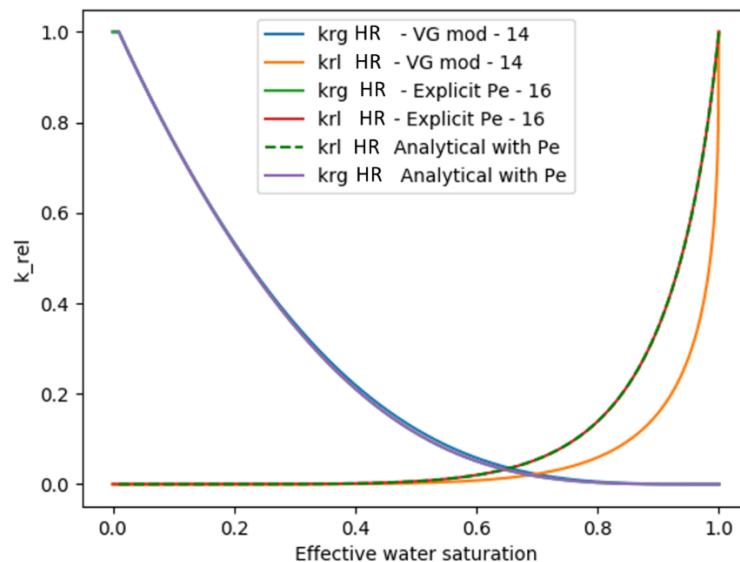


Figure 3-48 Relative permeability curves for Host Rock (HR) with different implementations of the relative permeability law. $P_r = 1.47 \cdot 10^7$ Pa, $m = 0.375$, $n = 1.6$, $P_e = 4$ MPa (for analytical solution and IRP=16 only).

4. Contribution of BGR

(Tom Schintgen, Michael Pitz, Gesa Ziefle)

As discussed in the EURAD-GAS “Generic repository” exercise description (Wendling, 2020), Task 4 of the WP GAS is dedicated to the conceptualization of a numerical model set-up and the evaluation at the repository scale. In addition to that, Task 2 and Task 3 of the WP GAS aim at the development of numerical modelling approaches considering different kinds of gas transport like advective and diffusive transport of dissolved gas, two-phase flow considering a gaseous and a liquid phase as well as dilatancy-controlled gas flow along pathways and gas transport in fractures. These effects are investigated by laboratory and in-situ experiments and related numerical approaches are developed. Considering these complex processes on the scale of a repository is a major numerical challenge. Since the individual processes are not of central importance in all parts of the repository, this exercise is also about finding suitable approaches to make safety-relevant statements on the repository scale.

As a matter of fact, the presented approach is characterized by simplifications with regard to the geometry, the time scale but also the mathematical description of the mentioned effects. It aims at the identification of critical processes, areas and times which must be considered in the safety assessment or whose relevance should already be taken into account in the repository design. The presented numerical model is based on a fully coupled TH²M approach, implemented in OpenGeoSys 6 (OGS-6). It is under development and validation in the context of Task 2 and Task 3 and is discussed very briefly in this contribution.

4.1 Model approach

A fully coupled thermo-hydro-mechanical model approach, considering two-phase two-component flow in deformable porous media (TH²M) is considered. This model approach is implemented in the open-source finite-element code OpenGeoSys 6 (OGS-6) (Bilke et al., 2019) and referenced as TH²M in the following. The set of governing equations as implemented in TH²M is summarized here. More details can be found in Grunwald et al. (2022) and Pitz et al. (2023a). For the sake of clarity, different indices for liquid and gaseous phases (L and G, respectively) as well as for water and gas components in each phase (W and C, respectively) are used.

Grunwald et al. (2022) present a TH²M implementation in which a liquid and a gaseous phase, $\alpha \in \{L, G\}$, occupy the pore space of a deformable porous solid $\alpha \equiv S$. Each fluid phase is populated by the constituents/components ζ . In our case, one of the components is water, while the other is hydrogen gas, i.e. $\zeta \in \{W, H_2\}$. In this work and for simplification, we assume the absence of vapor, thus water does not exist in gaseous phase. The coupled processes of energy transport, deformation and two-phase two-component hydraulics are solved using four balance equations with temperature T , solid displacement vector \mathbf{u}_S , gas pressure p_{GR} and capillary pressure p_{cap} as primary variables. A further simplification made in this work is the assumption that $\mathbf{u}_S = 0$, i.e. medium deformation is neglected and prevented in the numerical model. The liquid phase pressure p_{LR} is expressed in terms of the primary variables:

$$p_{LR} = p_{GR} - p_{cap}$$

The two TH²M mass balance equations are written in a component (i.e. water and hydrogen component) form with $\zeta \in \{W, H_2\}$ and read:

$$0 = \rho_{FR}^{\zeta} (\alpha_B - \phi) \beta_{p,SR} \frac{dp_{GR}}{dt} - \rho_{FR}^{\zeta} (\alpha_B - \phi) \beta_{p,SR} S_L \frac{dp_{cap}}{dt} - \rho_{FR}^{\zeta} (\alpha_B - \phi) \text{tr}(\alpha_{T,SR}) \frac{dT}{dt} + \text{div}(A^{\zeta} + J^{\zeta}) \\ + \phi \left[(1 - S_L) \frac{d\rho_{GR}^{\zeta}}{dt} + S_L \frac{d\rho_{LR}^{\zeta}}{dt} \right] + [\phi(\rho_{LR}^{\zeta} - \rho_{GR}^{\zeta}) - \rho_{FR}^{\zeta} p_{cap} (\alpha_B - \phi) \beta_{p,SR}] \frac{dS_L}{dt}$$

where α_B and ϕ represent the Biot-Willis coefficient and porosity, respectively, $\beta_{p,SR}$ is the solid grain compressibility and $\alpha_{T,SR}$ is a diagonal matrix for the linear solid thermal expansion coefficients in all coordinate directions such that $\text{tr}(\alpha_{T,SR})$ gives the volume thermal expansion coefficient of the solid. The effective density of component ζ in both fluid phases is given by:

$$\rho_{FR}^{\zeta} = (1 - S_L) \rho_{GR}^{\zeta} + S_L \rho_{LR}^{\zeta}$$

with ρ_{GR}^{ζ} and ρ_{LR}^{ζ} as the density of component ζ in each respective phase. The “R” in the index of a variable denotes an intensive property. In case of densities, it therefore refers to the intrinsic density independent of the volumetric frame of reference. The phase densities themselves can be considered as the sum of both component densities in the respective phase (Pitz et al., 2023a for more details) and are temperature, pressure and composition dependent. The liquid phase density ρ_{LR} is given by a multilinear function (Grunwald et al., 2022):

$$\rho_{LR} = \rho_{LR,ref} (1 + \beta_{p,LR} (p_{LR} - p_{LR,ref}) - \beta_{T,LR} (T - T_{ref}) + \beta_{c,LR} c_L^C)$$

with $\beta_{p,LR}$, $\beta_{T,LR}$, and $\beta_{c,LR}$ as the liquid compressibility, thermal expansion coefficient and liquid expansion due to hydrogen dissolution, respectively. Since in this numerical model, water vapour is neglected, the binary composition of the gas phase discussed in Grunwald et al. (2022) and Pitz et al. (2023) reduces to a unary composition:

$$\rho_{GR}^W = 0$$

Hence, the gas phase pressure p_{GR} and density ρ_{GR} are equal to the hydrogen partial pressure and density, respectively. The latter is given by the ideal gas law:

$$\rho_{GR}^{H_2} \equiv \rho_{GR} = \frac{p_{GR} M_{H_2}}{RT}$$

where R is the universal gas constant and the effective molar mass of molecular hydrogen is represented by M_{H_2} . Partial component densities in the liquid phase are defined further below. The liquid saturation S_L is a function of capillary pressure p_{cap} and is given according to the van Genuchten model (van Genuchten, 1980) with:

$$S_L = S_e (S_{L,max} - S_{L,res}) + S_{L,res}$$

where the effective saturation S_e is given according to:

$$S_e = \begin{cases} \left(1 + \left(\frac{p_{cap}}{p_e}\right)^n\right)^{\frac{1}{n}-1}, & \text{if } p_{cap} > 0 \\ 1, & \text{if } p_{cap} \leq 0 \end{cases}$$

It can be seen in above equation, that OGS computes a partial saturation if the capillary pressure is positive – this is the case whenever gas pressure exceeds liquid pressure. Therefore, the used liquid saturation-capillary pressure relation used here represents a difference to the modified equation given

in the generic repository exercise, where an explicit gas entry pressure is considered. Its impact on the results is discussed later on in this contribution.

Mass transfer of hydrogen can theoretically occur in both fluid phases advectively with $\mathbf{A}^\zeta = \mathbf{A}_L^\zeta + \mathbf{A}_G^\zeta$. Since water vapour is neglected, the water component mass transfer is restricted to advection in the liquid phase with $\mathbf{A}_G^W = 0$. The advective mass flux of component ζ in phase α is governed by the Darcy flux of a phase and the respective component density:

$$\mathbf{A}_\alpha^\zeta = -\rho_{\alpha R}^\zeta \frac{k_\alpha^{\text{rel}} \mathbf{k}_S}{\mu_{\alpha R}} (\text{grad } p_{\alpha R} - \rho_{\alpha R} \mathbf{g})$$

where \mathbf{k}_S represents the intrinsic permeability tensor, k_α^{rel} is the relative permeability according to Mualem (1976) and $\mu_{\alpha R}$ is the phase viscosity (assumed to be constant in this first modelling attempt) and \mathbf{g} represents the earth's gravitational acceleration. Component mass transport can also occur via diffusive transport. Since water vaporization is neglected, there is no diffusion in the unary gas phase, but in the liquid phase, diffusion occurs and it is driven by the mass fraction gradient of the respective component, obeying Fick's law

$$\mathbf{J}^\zeta = \underbrace{\mathbf{J}_G^\zeta}_{=0} + \mathbf{J}_L^\zeta$$

and

$$\mathbf{J}_L^\zeta = -\rho_{LR} \mathbf{D}_L \text{grad } x_{m,L}^\zeta$$

The Fick diffusion coefficient in the liquid phase \mathbf{D}_L needs to be calculated using the Millington-Quirk relation. The latter links the dissolved hydrogen diffusion D_0 in pure water provided in the generic repository exercise to the effective dissolved hydrogen diffusion in the porous medium \mathbf{D}_L :

$$\mathbf{D}_L = D_0 \phi^{1+a} S_L^b \mathbf{I}$$

with ϕ the porosity and \mathbf{I} as the identity; a and b are material parameters specified in the generic repository exercise. Since Millington-Quirk is not implemented in OGS-6, we calculate D_0 assuming $a = 0$ and $b = 1$ as Millington-Quirk-parameters. The density of dissolved hydrogen obeys Henry's law and is proportional to the partial hydrogen pressure in the gas phase

$$\rho_{LR}^{\text{H}_2} = p_{\text{H}_2} M_{\text{H}_2} H_{\text{H}_2}$$

With H_{H_2} designating the constant Henry's coefficient. In the repository exercise, the Henry coefficient is given in Pa^{-1} , whereas OGS interprets the same coefficient in terms of $\text{mol Pa}^{-1} \text{m}^{-3}$. The density of the water component within the liquid phase then results from the binary liquid composition:

$$\rho_{LR}^W = \rho_{LR} - \rho_{LR}^{\text{H}_2}$$

The component mass fraction in the liquid phase can then be calculated as the ratio of partial component density and liquid density:

$$x_{m,L}^\zeta = \frac{\rho_{LR}^\zeta}{\rho_{LR}}$$

The energy balance in the TH²M implementation is expressed in terms of internal energy u_α and specific enthalpy h_α of each phase $\alpha \in \{L, G, S\}$:

$$0 = \underbrace{\frac{d}{dt}(\Sigma_\alpha \rho_\alpha u_\alpha)}_{\text{storage}} + \underbrace{\text{div}(\Sigma_\alpha h_\alpha \mathbf{A}_\alpha)}_{\text{transport by advection}} + \underbrace{\text{div}(\Sigma_\alpha \Sigma_\zeta h_\alpha^\zeta \mathbf{J}_\alpha^\zeta)}_{\text{transport by diffusion}} + \underbrace{(\Sigma_\alpha \rho_\alpha h_\alpha) \text{div}\left(\frac{d\mathbf{u}_s}{dt}\right)}_{\text{medium volume change}} - \underbrace{\Sigma_\alpha \mathbf{g} \cdot \mathbf{A}_\alpha}_{\text{gravitation work}} - \underbrace{\text{div}(\lambda_{\text{eff}} \text{grad } T)}_{\text{heat conduction}}$$

where ρ_α represents the apparent density of a phase in the porous medium with $\rho_L = \phi S_L \rho_{LR}$ and $\rho_G = \phi(1 - S_L) \rho_{GR}$ and $\rho_S = (1 - \phi) \rho_{SR}$. The effective medium thermal conductivity is given by a porosity-saturation based mixing rule with

$$\lambda_{\text{eff}} = (1 - \phi) \lambda_S + \phi(S_L \lambda_L + (1 - S_L) \lambda_G)$$

where λ_S , λ_G and λ_L are the solid, gaseous and liquid phase thermal conductivity tensors.

4.2 Model set-up and numerical details

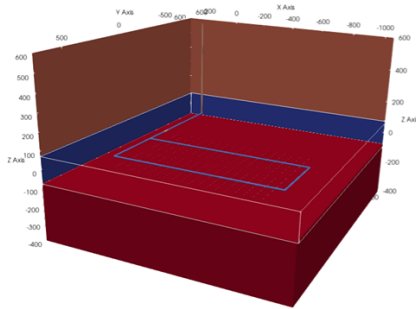
This section contains basic information about the following aspects of the model setup:

- Conceptual approach
- Geometry and material parameters
- Initial and boundary conditions
- Heat source
- Gas source
- Finite element mesh

Conceptual approach

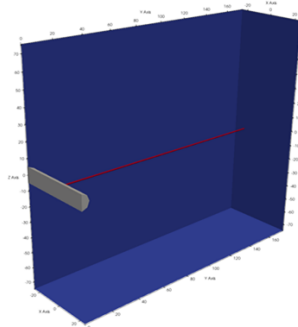
Aiming on the safety assessment of a potential repository, we propose a conceptual approach, which includes two numerical models of different size as presented in Figure 4-1. One model contains the whole repository as well as the host rock and lower and upper aquifer. In this report, we refer to it as “repository model”. This model allows the investigation of effects that would not be possible with a simplified geometry using partial symmetries, such as the flow through seals. The second model takes advantage of symmetric conditions and includes only one deposition tunnel. In this report it is referred to as “deposition tunnel model”. This smaller model enables a detailed investigation of e.g. mesh effects, the impact of complex geometric conditions around the deposition tunnel and complex physical behaviour like e.g. plastic deformations, while neglecting e.g. the gas flow towards the seal. While following this conceptual approach in general, this report focuses on the repository model.

Repository model with aquifers



- ~ 600k nodes
- ~ 4M cells
- Zone C, incl. seal.
- Host rock and upper/lower aquifer

Deposition tunnel model



- ~ 70k nodes
- ~ 425k cells
- Single deposition tunnel, full host rock thickness

Figure 4-1 Conceptual approach for the safety assessment on repository scale.

Geometry and material parameters

The 3D repository model described here is based on disposal zone C as defined in the EURAD-GAS "generic repository" exercise (Figure 4-2). The vertical extent (along the z-axis) of the model is 1000 m. Consideration of the host rock as well as lower and upper aquifer helps to avoid boundary problems as the aquifers have a significant impact on the transport processes occurring in the repository. However, the boundary conditions have been simplified significantly as the aquifers are parametrized by the same material properties as the host rock. The horizontal extent (along the x-axis) of the model is 1400 m. The width (along the y-axis) of the model is 1560 m. In order to simplify the model, only three material groups are used - namely host rock, backfill and seal. Geometrically, host rock material is assigned to host rock, lower and upper aquifers as well as inner and outer EDZ. The deposition tunnels, access gallery and shaft are assigned as "backfill material", including materials introduced/installed into the excavated drifts or shafts, such as waste, voids, concrete and steel liner. Additionally, the repository includes two seals: one in the shaft at the upper part of the host rock and one in the access gallery. The related volumes are defined as "seal" material neglecting the difference between bentonite, concrete liner and plug. The material and fluid (i.e. water and hydrogen) parameters used in the TH²M simulation are summarized in Figure 4-2. In the generic repository exercise, the medium thermal conductivity is defined for fully liquid saturated media. Since OGS takes thermal conductivities for each phase (solid, liquid, gas) and computes the effective medium thermal conductivity based on the arithmetic mean mixing model, a solid thermal conductivity for each medium was deduced using the above equation and assuming constant liquid and gas phase given in Figure 4-2.

Schematic horizontal slice at repository depth

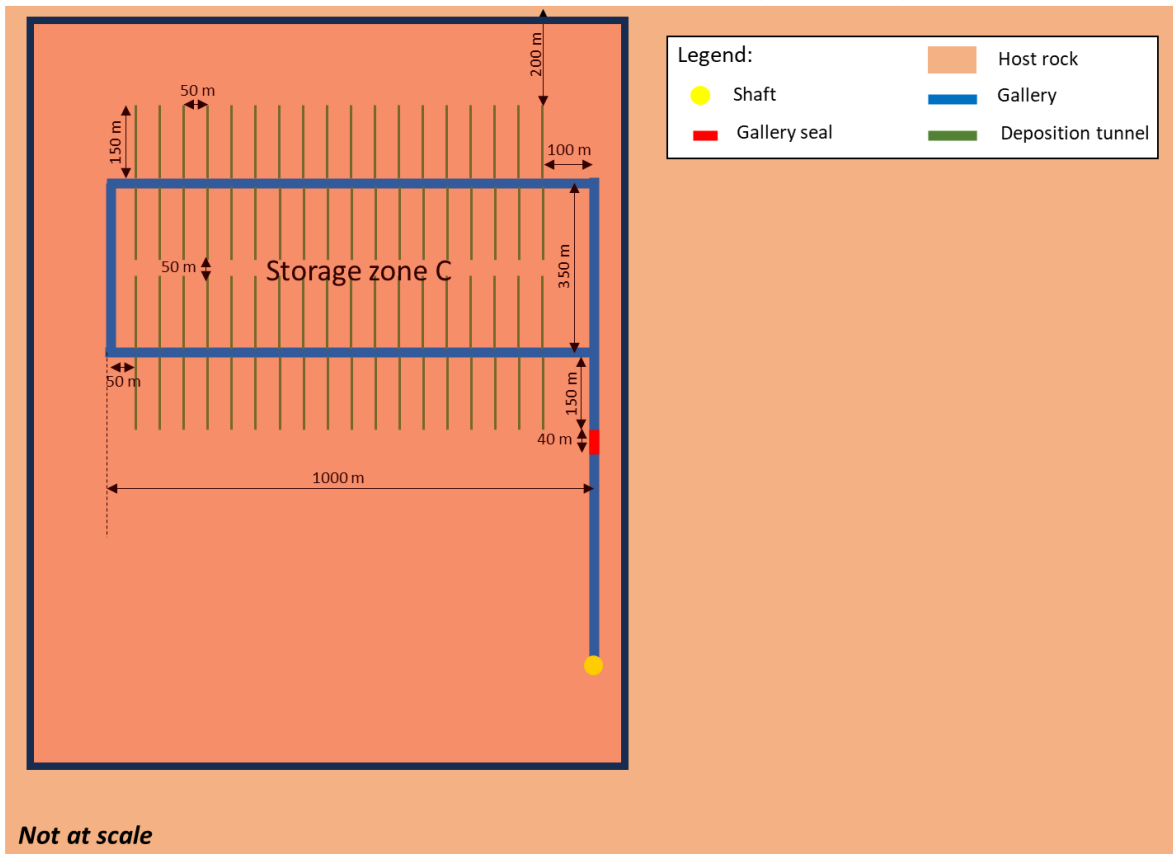


Figure 4-2: Overview of disposal zone C as defined in the generic repository exercise (Wendling, 2020). Location and approximate horizontal extent of the full 3D model are highlighted by the red box.

Table 4-1 Material and fluid parameters used for the TH2M simulation. Parameters which are not directly taken from the specification in the generic repository exercise are marked in grey.

Input parameters		Symbol	Unit	Material group				
				0, 5 and 6	1	2	4	3
				Host rock/ aquifers	Access gallery (mainly backfill)	Deposition tunnel (mainly waste)	Shaft (mainly backfill)	Seal (mainly bentonite and concrete)
				Parameters for host rock	Parameters for backfill			Parameters for bentonite
Thermal parameters	Solid density	ρ_s	kg m^{-3}	2550		2550		2550
	Solid thermal conductivity	λ_T^s	$\text{W m}^{-1} \text{K}^{-1}$	2,0		1,8		2,0
	Solid specific heat capacity	c_p^s	$\text{J kg}^{-1} \text{K}^{-1}$	720		500		700
	Solid thermal expansivity	β_s	K^{-1}	0		0		0
Hydraulic parameters	Porosity	Φ	-	0,2		0,4		0,35
	Water permeability	k_L	m^2	1,00E-20		1,00E-16		1,00E-19
	Van Genuchten 'n'	n	-	1,5		1,5		1,6
	Van Genuchten 'Pr'	Pr	Pa	2,3E+07		1,0E+06		2,0E+07
	Gas entry pressure 'Pe'	Pe	Pa	-		-		-
	Residual water saturation	S_{lr}	-	0		0		0
	Residual gas saturation	S_{gr}	-	0		0		0
	Minimum relative permeability	$k_{rel,min}$	-	1,0E-10		1,0E-10		1,0E-10
	Dissolved H2 'a' for Millington-Quirk	a	-	1,5		1,5		1,5
	Dissolved H2 'b' for Millington-Quirk	b	-	10		10		10
Henry's coefficient 'H' for H ₂	H	Pa^{-1}	1,4E-10		1,4E-10		1,4E-10	
Mechanical parameters	Pore compressibility	β_{pore}	Pa^{-1}			1,0E-10		
	Liquid phase compressibility	$\beta_{p,LR}$	Pa^{-1}			4,5E-10		
	Biot coefficient	α_B	-	1,0		1,0		1,0
	Young's modulus	E	Pa	5,0E+09		5,0E+09		5,0E+09
	Poisson's ratio	ν	-	0,3		0,3		0,3
Fluid parameters	Molar mass of water	M_L	kg mol^{-1}			0,018016		
	Water specific heat capacity	c_p^L	$\text{J kg}^{-1} \text{K}^{-1}$			4182		
	Water thermal conductivity	λ_T^L	$\text{W m}^{-1} \text{K}^{-1}$			0,6		
	Water density	ρ_{LR}	kg m^{-3}			1000		
	Water viscosity	μ_L	Pa s			1,00E-03		
	Dissolved H ₂ diffusion	D_0	$\text{m}^2 \text{s}^{-1}$			5,00E-09		
	Molar mass of hydrogen	M_G	kg mol^{-1}			0,002016		
	Hydrogen specific heat capacity	c_p^G	$\text{J kg}^{-1} \text{K}^{-1}$			14300		
	Hydrogen specific latent heat	L_G	J mol^{-1}			2258000		
	Hydrogen thermal conductivity	λ_T^G	$\text{W m}^{-1} \text{K}^{-1}$			0,18		
Hydrogen viscosity	μ_L	Pa s			1,00E-05			

Initial and boundary conditions

The initial conditions and the boundary conditions applied at the outer boundaries of the repository model result from the hydrostatic pressure gradient. Additional initial and boundary conditions within the repository are based on assumptions concerning the repository conditions during the ventilation phase (50 years) and at the beginning of the deposition phase. A summary of the related model set-up is presented in Figure 4-3. As a conservative assumption, we consider all lateral boundaries as no-flow boundaries for heat, liquid and gas. The model surface and bottom temperatures correspond to those

indicated in the generic repository exercise. The initial temperature inside the model domain is computed assuming a linear temperature gradient between the top and bottom boundaries (cf. Fig. 4-3)

The initial gas pressure in the entire model corresponds to atmospheric pressure of 0.1013 e6 Pa.

The model surface and bottom liquid pressures correspond to those indicated in the generic repository exercise. The initial liquid pressure condition p_{LR0} corresponds to the hydrostatic pressure gradient of 10150 Pa m⁻¹ derived from the model surface and bottom liquid pressures given in the task definition. We apply the initial capillary pressure (primary variable) by its relation to liquid pressure and gas pressure:

$$p_{cap0} = p_{GR0} - p_{LR0}$$

We do not consider the time period of the excavation and ventilation phases and thus begin the simulation at the moment of waste emplacement and closure of the repository at $t = 50$ years. However, we take into account the effect of ventilation as initial condition for capillary pressure and thus partial saturation.

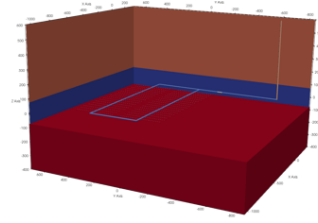
Considering instantaneous excavation of the entire repository, it is ventilated during 50 years before waste emplacement and closure. The ventilation uses air at 80 % of relative humidity RH. In the repository exercise, no ventilation is specified in the deposition tunnels (or cells) in zone C, but here we apply the same ventilation to both deposition tunnel and access gallery/shaft.

We calculate the corresponding capillary pressure p_{cap} by means of Kelvin's relation:

$$p_{cap} = \rho_{LR} \frac{RT_{ref}}{M_{H_2O}} \ln(RH)$$

Where the liquid density ρ_{LR} equals 1000 kg/m³, the universal gas constant R equals 8.314 J kg⁻¹mol⁻¹, the reference temperature T_{ref} equals 293.15 K and the molar mass of water equals 0.01801528 kg/mol. The resulting capillary pressure is 30.2 MPa. We apply this p_{cap} to a volume of 1 meter radius around the axes of deposition tunnels and to a volume of 10 meter radius around the axes of access galleries and the axis of the shaft. This leads to partial saturation of the different materials affected.

Model set-up



- **Initial conditions:**

- $T_0(x, y, z) = 293.15\text{K} - 0.025 \frac{\text{K}}{\text{m}} (z - 600\text{m})$

- $p_{\text{GR}0}(x, y, z) = 0.1013 \text{ MPa}$

- $p_{\text{cap}0}(x, y, z) = \begin{cases} 30.0 \text{ MPa} & \text{, in all repository materials} \\ 0.1\text{e}06 \text{ Pa} + 10150 \frac{\text{Pa}}{\text{m}} (z - 600\text{m}) & \text{, in all rock materials} \end{cases}$

- **Boundary conditions at top & bottom boundary:**

- $p_{\text{GR}}(t, x, y, z) = p_{\text{GR}0}(x, y, z)$
- $p_{\text{cap}}(t, x, y, z) = p_{\text{cap}0}(x, y, z)$
- $T(t, x, y, z) = T_0(x, y, z)$

- **Repository conditions during ventilation and deposition phase:**

Materials	Access Gallery + Shaft + Seals	Deposition Tunnels
Ventilation BC for $t < 50$ years	80% RH $\rightarrow p_{\text{cap}} = 30 \text{ MPa}$	80% RH $\rightarrow p_{\text{cap}} = 30 \text{ MPa}$
Instantaneous condition at $t = 50$ years	80% Saturation (proctor), p_{cap} results from retention curve	

Figure 4-3: Summary of the model set-up containing initial and boundary conditions as well as repository conditions during the ventilation and the deposition phase. The origin of the coordinate system lies in the centre of the repository, so that the top boundary has the vertical coordinate $z = 600 \text{ m}$.

Heat source

To represent the waste volume in the deposition tunnels, we apply an average equivalent waste heat according to the heat source term specified per m of canister. We apply the heat source term as a volumetric heat source that is evenly distributed in the volume of the deposition tunnel, corresponding to the waste, the void and the steel liner.

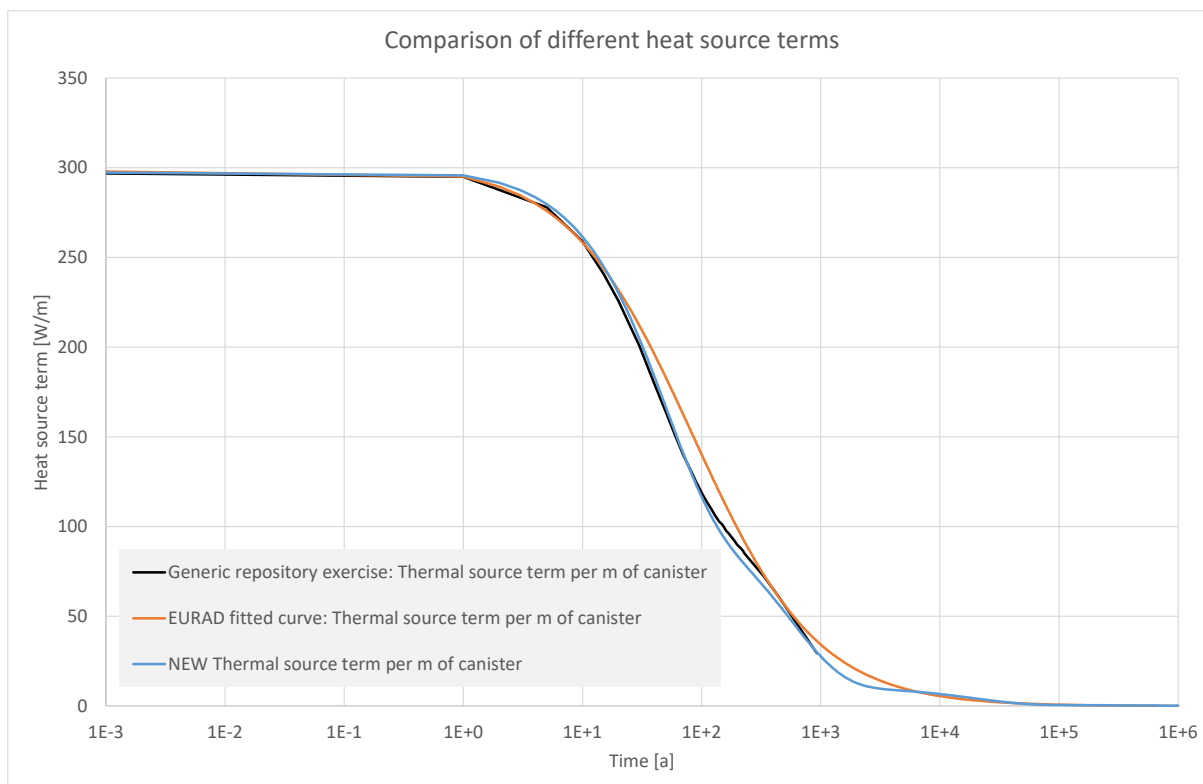


Figure 4-4: Comparison of the thermal source term for HLW canisters from the generic repository exercise (per m of canister) and the curves discussed in our model. The results presented in this report are based on the blue curve, which is based on the data from the generic repository exercise (Wendling, 2020) in combination with heat output as defined in the RESUS project (Alfarra et al. 2020 and Maßmann et al. 2022), which uses a thermal source term physically based on radioactive decay as summarized in Table 4-2.

Table 4-2: Parameters for the thermal source term equation based on radioactive decay

Nuclide	Heat output P [W]	Half-life $t_{1/2}$ [a]	Decay constant
1	1156.00	32.2	0.021526310
2	226.70	396.8	0.001746843
3	21.51	13670.0	0.000050706
4	0.9466	759300.0	0.000000913

In order to cover a time span of 1 000 000 years, the thermal source-term data range provided in the generic repository exercise has been expanded, using values from Table 4-2:

$$Q_{waste} = \left(1156 \cdot e^{\left(-\frac{t}{60 \cdot 60 \cdot 24 \cdot 365.25} + 50\right)} \cdot \frac{\ln(2)}{32.2} + 226.7 \cdot e^{\left(-\frac{t}{60 \cdot 60 \cdot 24 \cdot 365.25} + 50\right)} \cdot \frac{\ln(2)}{396.8} + 21.51 \cdot e^{\left(-\frac{t}{60 \cdot 60 \cdot 24 \cdot 365.25} + 50\right)} \cdot \frac{\ln(2)}{13670} + 0.9466 \cdot e^{\left(-\frac{t}{60 \cdot 60 \cdot 24 \cdot 365.25} + 50\right)} \cdot \frac{\ln(2)}{759300} \right) \cdot 0.48044$$

where Q_{waste} is the power of the heat source per m of canister in W and t is time in s.

To fit the thermal source term to our 3D model, more specifically to the heat produced by one meter of deposition tunnel Q_m in W, we multiply the equation as follows

$$Q_m = \frac{L_{\text{canister}}}{L_{\text{canister}} + L_{\text{void}}} \cdot Q_{\text{waste}} = \frac{1.5}{1.5 + 0.3} \cdot Q_{\text{waste}}$$

where L_{canister} is the length of one canister and L_{void} is the distance between adjacent canisters/waste packages in m. In addition, OGS-6 requires the transformation of the heat source term per m of deposition tunnel into a heat source term Q_{applied} in W m^{-1} of the deposition tunnel:

$$Q_{\text{applied}} = \frac{1}{\pi \cdot r^2} \cdot Q_m = \frac{1}{\pi \cdot 0.5^2} \cdot Q_m$$

With r the radius of the deposition tunnel.

Gas source

We apply two distinct gas source terms. On the one hand, we apply a volumetric gas source that is evenly distributed in the volume of the deposition tunnel (radius of 0.5 m), corresponding to the waste, the void and the steel liner. As specified, we consider a gas source term of 1.9 mol/y per meter of deposition tunnel from $t = 50$ to $t = 40\,000$ years. Considering a cross-sectional area of 0.7854 m^2 and a molar mass of hydrogen M_{H_2} of 0.002016 kg/mol, we apply a hydrogen gas source of $1.5454\text{e-}10 \text{ kg m}^{-3}\text{s}^{-1}$ (Figure 4-5).

On the other hand, we apply a volumetric gas source term that is evenly distributed in the volume of the access gallery and shaft (radius of 5 m), corresponding to the backfill and the concrete liner. As specified, we consider a gas source term of 21.5 mol/y per meter of access gallery and shaft from $t = 50$ to $t = 50\,000$ years. Considering a cross-sectional area of 78.54 m^2 and a molar mass of hydrogen M_{H_2} of 0.002016 kg/mol, we apply a hydrogen gas source of $1.7488\text{e-}11 \text{ kg m}^{-3}\text{s}^{-1}$ (Figure 4-5).

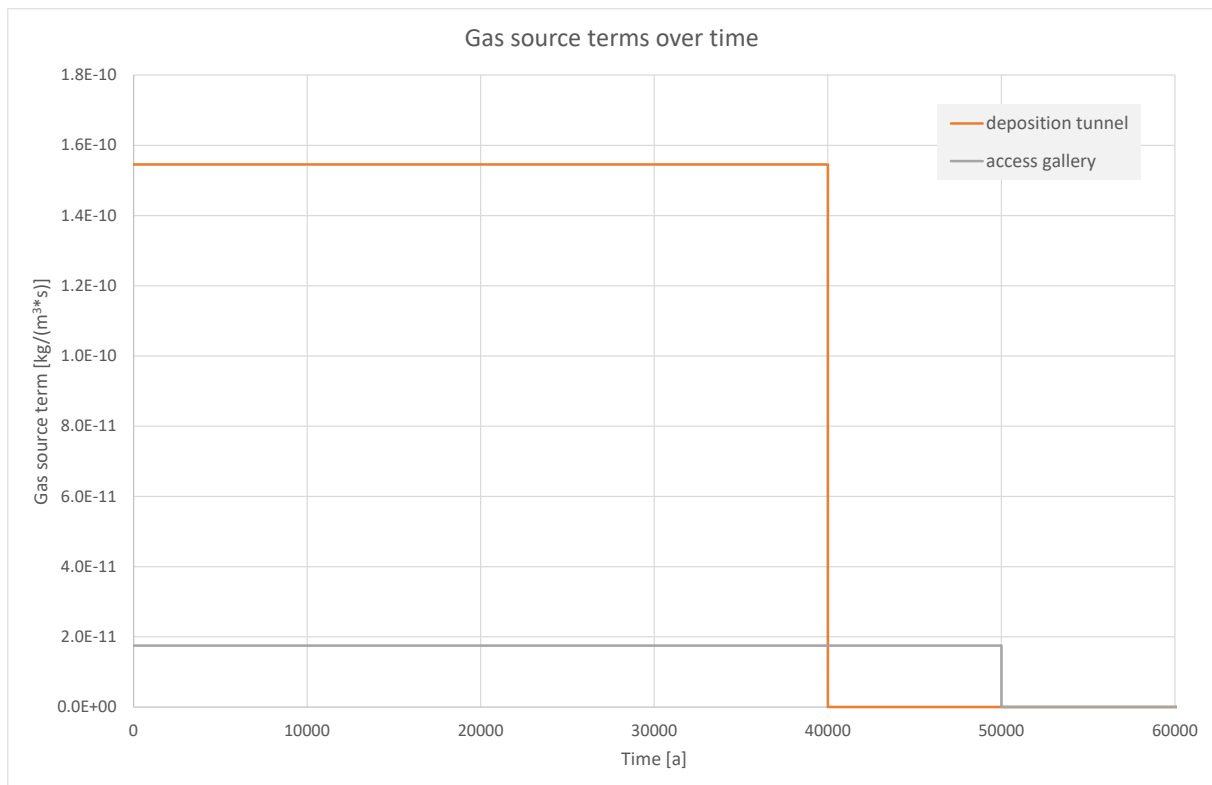


Figure 4-5: Gas source terms applied to the deposition tunnel as well as access galleries and shaft.

Finite element mesh

The mesh shown in Figure 4-6 is composed of > 600 000 nodes and > 4 million elements. The specific body force (i.e. gravity) is considered and is -9.81 m/s^2 in z-direction. The maximum time span modelled is about 300 000 years. Using conventional Linux-Servers with up to 100 cores, CPU time was about some weeks.

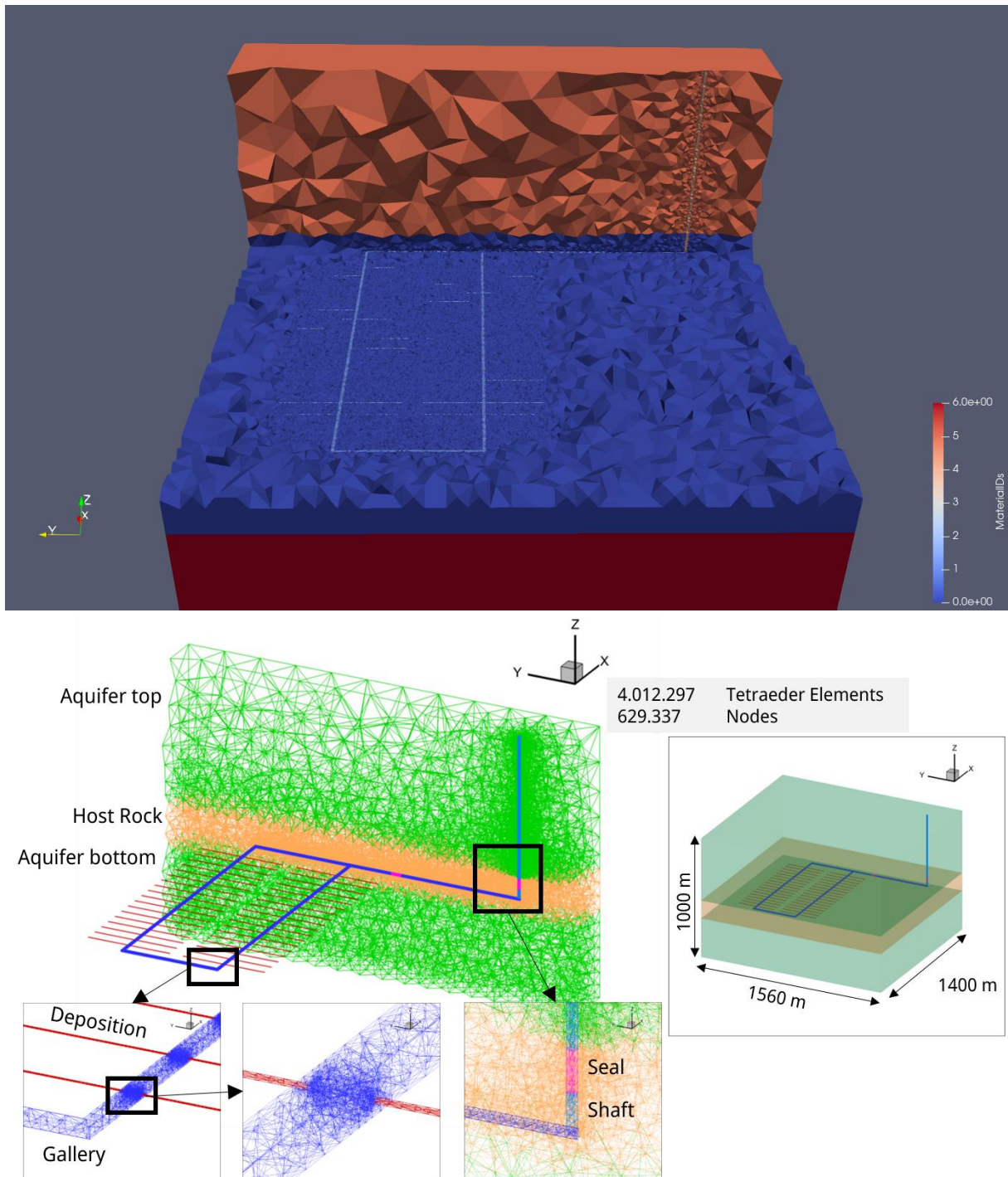


Figure 4-6: General view of the repository-scale 3D mesh (top) and details of the mesh (bottom).

4.3 Simulation results

The interpretation of the simulation results focuses on the evolution of temperature, gas and liquid pressure as well as saturation within and around the repository. The output points as defined by the task lead are summarized in Figure 4-7. Most of the output points are located directly in the repository: Some at the ends of the deposition tunnels (green labels), some at the entrance to the deposition tunnels, directly near the galleries (red labels). The points labelled in blue are located in the galleries. Some additional output points are located within (purple) and around the seals (orange/black). One output point lies in the host rock (light blue).

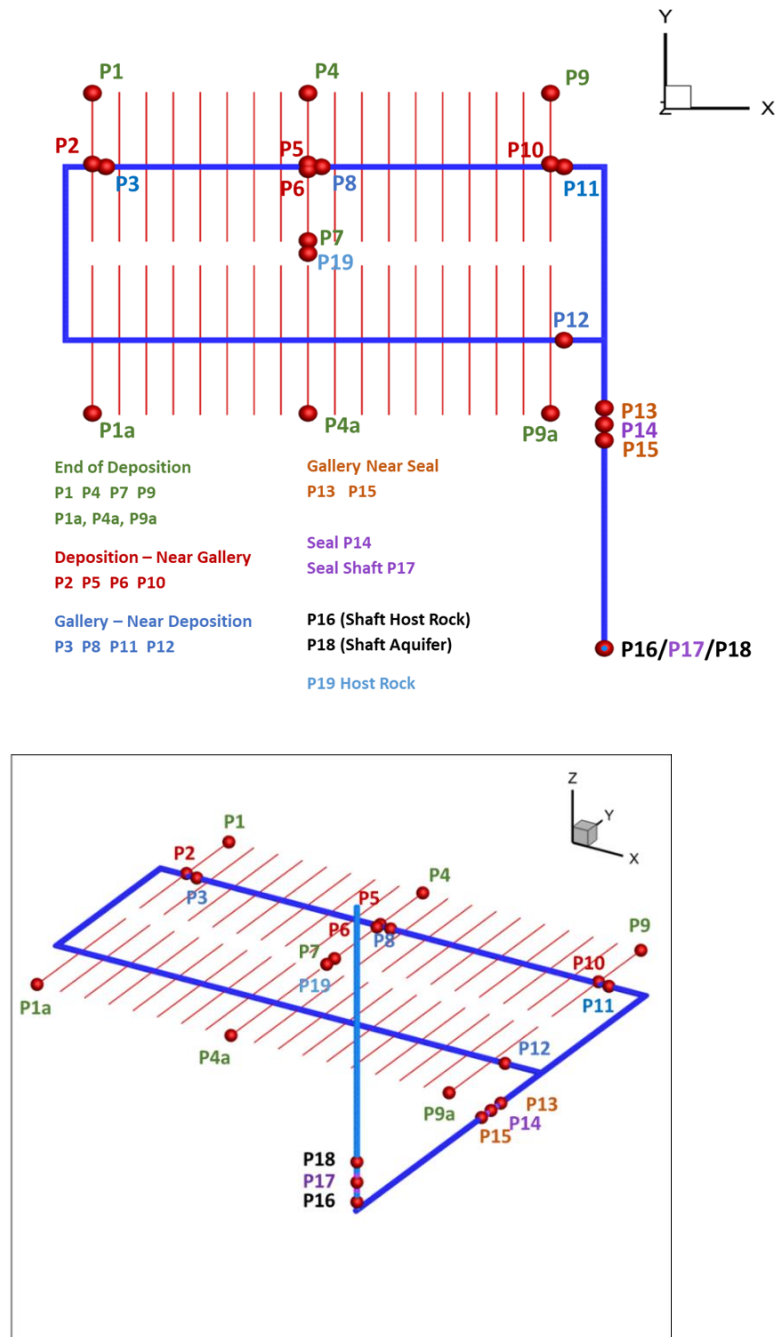


Figure 4-7: 2D (top) and 3D (bottom) plot of the output points as defined in Wendling (2020). Additional points have been introduced to investigate possible effects of the model boundaries. The labelling of these points ends with an “a”.

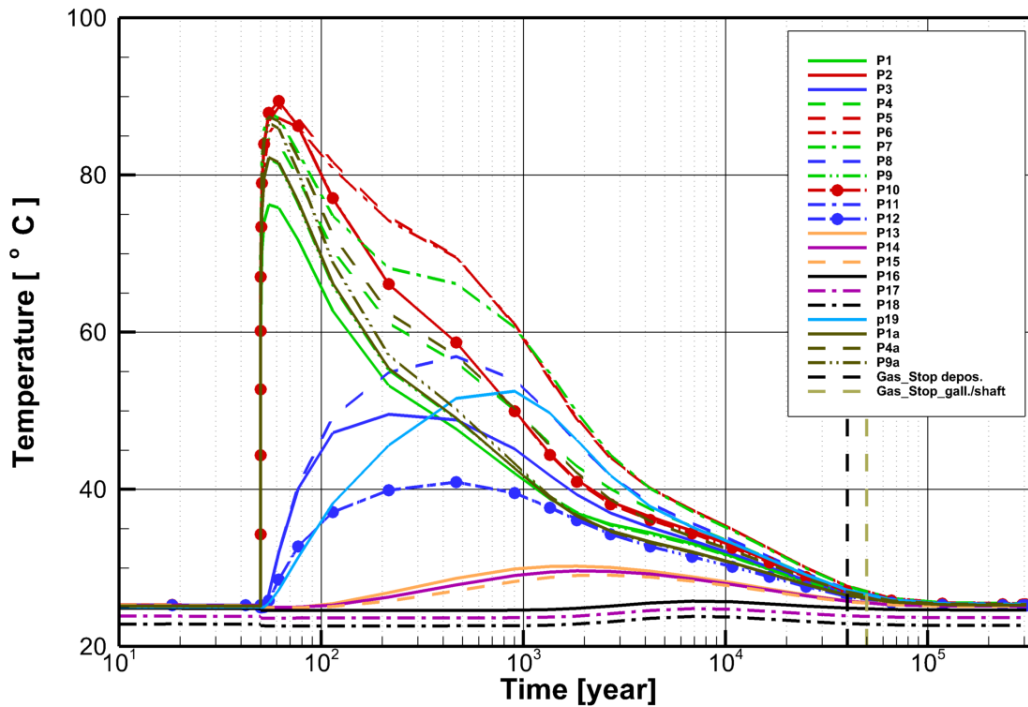


Figure 4-8: Temperature over time at the defined output locations given in Figure 4-7.

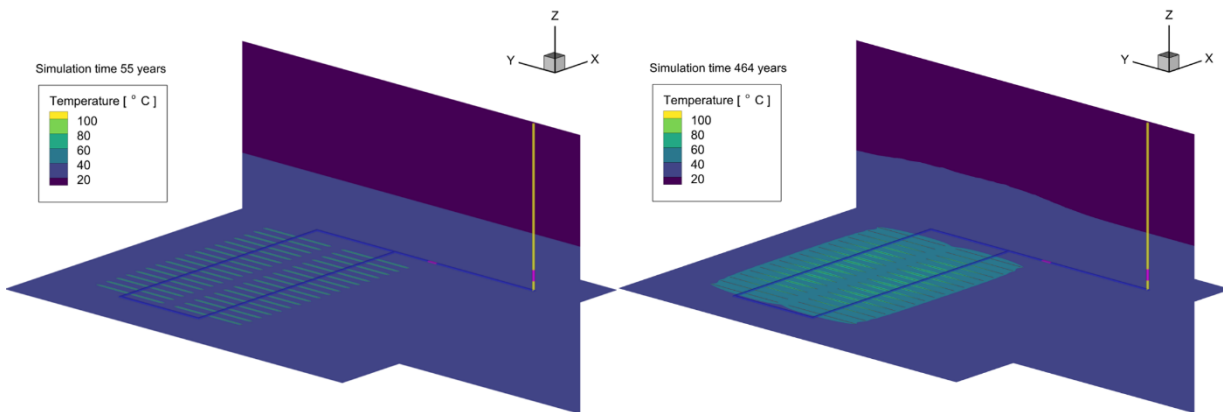


Figure 4-9: Contour plots of the temperature after 55 years (left) and ~450 years (right).

The temperature evolution over time at the defined output points is presented in Figure 4-8. After the ventilation phase of 50 years, the start of the deposition phase comes along with an immediate increase of temperature in the deposition tunnels (green and red lines) as expected. The maximal temperature is reached at about 60 years and yields about 90 °C. The highest value is reached at the output points located at the entrance of the deposition tunnels, near the access galleries. Due to the geometric situation there are some slight differences between the output points in the galleries: the highest temperature is reached in the central part of the repository. The temperature evolution in the galleries and also in the host rock is characterized by a delayed increase of the temperature. The maximal temperature at the given output points within the galleries reaches about 55 °C and is also corresponding to the point closest to the centre. The temperature increase in the seals is significantly smaller, with a maximum value of about 30 °C, which is reached after more than 1 000 years. Contour plots of the temperature for chosen output times (55 years, ~450 years) are given in Figure 4-9, indicating also the central area with maximal temperatures.

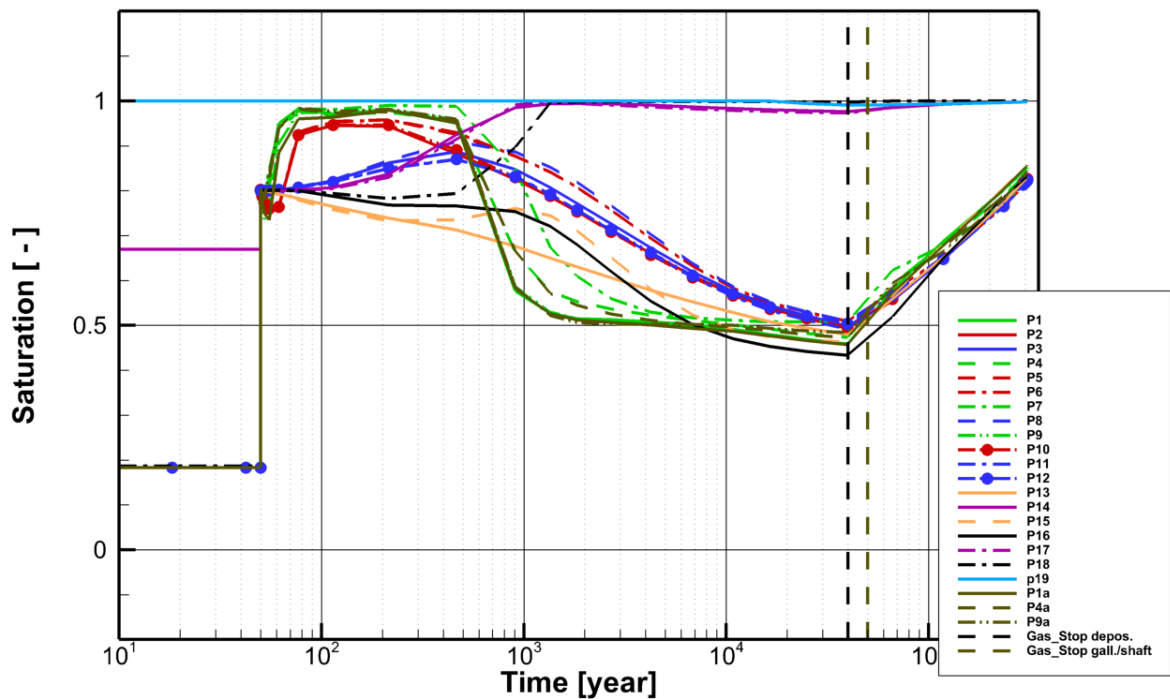


Figure 4-10: Saturation over time at the defined output locations given in Figure 4-7.

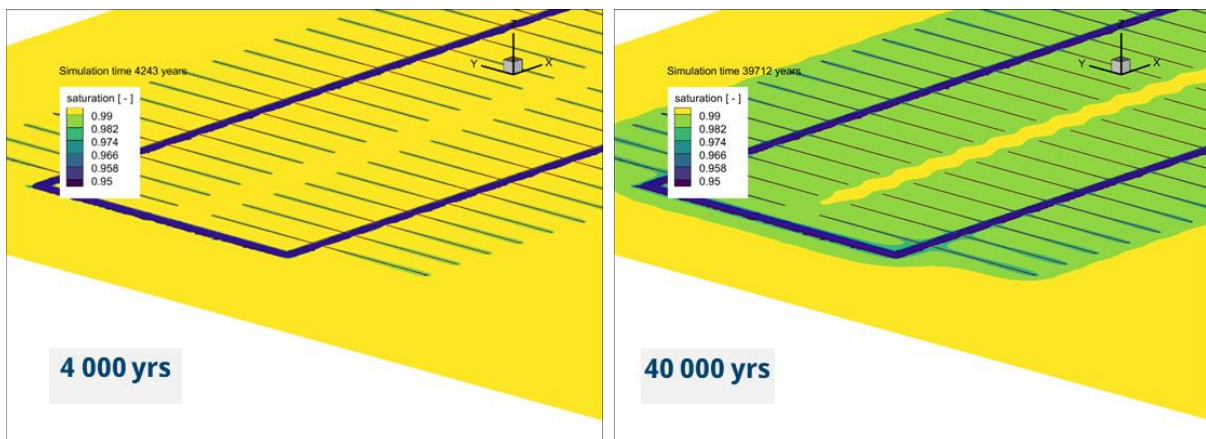


Figure 4-11: Contour plots of the saturation after ~4000 years (left) and ~40,000 years (right).

The evolution of the saturation in the different materials in and around the repository is presented in Figure 4-10. The saturation in the ventilation phase (up to 50 yrs) represents the defined boundary conditions as defined in Figure 4-3. Focusing on the deposition zones (green and red lines in Figure 4-10), the start of the deposition phase leads to a sudden decrease of saturation due to the desaturated host rock. After that, a resaturation takes place due seepage from the host rock as well as thermal liquid expansion. In a later phase, the gas production leads to a desaturation. The same behaviour can be observed in the galleries, albeit in a reduced form. The saturation evolution in the host rock is represented by the light blue line. It indicates a slight desaturation after > 40 000 years. It has to be

mentioned, that this desaturation depends significantly on the retention curve. With the chosen retention curve, desaturation is computed as soon as the gas pressure exceeds the liquid pressure. The result is an out-gassing of the gas previously dissolved in the liquid phase. If a high gas entry pressure were assumed, this effect would not be expected unless the sum of liquid and gas entry pressure was exceeded by the gas pressure. Therefore, one can also expect that the chosen retention curve affects the development of the gas and liquid pressure via the extent of the desaturated zone. The modelled extent of the desaturated zone is shown in Figure 4-11. It becomes obvious that the saturation in the host rock remains very high with minimal values of > 0.97 . In contrast, the strongest desaturation takes place in the seal of the shaft (black line).

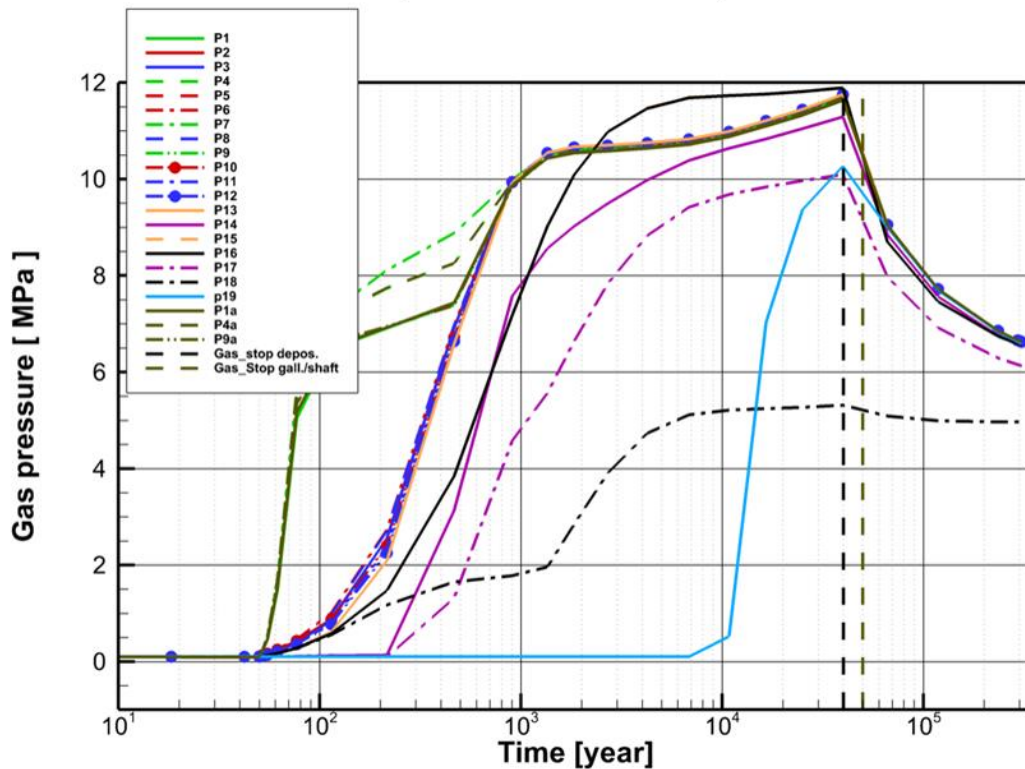


Figure 4-12: Gas pressure over time at the defined output locations given in Figure 4-7.

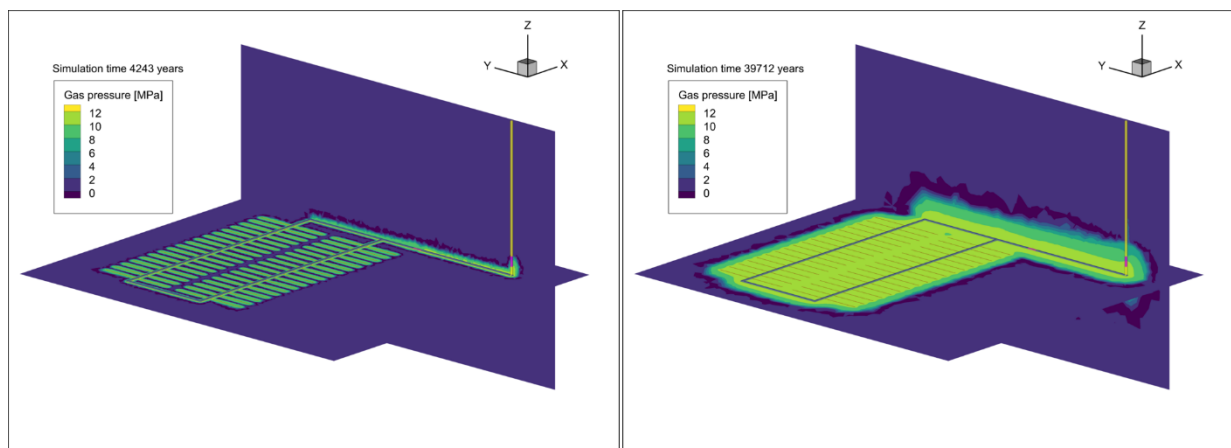


Figure 4-13: Contour plots of the gas pressure after ~4000 years (left) and ~40,000 years (right).

The gas pressure evolution is plotted in Figure 4-12 for the defined output locations. It indicates a faster increase and higher gas pressures at the end of the deposition tunnels (green lines) than at the entrance of the deposition tunnels (red lines), where the gas pressure follows that in the galleries (blue lines). The maximal gas pressure is reached at the end of the gas production time (40 000 years) with a value of ~12 MPa. In the host rock, the gas pressure increase starts at about 10 000 years, corresponding to the desaturation phase of the host rock. The maximum value reached is about 10 MPa. The distribution of gas pressure after ~4 000 and ~40 000 years is plotted in Figure 4-13. The highest values of gas pressure are reached between the seal in the gallery and the seal in the shaft.

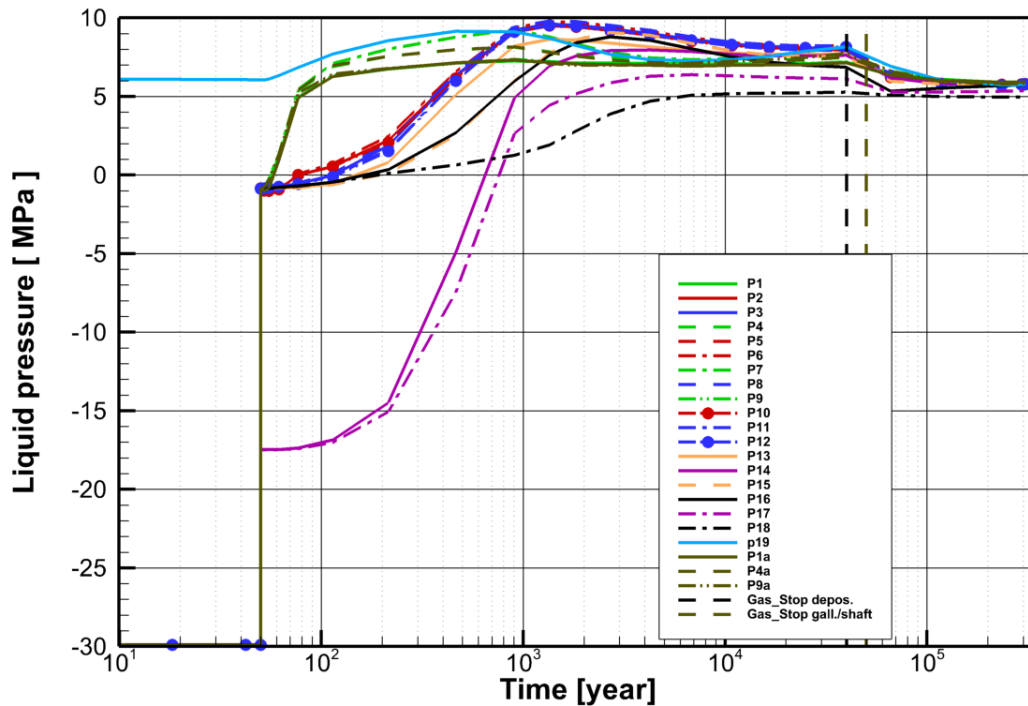


Figure 4-14: Liquid pressure over time at the defined output locations given in Figure 4-7.

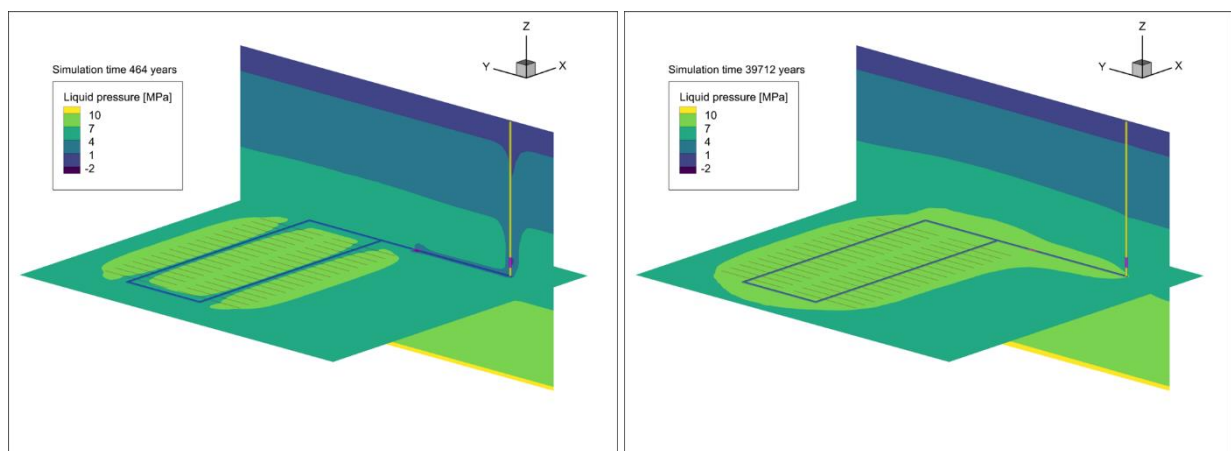


Figure 4-15: Contour plots of the liquid pressure after ~450 years (left) and ~40,000 years (right).

The evolution of liquid pressure is given in Figure 4-14. The conditions during the ventilation phase are evoked by the different retention curves of the material groups. An early increase of the liquid pressure at the end of the deposition tunnels and in the host rock can be seen. The maximum values are reached after about 500 years in the host rock (9 MPa) and after about 1500 years in the repository (10 MPa). The distribution of the liquid pressure is plotted in Figure 4-15 and Figure 4-16, indicating the zones with the highest liquid pressures. Figure 4-16 pictures the situation after 1834 years, which corresponds to the time with maximal values. The contour plot clearly indicates the impact of the boundary condition on the liquid pressure. To quantify this effect, some additional output points have been defined. These are plotted in Figure 4-7 and the labelling of these points ends with an “a” (P1a, P4a, P9a). They correspond to the respective output location (P1, P4, P9). Comparing these points in Figure 4-8, Figure 4-10, Figure 4-12 and Figure 4-14 indicates a low impact of this boundary on the results. Nevertheless, the extent of the model domain should be increased in further model set-ups.

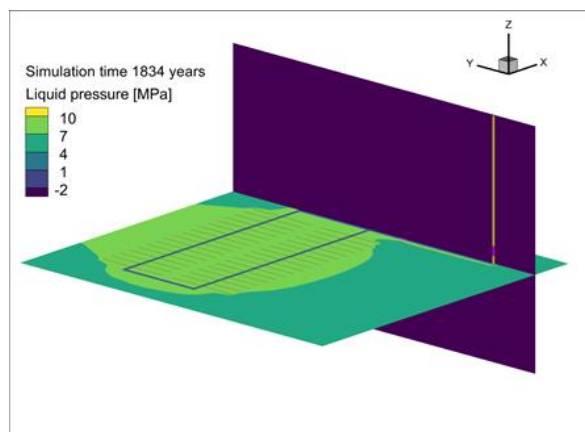


Figure 4-16: Contour plot of the liquid pressure after 1834 years, indicating the impact of the boundary condition.

4.4 Summary and future work

BGR has been involved in Task 2, Task 3 and Task 4 of the WP GAS. Based on the model validation against laboratory experiments conducted in Task 2 and 3, strategies to include gas transport processes on the repository scale have been developed in Task 4. In this context, the OGS 6 process class TH2M has been used and enables the modelling of coupled TH2M effects on the repository scale with specific focus on gas transport. Based on the generic repository description, a 3D model of disposal zone C was created. The presented model set-up enables an investigation of the coupled TH2 effects caused by the heat source of the radioactive waste and the gas production due to corrosion. The approach is characterised by some simplifications such as the homogenisation of the material parameters and the neglect of mechanical effects (as discussed in Pitz et al., 2023c). However, the model allows statements to be made about the development of temperature, saturation, gas and liquid pressure in and around the repository over several millennia. A comparison of the OGS 6 results with similar modelling results from other teams shows qualitatively and quantitatively a satisfactory agreement, although there are still details to be discussed.

Generally, the investigation of gas transport processes on the repository scale is numerically challenging, as complex and interacting effects arise on a large scale over a long time period. Therefore, it is necessary to get an understanding of the sensitivity of the results regarding physical effects, boundary conditions, material parameters and also parameters of the numerical set-up (density of mesh, numerical e.g. solver settings). Based on this process and system understanding, a numerical model can be built that is numerically manageable on the one hand and provides meaningful results on the other.

The presented BGR model focuses on TH2 effects, while the mechanical aspects are neglected. Assuming a gas pressure lower than the breakthrough pressure, the impact of the mechanical aspects is low. However, the model includes the lower and upper aquifer, because test simulations indicated that these areas have a significant impact on the flow processes within the repository. It has to be mentioned, that the aquifers have been simplified concerning their material parametrization. The impact of this simplification on the results has to be quantified. Setting reasonable boundary conditions is a very important part of the model set-up: the pressure distribution, degree of saturation and also the hydraulic conditions within the repository during ventilation and thereafter have a significant impact on the results. Additionally, the sensitivity of the material parameters has to be investigated and is an important basis for the modelling. While some parameters like the retention curve and the Henry coefficient have a significant impact on the gas transport processes, the impact of some other material parameters is minor. Finally, safety analysis requires a comprehensive understanding of the coupled processes, their sensitivities and the long-term interactions between the various effects. The model class TH2M of OGS 6 forms an extensively tested tool to simulate large scale geotechnical systems like the repository model aiming on an increased understanding of the safety relevant effects.

Nevertheless, there are still open questions: While effects like advective and diffusive gas transport of dissolved gas as well as two-phase flow are part of the modelling on repository scale, processes such as dilatancy-controlled gas flow along pathways and gas transport in tensile fractures have to be taken into account on a smaller scale. Furthermore, the impact of gas transport effects on radionuclide transport processes has not been investigated. The proposed conceptual approach, which includes models of different size and detail level enables investigation of effects like pressure build-up and gas transport on the repository scale and a focus of near field effects on the deposition tunnel scale.

4.5 References

Alfarra, A., Bertrams, N., Bollingerfehr, W., Eickemeier, R., Flügge, J., Frenzel, B., Maßmann, J., Mayer, K.-M., Mönig, J., Mrugalla, S., Müller-Hoeppe, N., Reinhold, K., Rübél, A., Schubarth-Engelschall, N., Simo, E., Thiedau, J., Thiemeyer, T., Weber, J.R. & Wolf, J. (2020): RESUS: Grundlagen zur Bewertung eines Endlagersystems in einer Tongesteinsformation größerer Mächtigkeit. GRS; 571; Köln (Gesellschaft für Anlagen- und Reaktorsicherheit (GRS) gGmbH).

Bilke, L., Flemisch, B., Kalbacher, T., Kolditz, O., Helmig, R., Nagel, T., (2019): Development of open-source porous media simulators: principles and experiences *Transp. Porous Media* 130 (1), 337 – 361

Jobmann, M., Bebiolka, A., Jahn, S., Lommerzheim, A., Maßmann, J., Meleshyn, A., Mrugalla, S., Reinhold, K., Rübél, A., Stark, L., Ziefle, G. (2017). Projekt ANSICHT: Sicherheits- und Nachweismethodik für ein Endlager im Tongestein in Deutschland. Synthesebericht TEC-19-2016-AB, DBE TECHNOLOGY GmbH, BGR, GRS, Peine, Hannover, Braunschweig.

Norbert Grunwald, Christoph Lehmann, Jobst Maßmann, Dmitri Naumov, Olaf Kolditz, Thomas Nagel (2022) “Non-isothermal two-phase flow in deformable porous media: Systematic open-source implementation and verification procedure (accepted)”. In: *Geomech. Geophys. Geo-energ. Geo-resou.*

Marschall, P., Horseman, S., Gimmi, T., 2005. Characterisation of gas transport properties of the Opalinus Clay, a potential host rock formation for radioactive waste disposal. *Oil & Gas Science and Technology* 60 (1), 121–139

Maßmann, J., Thiedau, J., Bittens, M., Kumar, V., Tran, T.V., Guevara Morel, C., Kneuker, T. & Schumacher, S. (2022): Methode und Berechnungen zur Integritätsanalyse der geologischen Barriere für ein generisches Endlagersystem im Tongestein. Projekt ANSICHT-II. Bundesanstalt für

Geowissenschaften und Rohstoffe (BGR), Ergebnisbericht; Hannover.
DOI:<https://doi.org/10.25928/n8ac-y452>

Pitz, M., Kaiser, S., Grunwald, N., Kumar, V., Buchwald, J., Wang, W., Naumov, D., Chaudhry, A. A., Maßmann, J., Thiedau, J., Kolditz, O., Nagel, T. (2023a): Non-isothermal consolidation: A systematic evaluation of two implementations based on multiphase and Richards equations. In: International Journal of Rock Mechanics and Mining Sciences, <https://doi.org/10.1016/j.ijrmms.2023.105534>.

Pitz, M., Jacobs, E., Grunwald, N., Ziefle, G., Nagel, T. (2023b): On Multicomponent Gas Migration in Single Phase Systems, In: Rock Mechanics and Rock Engineering (submitted).

Pitz, M., Ziefle, G., Kunz, H., Nagel, T., Maßmann, J. (2023c): A Numerical Large-Scale Investigation of Gas Transport Processes in a Generic Nuclear Waste Repository in Argillaceous Porous Media. (in prep.)

Wang, W., Shao, H., Nagel, T., Kolditz, O. (2021): Analysis of coupled thermal-hydro-mechanical processes during small scale in situ heater experiment in Callovo-Oxfordian clay rock introducing a failure-index permeability model. *Int. J. Rock Mech. And Min. Sci.* 142

Wang, W., Rutqvist, J., Görke, U.-J., Birkholzer, J.T., Kolditz, O. (2011): Non-isothermal flow in low permeable porous media: A comparison of Richards' and two-phase flow approaches. *Environmental Earth Sciences* 62, 1197-1207

Wendling, J. (2020): EURAD-GAS "Generic Repository" exercise. Internal report.

5. Contribution of IRSN

As discussed in the framework of WP DONUT (Deliverable 4.1, Ahusborde et al., 2021) the IRSN purpose in the WPs DONUT and GAS is to improve knowledge of the physics of two-phase (liquid-gas) two-component (water-hydrogen) flow and transport models at various scales of a disposal facility (Cell, Module, DGR) by incorporating important phenomena neglected in previous studies, as well as to quantify uncertainties due to these neglected phenomena. Among these phenomena are the capillary gas entry pressure and hysteresis which showed to be important for explaining two-phase flow in-situ and laboratory experiments (PhD, Amri, 2021; Amri et al., 2022, 2023).

The IRSN contribution to this task 4.2 exercise of the WP GAS consists in studying the impact of capillary gas entry pressure on hydrogen transfer in the stand-alone disposal zone C with shaft inside the clay host rock (module of 72 HLW cells, Figure 5-1(a)). The new Van Genuchten - Mualem hydrodynamic functions, accounting for an explicit representation of the capillary gas entry pressure (called VGM-PE), developed by Amri et al. (2022) in the framework of WP DONUT (Deliverable 4.1, SotA DONUT, Ahusborde et al., 2021) will be tested by considering the parametrization proposed in Milestone 61 for the host rock, EDZ and engineered barriers materials. The numerical model developed is based on the two-phase (liquid-gas) and two-component (water-hydrogen) equation of state EOS5 (Pruess et al., 1999, 2011) of TOUGH suite of codes (iTOUGH2, Finsterle, 2007; TOUGH2-MP, Zhang et al., 2008).

In this study, only a structured and rectilinear mesh is tested. Hysteresis, the coupling of geo-mechanics with two-phase flow, and the transport of radionuclides are not modelled.

5.1 Model description

Physical domain

The repository is located at 600 m depth from the surface ($z = 0$) in the center of the host rock layer of 150 m thickness (between $z = 525$ m and $z = 675$ m from the surface).

The purpose is to evaluate the contribution of HLW cells of disposal zone C (stand-alone disposal zone C with shaft) to gas phase flow and transport of hydrogen generated by metallic components in the cells (micro-tunnels) and the drifts to the shaft outlet (yellow disc in Figure 1(a)). The studied module is that bounded by dark broken lines shown in Figure 5-1 (a). It consists of 72 HLW cells, two access drifts, a main drift, and a shaft, all embedded within the host rock layer, as also shown in Figure 5-2 (3D view preprocessed under PetraSim). There is incorporation of seals in the main drift (red colour in Figure 5-1(a)) and in the shaft (not shown in Figure 5-1(a)). Geometries (length and section) of seals are shown in Figure 5-3(a) and Figure 5-3(b), and those of drifts and cells are shown in Figure 5-1 and Figure 5-4. In Figure 5-1, Figure 5-3 and Figure 5-4 one can see the inner and outer EDZs, and constitutive materials of the engineered barriers (concrete, bentonite, and backfill) attributed to these geometries. The domain volume is $2\,410 \times 1\,760 \times 150$ m³.

Preprocessing of the domain geometry is carried out using PetraSim (Thunderhead engineering INC). Figure 5-5 shows attribution of the material type to the different components of the cell, drift, shaft, and seals (in the main drift and in the shaft) with the surrounding EDZs.

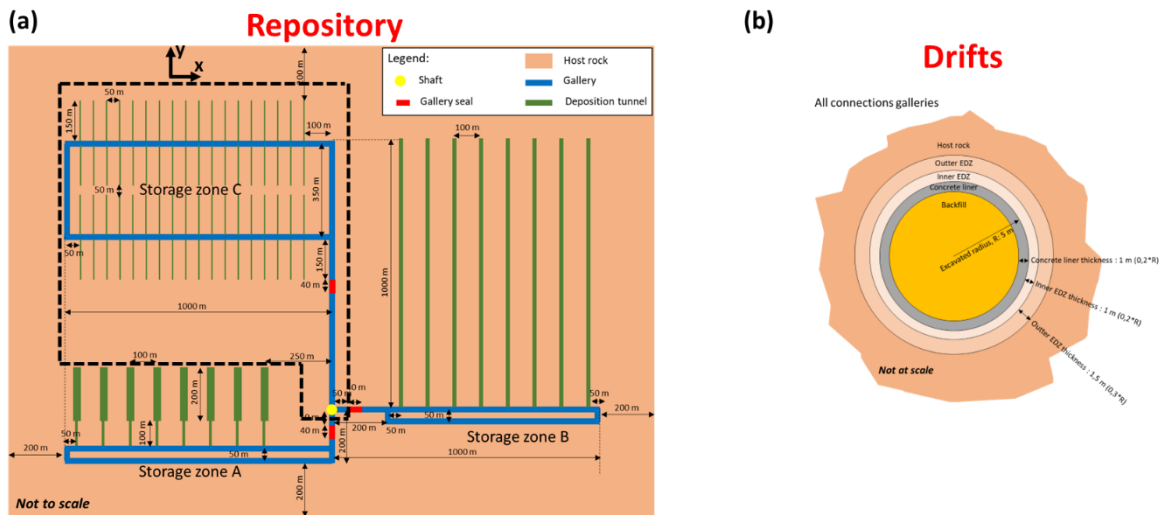


Figure 5-1 – (a) Schematic horizontal slice at generic repository depth. (b) Schematic vertical slice of a gallery.

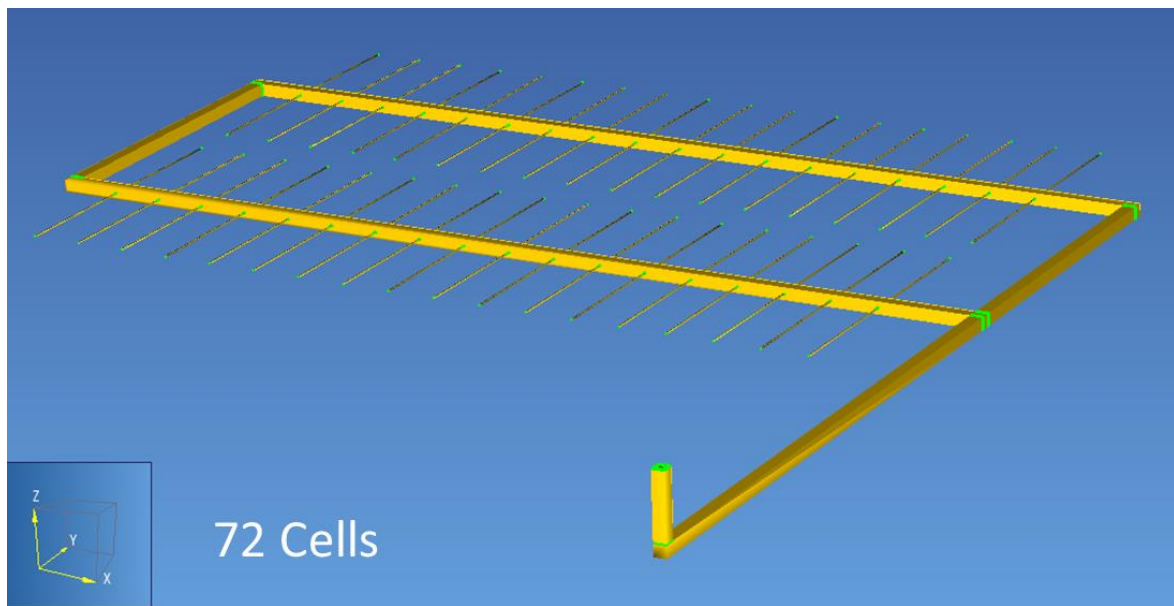


Figure 5-2 – 3D view of the stand-alone module of 72 HLW cells with shaft embedded within the host rock layer (PetraSim preprocessing; Thunderhead engineering inc.).

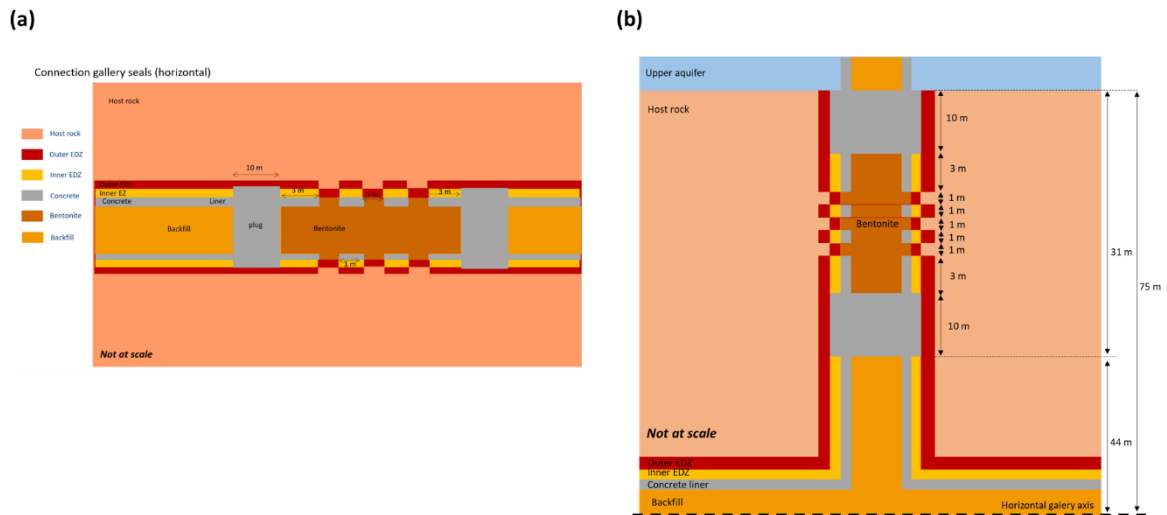


Figure 5-3 – (a) Schematic representation of a connection gallery seal. (b) Schematic representation of the shaft seal.

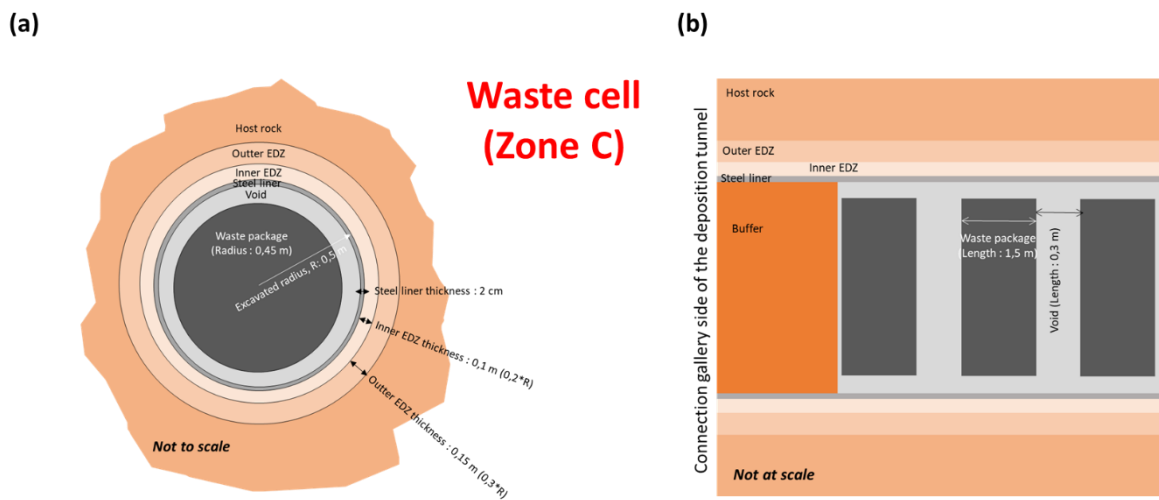


Figure 5-4– Schematic representation of a deposition tunnel in disposal zone C (inspired by Andra HLW deposition micro-tunnel): a/ Cross section inside the waste cell; b/ Longitudinal side of the waste cell.

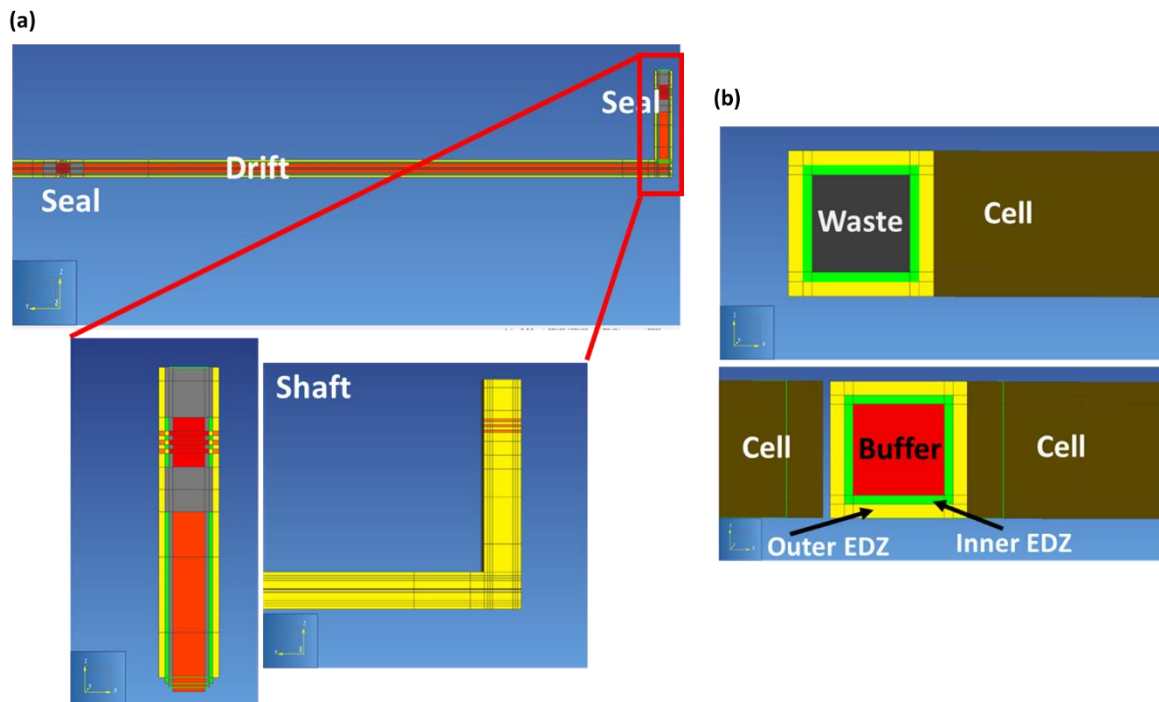


Figure 5-5 – (a) Materials defining drift and shaft seals. (b) Materials defining the waste cell.

As deviations from the benchmark specifications: (i) The radial sections of the cell, drift and shaft are assumed rectangular (Figure 5-2 and Figure 5-5) to avoid the problem of intersection between curvilinear shapes of surfaces, i.e., between the micro-tunnel of the waste cell and the drift, and between the main drift and the shaft; (ii) Properties of the steel-liner (2 cm thickness) adjacent to waste packages are considered as those of the cell void, whereas properties of the steel-liner adjacent to the buffer (bentonite) are considered as those of the cell buffer (Figure 5-5(b)).

Modelled phenomena

The performed model is based on the fluid property equation of state EOS5 (Pruess et al., 1999, 2011) of TOUGH (iTOUGH2 and TOUGH2-MP) to solve the problem of non-isothermal two-phase (liquid-gas) flow and two components (water-hydrogen) transport in both liquid and gas phases in the different porous materials. The EOS5 code assumes that hydrogen transport occurs by advection and diffusion in both liquid and gas phases according to Darcy and Fick laws, with a partition of hydrogen between the two phases according to Henry's law. The EOS5 code has been modified to account for gas-entry pressure with the new hydraulic properties' curves VGM-PE (Amri et al., 2022).

In the mass balance equation of hydrogen, production of hydrogen due to anoxic corrosion of metals is modelled as a source term.

The generic gas source term is supposed to be composed solely by hydrogen generated by anoxic corrosion of only non-allied steel (i.e., no other metallic component, no radiolysis, and no bacterial activity).

The hydrogen generation rate is approximated as follows:

$$(1) \quad F_{H_2} = S \times CR \times C$$

With:

F: hydrogen generation flux (mol/y),

S: available surface of metallic component (m²),

CR: Corrosion Rate (m/y),

C: constant coefficient to pass from m³/y to mol/y (mol/m³). For Hydrogen and non-allied steel C, it can be approximated by 215 000 mol/m³.

For **all galleries**, this flux is calculated per unit length of the drift knowing that the surface of the metallic components (concrete rebars of 0.5 cm thickness) is 1000 m² which corrode at a rate of 10⁻⁷ m/y (low value because of the alkaline environment). This leads to a constant gas source term of 21.5 mol/y (per meter of gallery) lasting 50 000 y (time needed to corrode 0.5 cm of thickness).

For **HLW waste cell** in disposal zone C, the flux is due to the metallic liner and waste container, its average per unit meter length of the cell (not including the buffer part) is calculated knowing that the surface of the metallic component is 9 m², the thickness of the metallic component is 4 cm, and the corrosion rate is 10⁻⁶ m/y (no passivation linked to an alkaline environment). This leads to a gas source term of around 1.9 mol/y (per meter of zone C HLW cell) during 40 000 y. No metallic component in the waste (assumed to be made of nuclear glass).

A schematic representation of the emplacement of the different gas source terms described is shown in Figure 5-1(b) and Figure 5-4. The H₂ source terms in the micro-tunnel are in the liner and waste containers of the cell, while those in the drifts are in the concrete liners. These source terms are modelled by injection of H₂ fluxes in the WASTE material (voids and canisters in the micro-tunnel, Figure 5-5(b)), and in the concrete liners of the drift (Figure 5-5(a)).

The thermal power generated by waste wells is also modelled but as time-dependent source term in the heat transfer equation according to the tabulated data given in Levasseur et al. (2021) (see their table in Figure 5-10 for thermal power values varying between 300 to 29,5 Watt/m canister' for years between 0 and 930, respectively).

The model needs to specify physical, thermal, hydraulic, and hydrogen transfer properties for each porous medium as well as initial and boundary conditions, as will be discussed below.

Equations and transfer properties

The new model VGM-PE (Amri et al., 2022) is a generalization of Vogel et al. (2001) model for two-phase flow with a non-zero capillary gas entry pressure $P_{c,e}$ (Pa) in the constitutive Van Genuchten-Mualem (Mualem, 1976; Van Genuchten, 1980; Parker et al., 1987) relationships for the water retention curve $P_c(S_l)$ and the relative permeability to liquid and gas curves $k_{r,\beta=l,g}(S_l)$. This model is described by the following equations:

$$(2a) \quad P_c(S_l) = \begin{cases} -\frac{1}{\alpha} \left[(S_e^* S_e)^{-\frac{1}{m}} - 1 \right]^{\frac{1}{n}} & \text{if } S_e \leq 1 \\ 0 & \text{elsewhere} \end{cases}$$

$$(2b) \quad k_{r,l}(S_l) = \frac{k_l(S_l)}{k_{0,l}} = \begin{cases} [S_e]^\tau \left[\frac{1 - (1 - (S_e^* S_e)^{\frac{1}{m}})^m}{1 - (1 - (S_e^*)^{\frac{1}{m}})^m} \right]^2 & \text{if } S_e < 1 \\ 1 & \text{if } S_e = 1 \end{cases}$$

$$(2c) \quad k_{r,g}(S_l) = \frac{k_g(S_l)}{k_{0,g}} = \begin{cases} [1 - S_e]^{\tau'} \left[1 - \frac{1 - (1 - (S_e^* S_e)^{\frac{1}{m}})^m}{1 - (1 - (S_e^*)^{\frac{1}{m}})^m} \right]^2 & \text{if } S_e < 1 \\ 0 & \text{if } S_e = 1 \end{cases}$$

With:

$$(3) \quad S_e^* = \frac{S_{ls} - S_{lr}}{S_{ls}^* - S_{lr}} = [1 + (\alpha P_{c,e})^n]^{-m} \quad S_e = \frac{S_l - S_{lr}}{S_{ls} - S_{lr}}$$

In equations (2) and (3), we have:

m and n : are dimensionless shape parameters related by the equation $m = 1 - \frac{1}{n}$.

α : is a scaling pressure parameter (Pa^{-1}), $\alpha = -\frac{1}{P_r}$ (> 0 ; because P_r is negative).

τ and τ' : are dimensionless parameters representing tortuosity for relative permeability to liquid and gas respectively. In this study $\tau = \tau' = 0.5$.

S_{lr} and S_{ls} : are residual and maximum (or full) liquid saturation, respectively (-). In this study, $S_{lr} = 0$ and $S_{ls} = 1$.

S_e : is the effective saturation of liquid phase (-).

$S_e^* S_e$: is the new effective liquid saturation, which reaches its maximal value when $S_l = S_{ls} = 1$.

$k_{0,l}$ and $k_{0,g}$: are scaling permeability parameters, defined as intrinsic permeabilities to liquid and gas, respectively (m^2).

In Eq. (2a) the water retention curve is extended beyond the full liquid saturation ($S_{ls} = 1$) by introducing the parameter $S_{ls}^* \geq 1$ in the capillary model of Van Genuchten (VG) as illustrated in Figure 6.

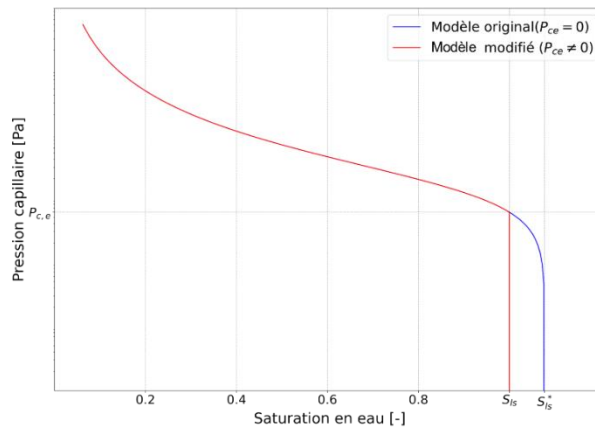


Figure 5-6 - Vogel et al. (2001) model with non-zero $P_{c,e}$ in the VGM water retention curve.

Values of the shape (m, n) and scale ($\alpha, P_{c,e}, k_{0,l}, k_{0,g}$) parameters of the VGM-PE hydraulic properties (i.e., Eqs. (2)) as well as values of the physical, thermal and mechanical parameters of each constitutive material of the domain (undisturbed host rock, outer and inner EDZ, bentonite, concrete, backfill), such as porosity, liquid and gas intrinsic permeability, pore compressibility and expansivity, heat conductivity, dry material specific heat, Young modulus, Poisson ratio and Biot coefficient, are those tabulated in Levasseur et al. (2021). Recall here that $P_{c,e}$ values are taken equal to 6.0, 4.0 and 2.0 MPa for the host rock, bentonite and outer-EDZ, respectively. For the other materials (inner-EDZ, backfill, concrete), $P_{c,e} = 0$.

The effective diffusion coefficients of water vapor and hydrogen in two-phase porous materials $D_{\beta=l,g}^{\kappa=H_2O,H_2}$ (m²/s) are deduced from their diffusion coefficients in free liquid and gas phase $D_{0,\beta=l,g}^{\kappa=H_2O,H_2}$ (m²/s) through a proportionality parameter (tortuosity factor), originally introduced by Millington and Quirk (1961) (MQ), but modified here according to the following equation:

$$(5) \quad D_{\beta}^{\kappa} = D_{0,\beta}^{\kappa} \omega^{1+\alpha_{\beta}} (S_e)^{b_{\beta}} \quad \kappa = H_2O, H_2 \quad \beta = l, g$$

with ω is the porosity; α_{β} and b_{β} are liquid or gas phase and material dependent parameters. As an example, for the host rock material, we have for the gaseous H₂, $a_g = b_g = 2.5$, and for the dissolved H₂, $a_l = 1.5$ and $b_l = 10$; For the bentonite material, we have for the gaseous H₂, $a_g = b_g = 3.0$, and for the dissolved H₂, $a_l = 2.5$ and $b_l = 15$.

Diffusion coefficients of hydrogen in free liquid and gas phases are equal to 5.0×10^{-9} and 9.0×10^{-5} m²/s, respectively, whereas those of water vapor in free liquid and gas phases are equal to 1.0×10^{-9} and 9×10^{-5} m²/s, respectively. The inverse Henry's constant of hydrogen is equal to 1.4×10^{-10} Pa⁻¹. These values are like those specified in the generic exercise.

Initial and boundary conditions

Initial conditions are such that temperature is constant equal to 25 °C in the whole domain and the pressure is hydrostatic between depths $z = 525$ m and $z = 675$ m before the micro-tunnel and drift excavation. Thereafter, all engineered barriers materials implemented in the micro-tunnel and the drift are initialized with a water saturation of 80 %. At top ($z = 525$ m) and bottom ($z = 675$ m) of the domain, liquid phase pressures are fixed to their hydrostatic ones, and temperatures are fixed to 23 °C and 27 °C, respectively. At all lateral boundaries, zero fluxes are considered.

Deviations from generic repository specifications

As described above, the following are the main deviations from the benchmark specifications:

- Geo-mechanics, and transport of radionuclides are not modelled.
- Properties of the cell steel-liner (2 cm thickness) are homogenized to those of their adjacent materials, i.e., voids and buffer bentonite (Figure 5-5(b)).
- The radial sections of the cell micro-tunnel, drifts and shaft are assumed rectangular (Figure 5-5).
- The model domain is limited to the host rock layer (i.e., 150 m) to reduce CPU times.

A priori simulations are carried out by TOUGH2-MP/EOS5. Three scenarios#1,2,3 have been proposed considering other deviations from the benchmark specifications (from phenomenological point of view):

✓ Scenario#1

- i) *Isothermal two-phase flow.*
- ii) *Diffusion coefficient:* the original MQ-model for the tortuosity factor is used instead of that of Eq. (5). The porosity and phase saturation power parameters a_β and b_β are assumed identical for any porous material type and for both liquid and gas phases, i.e., are taken equal to 1/3 and 10/3, respectively.
- iii) *Intrinsic permeability to water and gas:* assumed identical for the host rock and outer-EDZ (i.e., $k_{0,l} = k_{0,g} = k_0$).
- iv) *VGM-PE $P_c(S_l)$ (Eq. (2)):* implicit $P_{c,e}$, SGM method (Amri et al., 2022) without any linearization near full liquid saturation ($S_l = 1$).

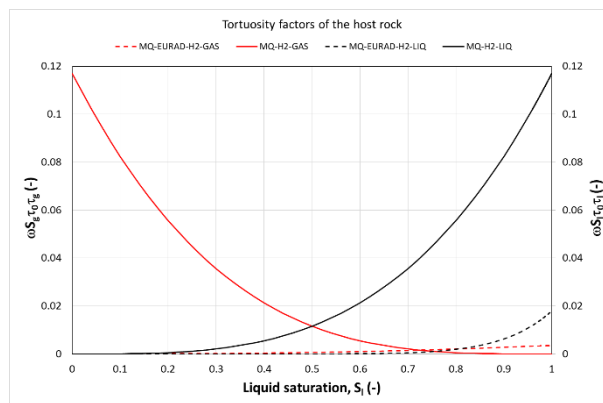


Figure 5-7 – Original (continuous lines) vs modified (dashed lines) MQ-model for the unsaturated tortuosity factor of the host rock, for liquid and gas phases.

Figure 5-7 shows, for the host rock material, a comparison between tortuosity factors simulated by the original and the modified MQ models. This comparison implies that the diffusion coefficient in liquid phase simulated by the classical model is much higher than that is simulated by the new model, and this for the whole range of liquid saturation variations. However, for the diffusion coefficient of H₂ in gas phase, overestimation of the new model is observed only in the range of liquid saturation 0.0 - 0.8. In the range 0.8 – 1.0, near full liquid-water saturation, differences between the models are very small. Therefore, it is expected to simulate a substantial accumulation of gas in the drift network of the repository by application of this new model.

✓ Scenario#2

Idem hypotheses in S#1 but simulations are performed with a parameterization $P_{c,e} = 0$, with a linearization near full liquid saturation ($S_l = 1$).

✓ Scenario#3

- i) *Non-isothermal two-phase flow.*
- ii) *Diffusion coefficient:* idem S#1 (original MQ-model).
- iii) *Intrinsic permeability to water and gas:* $k_{0,l} \neq k_{0,g}$ for the host rock and outer-EDZ.

- iv) *VGM-PE* $P_c(S_l)$ (Eq. (2)): explicit $P_{c,e}$ with linearization near full liquid saturation ($S_l = 1$), i.e. between $P_c(S_l = 1 - \varepsilon)$ and $P_c(S_l = 1)$, with ε is an infinitesimal value equal to 0.01 or 0.001 (Levasseur et al., 2021).

N.B. Parametrization of scenario#3 differs from that specified in the benchmark specifications only by the new formulation for the diffusion coefficient that has not yet been implemented in iTOUGH2 and TOUGH2-MP.

5.2 Numerical details

The mesh used by the model is structured and rectilinear (Figure 5-8). It consists of 276 192 elements (137 x 63 x 32). Although of this high number of elements, this mesh guarantees the orthogonality of the distance between the centre of mass of any element and any surface connection of its neighbour (VORONOI approximation).

The three scenarios are simulated for a maximum period of 100 000 y. Simulation results of S#1 are not presented, because the numerical solution diverges earlier as is the case of a HLW cell model (M174 Progress Report 2022, EURAD WP6 GAS; IRSN contribution). This divergence occurs essentially when gas pressure becomes much higher in the backfilled drift (~ 20 MPa) and the latter becomes highly desaturated (gas saturation $S_g \sim 0.5$).

Only the results from simulations by scenarios #2,3 are presented because the period 100 000 y is completely simulated. For both scenarios, simulations last ~ 3 weeks with 32 CPUs.

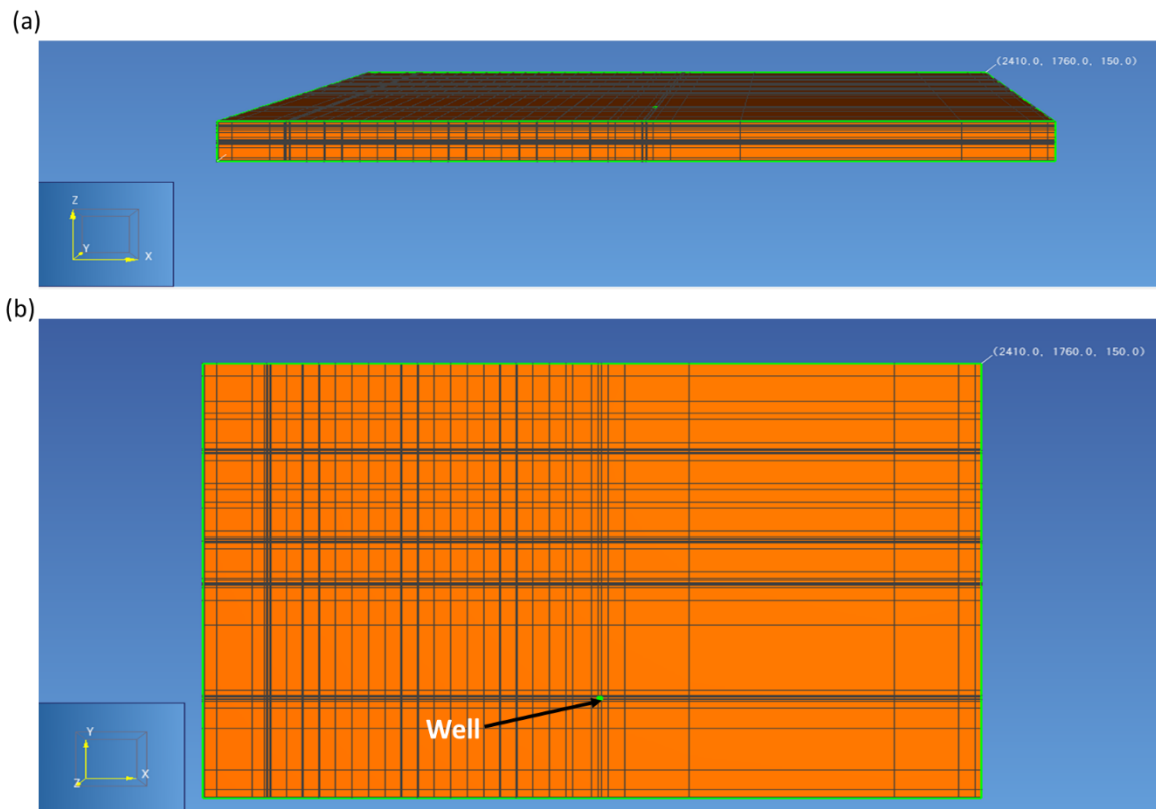


Figure 5-8 – (a) Vertical mesh along OXZ plane. (b) Lateral mesh along OXY plane.

The purpose is to follow the time evolution of temperature, gas pressure and gas saturation at the elements' points P1 to P19, shown in Figure 5-9.

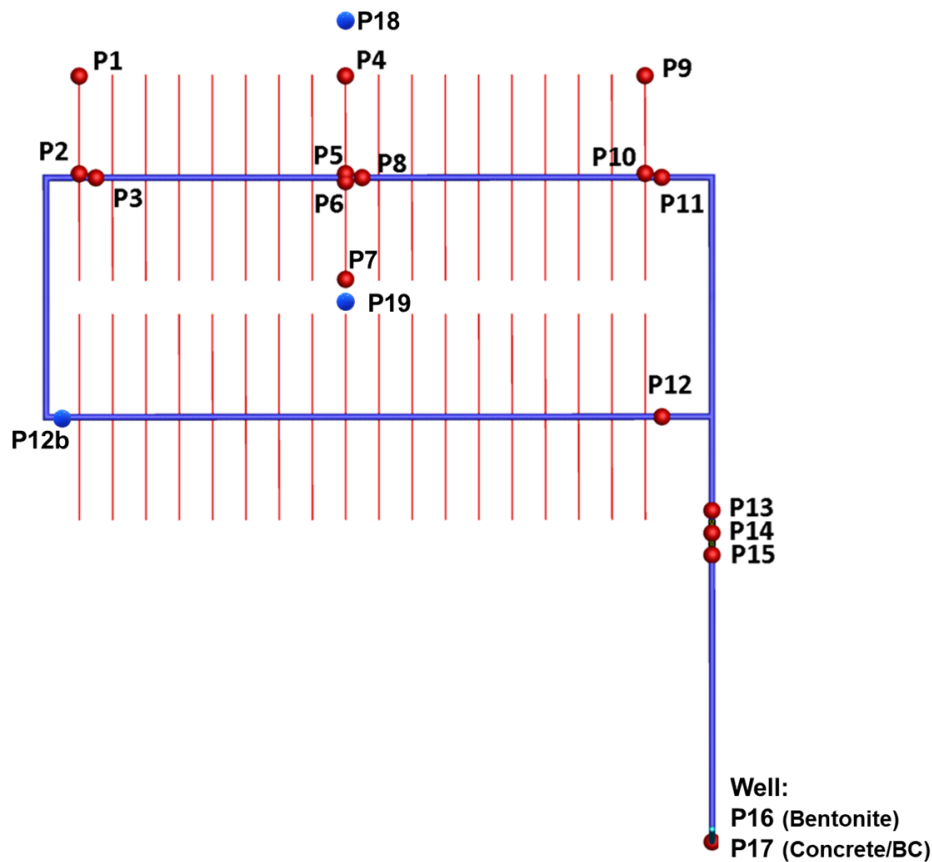


Figure 5-9 – Points P1-P19 where results of temperature, gas pressure and gas saturation vs time are plotted. Blue points are new points not specified in the benchmark. Points in the host rock: P18 (adjacent to BC) and P19.

5.3 Simulation results

Scenario#3 – Cells, access drifts, seals, and host rock

Figures 10(a) shows time-evolutions of temperature in the elements points P1-P12, P12b, P18, and P19, simulated by scenario#3 with parametrization $P_{c,e} \neq 0$. In the cells, for elements points P1, P4, P7, and P9 located in the WASTE material (voids + canisters) there is an instantaneous increase of temperature from the initial state (25 °C) during the first years reaching about 97 °C in points P4 and P7. This result is obvious because canisters are the main sources of heat generation. Temperature at these points decreases during ~930 y corresponding to the period of the decrease of the thermal power generated by radioactive waste in the canisters. During this period of heat generation, there is a small increase in temperature later in time by about 7.5 °C from the initial temperature 25 °C in elements points P2, P5, P6 and P10 located in the cells' buffers (bentonite), Figure 5-10(a), and in elements points P3, P8, P11, P12, P12b located in the access drifts, Figure 5-10(c) (maximum temperature is ~32.5 °C). The host rock zone between the two modules of cells (e.g., element point P19) are heated by adjacent cell canisters, which explains the temperature increase in this zone by about 5 °C reaching a maximum of ~30 °C (Figure 5-10(b)). Far away from the module in the host rock, near the boundary $Y = 1.76$ km

(e.g., point P18), the temperature variation is very negligible. After the period of heat generation, the temperature becomes constant and equal to the initial temperature 25 °C in the whole domain.

Simulated temperature profiles at slice plane $z = 75$ m, at times $t = 100, 929$ y, Figure 5-11, confirm well the plotted curves of temperature at elements points shown in Figure 5-10. There is a net decrease of temperature in the two modules of zone disposal C from time 100 to 929 y. Although temperature in the host rock zone vary slightly from the initial temperature, but one can see that the heat transfer is extended to many hundreds of meters in the host rock and can reach the boundaries $X = 0$ and $Y = 1.76$ km at time 930 y.

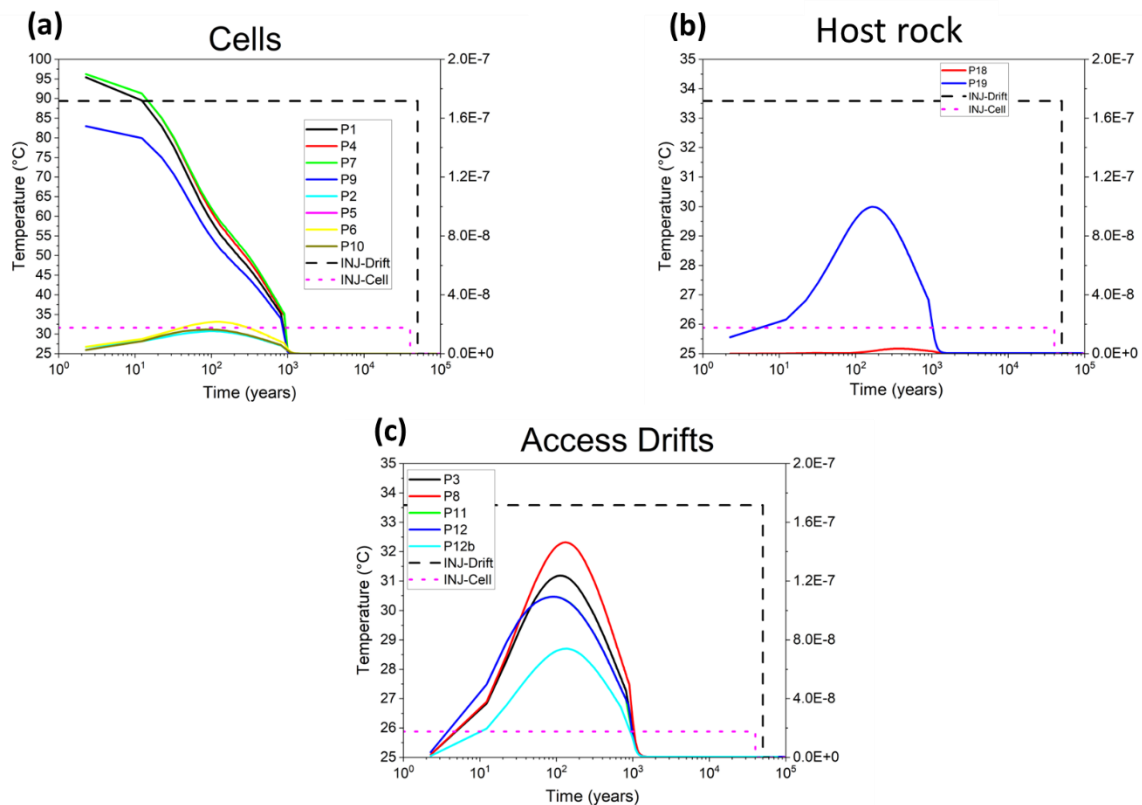


Figure 5-10– Temperature variation in time simulated by scenario#3 ($P_{c,e} \neq 0$) at elements points P1-P19. (a) Cells. (b) host rock. (c) Access drifts.

We simulate a gas pressure build-up in the drift network during the periods of hydrogen generation in both cells WASTE and backfilled drifts (discontinuous lines), which later stabilizes at a maximum value from ~ 1 000 y (Figure 12(c)). In parallel to this pressure build-up, the drifts backfill highly desaturates (Figure 12(d)).

The high increase of gas saturation to a maximum of ~ 0.8 at 40 000 y in the cells WASTE materials (Figure 5-12(b): points P1, P4, P7, P9) is due to the substantial accumulation of gas in these materials, showing that these materials behave as a big reservoir of gas storage during the period of gas generation. The presence of this reservoir reduces the maximum gas pressure to about 10.2 MPa at time 40 000 y in the WASTE material (Figure 5-12(a): points P1, P4, P7, P9) and consequently that in the backfilled access drifts (10.5 MPa; Figure 5-12(c): points P3, P8, P11, P12 and P12b).

Although of the very small (negligible) variation of gas saturation in the cells' buffers bentonite (Figure 5-12(b): points P2, P5, P6, P10) due to its re-saturation during a period of 1000 y, the maximum gas pressure reaches about 10.5 MPa at 40 000 y.

Gas pressure in the backfilled access drifts evolves in time and in magnitude like in the cells' buffers. However, the gas saturation in the access drifts is much higher than that in the buffers and can reach about 0.54. This is due to the permeable nature of the backfill. In addition, one can see an overlap of the curves of gas pressure and gas saturation vs time in all points located in the access drifts (Figure 5-12(c) and Figure 5-12(d): P3, P8, P11, P12 and P12b), showing the instantaneous migration of hydrogen from the cells' buffers to the access drifts.

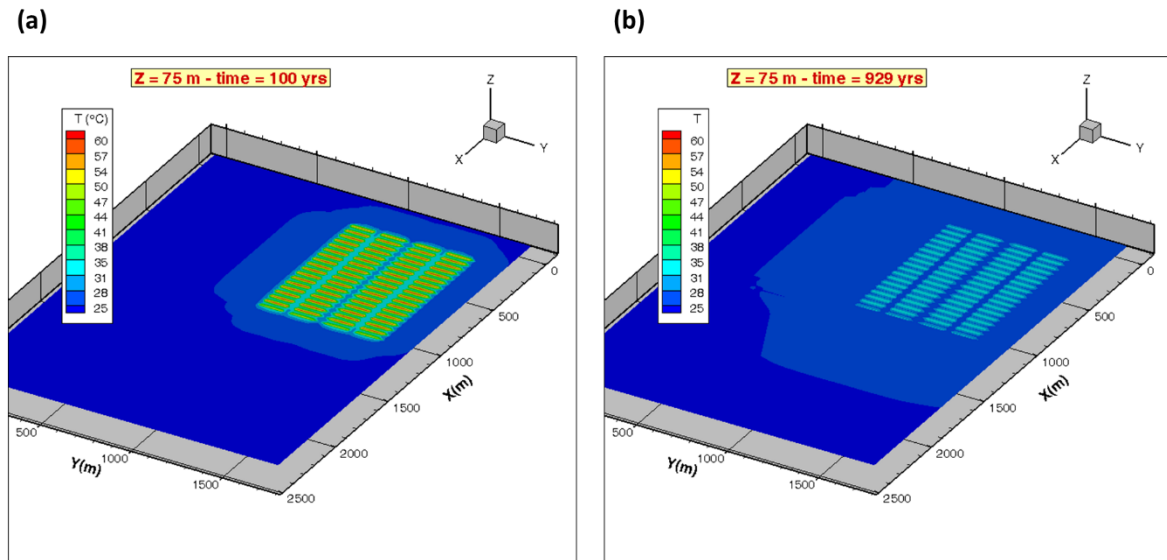


Figure 5-11 – Simulated temperature profiles at slice plane Z = 75 m simulated by scenario#3 ($P_{c,e} \neq 0$). (a) Time $t = 100$ y. (b) Time $t = 929$ y.

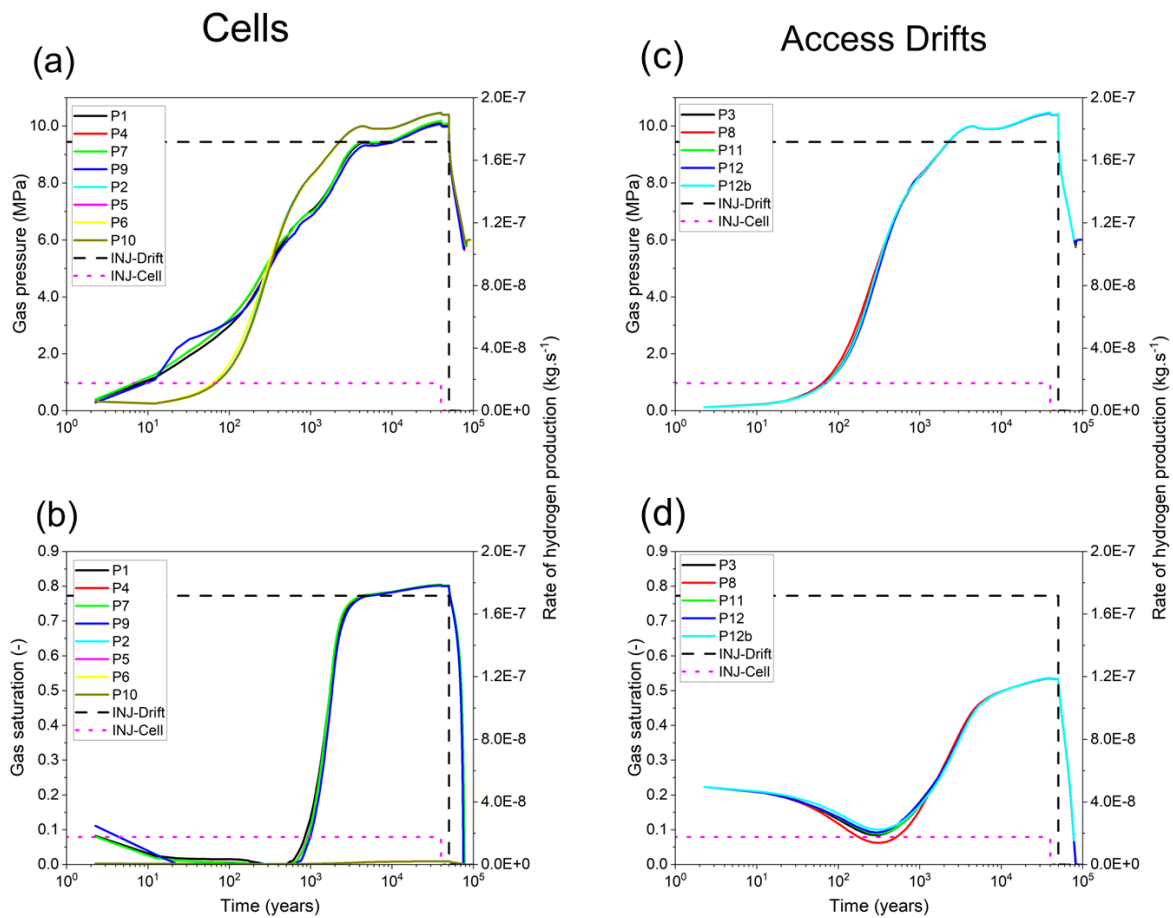


Figure 5-12 – Time evolution of gas pressure (above) and gas saturation (below) at elements points P1-P12 and P12b, simulated by scenario S#3. (a,b) Cells (WASTE and buffer bentonite). (c,d) Access drifts (backfill).

There is a small desaturation of the host rock zone between the two modules (i.e., point P19) leading to a maximum of gas saturation $S_g = 0.0039$ at 50 ky (Figure 5-13(b)), and so to the increase of gas pressure to a maximum of 8.46 MPa at 50 ky (Figure 5-13(a)). The point P18, far away from the module, remains saturated (Figure 5-13(b)) at its hydrostatic pressure of ~6 MPa (Figure 5-13(a)).

The cells and access drifts become fully saturated after periods of about 75 000 and 80 000 y, respectively.

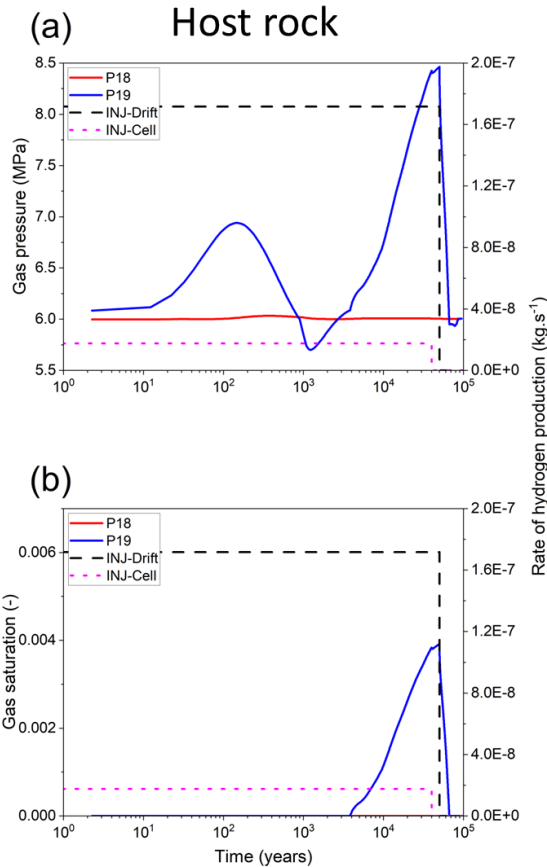


Figure 5-13 – Time evolution of (a) gas pressure (b) gas saturation at elements points P18 and P19 in the host rock.

Profiles of pressure and gas saturation at slice plane $z = 75$ m simulated by scenario#3 at time 50 000 y (~ time of maximum P_g and S_g in cells and drifts; Figure 5-14), illustrate well simulations at points P1-P12, P12b, P18, and P19 (Figure 5-12 and Figure 5-13). The maximum gas pressures and gas saturations are shown in access drifts and main drift upstream of the seal. There is a high-water drainage in the drift network, and a small desaturation of the host rock around the module.

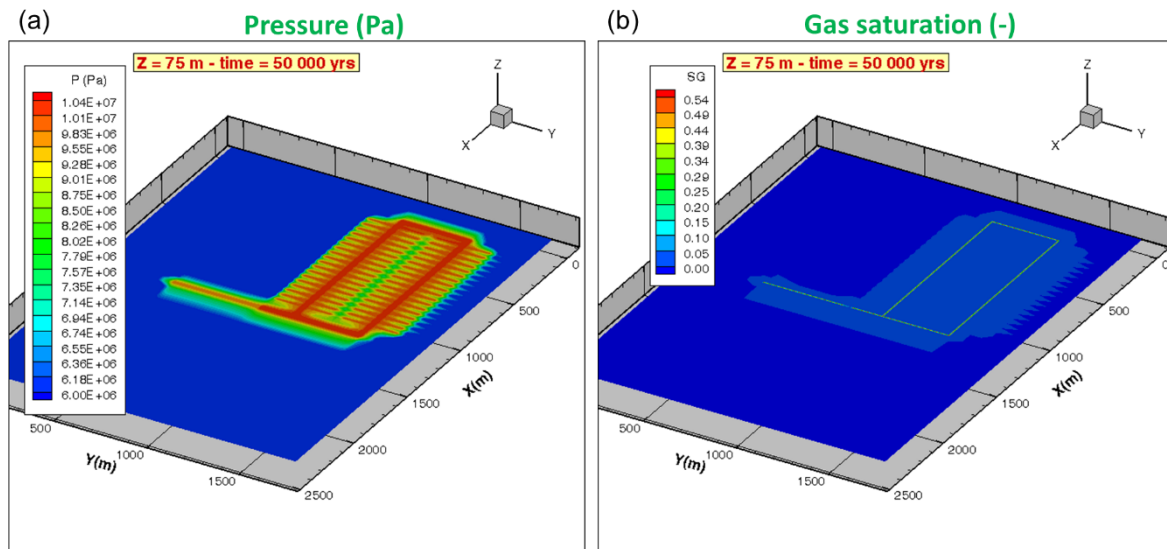


Figure 5-14– Simulated profiles of (a) pressure and (b) gas saturation at the slice plane $z = 75$ m simulated by scenario#3 ($P_{c,e} \neq 0$) at time 50 000 y.

Seals (drift and shaft)

In the main drift, the presence of the seal decreases the gas pressure and gas saturation downstream the seal during the period of maximum gas pressures as shown in Figure 5-15(a) and Figure 5-15(b). In fact, at time 40 000 y, the maximum gas pressure is reduced from ~ 10.45 MPa at point P13 to ~ 9.7 MPa at point P15 (Figure 5-15(a)). Idem for the gas saturation, which is reduced from ~ 0.54 at point P13 to ~ 0.5 at point P15 (Figure 5-15(b)). As for the cell buffer, there is small desaturation of the main drift seal (Figure 5-15(b)), but a high increase of gas pressure reaching a maximum of 10.2 MPa at 40 000 y, which is of the same order of magnitude to that simulated at the upstream of the seal (e.g., point P13).

There is a small desaturation of the shaft seal and the concrete adjacent to the saturated surface boundary (Figure 5-15(d): points P16 and P17). This leads to the increase of gas pressure in the shaft seal to a maximum of 8.9 MPa at $t = 40$ 000 y, but not in the concrete which is permanently saturated from the above aquifer.

These results are well illustrated by the 2D profiles of gas pressure in Figure 5-14(a) and Figure 16(a) at slice plane $z = 75$ m, simulated at time 50 000 y. Notice, however, the small desaturation of the host rock around the main drift and the shaft (all along the host rock layer 150 m and the main drift length), as shown in Figure 5-16(b), leading to an increase of gas pressure in the host rock to a maximum of 8.46 MPa at 50 000 y, Figure 5-16(a).

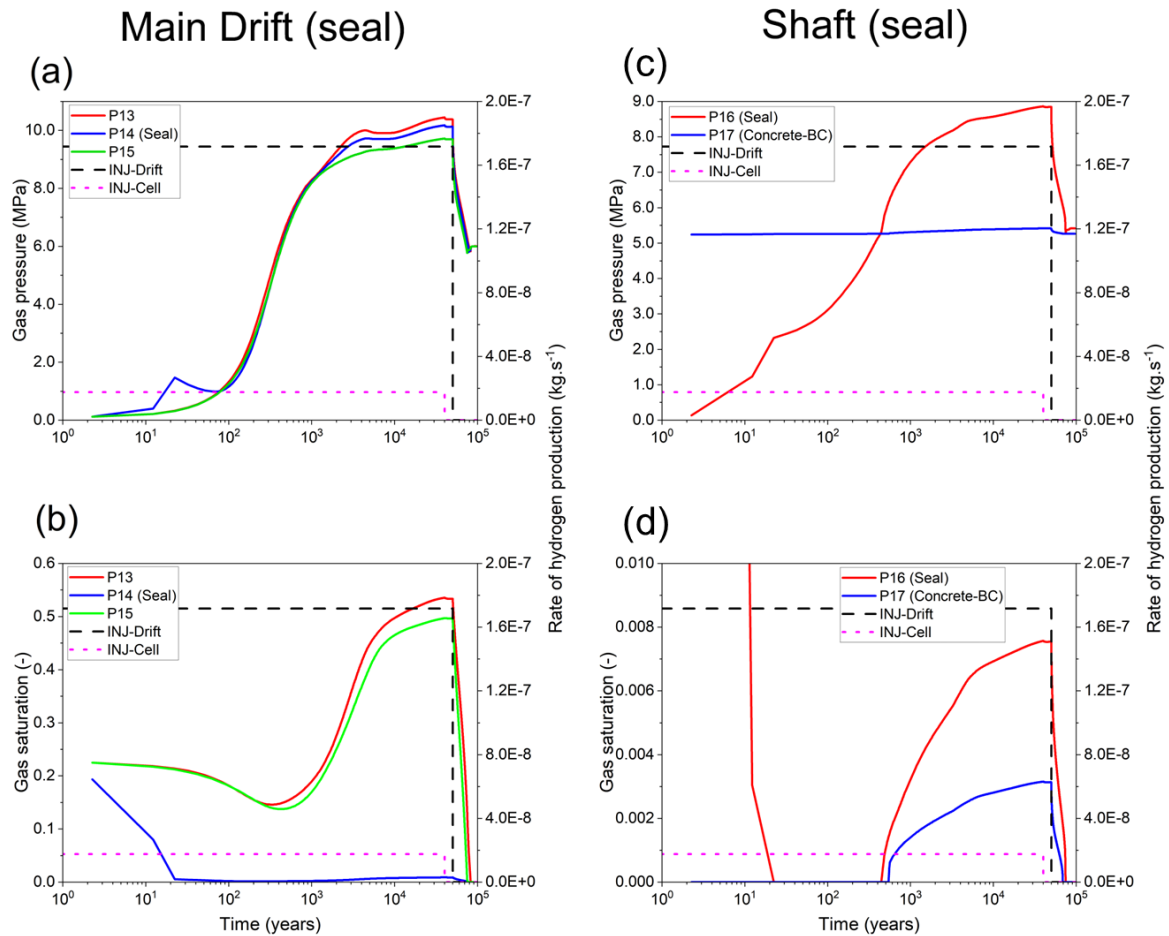


Figure 5-15 – Time evolution of gas pressure (above) and gas saturation (below) at elements points P13-P17 simulated by scenario S#3. (a,b) Main drift seal. (c,d) Shaft seal.

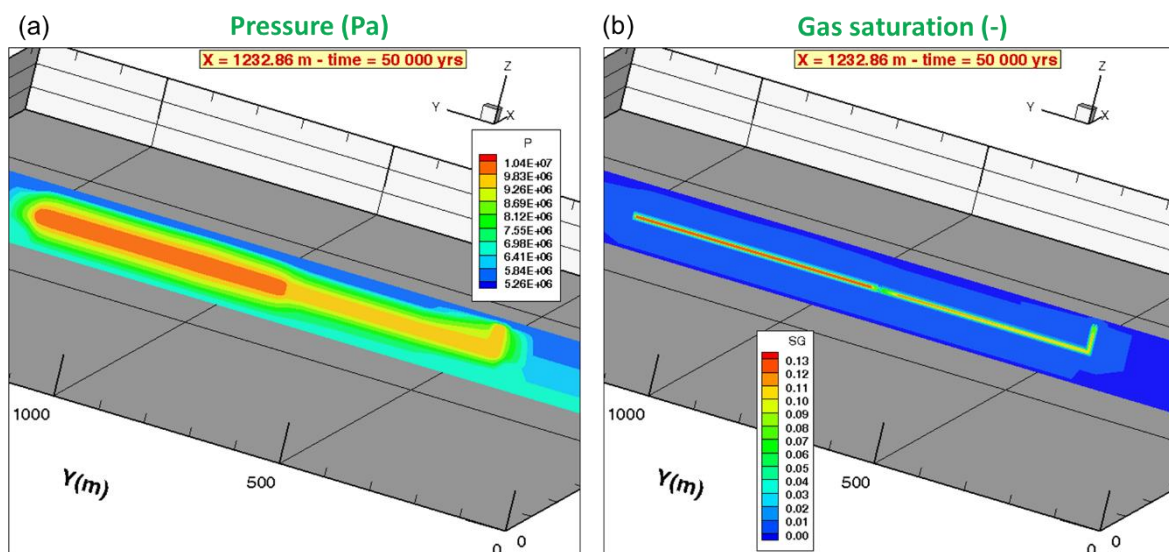


Figure 5-16– Profiles of (a) pressure and (b) gas saturation at slice plane X = 1232.86 m, simulated by scenario#3 ($P_{c,e} \neq 0$) at time 50 000 y.

Scenario#2 ($P_{c,e} = 0$) vs Scenario#3 ($P_{c,e} \neq 0$)

Simulations by scenario#2 with a parametrization $P_{c,e} = 0$ show that gas pressure in the buffer, access drift, and host rock is reduced by about ~1.2 to 1.3 MPa compared to that simulated by scenario#3 (reduction from 10.5 to 9.2 MPa in the buffer and access drifts, Figure 5-17(a) and Figure 5-17(c); and reduction from 8.5 to 7.2 MPa in the host rock, Figure 5-17(e)). The slight decrease of gas saturation in the bentonite of the cell buffer and host rock (heavily clayey materials) simulated by scenario #3 compared to that of scenario 2 (Figure 5-17(b) and Figure 5-17(f)) is explained by their higher $P_{c,e}$ values (4 and 6 MPa) that probably reduce gas entry in these materials. However, the backfill of the access drifts, which has the smallest $P_{c,e}$ value (0 MPa), does not present a capillary barrier for the gas entry, and therefore the accumulation of gas in this material becomes substantial leading to the increase of its desaturation by the gas.

The explanations above also apply to the results of gas pressure and gas saturation simulated by both scenarios #2 and #3 in the backfill and seal bentonite of the main drift (Figure 5-18(a) and Figure 5-18(b)), as well as to those in the seal and concrete of the shaft (Figure 5-18(c) and Figure 5-18(d)).

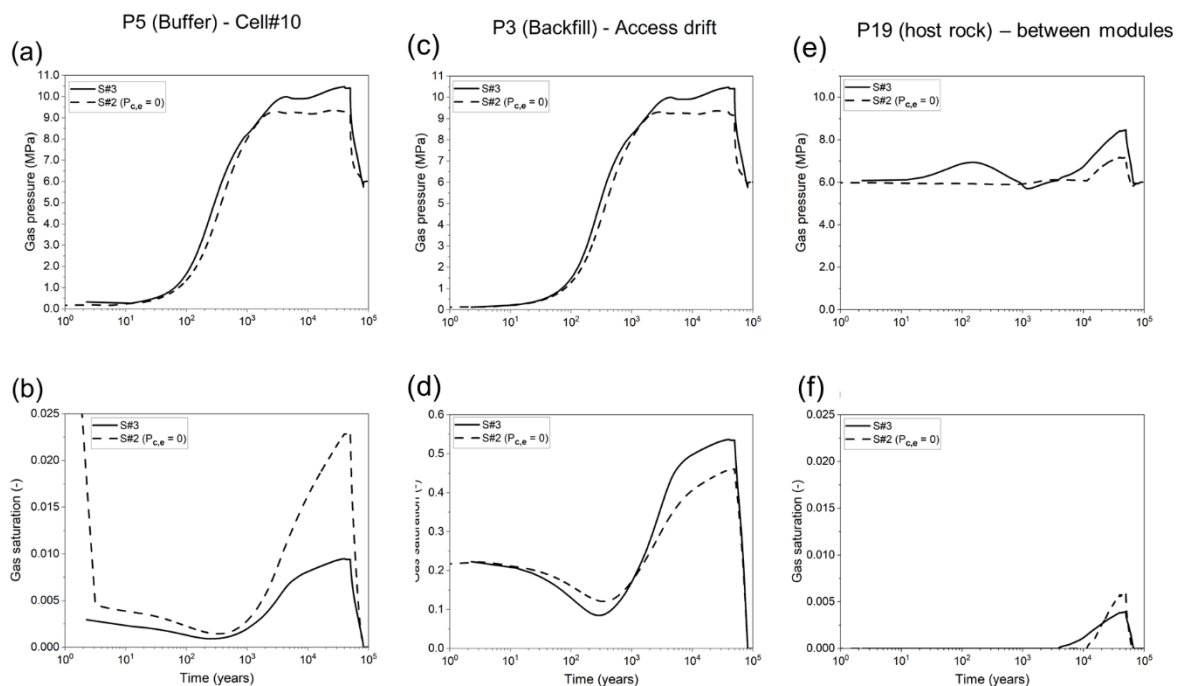


Figure 5-17– Time evolution of gas pressure (above) and gas saturation (below) at elements points P3, P5, and P19 simulated by scenarios S#2 ($P_{c,e} = 0$) and S#3 ($P_{c,e} \neq 0$). (a,b) Cell buffer; (c,d) Access drift; (e,f) host rock between modules.

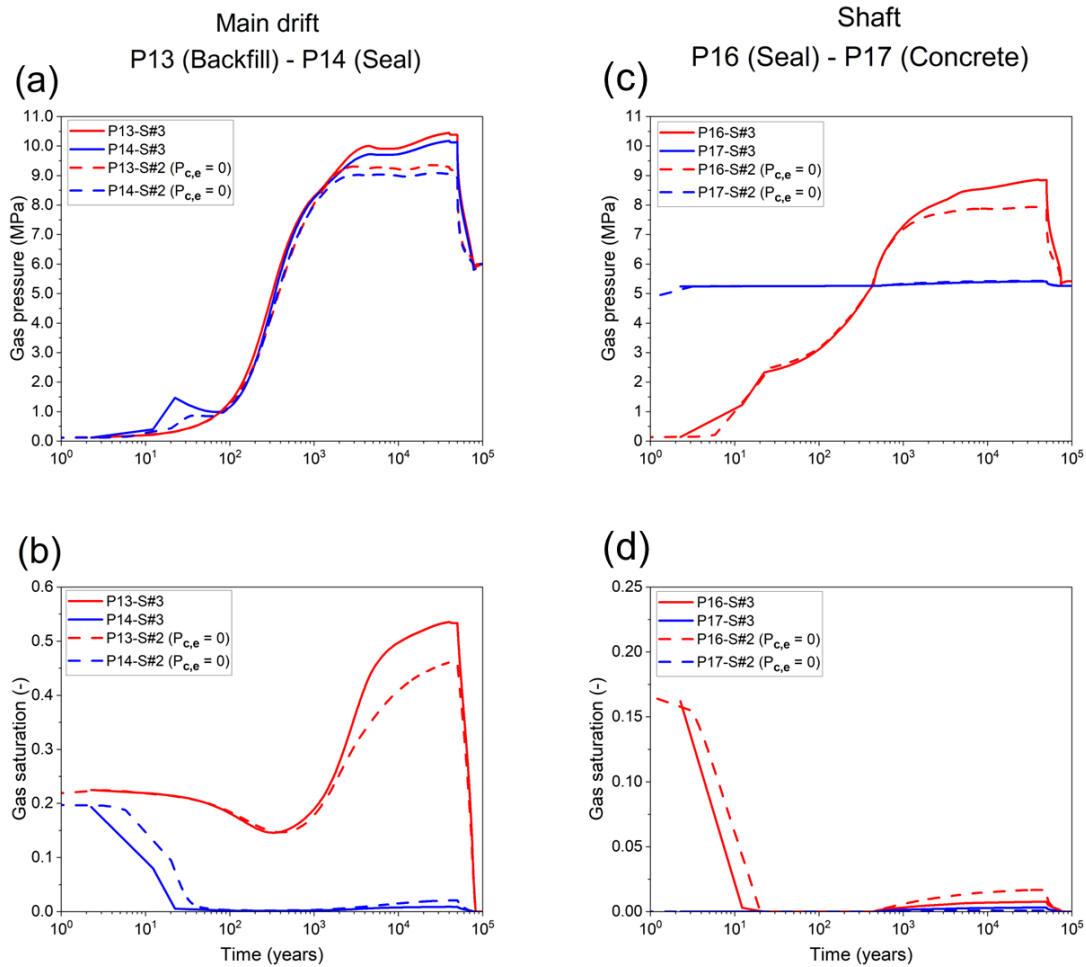


Figure 5-18– Time evolution of gas pressure (above) and gas saturation (below) at elements points P13, P14, P16 and P17. (a,b) Main drift backfill and seal; (c,d) Shaft seal and concrete.

5.4 Conclusions and perspectives

The capillary gas entry pressure model VGM-PE (Amri et al., 2022) developed in the framework of WP DONUT has been verified, validated, and introduced in this benchmark for the modeling of gas migration at the repository scale.

A priori, application of VGM-PE by using the numerical scheme SGM for solving the problem of gas migration at cell and module scales (disposal zone C) fails to simulate the long-term behavior of the gas transfer within the sub-structure of the stand-alone zone C with shaft within the host rock. This is essentially due to the highest $P_{c,e}$ value of the host rock which leads to the gas accumulation in the drifts and gas pressure build-up. The gas pressure reaches earlier ~20 MPa than expected at ~ 1000 y (scenario #1).

The simplification made (linearization) to the water retention curve $P_c(S_l)$ of the VGM-PE model near full liquid saturation allowed convergence of the TOUGH2-MP numerical solution for 100 000 y, but probably it underestimates the maximum gas pressure within the drift network (at the expense of the improvement of the physics of gas transfer in the porous materials).

If we exclude geomechanics and radionuclides transport in the stand-alone disposal zone C with shaft, and geometry simplification from the specifications of this benchmark, our deviations from this benchmark consider only, from phenomenological point of view, the model of the diffusion coefficient of hydrogen by using the classical MQ-model instead of the new one for the tortuosity factor. As shown in Figure 5-7, the new MQ-model of the diffusion coefficient of hydrogen in liquid phase within the host rock is very low compared to that of the original one. Therefore, it is expected to simulate greater gas pressures in the drift network by this new MQ-model. This explain probably why the maximum gas pressure simulated by our model (~10.5 MPa) is smaller than those calculated by BGR (~12 MPa) and by Andra (~16 MPa).

Finally, to enhance results of our contribution to this benchmark, many tasks must be addressed in our future studies as described below:

- Testing the numerical scheme PCM (Amri et al., 2022) instead of SGM with new meshes types for the parametrization $P_{C,E} \neq 0$ to deal with the problem of gas transfer at the cell scale before dealing with that at the repository scale. Therefore, it is worthwhile to study scenarios with structured and unstructured meshes with different sizes to quantify errors due to meshing.
- Try scenarios with explicit steel-liner in the cell model and implement the modified diffusion coefficient model of MQ in TOUGH2-MP as specified in the benchmark.
- Analyze H_2 maximum gas pressure and fluxes with a sensitivity analysis to H_2 source term reduction. On occasion it will be possible to know for which source term the numerical solution of TOUGH2-MP implicit SGM or PCM scheme would converge.
- ✓ Study the problem of HM-coupling of an elastic mechanical deformation model to a two-phase flow model at cell scale before dealing with the problem at the repository scale.

5.5 References

Ahusborde, E., Amaziane, B., Baksay, A., Bátor, G., Becker, D., Bednár, A., Béreš, M., Blaheta, R., Böhti, Z., Bracke, G., Brazda, L., Brendler, V., Brenner, K., Březina, J., Cancès, C., Chainais-Hillairet, C., Chave, F., Claret, F., Domesová, S., Havlova, V., Hokr, M., Horák, D., Jacques, D., Jankovsky, F., Kazymyrenko, C., Kolditz, O., Koudelka, T., Kovács, T., Krejci, T., Kruis, J., Laloy, E., Landa, J., Lipping, T., Lukin, D., Mašin, D., Masson, R., Meeussen, J.C.L., Mollaali, M., Mon, A., Montenegro, L., Montoya, V., Pepin, G., Poonoosamy, J., Prasianakis, N., Saâdi, Z., Samper, J., Scaringi, G., Sochala, P., Tournassat, C., Yoshioka, K., Yuankai, Y. (2021): State Of the Art Report in the fields of numerical analysis and scientific computing. Final version as of 16/02/2020 of deliverable D4.1 of the HORIZON 2020 project EURAD. EC Grant agreement no: 847593. <https://hal.archives-ouvertes.fr/hal-03165686>

Amri A., Z. Saâdi, R. Ababou, 2023. Modeling two-phase flow with hysteresis: comparative study of hysteresis models and application. Rock Mechanics and Rock Engineering <https://doi.org/10.1007/s00603-023-03501-1>

Amri A., Z. Saâdi, R. Ababou, 2022. Parametric sensitivity to gas-entry pressure in two-phase flow models for a deep geologic repository of radioactive waste. Transp. Porous Med. 145: 13–43. <https://doi.org/10.1007/s11242-022-01780-w>

Amri A. (2021): A revisited hydrogen transfer model for the study of hydraulics-gas transient in a deep geological disposal facility. PhD Thesis, Toulouse University, Institut National Polytechnique de Toulouse (INP Toulouse), 213p.

Finsterle S. (2007): iTOUGH2 User's Guide. LBNL-40040, Earth Sciences Division, Lawrence Berkeley National Laboratory, University of California, Berkeley, CA 94720, February 2007.

Millington R.J., J.M. Quirk, 1961. Permeability of porous solids. Faraday Society Transactions 57(7): 1200-1207.

Mualem Y., 1976. A new model for predicting the hydraulic conductivity of unsaturated porous media. Water Resources Research, t. 12, no 3, p. 513-522, 1976.

Parker J., R. Lenhard, T. Kuppasamy, 1987. A parametric model for constitutive properties governing multiphase flow in porous media. Water Resources Research, t. 23, no 4, p. 618- 624, 1987.

Pruess K., C. Oldenburg, G.J. Moridis (2011): TOUGH2 User's Guide, Version 2.1. Report LBNL-43134 (revised), Lawrence Berkeley National Laboratory, Berkeley, California, USA, 197 p.

Pruess K., C. Oldenburg, G.J. Moridis (1999): TOUGH2 User's Guide, Version 2.0. LBNL-43134, Lawrence Berkeley National Laboratory, Berkeley, California, USA, 197 p.

Van Genuchten M. Th., 1980. A closed form equation for predicting the hydraulic conductivity of unsaturated soils. Soil Sci Soc. Am. J., 44:892–898, 1980.

Vogel T., M. Th. Van Genuchten, M. Cislérova, 2001. Effect of the shape of the soil hydraulic functions near saturation on variably-saturated flow predictions. Advances in Water Resources, t. 24, no 2, p. 133-144, 2001.

Zhang K., Y.-S. Wu, K. Pruess (2008): User's Guide for TOUGH2-MP — A Massively Parallel Version of the TOUGH2 Code. LBNL-315E, Lawrence Berkeley National Laboratory, University of California, Berkeley, CA 94720.

6. Contribution of EDF

6.1 Contributions of EDF

EDF's contribution is dedicated to **zone C** of the generic repository. Two main configurations have been considered: a "local" 3D domain and a 2D vertical cross section.

The first part of the work consists in the "local" 3D modeling, which includes the crossing of a gallery with a cell (also known as "tunnel") as shown Figure 6-3. For symmetrical reasons, it corresponds to the middle of the C gallery (in this case, equivalent to an infinite gallery in a closed system). It is reasonable to assume that the maximum gas pressure of zone C will be reached in this area due to these symmetrical reasons. This "local 3D" modelling is conservative compared to a "global 3D" modeling i.e. a modeling at the scale of the repository provided by Andra (see corresponding section). Comparisons of these 2 approaches will be discussed at the end of this report. These 3D computations will be fully described in section 6.4.1.

The second part of the work consists in a 2D modeling of a vertical section around the tunnel in order to make a sensitivity analysis on several parameters and increase the understanding of the processes. These 2D computations will be fully described and discussed in section 6.4.2.

For all these computations, a finite element (FE) homemade software called Code_Aster is used, including a classical thermohydrmechanical (THM) two-phase flow poro-elastic mode [1].

6.2 Model description

6.2.1 Physical model

We consider an unsaturated biphasic THM model. Details of the THM model are available in [1]. We recall hereafter the main equations and assumptions of the model.

We consider 2 components (H₂ and H₂O) present in 2 phases (liquid (l) and gas (g)).

In our study and for reasons of simplifications, we consider that there is no vapor; hence, water does not exist in a gaseous phase. The gaseous phase is therefore only composed of Hydrogen and the liquid phase is composed of water and dissolved hydrogen.

The thermal unknown is the temperature, mechanical unknowns are displacements $u = (u_x, u_y, u_z)$. hydraulic unknowns are liquid pressure $p_l = p_l^{H_2O} + p_l^{H_2}$ and gas pressure $p_g = p_g^{H_2}$. They are related by the capillary pressure p_c , following the equation $p_c = p_g - p_l$. As indicated in the generic repository specifications (milestone 61), the capillary pressure p_c is related to the water saturation S_l by a modified Van-Genuchten relation, and including entry pressure parameter such as:

$$p_c = \frac{1}{\alpha} \left((S_e^* S_e)^{\frac{1}{m}} - 1 \right)^{\frac{1}{n}}, \text{ if } S_e \leq 1 - \varepsilon \quad \text{Equation 7}$$

$$\text{with: } S_e^* = (1 + (\alpha p_e)^n)^{-m}$$

$$S_e = \frac{S_l - S_{lr}}{1 - S_{lr}} \quad m = 1 - 1/n, \text{ and } \alpha = 1/P_r$$

and

$$-\frac{1}{\alpha} \left((S_e^* S_e)^{\frac{1}{m}} - 1 \right)^{-\frac{1}{n}} \cdot \frac{1 - S_e}{\varepsilon}, \text{ if } (1 - \varepsilon) < S_e < 1$$

Equation 8

Where S_r is the residual saturation, S_e the effective saturation, α , n and m Van-Genuchten parameters such as: $m = 1 - 1/n$. ε is a numerical parameter that is taken equal to 0,001.

In Code_Aster, the capillary pressure and gas pressure are the main numerical unknowns, and a function $S(P_c)$ has to be entered in the model Inverting the previous function gives the following relationship:

$$S_e = \frac{1}{S_e^* (1 + (\alpha P_c)^n)^m}, \text{ if } S_e \leq 1 - \varepsilon$$

Equation 9

When $S_e > 1 - \varepsilon$, it is not possible to directly inverse Equation 8, hence the aforementioned equation is completed by an hyperbolic function in order for S to tend to 1 when P_c tends to $-\infty$:

$$S_e = 1 - \frac{a}{b - P_c}$$

Equation 10

a and b are computed for the function to remain $C1$ when $S_e = 1 - \varepsilon$.

Given the parameters indicated in Table 6-1, the extension of the Van-Genuchten curve is shown on Figure 6-1 (this model will be referred to "VGE" in the following). The "original treatment" corresponds to the treatment given in Equation 8. Consequences of these differences on the results will be discussed in section 6.4.2.

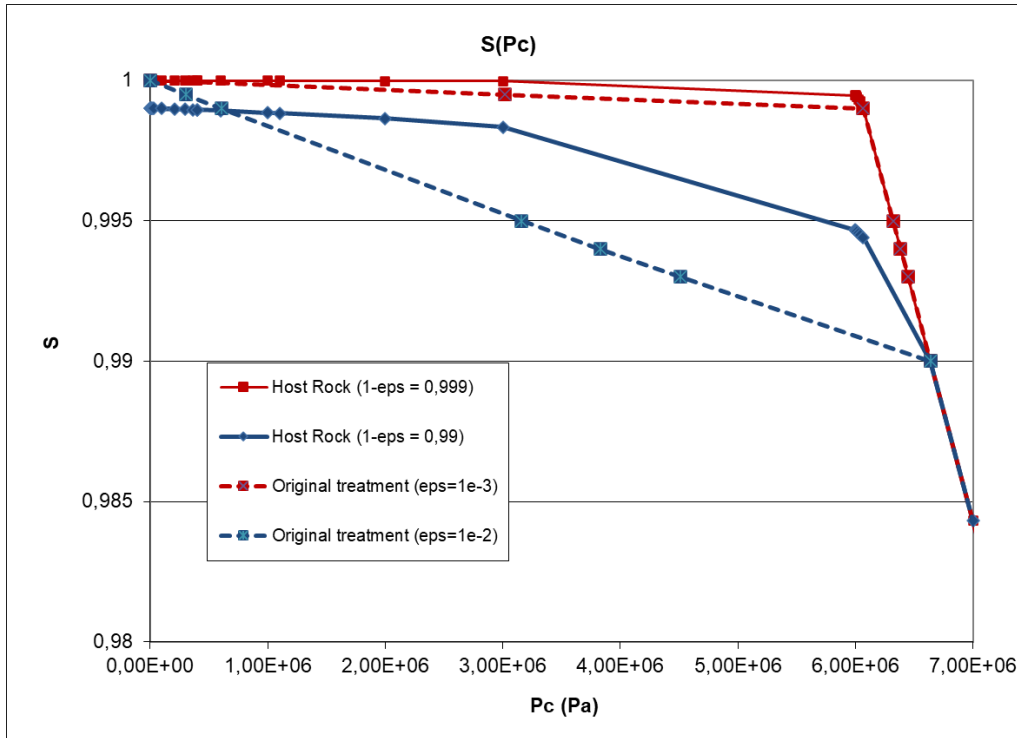


Figure 6-1: Prolongation of Van-Genurchten function when $S > \varepsilon$

The main equations governing the system's evolution are the momentum equilibrium, fluid mass conservations and energy conservation:

- Equilibrium momentum equation is

$$\nabla \cdot \sigma(u, p_c, p_g) + \rho_0 \mathbf{G} = 0$$

With σ the total stress, \mathbf{G} the gravity and ρ_0 the global density of the saturated rock.

- Mass conservation reads for each component c ($c = H_2O; H_2$):

$$\dot{m}_c + \nabla \cdot (F_l^c + F_g^c) = 0$$

where m_c (resp. F_l^c , F_g^c) designates the mass inflow (resp. liquid, gaseous flux) of component c .

- Energy conservation is

$$\sum_{c=H_2O, H_2; p=l, g} h_p^c \dot{m}_p^c + \dot{Q}' + \nabla \cdot (q) = \theta$$

With h_p^c the massic enthalpy of component c in phase p , Q' the non convected heat, q the heat flux and θ the heat source.

This system is completed by the following relations:

For each phase p ($p=l,g$), hydraulic fluxes obey to Darcy's law:

$$\mathbf{F}_p = \frac{k \cdot I \cdot k_{rp}^{\square}(S_l)}{\mu_p} (-\nabla p_p + \rho_l \mathbf{G})$$

k stands for isotropic intrinsic permeability, k_{rp}^{\square} for relative permeability, and μ_p for dynamic viscosity of phase p .

As for capillary pressure, modified relations for relative permeabilities are introduced in the model.

The following relation gives liquid and gas relative permeability (respectively k_{rl} and k_{rg}):

$$k_{rl} = \begin{cases} \sqrt{S_e} \cdot \left[\frac{1 - (1 - (S_e^* S_e)^{1/m})^m}{1 - (1 - S_e^{*1/m})^m} \right]^2, & \text{if } S_e < 1 \\ 1, & \text{if } S_e = 1 \end{cases} ;$$

$$k_{rg} = \begin{cases} f_g \cdot \sqrt{1 - S_e} \cdot \left[\frac{(1 - S_e^{*1/m})^m - (1 - (S_e^* S_e)^{1/m})^m}{(1 - S_e^{*1/m})^m - 1} \right]^2, & \text{if } S_e < 1 \\ 0, & \text{if } S_e = 1 \end{cases}$$

f_g is the ratio between gas permeability and water permeability.

Diffusion in the liquid phase obeys to Fick's law.

$$\frac{F_l^{H_2O}}{\rho_l^{H_2O}} + \frac{F_l^{H_2}}{\rho_l^{NH_2}} = -D_l \nabla \rho_l^{H_2}$$

where D_l stands for Fick diffusion coefficient in liquid phase.

As indicated in milestone 61, Millington Quirck relation is used to link the dissolved hydrogen diffusion D_0 to the effective dissolved H_2 diffusion which is equal to the diffusion coefficient in liquid phase D_l :

$$D_l = D_0 \phi_{\square}^{1+a} S_l^b$$

With ϕ the porosity; a and b material parameters.

Hydrogen H_2 obeys the ideal gas law:

$$p_g^{H_2} = \frac{\rho_g^{H_2}}{M_{H_2}} RT$$

Where $\rho_g^{H_2}$ is the gas density, M_{H_2} the hydrogen molar mass, R the perfect gas constant and T the temperature.

Water is slightly compressible; hence we have the relation depending on liquid pressure and temperature:

$$\frac{d\rho_l^w}{\rho_l} = \frac{dp_l^w}{K_l} - 3\alpha_l dT$$

Where coefficient K_l denotes water compressibility and α_l the linear liquid thermal dilatation.

Hydrogen dissolution obeys to Henry's law

$$\frac{\rho_l^{H_2}}{M_{H_2}^{ol}} = \frac{p_g^{H_2}}{K_H}$$

Where K_H designates Henry's constant.

The stress tensor is decomposed in effective stress tensor σ' and pressure stress tensor σ_p according to the Biot relation:

$$\sigma(u, p_c, p_g) = \sigma'(u) + \sigma_p(p_c, p_g)$$

Incremental form of pressure stress tensor reads:

$$d\sigma_p = -b(dp_g - S_l dp_c)$$

Where b designates Biot coefficient and S_l water saturation.

The variation of porosity $d\phi$ is given by the eulerian representation for small displacements:

$$d\phi = (b - \phi) \left(d\varepsilon_v - 3\alpha_0 dT + \frac{S_g dp_g + S_l dp_l}{K_S} \right)$$

With ε_v is volumetric strain, α_0 the solid thermal dilatation (linear) and K_S the compressibility of the skeleton.

The hypothesis of an elastic law is kept for mechanical behaviour.

The thermal model used in this study is finely described in [1] and is mainly governed by conductivity. We remind that water enthalpy h_l^w is governed by

$$dh_l^w = (1 - 3 \cdot \alpha_l) \frac{dp_l^w}{\rho_l} + C_l^w dT$$

with C_l^w the specific heat of water

For the gas, following equation is to be considered:

$$dh_g^c = C_g^c dT$$

with C_g^c the specific heat of gaseous component.

6.2.2 Physical parameters

All parameters used for the present study are taken from the generic repository specifications (milestone 61). They concern Host rock (intact or disturbed, voids, backfill, concrete and waste. Nevertheless, some precisions must be added:

- As we take into account the mechanical behavior of the host rock (via an elastic law), the pore compressibility given in the specifications is not considered as it is directly linked to the other parameters (see discussion in 6.4.2.5). In Code_Aster, Henry's coefficient K_H is given in Pa.m³/mol such as: $K_H = \frac{M_{H_2O}^{ol}}{H\rho_l}$ with H the value is indicated in the specification.
- The linear liquid thermal dilatation α_l depends on temperature and is given Table 6-3 (hypothesis).
- We apply the same density for all materials in order to have a global linear equilibrium with the specified boundary condition on the total stress.

Finally, the materials parameters used in the computations are defined in Table 6-1 (Note that aquifer is considered as host rock). The parameters who differ from the initial specifications listed in Milestone 61 are indicated with a grey cell. Fluid parameters are given in Table 6-2 and Table 6-3.

Table 6-1 Materials parameters values. Parameters who differ from Milestone 61 are highlighted in grey

Parameter	Host rock			Concrete	Backfill	waste	voids
	Undisturbed	Outer EDZ*	Inner EDZ**				
Initial porosity « ϕ » (-)	0,2			0,15	0,4	0,4	0,9
Water permeability k (m ²)	10 ⁻²⁰	10 ⁻¹⁸	10 ⁻¹⁶	10 ⁻¹⁶	10 ⁻¹⁶	10 ⁻¹³	10 ⁻¹³
Gas permeability $k \cdot f_g$ (m ²)	10 ⁻¹⁸	10 ⁻¹⁷	10 ⁻¹⁶	10 ⁻¹⁶	10 ⁻¹⁶	10 ⁻¹³	10 ⁻¹³
Van Genuchten « n » (-)	1,5			1,5	1,5	1,5	1,5
Van-Genuchten « Pr » (MPa)	16			10	1	0.1	0.1
Gas entry pressure « Pe » (MPa)	6	2	0	0	0	0	0
Residual water saturation "Slr" (-)	0						
Dissolved H ₂ « a » and « b » for Millington-Quirk (-)	a = 1,5 b = 10	a = 1,5 b = 10	a = 1,5 b = 10	a = 2 b = 4	a = 1 b = 15	a = 1 b = 15	a = 1 b = 15

Parameter	Host rock			Concrete	Backfill	waste	voids
	Undisturbed	Outer EDZ*	Inner EDZ**				
Henry's coefficient "H" for H ₂ (Pa ⁻¹)	1.4 10 ⁻¹⁰						
Heat conductivity (w/m/°C) (assumed constant with saturation)	1,7			2,3	1,3	1,3	1,3
Dry material specific heat (J/Kg/°C)	720			900	500	500	500
Pore expansivity (volumic thermal dilatation of solid matrix 3. α_0) (1/°C)	4 10 ⁻⁵			2 10 ⁻⁵	2 10 ⁻⁵	2 10 ⁻⁵	2 10 ⁻⁵
Young modulus (MPa)	5 000	5 000	500	40 000	120	500	1
Poisson ratio (-)	0,3			0,25	0,3	0,3	0,3
Material density ρ_0 (kg/m ³)	2501						
Biot coefficient (-)	0,8			1	1	1	1

Table 6-2 fluid properties

Liquid Viscosity μ_l (Pa.s)	10 ⁻³
Gas Viscosity μ_g (Pa.s)	10 ⁻⁵
Initial liquid density ρ_l (kg/m ³)	1 000
Inverse of liquid compressibility $1/K_l$ (Pa)	5 10 ⁻¹⁰
Specific heat C_l^w (J/Kg/°C)	4 180
Dissolved H ₂ diffusion D_0 (m ² /s)	5 10 ⁻⁹

Table 6-3: linear liquid thermal dilatation α_l

Temperature (K)	Thermal dilatation α_l (K ⁻¹)
293	6.67 10 ⁻⁵
298	8.57 10 ⁻⁵
303	1.01 10 ⁻⁴
308	1.15 10 ⁻⁴

Temperature (K)	Thermal dilatation α_l (K^{-1})
313	$1.28 \cdot 10^{-4}$
318	$1.40 \cdot 10^{-4}$
323	$1.51 \cdot 10^{-4}$
328	$1.62 \cdot 10^{-4}$
333	$1.72 \cdot 10^{-4}$
338	$1.81 \cdot 10^{-4}$
348	$1.99 \cdot 10^{-4}$
353	$2.07 \cdot 10^{-4}$
358	$2.15 \cdot 10^{-4}$
363	$2.22 \cdot 10^{-4}$

6.3 Numerical details

6.3.1 Geometry of the modelling domain

Given the goal of the exercise - consisting in evaluating the gas maximum pressure for each zone - we consider a cross section between a cell and the gallery in the middle of zone C (see Figure 6-2, rectangle with red dotted line). Indeed, symmetrical conditions between cells and gallery can be applied in this area. Even if it is conservative, it seems reasonable to consider here a closed system (the gas escape by the shaft is not taken into account). This assumption will be discussed at the end of this report. Vertically, the entire depth (1000 m) is considered in order to avoid boundary problems. Figure 6-3 gives the geometries that will be employed for 3D and then for 2D computations.

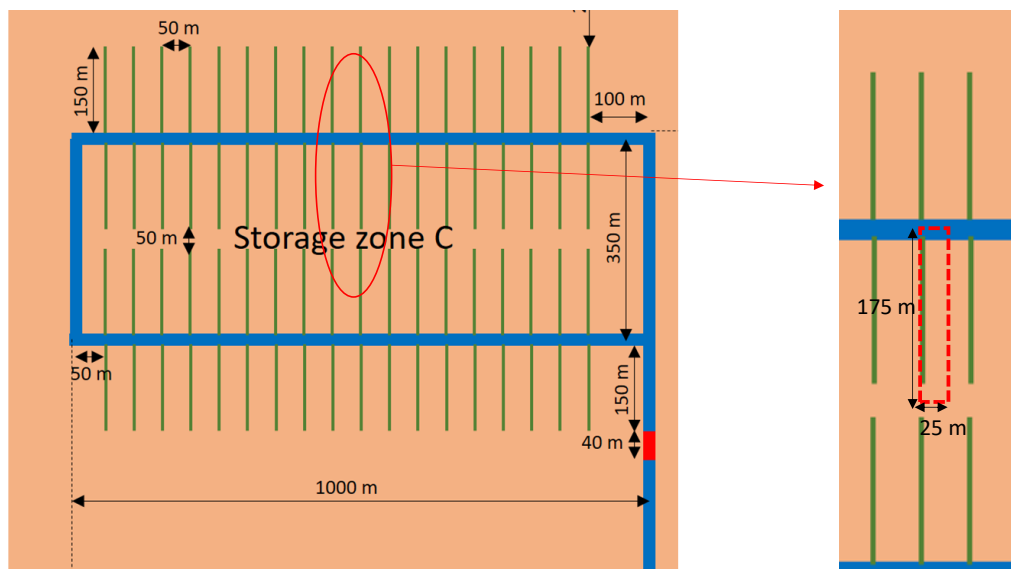


Figure 6-2: Representation of the modelling domain in the zone C (horizontal plan)

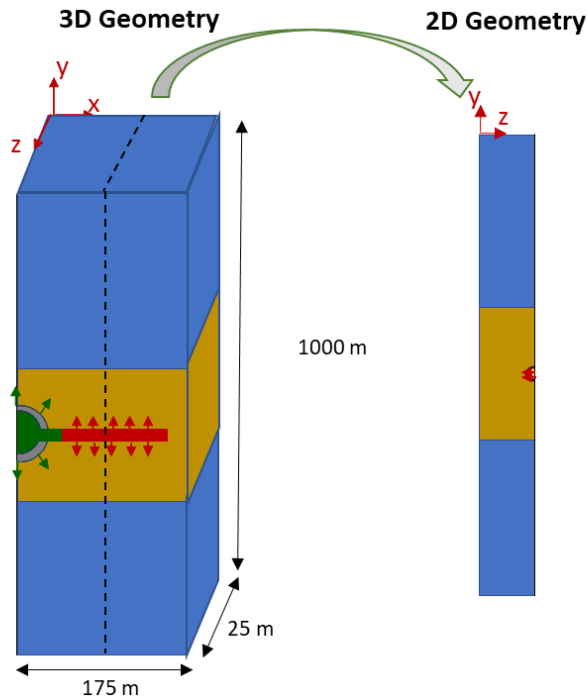


Figure 6-3: scheme of the modeling geometry for 3D and 2D computations

6.3.2 Mesh

A mesh has to be established for all materials to be modeled. In this domain, the materials taken into account are the host rock (intact, inner and outer damage zone around gallery and cell), backfill for gallery and plug, concrete around the gallery, waste canisters and voids between waste and rock. We do not consider the voids between the waste canisters in our simulation except in the thermal flow. The steel liner present in the tunnel is not modelled but is included in the evaluation of the gas production. A CAO EDF tool called “shaper” provides the geometry to be used for the simulation and the Salome platform computes the mesh (see <https://www.salome-platform.org>).

The mesh is composed of 1.06 million of tetrahedrons and 192 000 triangles (see Figure 6-3).

Considering a full THM model (3D_THH2MS model in Code_Aster), a computation of 5 million of degrees of freedom has been conducted to simulate 50 000 years. Table 6-4 gives the mesh repartition.

We remind the reader that in all the modeling, **the aquifer is modeled by the same material as the host rock.** This part is meshed in order to avoid boundary conditions problems at the top of the host rock.

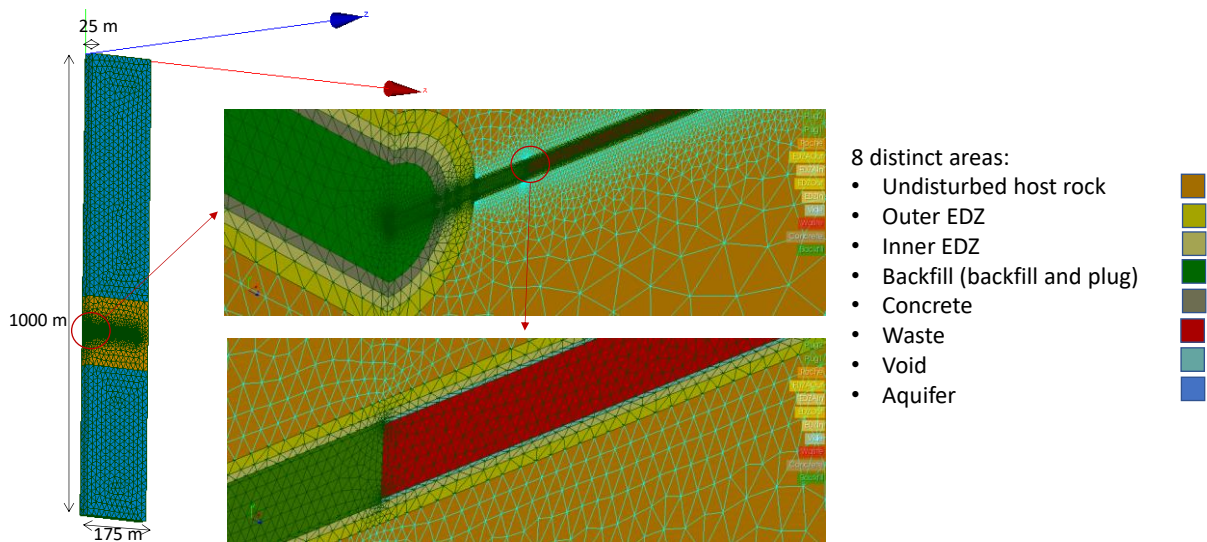


Figure 6-4: 3D mesh of the considered cross section (general view and zooms)

Table 6-4: 3D Mesh repartition

Material	Mesh number
Aquifer	8812
Undisturbed host rock	436470
Outer EDZ	132732
Inner EDZ	123601
Backfill	36347
Plug	26409
Concrete	10750
Waste	177685
Void	108084

The mesh used for the 2D computations (see 6.4.2) is composed of 21022 triangles. A zoom of this mesh is presented in Figure 6-5. Table 6-6 gives the mesh repartition.

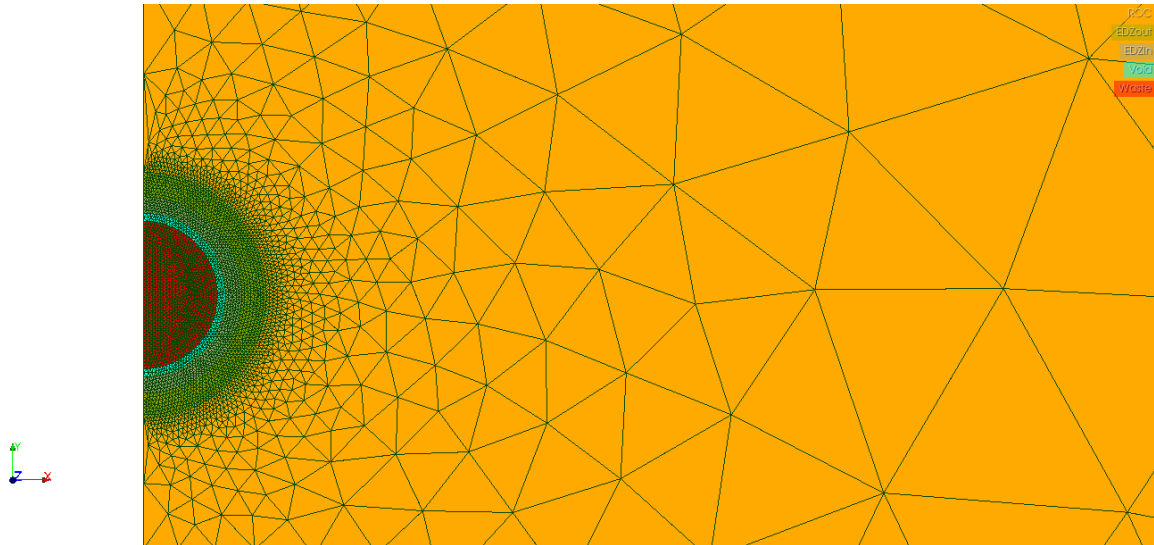


Figure 6-5: 2D Mesh (zoom around the tunnel)

Table 6-5: Mesh repartition

Material	Mesh number
Undisturbed host rock+ Aquifer	15845
Outer EDZ	1730
Inner EDZ	989
Waste	2036
Void	422

6.3.3 Boundary conditions

2 time (t) frames are considered: before and after 50 years. 50 years corresponds to the placement of the wastes and the closure of the gallery.

- For $t < 50$ years: Considering an instantaneous excavation of the whole repository, all the excavation area is ventilated with air at 80% of relative humidity (HR). Considering Kelvin's relation:

$$\frac{P_c}{\rho_l} = \frac{RT_{ref}}{M_{H_2O}^{ol}} \ln(HR)$$

with $M_{H_2O}^{ol}$ the water molar mass, it involves applying a capillary pressure $P_c=30,2$ MPa.

In the generic repository specifications, there is no ventilation in the *cells* of zone C, but for reasons of simplification, the same ventilation is applied in both the cell *and* the gallery. This choice is without consequences on the results, due to the small size of the cell (see section

6.4.2) compared to the gallery. All boundary conditions used for the simulations are summarized in Figure 6-4: 3D mesh of the considered cross section (general view and zooms).

- For $t \geq 50$ years: Backfill, plug, concrete, wastes and “voids” are instantly placed. Gas flows are applied on gallery and cell and thermal flow on cell only. All boundary conditions are summarized in Figure 6-5. Gas and thermal source terms are detailed below.

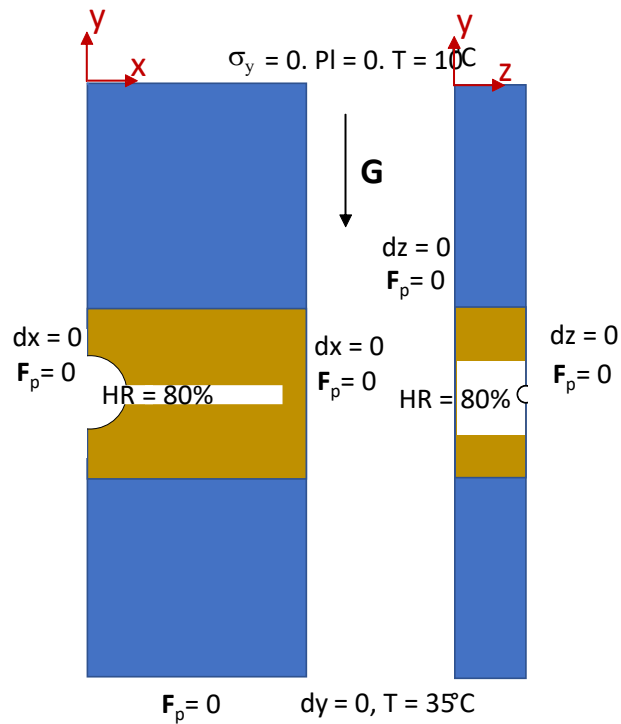


Figure 6-6: 3D boundary conditions for $T < 50$ years

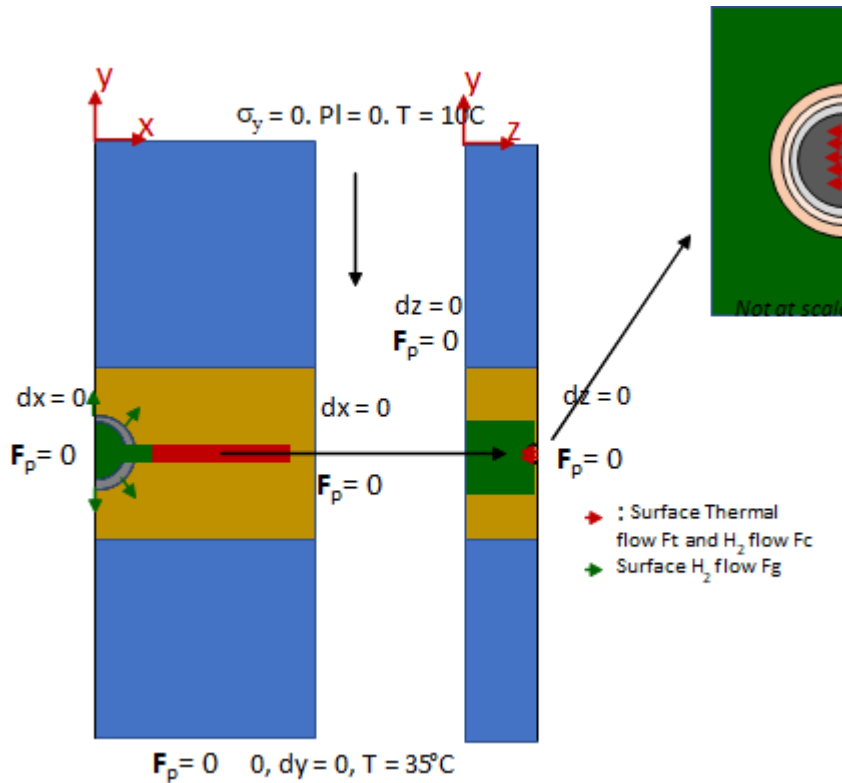


Figure 6-7: 3D boundary conditions for $T \geq 50$ years

For the 2D computations, the same 2 steps are applied Figure 6-7: 3D boundary conditions for $T \geq 50$ years summarizes the 2 steps (before 50 years, HR=80% is applied at the rock).

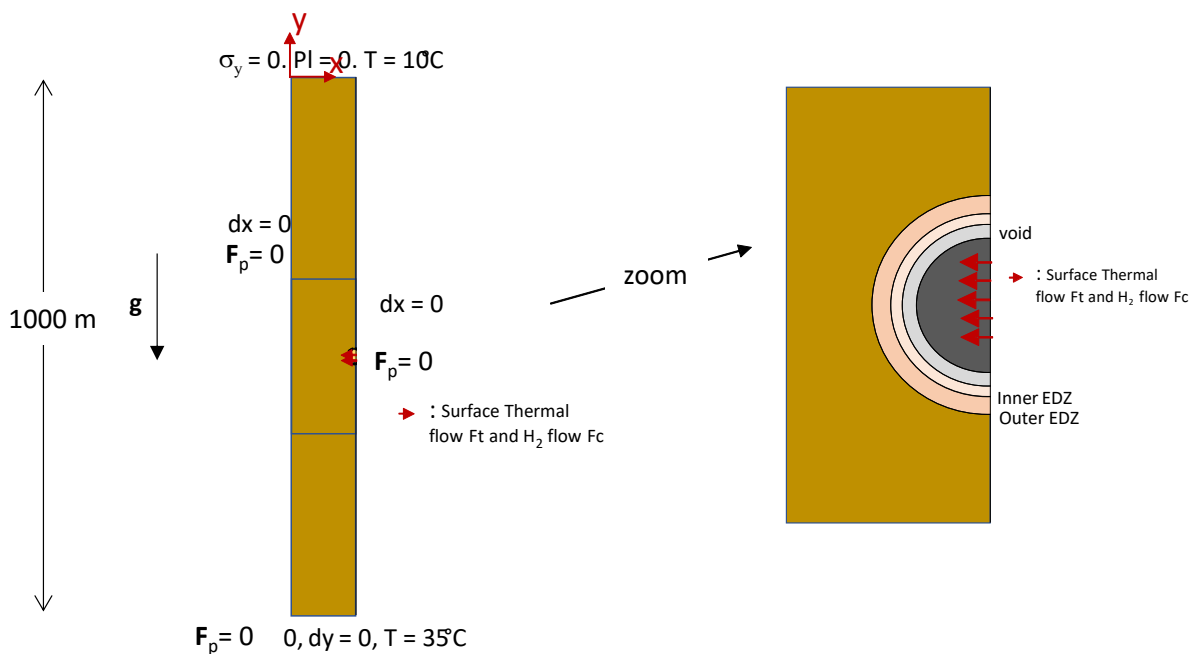


Figure 6-8: 2D boundary conditions (vertical section around a HLW C) $t \geq 50$ years

To complete this scheme, we explicit now the source terms used in the computations.

Source terms:

It is stated in the specifications that source terms don't correspond to given existing wastes/component: they just must be of the right order of magnitude concerning the values and the duration. The required terms are given bellow.

✓ **Around the gallery:**

A gas source term of 21.5 mol/y per meter of gallery from T=0 to T=50 000 y (time needed to corrode 0.5 cm of thickness) is considered.

In Code_Aster surface flow is required in kg/m²/s which implies the need for an equivalence with the previous gas term source.

Assuming that the surface flow Fg is applied around the concrete boundary (radius = 5 m, which means a unit surface Sg = 31,4 m²) and that $M_{H_2}^{ol} = 0,002 \text{ kg.mol}^{-1}$, the applied hydrogen flow is $Fg = 4,3 \cdot 10^{-11} \text{ kg/m}^2/\text{s}$.

✓ **Around the cell:**

A gas source term of 1.9 mol/y per meter of zone C HLW cell during 40 000 years is considered. The flow is applied at the internal boundary of the cell (symmetry plan see Figure 6-5, which means a unit surface Sc = 1,8 m²) and corresponds to $Fc = 6.7 \cdot 10^{-11} \text{ kg/m}^2/\text{s}$. This flux is applied along the cell except for the buffer (red part Figure 6-7, i.e. 143 m long).

The thermal flow indicated in Figure 6-6 is applied on the same boundary (the same surface Sc is considered to convert this flow in W/m²). Moreover, the flux is given by meter of canister. As it is applied along all the cell board (except the buffer) a ratio of 1,5/1,8 is used. We consider that the flow reaches zero at 1600 years (linear between 900 and 1600 years). We make the arbitrary hypothesis that thermal flow reaches zero at 1600 years. This is an arbitrary choice that will be discussed in section 6.4.2.3.

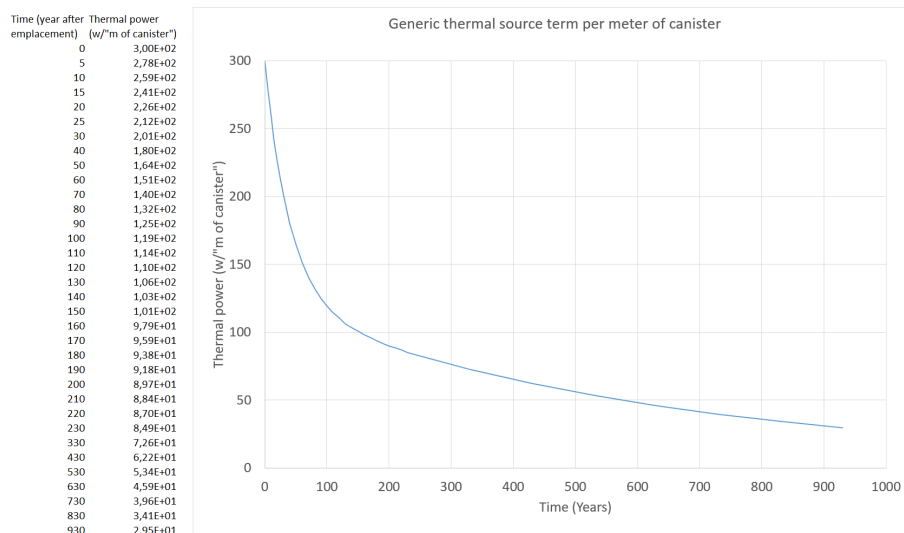


Figure 6-9: thermal source term per meter of canister

6.3.4 Initial conditions

The time varying elements are as follows:

- $t = 0$: The media is fully saturated with an initial pressure corresponding to the hydrostatic pressure p_0 . We consider also mechanical equilibrium considering gravity and boundary conditions.

Considering isotropic state of stress, we have at -525m deep:

$$\sigma_{y=-525m}^0 = \sigma_{y=-525m}^0 = \sigma_{z=-525m}^0 - 13,13MPa$$

$$\sigma_x(y, t = 0) = \sigma_y(y, t = 0) = \sigma_z(y, t = 0) = \rho_0 \cdot G \cdot (y + 525) + \sigma_{y=-525m}^0$$

With $G = 10 \text{ m} \cdot \text{s}^{-2}$

Hydrostatic equilibrium is also written for water pressure:

$$p_l^0(y) = -\rho_l^0 G y$$

Considering boundary conditions given for temperature, we apply (T in °C):

$$T_{\text{ini}}^0(y) = -0,025 \cdot y + 10$$

- $t = 50$ years: instantaneous appearance of the waste canisters in the model and closure of the whole repository. All emplaced materials are assumed to have an initial water saturation of 0.8, a temperature equal to 25°C and an initial stress equal to zero.

6.4 Simulation results

Except preliminary 2D computations shown in section 6.4.2.2, all the following results are represented in chronological order.

6.4.1 3D modelling case

6.4.1.1 Reference computation

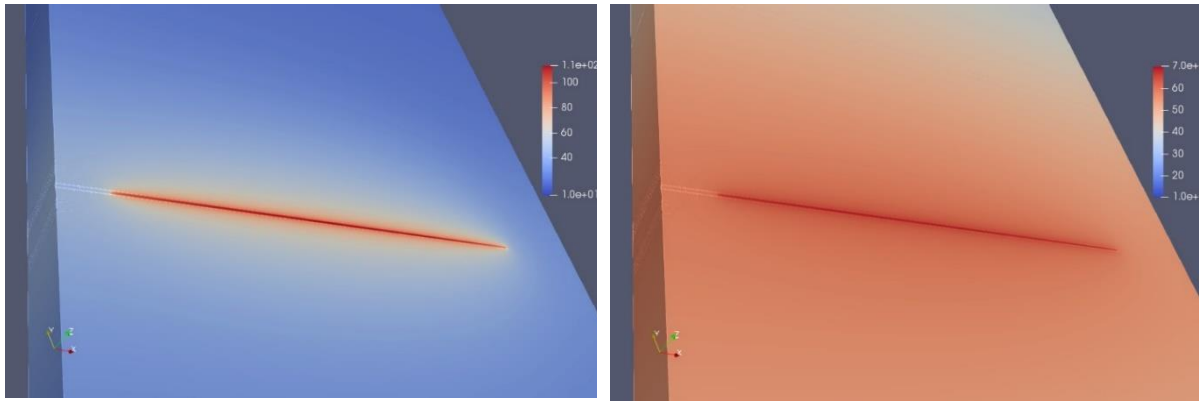
In this section, the results obtained with all the previously described parameters are given. Isovalues are first presented (from Figure 6-10 to Figure 6-12) to give main tendencies and to observe the strong 3D aspect of this simulation. For precise and quantitative, results curves are given in the following.

Figure 6-10: temperature isovalues show temperatures map for “early times” (100 and 1000 years) when thermal phase is important (thermal flow is only indicated before 1000 years, see Figure 6-9). These pictures allows to point the localized temperature around the cell and its progressive diffusion in all the material

Figure 6-11 and Figure 6-10 show gas pressure maps for different times (from 100 to 50 000 years). From these figures it can be noted that at 100 years, gas pressure is more important in the cell than in gallery, and after 1000 years, this pressure is the same in all the excavated part. Logically the temperature is focused around the tunnel.

Figure 6-12 shows gas pressure isovalues in the host rock only (the underlying and overlaying aquifer are not considered in the picture) with the same scale used between 1 bar and 1 MPa. This figure shows

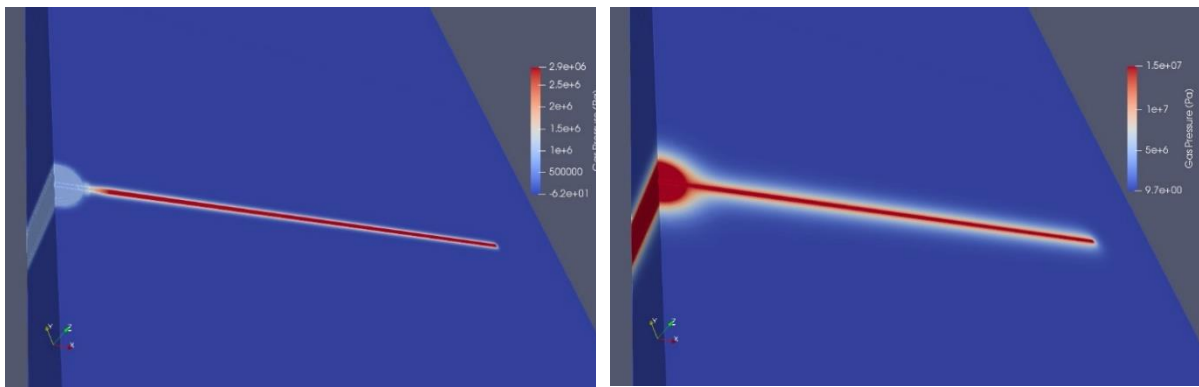
the impact of representing the entire the domain rather than only the host rock: it avoids boundary effects. This was the original goal of this choice, but it is questionable (see also section 6.4.2.6). Indeed, representation of aquifer in a closed system (compared to the full repository) is questionable: even aquifer would has been represented with appropriated parameters, system stays closed and fluids are not able to escape laterally. This is the point which probably differs mainly from Andra's representation (see corresponding section and discussion chapter) and highlight the limitation of the "local 3D model" compared to repository scale representation.



100 years

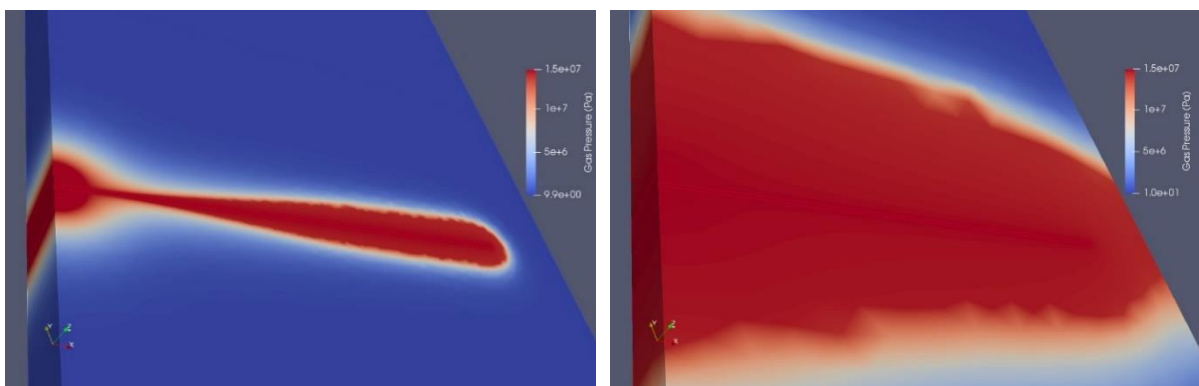
1000 years

Figure 6-10: temperature isovalues



100 years

1000 years



5000 years

50 000 years

Figure 6-11: gas pressure isovalues

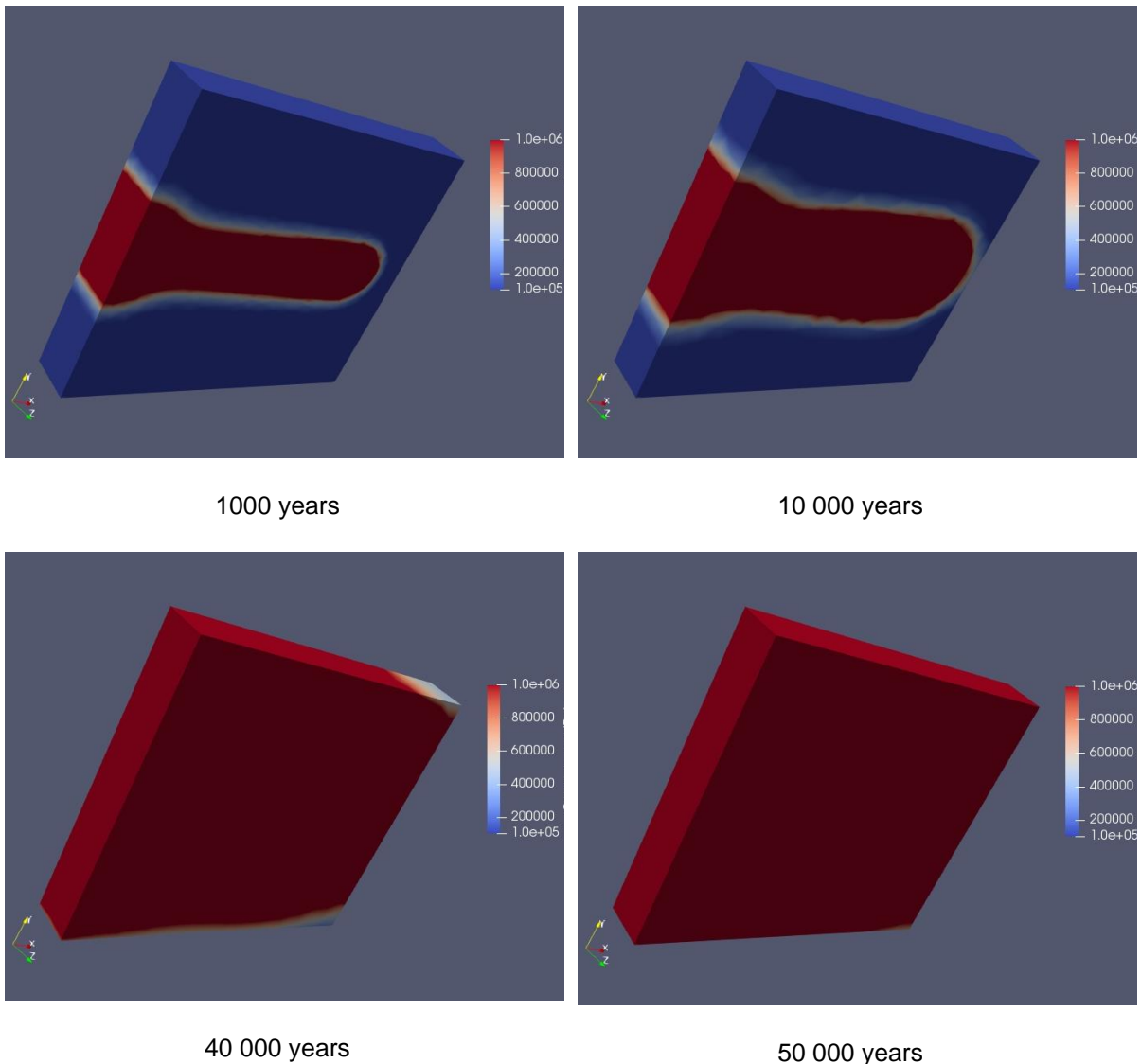


Figure 6-12: gas pressure isovalues (host rock only)

Evolution of different values on defined output points are now studied in detail. These output points are taken on an horizontal plan at 600 m of depth (cell level) and are shown on Figure 6-13. In this figure, colors are the same than those defined in Figure 6-4. Values are also presented at several time steps on an horizontal profile crossing the cell (dotted line on Figure 6-13). Figure 6-14, Figure 6-15, Figure 6-16 and Figure 6-17 show respectively temperature, gas pressure, saturation and capillary pressure evolution on output points (a) and on the horizontal line (b).

The temperature reaches its maximum value 10 years after the waste canister emplacement in the repository (i.e. 60 years after the beginning of simulation). This value is equal to 130°C in the middle of the waste canister on the injection board (point MT). At the edge of the clay, this value is equal to 95°C. The temperature decreases quickly from the boundary injection (Figure 6-14 b). The high value on injection board is due to the fact that flow is applied only on this surface and not distributed on all the waste volume (which is not possible with Code_Aster). This causes a boundary effect which remains very local and doesn't impact temperature in the rock.

Gas pressure first increases very quickly until around 70 years in the tunnel (point MT on Figure 6-13) due to the quick rise of temperature. After that, the pressure continues to increase more gradually and after around 300 years, we observe an homogenization of the pressure in all the excavated part. **The maximum gas pressure is reached at around 3000 years and is equal to 16 MPa** due to the combination of gas production and temperature. After that, pressure decreases a little in both the tunnel and the gallery, which can be attributed to the desaturation of the clay rock. Indeed, according to Figure 6-16, gas enters in the clay between 3000 and 4000 years. Then gas pressure increases a little until the end of injection (50 000 years). It is worth noting that the first “gas pressure” peak (at 3000 years) is higher than the one obtained at the end of the production phase. This observation - which is different from results obtained at the scale of the repository (for Andra for example, this first peak exists but is smaller) should be discussed in the future.

Looking at the saturation evolution in the gallery, we observe a resaturation due to water coming from the rock before 500 years and then desaturation due to hydrogen production. The minimum value is observed after 10 000 years. In the tunnel, the process is the same as in the gallery but faster, as expected: the resaturation is done in less than 100 years and the minimal saturation is reached around 3000 years. As previously said, we observe a weak desaturation ($>0,98$) of the host rock after 3000 years.

It is worth noting that regarding Figure 6-14, capillary pressure is always strictly positive in the gallery and tunnel, which means that gas is really expressed (and not on a dissolved phase). As said previously, the point placed in host rock (C1 on Figure 6-13) is desaturated only after 3 000 years (when $P_c > 6$ MPa). Before that “gas pressure” corresponds only to solved hydrogen ($p_g^{H_2} = K_H \cdot \frac{\rho_L}{M_{H_2}}$).

As previously detailed, the 3D aspect is clearly important and will be discussed in section 6.4.2. Nevertheless, due to the boundary conditions (hydraulic flows equal to zero on boundary conditions), gas can't escape in the gallery, as it would normally be the case. That is why we call this modeling a “local 3D” modeling.

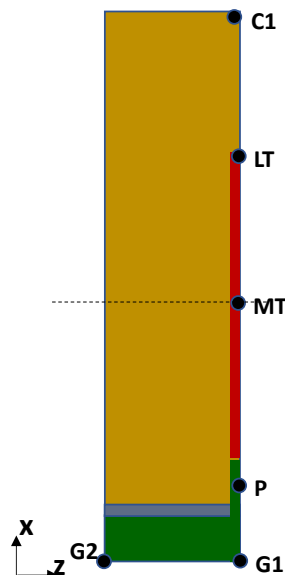
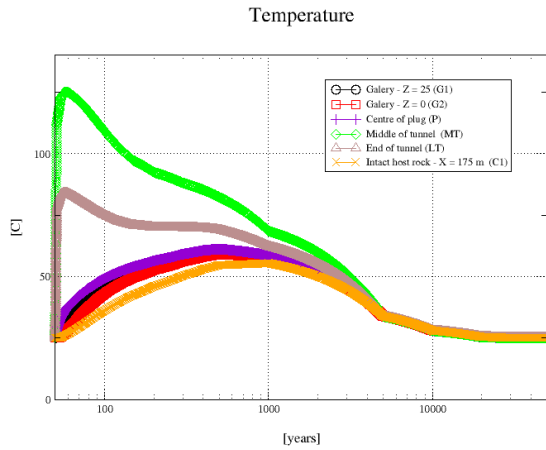
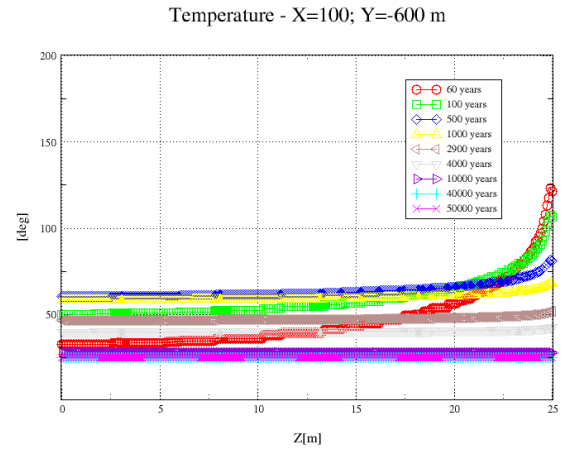


Figure 6-13: output points ($y = -600$ m) (C1, LT, MT, P, G1, G2)

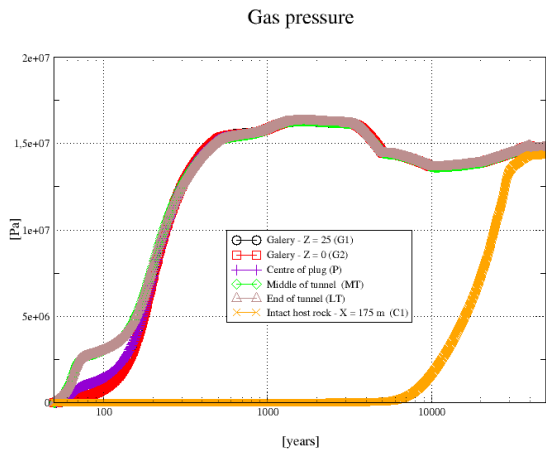


(a)

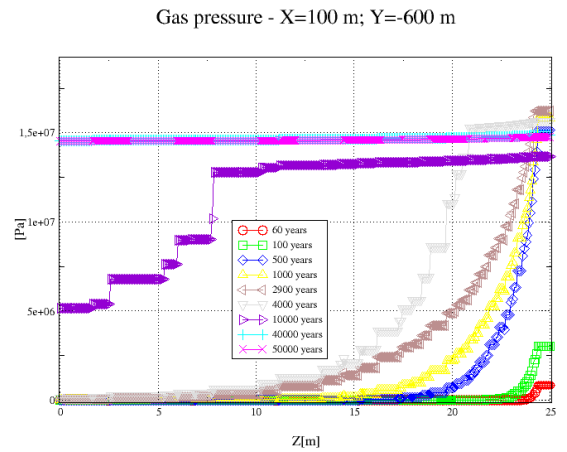


(b)

Figure 6-14: temperature on output points (a) and on profile (b)



(a)



(b)

Figure 6-15: gas pressure on output points (a) and on profile (b)

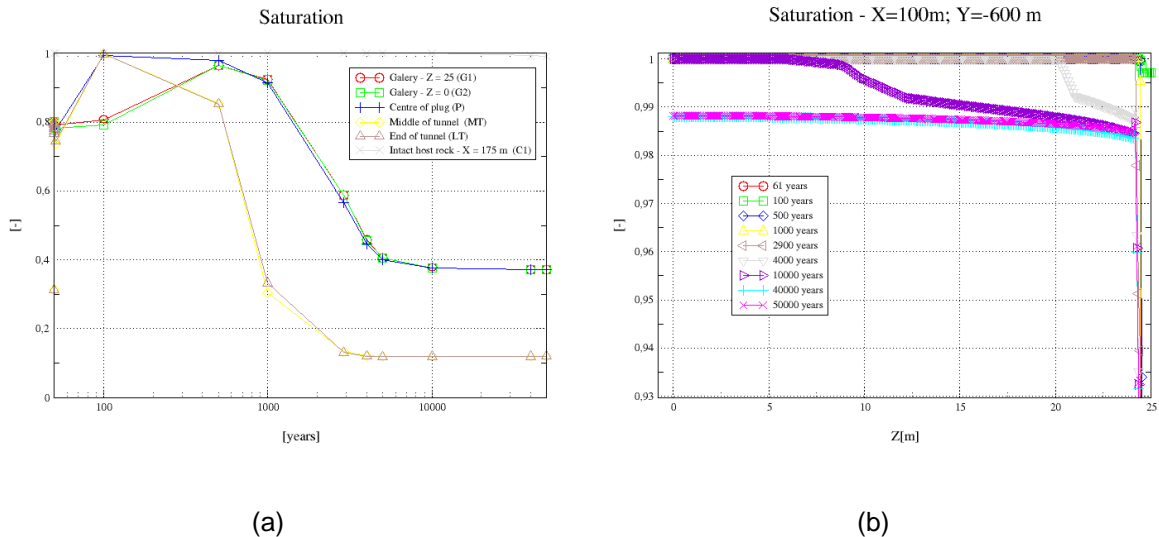


Figure 6-16: saturation on output points (a) and on profile (b)

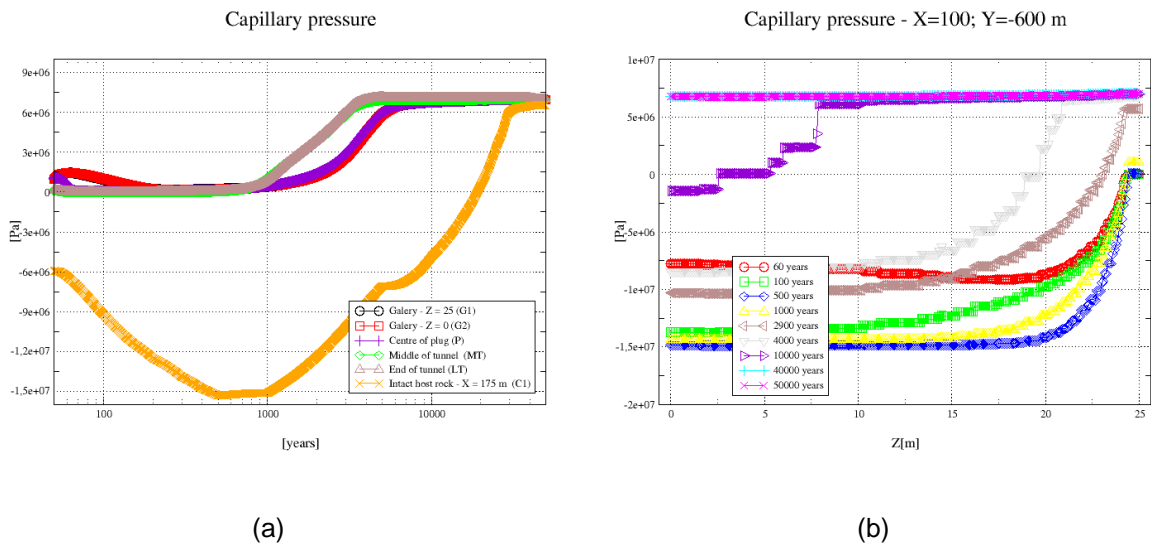


Figure 6-17: capillary pressure on output points (a) and on profile (b)

6.4.1.2 Sensitivity analysis on 3D computations

Sensitive analysis on 3D configuration is almost impossible due to the cost of such a computation. Nevertheless, to enhance the impact of temperature on gas pressure, same computation is done without thermal flow. Comparison of evolution of gas pressure is showed Figure 6-14. Logically, without a thermal flow, the gas pressure increases much more progressively. The maximum gas pressure equal to 16 MPa after 3000 years is not reached. Naturally, after an important time (about 10 000 years), the gas pressure evolutions become the same as in the former model. In the host rock, far from the cell (C1), the temperature has logically no impact on gas pressure.

Gas pressure - impact of temperature

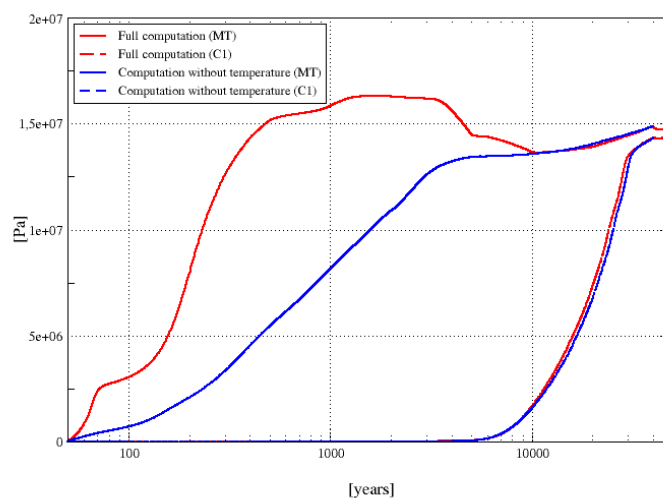


Figure 6-18: gas pressure evolution – comparison of 3D computations with or without thermal flow

6.4.1.3 Difficulties and performance analyses

We remind the reader that this computation has required 5 million of degrees of freedom and has been conducted in order to simulate a period of 50 000 years (corresponding to the final time of gas injection).

This computation has been performed on 48 processors (6 number of OpenMP threads and 8 nodes) on EDF's cluster. Several steps have been necessary to succeed in these computations. Indeed, because hydromechanical processes don't affect the temperature in the porous media, a pure thermal computation (degrees of freedom of pressures are blocked) has first been made and projected as a boundary condition on the full THM model. This has considerably reduced convergence problems. However, convergence problems are proving to be still important especially during the simulation period between 1000 and 3500 years. Time steps refinements have therefore been necessary, numerous and sometimes unexpected. Convergence difficulties are due to high non-linearities and materials contrasts. 3D effects reinforce these aspects (gas front evolves in different ways, hence difficulties appears at different times). Numerous continuations of the calculation have been necessary in order to resize the time step or the Newton's residual (between 10^{-6} and 10^{-10}).

Actually more than 9000 time steps have been required to complete the calculation. Each time step cost between 1 mn and 5 mn.

An iterative linear solver from PETSc library has been used with following CODE_ASTER parameters:

```
METHODE = 'PETSC'; PRE_COND='LDLT_DP', ALGORITHME = 'FGMRES', RENUM =
'PARMETIS', ACCELERATION = 'BLR+', PCENT_PIVOT=50
```

The efficiency of this solver is huge: it is 4 times faster than a direct solver ('MUMPS') but is less robust (which is well-known by the scientific community).

6.4.2 2D modelling

Sensitivity analyses are performed in order to understand differences with other teams. For that, 2D computations are performed. These modellings treat a vertical section at the middle of the tunnel (as previously schematized on Figure 6-7). In this case, the gallery is not considered anymore.

In a first part, the same hypothesis as in the 3D modelling are kept in order to compare the results between 2D and 3D computations (section 6.4.2.1). Some hypotheses concerning the boundary conditions around the cell are then questioned (section 6.4.2.2) in order to verify the 3D hypothesis. In a second part, a sensitivity analysis on material parameters is done (section 6.4.2.3 to 6.4.2.5). At least, goal of boundary conditions (linked to aquifer representation) are studied in 6.4.2.6.

6.4.2.1 Comparison with 3D computations (considering same hypotheses)

In this section, 2D results are compared with the reference 3D computation at the center of the tunnel (MT point Figure 6-13 for 3D computation). All the hypotheses - except the geometry - are the same in the 2D and 3D modelling. Temperature, gas pressure, capillary pressure and water pressure evolution in the cell center are respectively shown on Figure 6-18, Figure 6-19 Figure 6-20 and Figure 6-21. Temperature evolutions are very close which is logical since thermal flow is only applied at the left side of the cell and the temperature peak arrives quickly compared to gas production and hydraulic phenomena. On the other hand, the 2D computation greatly overestimates gas pressure during at least 2000 years of simulation and at the end underestimate it. The first gas pressure peak in 2D leads to 20 MPa around 550 years compared to 16 MPa at 2800 years in 3D. Indeed, even if there is no gas production around the gallery, the gas can't escape (no more backfill volume) and the cell is modelled as an "infinite" one. Liquid pressure evolution corresponds logically to those of gas pressure. In 2D, a second peak of gas appears around 2800 years. This happens when gas enters the rocks: capillary pressure suddenly increases and exceeds the gas entry pressure. This effect – more pronounced in 2D - may be reinforced by the chosen Van-Genuchten model. It will be discussed in section 6.4.2.4.

Finally, at the end of the gas production phase around the cell (happening at around 40 000 years), gas pressure is higher in 3D than in 2D which is due to gas production in the gallery.

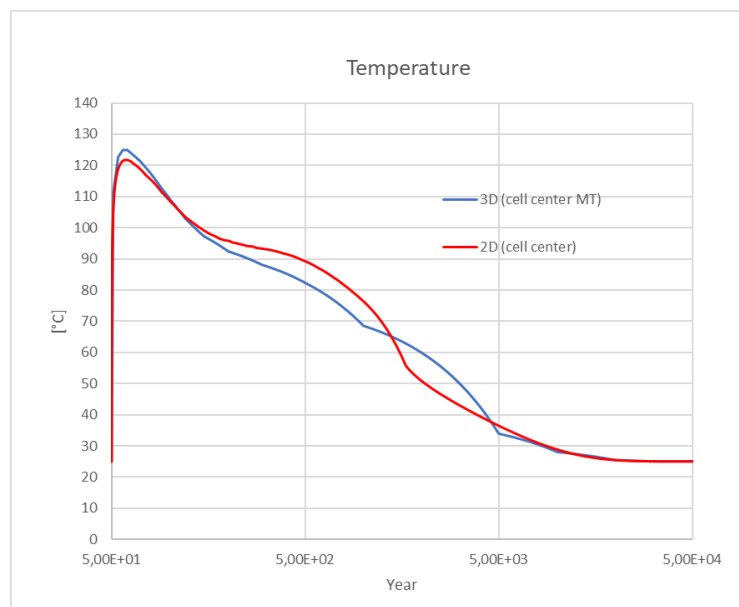


Figure 6-19: temperature evolution - comparison between 3D and 2D computations

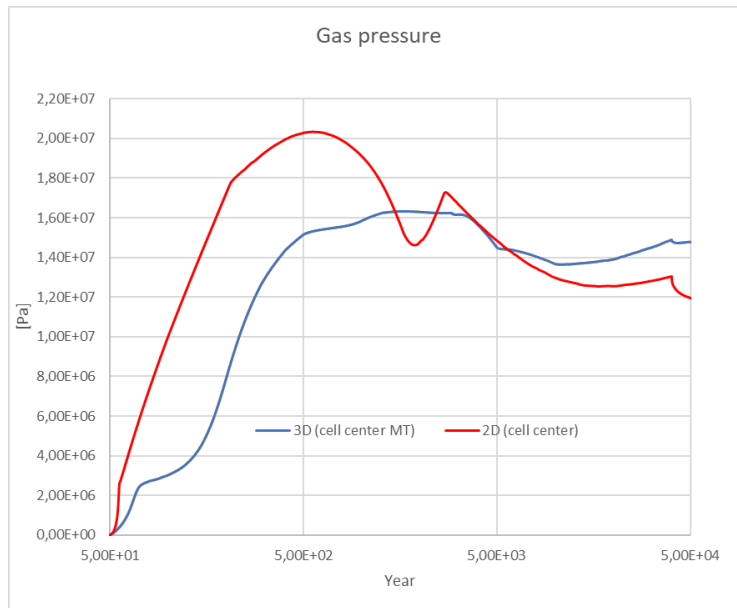


Figure 6-20: gas pressure evolution - comparison between 3D and 2D computations

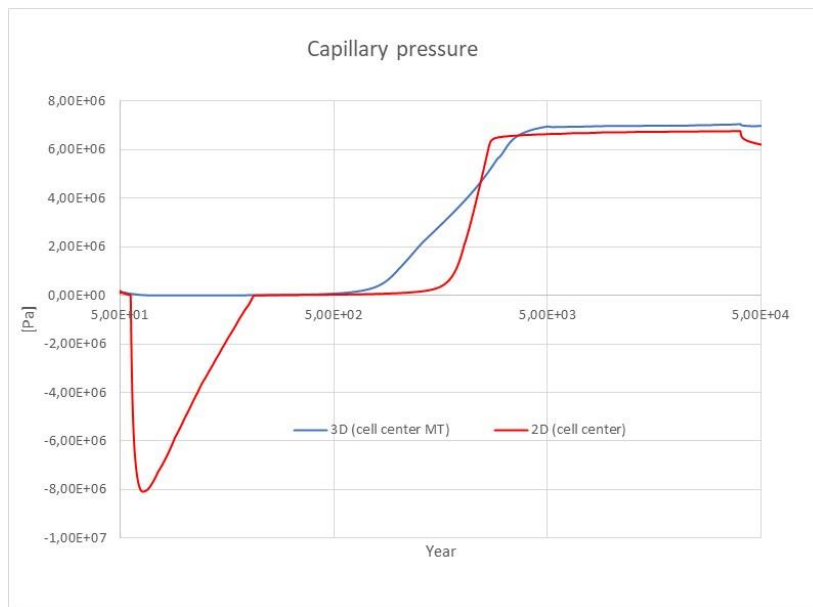


Figure 6-21: capillary pressure evolution - comparison between 3D and 2D computations

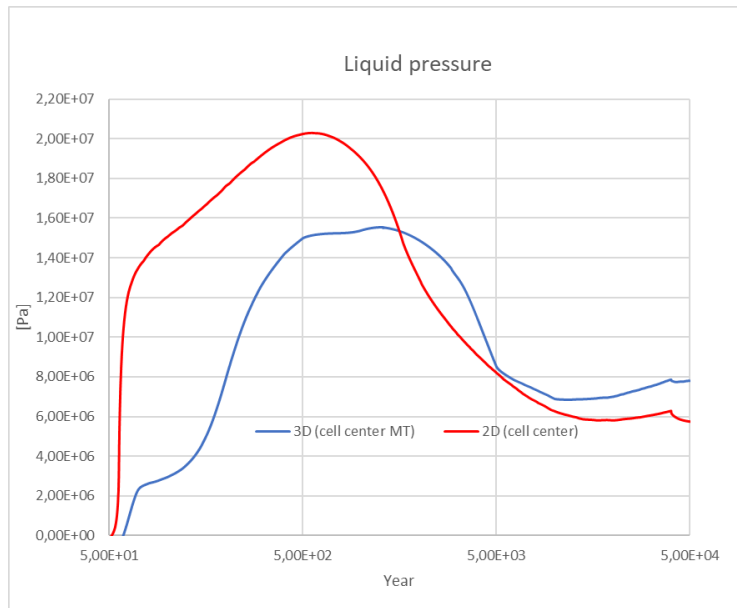


Figure 6-22: liquid pressure evolution - comparison between 3D and 2D computations

6.4.2.2 Preliminary computations with comparisons on boundary conditions around the cell

Prior to establishing the 3D modelling, several 2D computations have been performed in order to check the hypotheses on hygrometry which were then used in 3D, as to know:

- A full modeling taking into account the ventilation_ HR = 80% (reference solution)
- A modeling without the hygrometry condition
- A modeling with the ventilation (HR = 80%) but without the thermal flow

Figure 6-22 shows the gas pressure evolution in the middle of the waste canister for the different hypotheses. As shown previously for the reference computation, maximum gas pressure is equal to 20 MPa after 550 years. Modeling without ventilation gives exactly the same results due to the weak dimension of the cell. It justifies the hypothesis to take the same boundary conditions in cells and gallery (see section 6.3.3). Considering the modeling without thermal aspects (in blue), the maximum gas pressure is obtained at the end of the injection phase (13 MPa). As already described for the 3D

computation (section 6.4.1.2), the first gas peak (corresponding to the maximal gas pressure for the whole computation) observed with fully THM model is clearly linked to the thermal phase.

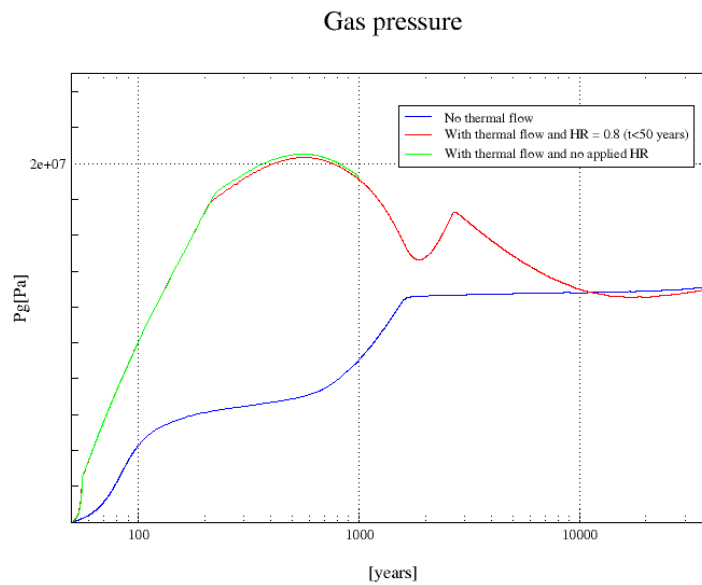


Figure 6-23: gas pressure evolution in the cell

6.4.2.3 Sensitivity analysis on thermal parameters

In order to benchmark our results with other teams (see ULiège section for comparisons), it has been decided to adopt common hypotheses for thermal flow, namely, to consider that the thermal flow reaches zero at 3000 years (instead of 1600 years as in the previous computations). A linear evolution between 930 years (corresponding to Figure 6-9) and 3000 years is applied.

Common nodes coordinates (depending on the mesh of each team) are also chosen in order to compare gas pressure, capillary pressure, water pressure and temperature (coordinates in brackets) in the same point:

- Waste Center [0;-600]
- EDZ In [0.55;-600]
- EDZ Out [0.67;-600]
- Host rock [0.95;-600]

In this section, we present the results corresponding to the following 3 cases:

- **Case 1:** reference case with all the hypotheses defined previously for 3D computations (i.e. thermal flow equal to zero at 1600 years).
- **Case 2:** same as case 1 but with thermal flow equal to zero at 3000 years.
- **Case 3:** same as case 2 with viscosity depending on temperature (instead of constant) according to following relationship proposed by ULiège (and represented on Figure 6-19).

$$\mu(T) = 10^{-3} \cdot \exp\left(-3,719 + \frac{578,919}{T - 137,546}\right)$$

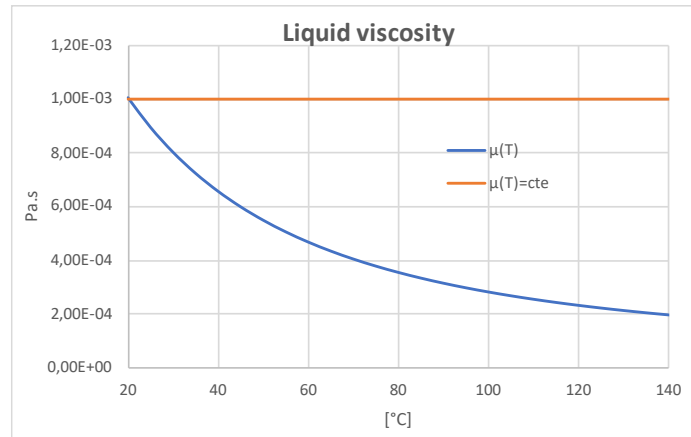


Figure 6-24: dynamic liquid viscosities used in the computations

A comparison between case 1 (dotted line) and case 2 (full line) is first proposed in Figure 6-24, Figure 6-25, Figure 6-26 and Figure 6-27 for temperature, gas pressure, capillary pressure and liquid pressure, respectively. Weak differences are observed. As expected, the temperature decreases a little bit slower for case 2 after 1600 years; the second gas pressure peak for case 1 is 17,1 MPa at 2900 years and for case 2 18,9 MPa at 3220 years. Gas entry pressure is a little bit delayed with $\mu(T)$ and logically the decrease of water pressure is slower. This highlights the importance of taking correctly into account the thermal flow for a long period and not only at short term.

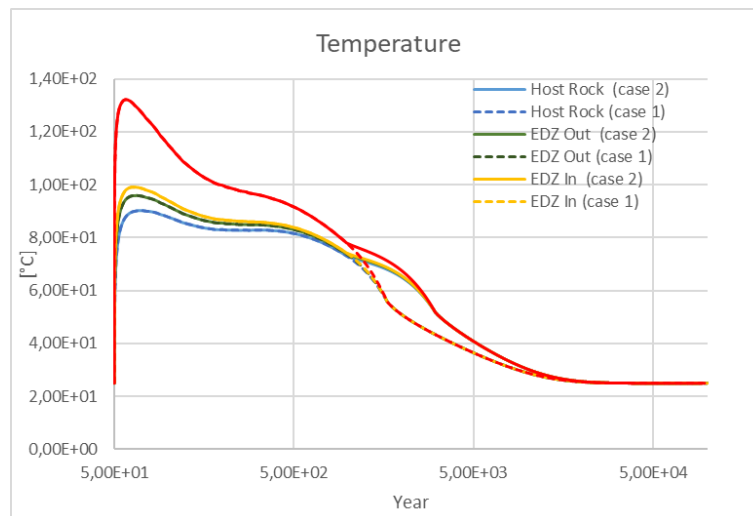


Figure 6-25: temperature evolution (cases 1 & 2)

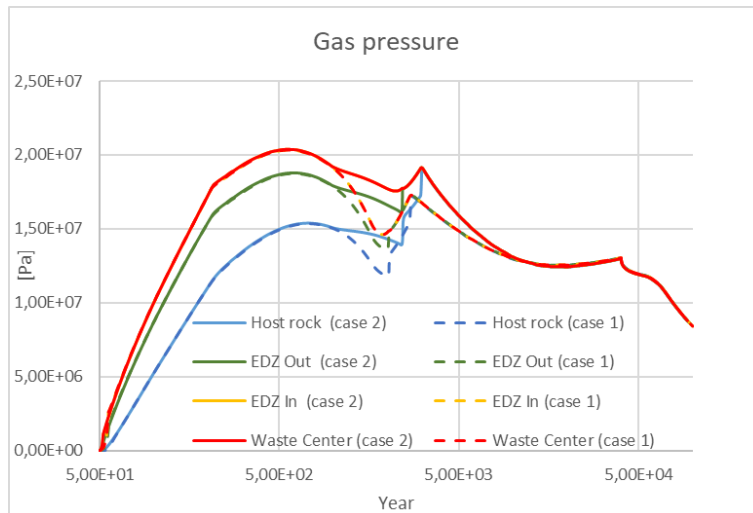


Figure 6-26: gas pressure evolution (cases 1 &2)

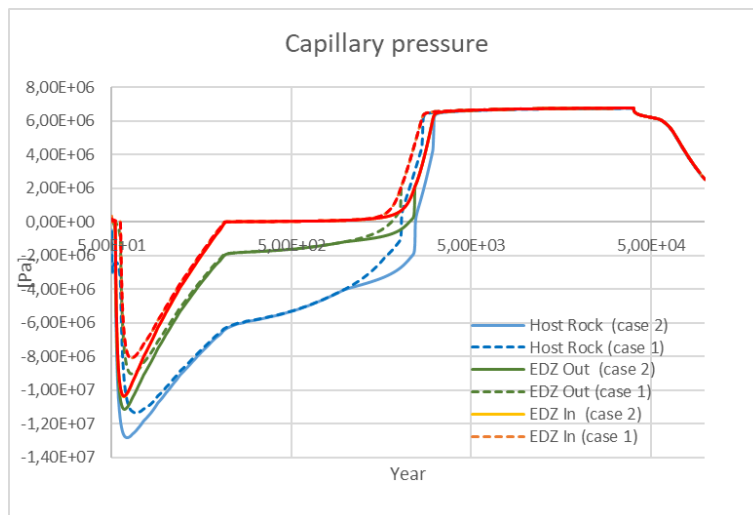


Figure 6-27: capillary pressure evolution (cases 1 &2)

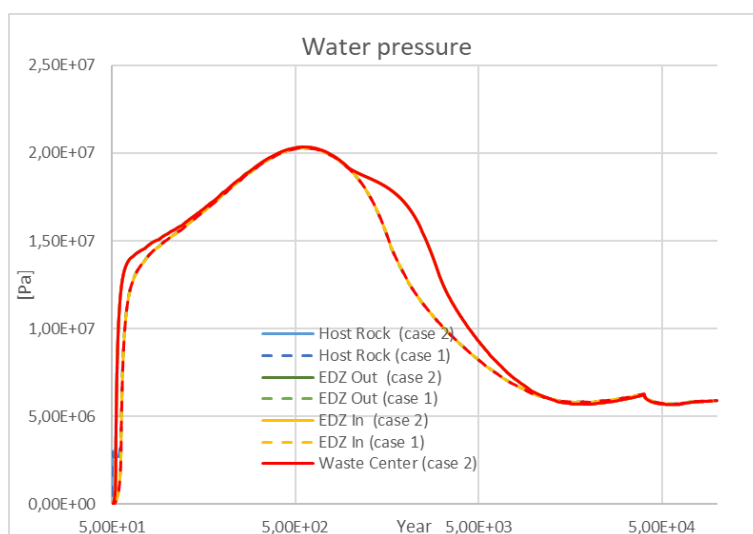


Figure 6-28: liquid pressure evolution (cases 1 &2)

In order to estimate the viscosity variation, we compare below the results obtained for case 2 (full line) and case 3 (dotted line) respectively on Figure 6-28, Figure 6-29 and Figure 6-30 for gas pressure, capillary pressure and liquid pressure (of course, this parameter has no influence on temperature).

Considering a constant viscosity equal to 10^{-3} Pa.s - as done in the previous computations - overestimates the pressure compared to the more realistic case (case 3). The overestimation is about 1MPa for both liquid and gas pressures. This result is logical: increasing the viscosity reduces the velocity of the fluid and its possibility to escape.

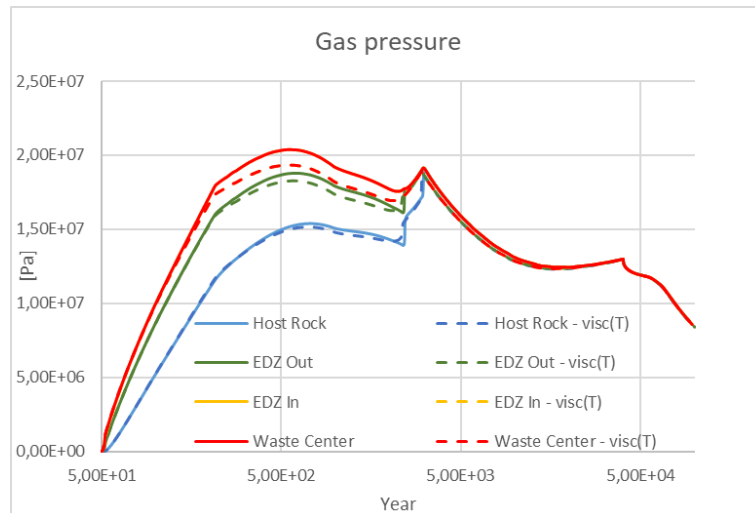


Figure 6-29: gas pressure evolution (cases 2 & 3)

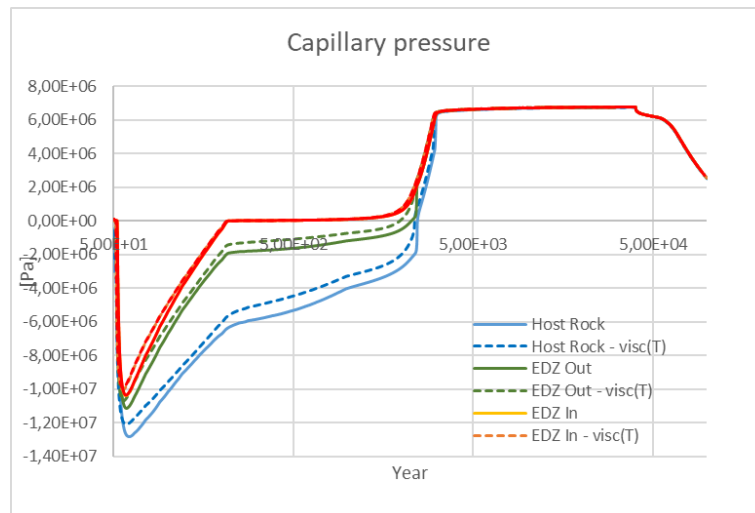


Figure 6-30: capillary pressure evolution (cases 2 & 3)

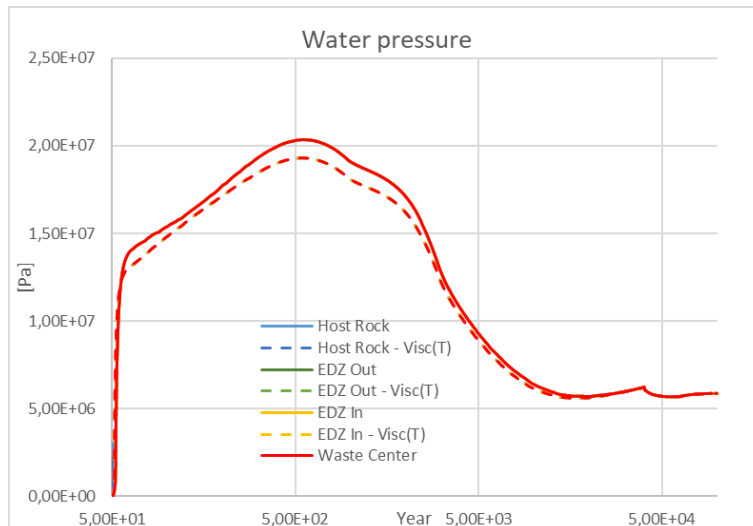


Figure 6-31: liquid pressure evolution (cases 2 &3)

Finally, **case 3 is considered as a new reference case** for the following sensitivity studies. In addition, we add on Figure 6-31 “expressed” gas pressure for this case. Indeed, gas exists only when $S < 1$, i.e. when the capillary pressure exceeds the entry pressure. In the previous figures, gas pressure evolution includes the part where hydrogen appears only on dissolved expression ($S=1$). For this case 3, gas appears in the tunnel and inner EDZ after around 230 years, in the outer EDZ after 2370 years and in the Host Rock after 3000 years.

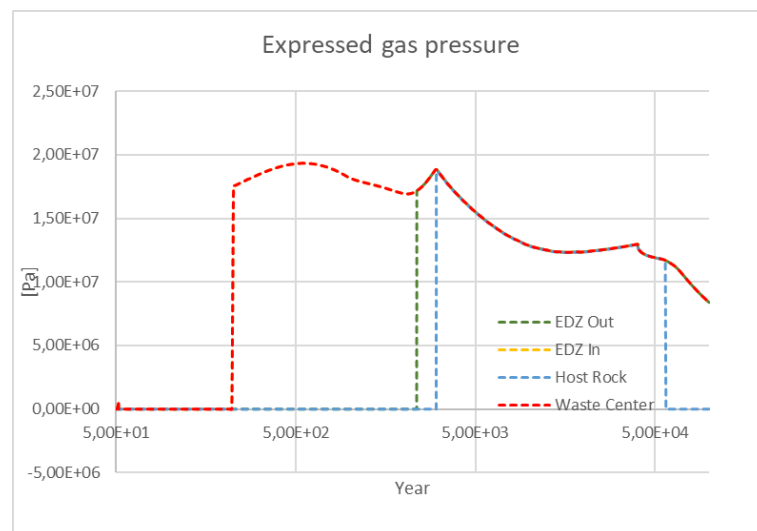


Figure 6-32: expressed gas pressure evolution (case 3)

6.4.2.4 Sensitivity analysis on transfer terms (Van-Genuchten model)

In the following, discussions about Van-Genuchten curves are made. A first sensitivity analysis is done playing with ε parameter (or $S_{max}=1-\varepsilon$) used for “modified” Van-Genuchten curves. The “modified” Van-Genuchten law (VGE) takes into account an entry pressure and a specific treatment when S reaches the numerical parameter S_{max} (see section 6.2.1). A 4th case is therefore considered, in addition to the 3 ones detailed in the previous sections, as to knows:

- Case 4:** same case as case 3 with $S_{max} = 0,99$ instead of $0,999$ for VGE law (see section 6.2.1) We compare below the results obtained for case 4 (full line) and case 3 (dotted line) on Figure 6-32, Figure 6-33 and Figure 6-34 for expressed gas pressure, capillary pressure and liquid pressure, respectively. This parameter S_{max} has no influence on the first peak of gas pressure but has an influence on the time of gas entry (or desaturation) and thus on its gas “expression”. This observation is logical since the S_{max} parameter concerns numerical treatments close to saturation. The first peak corresponds to gas expression (or liquid desaturation) in the tunnel and inner EDZ; in these materials entry pressure is equal to zero.

A more questionable point concerns the peak at 3150 years corresponding to gas entry in the host rocks. The value of S_{max} modifies substantially this peak and it is reasonable to think that it is due to the numerical treatment used for the Modified Van-Genuchten curve (see section 6.2.1, Equation 10). This hypothesis has been confirmed by the ULiège computation (see related section).

Except for this peak, main tendencies are the same. S_{max} has no influence on liquid pressure.

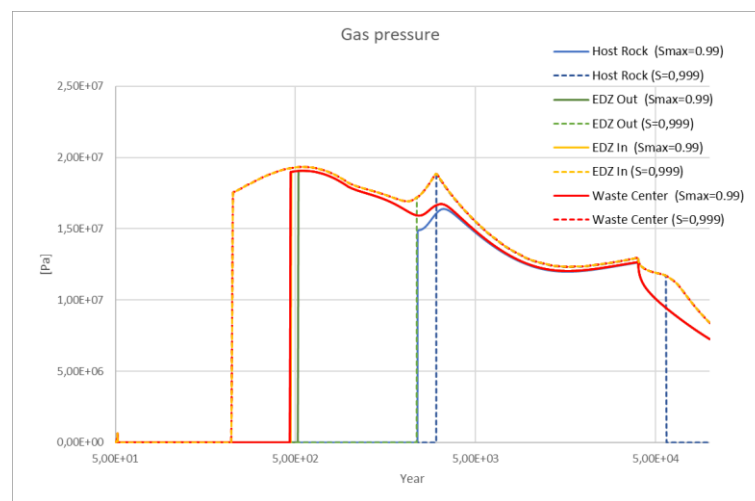


Figure 6-33: expressed gas pressure evolution (cases 3&4)

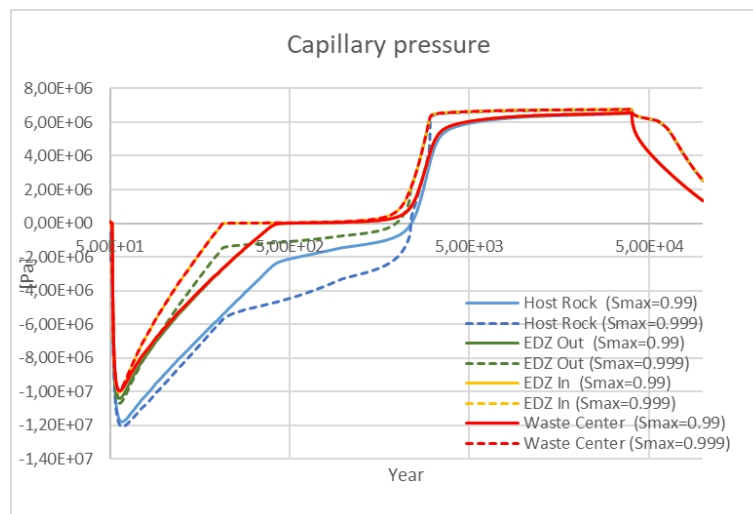


Figure 6-34: capillary pressure evolution (cases 3&4)

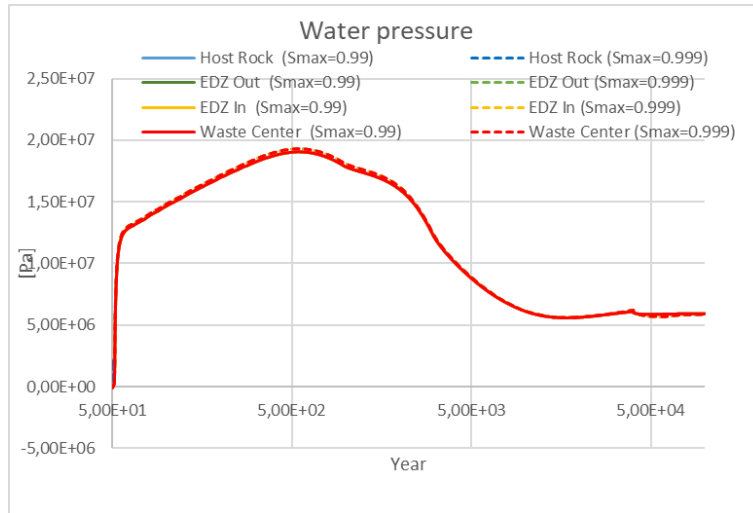


Figure 6-35: liquid pressure evolution (cases 3 & 4)

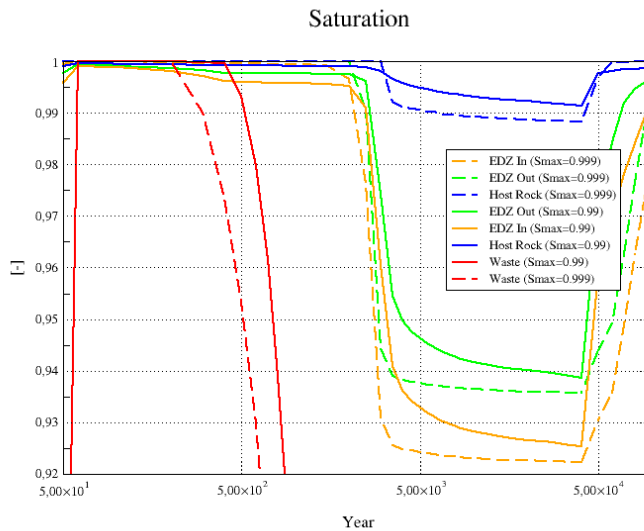


Figure 6-36: saturation evolution (cases 3 & 4)

In order to understand the numerical difficulties due to the “modified” Van-Genuchten law (VGE), the original law is now considered. Indeed, the VGE model defined in milestone 61 considers an entry pressure and a specific treatment at the interface for capillary pressure and for relative permeabilities. An alternative is to consider the classical Van-Genuchten Mualem (VGM) model (i.e. with $Pe=0$) with appropriate parameters. For that, “equivalent parameters” are proposed by ULiège (see appropriated section) and are indicated in Table 6-6 for capillary pressure. As previously, the relation is completed by an hyperbolic function when $S > 1-\varepsilon$ (see section 6.2.1). The corresponding curves are indicated Figure 6-33: even with chosen parameters, differences between VGE and VGM are quite important but the tendencies are the same. The goal of this part of work is essentially to understand the impact of the numerical treatment when S reaches $1-\varepsilon$ for both VGE and VGM curves.

For the relative permeabilities, the power m applied to the law is disconnected from the previous one and an additional power term l is used for gas permeability:

$$k_{rw}(S) = \sqrt{S_e} \cdot \left[1 - \left(1 - S_e^{1/m} \right)^m \right]^2$$

$$k_{rg} = f_g \cdot (1 - S_e)^l$$

The parameters proposed by ULg are indicated in Table 6-6.

	Host Rock	EDZ in	EDZ Out
Pr(MPa)=1/α	23	16	17
n	1,5	1,5	1,5
m	=1-1/n		
ε	10 ⁻³		

Table 6-6: ULiège parameters used for capillary pressure (case 5)

	Host Rock	EDZ in	EDZ Out
m	0,6	0,33	0,5
l	1,5	0,88	1,3

Table 6-7: ULiège parameters used for relative permeabilities (case 5)

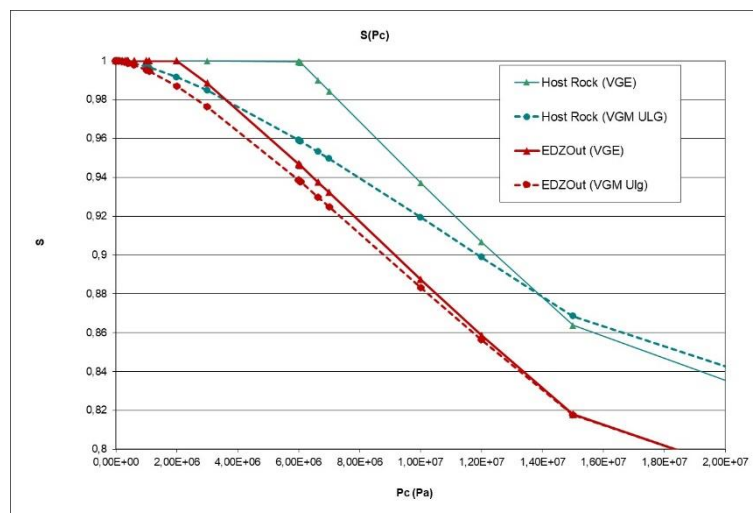


Figure 6-37: comparison of capillary pressure curves used for case 3 (VGE) and for case 5 (VGM with ULiège parameters)

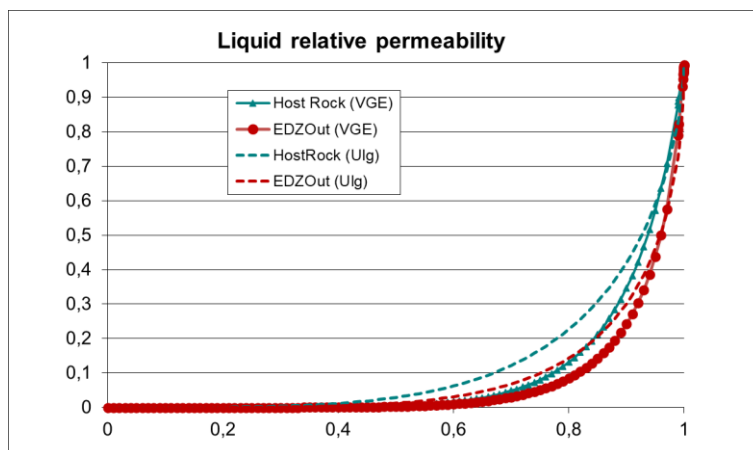


Figure 6-38: comparison of liquid relative permeabilities curves used for case 3 (VGE) and for case 5 (VGM with ULiège parameters)

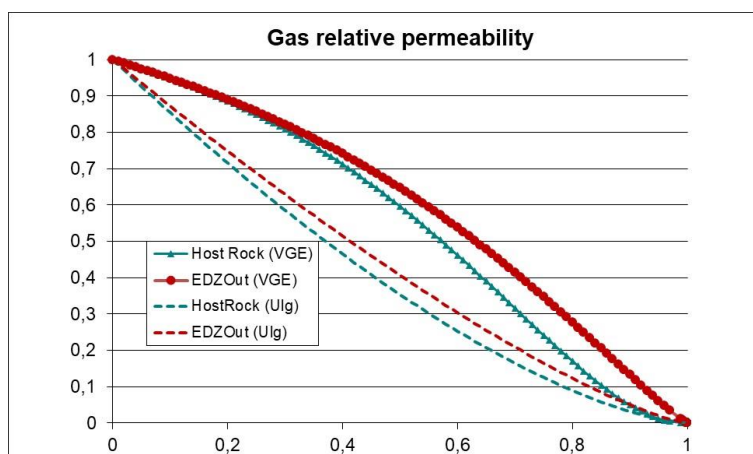


Figure 6-39: gas relative permeabilities curves (f_g) used for case 3 (VGE) and for case 5 (VGM with ULiège parameters)

A 5th case is therefore considered:

Case 5: same case than case 3 with parameters from ULiège (Table 6-6 and Table 6-7).

We compare below the results obtained for case 3 (full line) and case 5 (dotted line) on Figure 6-39, Figure 6-40, Figure 6-41 and Figure 6-42 for gas pressure (global and expressed), capillary pressure and liquid pressure, respectively. We recall that this parameter has no influence on temperature. It is clear that the second peak around 3000 years (corresponding to gas entry in the rocks) disappears with the classical VGM model. For a better understanding, we plot in Figure 6-43 the evolution of saturation. The gas pressure peak corresponds to an important desaturation which is much smoother with the VGM curves. Desaturation is logically linked to entry pressure which plays a role at this stage. Water pressure remains the same. These results are comforted with comparisons with ULiège (very closed results between EDF and ULiège with the same parameters).

The choice to treat the transition when $S=1-\varepsilon$ for modified Van-Genuchten curve (see Figure 6-1 and Equation 10 in section 6.2.1) differs from Andra due to the fact that Aster needs $S(P_c)$ instead of $P_c(S)$. This choice probably introduced a numerical bias. Indeed, ULiège also developed a VGE model but with a choice closer to Andra's treatment with a numerical inversion of Equation 9. Doing that avoids this "numerical peak" (see corresponding section) and some inaccurate results once host rock is desaturated.

One finding from this study is the importance of taken into account the entry pressure and the adopted numerical treatment when saturation approaches 1. This difficulty is reinforced by the choice of the unknowns ($P_c(S)$ instead of $S(P_c)$). Future works will have to be done either on the law's formulation or on the numerical treatment near to 1 in order to better capture gas pressure when entry pressure is reached.

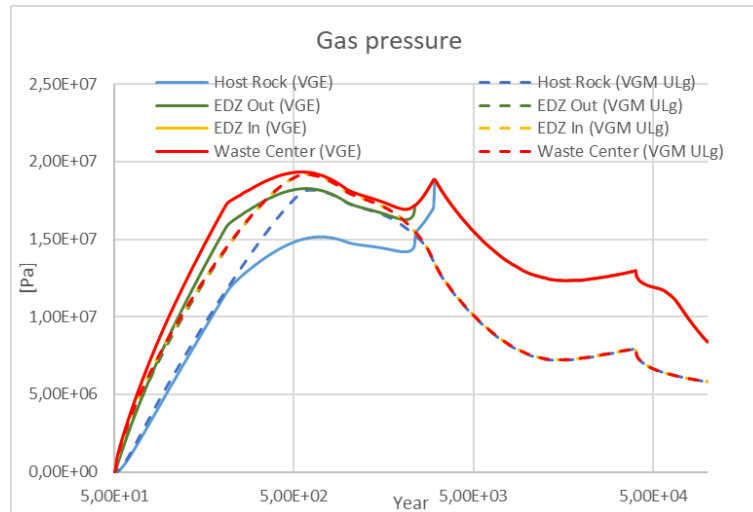


Figure 6-40: gas pressure evolution (cases 3 & 5)

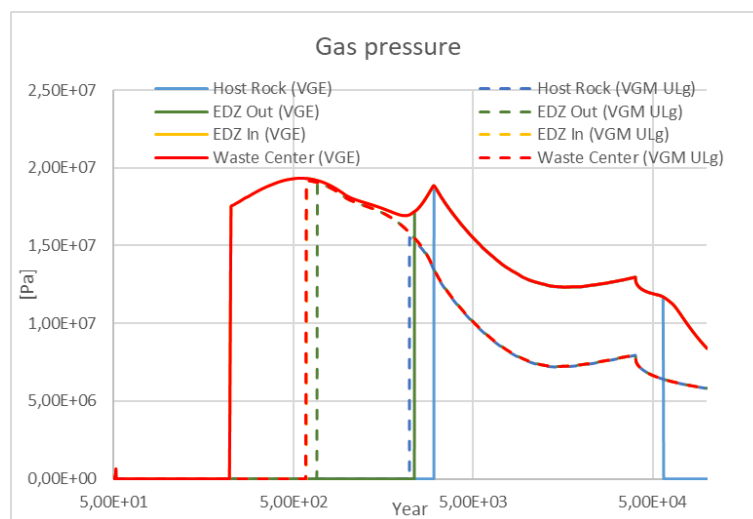


Figure 6-41: expressed gas pressure evolution (cases 3 & 5)

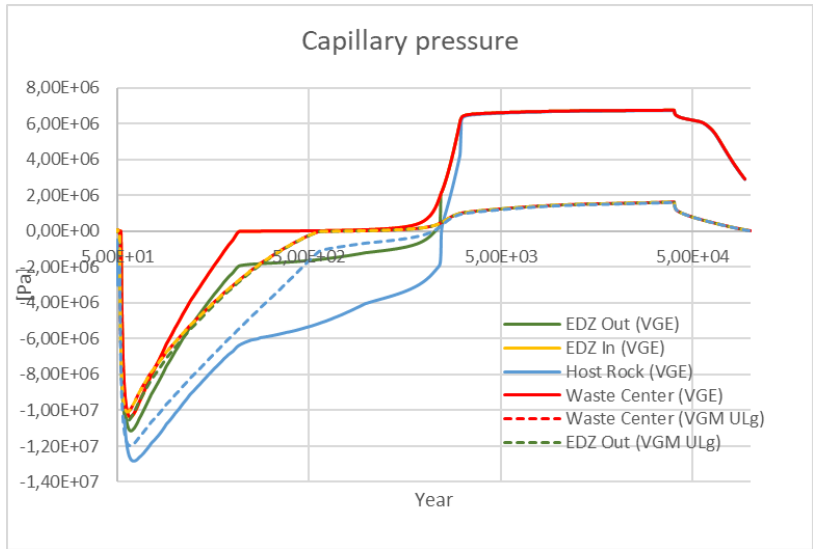


Figure 6-42: capillary pressure evolution (cases 3 &5)

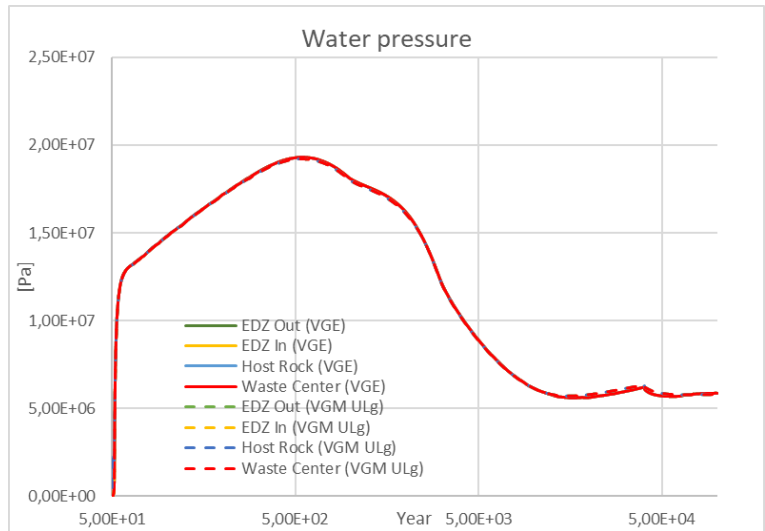


Figure 6-43: liquid pressure evolution (cases 3 &5)

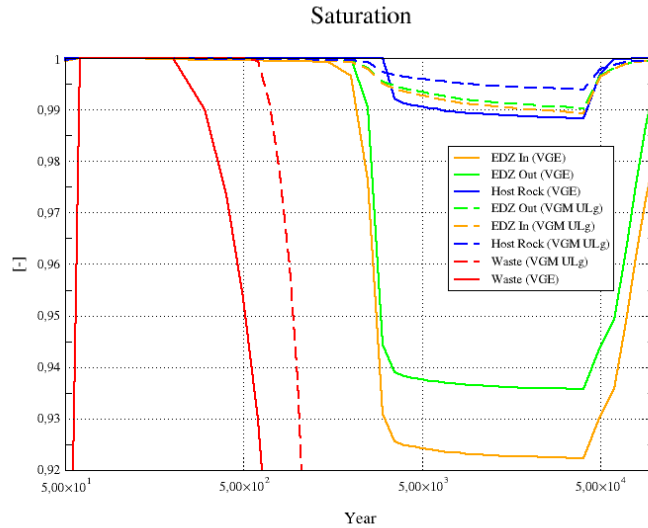


Figure 6-44: saturation evolution (cases 3 &5)

6.4.2.5 Sensitivity analysis on mechanical parameters

A lot of softwares don't directly consider the elastic behavior of the rock. Nevertheless, most of these codes use a storage capacity including compressibility of rocks and water to compensate that. For the two-phase flow model, it is equivalent to treat elasticity explicitly by a poromechanical model or with this kind of approach. Obviously, it is crucial to be consistent in the choice of the parameters.

For example, for Tough2 used by Andra, storage coefficient is written as a specific storage S_s as:

$$S_s = \left(\frac{1}{K_l} + \frac{1}{K_s} \right) \cdot \varphi$$

For other softwares (depending if it is a Lagrangian or Eulerian formulation), the storage coefficient of pore space could also be written as S_ε :

$$S_\varepsilon = \left(\frac{\varphi}{K_l} + \frac{b - \varphi}{K_s} \right)$$

We recall that solid compressibility K_s is classically expressed as $\frac{1}{K_s} = \frac{1-b}{K_0}$ with K_0 the drained compressibility coefficient of the porous media such as:

$$K_0 = \frac{E}{3(1-2\nu)}$$

We compute this coefficient in Table 6-8 with the reference parameters defined in Table 6-1. We also define a new case (case 6) with a Young modulus much smaller than the original one (see Table 6-1) and the equivalent storage coefficients. Other parameters correspond to case 5. Figure 6-44 and Figure 6-45 compare cases 5 and 6 (i.e. considering $E = 5\,000$ MPa or $1\,000$ MPa) for expressed gas pressure and liquid pressure, respectively. As expected, the difference of fluid pressures between the two cases is important for the first peak, mainly due to thermal phase. In this phase, pressure increase is mainly caused by water dilatation. The less the material is rigid (E smaller), the more the porosity could expand, and the more gas and water have available space, involving a decrease of pressure. After 10 000 years, Young modulus is no more a critical parameter.

Parameters	Host Rock (ref Case – case 5)	Modified Host Rock (Case6)
E (MPa)	5 000	1 000
ν	0,3	0,3
b	0,8	0,8
ϕ	0,2	0,2
$1/K_0$ (Pa ⁻¹)	$2,4 \cdot 10^{-10}$	$1,2 \cdot 10^{-9}$
$1/K_s$ (Pa ⁻¹)	$4,8 \cdot 10^{-11}$	$2,4 \cdot 10^{-10}$
S_ε (Pa⁻¹)	$1,29 \cdot 10^{-10}$	$4,48 \cdot 10^{-10}$
S_s (Pa⁻¹)	$1,1 \cdot 10^{-10}$	$1,48 \cdot 10^{-10}$

Table 6-8: mechanical parameters for reference case and case 6

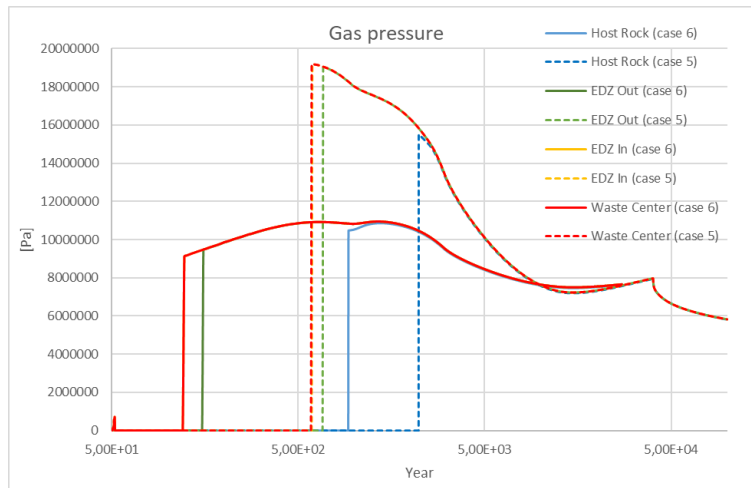


Figure 6-45: gas pressure evolution (cases 5 & 6)

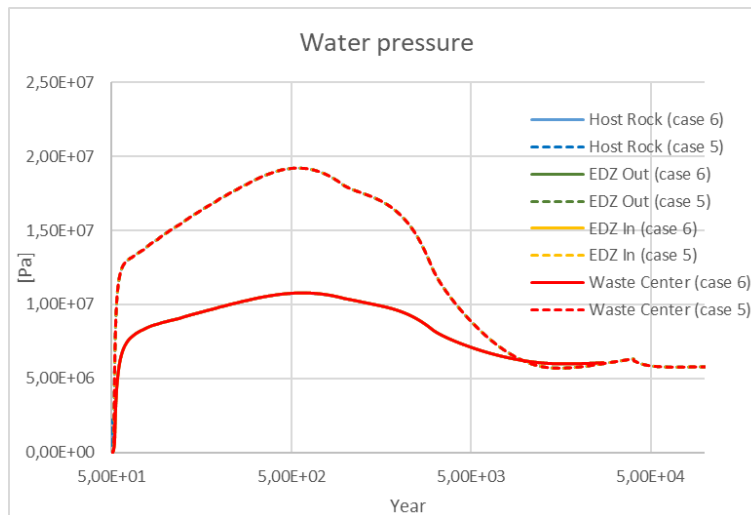


Figure 6-46: liquid pressure evolution (cases 5 & 6)

6.4.2.6 Sensitivity analysis on boundary conditions

In the previous study the aquifers are taken into account in the geometry and modeled by the same material than host rock. Initially, a gradient is applied to pressure, temperature and stress corresponding to hydrostatic initial state (see section 6.3.4) and then these values evolve, with time, beyond the host rock layer. Actually, the aquifer allows to evacuate heat and water through a lateral flow. For this reason, in the Andra model, only the Host Rock layer is represented with pressure applied on top and bottom

(Dirichlet boundary conditions). In this section, a 2D model is done with this kind of boundary conditions and is summarized Figure 6-46. This configuration will be called in the following BC2 (the previous ones are noted BC ref). The initial conditions are the same than previously (hydrostatic gradient).

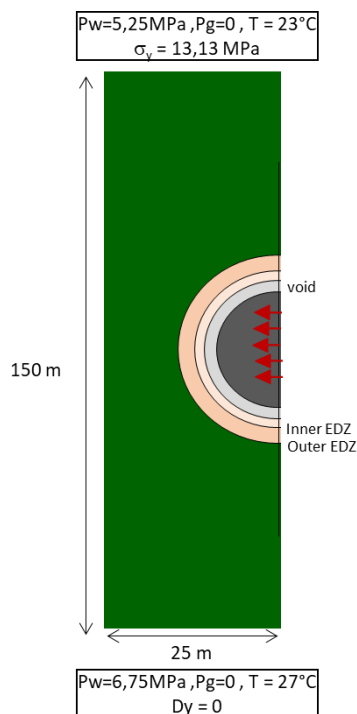


Figure 6-47: Configuration BC2 considering only host rock

We create case 7 with this BC2 configuration:

- **Case 7:** same than case 5 (VGM ULiège curves) with BC2

We compare below on the same curve the results obtained for case 7 (full line) and case 5 (dotted line) on Figure 6-47, Figure 6-48, Figure 6-49 Figure 6-50 and Figure 6-51 for gas and expressed gas pressure, capillary pressure, liquid pressure and temperature, respectively. If the maximum temperatures and the short-term behavior are the same, temperature with BC2 decreases logically faster due to boundary condition (gas can't diffuse in the layer up and down and the temperature remains equal to initial conditions). For gas and liquid, since the pressure peak is reached later than temperature, the maximal pressure with BC2 is lower than with BC ref; and values remains smaller. Nevertheless and contrary to Andra's results, the peak of pressure appears essentially in the thermal phase (before 1000 years). Whatever are the boundary conditions, liquid and gas pressures are higher before 1000 years than at the end of the gas injection phase. This major observation, also done by ULiège teams, is probably due to the closed condition of the 2D computation (and also of the "3D local" computation). There is no possibility for the gas to escape laterally. This point shows the importance of a modelling at the full scale.

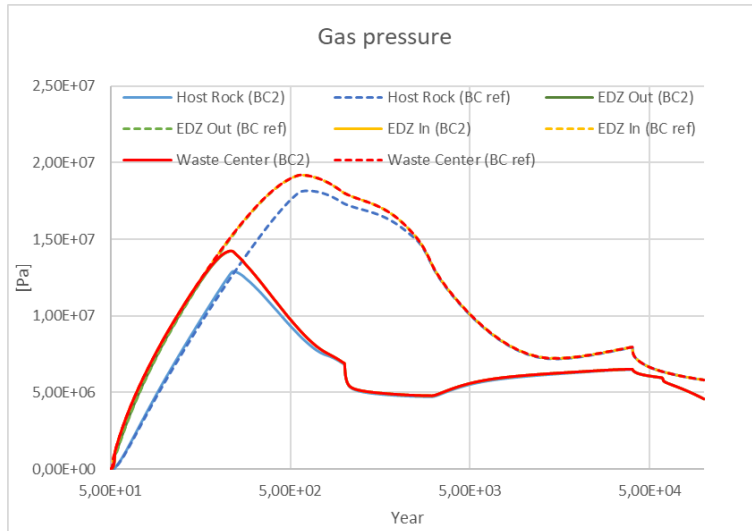


Figure 6-48: gas pressure evolution (cases 5 & 7)

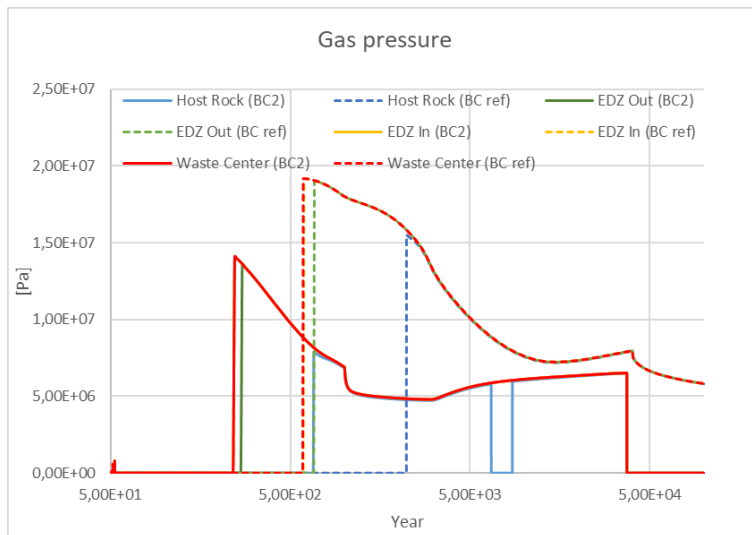


Figure 6-49: expressed gas pressure evolution (cases 5 & 7)

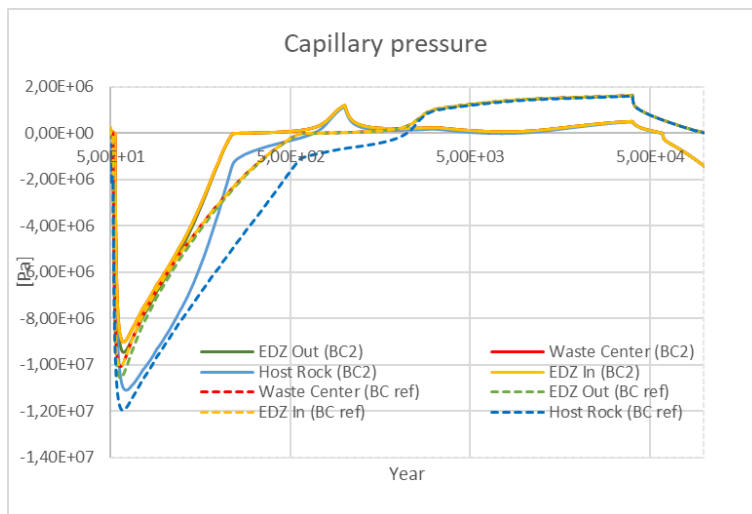


Figure 6-50: capillary pressure evolution (cases 5 & 7)

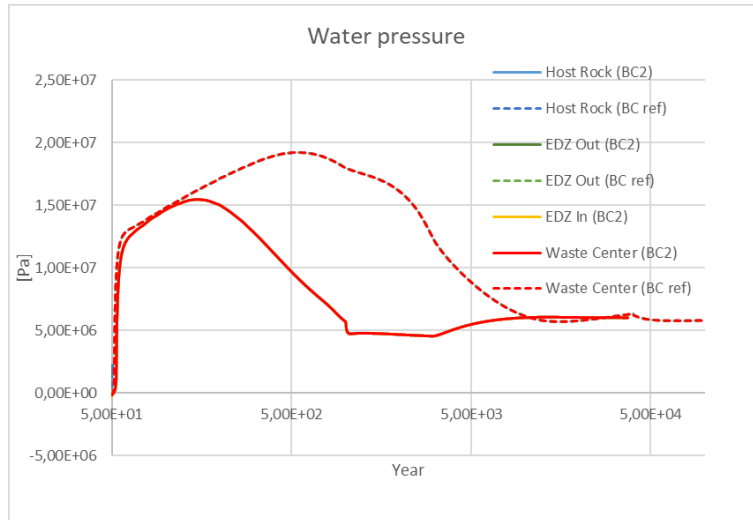


Figure 6-51: liquid pressure evolution (cases 5 & 7)

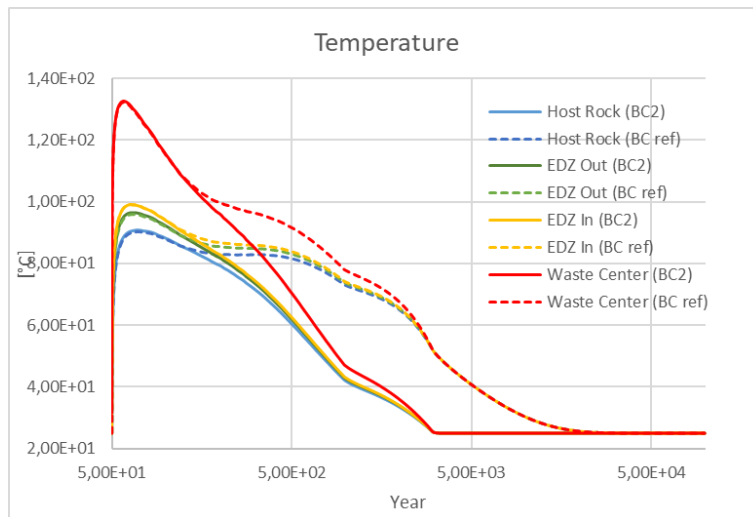


Figure 6-52: temperature evolution (cases 5 & 7)

6.4.2.7 Summary of 2D computations

All the 2D computations are summarized in Table 6-9.

Case	Time of thermal flow extension (years)	Liquid viscosity (Pa.s)	Smax	Van Genuchten	E (MPa)	BC
Case 1	1600	cte	0,999	VGE	5000	BC ref
Case 2	3000.	cte	0,999	VGE	5000	BC ref
Case 3	3000.	$\mu(T)$	0,999	VGE	5000	BC ref
Case 4	3000.	$\mu(T)$	0,99	VGE	5000	BC ref

Case	Time of thermal flow extension (years)	Liquid viscosity (Pa.s)	Smax	Van Genuchten	E (MPa)	BC
Case 5	3000.	$\mu(T)$	0,999	VGM ULiège	5000	BC ref
Case 6	3000.	$\mu(T)$	0,999	VGM ULiège	1000	BC ref
Case 7	3000.	$\mu(T)$	0,999	VGM ULiège	5000	BC 2

Table 6-9: cases for sensitive analysis in 2D.

6.5 Conclusions

EDF's contribution to this work has been dedicated to **zone C** (generic concept representative of the France concept). First a closed "local" 3D modeling has been made. Then, 2D computations of a vertical section around the tunnel have been performed to allow for a sensitivity analysis and help to understand the impact of different processes or parameters. For all these computations, Code_Aster has been used, with a classical THM two-phase flow model. We can separate the main key findings into different points:

- *Numerical aspects for the 3D computation*

A 3D THM computation has been done including the crossing of a gallery with a cell in the middle of zone C. Indeed, it is reasonable to expect that maximum gas pressure of this zone C will be reached in this area. With symmetrical conditions (gas couldn't escape in the gallery), the computation gives a maximum gas pressure equal to 16 MPa after 3 000 years.

This 3D HPC computation shows the feasibility of a 3D fully-coupled unsaturated THM study with several materials. It is a first reference study with Code_Aster and it opens prospects to the future. Nevertheless, it also shows its limitations at the current state. More than the important CPU times, this calculation requires a lot of human interventions due to convergence problems. For now, such a study is not reasonable if necessary at larger scales. For example, it seriously hinders the sensitivity analyses. Nevertheless other computations have been done without thermic, highlighting logically the importance thermal phase.

This 3D computation could be enhanced in the future: first, simply with mesh improved in order to gain degrees of freedom. Secondly, the current refactoring of parallelism in Code_Aster (introduction of more parallelism with domain splitting) is an opportunity. It could be tested and exploited in the near future to allow for more rapid computations. Work on linear solvers dedicated to two-phase flow models is also in progress following [2] and could considerably speed up these computations.

Nevertheless, such a "local 3D" computation seems not to be enough to represent the main phenomena. Indeed, with a closed system, fluid, can't be evacuate neither by the shaft nor by the aquifer, and goal of thermal phase seems to be overestimated. Modeling at the scale of the repository seems necessary. For that, adapted numerical schemes and meshes (non-conforming mesh, etc.) have to be developed.

- *Sensitivity analyses*

In addition to the 3D computations, several 2D computations have been conducted. They are logically conservative, but they allow to better understand different aspects of the computations such the impact of mechanical parameters, transfer terms, etc. on the results. A Main finding of these computations is the important impact of entry pressure. There are different manners to consider it. If modified Van-Genuchten function proposed in milestone 61 is chosen, attention must be paid to numerical treatment

when saturation is close to 1. An inadequate treatment could produce significant errors on gas pressure evolution. Liquid pressures are not impacted by this choice.

- *General conclusion*

These computations give numerous ways of improving. They confirm the limitation of modeling a closed system (2D or local 3D) to capture the maximum gas pressure reached in a deep geological repository. Modeling at the repository scale allows not only to model gas escape by the vertical shaft but also by the aquifer. This approach changes deeply the understanding of the different steps of the process.

More generally, the complexity of the problem requires many simplifications hypotheses. It means that choices must be done on the retained geometry, on the numerical treatment of the non-linearities, on neglecting or not a material or a dependency, etc. These choices are numerous and could lead to significant differences when compared to results from other modelling teams (see Chapter 11, Task 4 global synthesis). For this reason, quantitative results – especially for gas pressure – should always be treated with caution.

6.6 References

- [1] Modèles de comportement THHM. Documentation Code_Aster R7.01.11
- [2] A.C. Ordonez, N. Tardieu, C. Kruse, S. Granet, D. Ruiz, “Scalable block preconditioners for saturated thermo-hydro-mechanics problems”. Adv. Model. and Simul. in Eng. Sci. 10, 10 (2023).

7. Contribution of LEI

7.1 Model description

The generic repository concept proposed in EURAD-GAS “Task 4 Technical Note defining a generic repository configuration, sets of parameters, conditions and relevant indicators” (hereafter referred as specification) [1], is presented in Figure 7-1):

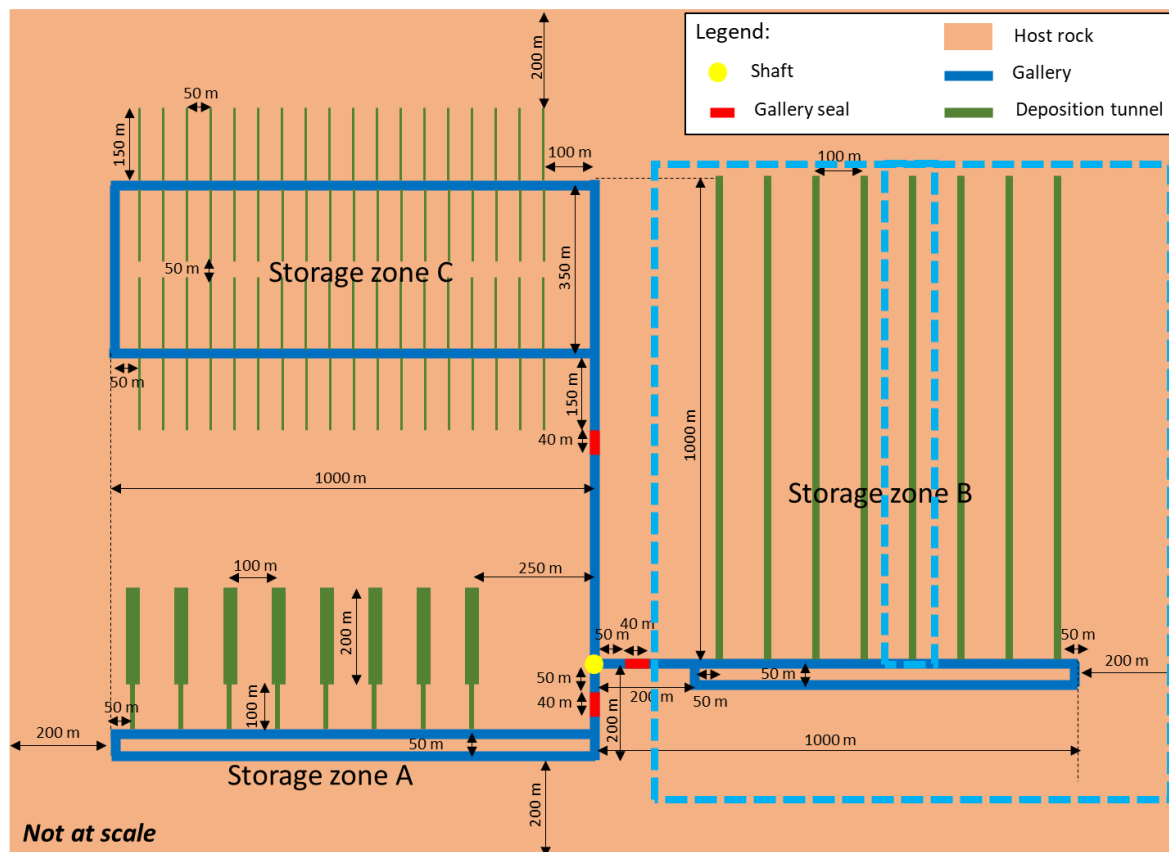


Figure 7-1– Schematic view of generic repository concept [1]. Blue dotted lines show LEI modelling domains in EURAD-GAS activities.

“The Development Programme for Decommissioning of Nuclear Power Facilities and Radioactive Waste Management for 2021–2030”, which was approved by the Government of Lithuania on February 3, 2021, foreseen the construction of a deep geological repository in Lithuania for long-lived waste including spent nuclear fuel. Despite repository concept is not defined yet in Lithuania, gas migration modelling in disposal zones for HLW is more relevant for national programme. For this reason and complexity of the whole exercise, only “HLW Disposal zone B” (further referred as Zone B) was selected for the analysis.

7.1.1 Modelling tool

Modelling of H₂ gas transport was modelled with numerical model implemented in COMSOL Multiphysics. For two component two-phase flow thermos-hydraulic analysis, the following phenomena were taken into account:

- Advective flow was described by Darcy's law for liquid and gas phase including relative permeability's and capillary pressure depending upon liquid saturation;
- Binary gaseous phases diffusion was described by Fick's law;
- Gas dissolution in liquid was described by Henry's law;
- Liquid phase contains water and dissolved gas;
- Gas phase contains water vapour and gas;
- Energy transport by movement of water and gas in both phases, conduction.

Mathematical equations representing mass balance of fluids was revised. It was assumed that the mass of air phase is insignificant thus gas phase consists of hydrogen and water vapor and liquid phase consists of water and dissolved hydrogen. Diffusive flux $i_{H2,d}$ of dissolved hydrogen was introduced:

$$i_{H2,d} = -\rho_w D_e \nabla \left(\frac{\rho_{H2,d}}{\rho_w} \right) \quad (1)$$

$$D_e = \tau n S_w D_0 \quad (2)$$

$$\rho_{H2,d} = H(T) \rho_{H2} \quad (3)$$

Here ρ_w - water density, τ – tortuosity, n – porosity, S_w – liquid saturation, $D_{H2,d}$ – dissolved hydrogen diffusion coefficient (m²/s), $\rho_{H2,d}$ - density of dissolved hydrogen (kg/m³), ρ_{H2} – density of hydrogen gas (kg/m³), $H(T)$ – Henry's constant for hydrogen (unitless).

Vapor pressure lowering (Raoult's law) due to dissolved gas was also introduced:

$$P_v^{\square} = P_v^{\square}(T, RH) \left[\frac{\rho_w}{\rho_w + \frac{M_w}{M_{H2}} \rho_{H2,d}} \right] \quad (4)$$

Here M_w and M_{H2} are molar mass of water and hydrogen respectively, P_v^{\square} is vapor pressure at particular temperature and relative humidity.

Component mass balance equations [6, 7] were defined with coefficient based PDE interface and solved with finite element method:

$$\frac{\partial m_*}{\partial t} + \nabla \cdot \vec{l}_* = Q, \quad m_* = m_w, m_{H2}, h \quad (5)$$

Mass of components (volumetric density) and enthalpy were defined as follows:

$$m_w = m_L + m_V = \rho_w \frac{e S_w}{1+e} + \rho_v \frac{e(1-S_w)}{1+e} \quad (6)$$

$$m_{H2} = m_{H2,d} + m_{H2} = \rho_{H2} n (1 - S_w (1 - H)) \quad (7)$$

$$h = \frac{\rho_s h_s}{1+e} + m_L h_{ML} + m_V h_V + m_{H2} h_{H2} \quad (8)$$

here m_w is total mass of water as a sum of liquid water and vapor, m_{H_2} is total mass of hydrogen as a sum of dissolved hydrogen and in gas phase, e is void ratio.

Fluxes were defined:

$$\vec{l}_w = (\rho_w \mathbf{q}_G) + \mathbf{i}_v + (\rho_w H \mathbf{q}_L); \quad (9)$$

$$\vec{l}_{H_2} = (\rho_{H_2} \mathbf{q}_G) + \mathbf{i}_{H_2} + (\rho_{H_2} H \mathbf{q}_L) + \mathbf{i}_{H_2-d}; \quad (10)$$

$$\vec{l}_h = \rho_w h_L \mathbf{q}_L + h_V (\rho_V \mathbf{q}_G + \mathbf{i}_V) + h_{H_2} (\rho_{H_2} \mathbf{q}_G + \mathbf{i}_{H_2} + \rho_{H_2} H \mathbf{q}_L) - \lambda \nabla T \quad (11)$$

The advective flowrate for liquid and gas phase were described by extended Darcy law:

$$\mathbf{q}_L = -\frac{k_{ML} k_{rML}}{\mu_w} (\nabla P_L + \rho_w \mathbf{g}) \quad (12)$$

$$\mathbf{q}_G = -\frac{k_G k_{rG}}{\mu_G} (\nabla P_G) \quad (13)$$

Diffusive fluxes were described:

$$\mathbf{i}_{H_2-d} = -\rho_w D_e \nabla \left(\frac{\rho_{H_2-d}}{\rho_w} \right) \quad (14)$$

$$\mathbf{i}_{H_2} = -\rho_w D_{e,g} \nabla \left(\frac{\rho_{H_2}}{\rho_w} \right) \quad (15)$$

$$\mathbf{i}_v = -\mathbf{i}_{H_2} \quad (16)$$

Mechanical force balance equation is defined:

$$\nabla \cdot \boldsymbol{\sigma} = -\mathbf{F}_v$$

Here $\boldsymbol{\sigma}$ is total stress tensor, \mathbf{F}_v – body force. Gravity is not considered in the analysis, thus $\mathbf{F}_v=0$.

The strains in porous material are caused by effective stresses described as follows:

$$\sigma_{ij}' = \sigma_{ij} - \alpha \cdot \bar{P}$$

Here σ_{ij}' is effective stress (Pa), α is Biot coefficient (-).

In summary, the primary variables for are liquid pressure P_l , gas pressure P_g , temperature T , displacement u .

Model updates were tested by several tests. The fully saturated sample of 1 cm long and 0.1 cm of radius was considered based on [2]. The material parameters are summarized in table Table 7-1.

Parameter	Value
Henry constant for nitrogen H^{cp} , (mol/(Pa·m ³))	6.4E-06
Molar mass of nitrogen M , (kg/mol)	0.028

Parameter	Value
Porosity n , (m^3/m^3)	0.2
Tortuosity τ (-)	1
Liquid saturation S_w (-)	1
Diffusion coefficient of dissolved nitrogen D_0 (m^2/s)	2E-09

Table 7-1 – Parameters used in modelling diffusive flux of dissolved gas.

Proper initial and boundary conditions were set to represent fully modelled system state:

- Liquid pressure on top and bottom boundary and initially in the sample was set equal to 1 MPa do not induce advective water flow;
- Gas phase pressure on the top boundary was fixed at 1 MPa, this resulted in zero suction and represented fully water saturated sample and no gas flow in gas phase;
- Gas phase pressure on the bottom boundary was set a small number (non zero value due to numerical reasons, 100 Pa), to represent lower concentration of dissolved gas on the bottom;
- Initial partial gas pressure was set 100 Pa.

Model run for $5 \cdot 10^7$ seconds. Modelling results of simulated gas profile at different times were compared to simulation results of OpenGeoSys presented in [2]. The comparison (Figure 7-2) showed a very good agreement between software.

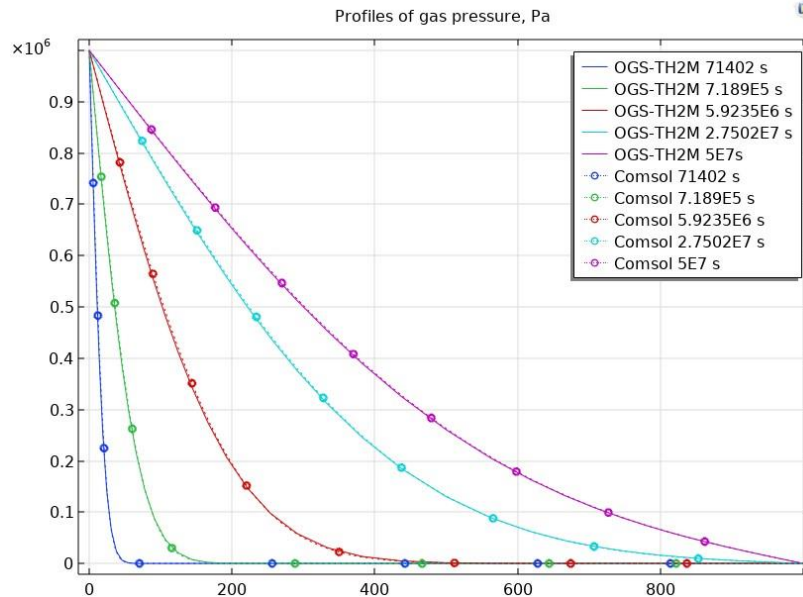


Figure 7-2 – Comparison of gas profiles at different times specified (solid lines) [2] and TH model formulation for hydrogen in COMSOL Mutliphysics (dotted lines with marker).

Implemented mathematical term describing diffusive gas flux was tested via modelling of SCK CEN diffusion test described in [3]. Scheme of experimental set-up is presented in Figure 7-3.

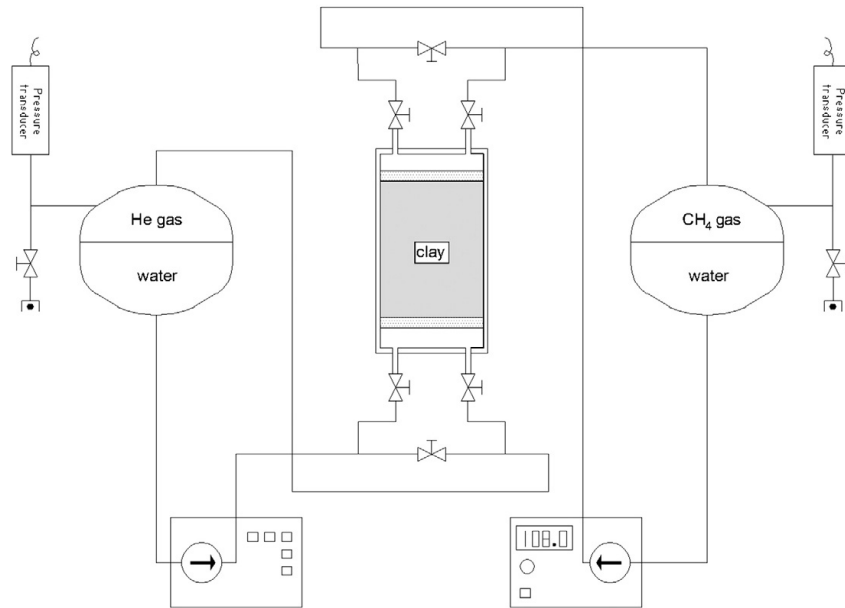


Figure 7-3 – SCK CEN diffusion test scheme [3].

Modelled clay sample (perpendicular orientation wrt bedding plane) dimensions were: diameter 80 mm, length 30 mm. Volume of vessels: 1 l, filled with 500 ml water and 500 ml gas (at 10 bar). Since numerical model formulation implemented in COMSOL Multiphysics was not applicable for multicomponent gas diffusion and experimental boundary conditions allow treatment of selected gas separately (there is no total gas phase or liquid phase pressure gradient imposed across the sample.), modelling of He and CH₄ gas diffusion was performed separately. Model parameters are summarized in Table 7-2.

	He	CH ₄
Henry constant for H ^{cp} (mol/(Pa·m ³))	3.8E-6	1.3E-5
Diffusion coefficient of dissolved gas D ₀ (m ² /s)	1.3E-9	2.46E-10
Molar mass M (kg/mol)	4E-03	1.6E-02
Dynamic viscosity of liquid μ (Pa·s)	5E-4	5E-4
Porosity n (m ³ /m ³)	0.37	0.37
Tortuosity τ (-)	1	1
Liquid saturation S _w (-)	1	1
Liquid density ρ _w (kg/m ³)	1000	1000
Intrinsic permeability k (m ²)	3.3E-19	3.3E-19

Table 7-2 – Parameters used in modelling diffusive flux of dissolved He and CH₄.

Proper initial and boundary conditions were set to represent fully modelled system state:

- Liquid pressure on top and bottom model boundary and initially in the sample was set equal to 1 MPa to represent absence of advective flow;
- Gas phase pressure on the top boundary was measured in experiment and decreasing with time from 1 MPa;
- Gas pressure remained lower than liquid pressure, meaning that saturated conditions prevailed;
- Gas phase pressure on the bottom boundary is set low (non zero value 100 Pa –concentration of dissolved gas in the downstream vessel is very low);
- Initial partial gas pressure was 100 Pa.

Because the gas pressure in the upstream and downstream vessels were the same, meaning no advective gas flow was imposed in the experiment. He and CH₄ were dissolving and diffusing through clay sample towards the opposite vessel. Simulation runs for 70 days. Modelling results as cumulative gas flux was compared to the modelling results presented in [2]. As presented in Figure 7-4, modelling results obtained with numerical models implemented in different software agreed well.

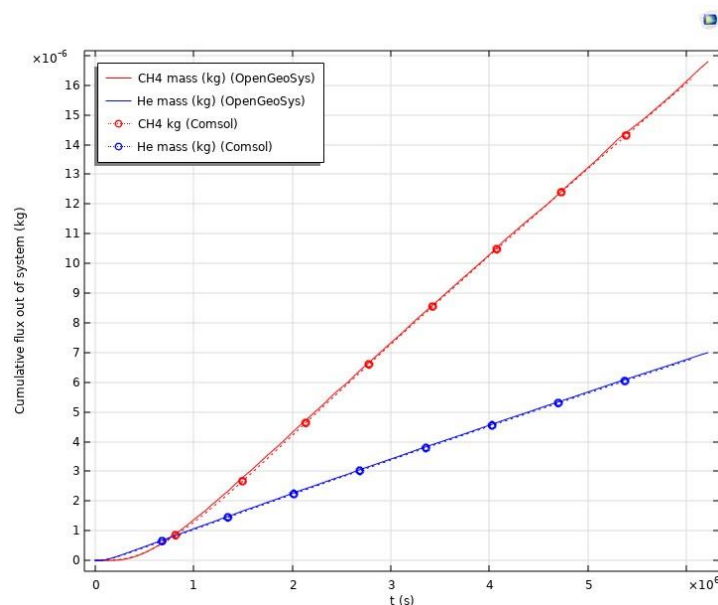


Figure 7-4 – Modelling results of cumulative gas flux out of the system: solid line – results from [2], dotted lines with markers – model results in COMSOL Multiphysics.

Modelling results were postprocessed following the approach presented in [2] and compared to measured gas concentration in ppm. The comparison of dissolved and diffused through clay gas versus measurements showed a very reasonable agreement and proper model implementation to represent this phenomenon.

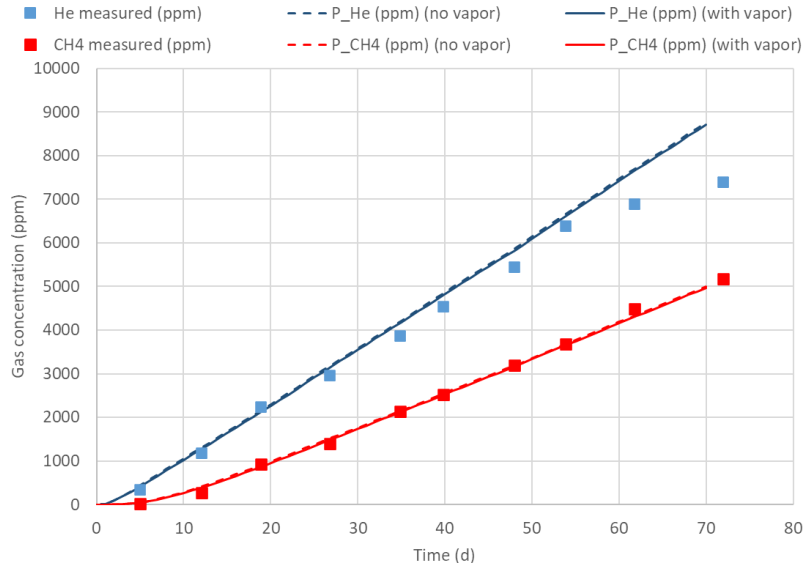


Figure 7-5 – Comparison of modelling results with measurements presented in [2]

This numerical formulation was further adapted for modelling H₂ gas in the zone B. For this particular task the additional modifications were done to follow the specification [1]. Nonlinear dependence of effective diffusion coefficient on porous media saturation and tortuosity was defined (Millington-Quirk relation for dissolved hydrogen):

$$D_{e,w} = n^{1+a} (S_{w,e})^b \cdot D_0 \quad (17)$$

$$D_{e,g} = n^{1+a} (1 - S_{w,e})^b \cdot D_0 \quad (18)$$

$$S_{w,e} = \frac{S_w - S_{wr}}{1 - S_{wr}} \quad (19)$$

Here $S_{w,e}$ is effective saturation, a and b are material parameters, S_w is liquid saturation, S_{wr} is residual liquid saturation.

TH model for H₂ gas was enhanced with relevant TH, TM, HM process couplings. Thermal load will impact fluid's density, viscosity, thermal expansion coefficient, heat will also induce strains due to thermal expansion, the changes in liquid and gas pressures will affect effective stress and lead to some volumetric strains in porous medium. These interactions were described as porosity change following [4], it was solved in parallel to mass and energy balance equations. Updated porosity was fed into the component mass balance equations (two-way coupling):

$$\frac{\partial n}{\partial t} = \frac{(\alpha - n)(1 - \alpha)}{K_D} \frac{\partial \bar{P}}{\partial t} + [(1 - \alpha)\beta_{TD} - (1 - n)\beta_{Tg}] \frac{\partial T}{\partial t} + \alpha \frac{de_v}{dt} \quad (20)$$

$$\bar{P} = S_w \cdot P_l + (1 - S_w) \cdot P_g \quad (21)$$

$$\alpha = 1 - \frac{K_D}{K_g} \quad (22)$$

$$K_g = \frac{K_D}{1 - \alpha} \quad (23)$$

Here \bar{P} is equivalent pore pressure (Pa), α is Biot coefficient (-), K_D is drained bulk modulus of the material (Pa), K_g is solid (grain) bulk modulus (Pa), β_{TD} is thermal expansion coefficient of porous medium (1/°C), β_{Tg} is thermal expansion coefficient of solid (1/°C), e_v is volumetric strain (-).

7.1.2 Deviations from specification

7.1.2.1 Retention curve

Numerical model formulation implemented by modeller in COMSOL Multiphysics using Coefficient PDE physics enable to control parameters representing material and fluid properties. The specification [1] provides the definition of modified Van Genuchten water retention curves (WRC) formulation taking into account explicit gas entry pressure with linalisation near $S_e=1$. WRC was provided in terms of capillary pressure as a function of effective saturation. Such definition was not directly applicable to our numerical model formulation as our primary variables were P_g and P_l giving the capillary pressure (suction) $P_c=P_g-P_l$. Therefore, the formulation presented in [5] was implemented in COMSOL Multiphysics model:

$$S_w(P_c) = \begin{cases} S_{wr} + \frac{S_{ws}^* - S_{wr}^{\square}}{(1 + (\alpha P_c)^n)^m}, & \text{if } P_c \geq P_e \\ S_{ws}, & \text{if } P_c \leq P_e \end{cases} \quad (1)$$

here: $S_{ws}^* = S_{wr}^{\square} + (S_{ws}^{\square} - S_{wr}^{\square})(1 + (\alpha P_e)^n)^m$, $m = 1 - 1/n$ and $\alpha = 1/P_e$.

This formulation provides the same results as the one in specification except it does not contain the linalisation part near $S_e=1$. With selected primary variables P_g and P_l there were no numerical issues close to full water saturation. As it is stated in [5] this water retention curve definition reduces to classical van Genuchten WRC with zero gas entry pressure, thus there was no need to define different WRC or adapt classical van Genuchten WRC with parameter values others than specified for materials with non zero gas entry pressure (mainly host rock, EDZ). The differences of the material are fully represented with WRC parameter values given in Table 1 of specification [1].

7.1.2.2 Relative permeability

Relative permeability for liquid phase (k_{rl}) and gas phase (k_{rg}) was implemented as follows [5]:

$$k_{rl} = \begin{cases} \left[\frac{S_{we}^{\square}}{S_{we}^*} \right]^{\tau} \left[\frac{1 - (1 - (S_{we}^{\square}(P_c))^{1/m})^m}{1 - (1 - S_{we}^{*1/m})^m} \right]^2, & \text{if } P_c \geq P_e \\ 1, & \text{if } P_c \leq P_e \end{cases} \quad (3)$$

$$k_{rg} = \begin{cases} \left[\frac{S_{we}^{\square}}{S_{we}^*} \right]^{\tau'} \cdot \left[1 - \frac{1 - (1 - (S_{we}^{\square}(P_c))^{1/m})^m}{1 - (1 - S_{we}^{*1/m})^m} \right]^2, & P_c \geq P_e \\ 0, & \text{if } P_c \leq P_e \end{cases} \quad (5)$$

Here $S_{we} = \frac{S_w(P_c) - S_{wr}}{S_{ws}^* - S_{wr}}$ is new effective saturation, $S_{we}^* = \frac{S_{ws} - S_{wr}}{S_{ws}^* - S_{wr}}$ is the maximum effective saturation.

It is in line with WRC definition presented above and corresponds to the one defined in specification [1] with $\tau=0.5$ and $\tau'=0.5$. With $P_e=0$ it reduces to classical Van Genuchten-Mualem permeability functions, thus there was no need to define different functions for analysed materials in zone B or to adapt classical van Genuchten-Mualem permeability functions with parameter values others than specified. The differences of the material were fully represented with parameter values given in specification [1] Table 7-1. It should be reminded, that with this formulation unsaturated conditions prevail when $P_g - P_l > P_e$. i.e., even gas pressure is higher than liquid pressure, but difference of those pressures is lower than the gas entry pressure, the material remains unsaturated under such conditions.

7.1.2.3 Mechanical model

The host rock, EDZ and concrete were described as linear elastic materials according to specification [1]. The backfill was also assumed to be linearly elastic material and the concrete mechanical properties were assigned (deviation from specification).

7.2 Numerical details

For the analysis of H₂ gas behaviour in the deposition tunnel of generic repository (Zone B) a 2D axisymmetric model was created (R=50 m, Z=0.1 m). Such model configuration will allow analyse the evolution of water and corrosion induced gas flow around deposition tunnel without gradient along tunnel. The extent of the model took into account a half distance between two adjacent deposition tunnels and is 50 m long (see Figure 7-6). A simplification regarding Zone B materials was made - cementitious backfill was represented instead of Canister & overpack (r=0.25 m) and Envelope (d=0.02 m). For this reason, 5 different materials were defined in the numerical model.

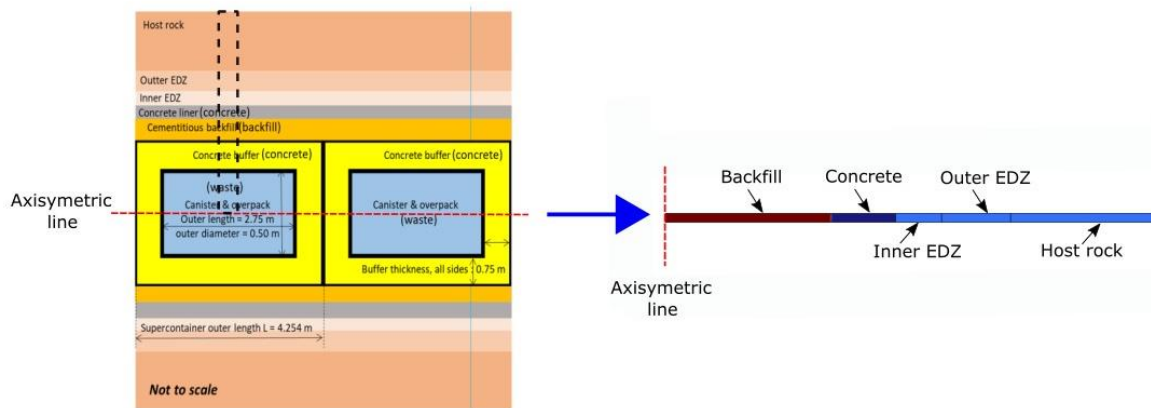


Figure 7-6 – Schematic representation of deposition tunnel in Zone B specified in [1] and in COMSOL Multiphysics model.

The modelling domain was discretized into triangular mesh elements (<4000).

7.2.1 Initial and boundary conditions

Initial and boundary conditions for numerical model was interpreted considering the information provided in specification [1]. It was assumed that deposition tunnel was excavated instantly and all materials were placed. Backfill and concrete was initially unsaturated (~80 %). Then the interface (at r=2.5 m) between concrete and inner EDZ was ventilated for 50 years (at RH=80 %, corresponding to constant suction of 30.6 MPa). Initially liquid and gas pressure in the host rock was 6.075 MPa and 0.1 MPa, respectively. On the model boundary at 50 m constant and Dirichlet boundary conditions were imposed (fixed liquid and gas pressures of 6.075 MPa and 0.1 MPa) (Figure 7-7). Liquid pressure corresponds to the groundwater pressure at repository level.

Gas injection started after 50 years of ventilation (0.25 mol/y or $1.5 \cdot 10^{-11}$ kg/(m²·s), it was specified at interface between backfill and concrete (at r=1.8 m). Hydrogen gas generation in deposition tunnel last from T=50 up to T=100 000 years. After 100 000 years resaturation phase started and simulated till 150 000 years.

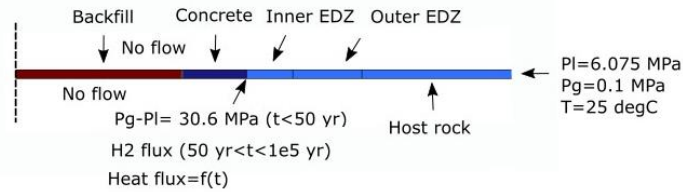


Figure 7-7 – Boundary conditions for TH model

Initial temperature in the model domains and on the host rock boundary (at 50 m) was set equal the temperature at repository level (25 °C). Heat load from the disposal canister was represented via time dependent (decreasing) heat flux specified at backfill-concrete interface (at $r=1.8$ m) (Table 7-3).

Time from waste emplacement (years)	Heat flux (W/m ²)	Time from emplacement (years)	Heat flux (W/m ²)
0	2.65E+01	140	9.11E+00
5	2.46E+01	150	8.93E+00
10	2.29E+01	160	8.66E+00
15	2.13E+01	170	8.48E+00
20	2.00E+01	180	8.29E+00
25	1.87E+01	190	8.12E+00
30	1.78E+01	200	7.93E+00
40	1.59E+01	210	7.82E+00
50	1.45E+01	220	7.69E+00
60	1.34E+01	230	7.51E+00
70	1.24E+01	330	6.42E+00
80	1.17E+01	430	5.50E+00
90	1.11E+01	530	4.72E+00
100	1.05E+01	630	4.06E+00
110	1.01E+01	730	3.50E+00
120	9.73E+00	830	3.02E+00
130	9.37E+00	930	2.61E+00

Table 7-3 – Time dependent heat flux specified in deposition tunnel model

For mechanical analysis the initial stress in the host rock and EDZ was simulated firstly with selected boundary conditions (Figure 7-8). The boundary load for axisymmetric model geometry was assigned

equal to compressive total stress at repository level (15 MPa). Steady state stress distribution was set as initial stress for transient analysis.

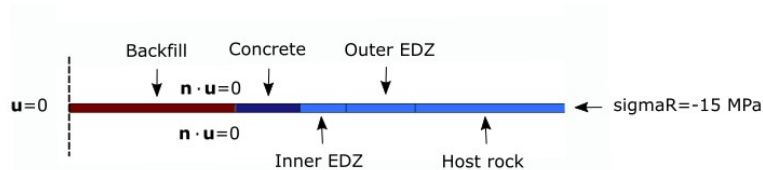


Figure 7-8 – Boundary conditions for M model

7.3 Simulation results

For the analysis of the hydrogen generation impact on relevant indicators such as liquid and gas pressure several cases were defined. Firstly, the evolution of pore pressure and gas pressure around the deposition tunnel was analysed without heat load. The impact of water retention curve was also tested. Then the pressure evolution and desaturation/resaturation was simulated considering heat load. Finally, the mechanical processes (poroelasticity) were considered.

7.3.1 Isothermal conditions

Modelling of transient of hydraulic conditions around the deposition tunnel was performed considering H₂ generation and without it. For the analysis several observation points were defined as indicated in Table 7-4.

Material	Coordinates (R, Z)	Notes
Backfill	(0.9 m, 0.05m)	Middle point
Concrete	(2.15 m, 0.05 m)	Middle point
Inner EDZ	(2.8 m, 0.05 m)	Middle point
Outer EDZ	(3.375 m, 0.05 m)	Middle point
Host rock	(4.5 m, 0.05 m)	2 m from tunnel wall

Table 7-4 – Observation points for the analysis.

The simulation of liquid and gas pressure evolution around the deposition tunnel showed that 50 years of ventilation led to desaturation of inner and outer EDZ and part of the host rock. It also led to decrease of initial saturation of backfill and concrete. When ventilation phase has finished the system re-saturation started by the groundwater coming from surrounding clayey host rock. Thus, the host rock undergoes resaturation first. The system transition from de-saturated to re-saturated is represented in Figure 7-9.

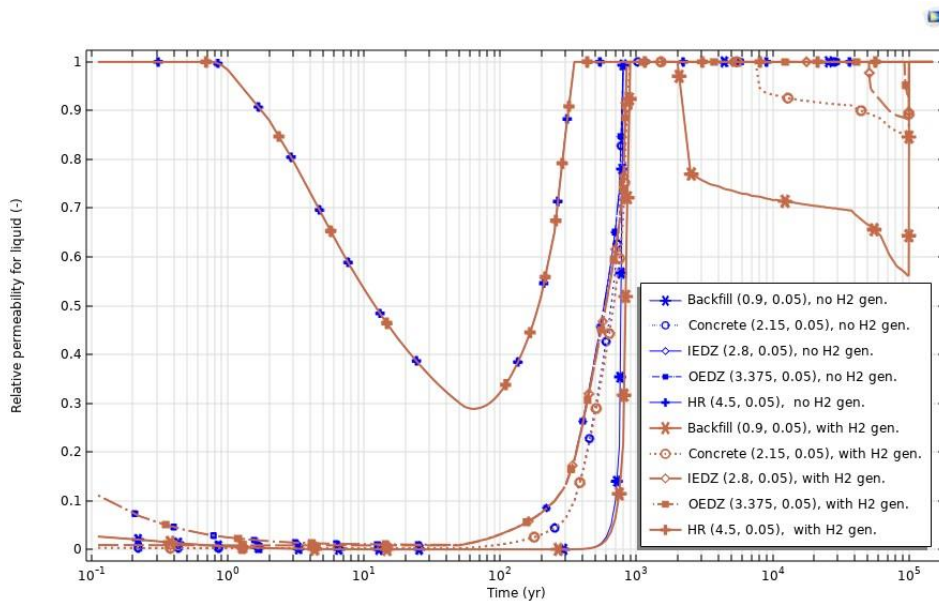
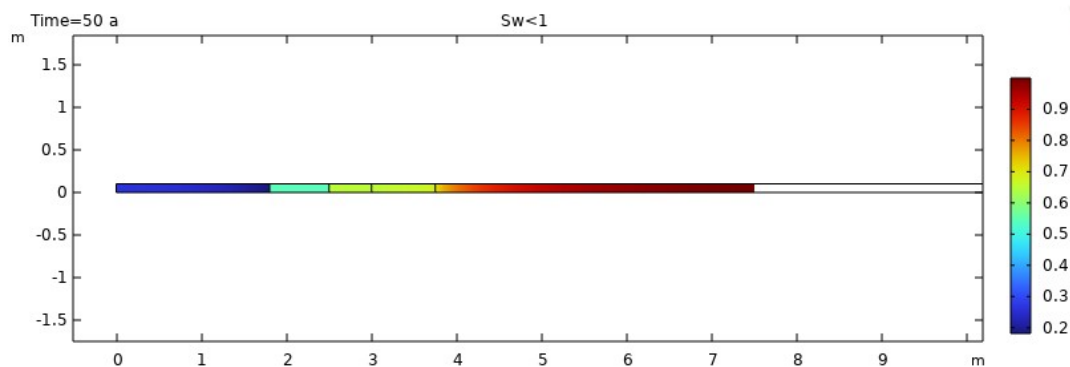


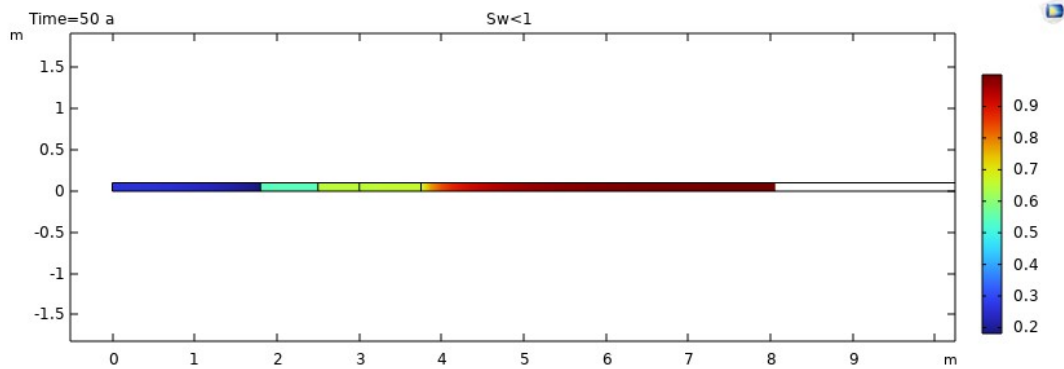
Figure 7-9 – Simulated evolution of relative permeability for liquid phase with and without H₂ gas generation in the tunnel

As it could be seen in the Figure 7-9, ventilation caused de-saturation of inner and outer EDZ and part of host rock, the engineered barriers (backfill, concrete) become more unsaturated than initially. Despite of H₂ gas injection start at 50 years the system continued to resaturate. Similar resaturation trends and time for full saturation for was obtained with H model (no gas injection) and HG model (with gas injection). The host rock at observation point (2 m away from tunnel wall) was resaturated by ~350 years, full water saturation at middle points of all other materials was achieved by ~800 years (H model) and 850-900 years (HG model). The evolution of relative permeability presented in Figure 7-9 clearly indicates that with continued H₂ gas injection the time to build up gas pressure was needed to de-saturate materials again. The materials closer to gas injection were de-saturated sooner and to a larger extend (backfill, concrete, inner and outer EDZ). However, the host rock 2 m away from tunnel wall was not desaturated continuous despite H₂ gas injection. Once the gas injection finished system quickly got fully water saturated.

Figure 7-10 a) presents the simulation results of liquid saturation distribution around the deposition tunnel after 50 years of ventilation. It indicates the maximal extend of desaturated region around the deposition tunnel during the simulation. As it could be seen from the Figure 7-10 a), considering explicitly WRC and relative permeability model as specified in specification [1] the host rock is de-saturated up to 7.5 m in the host rock by the end of ventilation.



a)

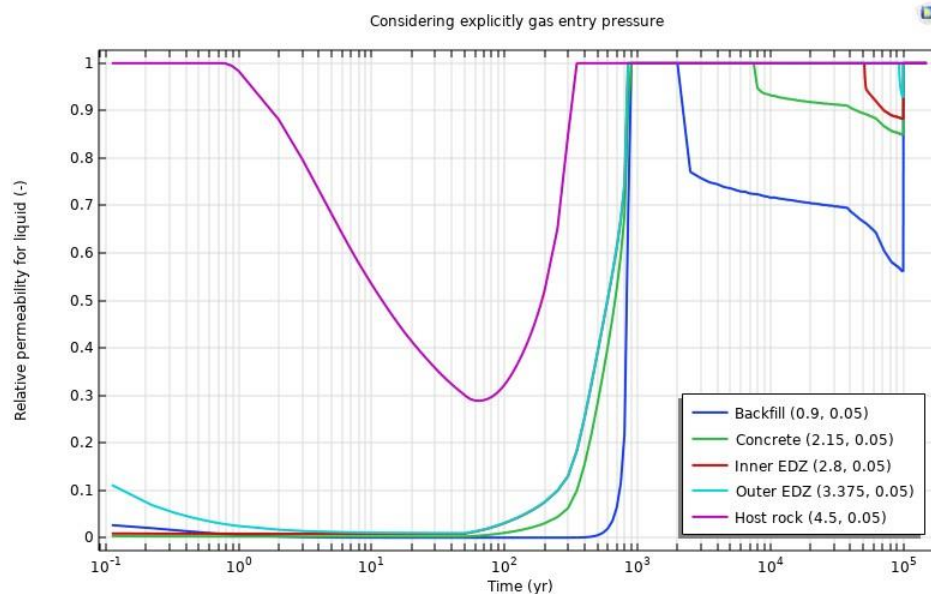


b)

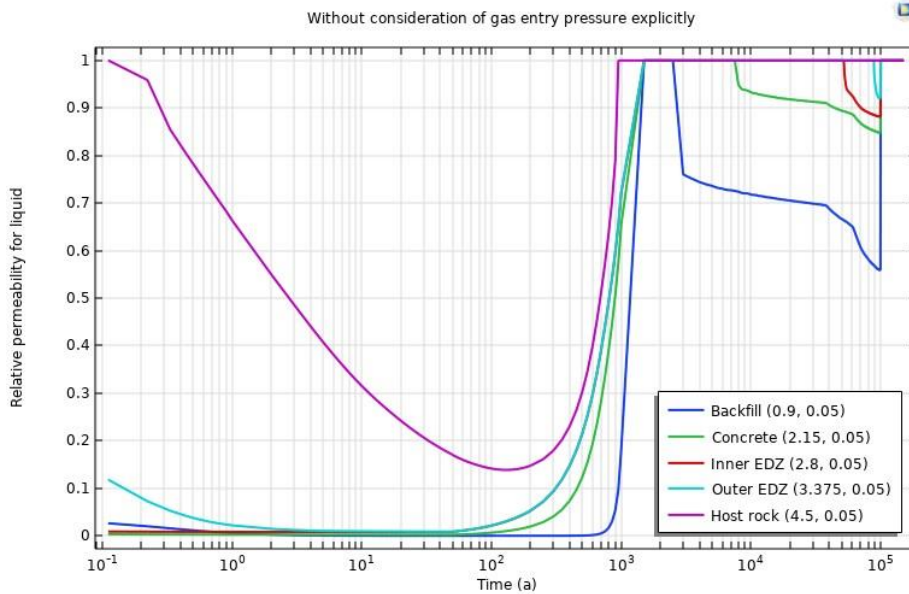
Figure 7-10 – Liquid saturation distribution around the deposition tunnel: a) considering modified Van Genuchten-Mulaem model with explicit gas entry pressure, b) unmodified Van Genuchten-Mulaem model (zero gas entry pressure)

For the comparison the saturation distribution was evaluated without considering explicitly gas entry pressure (setting gas entry pressure to zero) (Figure 7-10 b). Modelling without considering explicitly the gas entry pressure revealed that the host rock would be desaturated to higher extend (up to 8 m) by the end of ventilation.

The impact on WRC and relative permeability model on the state of analysed materials (saturated/unsaturated) could be perceived from relative permeability evolution presented in Figure 7-11. The extend of desaturated zone was larger without consideration of gas entry pressure explicitly, relative permeability zone was also extended and this prolonged the time of full first resaturation after the ventilation end (Figure 7-11 b). The host rock at observation point (2 m away from tunnel wall) was resaturated by ~350 years, full water saturation at middle points of all other materials was achieved by ~850-900 years (Figure 7-11 a). Meanwhile without consideration of gas entry pressure explicitly the observation point in the host rock (2 m away from tunnel wall) was resaturated by ~950 years, full water saturation at middle points of all other materials was achieved by ~1 500 years (Figure 7-11 a).



a)



b)

Figure 7-11 – Simulated evolution of relative permeability at observation points: a) considering modified Van Genuchten-Mulaem model with explicit gas entry pressure, b) unmodified Van Genuchten-Mulaem model (zero gas entry pressure)

The start of the second desaturation due to H₂ gas injection was predicted later with classical Van Genuchten-Mulaem model for backfill, while there was no significant impact on gas induced desaturation start for other materials. Thus, the selected/assumed water retention and relative permeability model would be important drawing conclusion on resaturation-gas induced desaturation time.

Relevant indicators such as liquid and gas pressure are presented in Figure 7-12 and Figure 7-13. As it is expected the liquid pressure was decreasing due to ventilation resulting in more de-saturated engineered materials and induced unsaturated conditions in EDZ and part of the host rock. Gas pressure increased gradually due to H₂ gas injection and subsequent dissolution and diffusion around deposition tunnel. Depending on the magnitude it caused the second desaturation only in the regions where it exceeded the liquid pressure and that difference was higher than explicit gas entry pressure for particular material.

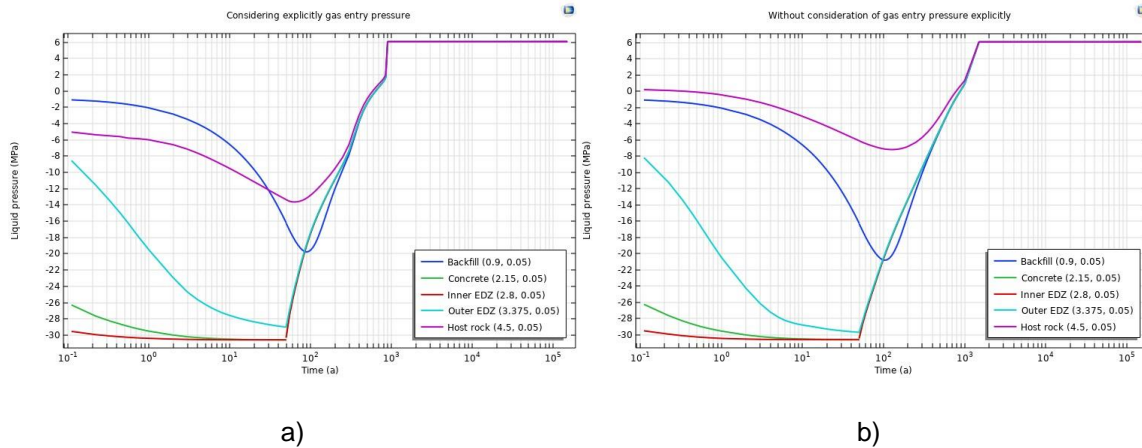


Figure 7-12 – Modelled evolution of liquid pressure at observation points: a) considering modified Van Genuchten-Mulaem model with explicit gas entry pressure, b) unmodified Van Genuchten-Mulaem model (zero gas entry pressure)

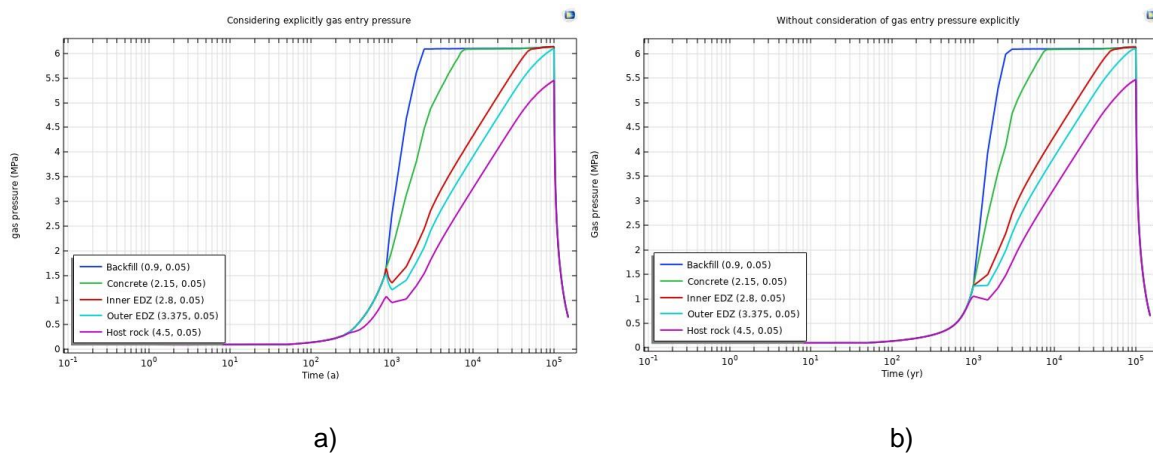


Figure 7-13 – Modelled evolution of gas pressure at observation points: a) considering modified Van Genuchten-Mulaem model with explicit gas entry pressure, b) unmodified Van Genuchten-Mulaem model (zero gas entry pressure)

It should be noted that under saturated conditions presented gas pressure (Figure 7-13) represents a partial pressure of dissolved H_2 .

As it could be seen from the plots above the selected water retention model had more significant effect on liquid pressure evolution than on gas pressure evolution trends. The gas pressure achieved its maximal value almost by the same time and the same magnitude ($P_g \sim 6.14$ MPa) in engineered barriers and EDZ. During gas injection phase (50-100 000 years) the dissolved gas concentration in the host rock (at 2 m away from tunnel) was lower resulting in lower partial pressure (<5.5 MPa).

7.3.2 Impact of temperature

HLW emplacement in the repository will impose a decay heat load on the engineered and natural barriers to some extent. With consideration a non-isothermal conditions the heat load from the HLW canister and its induced/dependent phenomena need to be taken into account. Different thermal expansion of water and porous low permeable medium could lead to thermal overpressurisation, redistribution of stresses, porosity change. Thermal properties of the materials are summarized in *Table 7-5*.

Properties	Backfill	Concrete	Inner EDZ	Outer EDZ	Host Rock
Thermal conductivity λ_s (W/m/K)	1.3	2.3	1.7	1.7	1.7
Solid specific heat $C_{p,s}$ (J/kg/K)	500	900	720	720	720
Thermal expansions of solids β_{Tg} (1/°C)	2.00E-05	2.00E-05	4.00E-05	4.00E-05	4.00E-05
Volumetric thermal expansion coefficient $\alpha_w \cdot 10^{-4}$ (1/°C)	$4E-06 \times T^3 - 0.001 \times T^2 + 0.1404 \times T - 0.3795$				T in °C
Density of water ρ_w	$998.2 \times \exp(5E-07(PL-100) - \alpha_w \cdot (T-12))$				PL in kPa, T in °C
Kinematic viscosity η (m ² /s) (dynamic viscosity= $\rho_w \cdot \eta$)	$1.384E-03 \times (T+50)^{-C1}$ $C_1(T) = 1.7-0.0156 \times (0.01 \times T)^{1.8}$				T in °C
Specific heat of water $C_{p,w}$ (J/kg/K)	$4190 \times (1+0.0025 \times (0.01 \times T))^{4.6}$				T in °C
Density of saturated vapour ρ_{v0} (kg/m ³)	$\exp(0.06374 \times T - 0.1634 \times 10^{-3} \times T^2)/194.4$				T in °C
Diffusivity of vapor D_v (m ² /s)	$5.9E-06 \times T^{2.3}/pG$				T in K
Dynamic viscosity of vapor μ_v (Pa·s)	273.15-373.15 K		$3E-08 \times T + 9E-6$		T in °C
	373.15-473.15 K		$4E-08 \times T + 8E-6$		T in °C
Specific enthalpy of vapor at T_0 h_{v0} (J/kg)	2.45E+06				
Specific heat of vapor $C_{p,v}$ (J/kg/K)	0-50 °C	$C1+C2 \times T + C3 \times T^2 + (p-p_{tr})/(C4+C5 \times T + C6 \times T^2)$		$C1=1877.2, C2=-0.49545, C3=8.1818E-03, C4=22.537, C5=0.49321, C6=0.048927, p_{tr}=611.657 \text{ Pa}, T \text{ in } ^\circ\text{C}$	
	Above 50 °C	$C7+C8 \times T + C9 \times T^2+(p-p_{tr})/(C4+C5 \times T+C6 \times T^2)$		$C7=1856.1, C8=0.28056, C9=6.9444E-04, C4=22.537, C5=0.49321, C6=0.048927, T \text{ in } ^\circ\text{C}$	
Specific heat of H2 (J/(g·K))	14.304				

Properties	Backfill	Concrete	Inner EDZ	Outer EDZ	Host Rock
Dynamic viscosity of H ₂ gas μ _{H2} (Pa·s)	1E-05				
Dynamic viscosity of gas mixture (H ₂ and vapor) μ _G (Pa·s)	$\frac{1}{\left(\frac{X_v}{\mu_v} + \frac{X_{H2}}{\mu_{H2}}\right)}$		X_v, X_{H2} – mass fraction of vapor and H ₂ gas		

Table 7-5 – Parameters considered in nonisothermal analysis.

Figure 7-14 present the temperature evolution in observation points. As it is expected the largest temperature was achieved in waste representing domain (backfill). Maximum temperature (~87 °C) was reached soon after waste emplacement (approximately after 20 years of heating (at 70 years from excavation)) and subsequently decreased. During 1000 years the temperature in all points remained below 100 °C.

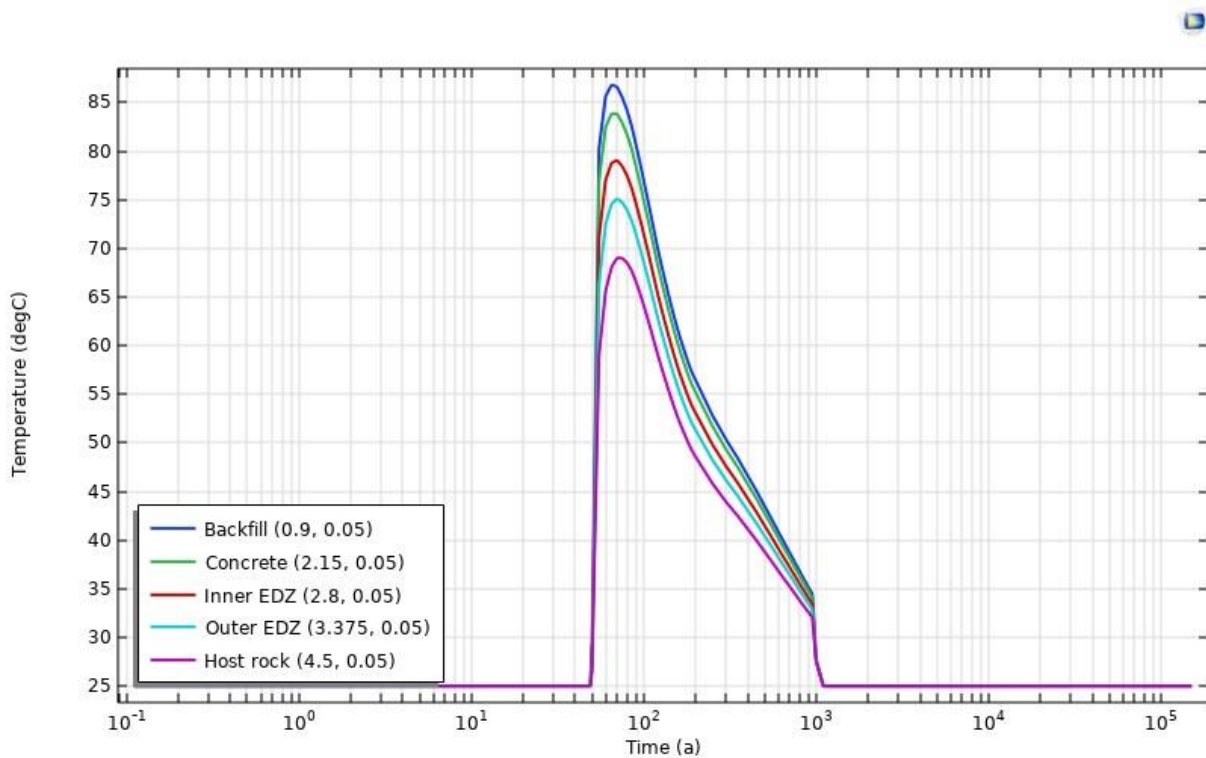


Figure 7-14 – Modelled temperature evolution at observations points

Figure 7-15 presents temperature distribution around deposition tunnel (geometry not to scale) at different times.

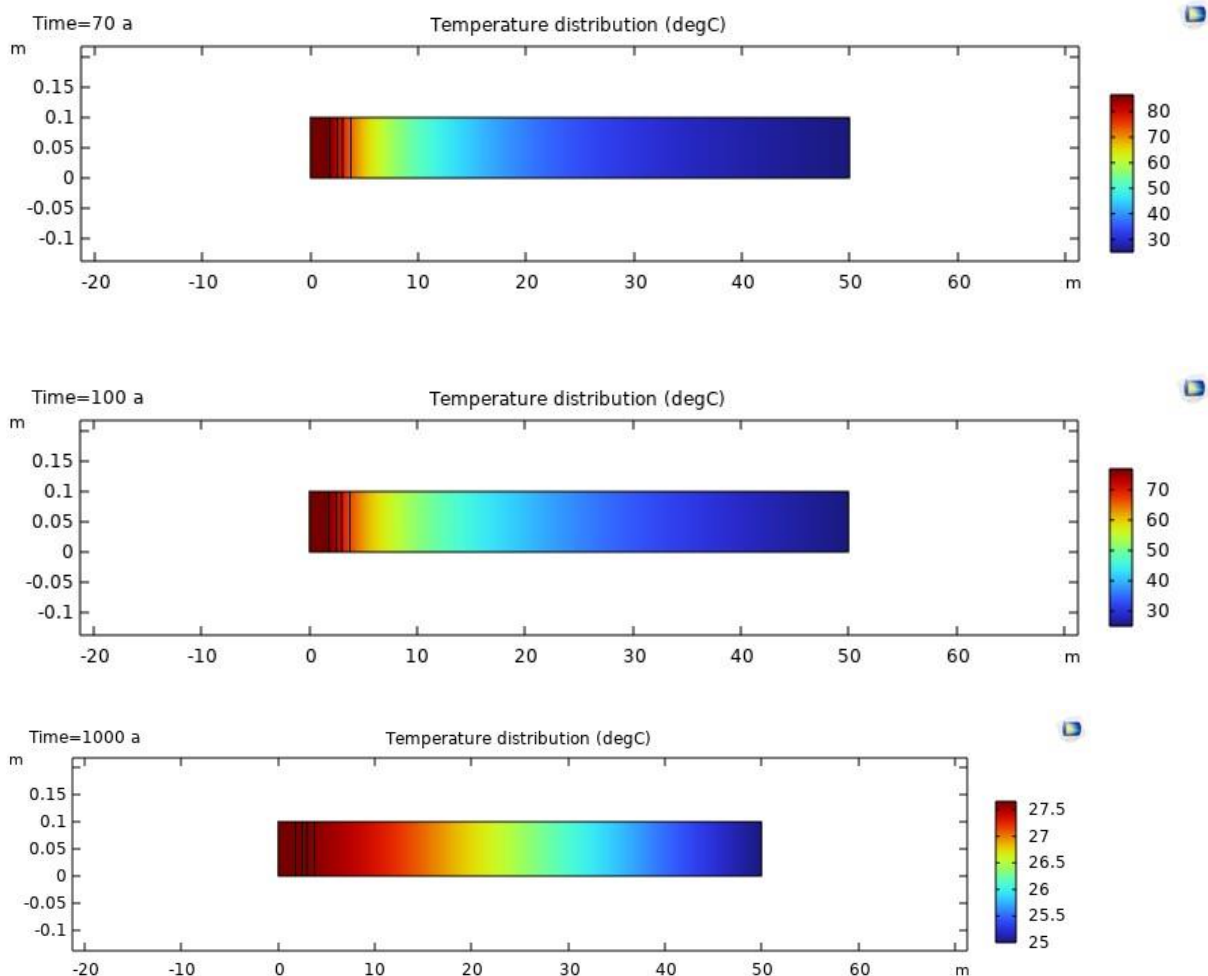


Figure 7-15 – Temperature distribution at different times (including time for ventilation)

By the end of heat emitting phase the temperature was approaching the initial temperature in the host rock (25 °C).

The evolution of system saturation under nonisothermal conditions is presented in Figure 7-16. For the comparison the saturation evolution is presented for isothermal case.

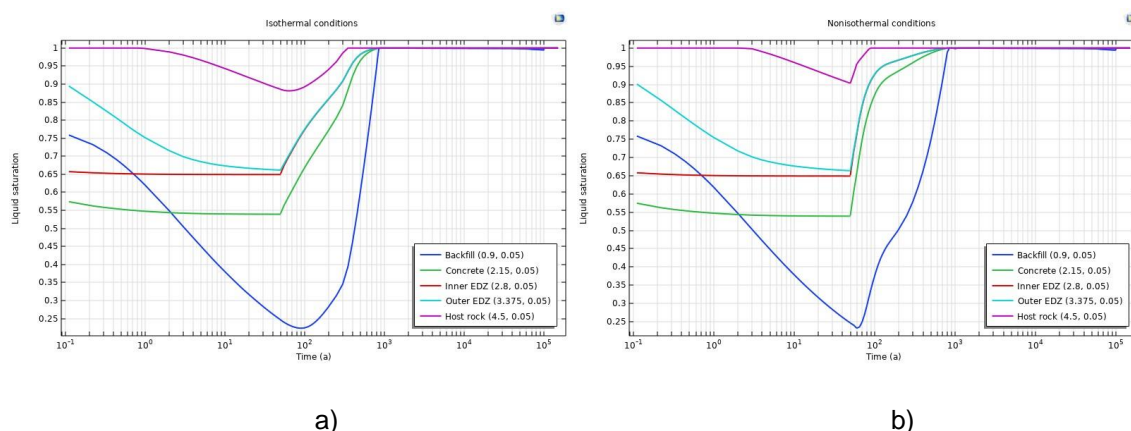


Figure 7-16 - Modelled evolution of liquid saturation evolution in observation points under: a) isothermal conditions, b) non-isothermal conditions

As it could be seen from Figure 7-16 the heat imposed more phenomena (vaporisation/condensation, advective gas flow, heat induced effective stress redistribution, etc.) which had an influence on re-saturation trend in all the materials. All material (except the host rock) were re-saturated later than under isothermal conditions. Meanwhile the re-saturation at observation point in the host rock (2 m from tunnel wall) occurred earlier than in isothermal case (at ~90 years vs ~350 years). Considering heat load and water thermodynamic properties as a function of temperature second de-saturation phase due to hydrogen gas started slightly earlier compared to isothermal case as could be seen from Figure 7-17.

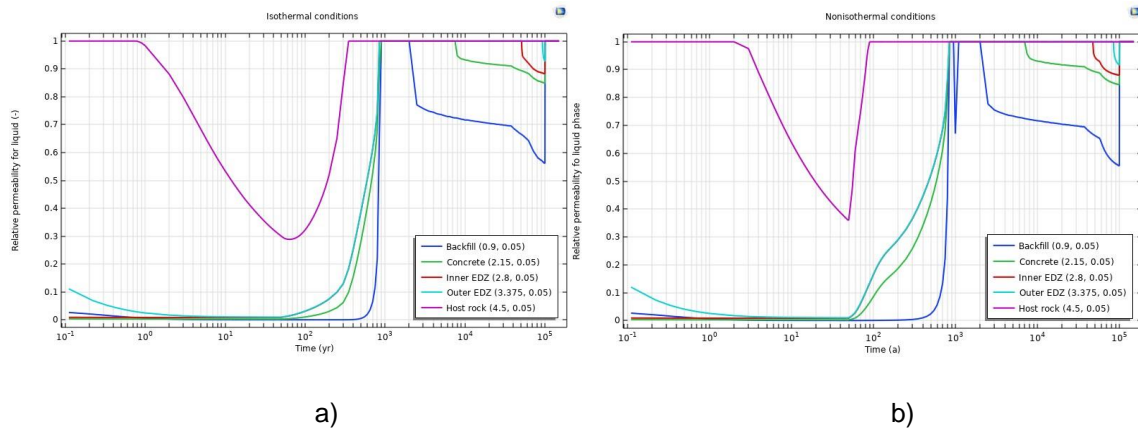
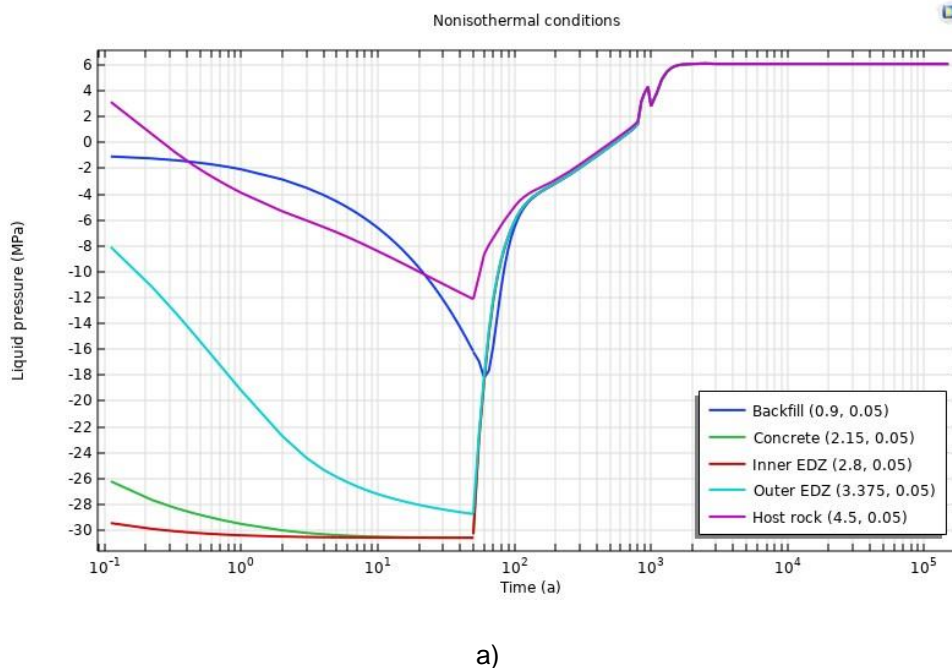
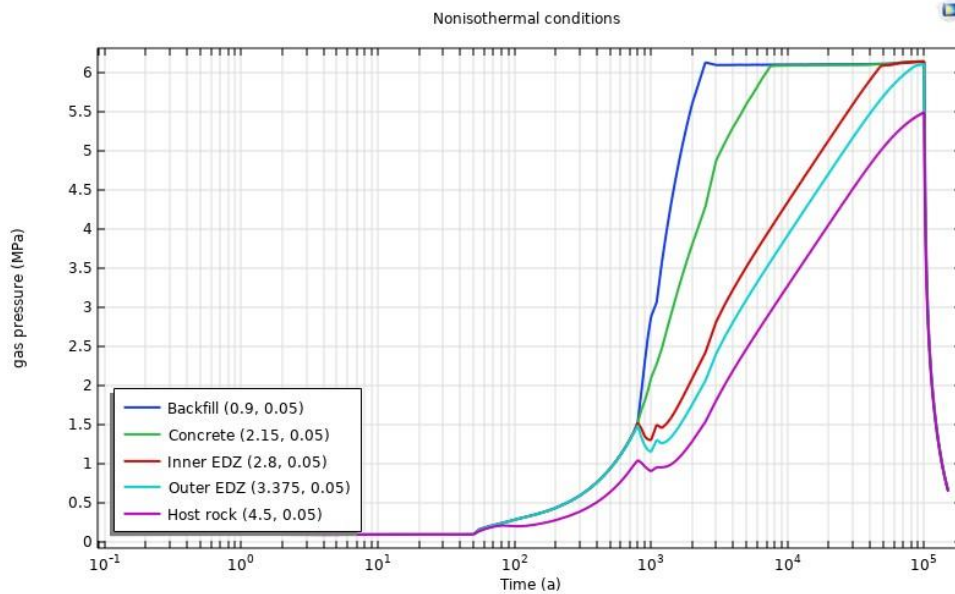


Figure 7-17 – Modelled evolution of relative permeability evolution in observation points under: a) isothermal conditions, b) non-isothermal conditions

Relevant indicators such as liquid and gas pressure are presented in Figure 7-18.



a)



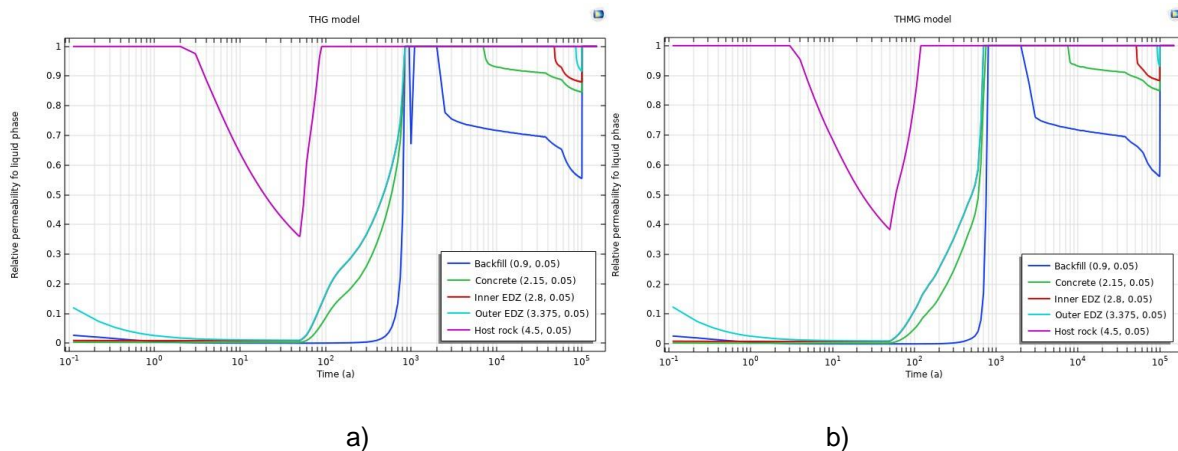
b)

Figure 7-18 – Modelled evolution of a) liquid and b) gas pressure at observation points

Compared to liquid pressure evolution under isothermal conditions (Figure 7-12 a), the liquid pressure build-up to maximal (pressure prevailing in-situ) was smoother under nonisothermal conditions. The evolution over time also showed some increase/decrease with a peak value less than in-situ porewater pressure. Meanwhile there were no significant influence on gas pressure evolution and on its maximum compared to isothermal conditions (Figure 7-13 a).

7.3.3 Impact of mechanical deformations

Considering HM, TM couplings allowed to assess the porosity change and subsequently impact on mass balance of components (water, hydrogen) (eq. 20). Considering porosity change due to mechanical processes the host rock re-saturation time after ventilation phase was slightly delayed as it could be observed from relative permeability evolution (Figure 7-18).



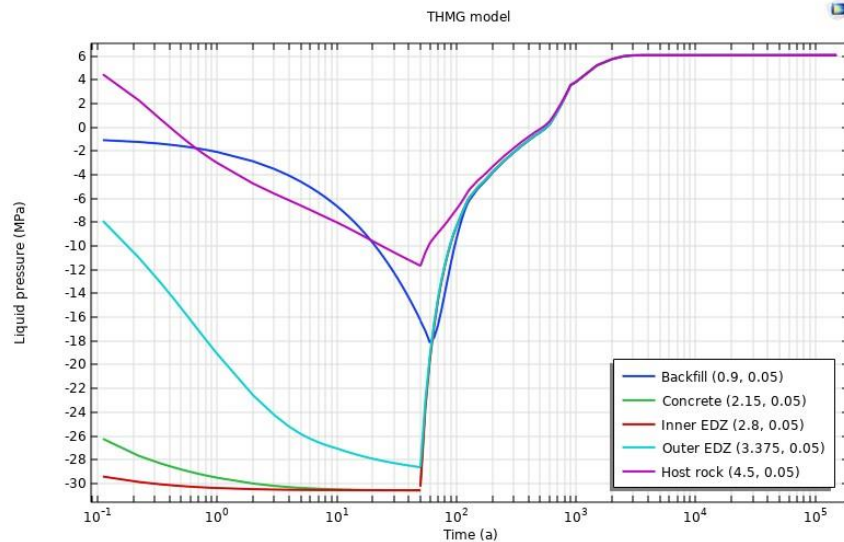
a)

b)

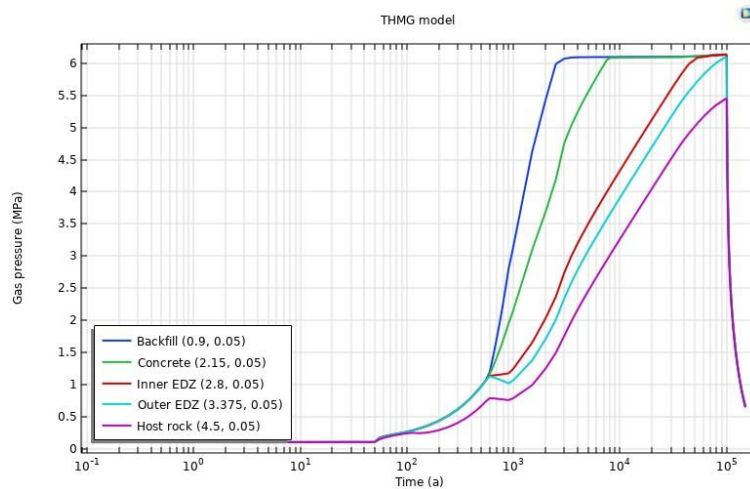
Figure 7-19 – Modelled evolution of relative permeability at observation points: a) without mechanical couplings, b) with mechanical couplings

Modelling results show that second de-saturation due to hydrogen gas generation started later for outer EDZ while for other materials there was no significant influence.

Modelling results on liquid and gas pressure derived with THG and THMG models are presented in Figure 7-20.



a)



b)

Figure 7-20 – Modelled evolution of a) liquid and b) gas pressure at observation points

Based on the results presented in Figure 7-20, some influence on liquid and gas pressure evolution within period 800-1500 years could be seen considering porosity change due to mechanical processes. However, no significant impact on maximal gas pressure (~6.14 MPa) was observed. This is mainly related to the high compressibility of the gas.

Nevertheless, besides the pore pressure evolution in observation points, its distribution in all modelled domains was analysed too. The Figure 7-21 present pore water pressure distribution in the modelled domain when the P_L reached its maximum value in the system.

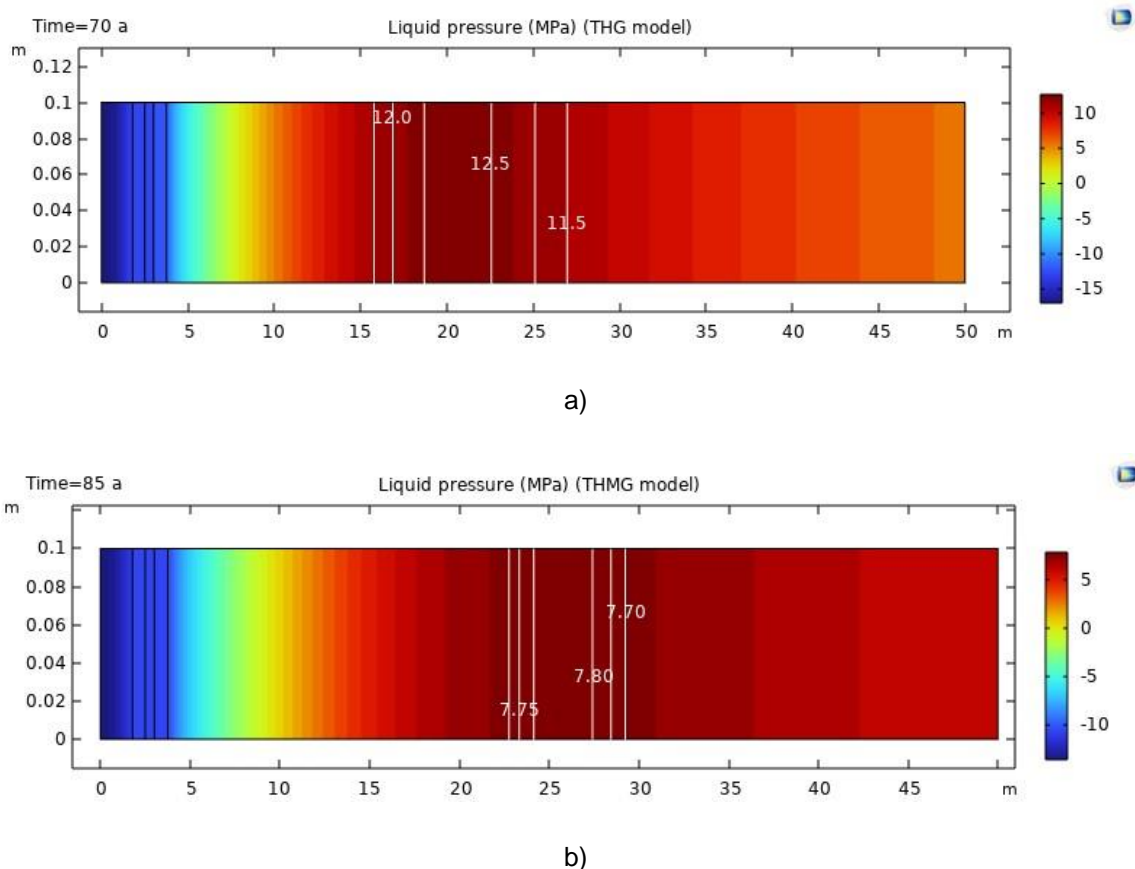


Figure 7-21 – Simulated distribution of liquid pressure a) without consideration mechanical processes (THG model) and b) considering mechanics related couplings (THMG model) (geometry not to scale)

Based on THG model results the maximum porewater pressure in modelled system was ~12.6 MPa and it was achieved at ~70 years after excavation. Meanwhile considering mechanical couplings the simulated maximum porewater pressure in modelled system was lower (~7.8 MPa) and it was achieved later (at ~85 years after excavation). It clearly indicates that omitting porosity change due to mechanical processes (thermal expansion of material and changes of effective stress) led to the overestimation of heat induced pore pressure increase in modelled system. Modelled heat induced pore pressure increase is still overestimated to some extent due to assumed model geometry (2D axisymmetric) as the heat transfer process take place in three directions in reality. Proper evaluation of porewater pressure in the system is important for the assessment of system state from mechanical point of view, i.e. whether system remain in compressive state or tensile stress conditions would develop.

7.3.4 Impact on radionuclide transport

Following the specification [1], soluble radionuclide I-129 transport should be analysed in Zone B. Radionuclide release starts from T=100 000 years (loss of tightness of the canister) and last 10 000 years (rapid degradation of the nuclear glass) (till T=110 000 years). Boundary conditions for contaminant transport is summarized in Figure 7-22.

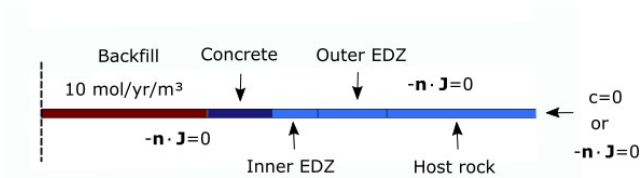
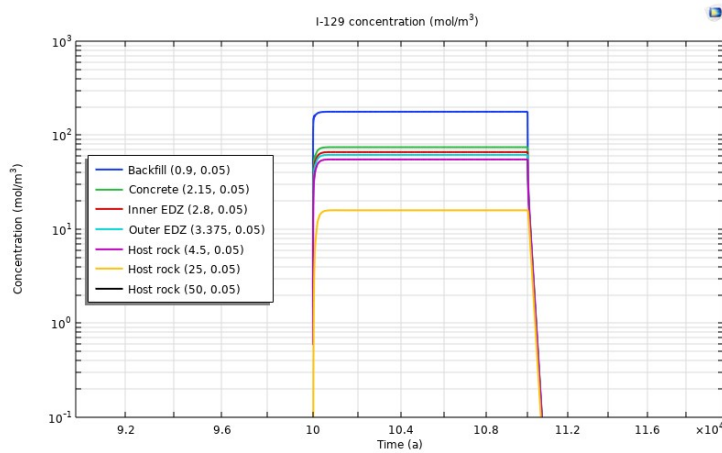
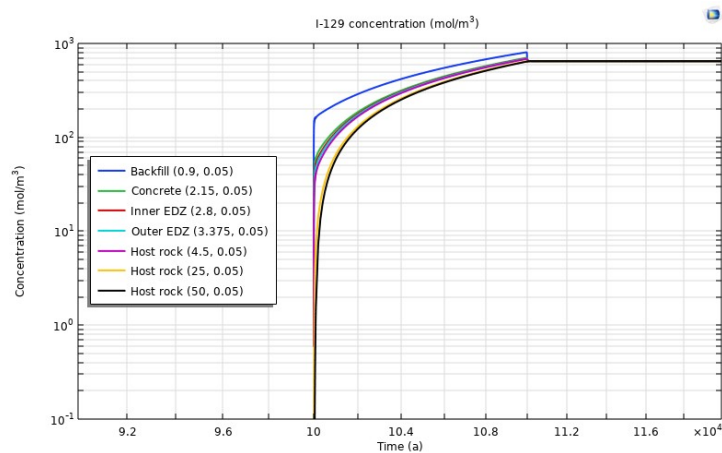


Figure 7-22 – Boundary conditions for I-129 transport in Zone B

Modelled concentration of I-129 in observations points and additionally in host rock further from the deposition tunnel (at 25 m and 50 m) is presented in Figure 7-23. As it was expected the concentration was the highest at the source domain. With constant influx it reached steady state rather quickly (Figure 7-23a). Maximal concentration was lower at the locations further away from the contaminant source. Once the radionuclide flux from the source stopped, the radionuclides were transported out of the modelled system (50 m around the tunnel) and the concentration decreased to zero. Such evolution was driven by accepted boundary condition (zero concentration on model boundary).



a)



b)

Figure 7-23 – Modelled I-129 concentration in observation points and further in host rock in Zone B under different boundary conditions

If no-flux boundary condition was assumed, the radionuclides released into the modelled system tended to equilibrate in the system once the influx was stopped (Figure 7-23 b). 2D axisymmetric geometry does not allow imposing different boundary conditions in different directions. Assumption of no-flux boundary condition at $r=50$ m would be more representative for the middle point in the half distance between deposition tunnels. Zero concentration on the boundary would be more representative for the aquifer layers above and below the host rock although they are at larger distance (75 m according to specification [1]).

Following the specification, the hydrogen injection started after 50 years and have stopped by the time radionuclide I-129 release started (100 000 years). I-129 is soluble nuclide and it is transported in dissolved form. Radionuclide transport in low permeable environment mainly take place via diffusion and the key parameter for diffusive radionuclide transport is effective diffusivity. The effective diffusivity is a function of porosity and liquid saturation (eq. 2). Therefore, the evolution of porosity and saturation need to be evaluated. As it has been already presented, the ventilation of 50 years led to desaturation of engineered barriers, EDZ and the part of the host rock. Subsequent re-saturation and hydrogen gas induced second de-saturation influenced the diffusivity. The evolution of effective diffusivity is shown in Figure 7-24.

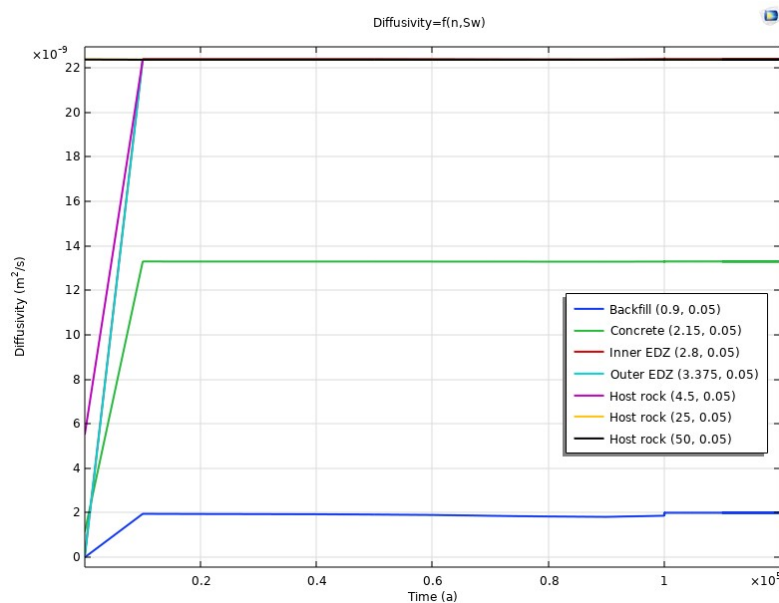


Figure 7-24 – Evolution of effective diffusivity of I-129 in different barriers

As the largest variation of liquid saturation were during ventilation and soon after it, the most influence on diffusivity was observed in this period too. Hydrogen gas injection does not lead to liquid saturation less than 0.994, thus the impact on diffusivity was not significant. By the time I-129 release from waste started, all the barriers were fully water saturated. Thus, under such conditions and radionuclide release start time, there were no impact of corrosion induced gas on radionuclide migration.

7.4 Conclusions

Within this task LEI revised and implemented mathematical model applicable for modelling of water and hydrogen evolution in the repository under isothermal and nonisothermal conditions. Mechanical processes and relevant couplings were considered too. This model formulation was used for numerical analysis of liquid and gas pressure evolution around one deposition tunnel (part of Zone B). 2D axisymmetric model was defined for the numerical analysis of the evolution of water and gas flow around deposition tunnel without gradient along tunnel.

Based on the modelling results under isothermal conditions it was observed that 50 years of ventilation led to the desaturation of inner and outer EDZ, a part of host rock and to decrease of initial saturation of engineered barriers. Considering gas entry pressure explicitly in water retention and relative permeability model, the host rock was de-saturated to smaller extend by the end of ventilation and re-saturated faster. Despite hydrogen gas injection all materials became water saturated before ~1500 years (with classical Van Genuchten model) and earlier (before 1000 years) with modified VG model (considering of gas entry pressure explicitly).

Second de-saturation (due to gas injection) occurred firstly in backfill, later in concrete, EDZ. Canister corrosion induced H₂ gas flux did not led to host rock de-saturation around deposition tunnel in this generic repository.

Modelling results under nonisothermal conditions showed that all materials except the host rock were fully re-saturated later compared to isothermal case. Consideration of water thermodynamic properties dependence on temperature had different influence on re-saturation time. Re-saturation at observation point in host rock (located 2 m from tunnel wall) occurred earlier than in isothermal case (~90 yrs vs ~350 yrs). Considering heat load and water thermodynamic properties as a function of temperature second de-saturation phase started slightly earlier compared to isothermal case. Nevertheless, no heat load impact on maximum gas pressure P_g in modelled system was observed.

Considering porosity change due to mechanical processes some influence on gas and water pressure evolution trend was seen within period 800-1500 years. Based on modelling results there were no significant impact on maximal gas pressure (~6.14 MPa) (related to high compressibility of the gas). There was no significant impact on maximal water pressure (~6.075 MPa) at observation points too. However, omitting porosity change due to mechanical processes (thermal expansion of material and changes of effective stress) would lead to the overestimation of heat induced pore pressure increase in the host rock. Proper pore pressure evolution is necessary while drawing conclusions on system state from mechanical point of view (compressive or tensile stress state).

Hydrogen gas injection does not lead to liquid saturation less than 0.994, thus the impact on diffusivity was not significant. By the time I-129 release from waste started in the deposition tunnel of Zone B, all the barriers had become fully water saturated. Thus, under such conditions and radionuclide release start time, there were no impact of corrosion induced gas on radionuclide migration.

Currently liquid and gas pressure evolution in access gallery and its impact on the deposition tunnel is not represented in the computational domain. It could be extended in the future by incorporation that evolution and influence via boundary conditions for the current model.

7.5 References

1. ANDRA. Task 4 Technical Note defining a generic repository configuration, sets of parameters, conditions and relevant indicators. EURAD WP GAS Milestone 61, 2021.
2. M. Pitz, E. Jacops, N. Grunwald, G. Ziefle, and T. Nagel. On Multicomponent Gas Migration in Single Phase Systems. In press.
3. E. Jacops, G. Volckaert, N. Maes, E. Weetjens, J. Govaerts. Determination of gas diffusion coefficients in saturated porous media: He and CH₄ diffusion in Boom Clay. Applied Clay Science 83–84 (2013) 217–223.
4. J. Rutqvist, L. Borgesson, M. Chijimatsu, A. Kobayashi, L. Jing, T.S. Nguyen, J. Noorishad, C.-F. Tsang. Thermohydromechanics of partially saturated geological media: governing equations and formulation of finite element models. International Journal of Rock Mechanics & Mining Sciences 38 (2001) 105-127.

5. A. Amri, Z. Saâdi, R. Ababou. Parametric Sensitivity to Capillary Entry Pressure in Two-Phase Water–Gas Flow Models: Deep Geologic Disposal of Radioactive Waste. *Transport in Porous Media* (2022) 145:13–43. <https://doi.org/10.1007/s11242-022-01780-w>
6. V. Navarro, L. Asensio, H. Gharbieh, G. De la Morena, V. Pulkkanen. Development of a multiphysics numerical solver for modeling the behavior of clay-based engineered barriers. *Nuclear Engineering and Technology*. Volume 51, Issue 4 (2019) Pages 1047-1059.
7. D.W. Pollock, Simulation of fluid flow and energy transport processes associated with high-level radioactive waste disposal in unsaturated alluvium, *Water Resour. Res.* 22 (5) (1986) 765-775

8. Contribution of SCK CEN

SCK CEN focused on the Thermal-Hydro-gas (THG) simulations of zone B, building the model stepwisely from 1D, 2D, and finally to a full 3D model at the repository scale. Firstly, the academic code Code_Bright has been used to investigate the disposal system behavior in response to gas accumulation and pressure build-up. Next, SCK CEN implemented the two-phase flow theory into the commercial software COMSOL Multiphysics. Comparisons between the two codes have been extensively performed. SCK CEN not only examined the differences and appropriateness of various approximation methods, but also investigated gas dissipation behavior at the repository scale as well as some relevant parameter sensitivities.

8.1 Model description

The exercise defined for task 4.2 (EURAD report Milestone 61) aims to simulate the gas migration in a generic repository, which includes three zones (zone A, zone B and zone C) corresponding to three different disposal concepts.

The host rock of the generic repository locates at a depth of 525 -675 m from the ground surface, with the repository located at $z=600$ m. Zone B has a total of 8 horizontal disposal cells. The disposal cell is 1000 meters long, with a distance of 100 meters between adjacent cells. There are two interconnected access galleries: one of them is connected to the shaft's bottom. The galleries and disposal cells have diameters of 5 and 2.5 meters, respectively. Aside from that, there are two seals: one in the access gallery and another in the shaft. The materials taken into account include backfill, liner, bentonite and plug, the inner and outer EDZ, and the intact host rock.

The geometry of a full 3D model for zone B and some mesh details are illustrated in Figure 8-1 and Figure 8-2. The geometry includes eight disposal cells, two access galleries and one shaft. Taking symmetry into account, only the upper half of zone B and a half shaft are included in the model. The model considers the surrounding host rock with a thickness of 50 m, which is a compromise between the inter-cell distance along the disposal cells and the thickness of the geological layer. The full 3D domain is meshed with 59453 nodes and 50632 hexahedral elements. Due to the computationally expensive 3D modelling, no mesh convergence was conducted.

8.1.1 Material properties

Constitutive laws and material properties used in the numerical model are defined as closely as possible to the exercise's specification. However, some constitutive laws and parameter values deviate from the definition due to limitations of the code used as well as convergence issues. This section explains the most important constitutional laws used in the simulation and Table 8-1 lists the major parameter values.

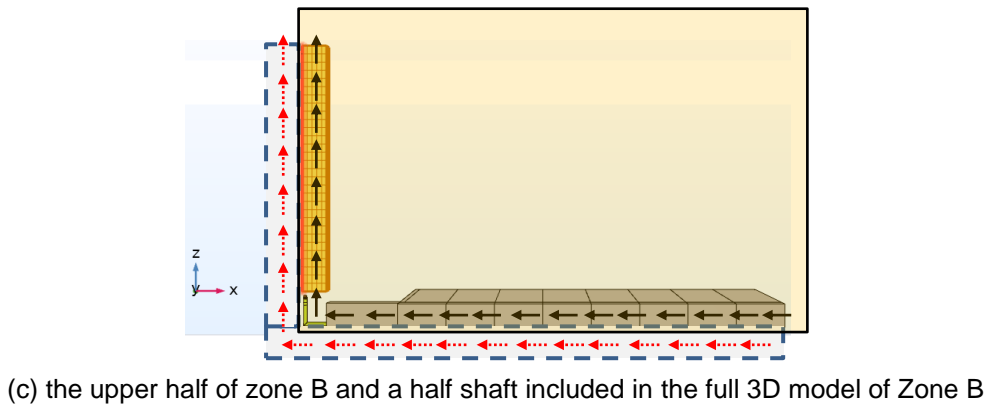
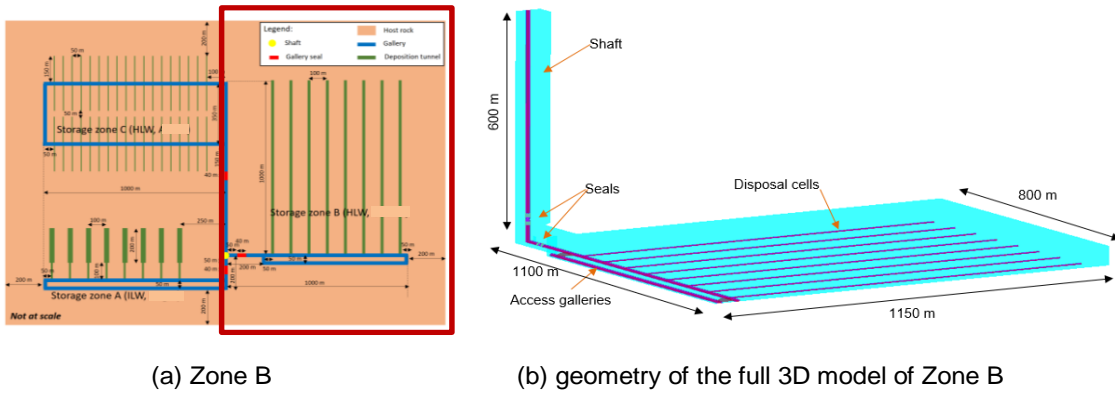


Figure 8-1 Geometry of the full 3D model of Zone B

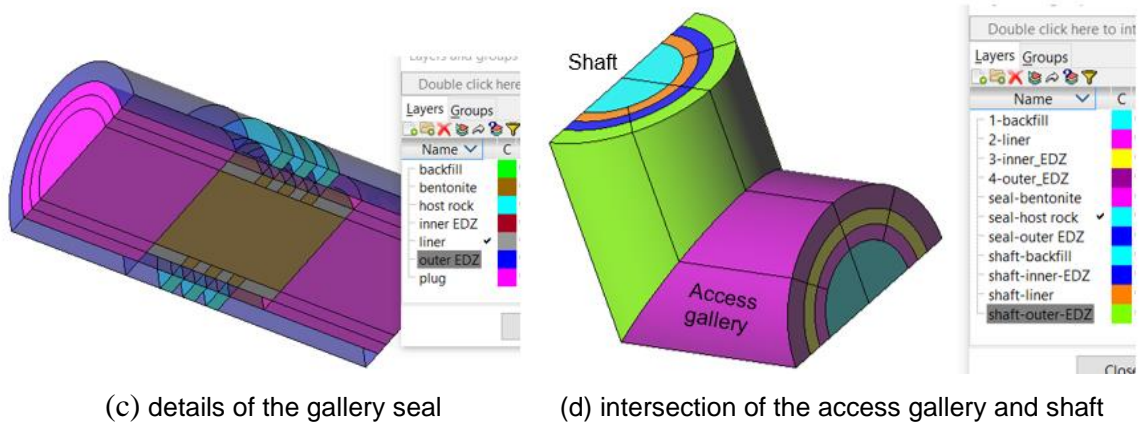
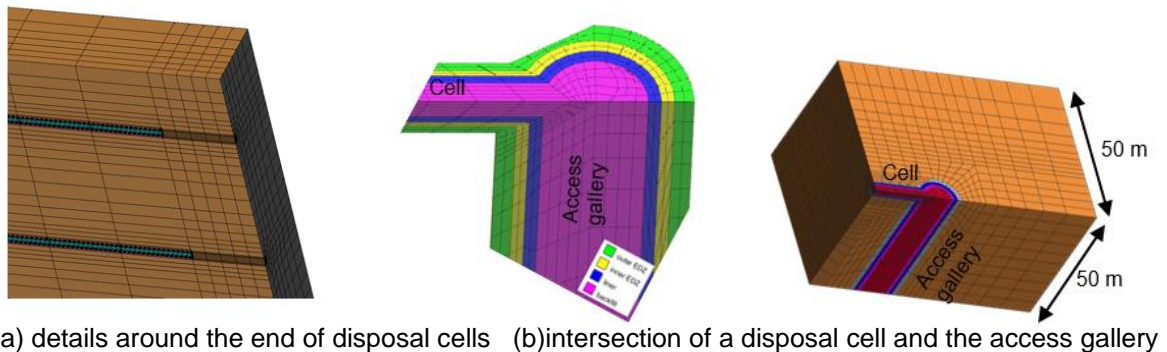


Figure 8-2 details of the full 3D model of Zone B

Table 8-1 Material properties

parameter	Unit	Host rock			backfill	liner	plug	bentonite
		Undisturbed	Outer EDZ	Inner EDZ				
porosity	η	-	0.2		0.4	0.15	0.15	0.35
Intrinsic permeability of water	K_{in}	m^2	10^{-20}	10^{-18}	10^{-16}	10^{-16}	10^{-16}	10^{-19}
Intrinsic permeability of gas	K_{in}	m^2	10^{-18}	10^{-17}	10^{-16}	10^{-16}	10^{-16}	10^{-19}
capillary pressure function								
shape parameter	n	-	1.5		1.5	1.5	1.5	1.6
fitting parameter	P_0	MPa	23	17	16	1	10	20
liquid density								
Storage coefficient [¶]	β	MPa^{-1}		7×10^{-4}	10^{-3}	10^{-3}	10^{-3}	2×10^{-3}
Heat conductivity (w/m/°C)				1.7	1.3	2.3	2.3	1.5
specific heat (J/Kg/°C)				720	500	900	900	700
thermal dilation of solid matrix (1/°C) ⁺				4×10^{-5}	2×10^{-5}	2×10^{-5}	2×10^{-5}	2×10^{-5}

[¶] In the exercise specification, these values are defined as pore compressibility. In the numerical simulations of Code_Bright, they are used as water compressibility alternatively.

⁺ The thermal dilation of solid matrix is mistakenly used as linear volumetric thermal expansion coefficient of solid grains in the numerical simulations of Code_Bright. This is corrected in the later COMSOL analysis.

8.1.1.1 water retention curve

The linearized V-G (Van Genuchten) retention curve defined in the exercise specification considers explicitly a small gas entry pressure P_e which is not available in Code_Bright. The introduction of P_e offsets the retention curves in the vicinity of fully saturation point. The original V-G retention formulation with a relatively higher P_0 as Equation 8-1 is alternatively used and Figure 8-3 shows the deviations.

$$S_e = \frac{S_l - S_{lr}}{S_{ls} - S_{lr}} = \left[1 + \left(\frac{P_g - P_l}{P_0} \right)^{\frac{1}{1-\lambda}} \right]^{-\lambda}$$

Equation 8-1

where P_0 and λ are fitting parameters, respectively: P_0 is commonly used as air entry pressure and $\lambda = 1 - \frac{1}{n}$ where n is the shape function defined in Table 8-1. S_e is the effective saturation; S_l is liquid saturation; S_{lr} and S_{ls} are residual and saturated saturation of liquid, respectively. The values of S_{lr} and S_{ls} are taken as 0 and 1, respectively in this exercise. P_g and P_l are gas and liquid pressure, respectively.

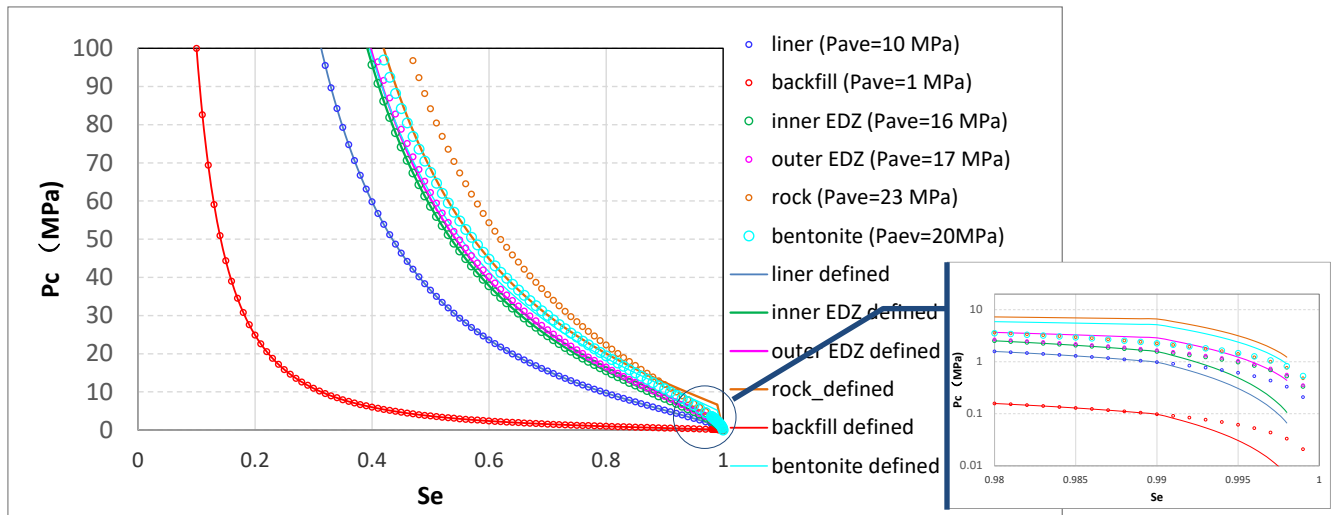


Figure 8-3: retention curves used in Code_Bright compared with retention curves in problem specification

8.1.1.2 relative permeability of water

The Van Genuchten model is used for the relative permeability of water:

$$k_{rl} = S_e^{0.5} \left[1 - \left(1 - S_e^{1/\lambda} \right)^\lambda \right]^2 \quad \text{Equation 8-2}$$

where the effective saturation S_e and fitting parameter λ are the same as before.

8.1.1.3 Intrinsic and relative permeability of gas

Intrinsic permeability of gas in the exercise is defined as being 0-2 orders higher than that of water. In the numerical model, the intrinsic permeability of gas is kept the same as water, but a coefficient A is used to simulate the higher permeability of gas:

$$k_{rg} = A(1 - S_e)^3 \quad \text{Equation 8-3}$$

where the coefficient A is the ratio between gas permeability (m^2) and water permeability (m^2) in Table 8-1.

8.1.1.4 Liquid/gas viscosity

$$\text{Liquid viscosity } \mu_l = 2.1 \times 10^{-12} \exp\left(\frac{1808.5}{273.15+T}\right) \text{ (MPa} \cdot \text{s)}$$

$$\text{Gas viscosity } \mu_g = 0.88 \times 10^{-11} \text{ (MPa} \cdot \text{s)}$$

8.1.1.5 Liquid density

Liquid density is expressed as $\rho_l = \rho_{l0} \exp(\beta_w(p_l - p_{l0}) + \alpha_T T)$ (Kgm^{-3}), where the reference density $\rho_{l0} = 1002.6 Kgm^{-3}$ and the reference pressure $p_{l0}=0.1MPa$. Water compressibility β_w is $4.5e-4[1/MPa]$ for the water. However, in order to take into account pore compressibility, β_w in simulations of Code_Bright takes the value of pore compressibility listed in Table 8-1. A temperature dependent thermal expansion coefficient of water $\alpha_T [1/^\circ C]$ is adopted:

$$\alpha_T = -(10^{-4}T^3 - 0.0314T^2 + 6.1649T + 106.61) \times 10^{-6}$$

8.1.1.6 Millington-Quirk diffusion of dissolved gas

Effective diffusion coefficient of dissolved H₂ in the porous material D_e is expressed in the problem specification as

$$D_e = D_0 \phi^{1+a} S_e^b \quad \text{Equation 8-4}$$

Where $D_0 = 5 \times 10^{-9} \text{ (m}^2\text{/s)}$ is diffusion coefficient of dissolved H₂ in water, ϕ is the porosity of the material. The exercise definition specifies the a and b values for each material. In Equation 8-4, $\phi^{1+a} S_e^b$ serves as tortuosity of the pores and it is expressed as a function of porosity and saturation degree of the porous material.

Diffusion of dissolved gas is the key mechanism of gas dissipation at the scale of the repository. Results of the gas pressure could be very different for different expressions of tortuosity. Instead of using Equation 8-4, results from Code_Bright in this report are obtained with a tortuosity of $\theta^{2+a} S_e^{b+1}$. Equation 8-4 is used in the later simulations with COMSOL. Results show that the maximum gas pressure from Code_Bright is much higher than that from COMSOL, which indicates that the dependence of effective diffusion coefficient on the porosity and saturation degree is very important to the maximum gas pressure induced in the system.

8.1.2 Initial and boundary conditions

The simulation considers the time-varying conditions listed in Table 8-2.

Table 8-2: time varying conditions considered in the simulation

Time (years)	conditions
0-50	Instantaneous excavation of the whole repository with a relative humidity of 80%
50-1E5	Instantaneous emplacement of waste and closure of the repository, with an instantaneous gas injection at a constant rate on the liner intrados, together with a decaying thermal load in THG analysis.
1E5-3E5	Gas production stops

The gas production rate in zone B is 0.25 mol/yr/m_{cell} for the disposal cells. Aside from that, there is a nearly 100-time higher gas production rate of 21.5 mol/yr/m_{gallery} for access galleries and shaft. The thermal load and gas production rate used in the full_3D THG model is presented in Figure 8-4. The initial and boundary conditions are defined in accordance with Table 8-2.

- 0—50 years: a constant suction of $\frac{-8.31432 \text{ J/mol/K} \times (273.15 + 25) \text{ K}}{0.001 \text{ m}^3/\text{kg} \times 0.018016 \text{ kg/mol}} = 30.7 \text{ MPa}^3$ at the intrados of liner (corresponding to a relative humidity of 80%).

³ The total suction is calculated based on Kelvin's equation: $suction = -\frac{RT}{v_{w0}\omega_v} \ln(RH)$, where v_{w0} is the specific volume of water and ω_v is the molecular mass of water vapour.

- 50—1E5 years: gas injection at the intrados of liner with a surface gas injection rate of disposal cells: 0.25 mol/yr/m (i.e. $\frac{0.25 \text{ mol/yr/m} \times 0.002 \text{ kg/mol}}{86400 \times 365 \text{ s} \times 2\pi \times 1.8 \text{ m}} = 0.14 \text{e-11 kg/s/m}^2$ at $r=1.8 \text{ m}$)
access galleries: 21.5 mol/yr/m (i.e. $\frac{21.5 \text{ mol/yr/m} \times 0.002 \text{ kg/mol}}{86400 \times 365 \text{ s} \times 2\pi \times 4 \text{ m}} = 5.425 \text{e-11 kg/s/m}^2$ at $r=4 \text{ m}$)
- 1E5 years afterwards, gas injection rate is set to zero.
- The top of the shaft is assigned with atmospheric gas pressure and hydrostatic water pressure: $P_g=0.1 \text{ MPa}$, $P_l=6.075 \text{ MPa}$ (in the 3D full model of Code_Bright) .
- all the external surfaces except symmetric surfaces:
Liquid pressure, gas pressure and temperature are fixed as 6.075 MPa , 0.1 MPa and 20°C respectively. No gas/liquid/thermal flux at symmetric surfaces.
- liner intrados:
Time < 50 years: $P_g=0.1 \text{ MPa}$ and $P_l=30.7 \text{ MPa}$. These conditions are released after 50 years.
during 50-1E5 years: $J_{\text{gas}}= 0.07 \text{E-11 kg/s}$ (disposal cells) and $J_{\text{gas}}= 2.7125 \text{E-11 kg/s}$ (galleries and shaft).
during 50-1E5 years: decaying thermal load J_E (disposal cells)
- backfill and seals
Time < 50 years: $P_l=-0.8685 \text{ MPa}$ (backfill) and $P_l=-18.37 \text{ MPa}$ (seals) with numerical artifact with extremely low permeability to simulate its non-existence. Restore the permeability after 50 years.

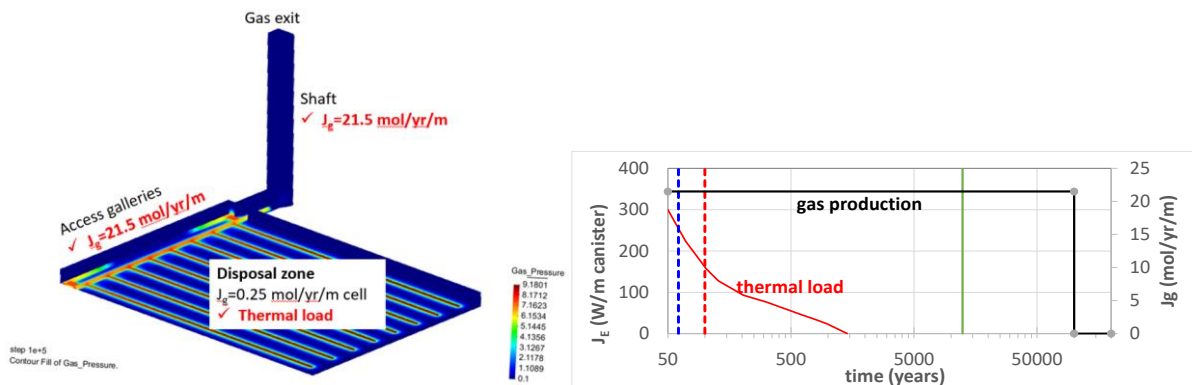
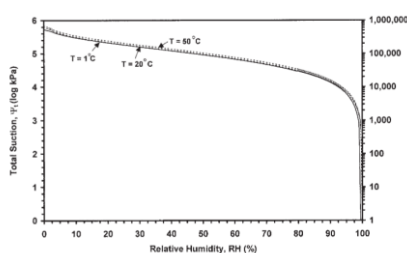


Figure 8-4: the thermal load and gas production rate in the 3D THG model for zone B



8.1.3 Software and results indicators

The problem is firstly solved with Code_Bright 3.0 developed by Technical University of Catalunya (UPC). Later, the two-phase flow theory was implemented into the multiphysics software COMSOL 6.

Results are investigated at 14 points as shown in Figure 8-5 (left): points 1-9 are on disposal cells, points 10-12 are around the gallery seal. Point 13 is within the shaft seal and point 14 is the middle point of the shaft. Gas flux is investigated at 12 sections as marked in Figure 8-5 (right)(Note: the surface area is only half of the backfill section area):

- Section 1-3 are on the intersections of three disposal cells (right: $x=950\text{m}$, middle: $x=550\text{m}$ and left: $x=250\text{m}$) at $Y=10\text{ m}$;
- Sections 4-8 are along the access gallery with $x=900\text{ m}$, 500 m , 240 m , 90 m (before gallery seal) & 40 m (after gallery seal);
- Section 9-10 are on the by-access gallery at $X= 900\text{ m}$ and 250 m ;
- Section 11 is under the shaft seal at $Z=35\text{ m}$;
- Section 12 is on the top of the shaft.

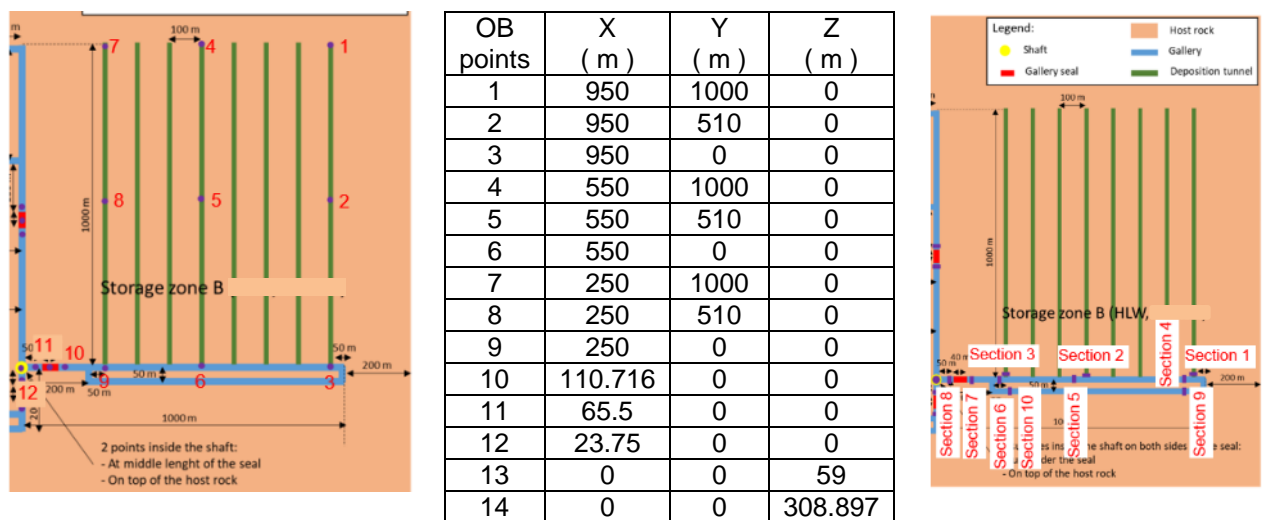


Figure 8-5: (left) 14 observation points and their coordinates (right) Schematic 12 surfaces (purple segments) for output of gas flux

8.2 EURAD GAS modelling results from Code_Bright

3D HG (Hydro-gas) modelling results for zone B considering gas produced in the disposal cells have been presented in the EURAD GAS progress report Milestone 174. This report presents the THG modelling results, considering gas produced in both disposal cells and galleries and shaft. Code_Bright was used to build models stepwisely from 1D, 2D, and finally to a full 3D model at repository scale, which analyzed qualitatively

- the differences and appropriateness of various approximation methods;
- gas dissipation pathway at the repository scale;
- sensitivity analysis of the seal at the repository scale.


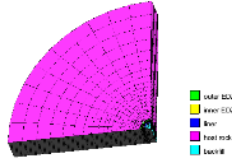

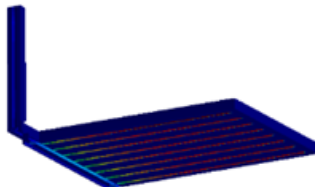
Yu et al. (2011)⁴ compares behaviors of Code_Bright and TOUGH in solving several THG problems. It should be noted that, the results from Code_Bright made in this study cannot be interpreted quantitatively because $D_e = D_0\theta^{2+a}S_e^{1+b}$ is used, while it is defined in problem specification as $D_e = D_0\theta^{1+a}S_e^b$. Obviously, the maximum gas pressure obtained from Code_Bright is much higher than the specification.

Although in the simulations with Code_Bright, there are several aspects that deviate from the problem specifications, the conclusions deduced from Code_Bright results are beneficial to the following implementation of the two-phase model in the COMSOL and the subsequent component-scale analysis based on COMSOL.

For a gas modelling at the repository scale, the domain size reaches as large as thousands of meters, and the time duration can be up to $\sim 10^5$ years. The element size varies from less than \sim dm within the seal up to tens of meters in the host rock. These increase the 3D model complexity and make the convergence hard to manage. As a result, a step-by-step scheme, as shown in Table 8-3, is used to ensure a smooth progress of model development.

This section starts with result comparison between 1D, 3D cell, and full 3D models, followed by the analysis of the full 3D model's results.

Table 8-3: the step-by-step scheme

		Total elements	Time cost	
Case 1	1D axisymmetric	205	2 mins	
Case 1a	Simple_3D extended from 1D	3750	1 hour	
Case 2	3D_cell	38625	2 days	
Case 3	Full_3D	50632	5 days	

⁴ L. Yu, E. Weetjens, J. Perko & D. Mallants (2011). Comparison of numerical tools through Thermo-Hydro-Gas transport modelling for a geological repository in Boom Clay. Nuclear Technology 174:411–423.

8.2.1 Comparisons between 1D-3D model results

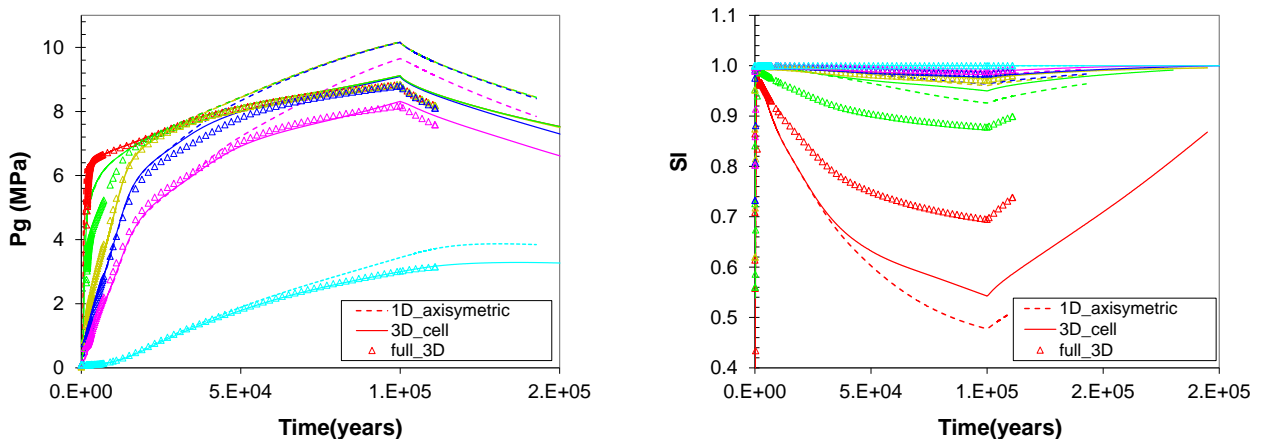
The comparisons between 1D-3D models are based on the results obtained in 2021, where the gas generated in the access galleries is not included. Except the full_3D model, the rest models are unable to account for gas migration through the access galleries and shaft. The gas pressure build-up in the region far from the access gallery and shaft is quite similar in all cases, owing to disposal cells with lengths as long as 1000 meters. In this section, the results of three models, including 1D axisymmetric model, 3D_cell model and full_3D model, are compared at the mid-section of the central disposal cell (point 5 in Figure 8-5: mid point Y=510 m of the central cell at X=550 m).

Figure 8-6 indicates that the gas pressure for all three models are quite similar, with the maximum gas pressure increasing from 3D to 1D. The difference in gas pressure between 1D and 3D models is approximately 1 MPa. Consequently, water saturation in the backfill drops from 3D to 1D. This observation implies that a simple 1D model is capable of providing a fast estimation of the maximum gas pressure in the system.

8.2.2 3D THG modelling results

8.2.2.1 Gas/water pressure and saturation degree

Evolution of gas/water pressure and water saturation at 14 observation points are demonstrated in Figure 8-7. Initially, the disposal cells, access galleries and shafts remain unsaturated after the ventilation ($t=50$ years). Once gas production starts, the gas pressure gradually builds up in the whole system. In the first 2000 years, there is a competition between gas pressure and liquid pressure. Re-saturation proceeds until ~2000 years when water pressure recovers to around 6 MPa. The gas amount is so high that the gallery and disposal cells can never become fully saturated.



r=1.5m (red, backfill)
 r=2.2m (green, liner)
 r=2.7m (Khaki, inner EDZ)
 r=3.5m (blue, outer EDZ)
 r=4.5m (fuchsia, near host rock)
 r=15m (aqua, far host rock)

Figure 8-6: Comparison of gas pressure and water saturation at the mid-section of the central disposal cell between 1D-3D models

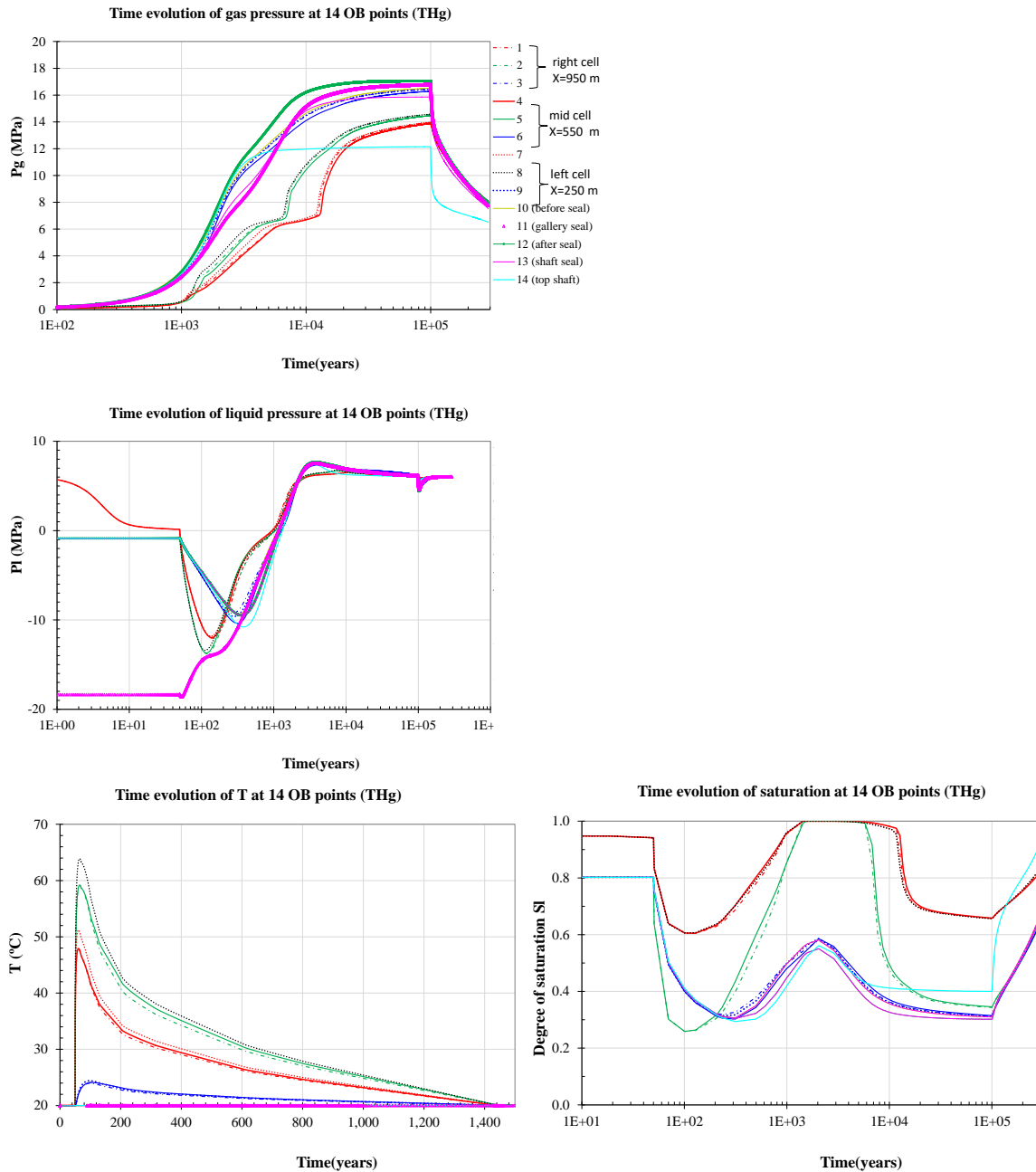


Figure 8-7: Evolution of gas pressure, water pressure, temperature and water saturation at 14 OB points from 3D THG simulation

Figure 8-8 presents snapshots of gas pressure and water saturation around two seals at ~2 000 years. After 2 000 years, the galleries and shaft remain unsaturated until gas production ceases.

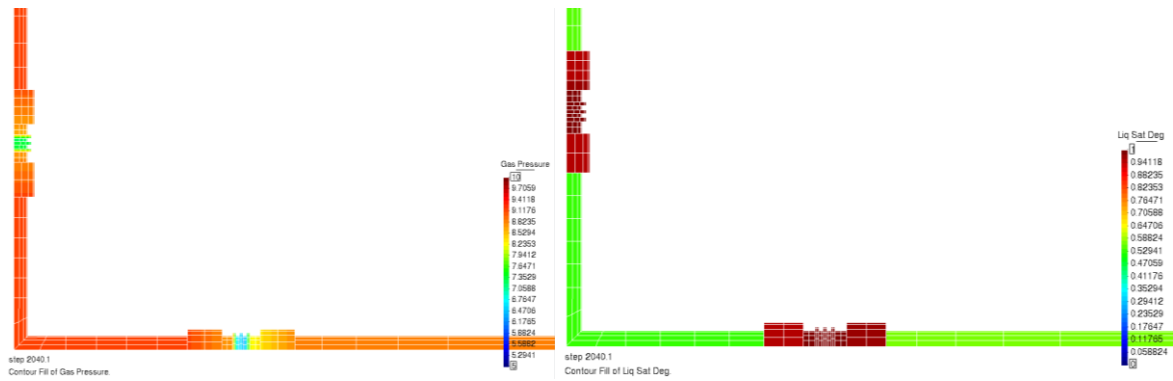


Figure 8-8: gas pressure(left) and water saturation(right) contour at ~2 000 years

The final gas pressure contour in the system at the end of gas generation is presented in Figure 8-9. Figure 8-10 illustrates the location with the maximum gas pressure ever appeared in the system (i.e. 17.728 MPa). The gas pressure profile at 1E5 years along section A-A (through the mid-point of the disposal cell and marked in Figure 8-10) at Z=0 m is presented in Figure 8-11, which visualizes a deep valley of gas pressure between disposal cells.

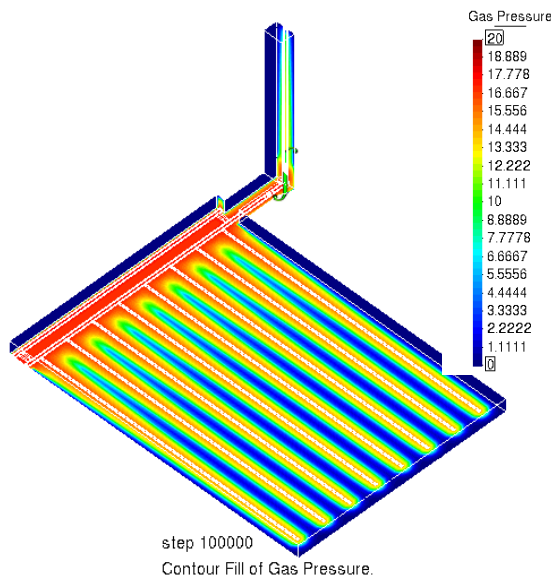


Figure 8-9: Contour of gas pressure at the end of gas injection (1E5 years) unit: MPa

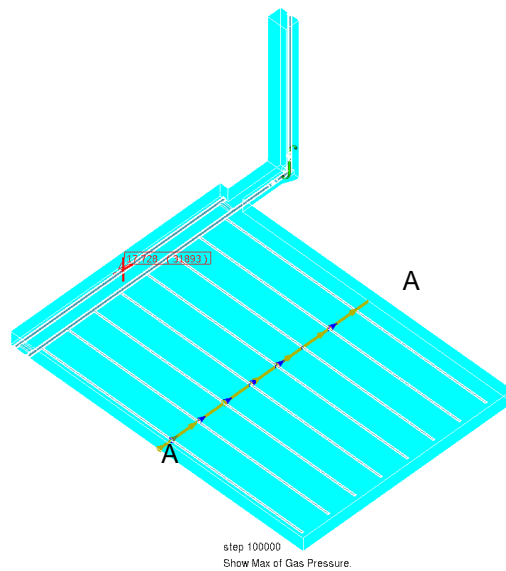


Figure 8-10: Section A-A and the location with the maximum gas pressure

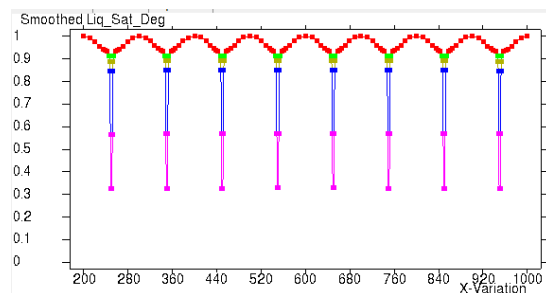
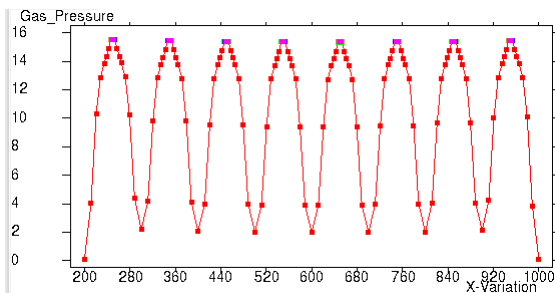


Figure 8-11: gas pressure (left, unit: MPa) and water saturation (right) profile along A-A section (Y=500 m, z=0) at 1E5 years

Figure 8-12 presents S_l and P_g contours at 1E5 years over the section A-A marked in Figure 8-12 (left). The EBS and the host rock within a radius of ~30 m around the disposal cells is de-saturated by the gas.

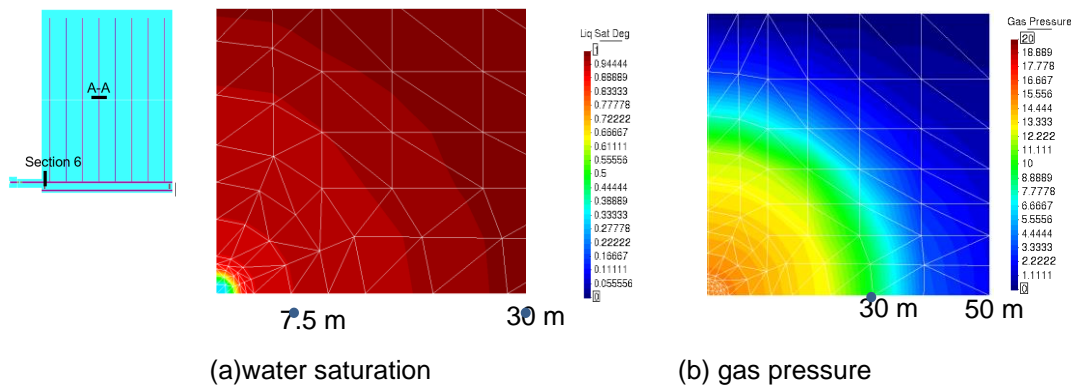


Figure 8-12: contours of S_l and P_g at section A-A at 1E5 years

Contours of gas pressure and water saturation of the access gallery at the cross section through observation point 10 ($X=90m$) is shown in Figure 8-13. The gas-induced desaturation extends deeply into the host rock and approaches the domain boundary, which means that the 50-m-thick host rock domain is not sufficient for the gas dissipation in the numerical modelling and needs to be extended in the future calculations.

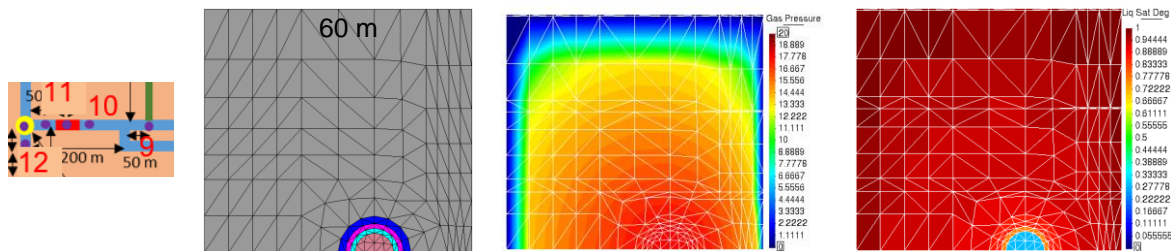
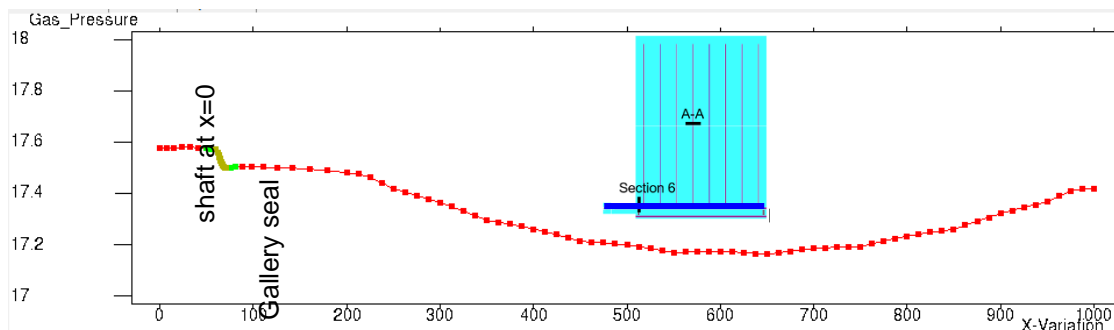


Figure 8-13: section at OB10 ($X=90m$) with materials from inner to outer are backfill, liner, inner_EDZ, outer_EDZ and host rock, respectively (left); contour of gas pressure (middle) and water saturation (right) at section OB10 at 1E5 years

Figure 8-14 displays some variable profiles along the access gallery at the end of gas generation. The blockage effect of gallery seal is obvious.



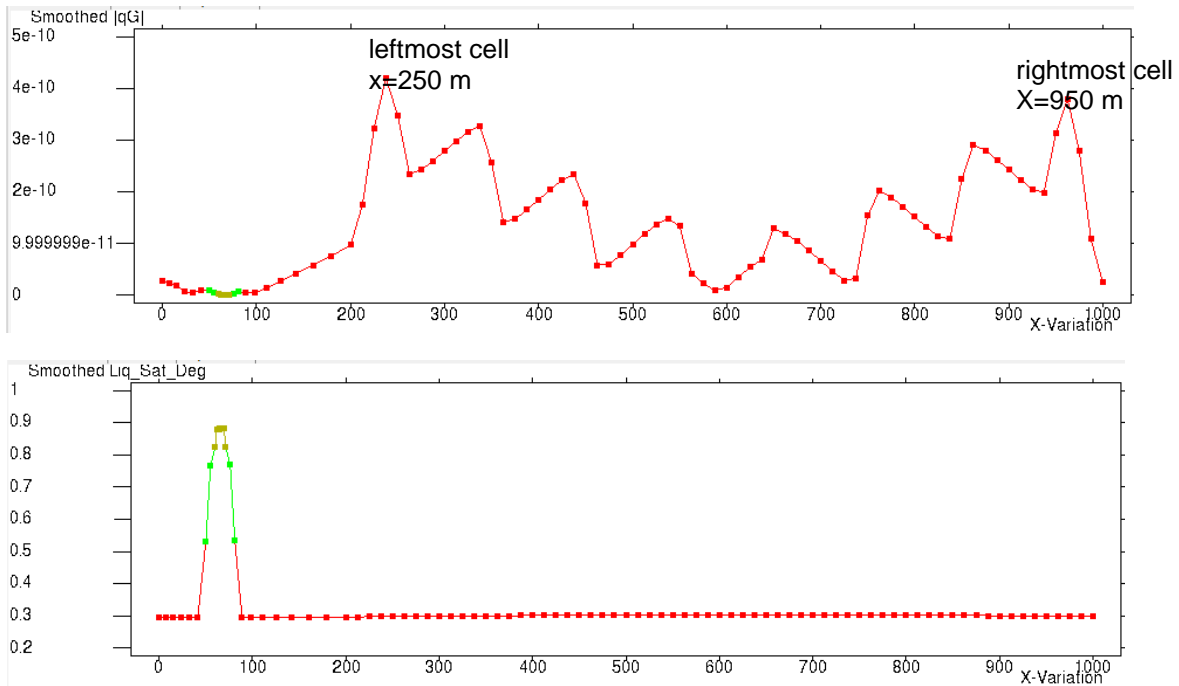
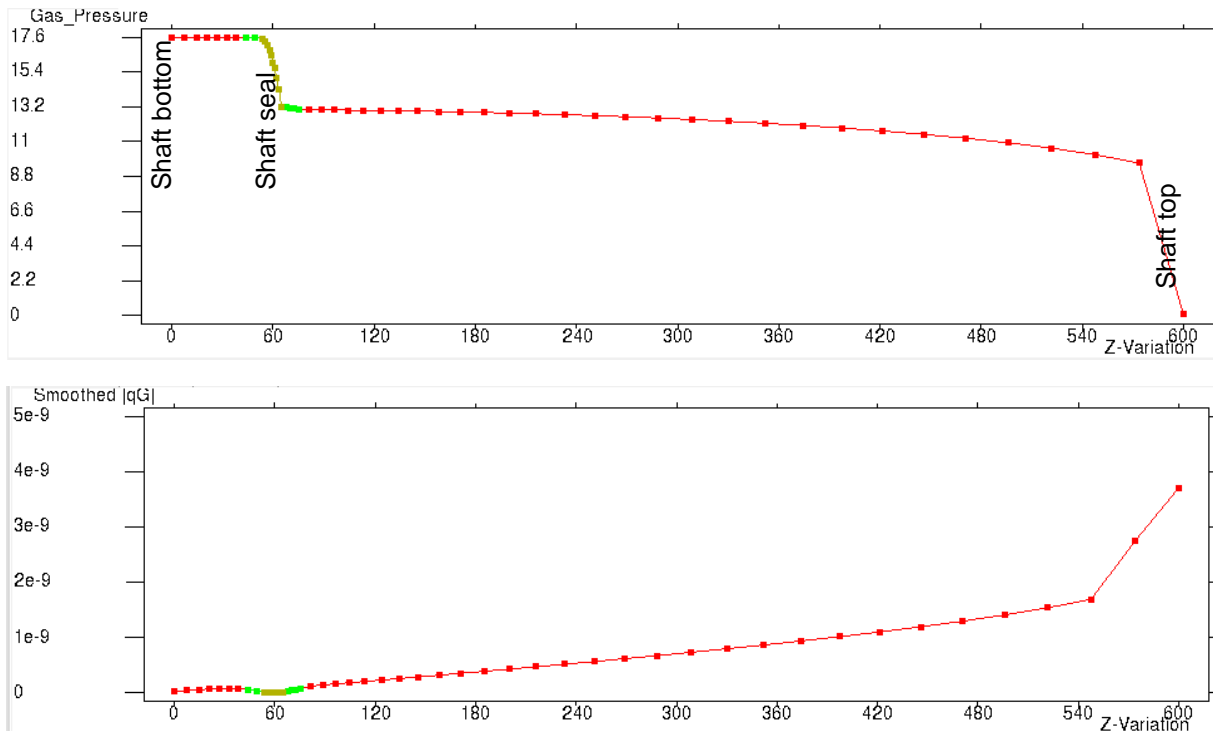


Figure 8-14: gas pressure (top), gas flux (middle) and water saturation (bottom) profile along the central line of the access gallery at 1E5 years

Figure 8-15 plots variable profiles along the shaft at the end of gas generation. The existence of gallery and shaft seals isolates the shaft from the rest repository. Gas produced in the shaft flows towards the shaft top. The gas pressure gradient over the shaft seal is quite large.



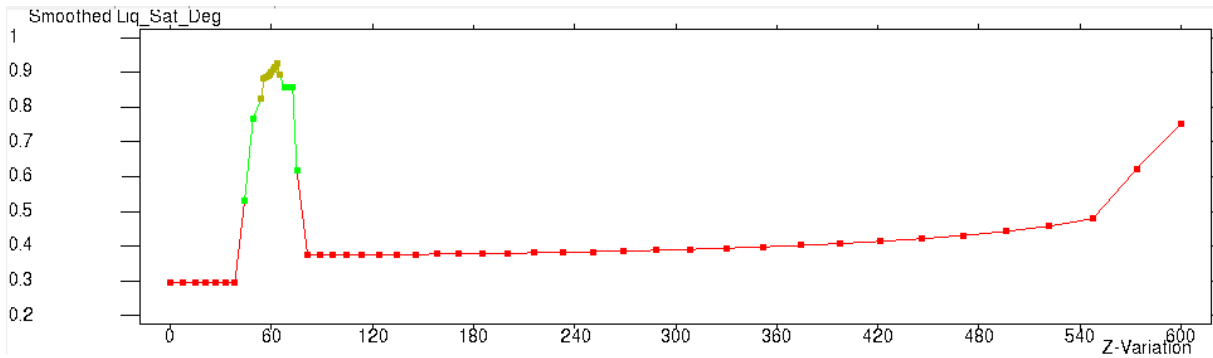
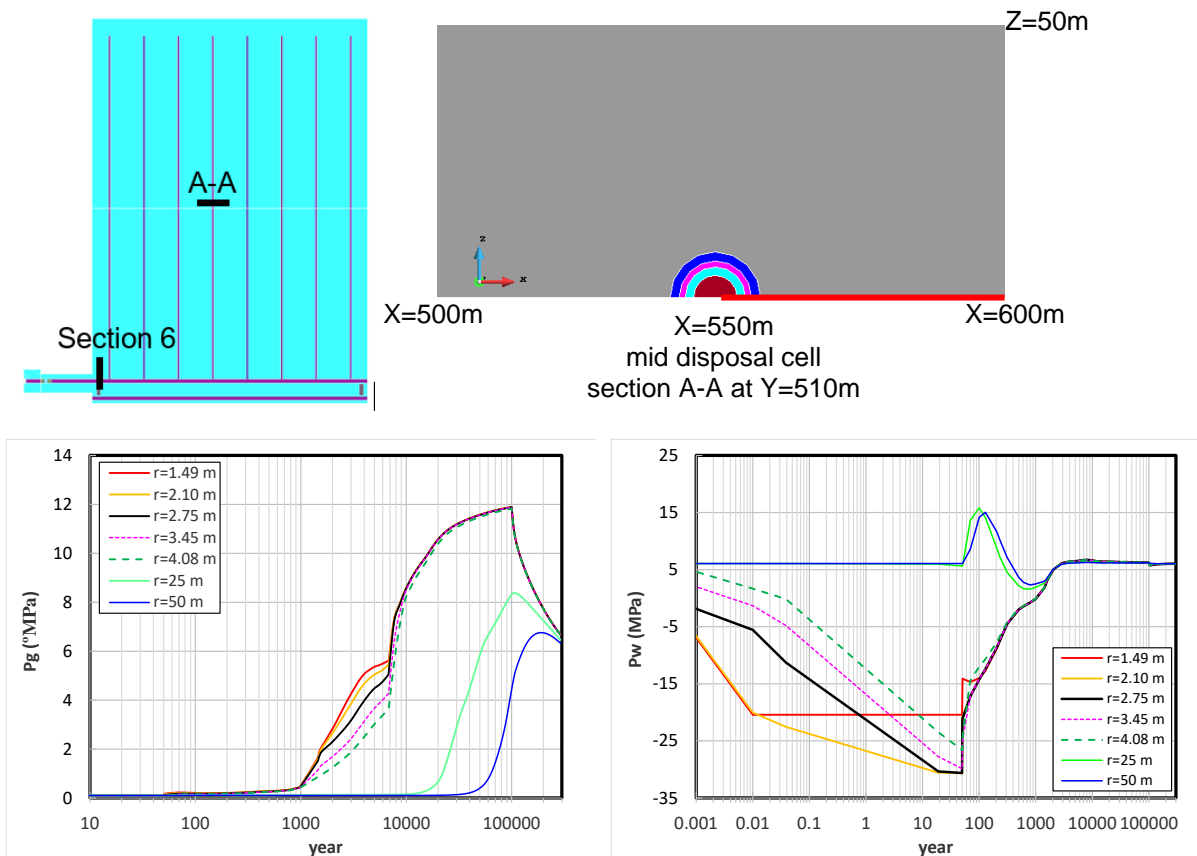


Figure 8-15: gas pressure (top), gas flux rate(middle) and water saturation (bottom) profile along the shaft

8.2.2.2 Results around the mid-point of the central disposal cell

Evolution of gas pressure, water pressure, temperature and water saturation are investigated around the mid-point of the central disposal cell , as marked in Figure 8-16.



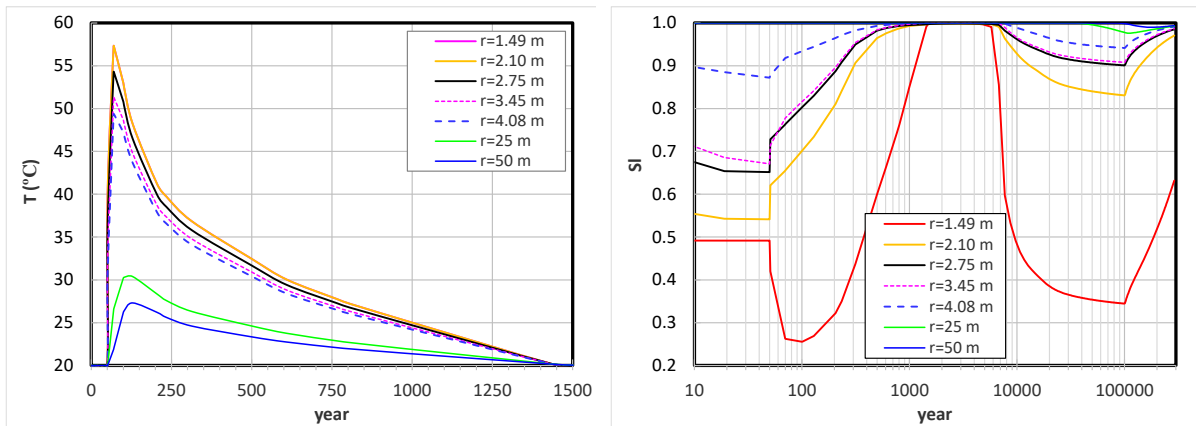


Figure 8-16: evolution of P_g, P_w, T and SI at seven points around the mid-point of the central disposal cell. The seven observation points locate along the red line marked in the uppermost graph.

8.2.2.3 Vector of gas flux

Figure 8-17 presents the advective gas flux integrated over the backfill (half circular backfill area) at 12 sections. Except the shaft top, four gallery sections: 4, 6, 9 and 10 (by-gallery) have the highest gas flux. Two sections close to gallery seal (7&8) have the lowest gas flux.

Regarding the gas flow in the gallery and disposal cells, results without considering gas produced in galleries and shaft (referred to as 2021 results hereafter) show that the gas produced in the disposal cells moves toward the access gallery. Results in Figure 8-18 considering both disposal cell and galleries and shaft (referred to as 2022 results hereafter) indicate that gallery gas dissipates along gallery, then into disposal cells where it drives the flow of disposal cell gas toward the far end of the disposal zone. While gas produced in the shaft is isolated by seals and dissipates steadily through shaft top exit. Obviously, gas flux through the shaft top steadily increases with gas production.

Figure 8-19 illustrates the gas flows along the by-gallery and afterwards enters into the disposal zone. Due to the blockage effect of gallery seal, all the gallery gas prefer flowing into the disposal zone. In the disposal zone, we take the central cell as an example, as shown in Figure 8-20. The higher gas production in galleries, determine that the gallery gas enters the disposal zone, driving disposal cell gas toward the end of the cells.

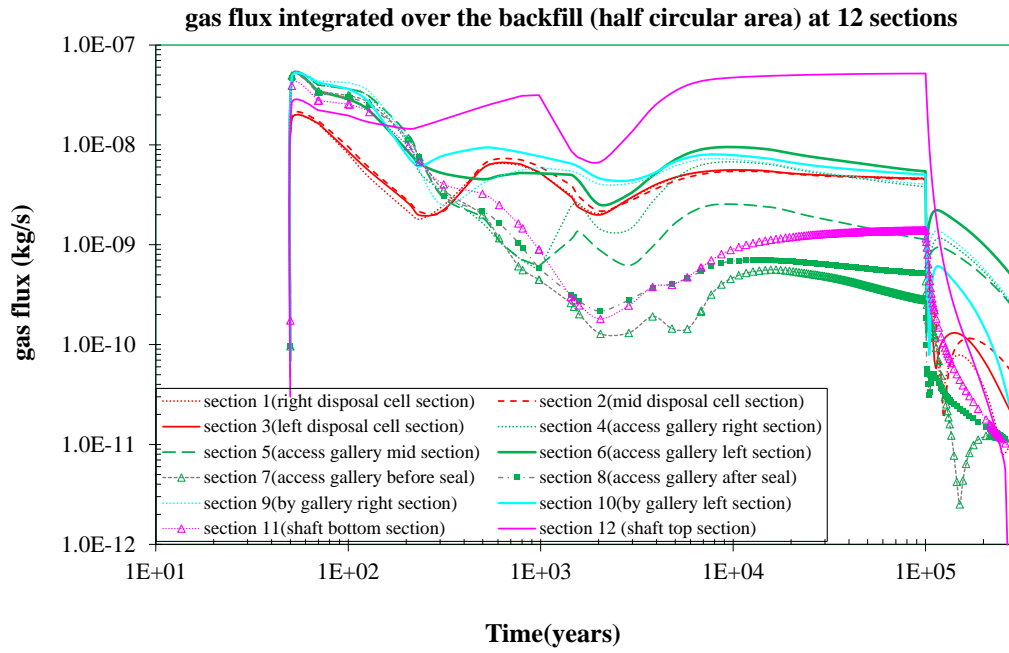


Figure 8-17: integrated advective gas flux through the backfill at 12 surfaces

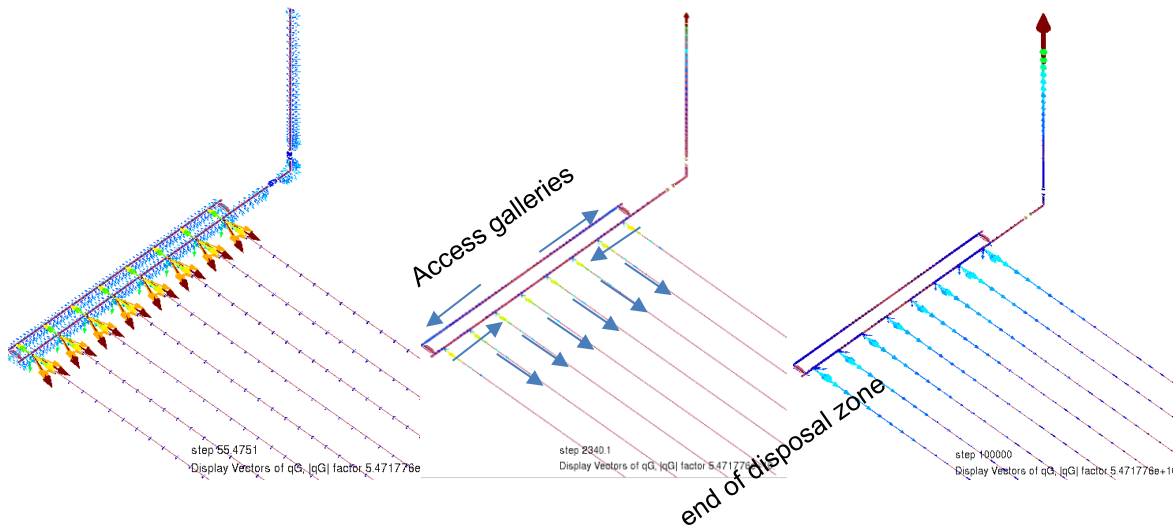


Figure 8-18: Vector of gas flux at 55 years(left), 2300 years (middle) and 1E5 years(right)

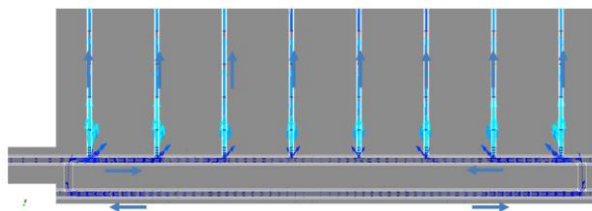


Figure 8-19: gas flux vector along access galleries: X=200-500m(left) x=700-1000m at 1E5 years

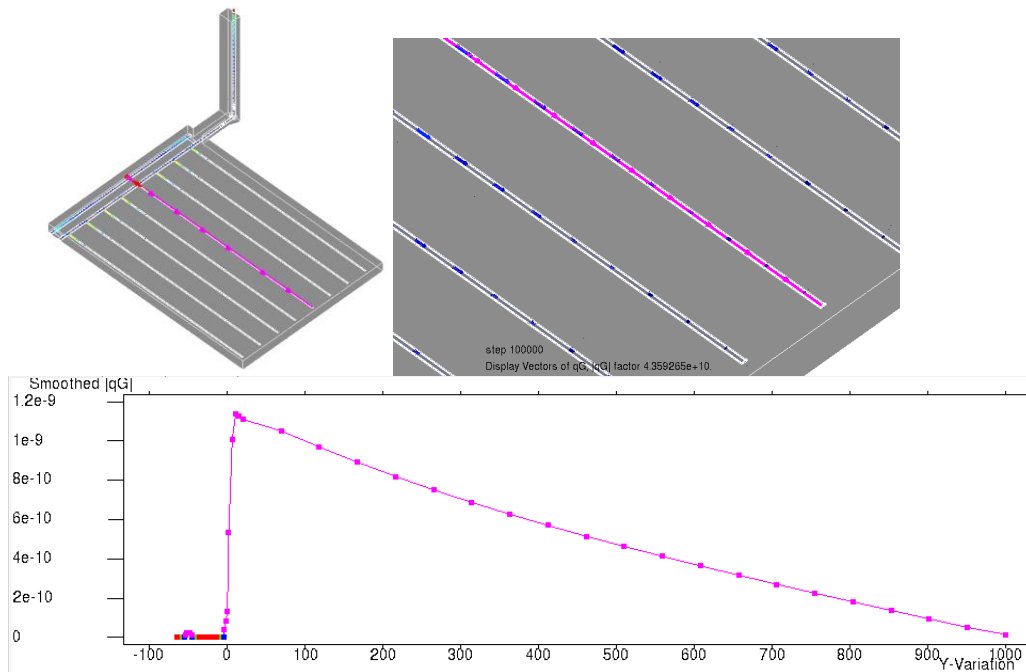


Figure 8-20: gas flux rate along the central cell (X=550) at 1E5 years

8.2.2.4 Gas flux in each material

The gas flux vector ($|q_g|$) in the mid-section of the central disposal cell at 1E5 years is demonstrated in Figure 8-21. Obviously, gas flows primarily along the backfill.

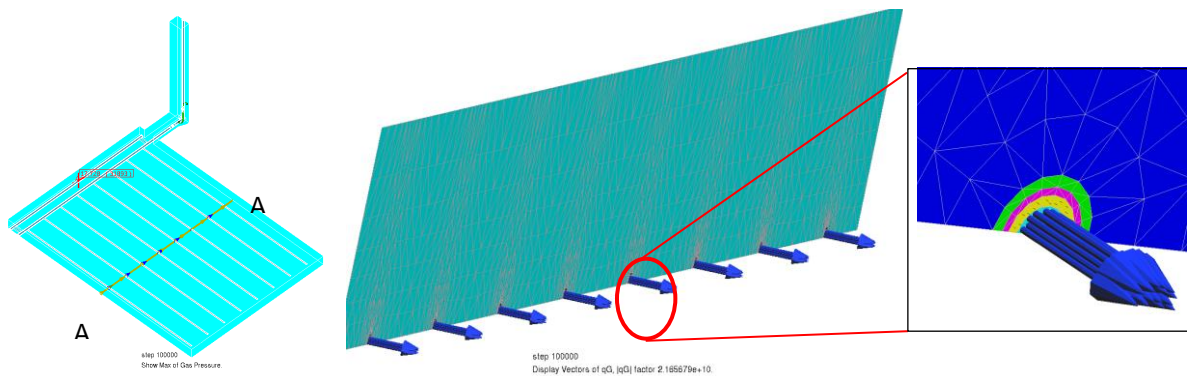


Figure 8-21: gas flux at the mid-section (Y=500 m) of disposal cells at 1E5 years, with materials from inner to outer are backfill, liner, inner_EDZ, outer_EDZ and host rock, respectively

Now we investigate quantitatively the advective gas flux through each material in the shaft. The gas production rate for the whole shaft is:

- $\frac{1}{2}$ section of shaft: $21.5 \text{ mol/yr/m} \times 0.002 \text{ kg/mol} \times 600 \text{ m} / 2 = 12.9 \text{ mol/year} = 4.1 \text{ E-7 kg/s}$
- The advective gas flux at the cross section close to the top exit integrated over the half section area is around 6.8 E-8 kg/s , as shown in Figure 8-22(right). Among the five materials, the majority (86%) flows within the backfill.

The total amount advective gas flux in the draft, i.e. 6.8 E-8 kg/s , is only 14% of the total gas produced in the shaft. This results implies that 14% of gas produced in the shaft flows advectively towards the shaft

exit, and the rest diffuses into the surrounding host rock. This observation is based on the boundary condition assumed for the shaft exit, where the top surface of the shaft remains saturated and prevents the gas flowing out. Results from the later model presented in section 8.6.2 where the top surface of shaft remains RH=80% lead to a completely different conclusion.

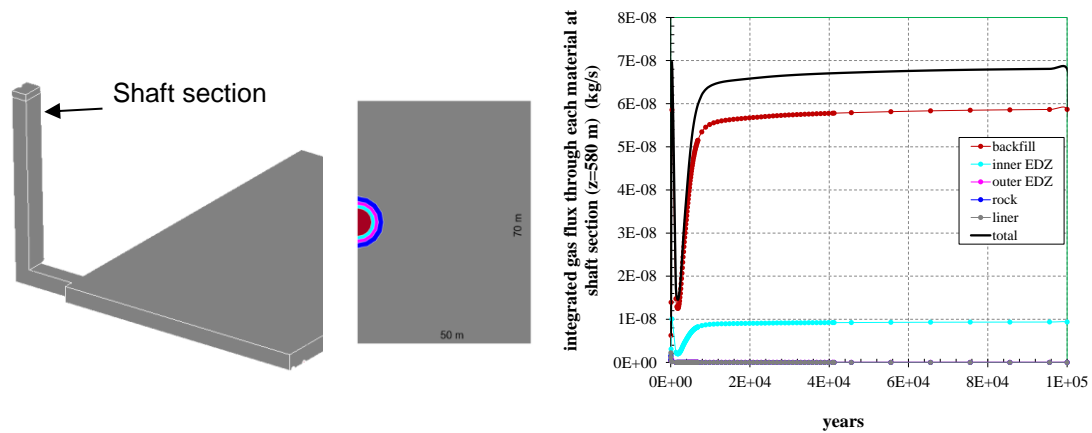
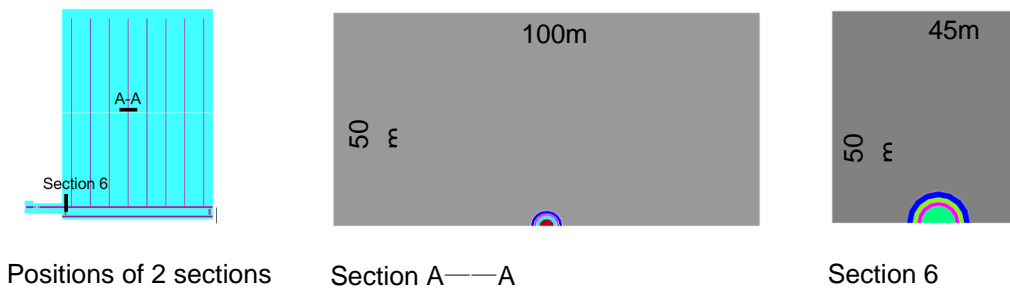
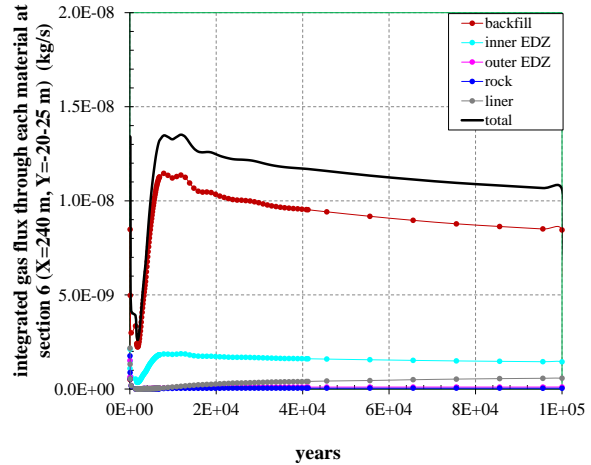
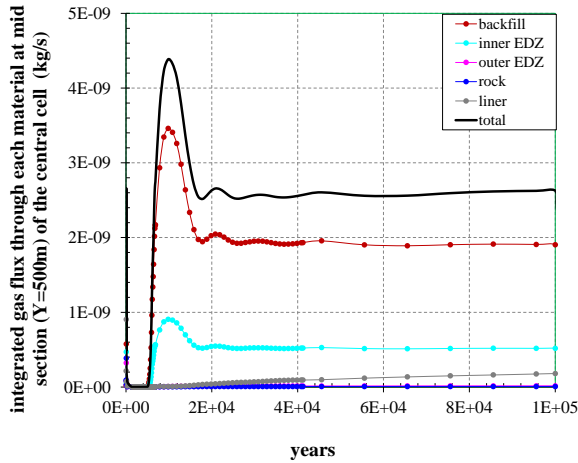


Figure 8-22: a horizontal cross section on the shaft at $z=580\text{m}$ (left) the cross sectional view (middle) integration of advective gas flux through the shaft cross section (right)

It is not straightforward to get a quantitative evaluation of gas flux in the repository due to the complex gas flows. We take two typical cross sections, as shown in Figure 8-23, as examples: section A-A is the mid-section of the central cell, and section 6 is chosen because it has the largest advective gas flux among the 12 sections under investigation. Gas fluxes at each section through various materials are presented in Figure 8-23. Compared to the total advective gas flux, the majority of gas flows along the backfill.





Section A—A

Section 6

Figure 8-23: advective gas flux through each material at section of one disposal cell (A-A) and one section at access gallery (section 6)

8.2.3 Impact of including gas production in galleries and shaft

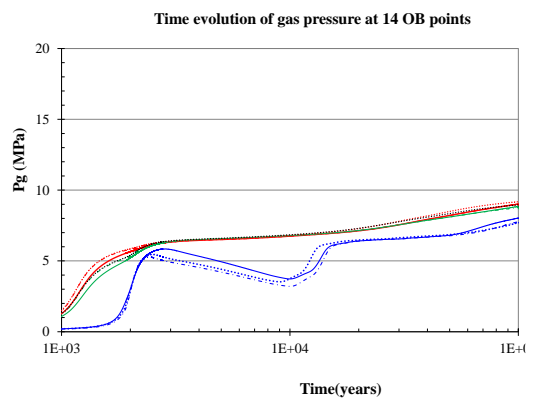
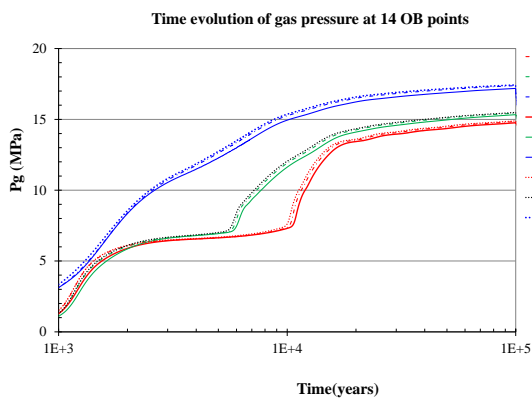
In the mid-term progress report of Milestone 174, only gas produced in disposal cells was considered (hereafter referred to as 2021 results). Simulations in year 2022 (hereafter referred to as 2022 results) considers gas produced in disposal cells, as well as gas produced in the access galleries and shaft.

The convergence problem encountered around 2400 years in 2021 results disappears in the 2022 results. This is consistent to previous findings in 2021 report, i.e. the case with a 100-time higher gas production rate in disposal cells has better convergence. The increased gas quantity makes the EBS harder to get re-saturated, and unsaturated gas dissipation pathways easier to maintain, resulting in a better numerical convergence.

The impacts of adding gallery gas on gas pressure at 14 observation points are shown in Figure 8-24. The gas pressure in the whole system increases dramatically compared to 2021 results, due to the enormous amount of gas produced in the access galleries and shaft.

2022 results

2021 results



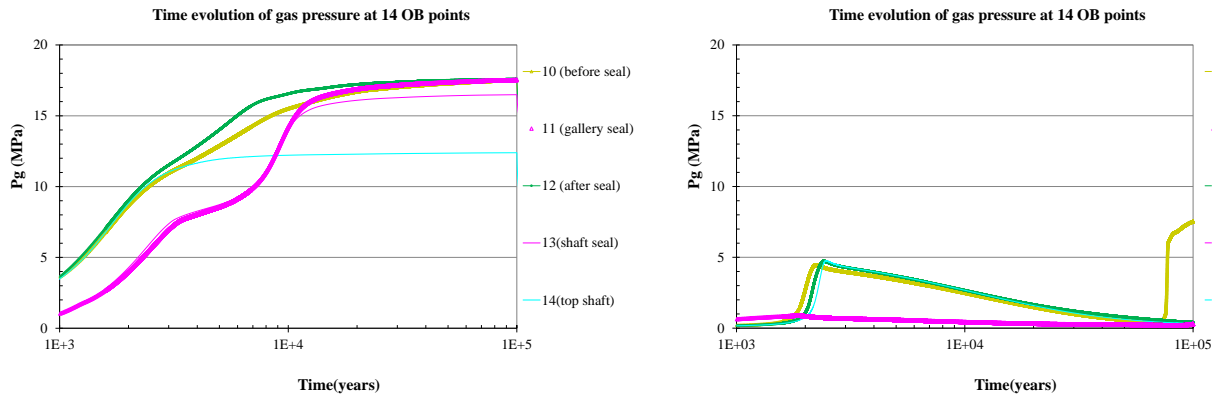


Figure 8-24: impact of including access gallery and shaft gas production on the gas pressure

8.2.4 Sensitivity of seal permeability

One alternative case considering bentonite with 100 times higher permeability is calculated to investigate the impact of seal permeability. Overall, the impact on gas pressure in the disposal zone is negligible. The gas pressure in the seal itself increases earlier than the base case, as shown in Figure 8-25. With a higher permeability of seal, more gas flows past the seal to the shaft top exit as shown in Figure 8-26.

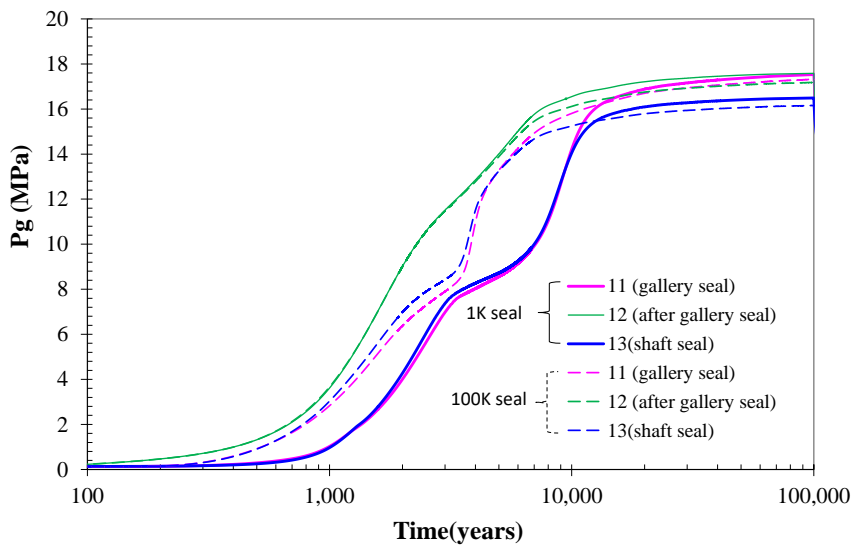


Figure 8-25: Comparisons of gas pressure around seals between the base case and an alternative case with 100 times higher permeability for the seal bentonite.

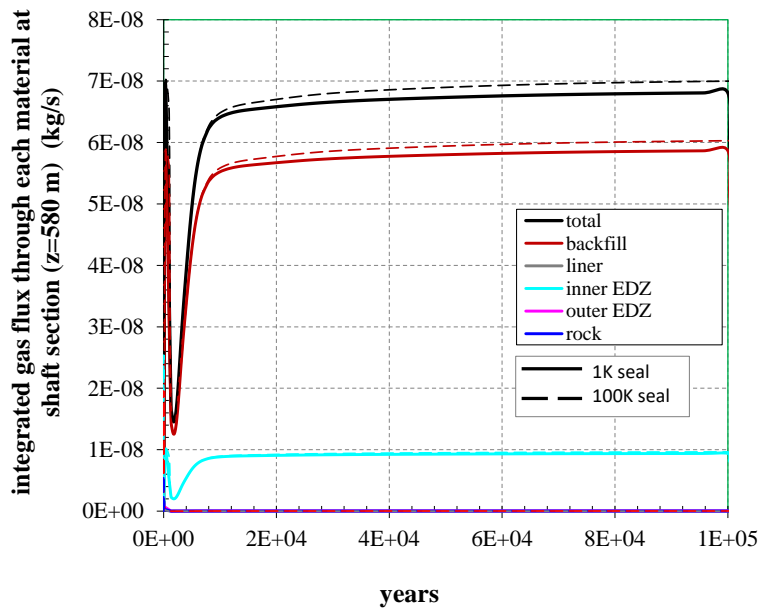
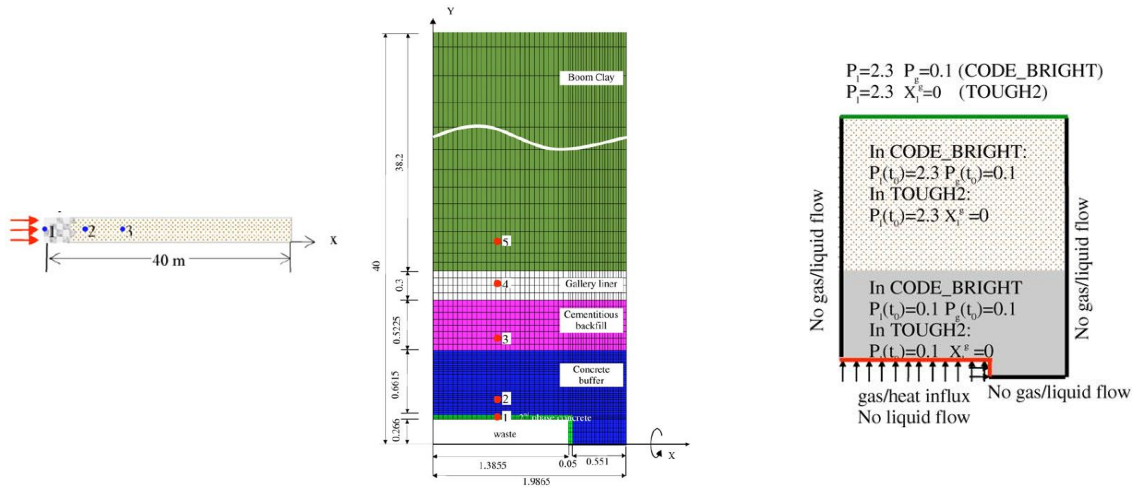


Figure 8-26: Comparisons of gas flux at shaft section ($Z=580\text{m}$) between the base case and an alternative case with 100 times higher permeability for the seal bentonite.

8.3 Development and verification of two-phase flow model in COMSOL

The two-phase flow model is implemented in the general-purpose commercial software package COMSOL Multiphysics. COMSOL is selected for the development because its user-friendly interface and its powerful internal modules. The two-phase flow model results from a combination of a set of governing equations regarding liquid, gas and heat transport and constitutive equations. The gas phase is a mixture of hydrogen and water vapor, and the liquid phase is water with dissolved hydrogen. COMSOL modules and physics interfaces are adopted to take account of the relevant physical processes involved in thermo-hydro-gas coupling analysis, such as diffusive transport of dissolved gas and vapor, advective transport of dissolved gas and gaseous gas, advective transport of pore water and vapor, and heat transfer. Essential changes are made to the internal variables of the physics interfaces either explicitly or in the weak form to ensure consistency in the evaluation of enriched solution fields. Currently, there are still several missing features in the COMSOL model, such as dry air in the gas mixture and the binary diffusion of multiple gas components.

In the absence of validation data for the complex problem of gas generation and transport in geological repositories, the confidence of the validity of the numerical tool in solving THG (thermo-hydro-gas) coupling problems was achieved by comparing benchmark results between various codes. Three exercises from 1D HG, 2D HG to 2D THG as depicted in Figure 8-27, were used to compare results from Code_Bright and TOUGH in solving THG problems (Yu et al. , 2011). The same three exercises are to be used in this section to compare results from Code_Bright and COMSOL. Parameters for various materials and constitutive laws used in the model can be found in Yu et al. (2011).



exercise 1 (1D HG) exercise 2 (2D-axisymmetric HG) & exercise 3 (2D-axisymmetric THG) Initial and boundary conditions
 Figure 8-27: schematic diagrams for three verification exercises used in Yu et al. (2011).

8.3.1 Exercise 1—1D HG problem

The 1st exercise is 1D gas-induced desaturation of an initially fully saturated system by a constant gas injection rate at the left boundary, as illustrated in the left figure of Figure 8-27. Comparisons of water and gas pressure at two observation points are depicted in Figure 8-28. Perfect agreements are obtained between Code_Bright and COMSOL.

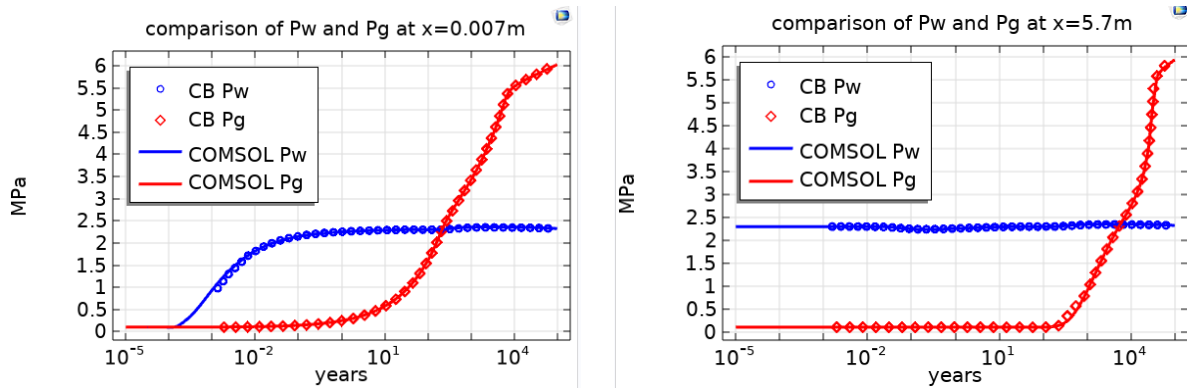


Figure 8-28: Result comparisons between COMSOL and Code_Bright for a 1D HG problem at two observation points (dots are from Code_Bright and lines are from COMSOL).

8.3.2 Exercise 2—2D-axisymmetric HG problem

The 2nd exercise is a 2D-axisymmetric gas-induced desaturation of an initially fully saturated system (with initial water pressure of 2.3MPa in clay (green domain) and 0.1MPa in the EBS system, initial gas pressure is 0.1MPa in the whole domain). A constant gas injection rate is assigned at $r=0.266\text{m}$. Result comparisons between Code_Bright and COMSOL at five points are presented in Figure 8-29.

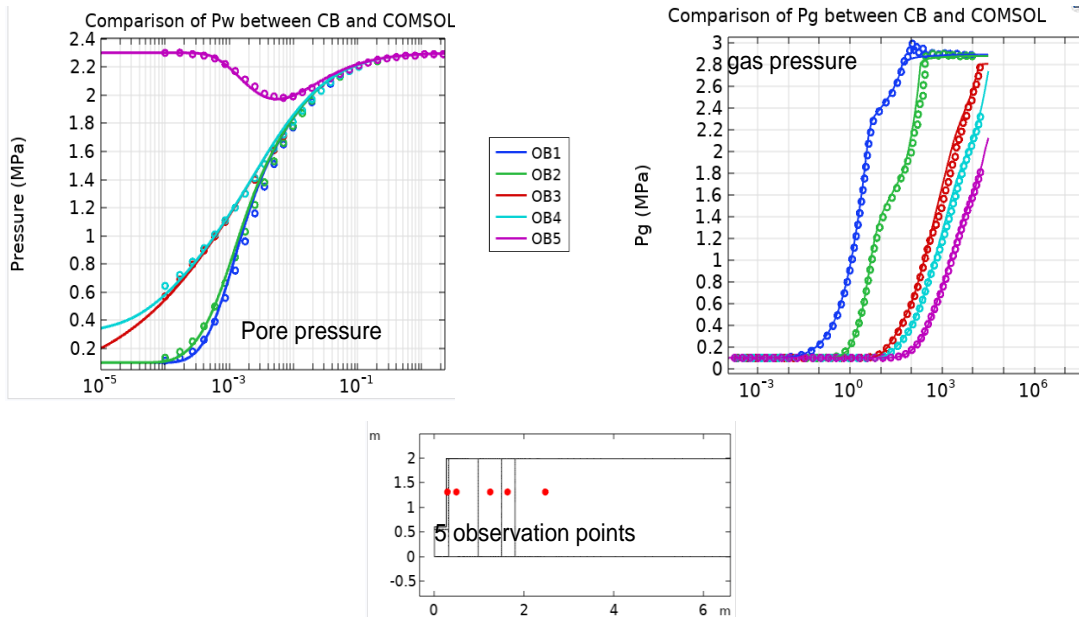
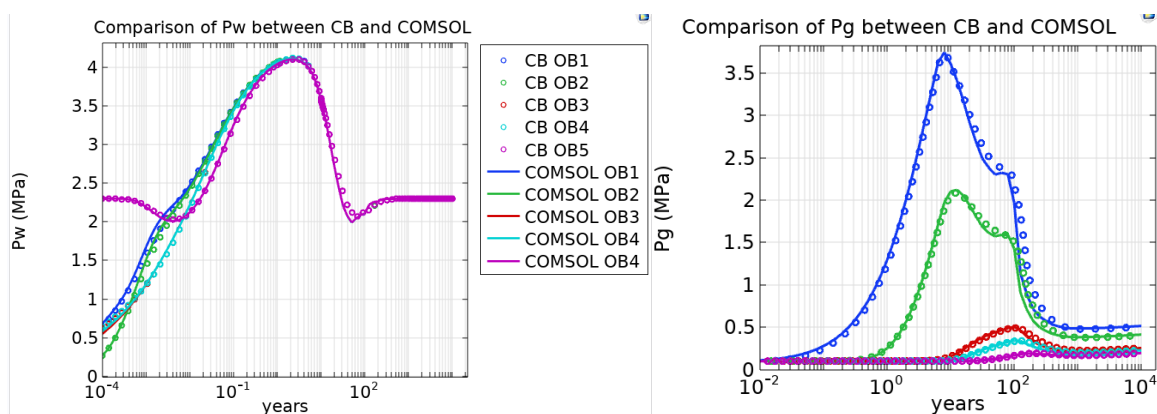


Figure 8-29: Result comparisons between COMSOL and Code_Bright for a 2D-axisymmetric HG problem at five observation points (dots are from Code_Bright and lines are from COMSOL).

8.3.3 Exercise 3—2D THG problem

The constant gas injection rate in the 2nd exercise is replaced with a decaying gas production rate and a decaying heat power (please refer to in Yu et al. (2011) for details). The system is initially saturated with a temperature of 15.7°C. The decaying gas injection and heat power are assigned at $r=0.266\text{m}$. Result comparisons between COMSOL and Code_Bright are presented in Figure 8-30. The comparisons are very similar to the comparison between Code_Bright and TOUGH presented in Yu et al. (2011). Because the source code of TOUGH could not be altered, we tried to match the constitutive laws and parameters between the two codes as well as possible. While in the development of the two-phase model in COMSOL, except the solver, all constitutive laws and parameters have been made exactly the same as those in Code_Bright.



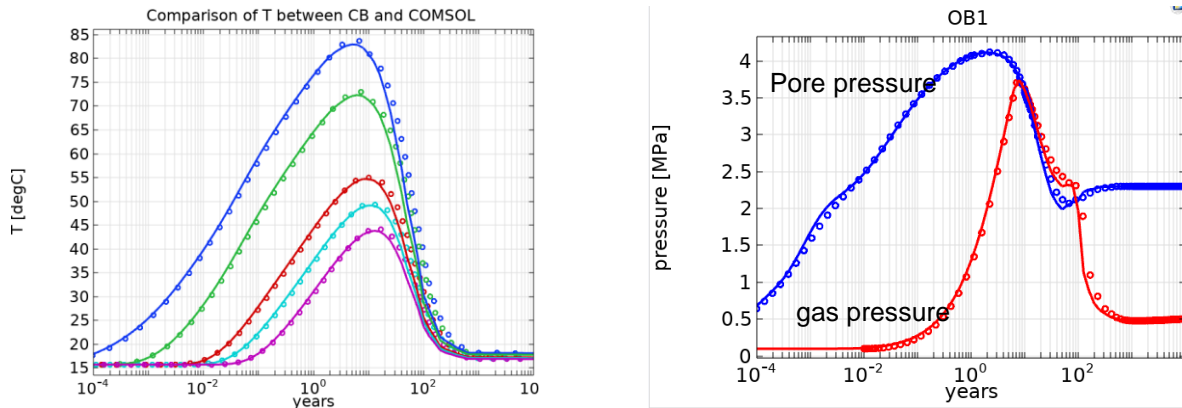


Figure 8-30: Results comparison between COMSOL and Code_Bright for a 2D-axisymmetric THG problem (dots are from Code_Bright and lines are from COMSOL).

8.4 Modelling results of the 2D-PS EURAD model from COMSOL

Following the three verification exercises mentioned above, the comparison between Code_Bright and COMSOL has further been elaborated using a 2D-PS TH(M)g case specific for the EURAD GAS project. After the comparison between two numerical tools, parameter sensitivities based on the 2D-PS model are presented in this section. No verification was made for the 3D full model of Zone B due to the fact that 3D modelling at repository scale is memory-demanding in COMSOL, and time-consuming in Code_Bright.

8.4.1 Description of the EURAD 2D-PS TH(M)g problem

A 2D plain strain (PS) model as shown in Figure 8-31 is set up for the EURAD GAS project. The same model is built in COMSOL and Code_Bright independently. The time duration of the thermal load applied in 2D-PS model extends from 1500 years to 3000 years (see Figure 8-32).

The geometry includes the upper and bottom aquifer and a vertical section of a half disposal cell with x varying from the center of the cell ($x=0$) and mid-point of two cells ($x=50\text{m}$). The horizontal boundaries at $x=0$ and 50 m are symmetry lines and set as impermeable boundaries. The top ($z=600\text{ m}$) and bottom ($z=-400\text{ m}$) boundaries are prescribed with constant water/gas pressures and temperature. The thermal load is applied at the intrados of the liner ($r=1.8\text{ m}$). The thermal load per meter of canister in zone B (length of canister of overpack 2.75 m), is equivalent to a surface thermal load acting at the inner surface of the liner ($r=1.8\text{ m}$) per m disposal cell: $\frac{J_E \times 2.75\text{m} / 4.254\text{m}}{2\pi \times 1.8\text{m}}$, as shown in Figure 8-32 right.

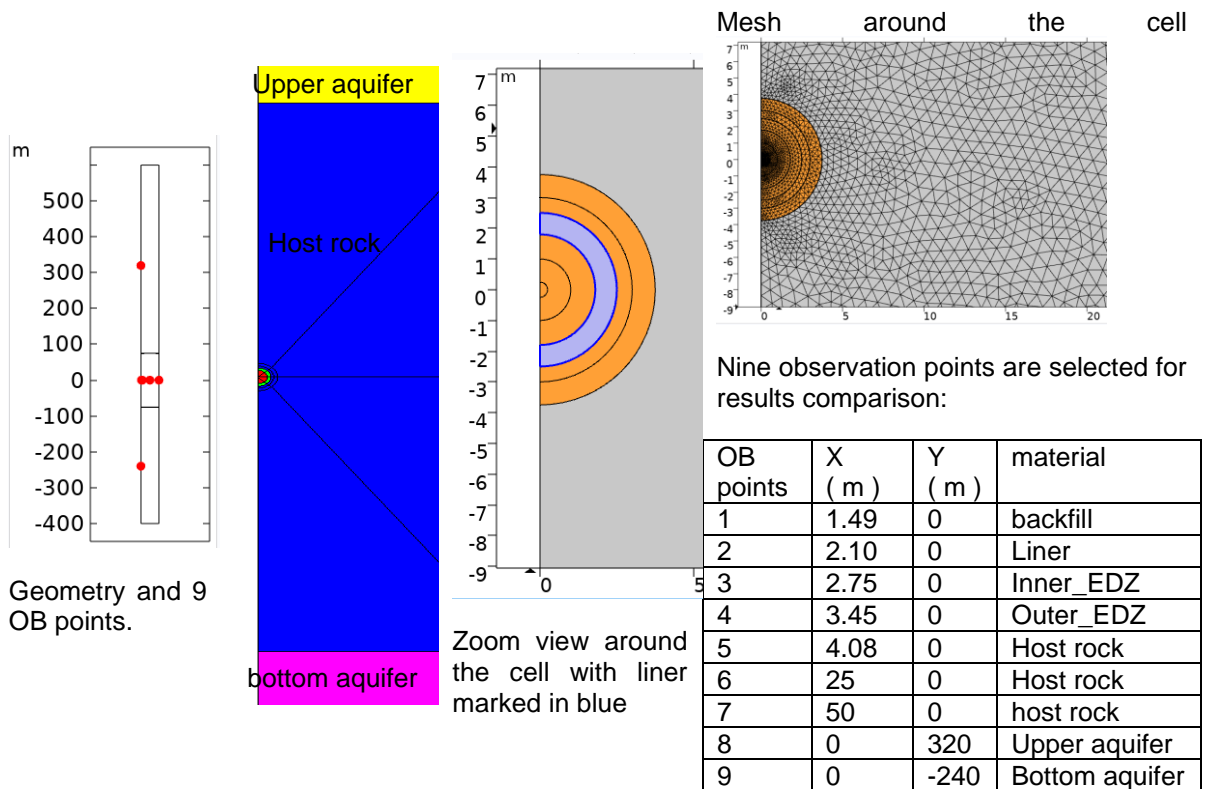


Figure 8-31: EURAD 2D-PS THG model geometry, mesh and observation points.

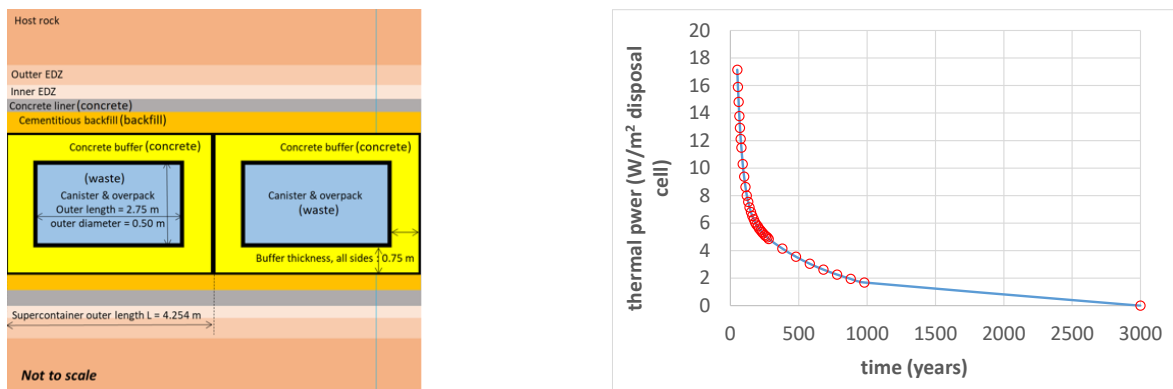


Figure 8-32: Thermal source term per meter of disposal cell in zone B (lasting from 50 years to 3000 years)

Initial conditions:

backfill ($r < 1.8$ m)	$P_w = -0.8685$ MPa (RH=80%), $P_g = 0.1$ MPa, $T = 25^\circ\text{C}$
liner ($r = 1.8$ - 2.5 m):	$P_w = P_g = 0.1$ MPa, $T = 25^\circ\text{C}$
bottom aquifer from $y = -400$ m to $y = -75$ m:	P_w linearly distributed between 10.25 - 7 MPa $p_g = 0.1$ T linearly distributed between 35°C - 27°C
Disposal cell locates within the host rock which is from $y = -75$ m to $y = 75$ m	P_w linearly distributed between 7 - 5.35 MPa $p_g = 0.1$ T linearly distributed between 27°C - 23°C
upper aquifer $y = 75$ m- 600 m:	P_w linearly distributed between 5.35 - 0.1 MPa $p_g = 0.1$ T linearly distributed between 23°C - 10°C

Boundary conditions:

At liner intrados $r = 1.8$ m (intrados of the liner)	with the time varying surface thermal load during 50-3000 years with a constant surface gas injection rate during 50- $1e5$ year, 0.25 mol/yr/m in disposal cells
At the top $y = 600$ m	$T = 10^\circ\text{C}$, $P_g = 0.1$ MPa, $P_w = 0.1$ MPa
At the bottom $y = -400$ m	$T = 35^\circ\text{C}$, $P_g = 0.1$ MPa, $P_w = 10.25$ MPa
all the rest boundaries are set impermeable.	

modelling phases:

0-0.01 day: Instantaneous excavation	The backfill does not exist $T = 25$, $P_w = P_g = 0.1$ MPa at liner intrados (at $r = 1.8$ m)
0.01 day -50 years: the whole repository with a relative humidity of 80%	a constant suction of 30.7 MPa at the intrados of liner (corresponding to a relative humidity of 80%). $T = 25$, $P_w = -30.7$ & $P_g = 0.1$ MPa at liner intrados (at $r = 1.8$ m)
50- $1E5$: Instantaneous emplacement of backfill, with an instantaneous gas injection at a constant rate and thermal load on the liner intrados	$J_g = 0.25$ mol/yr/m at $r = 1.8$ m) adding thermal load and gas injection rate at $r = 1.8$ m
1E5-3E5: Gas production stops	$J_g = 0$

Material properties:

A 2D-PS THG reference case as defined in Table 8-4 is used for the code verification and sensitivity analysis. To ease the task, the following simplified aspects are used in the reference case:

- Porosity remains constant;
- the thermal expansion of solid grains and matrix is excluded;
- the porous compressibility is excluded;
- the vapor effect is excluded.

Table 8-4: Material properties used in the 2D PS THG model (the reference case)

parameter		Unit	Host rock			backfill	liner
			Undisturbed	Outer EDZ	Inner EDZ		
Porosity0	θ_0	-	0.2			0.4	0.15
capillary pressure VG model							
shape parameter	n	-	1.5				
shape parameter $m=1-1/n$	m		0.333				
fitting parameter	P_0	MPa	23	17	16	1	10
Intrinsic permeability of water	K_{in}	m ²	1E-20	1E-18	1E-16	1E-16	1E-16
Relative permeability of water	k_{rw}		$(1 - (1 - S_{e,w}^{1/m})^m)^2 \sqrt{S_{e,w}}$				
Relative permeability of gas	k_{rg}		$fg(1 - S_{e,w})^3$				
	fg	-	100	10	1	1	1
Viscosity of water	μ_l	MPa · s	$22.1E - 12 * \exp(\frac{1808.5}{T[K]})$				
Viscosity of gas	μ_g	MPa · s	$0.88E - 11$				
Liquid density	ρ_w	Kg/m ³	$\rho_0 \exp(\beta_w(P_w - P_{ref}) + \alpha_w T[^\circ\text{C}])$				
Water compressibility	β_w	1/MPa	4.5E-4[1/Pa]				
	ρ_0	Kg/m ³	1002.6				
	P_{ref}	MPa	0.1				
volumetric thermal expansion coefficient of water	α_w	1/K	-3.4E-4				
diffusion coefficient of dissolved gas	D_0	m ² /s	5E-10				
Henry's coefficient	H	MPa	7215				
Molar mass of hydrogen		kg/mol	0.002				
Molar mass of water		kg/mol	0.018				
Thermal parameters							
Heat conductivity (w/m/°C)			1.7			1.3	2.3
specific heat of solid phase	C_s	J/Kg/°C	720			500	900
Solid density	ρ_s	kg/m ³	2639				
Bulk specific heat	C_{bulk}	J/Kg/°C	$(\rho_s C_s (1 - \theta) + \rho_w C_w \theta S_e) / \rho_{bulk}$				
Bulk density	ρ_{bulk}	kg/m ³	$\rho_s (1 - \theta) + \rho_w \theta S_e$				
the properties of the upper and below aquifers are considered the same as the host rock.							
Canister and buffer are replaced in the calculation with backfill.							
The effect of vapor is not considered in the reference case.							

8.4.2 Result comparisons between COMSOL and Code_Bright for the reference 2D-PS THG model

The THG reference model as described in 8.5.1 is established in Code_Bright and COMSOL, separately. The COMSOL model consists of 10345 triangle elements, and the calculation runs in less than 10 minutes. The Code_Bright model has 5100 quadrilateral elements and it costs more than 6 hours to finish the calculation. The long calculation time in Code_Bright is because the time stepping is strictly restricted in order to avoid any convergence problem. Results from Code_Bright and COMSOL agree very well. Comparisons for water/gas pressure, temperature and water saturation for the reference case are illustrated in Figure 8-33.

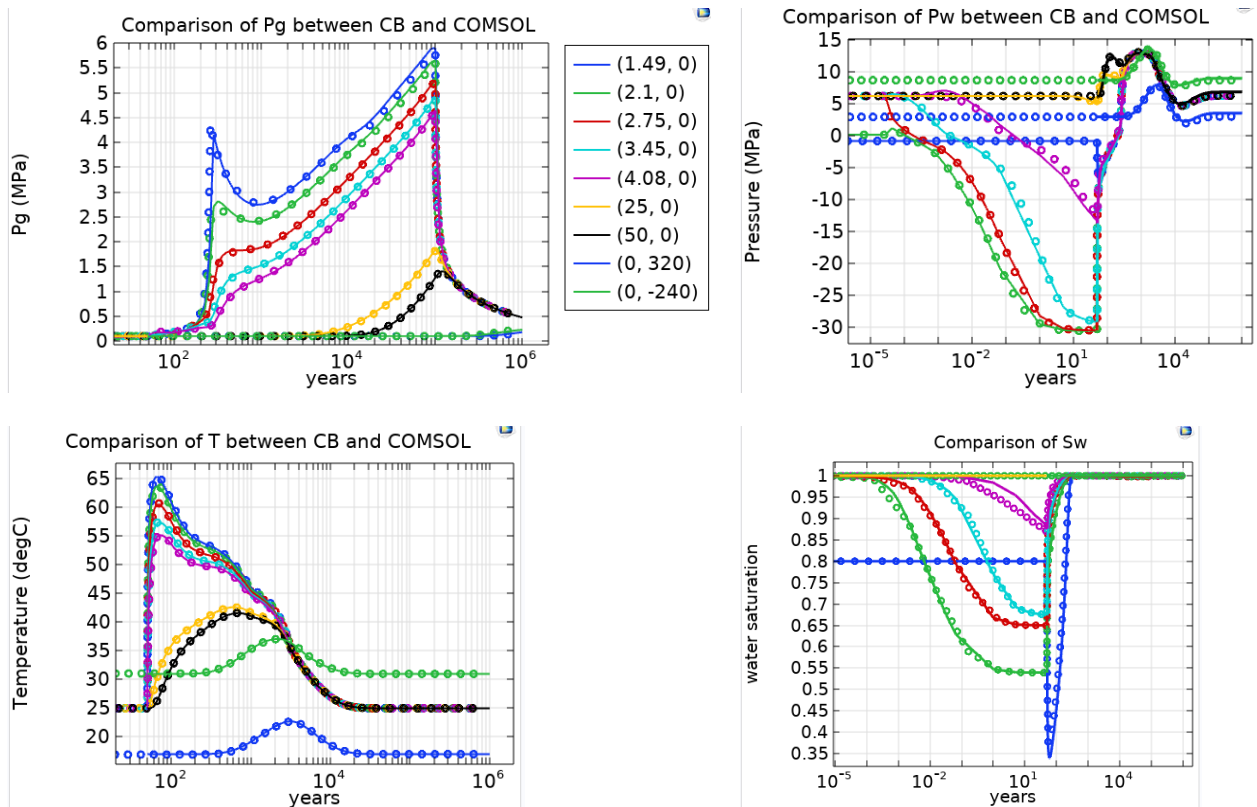


Figure 8-33: Result comparisons between COMSOL and Code_Bright for the 2D-PS THG reference case (dots are for Code_Bright and lines for COMSOL).

During the ventilation period ($t < 50$ years), water pressure in the near field of the gallery keeps decreasing. When the thermal power and gas injection start at 50 years, water pressure increases with the increased temperature. The maximum temperature reaches 65°C in the backfill. The system starts to become saturated at 280 years. After the first peak of gas pressure at the start of the thermal loading, the gas pressure keeps increasing and reaches its peak at the end of gas injection.

From the next section onwards, some sensitivity analysis have been done using COMSOL model.

8.4.3 Sensitivity of the diffusion coefficient of dissolved hydrogen

In the reference case, a constant diffusion coefficient $D_0 = 5 \times 10^{-10} (\text{m}^2/\text{s})$ for the dissolved gas is used: $\nabla \cdot (-D_0 \theta S_w \rho_w \nabla(\omega_l^a))$, where ω_l^a is the fraction of air in the liquid phase, θ is the porosity of the material, S_w is the water saturation degree and ρ_w is water density. Figure 8-34 compares gas pressure at the backfill observation point (1.49,0) for four cases with various D_0 values. Comparisons indicate that gas pressure is very sensitive to the value of D_0 .

Figure 8-34 also compares results for using Millington-Quirk diffusion for dissolved air: $\nabla \cdot (-D_0 \theta^{1+a} S_w^b \rho_w \nabla(\omega_l^a))$ where $D_0 = 5 \times 10^{-9} (\text{m}^2/\text{s})$. The Millington-Quirk diffusion considers a water saturation and porosity dependent tortuosity. The a and b values are defined in the EURAD gas T4.2 specifications for each material.

This result indicates that the relationship between effective diffusion coefficient and θ and S_w is one of the key factors for gas dissipation.

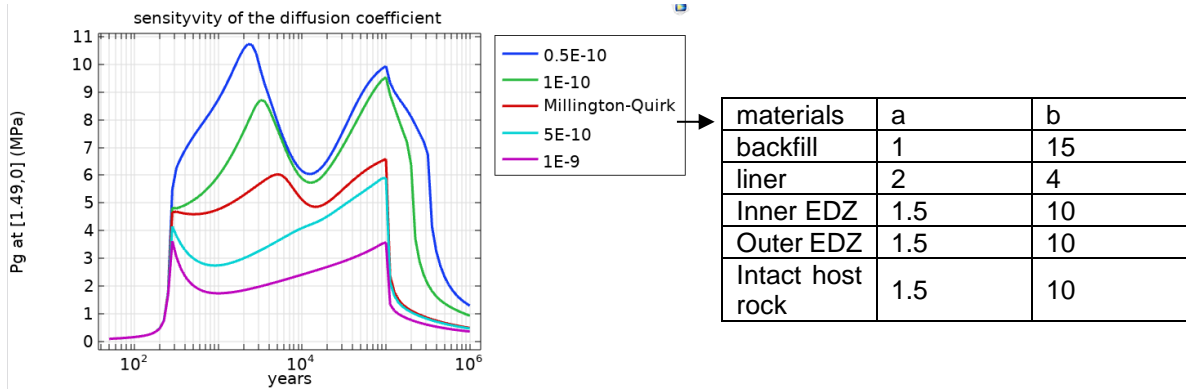


Figure 8-34: impacts of various diffusion coefficients on the gas pressure at the backfill point (1.49,0)

8.4.4 VG Retention curve

The exercise specifies the following modified Van-Genuchten(VG) retention formulations, where besides the fitting parameter of P_r and n , an explicit smaller gas entry pressure P_e is included, together with linearized treatment in the vicinity of saturation point:

$$P_c = \begin{cases} -\frac{1}{\alpha} \left((S_e^* S_e)^{-\frac{1}{m}} - 1 \right)^{\frac{1}{n}}, & \text{if } S_e \leq 1 - \varepsilon \\ -\frac{1}{\alpha} \left((S_e^* S_e)^{-\frac{1}{m}} - 1 \right)^{\frac{1}{n}} \cdot \frac{1 - S_e}{\varepsilon}, & \text{if } (1 - \varepsilon) < S_e < 1 \\ 0, & \text{if } S_e = 1 \end{cases}$$

With: $S_e^* = (1 + (\alpha p_e)^n)^{-m}$ and $m=1-1/n$, $\alpha = 1/P_r$. ε is a numerical parameter that should be small, in the order of 0.01 or 0.001, f_g is the ratio between gas permeability (m^2) and water permeability (m^2).

parameter	symbol	Unit	Host rock			backfill	liner	
			Undisturbed	Outer EDZ	Inner EDZ			
shape parameter	n	-	1.5					
shape parameter $m=1-1/n$	m		0.333					
VG parameter	P_r	MPa	16			1	10	
VG parameter	P_e	MPa	6	2	0	0	0	
Intrinsic permeability of water	K_{in}	m^2	1E-20	1E-18	1E-16	1E-16	1E-16	
Relative permeability of water	k_{rw}		$k_{rw} = \begin{cases} \sqrt{S_e} \cdot \left[\frac{1 - (1 - (S_e^* S_e)^{1/m})^m}{1 - (1 - S_e^{*1/m})^m} \right]^2, & \text{if } S_e < 1 \\ 1, & \text{if } S_e = 1 \end{cases}$					
Relative permeability of gas	k_{rg}		$k_{rg} = \begin{cases} f_g \cdot \sqrt{1 - S_e} \cdot \left[\frac{(1 - S_e^{*1/m})^m - (1 - (S_e^* S_e)^{1/m})^m}{(1 - S_e^{*1/m})^m - 1} \right]^2, & \text{if } S_e < 1 \\ 0, & \text{if } S_e = 1 \end{cases}$					
	f_g	-	100	10	1	1	1	

Figure 8-35 compares results from the reference model in Table 8-4 and the linearized VG model stated in this section. In spite of the differences in the retention curves near saturated point, comparison shows that the impacts are mainly on the pore water pressure during the ventilation stage.

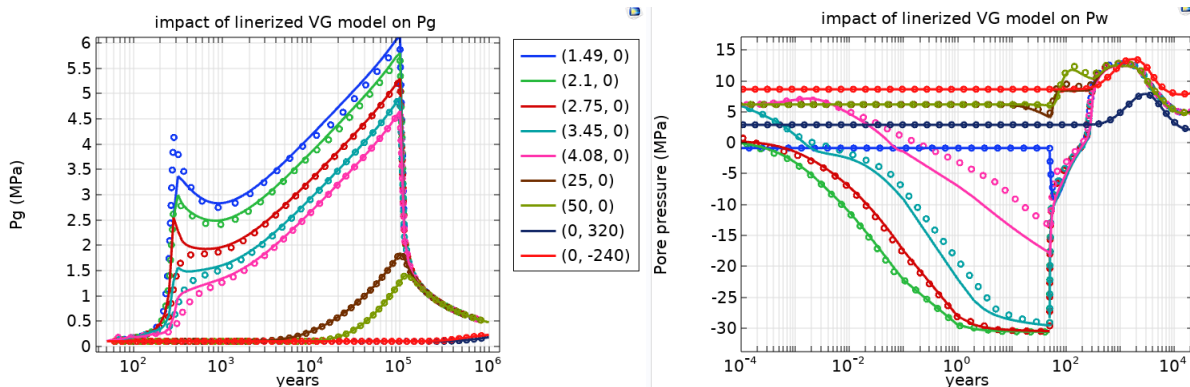


Figure 8-35: comparisons between VG model in Table 8-4 (circles) and linearized VG model (solid lines)

8.4.5 Effect of porosity variation induced by the thermal expansion

Thermal expansion of solid grains and solid matrix are not considered in the reference case and the porosity remains constant. Coupling of thermal load means including thermal-induced porosity variation in the HG model. In this section, two alternative cases are introduced to check the impact of different thermal-induced porosity variations on the gas dissipation:

- Case 1 only considers the thermal expansion of solid grains in a rigid solid matrix, and the porosity variation is $\Delta\theta = -\alpha_s\Delta T(1 - \theta_0)$, where α_s is volumetric thermal dilation coefficient and equal to $3e-5$ (1/°C).
- Case 2 considers the thermal expansion of both solid grains and solid matrix, assuming they have the same thermal expansion coefficient. The porosity variation is calculated as $\Delta\theta = +\alpha_s\Delta T\theta_0$.

Figure 8-36 compares the porosity variations induced by the thermal expansion between case 1 and case 2. For a rigid solid matrix as case 1, porosity decrease is due to the thermal expansion of solid grains; while for a deformable solid matrix such as case 2, porosity increase is a combined effect of expansion of both solid matrix and solid grains.

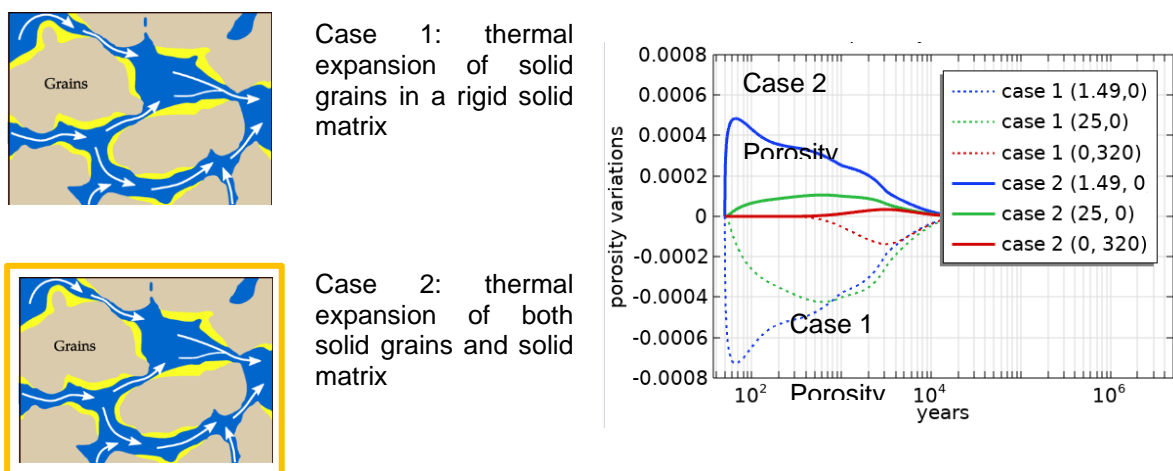


Figure 8-36: impacts of thermal expansion on porosity variation

Impact of thermal expansion on water pressure and gas pressure at three observation points is compared between the reference case, case 1 and case 2 in Figure 8-37. The comparison indicates that the thermal effects on the pore water pressure are more significant than on the gas pressure. The increased porosity in case 2 (solid line) lowers the water pressure, and the decreased porosity in case 1 significantly increases the water pressure, while affect not so much on the gas pressure.

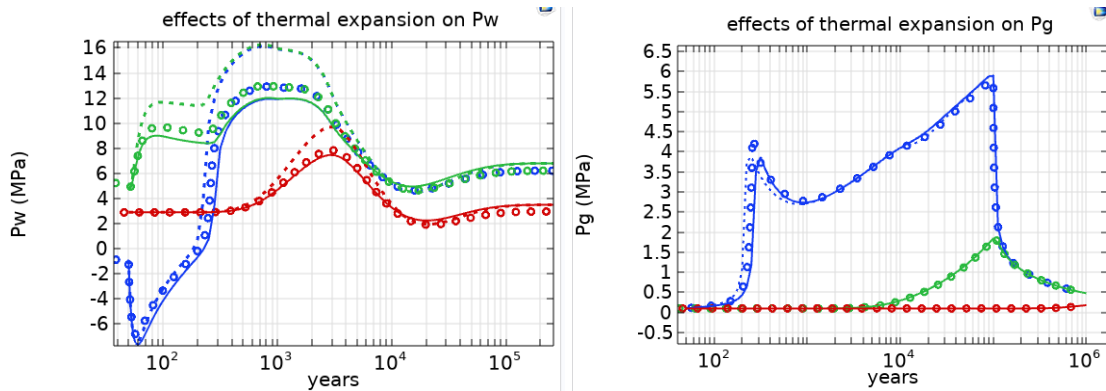


Figure 8-37: impact of thermal expansion on pore/gas pressure (circles are for the reference case, dotted lines are for case 1 and solid lines are for case 2)

8.4.6 Effect of including mechanical coupling

THMG analysis considers the gas dissipation in a deformable solid matrix through coupling a mechanical module into the reference model. The matrix deformation includes both stress-induced deformation and thermal-induced expansion. The initial stresses in host rock is equal to self-weight, varying linearly between -0.1[MPa] at $y=600\text{m}$ (top) to -20.1[MPa] at $y=-400\text{m}$ (bottom). We assume all materials are linear elastic with their respective Young's modulus and Poisson ratio as listed in Table 8-5.

Table 8-5: mechanical parameters used in the THMG model

parameter	Host clay			Liner	backfill
	undisturbed	outer EDZ	inner EDZ		
Young's Modulus E [MPa]	5000	5000	500	40000	500
Poisson ratio	0.3			0.25	0.3
Biot's coefficient	0.8			1	1

An effective stress framework is adopted in the coupled THMG analysis as $\sigma = \sigma' - \alpha_B (S_g \cdot p_g + S_w \cdot p_w)$, where, σ is the total stress, σ' is the effective stress, α_B is the Biot's coefficient, S_w is degree of saturation for water, p_g is the gas pressure, and p_w is the pore water pressure.

Variation of volumetric strain is a combined effect of stress-induced and thermal-induced volumetric strain variations. These two components are compared at 9 observation points in Figure 8-38. The backfill and liner are under tension due to the increased pore and gas pressure. The impact of matrix deformation on pore water and gas pressure is depicted in Figure 8-39. Considering matrix deformation has more impact on the water pressure, while the impact on the gas pressure is quite limited.

The time evolution of the effective circumferential stresses at six points along the horizontal line from the cell center is presented in Figure 8-40. Tensile effective circumferential stress may appear in the

liner due to the high gas pressure. Figure 8-40 cannot be quantitatively used to interpret the liner stress because excavation-induced stress release and host rock convergence are not considered in the model.

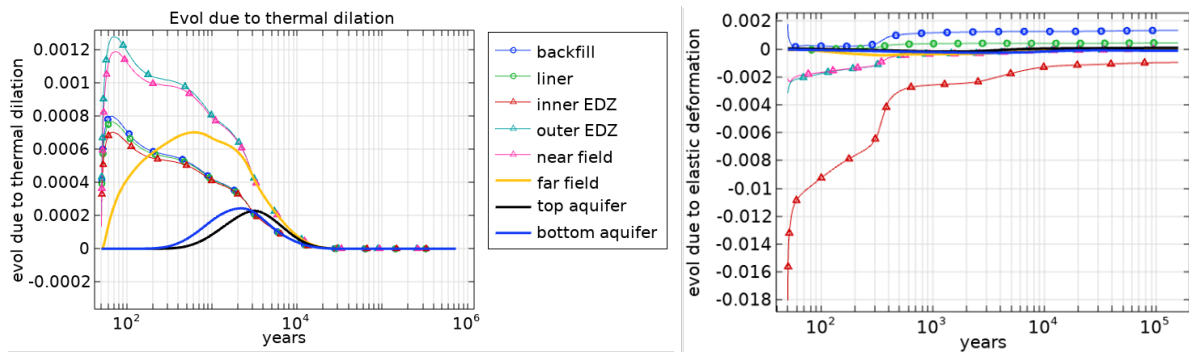


Figure 8-38: comparison of thermal-induced and stress-induced volumetric strain in THMG analysis

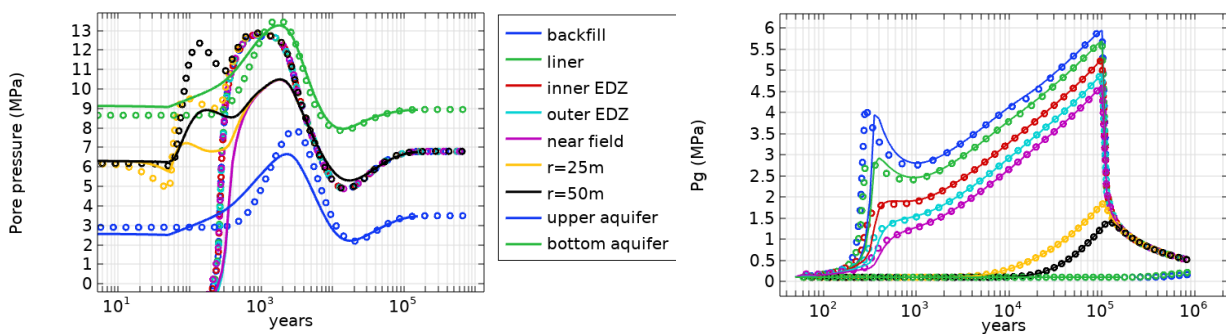


Figure 8-39: comparison between THMG and THG models (dots are for the reference THG model and solid lines are for THMG model)

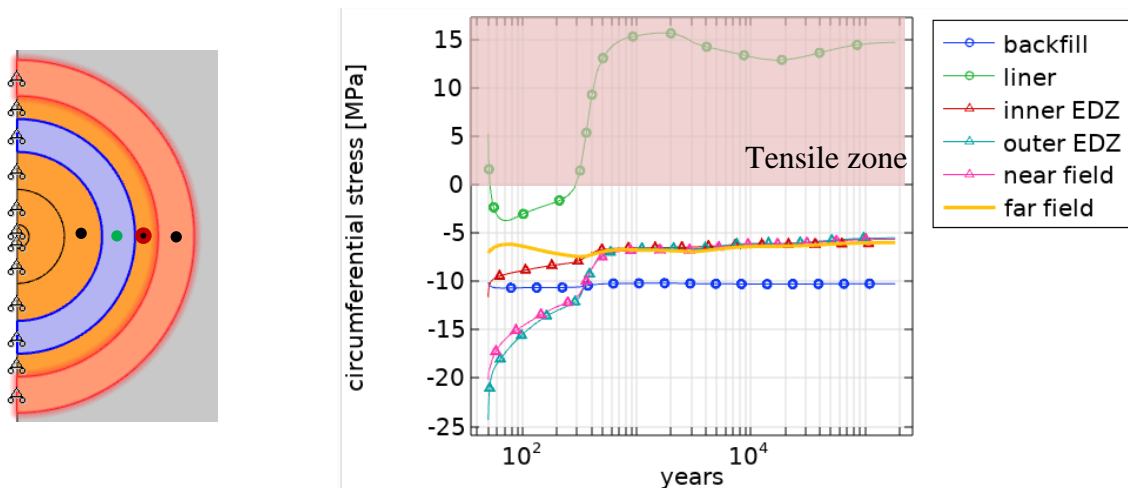


Figure 8-40: time evolution of the effective circumferential stresses from the THMG model

8.4.7 Effect of considering vapor

When adding vapor in the reference case with a diffusion coefficient of vapor of $5.9 \times 10^{-6} \times (T[K])^{2.3} / P_g [Pa]$, Figure 8-41(left) depicts the percentage of vapor pressure in the gas pressure. It is obvious that the vapor percentage follows the T trend and reaches its maximum value at the start of thermal loading, about 13%, then keeps decreasing until the end of gas production. Figure 8-41(right) presents the vapor effects on the gas pressure at nine observation points. Results show that considering vapor decreases

the gas pressure in the backfill, while increasing P_g in the vicinity of the host rock. There is no discernible effect on the pore water pressure.

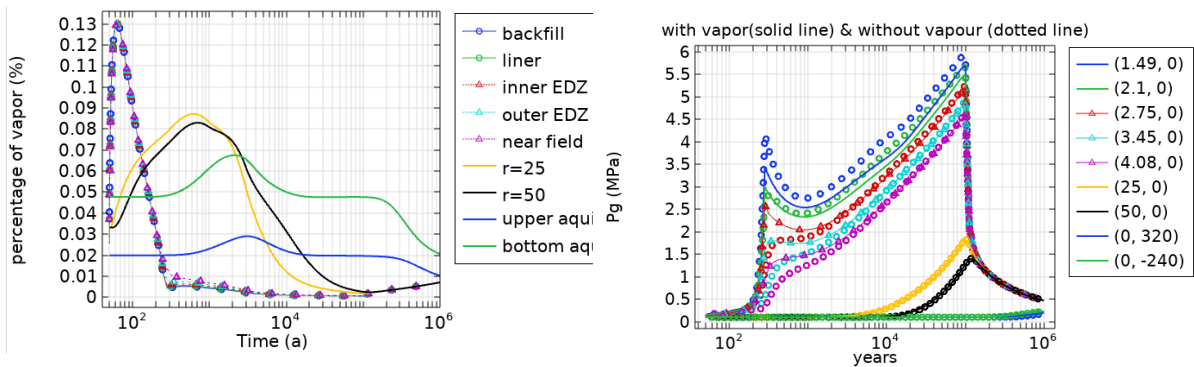


Figure 8-41: percentage of vapour pressure in the total gas pressure(left) and effect of vapour on the gas pressure(right).

Figure 8-42 compares the total gaseous and the total dissolved H_2 in the system, together with the total injected H_2 and variations of the gas saturation in the backfill. Results show that the majority of the injected H_2 exists as dissolved gas in the system. There are very limited differences between the two cases with and without considering vapor.

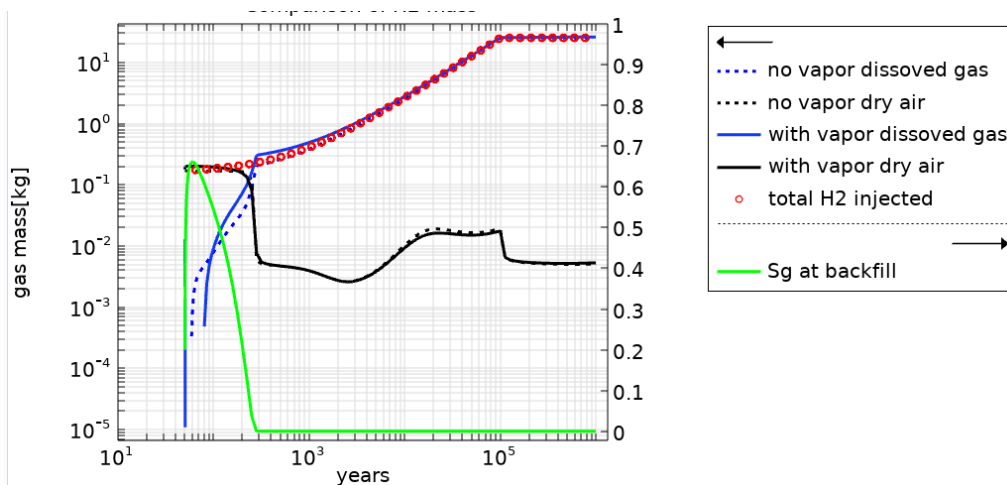


Figure 8-42: Effects of vapour on the total dissolved and total gaseous H_2 in the system

8.4.8 The final case of EURAD 2D-PS THMG

In the final case, the 2D-PS THMG model is built up as closely as possible to the problem definition in Milestone 61. Details are listed in Table 8-6. Comparisons of results with the reference case in Table 8-4 is presented in Figure 8-43.

Table 8-6: Material properties used in the 2D-PS THMG model (the final case)

parameter		Unit	Host rock			backfill	liner
			Undisturbed	Outer EDZ	Inner EDZ		
Porosity $\theta = \theta_0 + \varepsilon_{elastic} + \alpha_T(T - T_{ini}) + (\beta_s(p_w - p_{w_{ini}}) - \alpha_s(T - T_{ini})) (1 - \theta_0)$							
Porosity0	θ_0	-	0.2			0.4	0.15
Compressibility of solid grains	β_s	1/Pa	3.33E-5				
Thermal expansion coefficient of solid grains	α_s	1/K	3E-5				
thermal expansion coefficient of solid matrix	α_T	1/K	4E-5			2×10^{-5}	2×10^{-5}
Young's modulus	E	MPa	5000	5000	500	40000	5000
Poisson ratio			0.3	0.3	0.3	0.25	0.3
Biot's coefficient			0.8			1	1
VG model							
shape parameter	n	-	1.5				
shape parameter $m=1-1/n$	m		0.333				
VG parameter	Pe	MPa	23	17	16	1	10
Gas/water permeability							
Intrinsic permeability of water	K_{in}	m ²	1E-20	1E-18	1E-16	1E-16	1E-16
Relative permeability of water	k_{rw}		$k_{rl} = S_e^{0.5} \left[1 - (1 - S_e^{1/\lambda})^\lambda \right]^2$				
Relative permeability of gas	k_{rg}		$k_{rg} = A(1 - S_e)^3$				
	fg	-	100	10	1	1	1
Viscosity of water	μ_l	Pa s	$2.1E - 6 * exp(1808.5/T[K])$				
Viscosity of gas	μ_g	Pa s	$8.8E - 6$				
Liquid density $\rho_0 \exp(\beta_w(P_w - P_{ref}) + \alpha_w T[^\circ C])$							
Water compressibility	β_w	1/Pa	4.5E-4				
	ρ_0	Kg/m ³	1002.6				
	P_{ref}	MPa	0.1				
volumetric thermal expansion coefficient of water	α_w	1/K	$-(10^{-4}T^3 - 0.0314T^2 + 6.1649T + 106.61) \times 10^{-6}$				
Diffusion of dissolved gas $\nabla \cdot (-D_0 \theta^{1+a} S_e^b \rho_w \nabla(\omega_l^a))$							
Millington-Quirk diffusion for dissolved air	D_0	m ² /s	5E-9				
parameter	a	-	1.5			1	2
parameter	b	-	10			15	4
Henry's coefficient	H	MPa	7215				
Molar mass of hydrogen		kg/mol	0.002				
Molar mass of water		kg/mol	0.018				
Diffusion of vapor and dry air $D_m^{vapor} = \tau D \left(\frac{(273.15 + T)^n}{P_g} \right)$							
diffusion coefficient	D_0	m ² /s	5.6E-6				
tortuosity	τ		1				
power	n		2.3				
Thermal parameters							
Heat conductivity (w/m/°C)			1.7			1.3	2.3
specific heat of solid phase	C_s	J/Kg/°C	720			500	900

Solid density	ρ_s	kg/m ³	2639
specific heat of Water			4180
Bulk specific heat	C_{bulk}	J/Kg/°C	$(\rho_s C_s (1 - \theta) + \rho_w C_w \theta S_e) / \rho_{bulk}$
Bulk density	ρ_{bulk}	kg/m ³	$\rho_s (1 - \theta) + \rho_w \theta S_e$

the properties of the upper and below aquifers are considered the same as the host rock.

Canister and buffer are replaced in the calculation with backfill.

The 3D THMG model cannot converge if using linearized VG retention model. Therefore, the VG retention curve as the ref case is used Instead

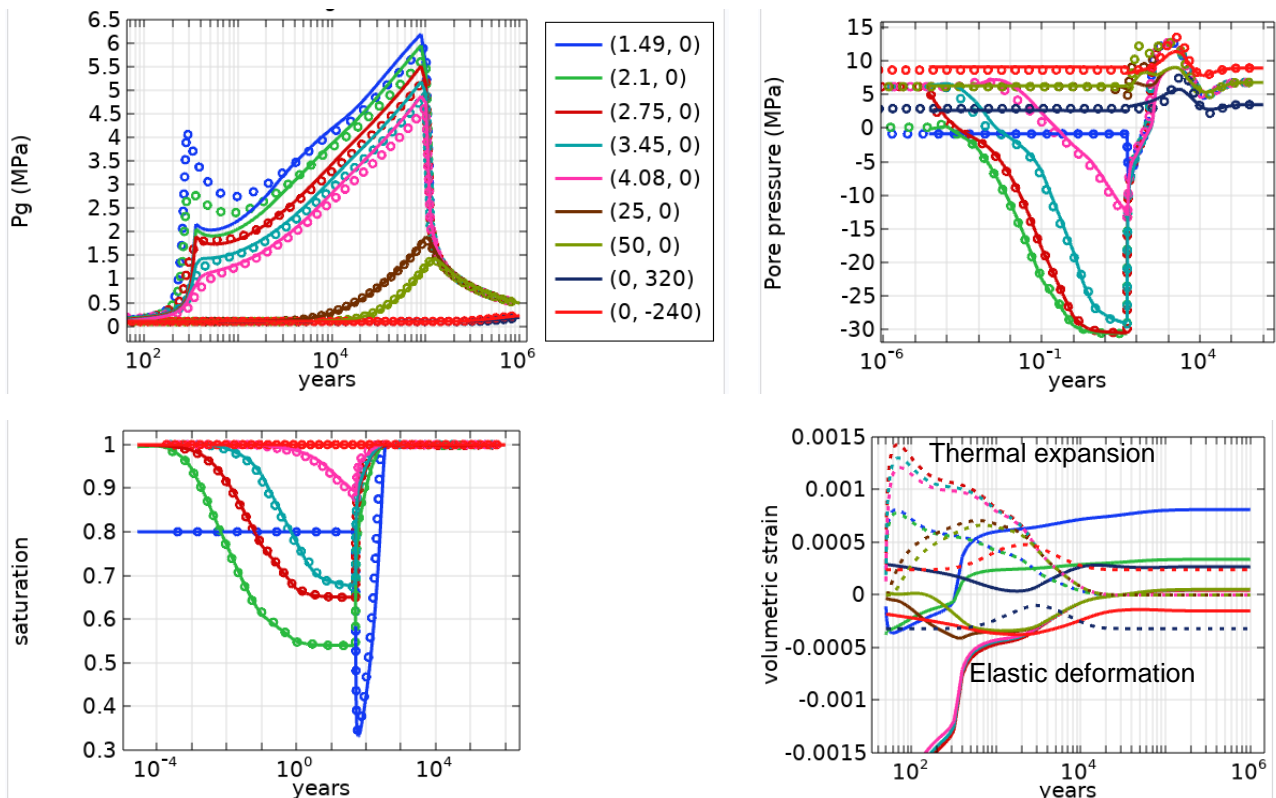


Figure 8-43: The final THMG case (solid lines) in Table 8-6 compared with the reference case in Table 8-4 (circles)

8.5 Results of component-scale models from COMSOL

The running of a full 3D THG model of Zone B is very slow in COMSOL, moreover the required memories exceed the capacity of a personal laptop. The result from Code_Bright for the full 3D model implies that the existence of two seals divides gas transport in Zone B into three rather separate zones: disposal zone, seal zone and shaft (see Figure 8-44). Therefore, COMSOL is used to do two simulations at component scale: one for a disposal cell and the other for the shaft.

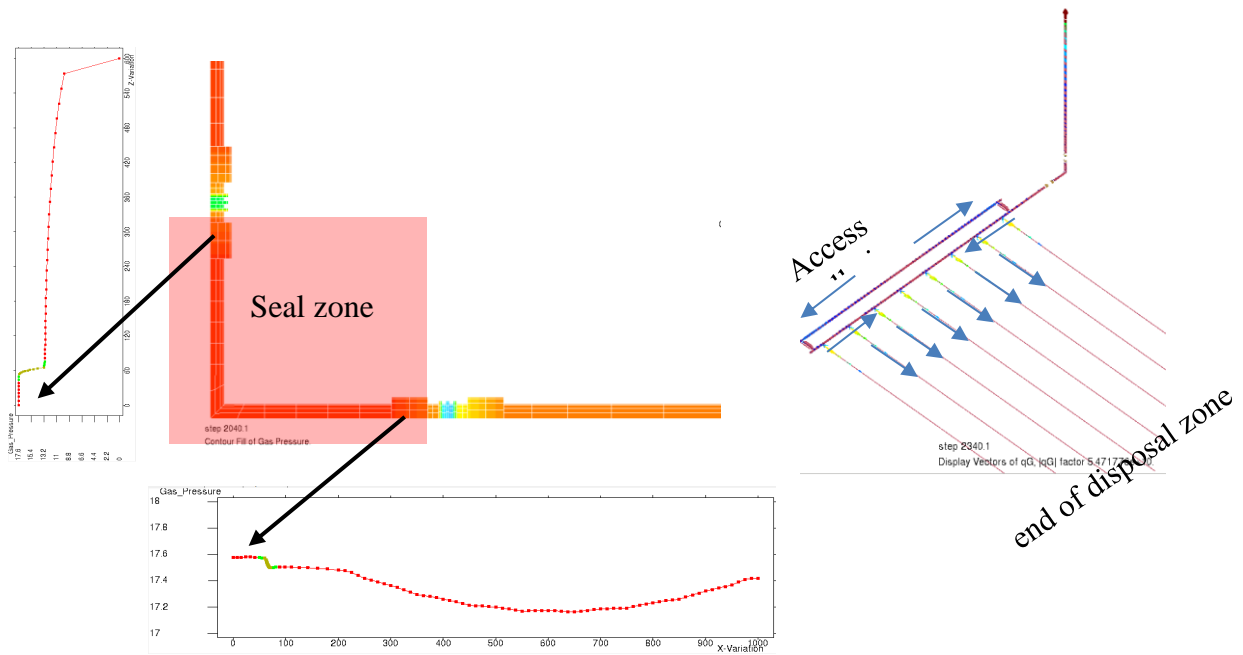


Figure 8-44: result from Code_Bright for the 3D full model of zone B: (left) P_g profile along the gallery and shaft at 1E5 years (right) schematic illustration of gas flux in zone B at around 2000 years

8.5.1 Model at cell scale

The disposal cell marked green in Figure 8-45 is selected for the analysis, which is 1150 m in length, 100 in width and 50 m in height. Gas is produced in the disposal cell and in the access galleries. The surfaces in contact with adjacent cells are set as no flux boundaries. Contour of gas pressure and water saturation degree at 1E5 years is presented in Figure 8-46. It is obvious that gas pressure around the access galleries is higher than the rest. The disposal cell and the access galleries remain unsaturated when the gas production stops.

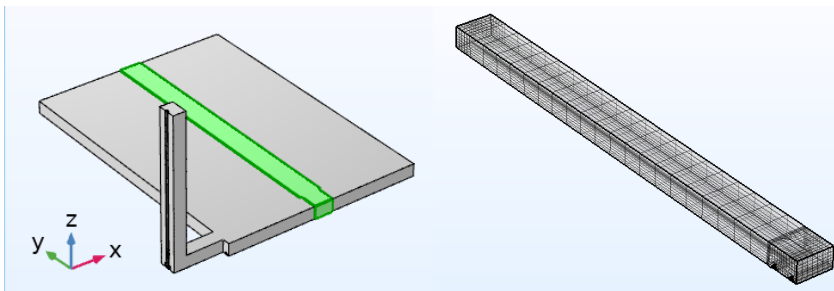


Figure 8-45: 3D COMSOL model at cell-scale (left) and mesh (right)

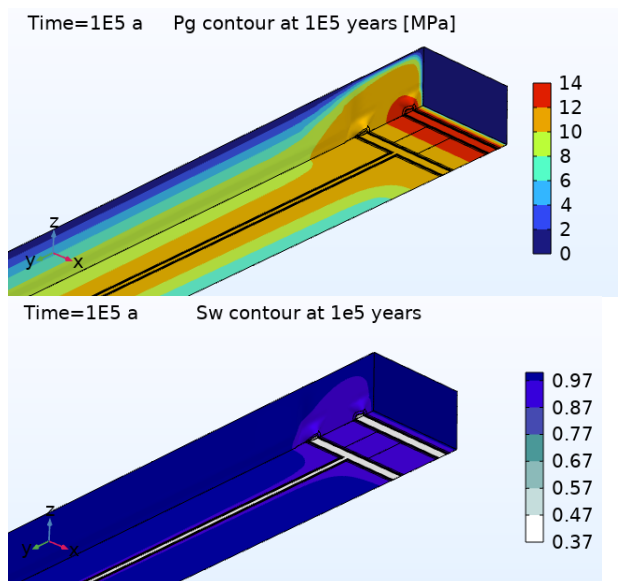
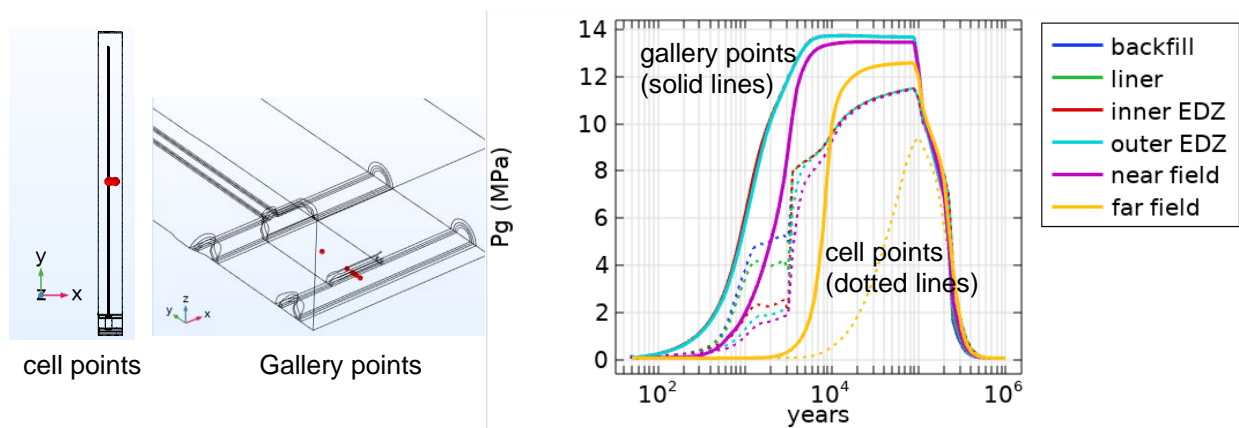


Figure 8-46: contour of Pg and Sw at 1E5 years from 3D COMSOL model at cell scale

A group of six observation points are selected around the mid point of the disposal cell. For comparison, another six observation points are selected around the mid section of the access gallery. Figure 8-47 compares the evolution of Pg, PI and Sw at the two groups of observation points. T at mid section of the disposal cell is presented as well.

The gas pressure in Figure 8-47 cannot be quantitatively compared with that shown in Figure 8-7 and Figure 8-43. Each model has its specific limitations, model parameters and boundary conditions. Model used for Figure 8-47 does not allow the migration of gas along the access gallery. Results in Figure 8-7 are obtained with lower effective diffusion coefficient. Figure 8-43 is based on 2D-PS model without considering gas flow along the disposal cell.



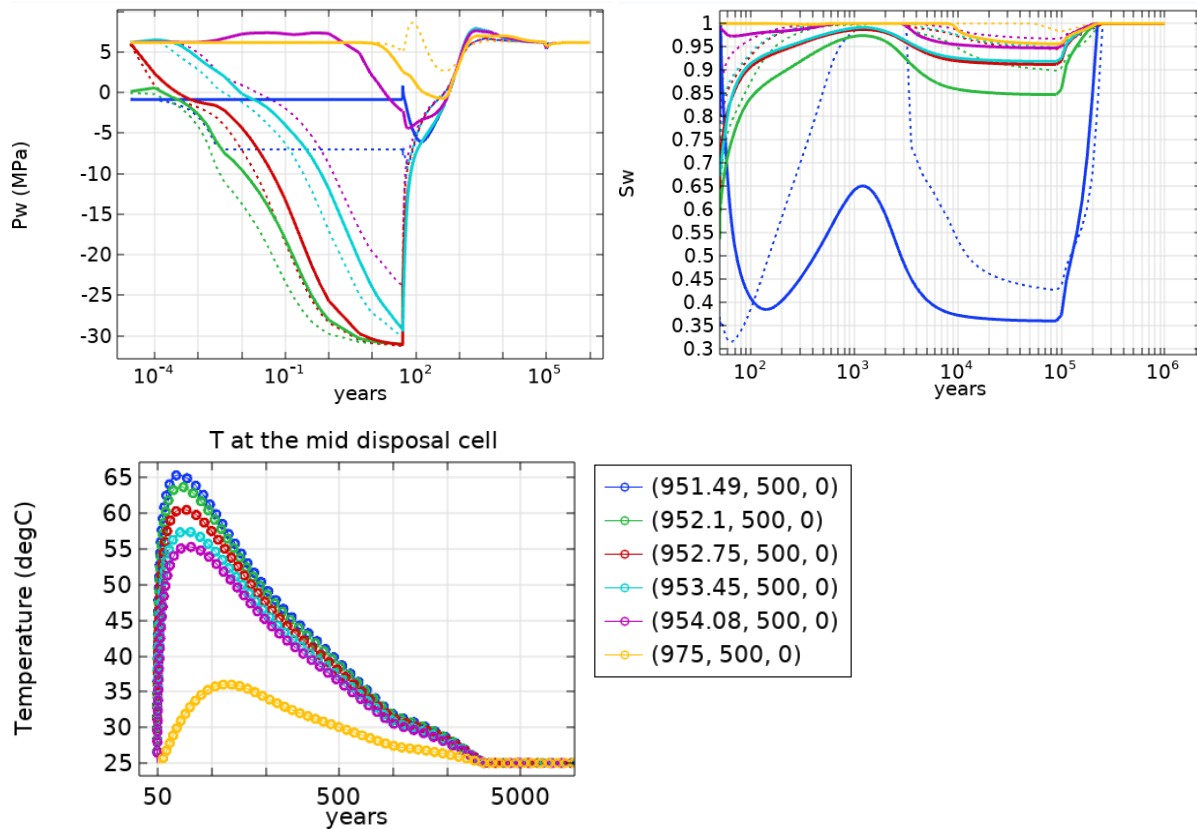


Figure 8-47: time evolution of P_g, P_w, S_w and T at cell points (dashed lines) and gallery points (solid lines) from 3D COMSOL cell model

Figure 8-48 compares the distribution of gaseous and dissolved gas mass in the system. The total gas produced in zone B is around 454773 kg, around 60% dissipates out of the surrounding host rock. This confirms the conclusion from 3D full model that the 50-m-thick host rock assumed in the model is not sufficient for the gas dissipation. Among the gas remains in the system, about 50% dissolves in the host rock (blue solid line). The rest 50% is gaseous gas and mainly exists in the backfill (green dotted line) and the host rock (blue dotted line).

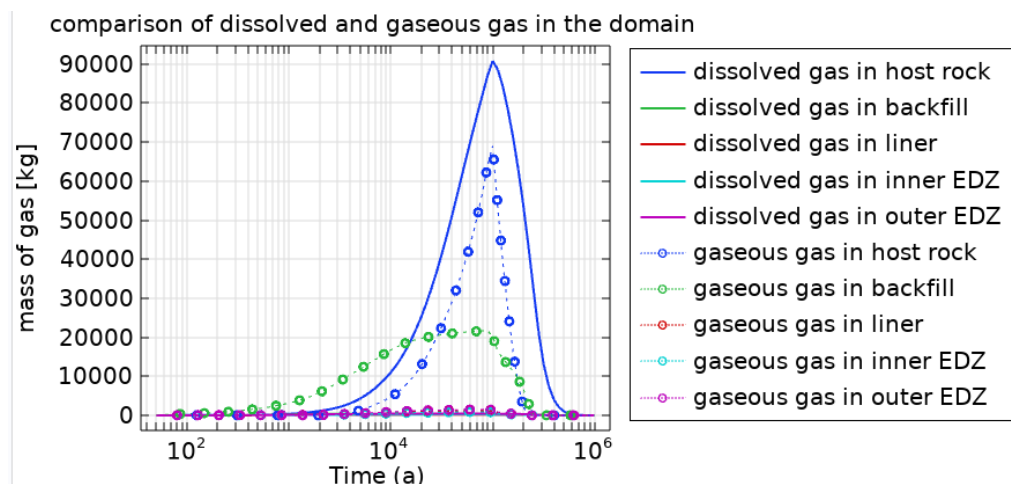


Figure 8-48: Comparison between gaseous and diffusive gas

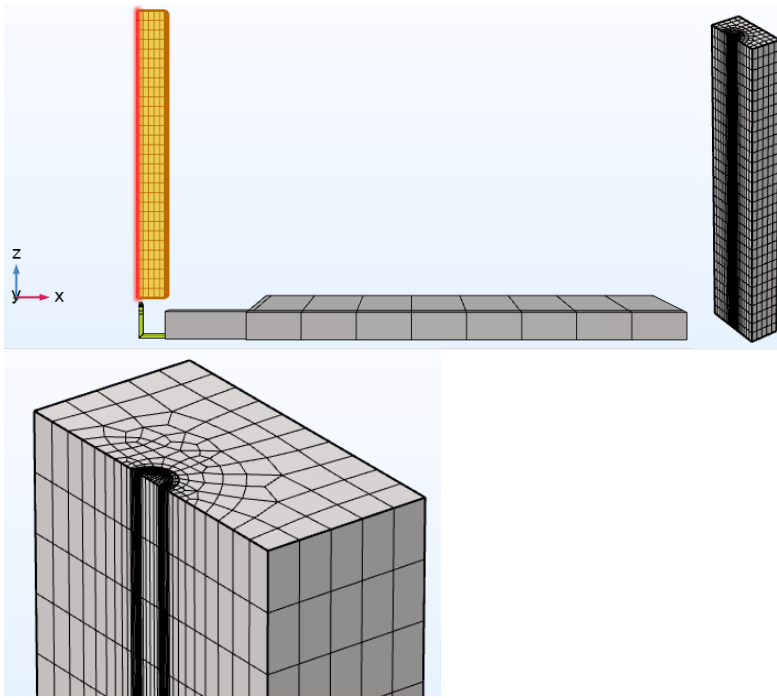


Figure 8-50: 3D COMSOL shaft model(left), mesh of shaft (middle) and zoomed view shaft exit (right)

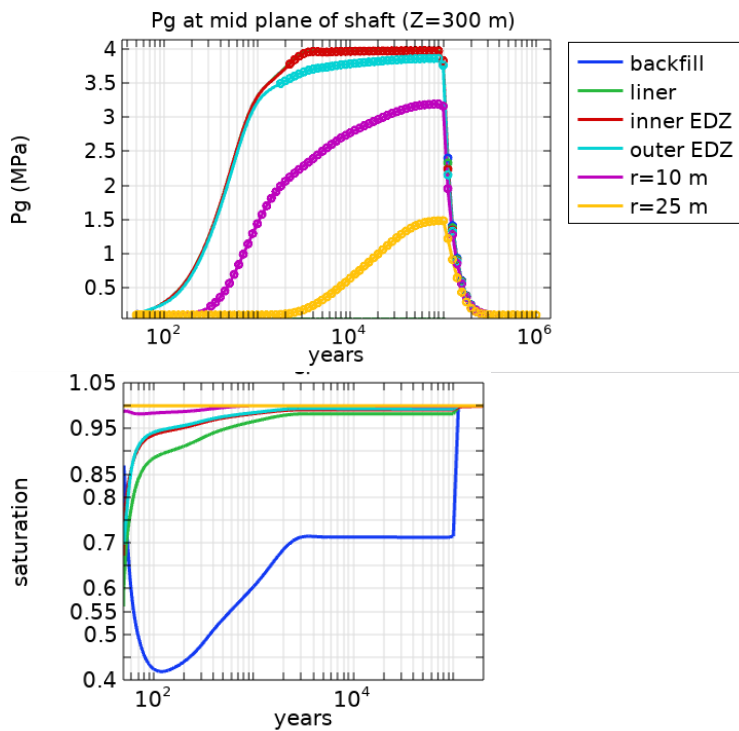


Figure 8-51: Evolution of gas pressure (left) and water saturation degree (right) at the mid-section of the shaft from the 3D COMSOL shaft model. The six observation points are located at x= 2, 4.5, 5.5, 6.75, 10, 25 m, Y=0 and Z=300m. Dots on the Pg curves marks the period when Sw >99%.

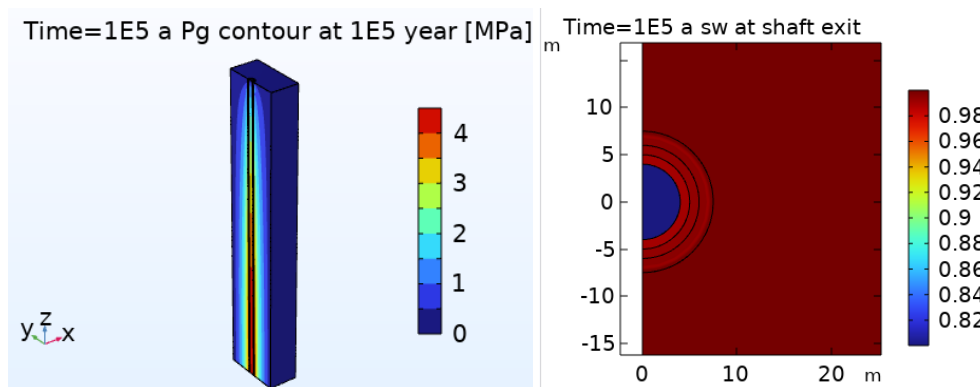


Figure 8-52: contour of gas pressure and water saturation degree at the shaft exit at 1E5 years.

Figure 8-53 indicates that after 1000 years, the gas production rate in the shaft equals the advective gas flux rate integrated over the backfill at the shaft exit, which implies that nearly all the gas exits the domain along the backfill. The total gas produced in half of the shaft in 1E5 years is 1130E3 kg. Of this, 1110E3 kg gas flows out from the shaft top, as shown in the right figure of Figure 8-53.

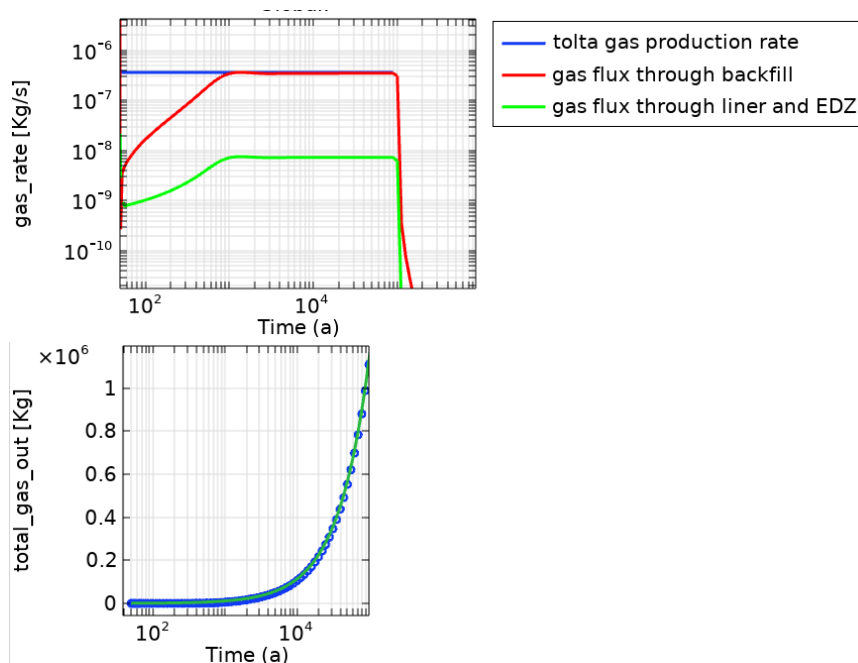


Figure 8-53: (left) comparison between the total gas production rate and integration of the advective gas flux over different materials at the shaft exit (right) total gas mass produced in the shaft compared to total advective gas at the shaft top surface.

8.5.3 Computation time

Although the shaft model and cell model are very similar, the calculation time is significantly different. The COMSOL cell model consists of only 4805 elements while the shaft model has 68853 hexahedral elements, the calculation for the former takes around 22 hours and 12 mins for the latter. Figure 8-54 compares the convergence process between the two model calculations. For the shaft model, there always remains a gas dissipation pathway along the backfill during gas production, therefore the time step steadily increases. However, the convergence for the cell mode becomes unstable when the system starts to be de-saturated by the gas after 2000 years (see Figure 8-55). The numerical aspects

of switching between saturated and unsaturated regimes are highly challenging for such a gas production problem.

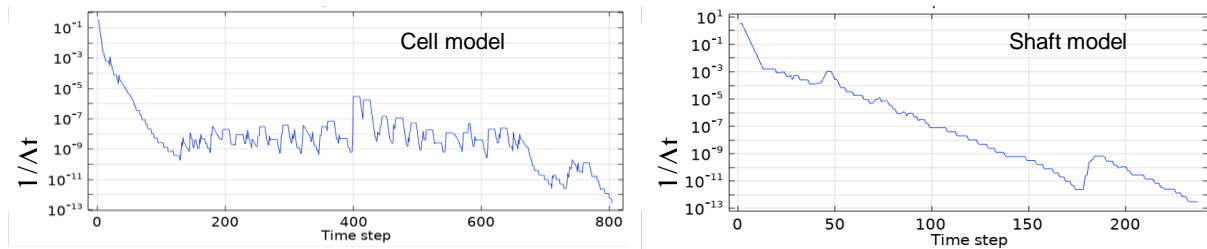


Figure 8-54: comparison of time step between cell model and shaft model

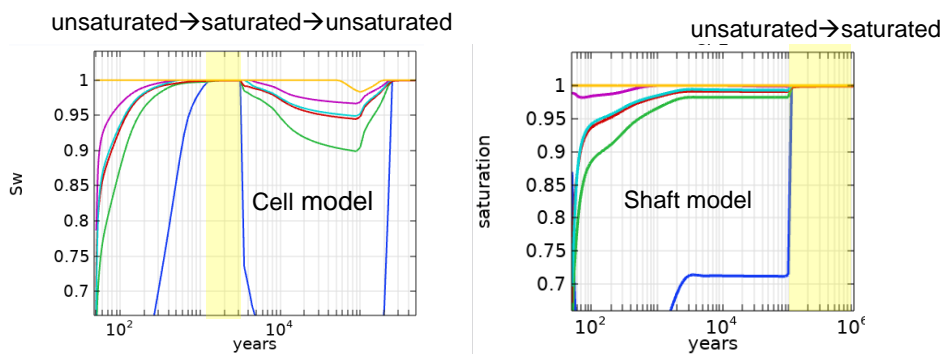


Figure 8-55: comparison of saturation degree between cell model and shaft model

8.6 Conclusions

Results from the 3D full model show:

- The maximum gas pressure in zone B appears in the access gallery, around 14 MPa (based on 3D COMSOL cell model) and 17 MPa (3D Code_Bright model). Both values are over-estimated due to model limitations in the former and the different expression used for $D_e = f(\theta, S_e)$ in the latter.
- Regarding the gaseous gas flow among the five materials, the majority (86%) flows within the backfill. By the end of gas production, 80% of the total gas exists as dissolved gas in the surrounding host rock. The rest stays in the repository as gaseous gas.
- The existence of gallery and shaft seals divides the system into three relatively isolated zones: disposal zone (including access galleries), seal zone and shaft. The gas produced in the galleries is blocked by the gallery seal and flows preferably into the disposal zone, driving disposal cell gas towards the end of the cells. Gas produced in the shaft dissipates steadily from the shaft top exit.

Through investigating various approximation methods, it is found that

- Result comparison between 1D, 3D cell, and full 3D models shows the gas pressure for all three models are quite similar, with the maximum gas pressure increasing from 3D to 1D. This

observation implies that a simple 1D model is capable of providing a fast estimation of the maximum gas pressure in the system.

- Results from the 3D full model imply that the existence of gallery and shaft seals divides the system into three relatively isolated zones: disposal zone (including access galleries), seal zone and shaft. Numerical simulations at component scale (such as shaft model, cell model) is an effective method to gain a quick understanding of the problem.
- A 2D-PS including top and bottom aquifer is an effective model too for sensitivity analysis. Results from the 3D full model indicate that the 50-m-thick host rock assumed in the model is not sufficient for the gas dissipation. The 2D-PS model therefore can be used beforehand to investigate the extent of the gas disturbed zone.

The sensitivity analysis based on the 2D-PS model shows:

- The relationship between the effective diffusion coefficient and θ and S_w is one of the key factors for gas dissipation.
- Pore water pressure is very sensitive to porosity variation. When doing code comparison, the method used to update thermal- and stress- induced porosity variation needs to be carefully checked.
- Tensile effective circumferential stress may appear in the liner due to the high gas pressure.

Other numerical issues:

- The boundary conditions assigned for the shaft exit determines the migration pathway of the shaft gas. Whether the shaft gas diffuses into the host rock or flows out of the shaft top exit depends completely on the boundary conditions assumed at the shaft top surface: either saturated or with a certain relative humidity.
- The time cost for a two-phase problem is problem dependent. If the phase change is uni-directional (such as unsaturated \rightarrow saturated or remains unsaturated), the convergence is steady and quick; if there exists multiple phase changes (such as unsaturated \rightarrow saturated \rightarrow desaturated), the convergence could become extremely slow and unstable.

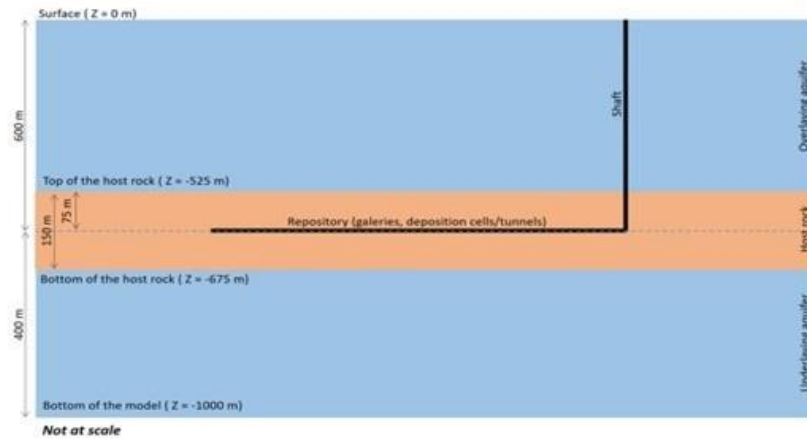
9. Contribution of University of Liège

Within the framework of EURAD-GAS joint research program, WP GAS: task 4.2 was dedicated to the conceptualization and evaluation of gas migration at the scale of a repository. In this regard, the contributions of the University of Liège are presented here.

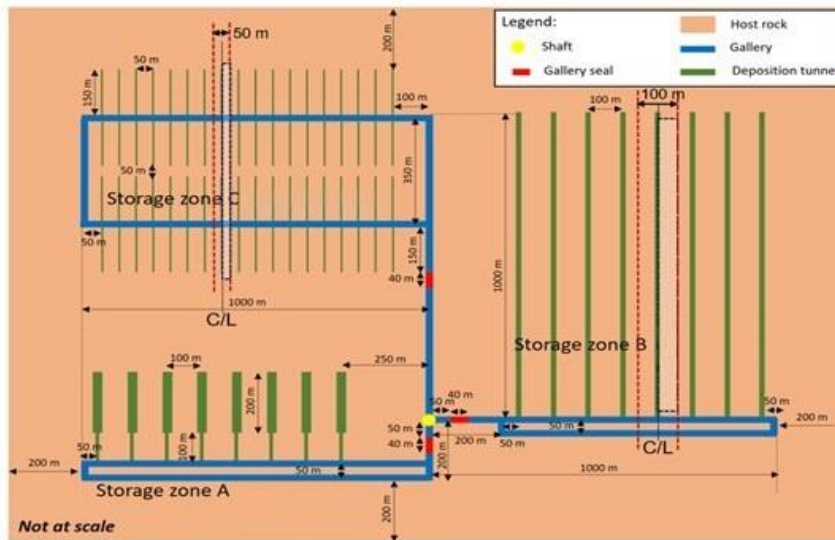
A two-dimensional (2D) plane strain finite element analysis was performed using our in-house FEM software LAGAMINE. The model dimensions, initial boundary conditions (i.e., mechanical, thermal, and hydraulic), time-varying boundary conditions, and the source terms for heat/gas flow were implemented as per the technical specifications of Zone B and Zone C. The governing equations of multiphase fluid and heat transport through a porous media are also discussed briefly in section 9.2. The simulation results are presented in section 9.5 mainly in terms of the evolution of relevant indicators such as temperature, pore water pressure, pore gas pressure, degree of saturation, and effective vertical stresses at the prescribed locations.

9.1 2D Model description

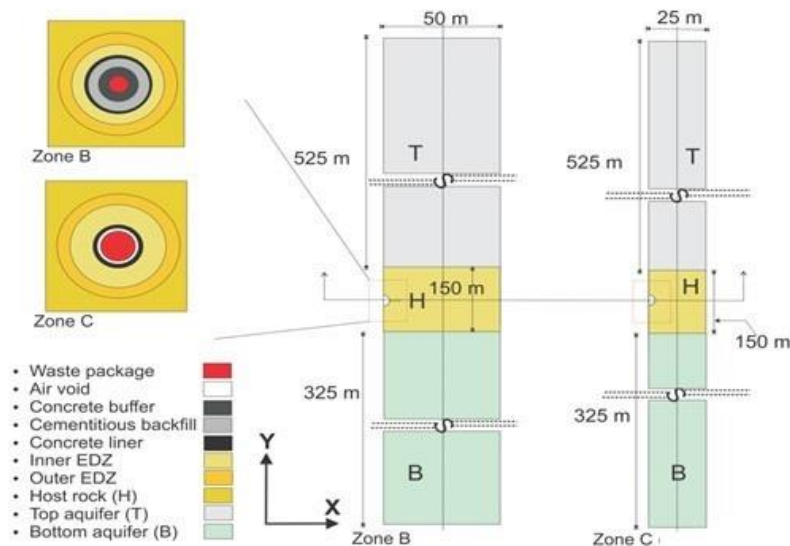
As shown in Figure 9-1, the overall height of 2D PS model was 1000 m in Y-direction for both Zone B and Zone C. The lithological features were adopted during the model creation based on the given vertical section of generic repository (see Figure 9-1a). The overall thickness of overlying aquifer, host rock, and underlying aquifer was 525 m, 150 m, and 325 m, respectively. Whereas the model width in X-direction was equal to the half of spacing between deposition tunnels i.e., in 50 m in Zone B, and 25 m in case of Zone C (see Figure 9-1b). As depicted in Figure 9-1c, Zone B disposal concept consists of canister overpack, concrete buffer, concrete backfill, and concrete liner, whereas Zone C consists of waste package, steel liner and air void between the waste package and steel liner.



(a): Schematic representation of vertical/longitudinal profile of a generic repository



(b): Schematic horizontal slice at generic repository depth, (Note: C/L = Disposal gallery/tunnel central line).



(c): Model dimensions for a 2D plane strain finite element analysis

Figure 9-1 Model dimensions and geometric features of 2D plane strain model.

9.2 Governing equations

In LAGAMINE, a bi-dimensional isoparametric finite element (MWAT) has been implemented for both 2D and 3D coupled flow and deformation analysis (Collin et al., 2002). The element for 2D-analysis possesses five degrees of freedom at each node: two displacements of the skeleton (X , Y), a liquid water pressure (P_w), a gas i.e., hydrogen + water vapor pressure ($P_{H_2} + P_v = P_g$), and temperature (T). The number of nodes is variable (three, four, six or eight) and the element is isoparametric, which means that the coordinates, velocities, pore pressure (water and gas) and temperature are discretized by the same shape functions.

9.2.1 Balance equations

9.2.1.1 Mass balance of water

The mass conservation equation for water species is obtained by summing the balance equation of liquid water and water vapor. The equation contains the variation of water storage and the divergence of water flows in both liquid and gas phases. Water vapor is one of the gas phase compounds. Therefore, vapor flows have two components: advective flux of the gaseous phase and the non-advective flux of water vapor related to vapor diffusion inside the gaseous phase.

$$\underbrace{\frac{\partial}{\partial t} (\rho_w \phi S_{rw}) + \nabla \cdot (\rho_w f_w)}_{\text{Liquid water}} + \underbrace{\frac{\partial}{\partial t} (\rho_v \phi S_{rg}) + \nabla \cdot (i_v + \rho_v f_g)}_{\text{Water vapor}} = 0 \dots \text{(Eq. 1)}$$

Where, ρ_w is liquid water density, ϕ is the porosity, S_{rw} is degree of water saturation, ρ_v is vapor density, S_{rg} is gas saturation, f_α is the macroscopic velocity of phase α ($\alpha = w$ or g), i_v is the non-advective flux of water vapor and t is the time.

9.2.1.2 Mass balance of Hydrogen

The equation of mass conservation for Hydrogen contains the dry Hydrogen and dissolved Hydrogen in water. The dry Hydrogen flows have two components: an advective flux related to gas phase motion and a non-advective flux corresponding to Hydrogen diffusion in the gaseous mixture.

$$\underbrace{\frac{\partial}{\partial t} (\rho_{H_2} \phi S_{rg}) + \nabla \cdot (i_{H_2} + \rho_{H_2} f_g)}_{\text{Dry Hydrogen in gas phase}} + \underbrace{\frac{\partial}{\partial t} (H \rho_{H_2} \phi S_{rw}) + \nabla \cdot (i_{dH_2} + \rho_{H_2} H f_w)}_{\text{Dissolved Hydrogen in water}} = 0 \text{ (Eq. 2)}$$

Where, ρ_{H_2} is dry Hydrogen density, ϕ is the porosity, S_{rw} is water saturation, H is Henry's coefficient, f_α is the macroscopic velocity of phase α , i_{H_2} is the non-advective flux of dry v, i_{dH_2} is the non-advective flux of dissolved Hydrogen, ρ_v is water vapor density, S_{rg} is gas saturation and t is the time. Henry's coefficient, H allows determining the dissolved Hydrogen volume in liquid water. The dissolved Hydrogen mass is supposed to be sufficiently low that water properties are not influenced.

9.2.1.3 Balance of heat

In the formulation of heat transfer in unsaturated porous medium, it was assumed that the different components are in a thermal equilibrium (i.e. $T_s = T_w = T_v = T_{H_2}$). A unique temperature is defined for

the medium and only one balance equation of energy is required. By neglecting the kinetic energy and pressure energy terms, the enthalpy balance equation can be written as:

$$\frac{\partial \phi}{\partial t} + LE_{H_2O}^{w \rightarrow v} + \nabla \cdot (q) - Q = 0 \dots \dots \dots (Eq. 3)$$

where, ϕ is the enthalpy of the medium, L is the latent heat of water vaporization, $E_{H_2O}^{w \rightarrow v}$ is the rate of water evaporation, q is the heat flow and Q is a volume heat source.

Evaporation rate may be evaluated from the water vapor balance equation (Eq. 4) and the enthalpy balance equation can be rewritten as per Eq. 5.

$$E_{H_2O}^{w \rightarrow v} = \frac{\partial}{\partial t} (\rho_v n S_{rg}) + \nabla \cdot (\rho_v f_g + i_v) \dots \dots \dots (Eq. 4)$$

$$\frac{\partial \phi}{\partial t} + L \frac{\partial}{\partial t} (\rho_v n S_{rg}) + \underbrace{L \nabla \cdot (\rho_v f_g + i_v)}_{\text{Heat transfer}} + \nabla \cdot (q) - Q = 0 \dots \dots \dots (Eq. 5)$$

Heat storage **Heat transfer**

9.2.1.4 Momentum balance for the medium

The momentum balance reduces to the equilibrium of stresses if the internal terms are neglected. Hence,

$$\nabla \cdot (\sigma_t) + b = 0 \dots \dots \dots (Eq. 6)$$

where, σ_t is the total Cauchy stress tensor (with compressive stress taken as positive), and b is the body force vector. If the only body force is gravity, b is equal to ρg , where ρ is the density of the mixture.

9.2.2 Constitutive equations

9.2.2.1 For mechanical behaviour

The linear elastic model is used to describe the mechanical behaviour of different components of Zone B and Zone C. The relevant mechanical properties adopted in the present simulation are summarized in **Appendix I (Table A1 to A4)**.

9.2.2.2 For hydraulic behaviour

The constitutive equations pertaining to the hydraulic behaviour consider the fluid flow in both liquid and gaseous phase. Each phase constitutes a mixture of two components i.e., dry Hydrogen and water vapor for the gas phase and liquid water and dissolved Hydrogen for liquid phase. As per Eq. 1 and 2 compositional approach is used to write the balance equations. The fluid flow occurs in advective form for liquid phase and diffusive form for gaseous phase. The advective flow of fluid is described by the generalized Darcy's law as per Eq. 7.

$$f_\alpha = - \frac{K_{int} k_{r,\alpha}}{\mu_\alpha} [\nabla p_\alpha + g \rho_\alpha \nabla y] \dots \dots \dots (Eq. 7)$$

Where, α is related to fluid species i.e., liquid or gas ($\alpha = \text{water or gas}$), μ_α is the dynamic viscosity of the fluid (water or gas), p_α is the fluid pressure (water or gas), g is the gravity acceleration, K_{int} is the intrinsic permeability of porous medium, $k_{r,\alpha}$ is the relative permeability of fluid and y is the vertical upward directed co-ordinate.

In LAGAMINE, there are different ways to describe $k_{r,\alpha}$ as a function of $S_{r,\alpha}$. Such as, the relative permeability $k_{r,\alpha}$, is derived from Mualem-van Genuchten closed form model,

$$k_{r,w} = \sqrt{S_{r,w}} \left(1 - \left(1 - S_{r,w}^{\frac{1}{m}} \right) \right)^m \dots\dots\dots (Eq. 8)$$

$$k_{r,g} = A. (1 - S_{r,w})^P \dots\dots\dots (Eq. 9)$$

where, m , A , and P are the material parameters which controls the relative permeability value with degree of saturation for liquid water/gas.

The variation of degree of saturation with total suction is described by the shape of water retention curve. In LAGAMINE, different water retention models are implemented. For an example van Genuchten model is described as below:

$$S_{r,w} = S_{res} + (S_{max} - S_{res}) \left(1 + \left(\frac{s}{P_r} \right)^{1-F} \right)^{-F} \dots\dots\dots (Eq. 10)$$

where, $S_{r,w}$ is the current degree of water saturation, S_{res} is the residual degree of saturation, S_{max} is the maximum degree of saturation, P_r is the parameters related with air-entry / air-expulsion suction, and F is a fitting parameter which controls the shape of water retention curve.

As per the technical guidelines for task 4.2, water retention curve and the relative permeability functions considering explicitly gas entry pressure were implemented. These functions are discussed below:

Water retention curve considering explicit gas entry pressure:

$$p_c = \begin{cases} -\frac{1}{\alpha} \left((S_e^* S_e)^{\frac{1}{m}} - 1 \right)^{\frac{1}{n}}, & \text{if } S_e \leq 1 - \varepsilon \quad \dots (Eq. 11) \\ -\frac{1}{\alpha} \left((S_e^* S_e)^{\frac{1}{m}} - 1 \right)^{\frac{1}{n}} \cdot \frac{1 - S_e}{\varepsilon}, & \text{if } (1 - \varepsilon) < S_e < 1 \quad \dots (Eq. 11a) \\ 0, & \text{if } S_e = 1 \end{cases}$$

$$S_e = \frac{S_l - S_r}{1 - S_r} \quad \dots (Eq. 11b)$$

$$S_e^* = (1 + (\alpha P_e)^n)^{-m} \quad \dots (Eq. 11c)$$

$$m = 1 - 1/n, \text{ and } \alpha = 1/P_r$$

In the above formulations, p_c is the capillary pressure ($p_c = p_{gas} - p_{water}$), α is the inverse of air-entry pressure i.e., P_r , S_e is the effective degree of water saturation, S_l is the degree of water saturation, S_r is residual degree of water saturation, S_e^* is the effective degree of saturation considering the explicit gas entry pressure i.e., P_e , ε is a numerical parameter (0.01 or 0.001), m and n are fitting parameters.

Relative permeability functions considering explicit gas entry pressure:

$$k_{rw} = \begin{cases} \sqrt{S_e} \cdot \left[\frac{1 - (1 - (S_e^* S_e)^{1/m})^m}{1 - (1 - S_e^{*1/m})^m} \right]^2, & \text{if } S_e < 1 \dots\dots\dots (Eq. 12) \\ 1, & \text{if } S_e = 1 \end{cases}$$

$$k_{rg} = \begin{cases} f_g \cdot \sqrt{1 - S_e} \cdot \left[\frac{(1 - S_e^{*1/m})^m - (1 - (S_e^* S_e)^{1/m})^m}{(1 - S_e^{*1/m})^{m-1}} \right]^2, & \text{if } S_e < 1 \dots\dots\dots (Eq. 13) \\ 0, & \text{if } S_e = 1 \end{cases}$$

In the above formulations for relative permeability functions for water (k_{rw}) and gas (k_{rg}), and f_g is the ratio between gas intrinsic permeability values.

The diffusive flux of water vapor (i_v^{\square}), dissolved Hydrogen (i_{dH2}^{\square}), and dry Hydrogen (i_{H2}^{\square}) is linked to gradient of mass fractions of species and follows the formulation as per Eq. 14 and 15.

$$i_v^{\square} = -D_g^{w*} \rho_g \nabla \left(\frac{\rho_v}{\rho_g} \right) = -i_a \dots\dots\dots (Eq. 14)$$

$$i_{dH2}^{\square} = -D_l^{H2*} \rho_w \nabla \left(\frac{\rho_l^{H2}}{\rho_w} \right) \dots\dots\dots (Eq. 15)$$

In the above equations, D_g^{w*} and D_l^{H2*} are effective diffusion coefficient of water vapor in gas and dissolved Hydrogen in liquid for a multiphase porous media, respectively. These coefficients depend on the porous volume of the material, its structure, and its water content, and can be expressed as:

$$D_g^{w*} = \phi(1 - S_{rw})\tau D_g^w \dots\dots (Eq. 16)$$

$$D_l^{H2*} = \phi S_{rw} \tau D_l^{H2} \dots\dots (Eq. 17)$$

where, ϕ is the porosity, S_{rw} is the degree of water saturation, τ is the tortuosity, and D_g^w and D_l^{H2} are the diffusion coefficients of water vapour in Hydrogen and dissolved Hydrogen in water, which are independent of the porous medium.

As per the given specifications for task 4.2, the diffusion coefficient formulation for dissolved gas in liquid water (Eq. 17) has been modified for hydrogen gas as per the Millington-Quirk relative diffusion coefficient formulation as shown below:

$$D_l^{hydrogen} = D_l^{H2} \phi^{1+a} S_e^b \dots\dots (Eq. 18)$$

where, $D_l^{hydrogen}$ is the effective diffusion coefficient of hydrogen in liquid water, a and b are material parameters, S_e^{\square} is the effective degree of saturation ($S_e = \frac{S_l - S_r}{1 - S_r}$), and D_l^{H2} is the diffusion coefficient of dissolved Hydrogen in liquid water.

The vapor is assumed to be in equilibrium with the liquid water and the vapor density ρ_v is expressed as:

$$\rho_v = \rho_{sat}(RH) \dots\dots\dots (Eq. 19)$$

where, ρ_{sat} is the saturated water vapor density and RH is the relative humidity. The relative humidity considers the adsorption phenomenon and the capillary effect. The Kelvin-Laplace equation relates suction with relative humidity as per Eq. 20.

$$RH = \exp\left(\frac{sM_w}{\rho_w R_v T}\right) \dots\dots\dots (Eq. 20)$$

Where, R_v is the gas constant of water vapor, s is the suction ($p_g^{\square} - p_w$) and T is the temperature.

Vapor is considered as a perfect gas and vapor pressure is computed using the ideal gas law, as shown below:

$$p_v = \left(\frac{n}{v}\right) R_v T \dots\dots\dots (Eq. 21)$$

$$p_v = \rho_v R_v T \dots\dots\dots (Eq. 22)$$

9.3 Material properties

The material properties related to the mechanical and hydraulic constitutive models as discussed in the previous section are listed in **Appendix I (Table A1 to A4)**. During the analysis, some reasonable assumptions were made concerning some of the missing material properties, as listed below:

- The properties of top/bottom aquifers were considered the same as host rock. In Zone C, steel liner was replaced with air void.
- In Zone B, waste canister and conc. buffer were replaced with cement backfill.
- The bulk density of different materials was calculated from the initial vertical stresses along the depth.
- The values of volumetric specific heat capacity (ρC_p) was calculated based on the formula as shown below, and it was kept constant during the analysis.

$$\rho C_p = C_s \rho_s (1 - n) + C_w \rho_w S_{rw} n + C_{H2} \rho_{H2} (1 - S_{rw}) n$$
- All the emplaced materials were assumed to have an initial water saturation of 80%, and the initial pore water pressure in these materials were in accordance with their water retention parameters.

The fluid (water / air / hydrogen) properties used in the present analysis are discussed in **Appendix 1 (Table A5)**. The liquid viscosity, density and the volumetric thermal expansion coefficient were considered as a function of temperature, as discussed below:

- For liquid viscosity:

$$\mu_l = 1 \times 10^{-3} \exp\left(-3.719 + \frac{578.919}{(T(^{\circ}K)-137.546)}\right) \text{ in (Pa} \cdot \text{s)}$$

- For liquid density:

$$\rho_l = \rho_{l0} \left(1 + (p_l - p_{l0}) \times B - \beta_W^T \times (T - T_0)\right)$$

where, the reference density $\rho_{l0} = 1000 \text{ Kg} \cdot \text{m}^{-3}$ and the reference pressure $p_{l0} = 0.1 \text{ MPa}$, B is liquid compressibility coefficient, and β_W^T is the liquid thermal expansion coefficient.

- For thermal expansion coefficient:

$$\beta_W^T = 1 \times 10^{-6} [1 \times 10^{-4} (T - 273.15)^3 - 0.0314 (T - 273.15)^2 + 6.1649 (T - 273.15) + 106.61]$$

9.4 Features of numerical analysis

9.4.1 Mesh generation

Figure 9-2 shows the finite element mesh used for the numerical analysis of Zone B and Zone C.

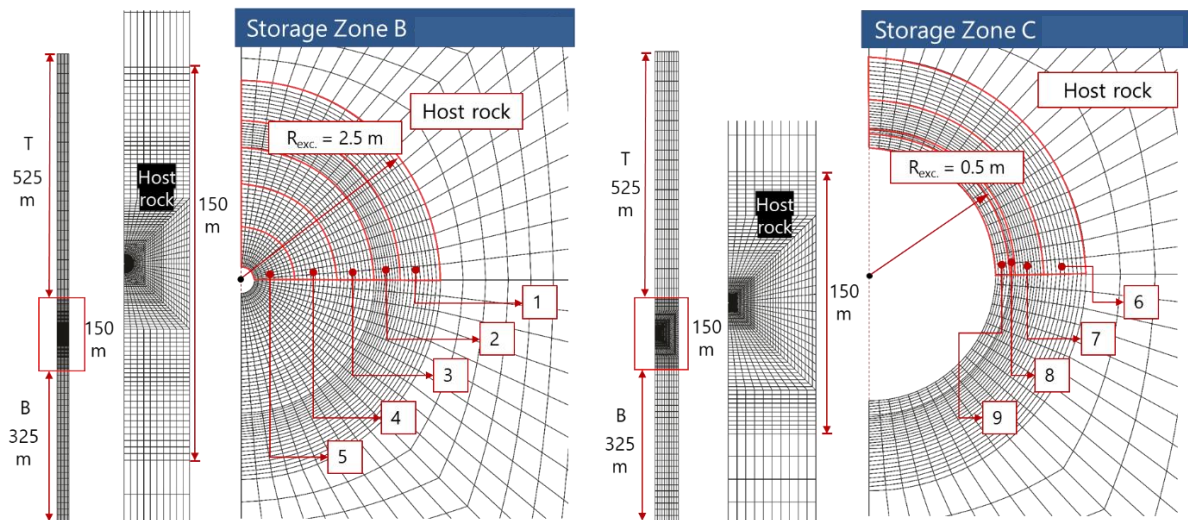


Figure 9-2 Finite element mesh (T = top aquifer, B = bottom aquifer; In Zone B: 1 = outer EDZ, 2 = inner EDZ, 3 = concrete liner, 4 = cementitious backfill, 5 = concrete buffer; In Zone C: 6 = outer EDZ, 7 = inner EDZ, 8 = steel liner, 9 = air void).

9.4.2 Initial boundary conditions

The initial boundary conditions are shown in Figure 9-3 with the Biot coefficient values as per the given specifications. The temperature and pore water pressure were kept constant at the top and bottom extremities of the 2D model in both Zone B and Zone C. The initial stresses (σ_v and σ_h) along the Y-axis are also shown along with the K_0 value which was considered 1 during the analysis.

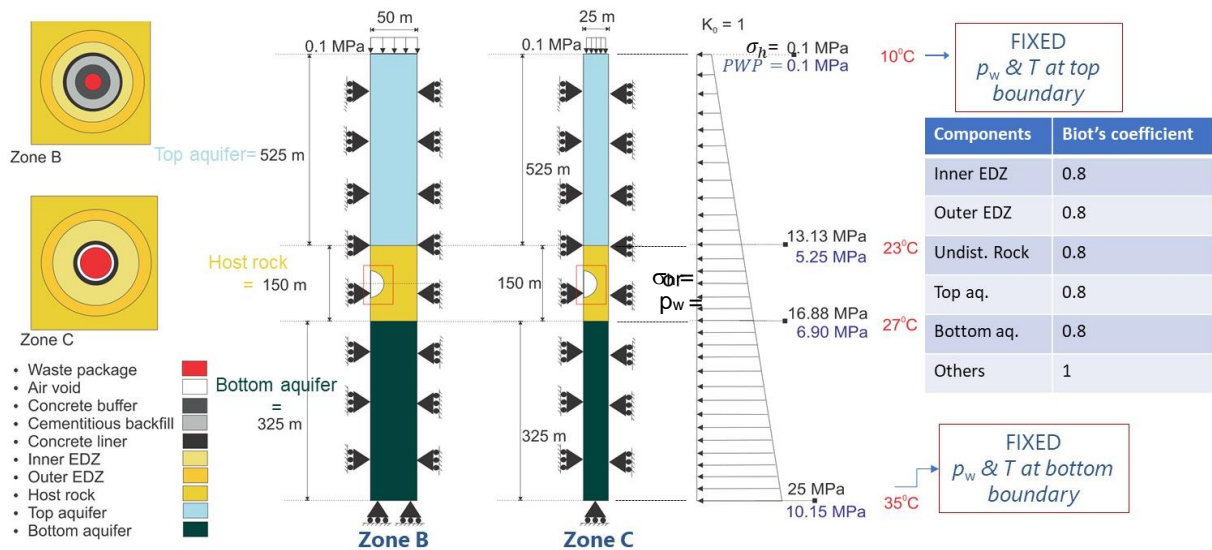


Figure 9-3 Initial boundary conditions for 2D PS analysis (Not at scale).

9.4.3 Time varying boundary conditions

The time-varying boundary conditions represents the different stages of a generic repository set up. For the analysis, these conditions were adopted from the technical document and are discussed in Table 9-1.

Table 9-1 Features of time-varying boundary conditions (Note: σ_v ; σ_h is vertical or horizontal stresses, p_w is pore water pressure, T is temperature along the depth, RH is relative humidity, and s_t is total suction).

Phase	Time [Years]	Scenario	Features
Initial	$T < 0$	No Repository (Instantaneous excavation)	<ul style="list-style-type: none"> In-situ stress regime (σ_v; σ_h) Hydrostatic pressure (p_w) Natural geothermal field (T)
Phase-I	$T = 0-50$	Ventilation (Zone B) Dewatering (Zone C)	<ul style="list-style-type: none"> Ventilation/Dewatering effect <ul style="list-style-type: none"> Zone B $\approx 80\% RH$ ($s_t = 30.60 MPa$) Zone C ($p_w \approx 0.1 MPa$)
Phase-II	$T = 50-100,000$	Instantaneous waste emplacement	<ul style="list-style-type: none"> Thermal load and gas generation (Hydrogen)

For the initial phase ($T < 0$), initial pore water pressure (p_w), in-situ stresses (σ_v and σ_h), and temperature (T) values were setup along the Y-axis (see Figure 9-4 a, b and c). In phase-I, the instantaneous excavation was numerically mimicked by reducing the in-situ normal stress to zero at the excavated face (i.e., $R_{exc.} = 0.5$ m for Zone C; $R_{exc.} = 2.5$ m for Zone B) as shown in Figure 9-5(a). The above change in the in-situ stresses was implemented in first 24 hours and kept constant during the ventilation/dewatering and waste emplacement stages.

The event of ventilation in Zone B and dewatering in Zone C was simulated by imposing the corresponding changes in the initial pore water pressure (i.e., 4.70 MPa to -30.60 MPa in Zone B and 0.10 MPa in Zone C), as depicted in Figure 9-5B. The applied change in the pore water pressure was

activated at the intrados of concrete liner ($r = 1.80\text{m}$) in Zone B, and at the excavated face in Zone C ($r = 0.5\text{m}$) as depicted in Figure 9-5c and 5d.

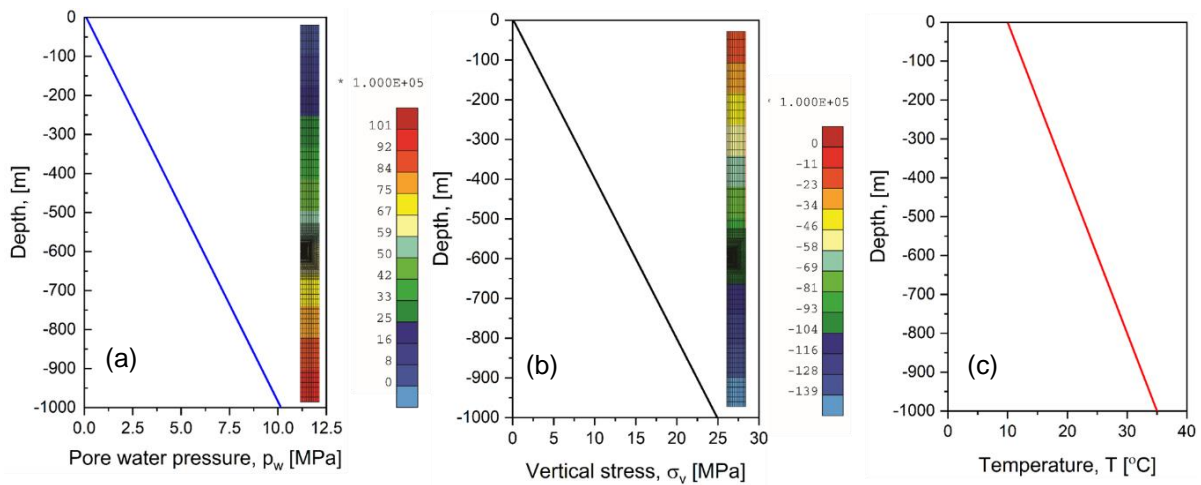


Figure 9-4 Setting up of initial boundary conditions, (a) pore water pressure, (b) vertical stress, and (c) temperature along the Y-direction or the depth.

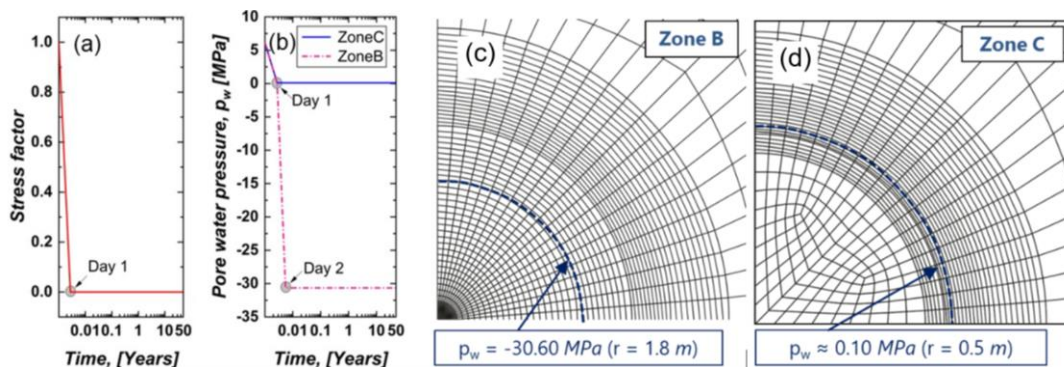


Figure 9-5 (a), (b) Initiation of tunnel excavation process using theory of deconfinement, and (c), (d) implementation of dewatering process in Zone C and ventilation process in Zone B.

Phase-II i.e., instantaneous waste emplacement signifies the activation of heat and gas (H_2) source terms at the relevant locations. The heat and gas source terms were deduced from the specifications as elaborated in Figure 9-6. The equivalent heat flow values (W/m^2) were calculated over the average length of waste canisters i.e., 4.254m for Zone B and 1.80m for Zone C. Similarly, the equivalent gas (H_2) flow values in $\text{kg}/\text{s}\cdot\text{m}^2$ were calculated from the given specifications and applied at the relevant locations.

The generic gas source term is supposed to be composed solely by hydrogen generated by anoxic corrosion of only non-allied steel (i.e. no other metallic component, no radiolysis, no bacterial activity, no radionuclides decay).

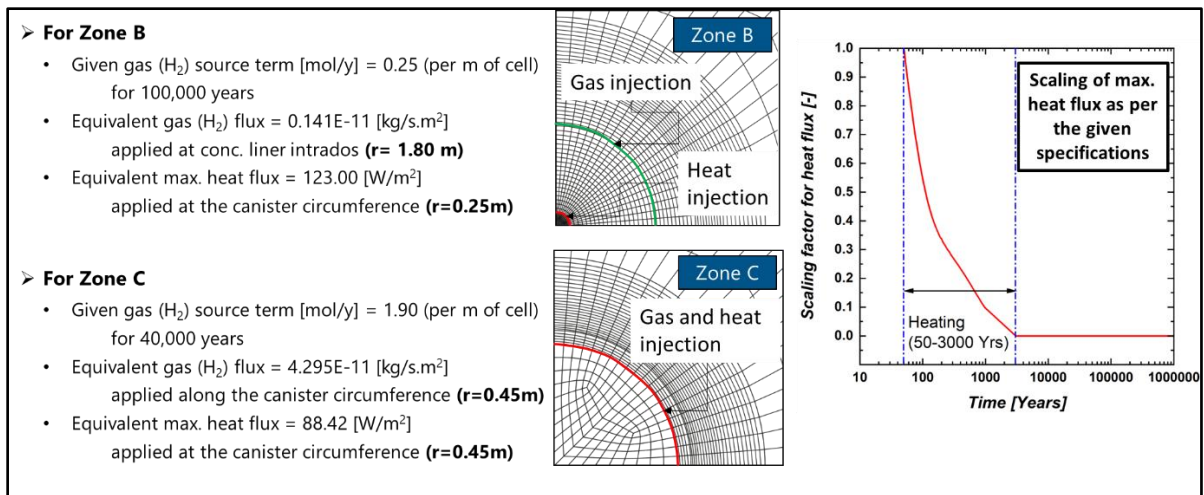


Figure 9-6 Gas (hydrogen) and thermal source term for Zone B and Zone C.

9.5 Simulation results

The simulation results are discussed to highlight the key observations and lessons learnt during the analysis; these are:

- Effect of SWRC formulations (role of gas-entry pressure)
- Effect of geometric features (consideration of top/bottom aquifers)
- Role of temperature on gas/porewater pressure evolution (THMG v/s HMG-coupling scenarios)
- Effect of gas (H₂) generation on simulation results (THMG v/s THM-coupling scenarios)

Evolutionary trend of key variables such as temperature, pore Hydrogen and water pressure, degree of water saturation, and the Biot's effective vertical stress were plotted at various locations as shown in Figure 9-7 and Figure 9-8.

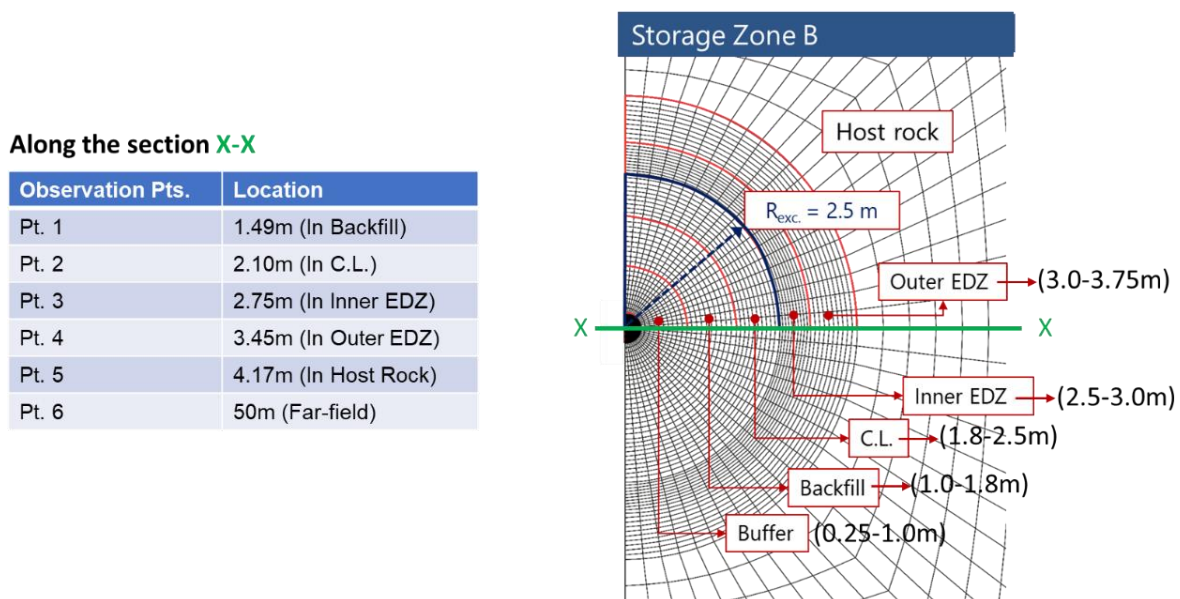


Figure 9-7 Observation points in Zone B.

Along the section X-X

Observation Pts.	Location
Pt. 1	0m (Canister center)
Pt. 2	0.12m (In waste)
Pt. 3	0.55m (In Inner EDZ)
Pt. 4	0.67m (In Outer EDZ)
Pt. 5	0.95m (In Host Rock)
Pt. 6	25m

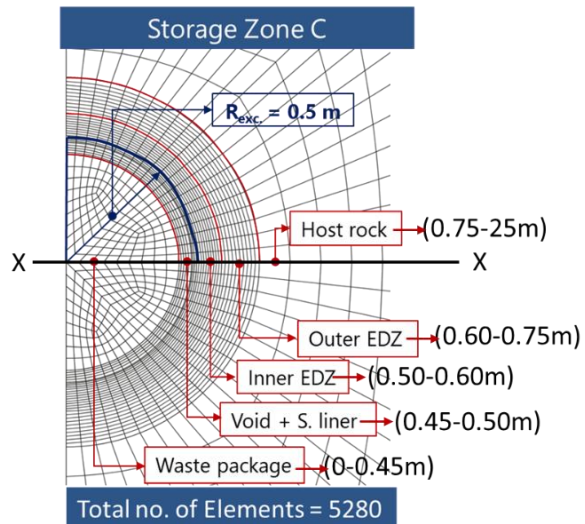


Figure 9-8 Observation points in Zone C.

9.5.1 Effect of SWRC formulation

One of the key features of given specifications for task 4.2 were water retention curve and relative permeability functions which consider the gas entry pressure in the formulation (see Eqs. 11 to 13). During the implementation of the given SWRC formulation in the case of Zone B, some numerical issues were observed. Hence, the given formulation was adopted for some selected materials as mentioned in Table 9-2.

For investigating the effect of SWRC formulation, two different cases were analyzed as shown in Table 9-3. Case 1 was dedicated to the idealized classical van Genuchten water retention model along with the specified relative permeability functions. Whereas case 2 represents the reference case based on the given technical specifications.

Table 9-2 Application of specified SWRC formulation in Zone B.

Material	Specified SWRC	Specified Rel. per. funs.
Top aquifer	✓	✓
Bottom aquifer	✓	✓
Host rock	✓	✓
Outer EDZ	✓	✓
Inner EDZ	✗	✓
Concrete liner	✗	✓
Cementitious backfill	✗	✓
Concrete buffer	✗	✓
Canister	✗	✓

Table 9-3 Case1 and case 2 for investigating the effect of SWRC formulation.

Cases	Classical SWRC	Given Rel. Per. Funs.	Specified SWRC	Coupling	Geometry Features
Case 1	✓	✓	✗	THMG	As specified
Case 2	✗	✓	✓	THMG	As specified

In case 1, the air entry pressure in the classical van Genuchten SWRC was modified in order to match the response of given SWRC in terms of effective degree of water saturation (S_e) and suction (s and p_o). These idealized air entry pressure values were used for the outer EDZ, host rock, and for the top and bottom aquifers as shown in Table 9-4. Fig. 9 shows the comparison between the idealized water retention curve with the specified one and highlights the role of parameter ε which separates the given SWRC in two different formulations at $S_e = 1 - \varepsilon$. An idealized SWRC is unable to produce such a response, as a result some variations were observed close to the saturation.

Table 9-4 Parameters for an idealized classical van Genuchten SWRC.

Material	Given gas entry pressure [MPa]	Given air entry pressure [MPa]	Idealized air entry pressure [MPa]	n [-]	m [-]
Inner EDZ	0	16	16	1.5	0.33
Outer EDZ	2	16	17	1.5	0.33
Host Rock	6	16	23	1.5	0.33
Top/Bottom aquifers	6	16	23	1.5	0.33

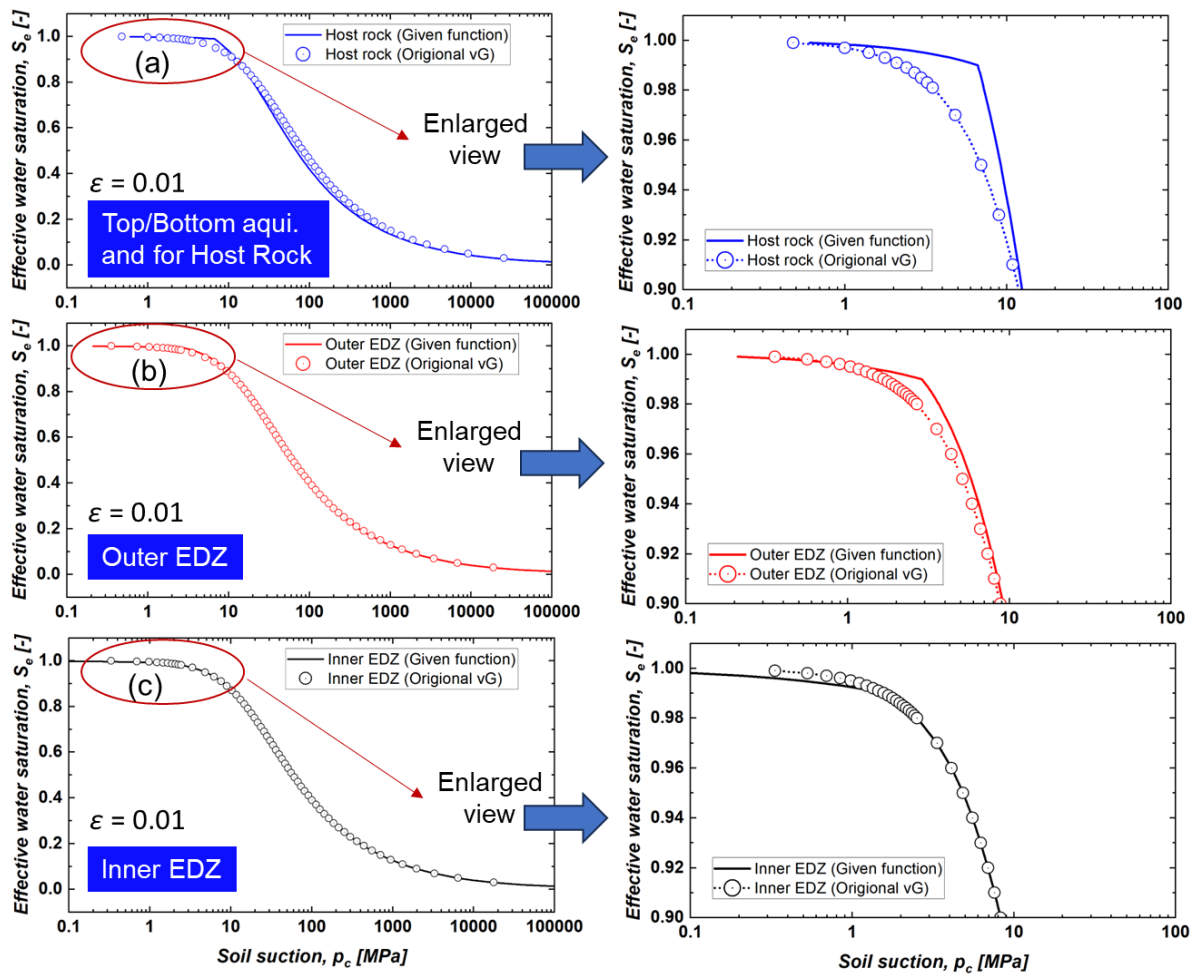


Figure 9-9 Comparison of an idealized van Genuchten water retention model with the specified water retention formulations considering the gas entry pressure with ϵ equals to 0.01.

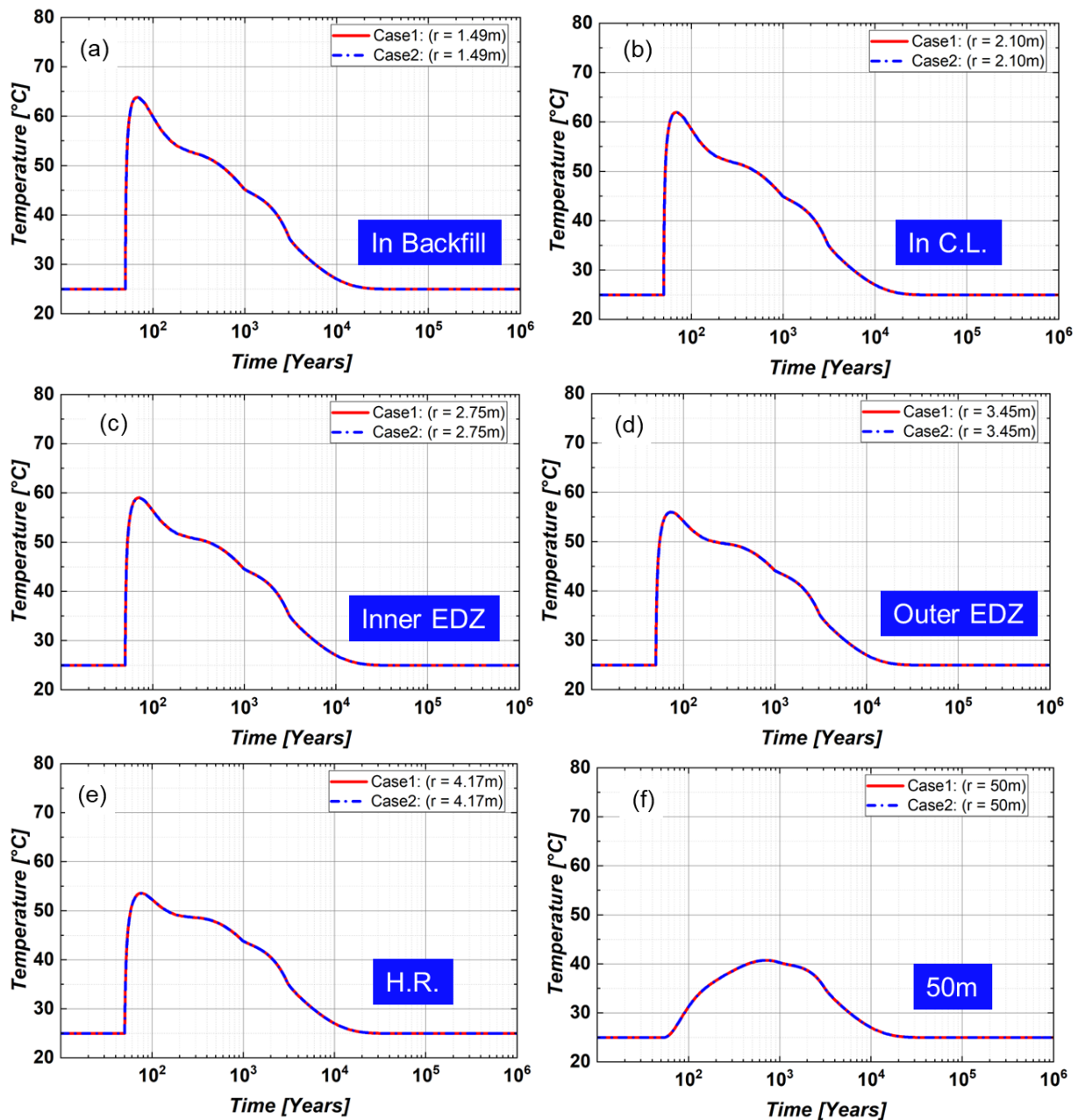


Figure 9-10 Evolution of temperature in Zone B (Case 1 v/s Case 2).

The evolution of temperature at different locations of Zone B and Zone C is shown in Figure 9-10 and Figure 9-11, respectively. It is worth mentioning here that the temperature at the level of deposition tunnel was kept constant (25°C) during the excavation and ventilation phase (0 to 50 years).

As evident from Figure 9-10 and Figure 9-11, temperature evolution did not depend on the SWRC formulation. Both in Zone B and Zone C, temperature increased immediately after the waste emplacement at the locations close to the waste canisters. In Zone B, the maximum temperature reached up to 64°C in backfill during the first 18 years of heating. While in Zone C it reached up to 100°C at the locations close to the waste canister such as inner EDZ.

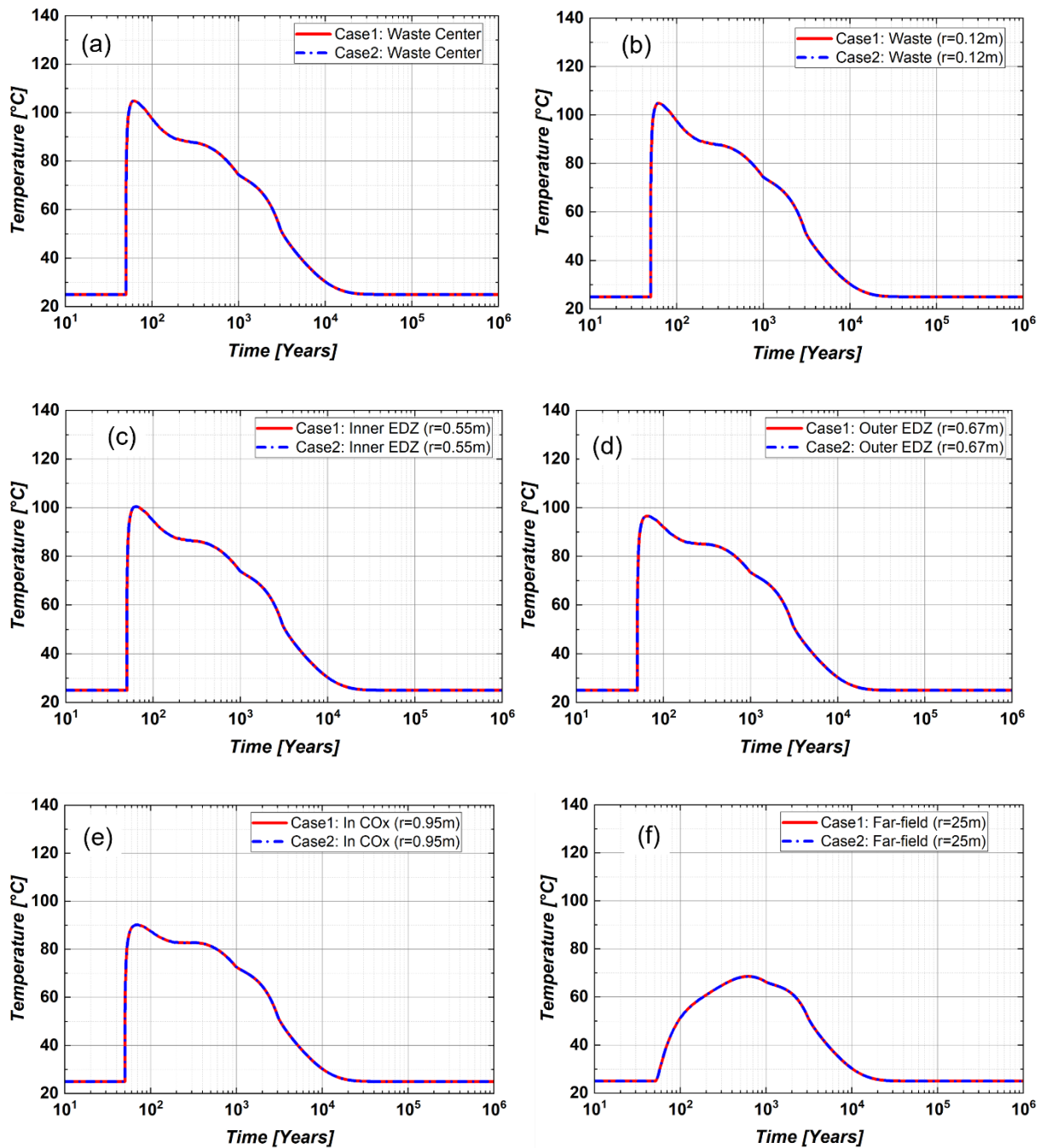


Figure 9-11 Evolution of temperature in Zone C (Case1 v/s Case 2).

With elapsed time, the temperature gradually decreased and attained the initial value in 30,000 years. The peak temperature varied with the distance from the injection point. At the boundary of 2D model in X-direction i.e., the half-spacing of the deposition tunnels (50 m in case of Zone B and 25 m in case of Zone C), the temperature reaches up to 41°C in 710 years in Zone B, and up to 68.5°C in 700 years in Zone C.

The evolution of pore water pressure at different locations is shown in Figure 9-12 for Zone B and in Figure 9-13 for Zone C. Before discussing the PWP distribution in Zone B, it should be noted here that the idealized SWRC was used for backfilling material, conc. liner and inner EDZ in both cases. As a result, the PWP distribution in these materials was found to be similar. Also, it is worth mentioning here that the backfilling material was placed instantaneously after the completion of ventilation phase.

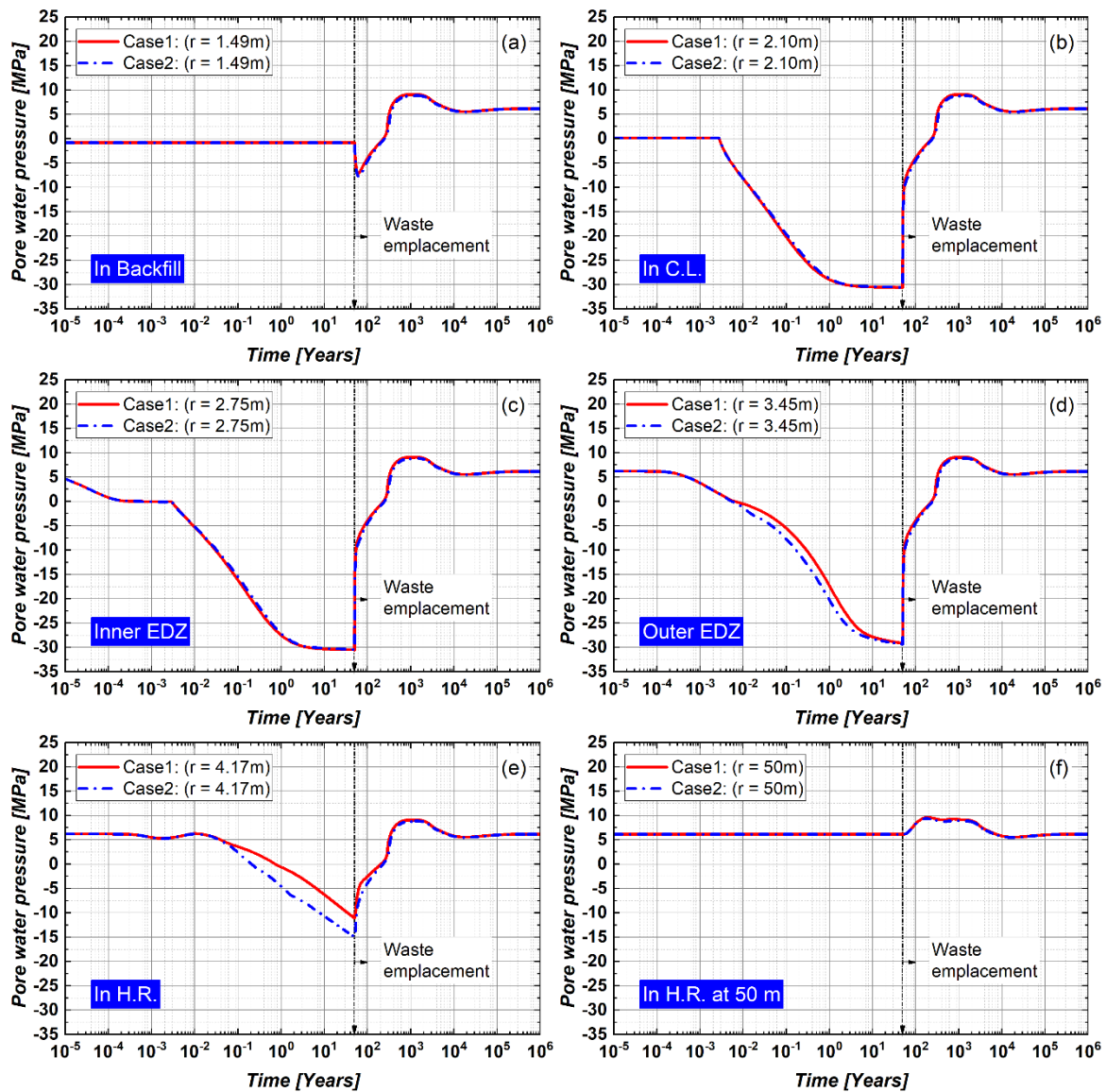


Figure 9-12 Evolution of pore water pressure in Zone B (Case 1 v/s Case 2).

For the other locations such as outer EDZ and nearby host rock, some minor variations were observed primarily during the ventilation phase. The ventilation-induced desaturation was more pronounced close to the excavated face, as a result, the PWP in concrete liner, inner EDZ, outer EDZ and nearby host rock decreased. The extent of ventilation-induced desaturation zone primarily depends on the relative humidity values and its seasonal variations during the ventilation period. Also, the hydraulic parameters such as intrinsic permeability etc. play a significant role. The moment of waste emplacement induced a rapid increase in PWP at all the locations due to the injected heat. It was observed that the peak value of temperature induced excess PWP was the same in both cases.

In Zone C (see Figure 9-13), the excavation was performed under drained conditions. As a result, the PWP decreased from its initial value to the atmospheric, particularly at the locations close to the excavated face (Figure 9-13a to 13e). After the completion of dewatering phase, the PWP increased rapidly similar to Zone B due to the temperature rise and reached up to 20.8 MPa. Comparing Figure 9-12 with Figure 9-13, it is evident that during the waste emplacement, the pore water pressure distribution was predominantly controlled by thermal response in both Zone B and Zone C.

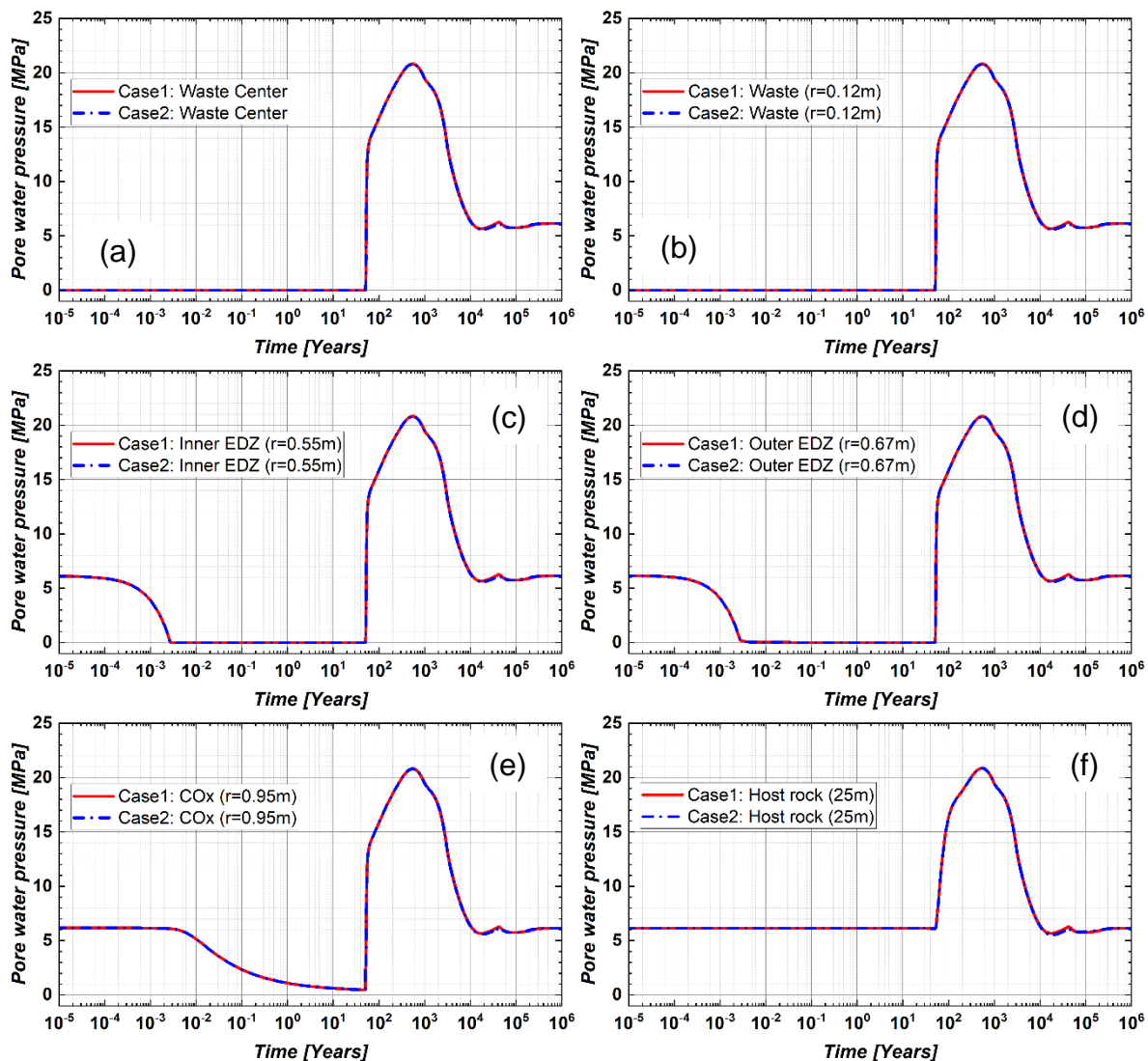


Figure 9-13 Evolution of pore water pressure in Zone C (Case 1 v/s Case 2).

Figure 9-14 shows the gas (H_2) pressure evolution in Zone B at different locations for case 1 and 2. In both cases, the gas pressure evolution was identical except for some minor variations during the occurrence of the first peak. A slightly higher peak was observed in case 2 as compared to case 1. However the maximum gas pressure values were the same in both the cases. Similar to the temperature evolution, the gas pressure was also found to be dependent on the distance from the injection point. The closer locations yield the higher gas pressure.

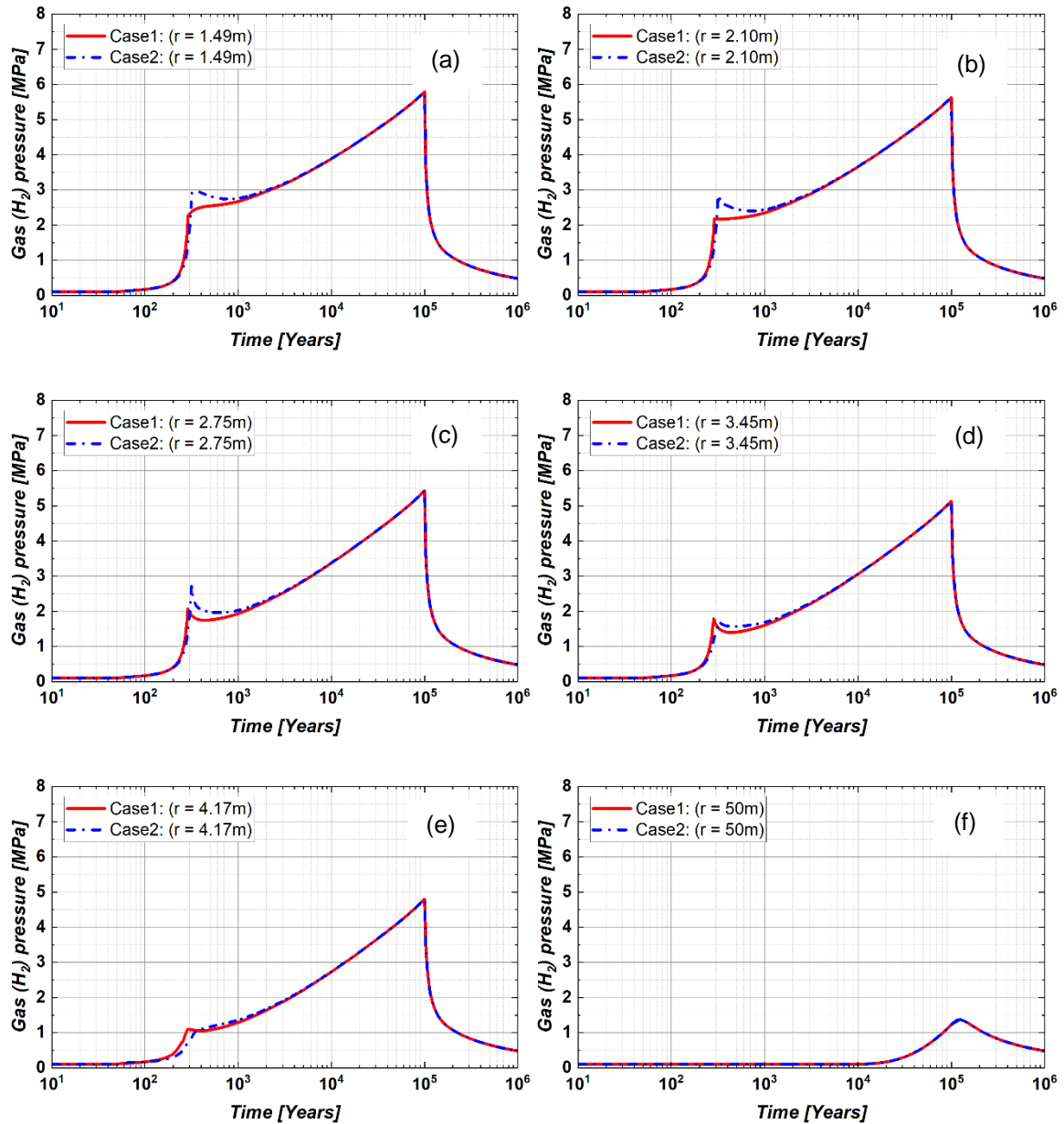


Figure 9-14 Evolution of gas (H₂) pressure in Zone B (Case 1 v/s Case 2).

Figure 9-15 shows the gas (H₂) pressure evolution in Zone C. Like Zone B, a quite similar gas pressure evolution was observed in both cases with some variation after the occurrence of peak pressure which was close to 20.8 MPa. Also, the gas pressure buildup was more pronounced at locations close to the injection point like Zone B. As evident from Figure 9-14 and Figure 9-15, a much higher gas pressure was observed in Zone C as compared to Zone B. One of the reasons is the higher source term for Zone C (1.90 mol/year). The degree of water saturation also plays a significant role as highlighted by the Millington-Quirk relative diffusion coefficient formulation:

$$D_l^{hydrogen} = D_l^{dH2} \phi^{1+a} S_e^b$$

Where, $D_l^{hydrogen}$ is the effective diffusion coefficient of hydrogen in liquid water, a and b are material parameters, S_e is the effective degree of saturation ($S_e = \frac{S_l - S_r}{1 - S_r}$), and D_l^{dH2} is the diffusion coefficient of dissolved Hydrogen in liquid water.

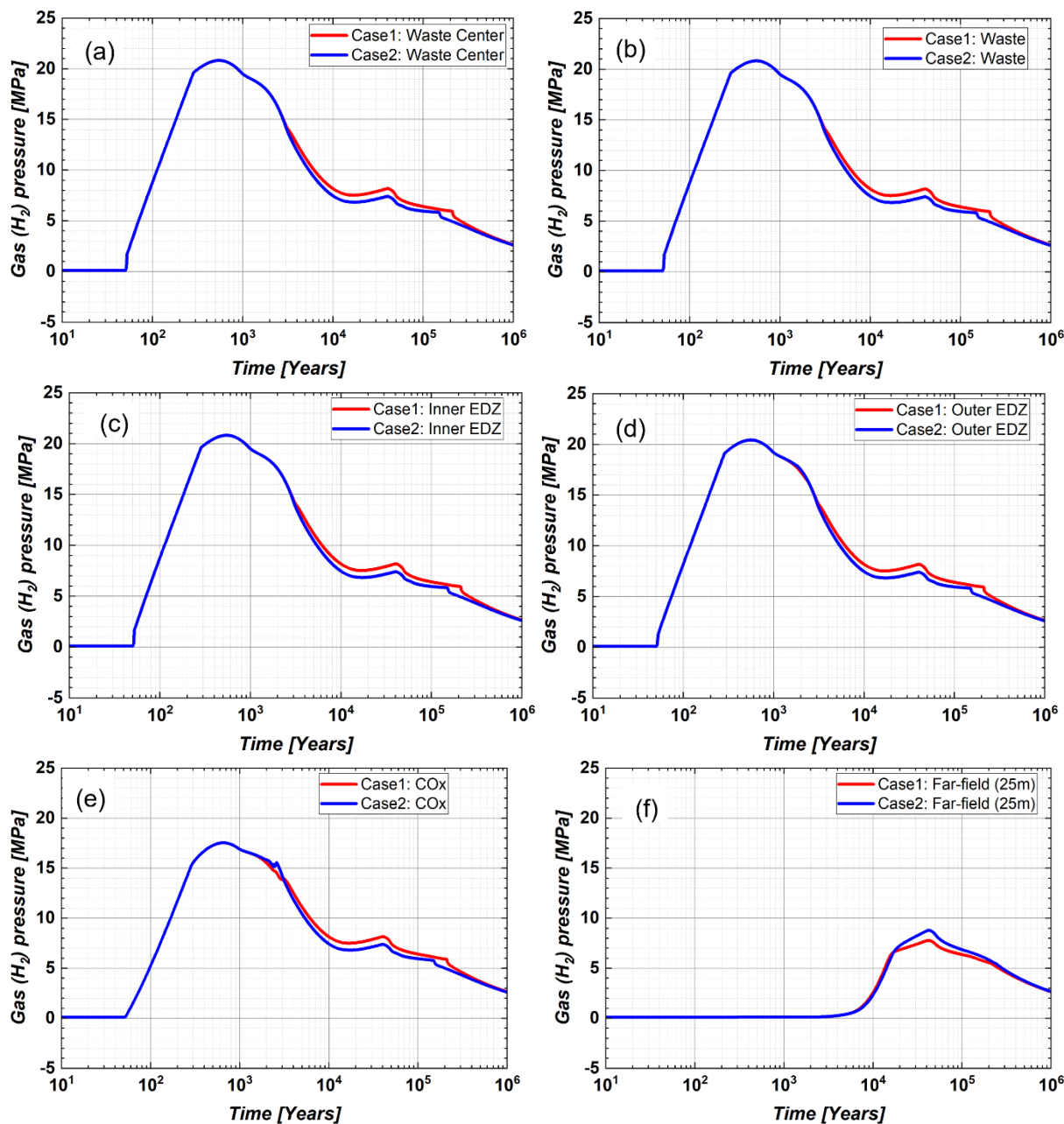


Figure 9-15 Evolution of gas (H₂) pressure in Zone C (Case 1 v/s Case 2).

Figure 9-16 shows the variation of water saturation in Zone B for locations in inner EDZ, outer EDZ and host rock. In the first 50 years, the effect of ventilation-induced desaturation was observed at the locations situated close to the excavated face. An instantaneous increase in the water saturation was observed at the locations close to the heat injection point which was due to the temperature-induced excess pore water pressure.

Figure 9-17 presents the variation of water saturation in Zone C for inner EDZ, outer EDZ and host rock. Initially from a fully saturated state, some minor variations were observed in the first 50 years. However during the waste emplacement, a rapid rise in temperature induced PWP occurred. In later years, desaturation occurred in both cases as a result of gas pressure increase in Zone C.

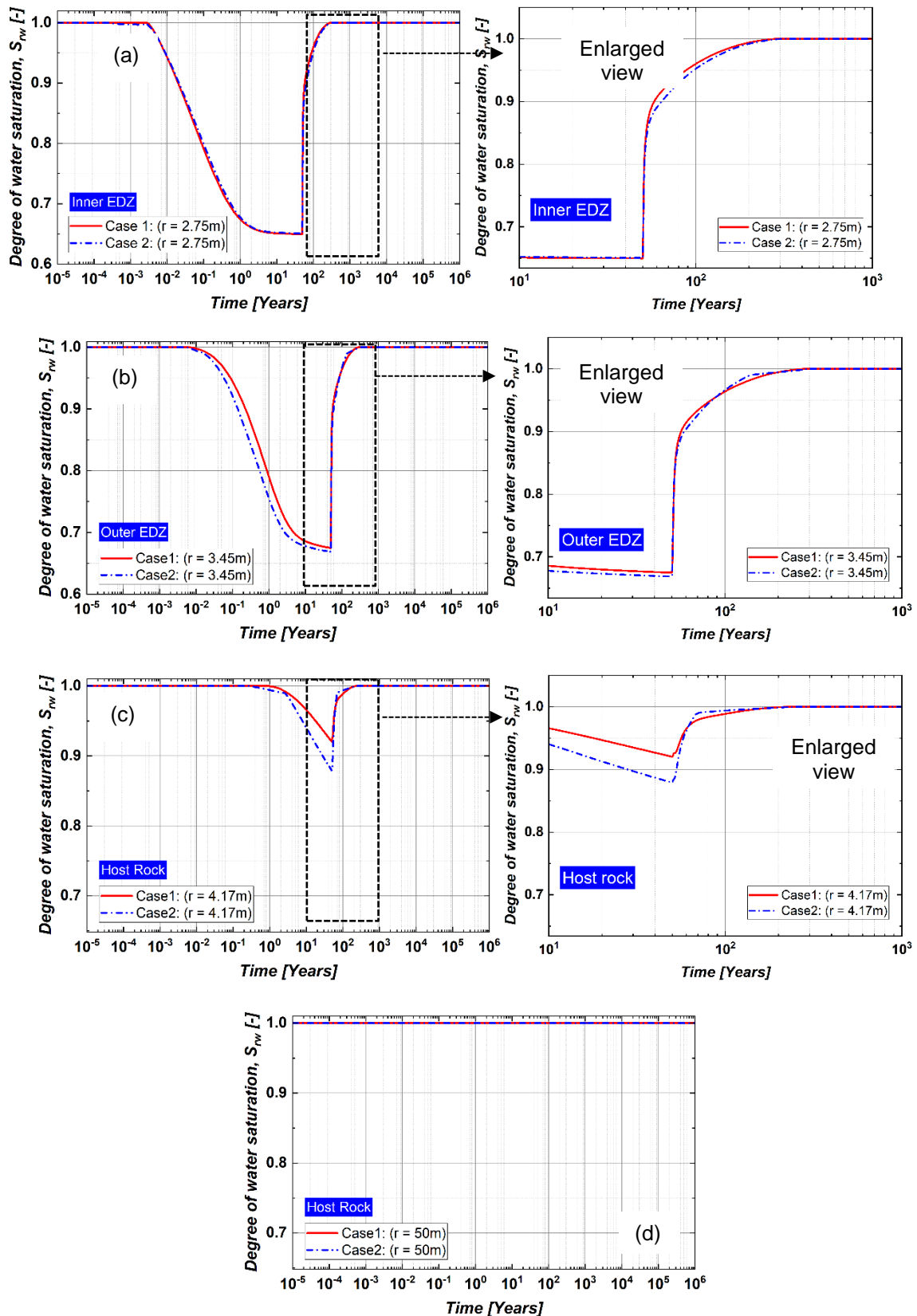


Figure 9-16 Evolution of water saturation in Zone B (Case 1 v/s Case 2).

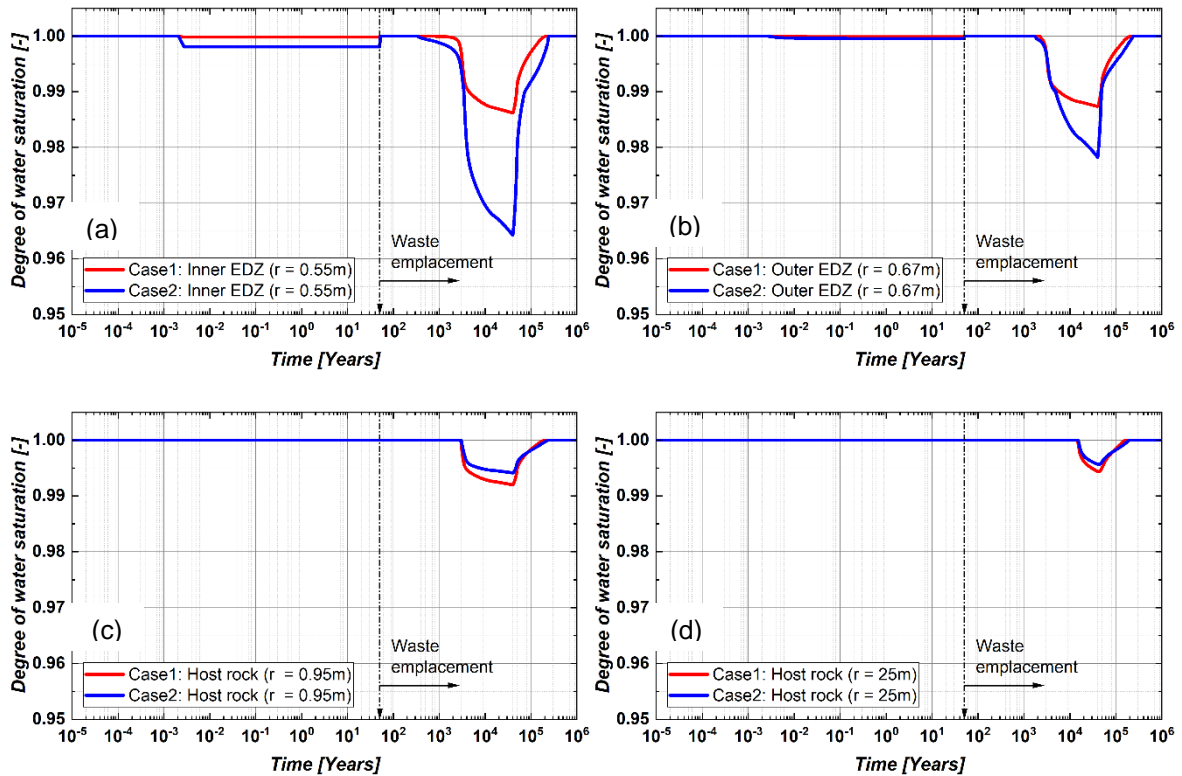


Figure 9-17 Evolution of water saturation in Zone C (Case 1 v/s Case 2).

The Biot's effective stress framework was adopted during the simulation, as explained in equation 23.

$$\sigma = \sigma' - b \cdot \left((1 - S_w) \cdot p_g + S_w \cdot p_w \right) \dots \dots \dots (Eq. 23)$$

Where, σ is the total stress, σ' is the effective stress, b is the Biot's coefficient, S_w is degree of water saturation, p_g is the pore gas pressure, and p_w is the pore water pressure.

Figure 9-18 shows the evolution of effective vertical stress in Zone B at various locations along the section that passes through the center of the deposition tunnel in X-direction. Prior to discussing the stress evolution, it is important to recall the relevant simulation features which may affect the mechanical response. To mimic the excavation process, stress reduction method was used in which the total stress at the excavated face was reduced to 0 within 24 hours under drained conditions. Later, the hydraulic BCs at the excavated face were adjusted to simulate the ventilation scenario in Zone B and dewatering in Zone C.

Initially, the effective vertical stress (≈ 10 MPa) was in accordance with the initial total stresses (≈ 15 MPa), initial PWP (≈ 6 MPa) along with other parameters ($b = 0.8$; $S_w = 1$). The excavation followed by ventilation in Zone B initiated redistribution of PWP, particularly at locations close to the excavation face (see Figure 9-18). Consequently, the PWP reduced, and the effective stresses (compression) increased. Once the ventilation was over and the waste canisters were emplaced, effective stress at all the locations decreased due to the temperature-induced excess pore water pressure. As evident from Figure 9-18, the SWRC formulation did not affect the effective vertical stress distribution along the horizontal axis of deposition tunnel of Zone B. Figure 9-19 presents the evolution of effective vertical stress in Zone C for case1 and case2.

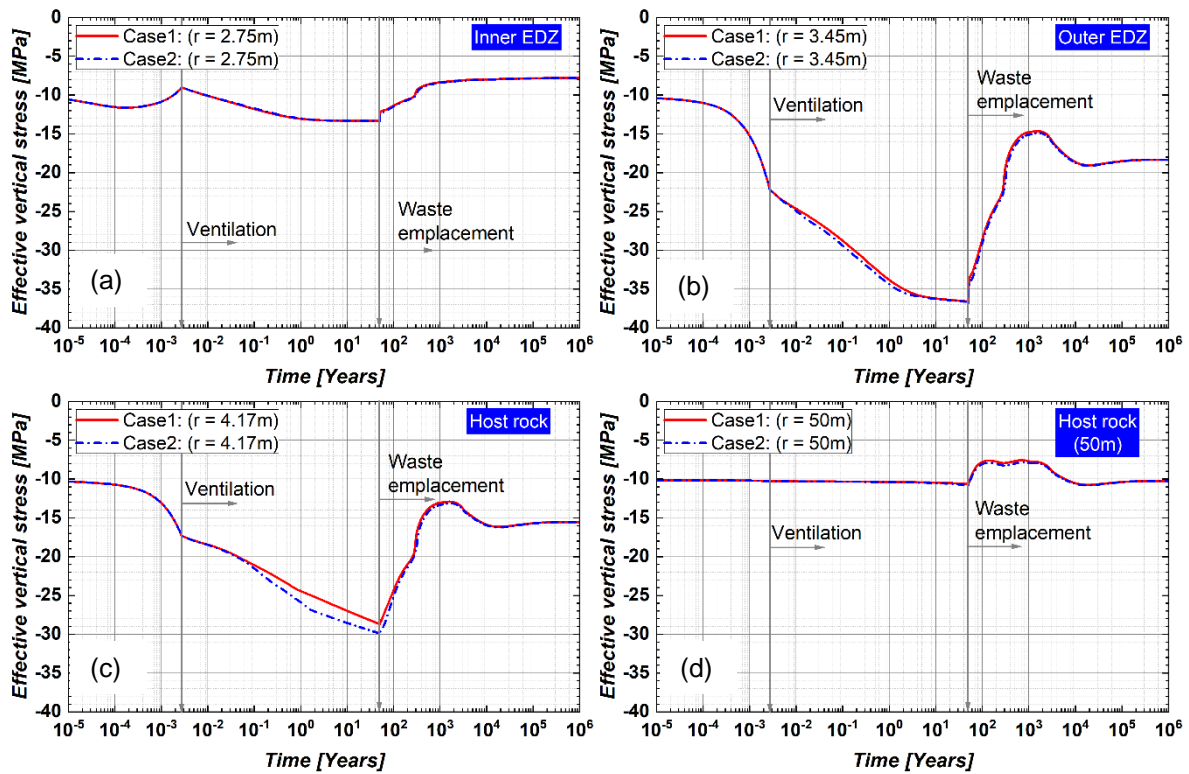


Figure 9-18 Evolution of effective vertical stress in Zone B (Case 1 v/s Case 2).

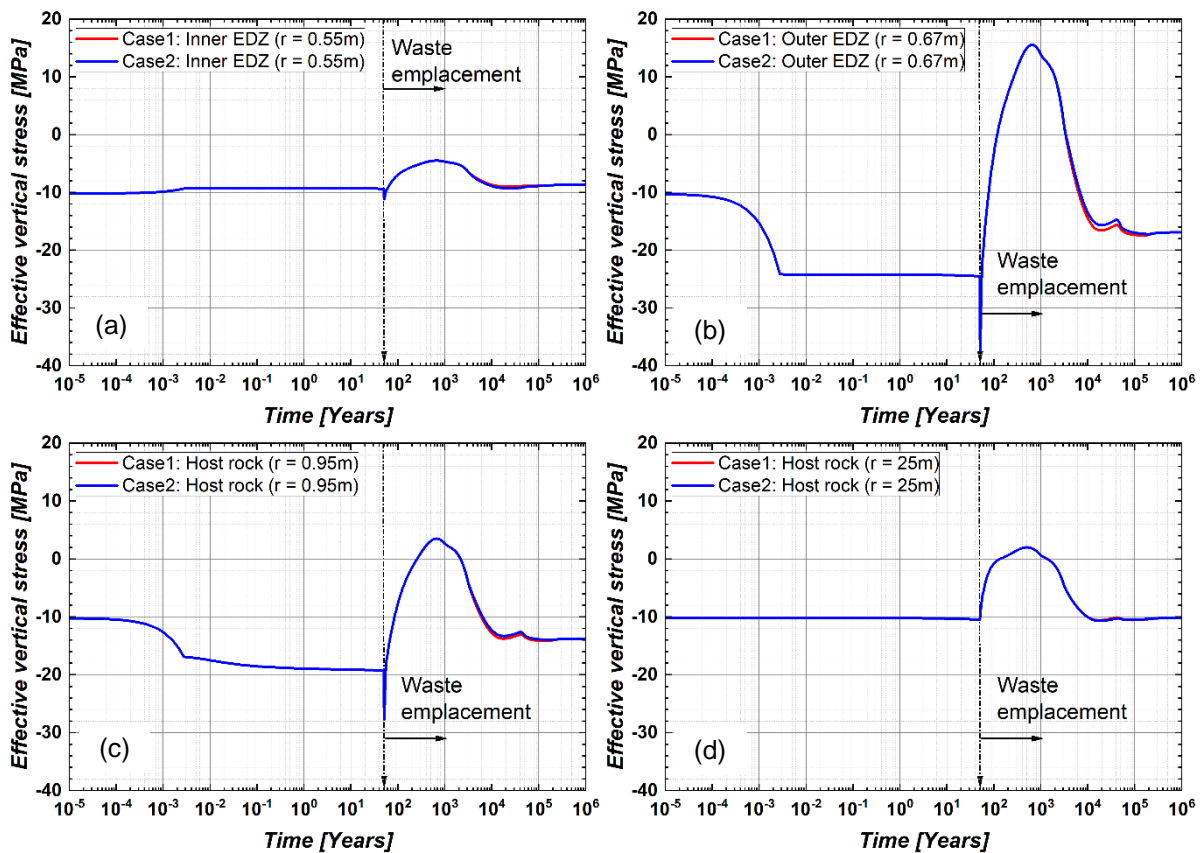


Figure 9-19 Evolution of effective vertical stress in Zone C (Case 1 v/s Case 2).

Similar to Zone B, it was observed that both cases yield an identical effective vertical stress distribution. The effect of excavation and dewatering phase was more predominant in outer EDZ and the surrounding host rock. During the instantaneous emplacement of waste and closure of the whole repository, effective stress at all the locations decreased due to temperature-induced excess pore water pressure. For the locations such as outer EDZ, nearby host rock and at 25m, the effective vertical stresses reached zero.

9.5.2 Effect of geometric features (consideration of top/bottom aquifers)

Table 9-5 outlines the features of numerical analysis for examining the effects of top/bottom aquifers on the simulation results. Case 2 represents the reference case which incorporates all the complexities of the given task. In case 3, the top/bottom aquifers have been deactivated by fixing the corresponding nodal values for pore water pressure (p_w), pore Hydrogen pressure (p_{H2}) and temperature (T). Specified water retention curve along with the water/gas relative permeability formulations were used in both these cases, however in Zone B these formulations were used only for outer EDZ, host rock and top/bottom aquifers due to having numerical issues.

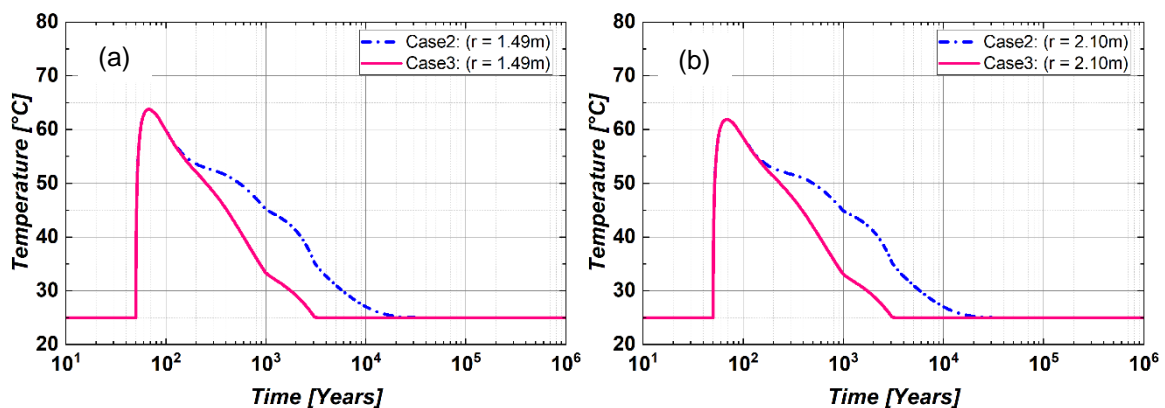
Table 9-5 Case 2 and case 3 for investigating the effect of geometry.

Cases	Given Rel. Per. Funs.	Specified SWRC	Coupling	Geometric Features
Case 2	✓	✓	THMG	As specified
Case 3	✓	✓	THMG	No top/bottom aquifers

Figure 9-20 and Figure 9-21 show the temperature evolution in Zone B and in Zone C, respectively. As evident from the figures, the presence of top and bottom aquifers affects the temperature evolution in both Zone B and Zone C.

It can be observed that the peak values in both cases were similar, particularly close to the injection point such as inner EDZ, outer EDZ, and nearby host rock. Whereas these peak values were different at location $r = 50\text{m}$ in Zone B and $r = 25\text{m}$ in Zone C. It signifies that the peak temperature close to the injection point primarily depends on the amount of the injected heat.

In both Zone B and Zone C, the post-peak evolution was different at all locations with a shorter thermal span of 3000 years in case 3 (without the top and bottom aquifers) as compared to case 2 (30,000 years). It is primarily due to the fixation of temperature in the overlaying and underlying aquifers which act as thermal boundary conditions for the host rock.



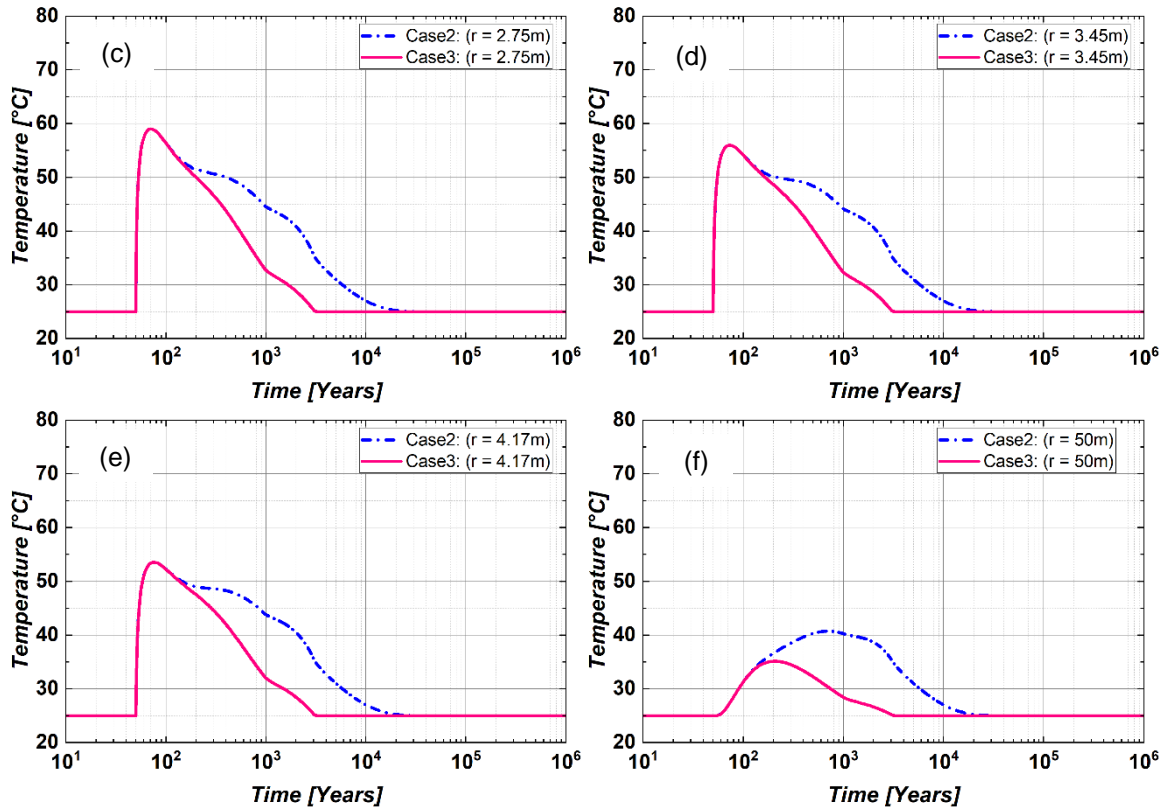
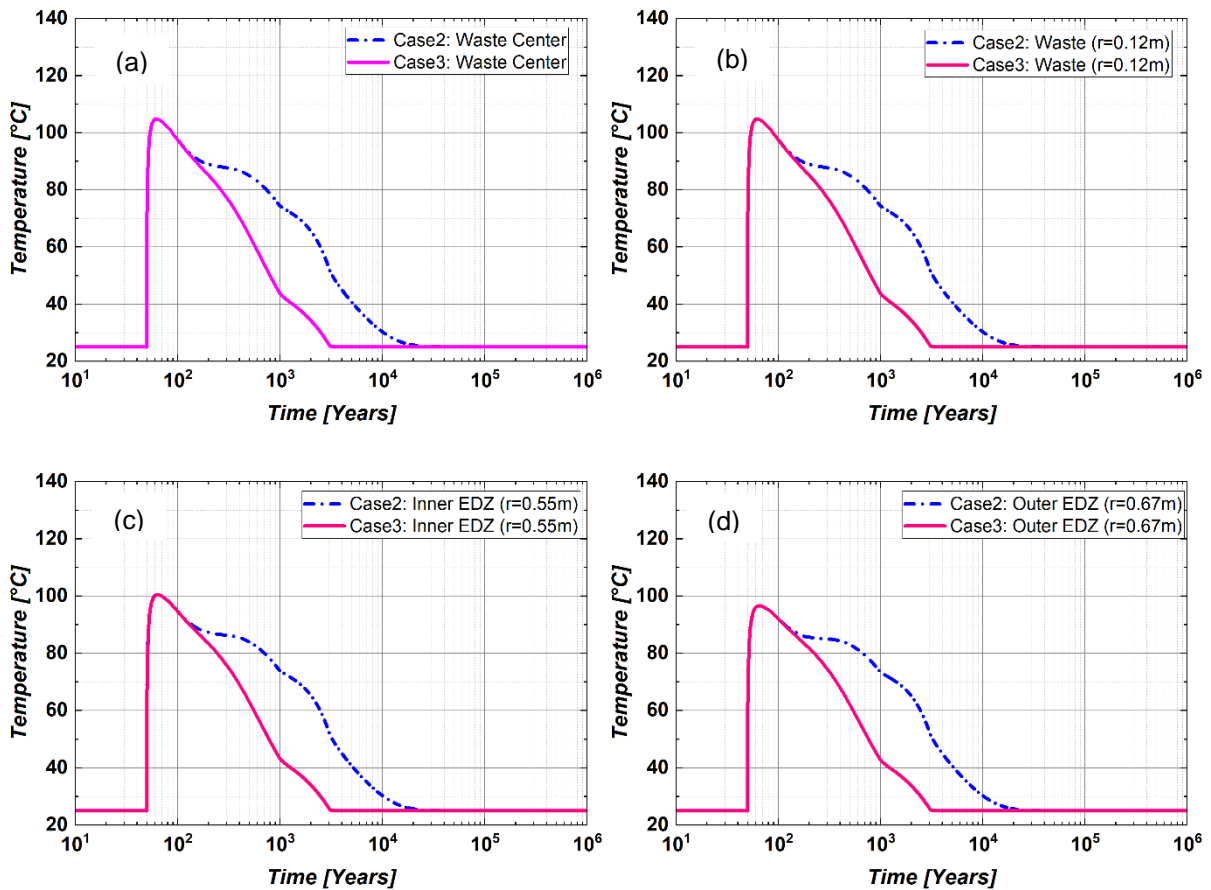


Figure 9-20 Evolution of temperature in Zone B (Case 2 v/s Case 3).



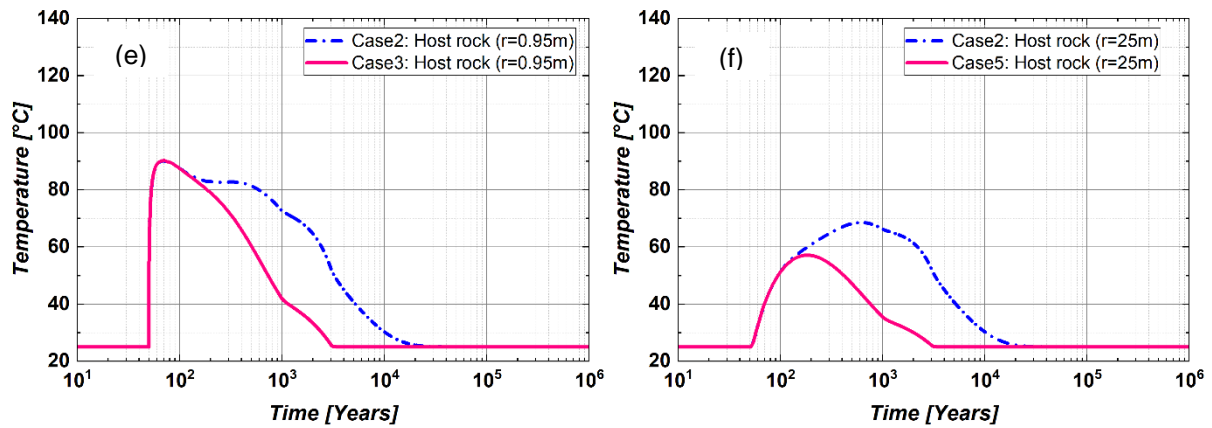
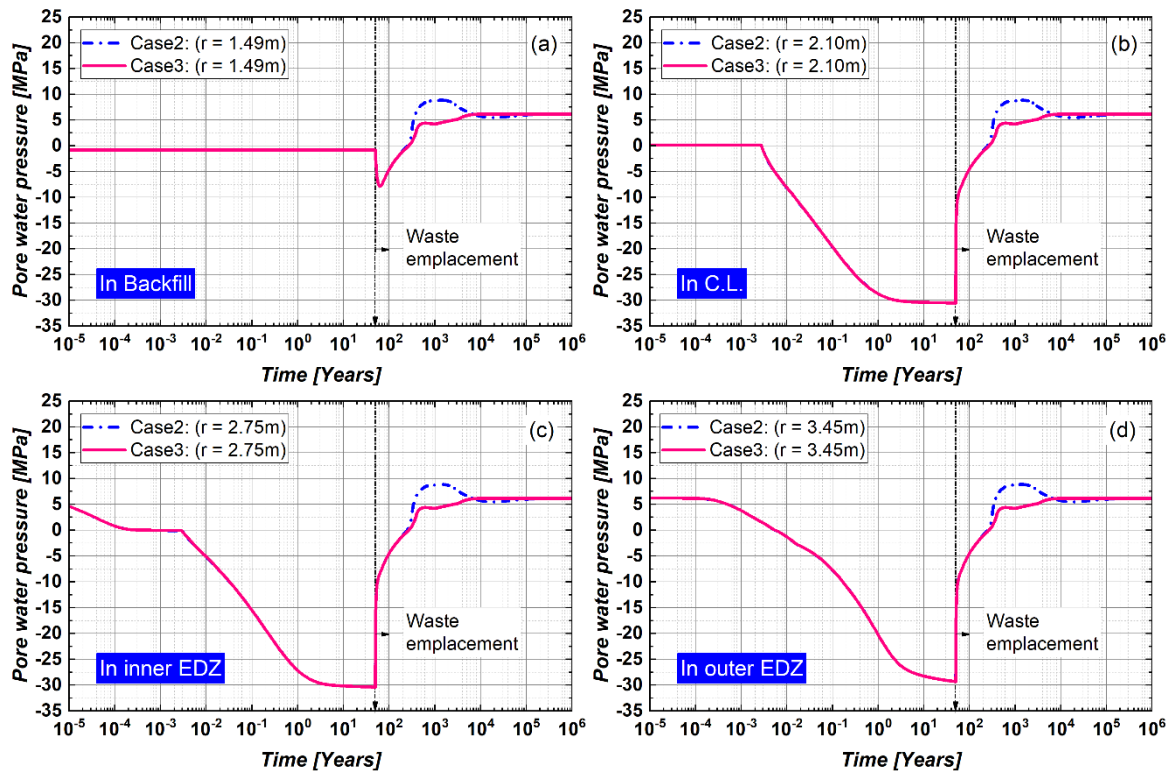


Figure 9-21 Evolution of temperature in Zone C (Case 2 v/s Case 3).

Figure 9-22 shows a significant effect of top and bottom aquifers on the pore water pressure evolution in Zone B which was primarily due to contrasting thermal responses of two cases. As discussed earlier, the presence of these aquifers in case 2 have much longer thermal period as compared to case 3. As a result, a much higher pore water pressure was observed in case 2.

The peak value of temperature-induced excess porewater pressure was close to 9 MPa, and it was same at all the locations despite having different peak temperatures. It is primarily due to the incompressibility of pore water in a saturated porous media, as a result, any spatial variation in pore water pressure also affects it's value at nearby locations.



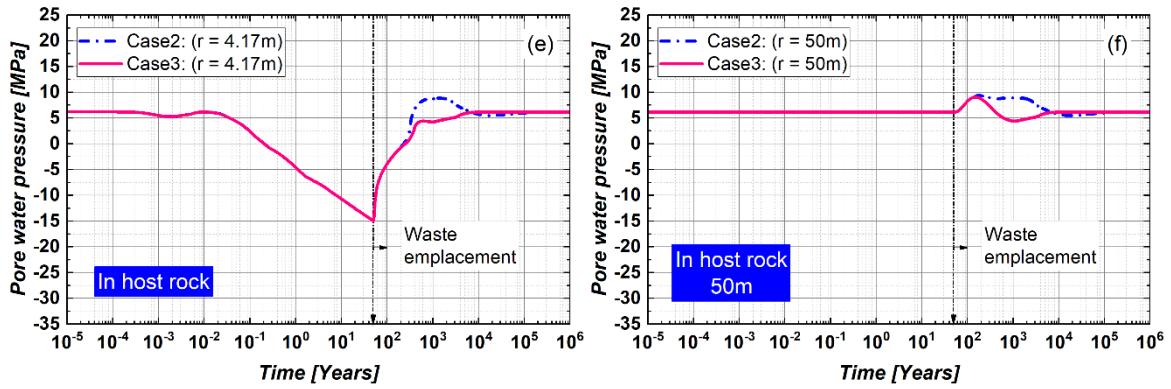
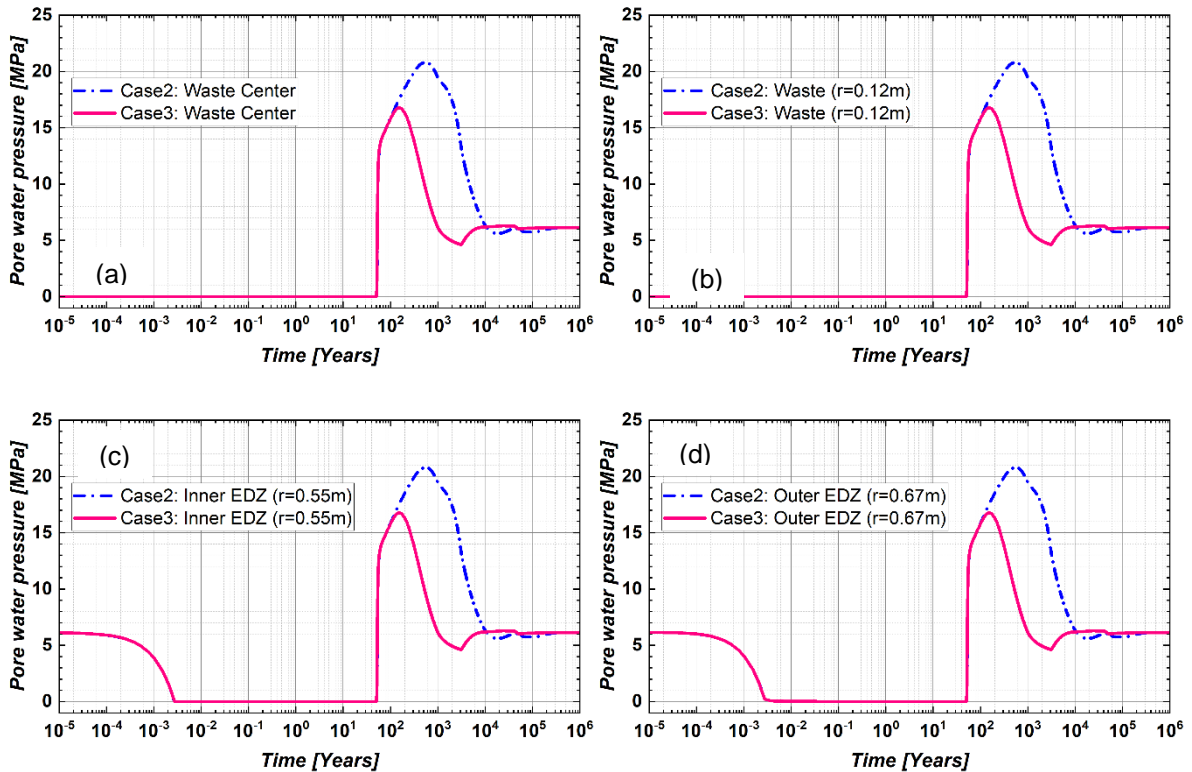


Figure 9-22 Evolution of pore water pressure in Zone B (Case 2 v/s Case 3).

Similarly, Figure 9-23 compares the evolution of PWP in Zone C for both cases. Likewise zone B, the presence of overlaying (top) and underlying (bottom) geological features significantly affects the temperature distribution, thus also affecting the pore water pressure evolution in a same manner as discussed for Zone B. The peak value of PWP reached 20.8 MPa in case 2, and 16.8 MPa in case 3.



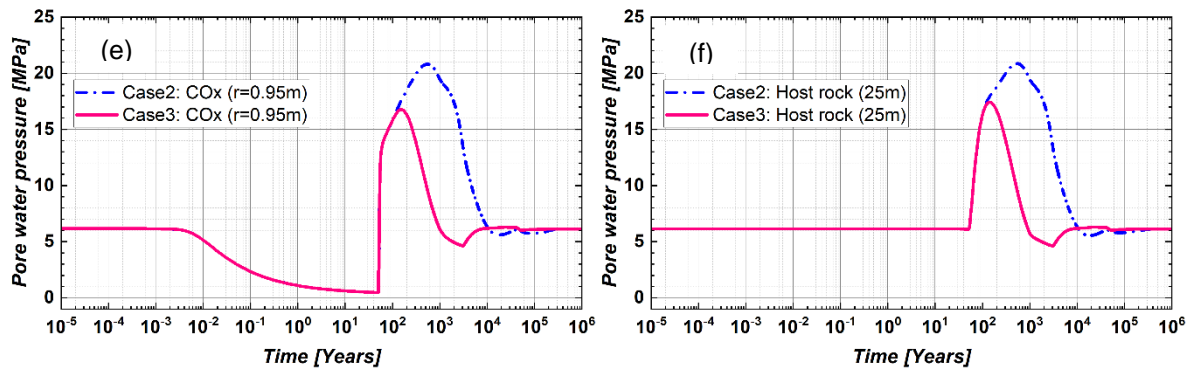
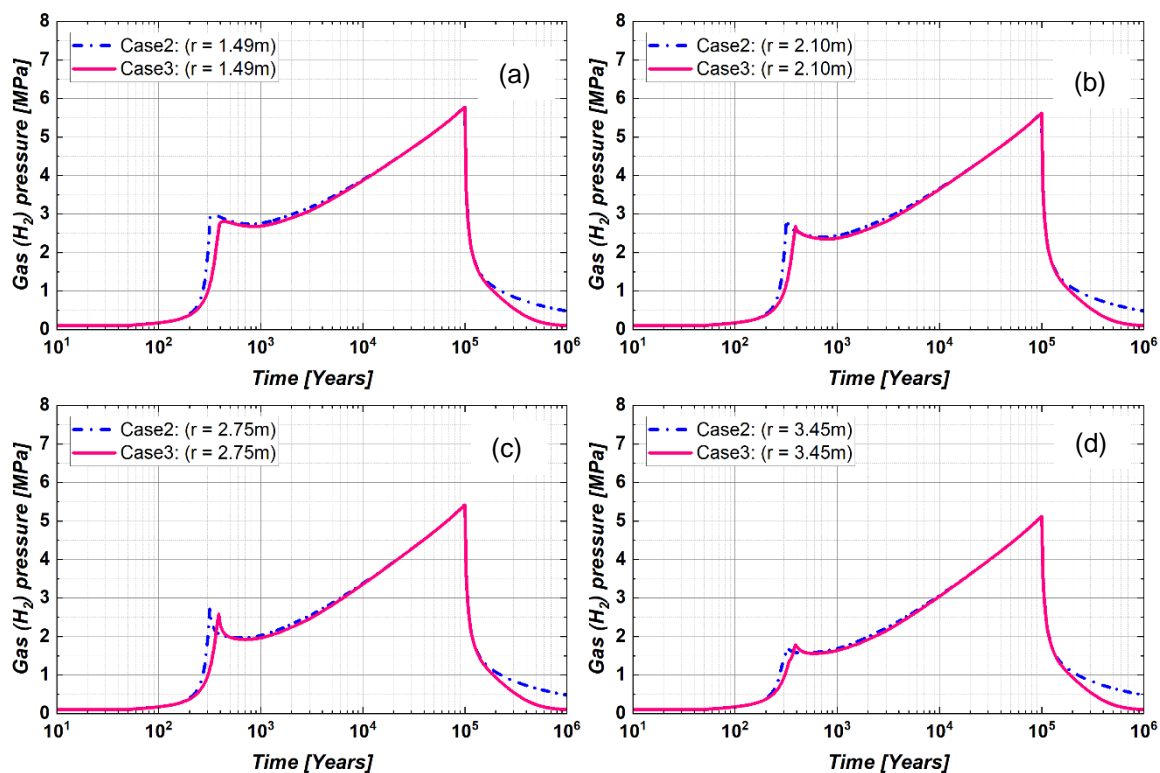


Figure 9-23 Evolution of pore water pressure in Zone C (Case 2 v/s Case 3).

Figure 9-24 and Figure 9-25 presents the gas pressure evolution in Zone B and in Zone C, respectively. The effect of top and bottom aquifers was more dominant in Zone C as compared to Zone B. As evident from Figure 9-24, the consideration of top/bottom aquifers does not affect the gas pressure evolution in Zone B. The maximum gas pressure in Zone B was close to 6 MPa (at $r = 1.49\text{m}$) which was identical in both cases. Unlike the porewater pressure evolution (see Figure 9-22 and Figure 9-23), the gas pressure varies with the distance from the point of gas injection.

In Zone C, a much higher gas pressure (≈ 20 MPa) was observed in case 2 as compared to case 3 where the maximum gas pressure reached up to 15 MPa for the locations close to the gas injection point (e.g., waste, and inner/outer EDZ). It is worth mentioning here that the ventilation-induced desaturation was present in Zone B prior to waste emplacement, while in Zone C the inner and outer EDZ along with the host rock was fully saturated.



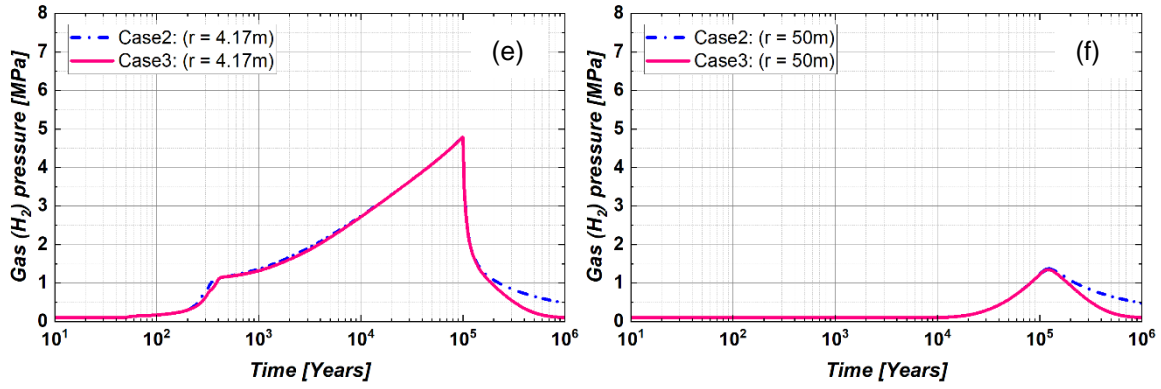


Figure 9-24 Evolution of gas pressure (H2) in Zone B (Case 2 v/s Case 3).

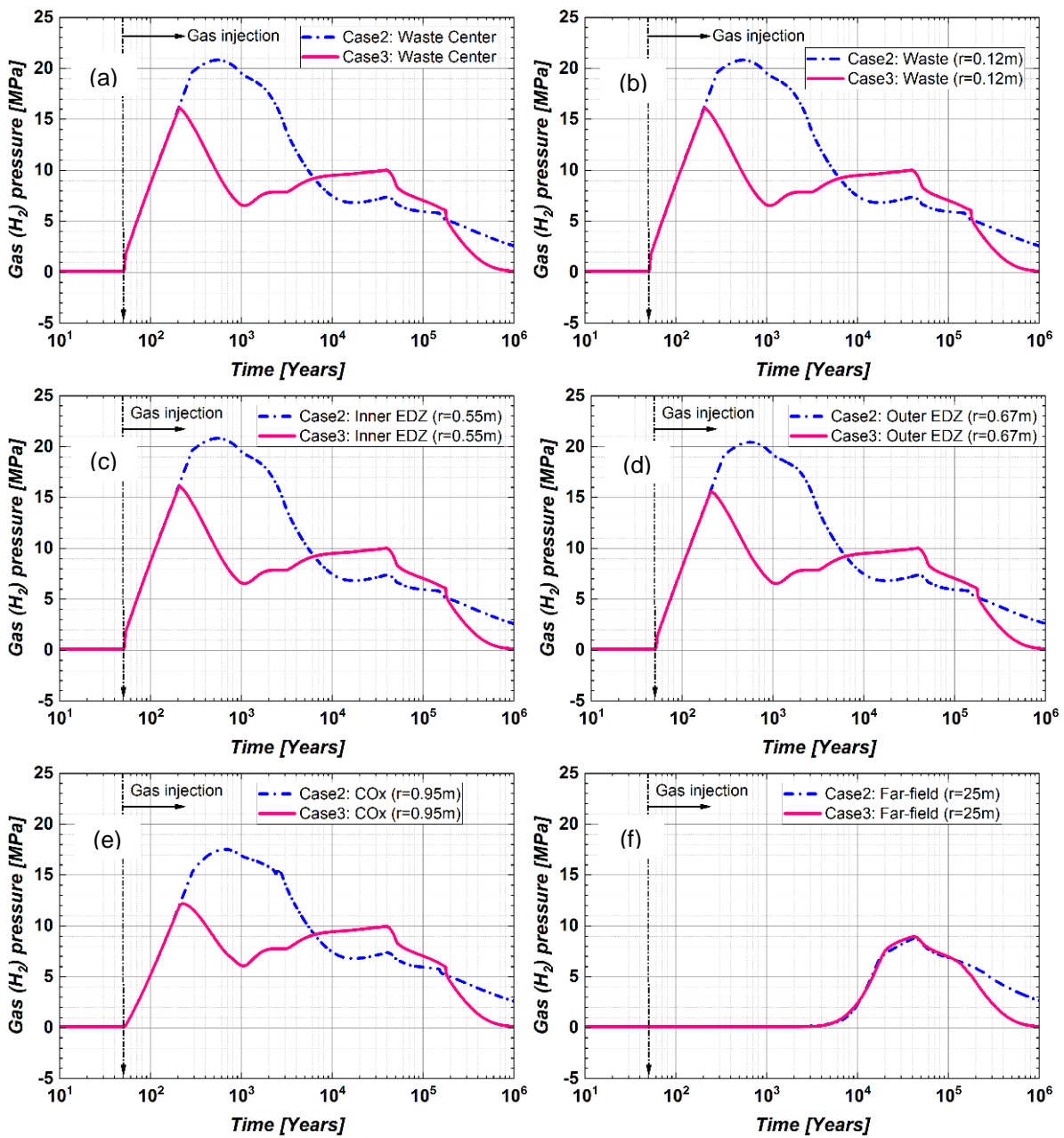


Figure 9-25 Evolution of gas pressure (H2) in Zone C (Case 2 v/s Case 3).

Figure 9-26 shows the evolution of water saturation in Zone B. Similar to the gas pressure evolution, the water saturation also remains unaffected from the considered geometric features. However in Zone C, a gas-induced desaturation event was observed in both scenarios with some minor differences as depicted in Figure 9-27.

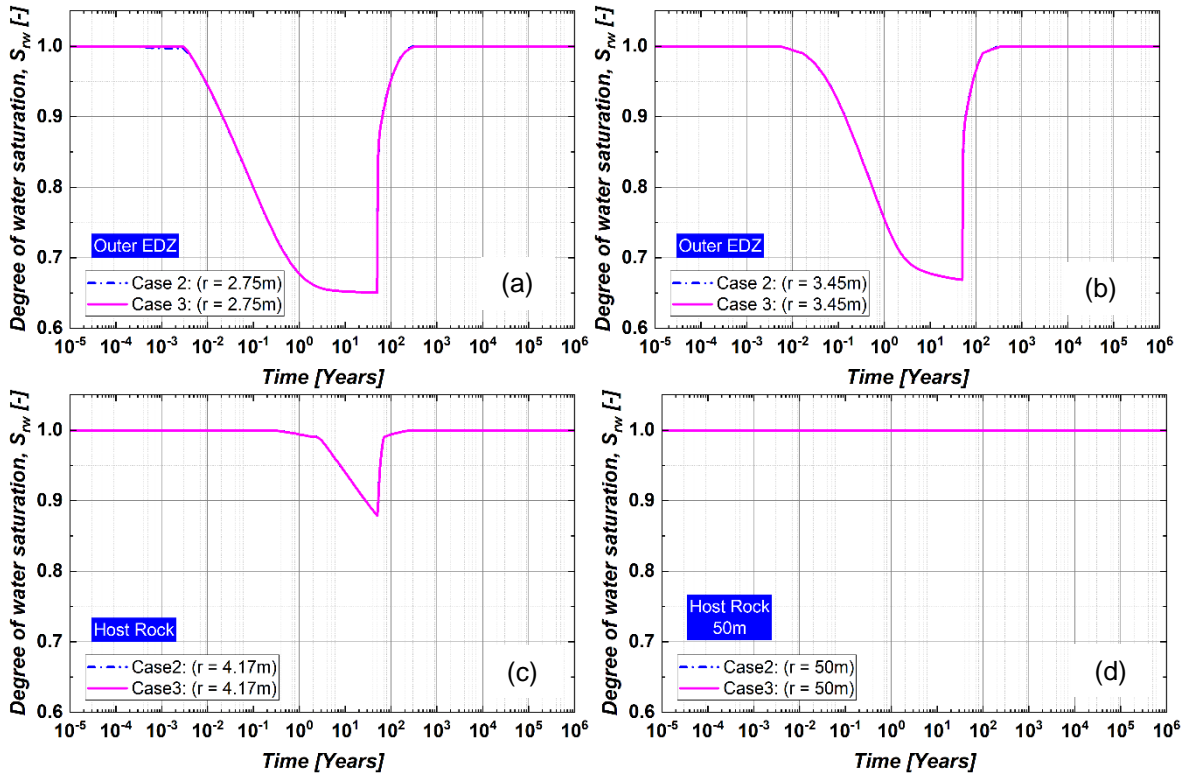


Figure 9-26 Evolution of water saturation in Zone B (Case 2 v/s Case 3).

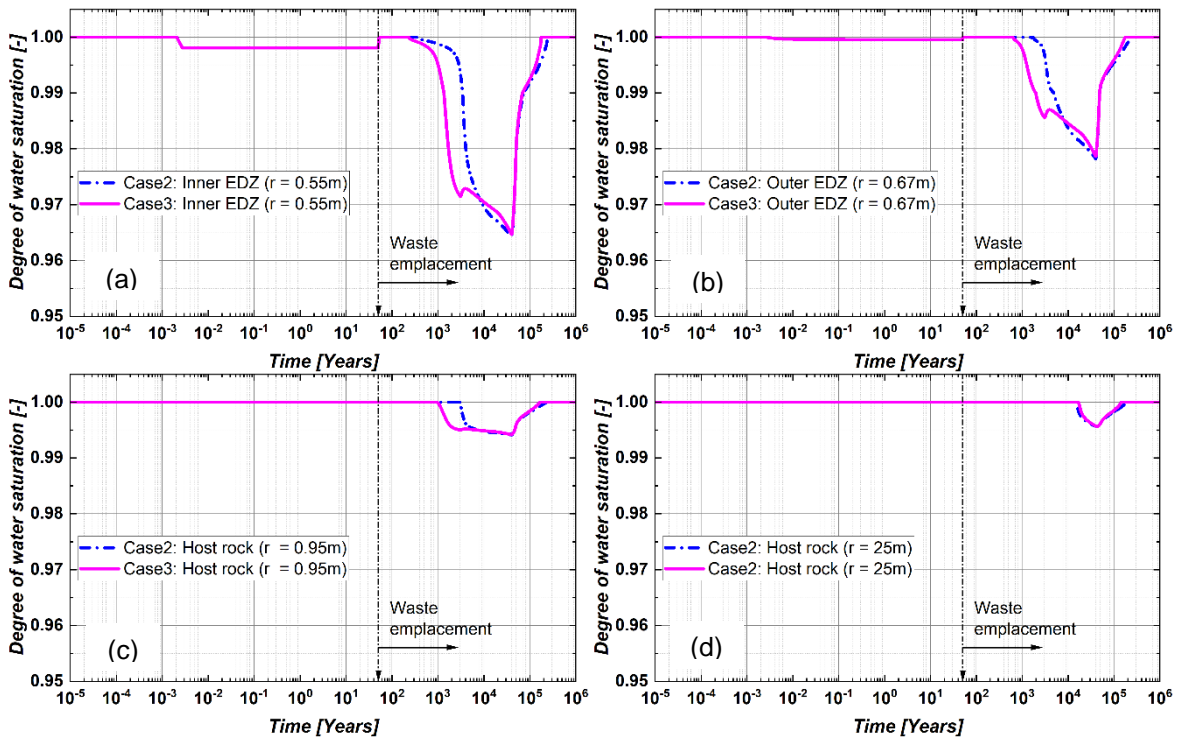


Figure 9-27 Evolution of water saturation in Zone C (Case 2 v/s Case 3).

Figure 9-28 and Figure 9-29 present the evolution of effective vertical stress in Zone B and Zone C, respectively. In Zone B, the effect of aquifers was more evident in outer EDZ and host rock as compared to inner EDZ. In the heating phase, a decrease in effective vertical stresses was more pronounced in case 2 due to having larger temperature induced excess PWP as compared to case 3.

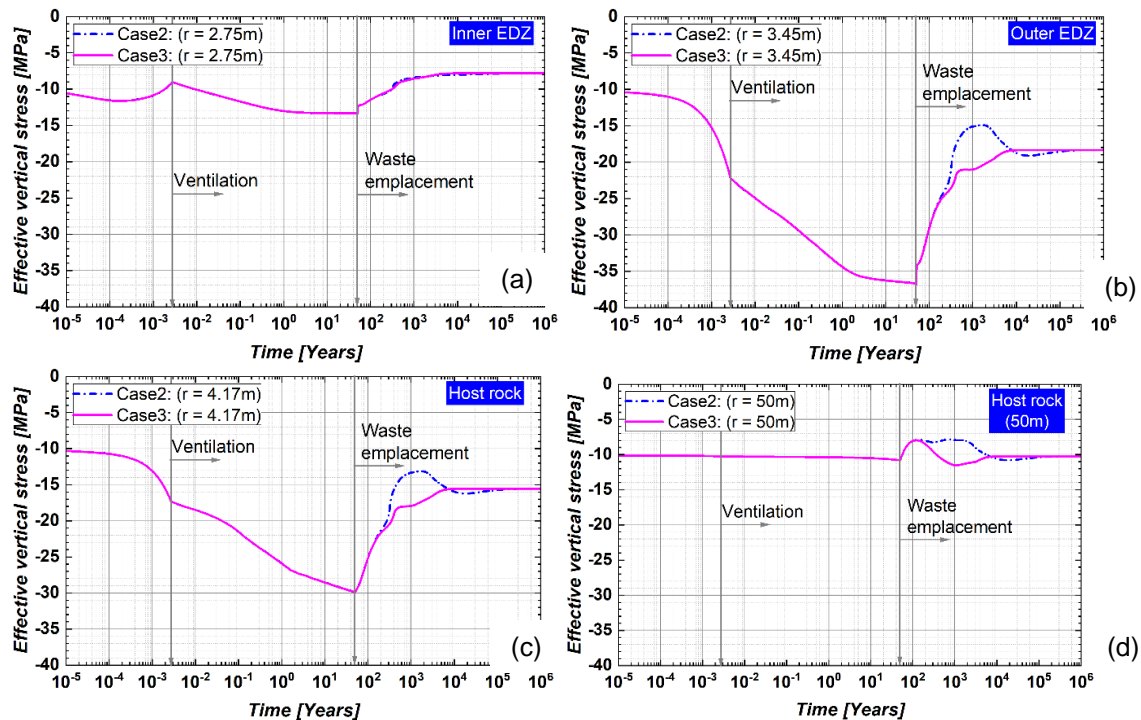


Figure 9-28 Evolution of effective vertical stress in Zone B (Case 2 v/s Case 3).

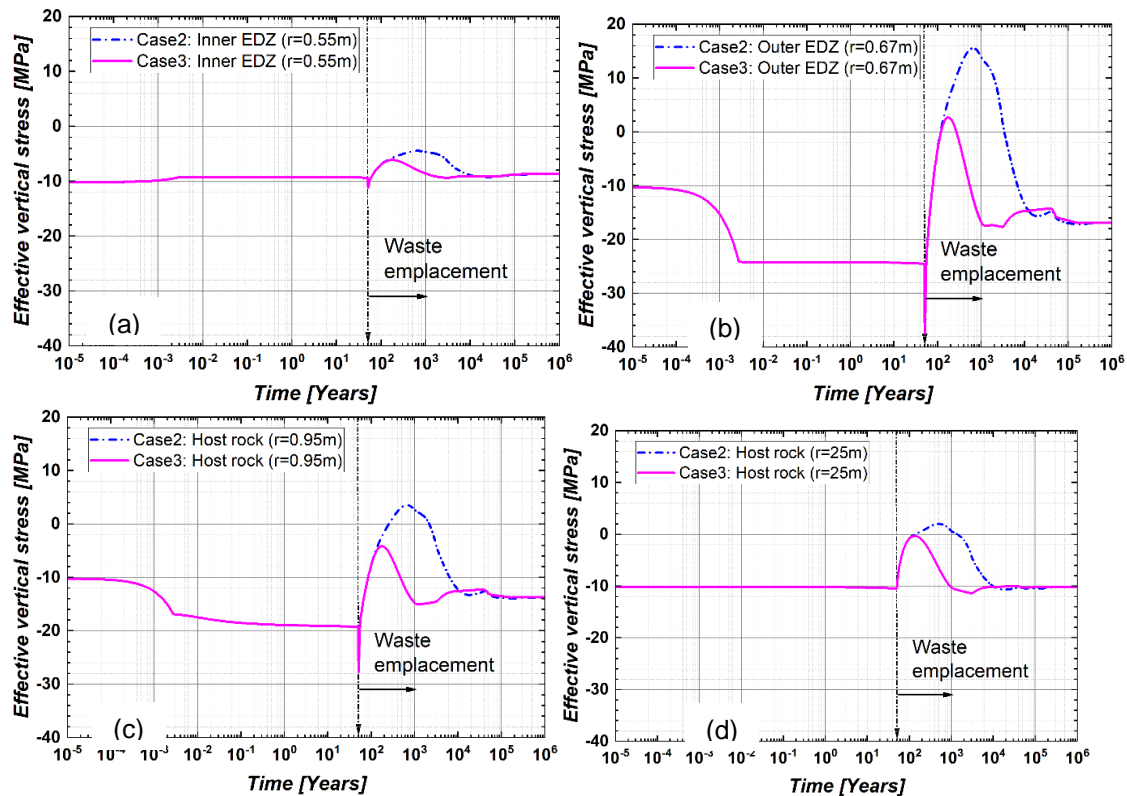


Figure 9-29 Evolution of effective vertical stress in Zone C (Case 2 v/s Case 3).

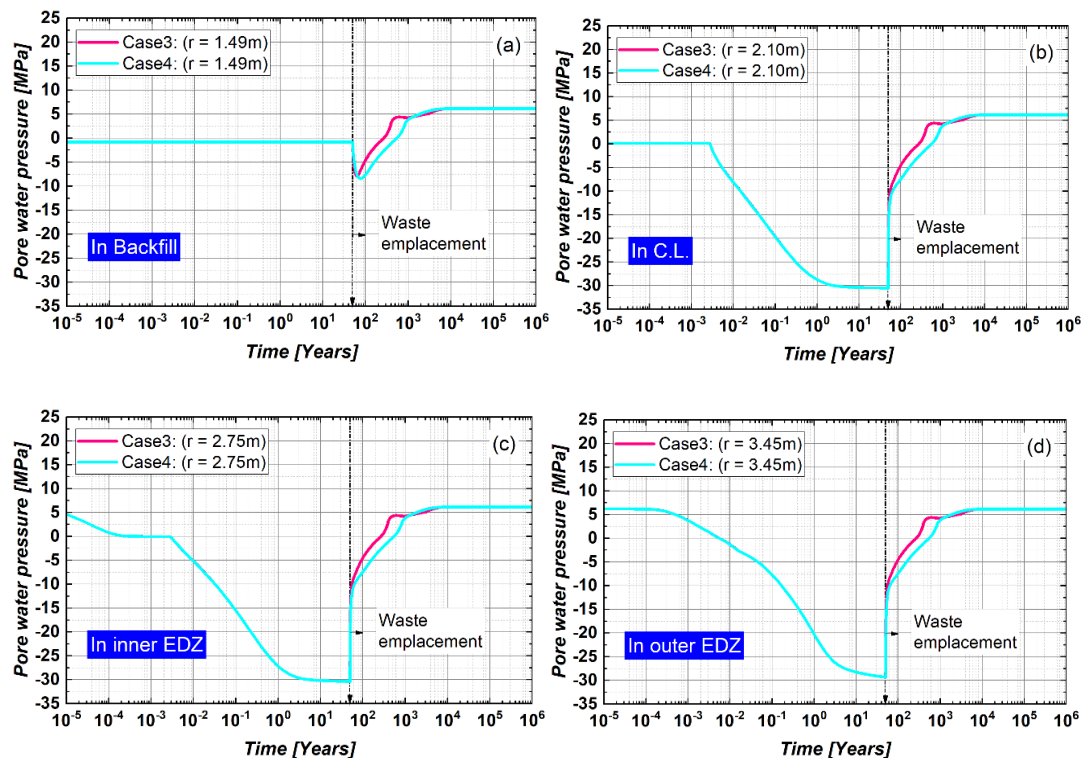
9.5.3 Role of temperature (THMG v/s HMG-coupling scenarios)

To investigate the effect of temperature, a fully coupled THMG case was compared with the HMG-coupling scenario. In both cases, the top and bottom aquifers were not considered during the analysis. Table 9-6 presents the features of simulation. Figure 9-30 presents the effect of temperature on the porewater pressure evolution in Zone B.

Table 9-6 Case 3 and case 4 for investigating the effect of temperature.

Cases	Given Rel. Per. Funs.	Specified SWRC	Coupling	Geometric Features
Case 3	✓	✓	THMG	No top/bottom aquifers
Case 4	✓	✓	HMG	No top/bottom aquifers

As evident from Figure 9-30, once the ventilation phase was over and the disposal cells were instantaneously filled, the porewater pressure equilibration took place rapidly under the influence of temperature and hydraulic gradient in case 3. Whereas in case 4, the porewater pressure equilibration took place with much slower rate under the effect of natural hydraulic gradient. Figure 9-31 presents the PWP evolution in Zone C and compares case 3 with case 4.



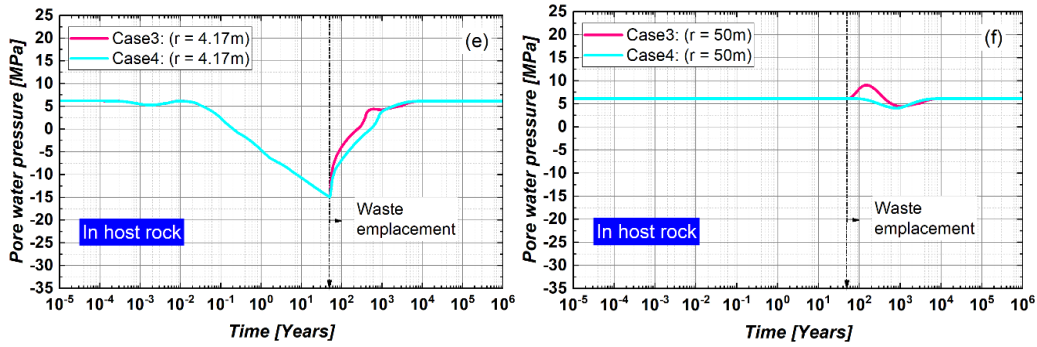


Figure 9-30 Evolution of pore water pressure in Zone B (THMG v/s HMG-coupling scenario).

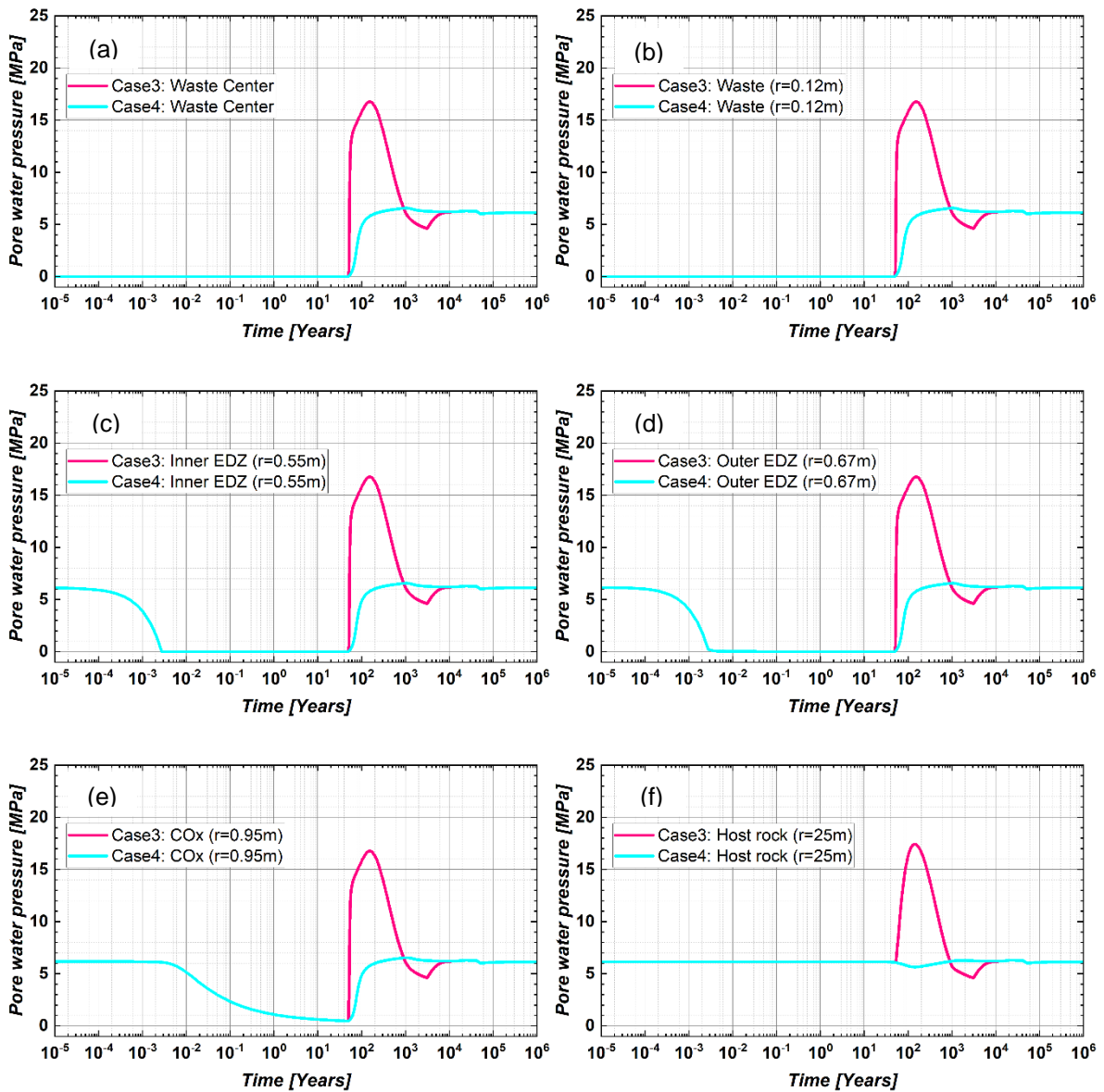


Figure 9-31 Evolution of pore water pressure in Zone C (THMG v/s HMG-coupling scenario).

As depicted in Figure 9-31, the in situ porewater pressure in Zone C reduced to atmospheric pressure at locations close to the excavated face (Figure 9-31a to e). During the waste emplacement, the temperature increased rapidly in case 3, and induced excess PWP at all the observed locations. Whereas in case 4, a gradual increase in PWP was observed under the existing natural hydraulic gradient. These observations in zone C agrees well with Zone B.

Figure 9-32 shows the gas pressure evolution in Zone B for a fully coupled THMG case versus HMG-coupling scenario.

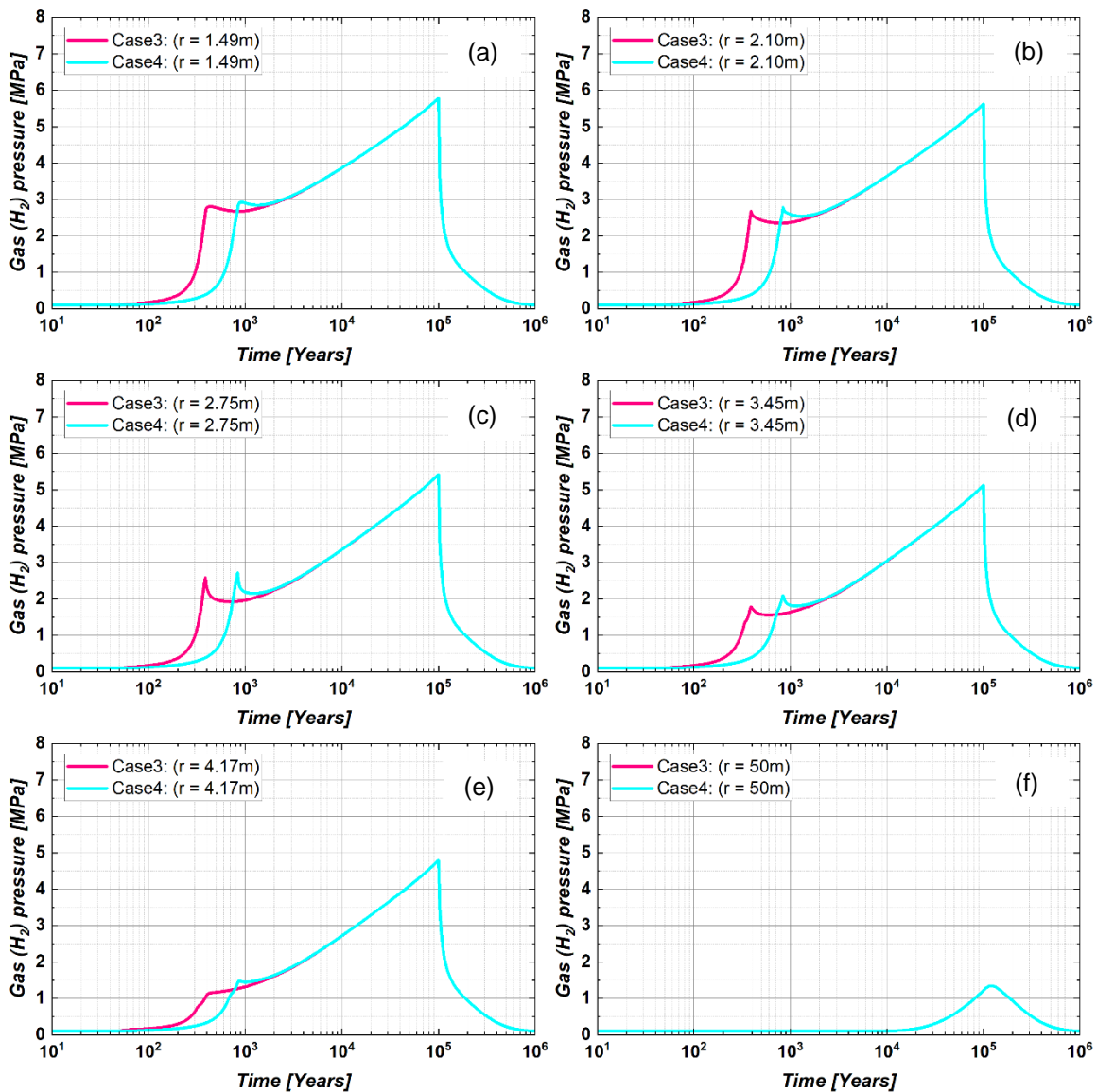


Figure 9-32 Evolution of gas pressure in Zone B (THMG v/s HMG-coupling scenarios).

Figure 9-32 reveals that the temperature has an insignificant effect on the gas pressure evolution in Zone B. The only effect was the occurrence of first peak which was earlier in case 3. Whereas the maximum gas pressure was same in both cases. The possible reason is the rate of water saturation, which was higher in case 3 (see Figure 9-33). The presence of temperature induces the excess PWP, as a result, the rate of water saturation is faster than the HMG-coupling case.

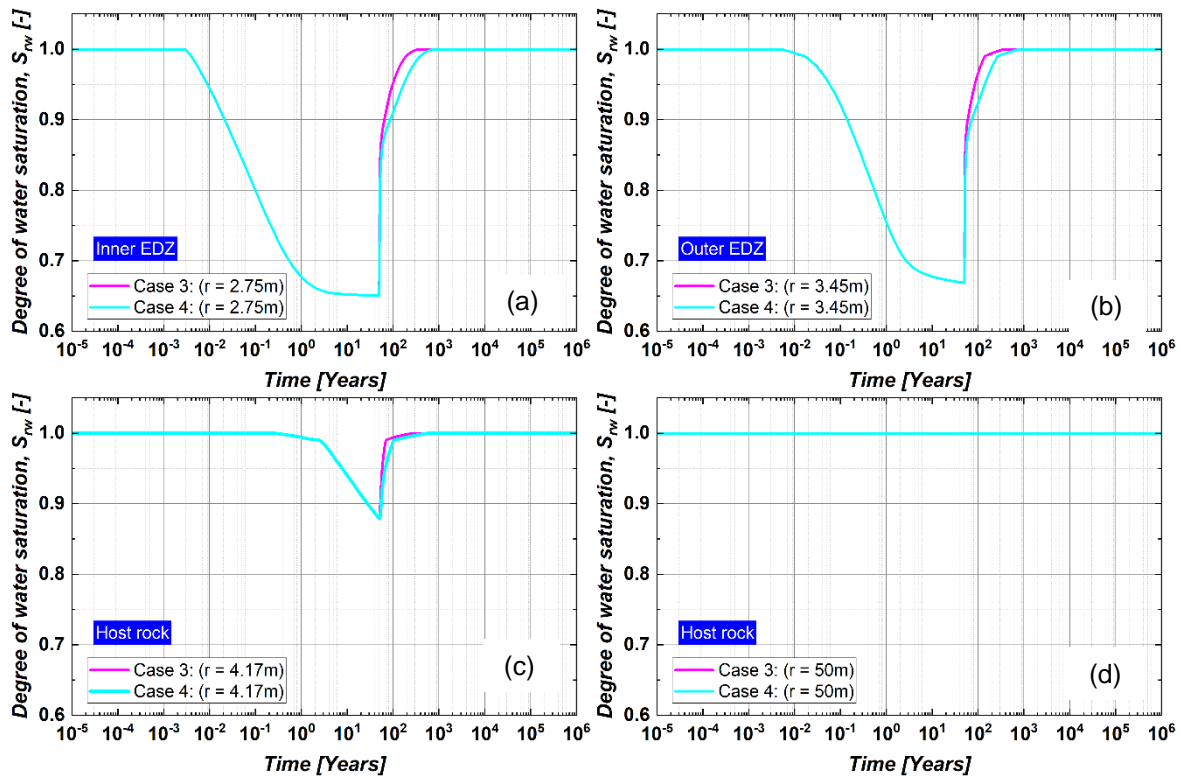


Figure 9-33 Evolution of water saturation in Zone B (THMG v/s HMG coupling scenarios).

Figure 9-34 shows the gas pressure evolution in Zone C and compares a fully coupled THMG case versus HMG-coupling scenario. In contrast to Zone B, both cases have a different gas pressure distribution in Zone C. A fully coupled THMG case yields much higher gas pressure than the HMG-coupling case.

Figure 9-35 presents the evolution of water saturation in Zone C for a fully coupled THMG (case 3) versus HMG (case 4) coupling scenario. The figure reveals the gas induced desaturation which was more pronounced close to the injection point. It is important to note that the evolution of water saturation was almost identical in both cases.

Figure 9-36 presents the evolution of effective vertical stress in Zone B and shows the effect of temperature on the stress distribution. The Biot's effective stress framework primarily consists of pore water pressure, pore gas pressure and degree of water saturation. Hence, variations in the above parameters due to the presence of temperature is naturally reflected in the evolution of effective vertical stress.

Figure 9-37 presents the evolution of effective vertical stress in Zone C for case 3 and 4. The effect of temperature on the stress distribution is more pronounced as compared to Zone B particularly for the locations close to the injection point.

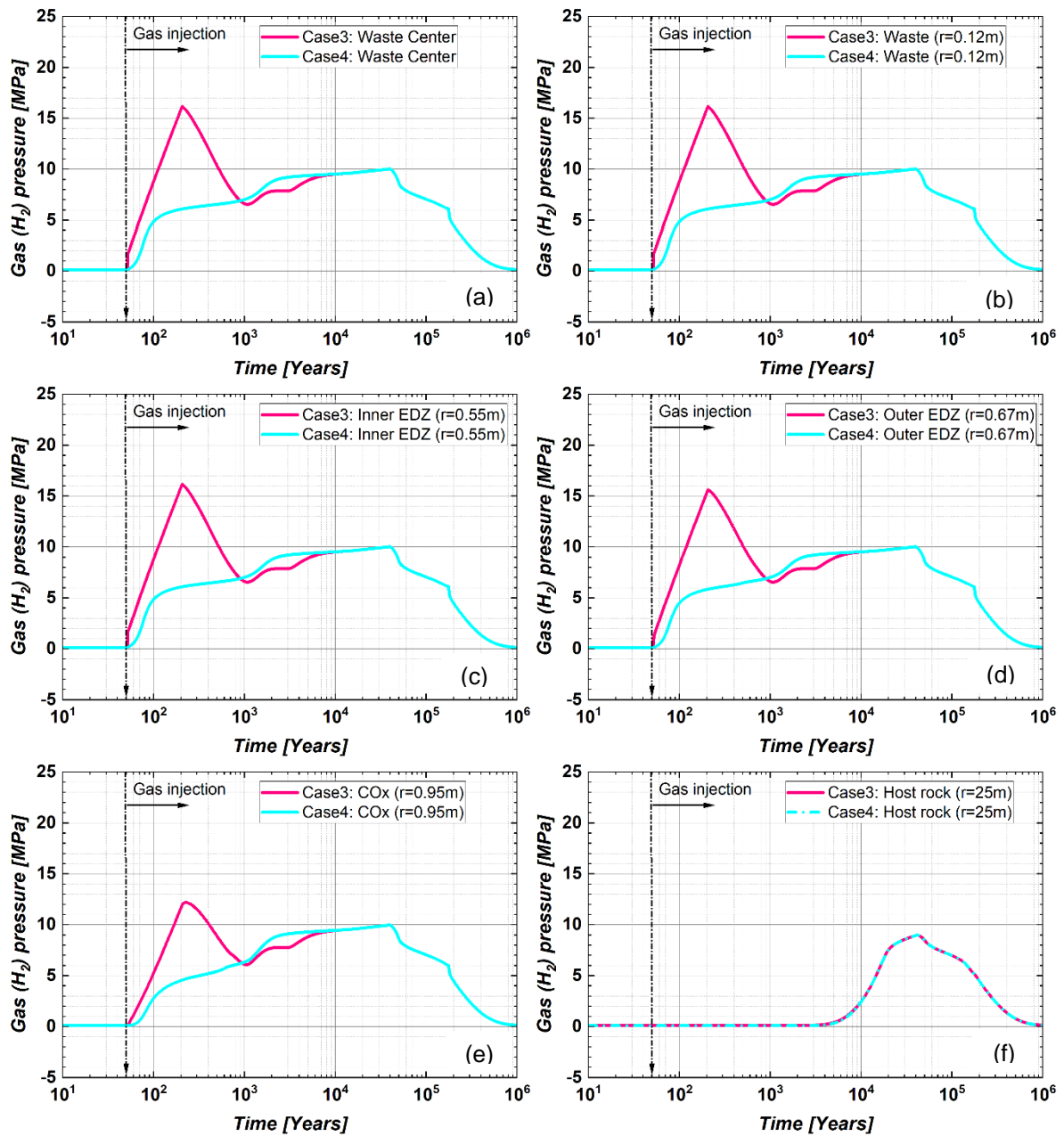


Figure 9-34 Evolution of gas pressure in Zone C (THMG v/s HMG case).

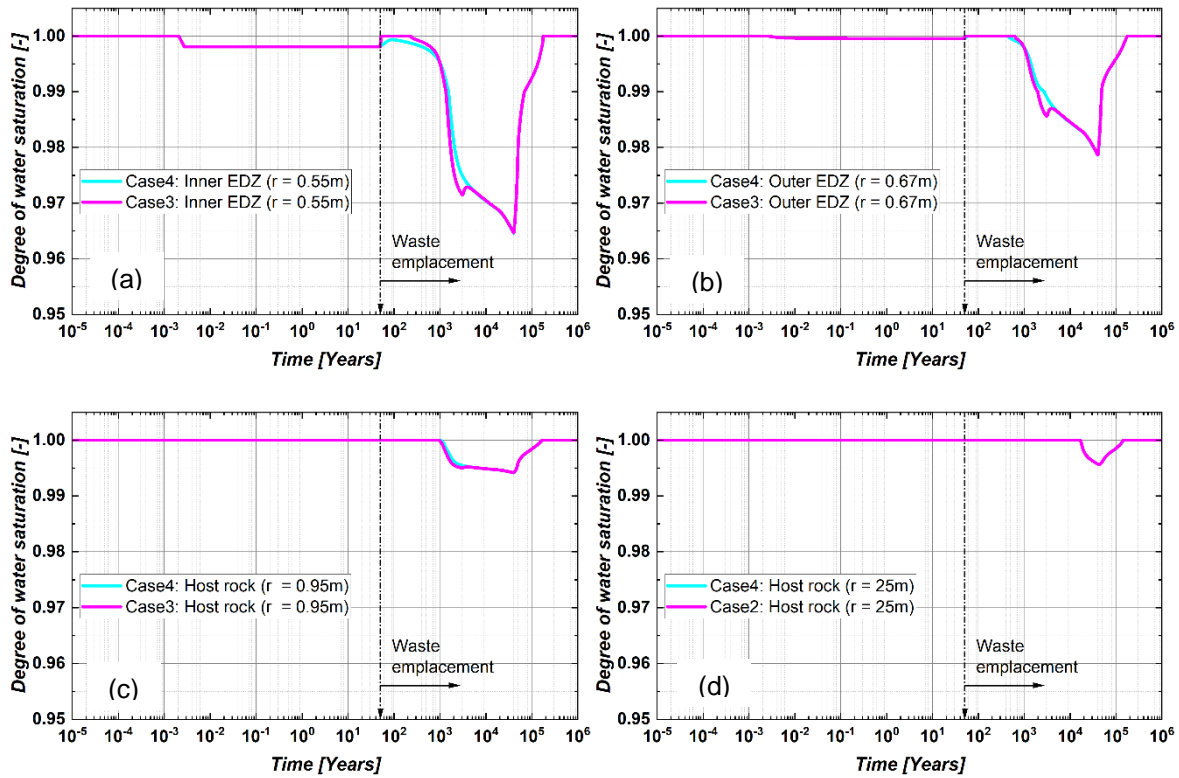


Figure 9-35 Evolution of water saturation in Zone C (THMG v/s HMG case).

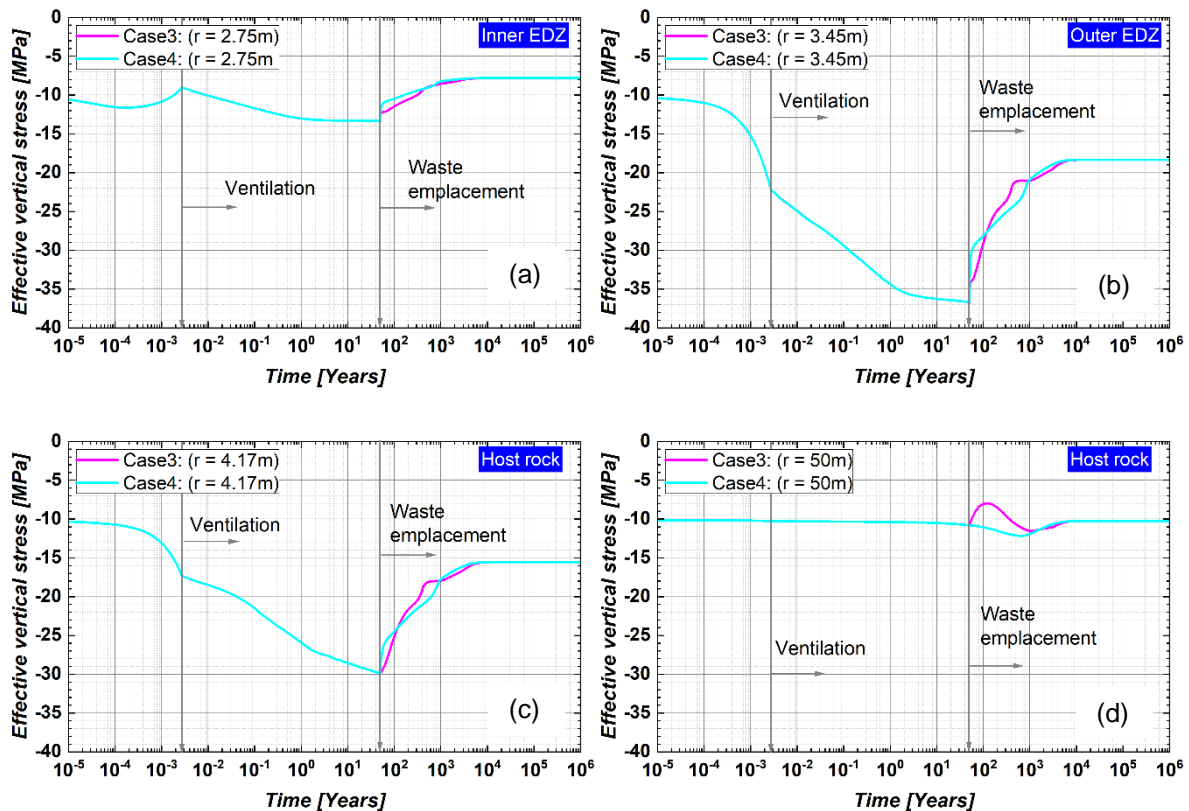


Figure 9-36 Evolution of effective vertical stress for case 3 and 4 (THMG v/s HMG coupling scenarios).

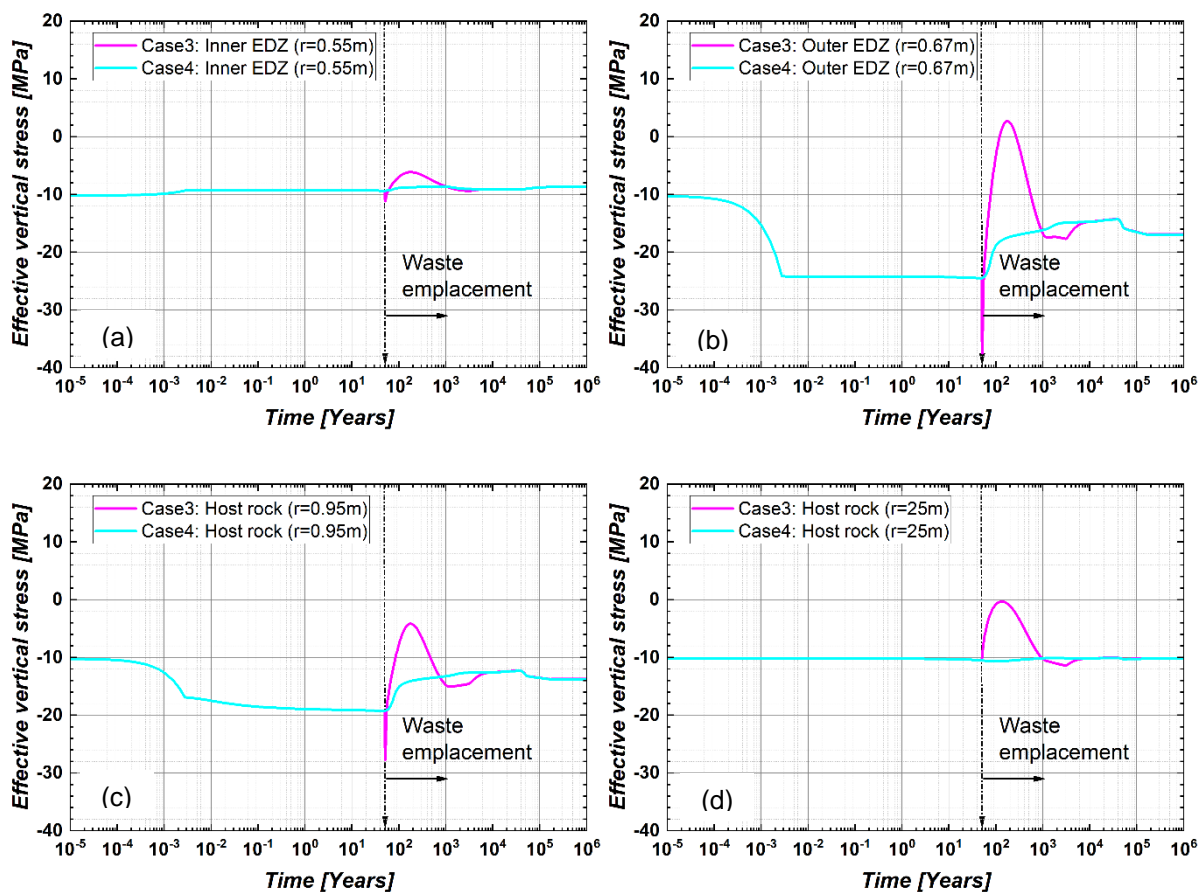


Figure 9-37 Evolution of effective vertical stress in Zone C (THMG v/s HMG case).

9.5.4 Effect of gas (H_2) generation on simulation results (THMG v/s THM-coupling scenario)

The simulation results are compared for a fully coupled THMG and THM case without the top and bottom aquifers (see Table 9-7). In both the cases, the specified relative permeability functions and water retention curves are adopted for the analysis. The results are discussed for both Zone B and Zone C.

Table 9-7 Case 3 and case 5 for investigating the effect of gas pressure on simulation results.

Cases	Given Rel. Per. Funs.	Specified SWRC	Coupling	Geometric Features
Case 3	✓	✓	THMG	No top/bottom aquifers
Case 5	✓	✓	THM	No top/bottom aquifers

Figure 9-38 and Figure 9-39 compare the temperature evolution in Zone B and in Zone C, respectively. The simulation results clearly show that the temperature evolution remains identical in both cases, hence the gas pressure does not affect the temperature distribution.

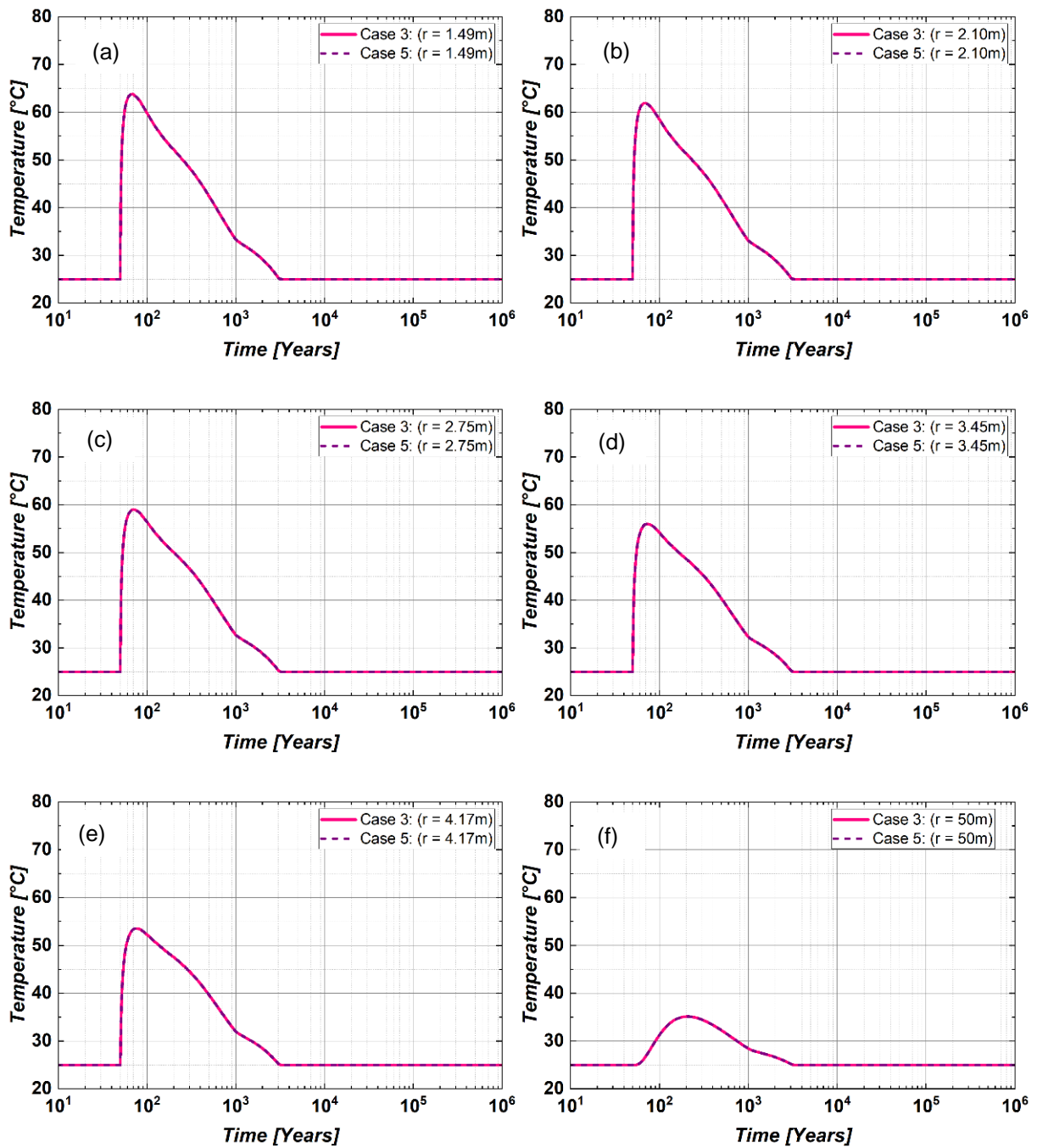


Figure 9-38 Evolution of temperature in Zone C (THMG v/s THM-coupling scenarios).

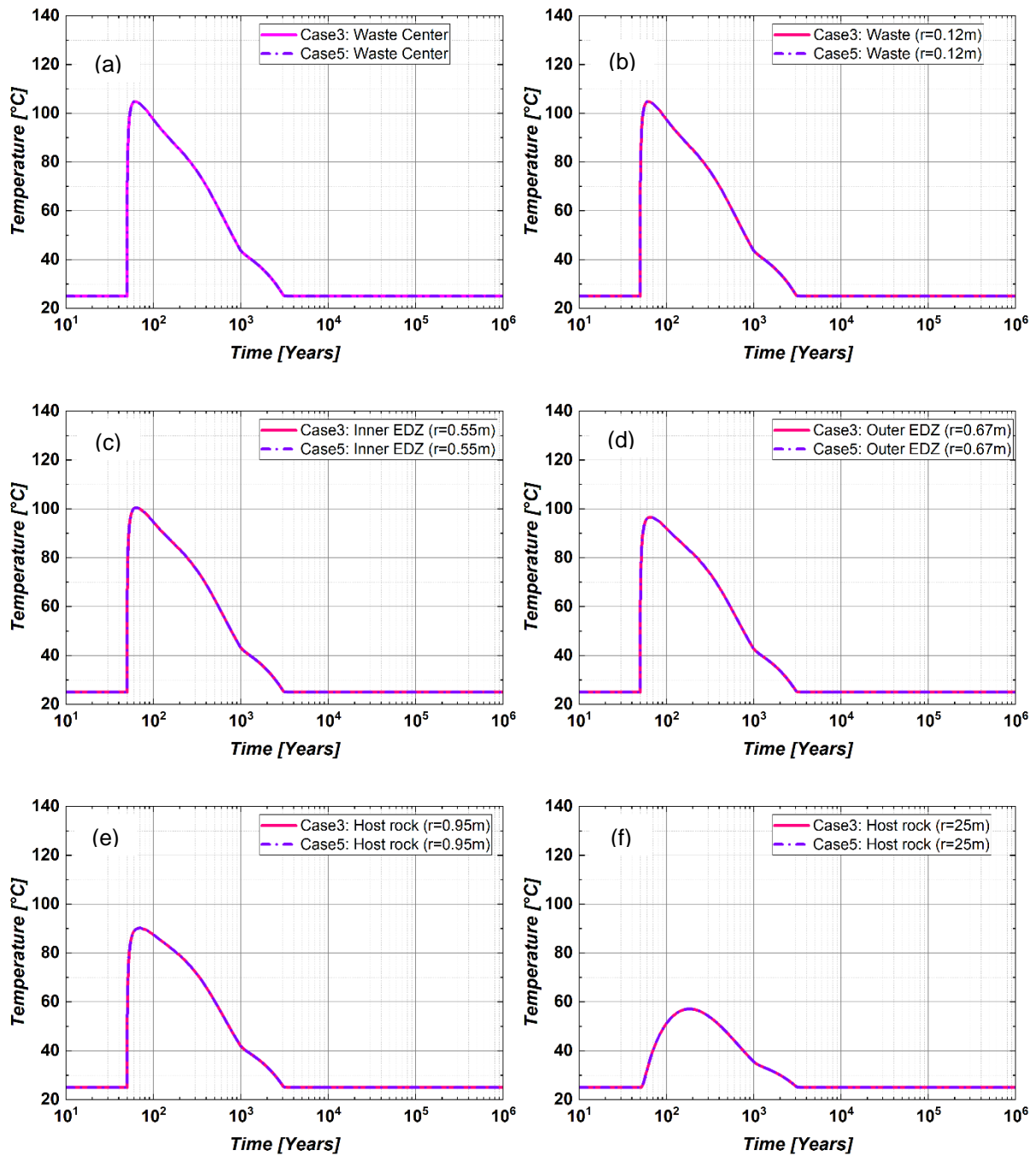


Figure 9-39 Temperature evolution in Zone C (THMG v/s THM-coupling scenario).

Similar to the temperature distribution, pore water pressure in both Zone B and Zone C is found to be independent from the gas pressure as shown in Figure 9-40 and Figure 9-41.

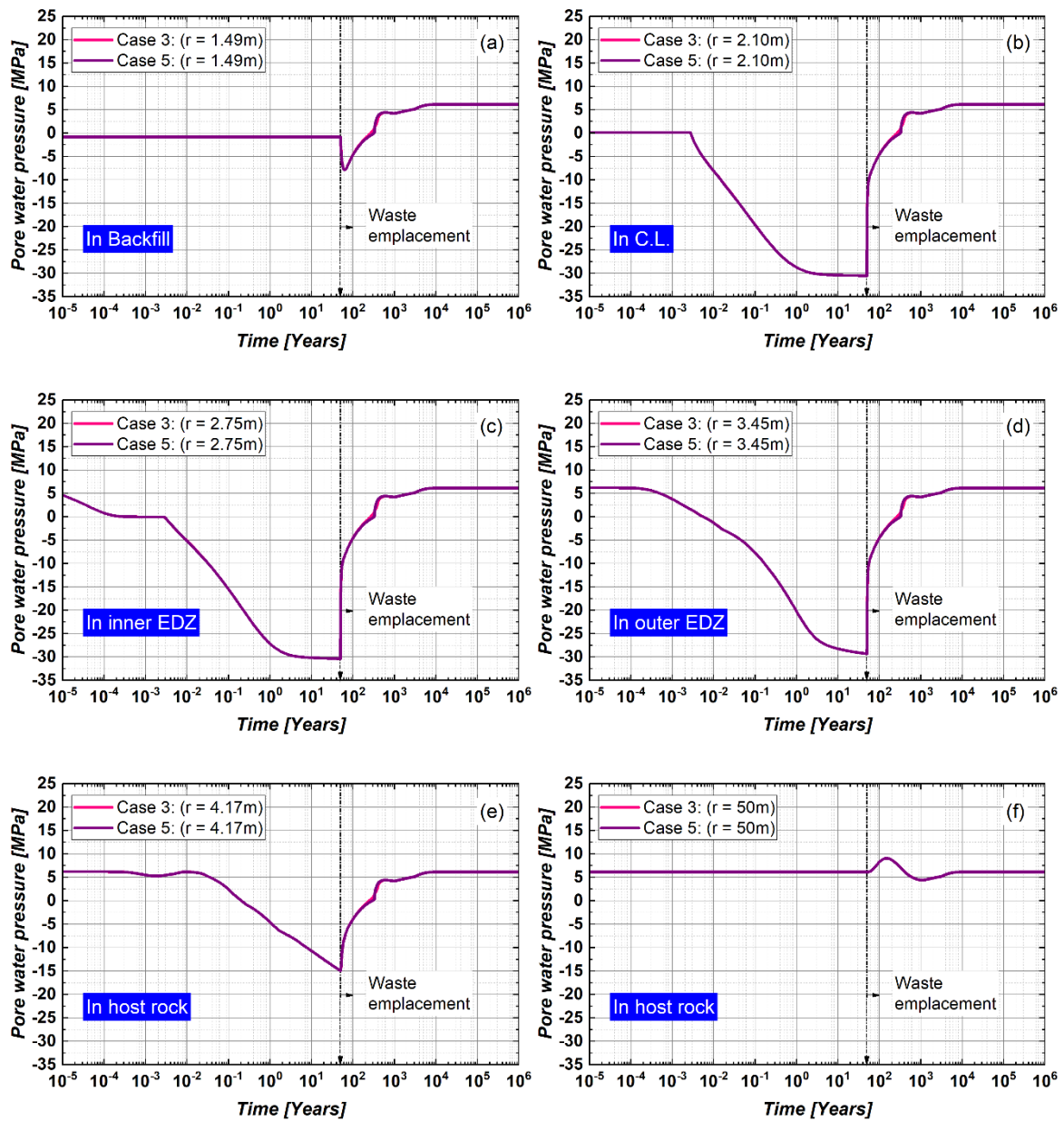
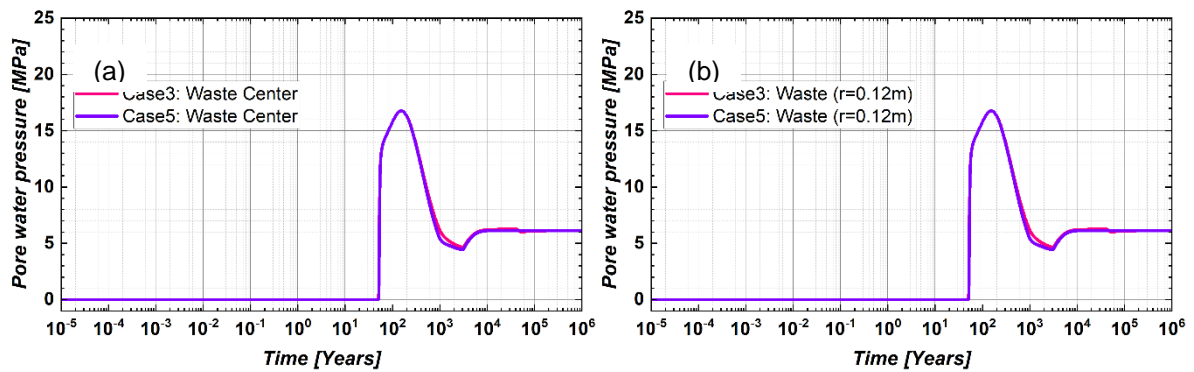


Figure 9-40 Evolution of gas pressure in Zone B (THMG v/s THM-coupling scenarios).



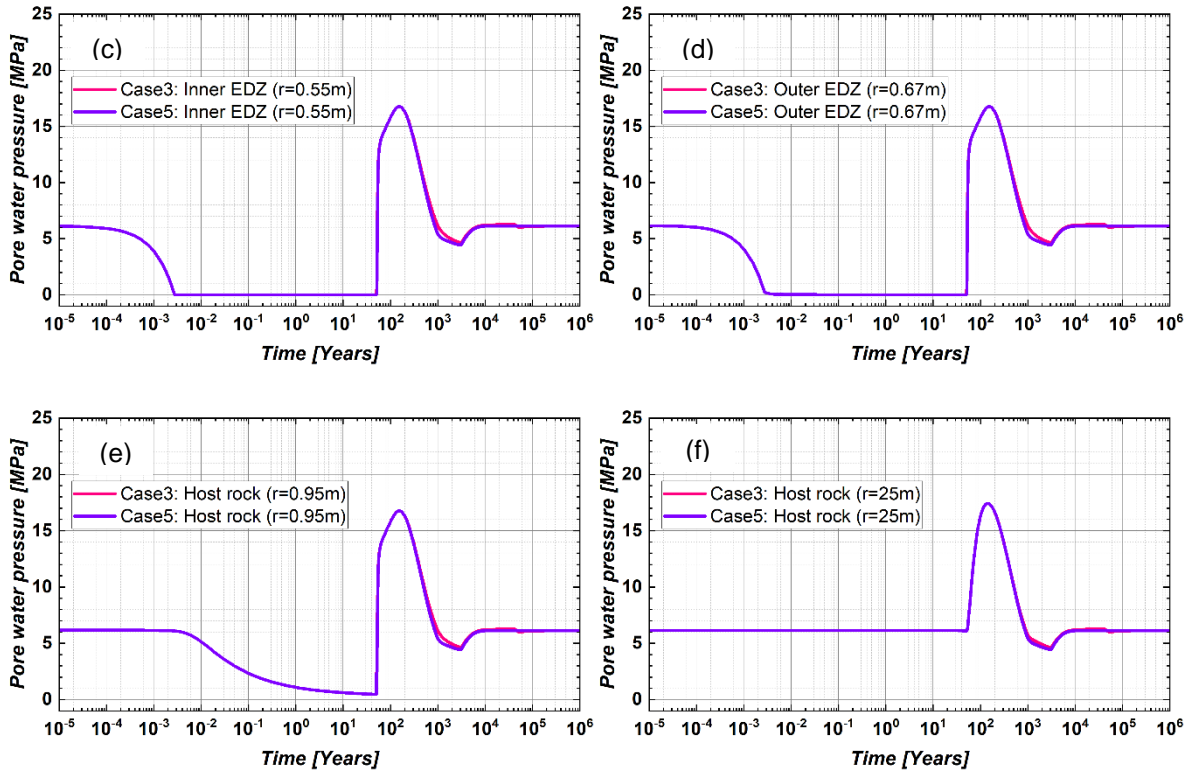


Figure 9-41 Pore water pressure evolution in Zone C (THMG v/s THM-coupling scenario).

Figure 9-42 and Figure 9-43 compare the evolution of water saturation in Zone B and in Zone C, respectively. In Zone B, the water saturation does not depend on the gas pressure. Whereas in Zone C, clearly shows the role of gas pressure in inducing desaturation in host rock.

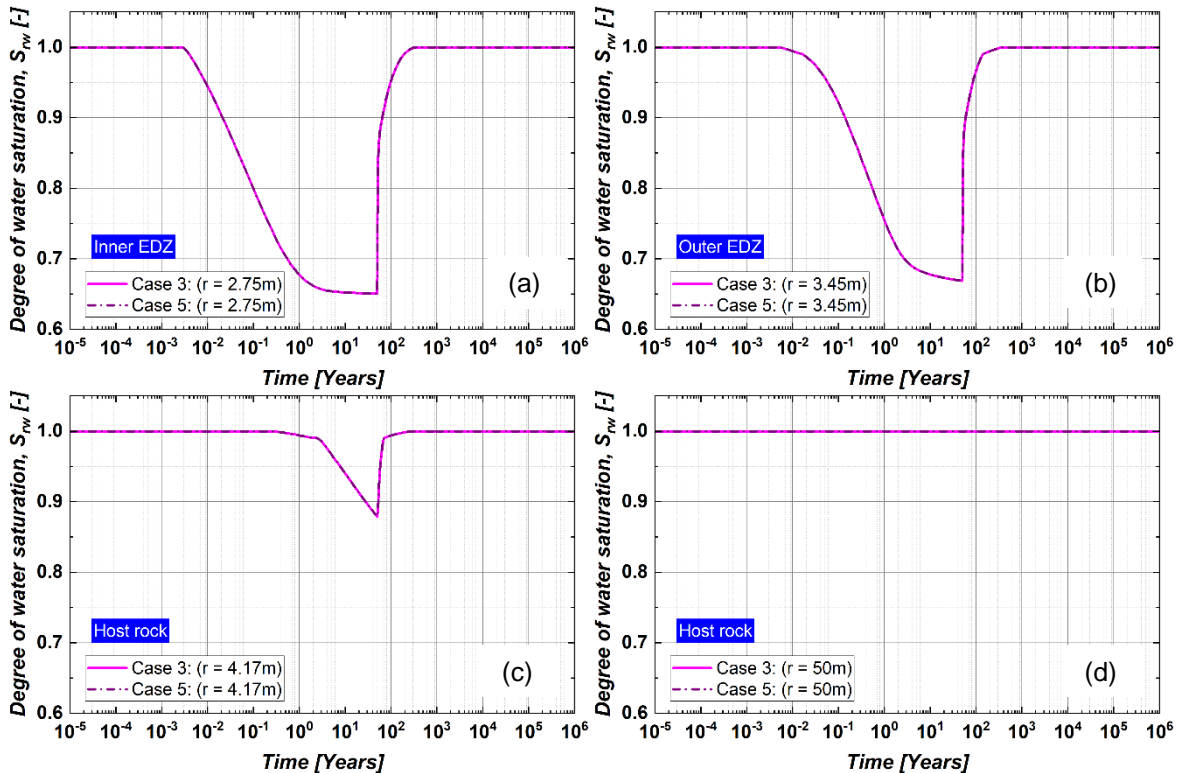


Figure 9-42 Evolution of water saturation in Zone B (THMG v/s THM-coupling scenarios).

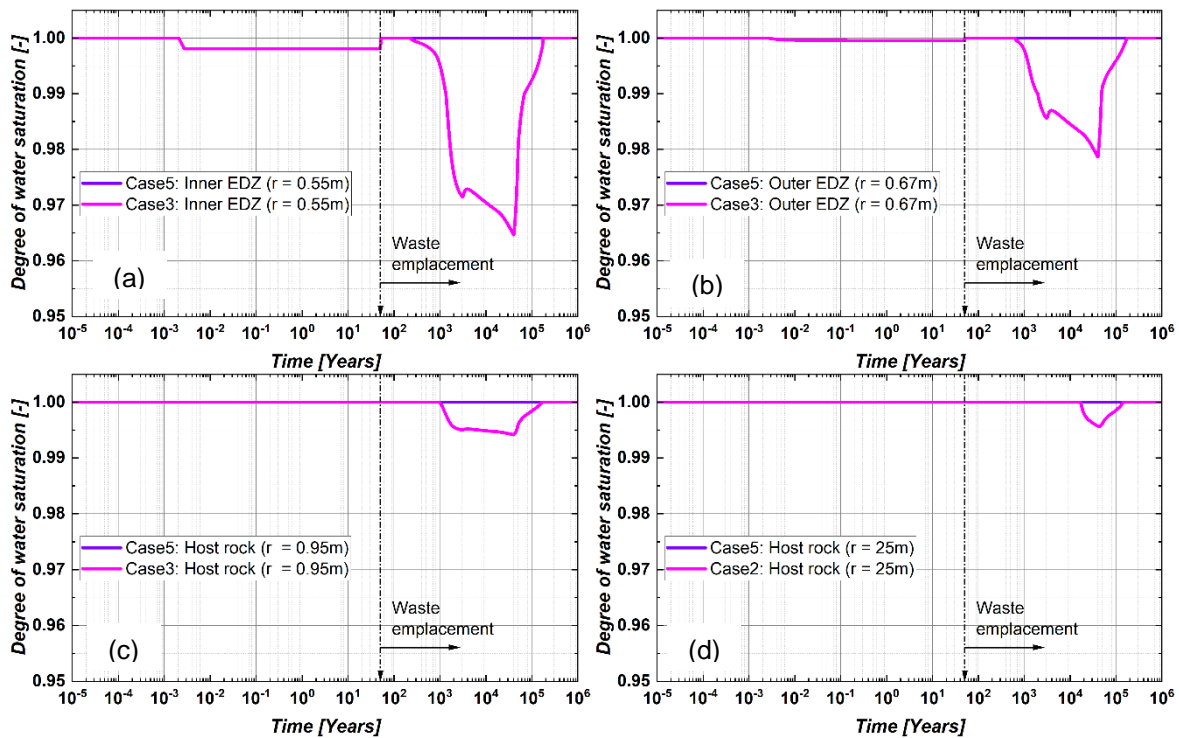


Figure 9-43 Evolution of water saturation in Zone C (THMG v/s THM-coupling scenario).

Figure 9-44 and Figure 9-45 present the effective stress distribution in Zone B and in Zone C, respectively. Both in Zone B and Zone C, stress distribution is unaffected by the presence of gas pressure.

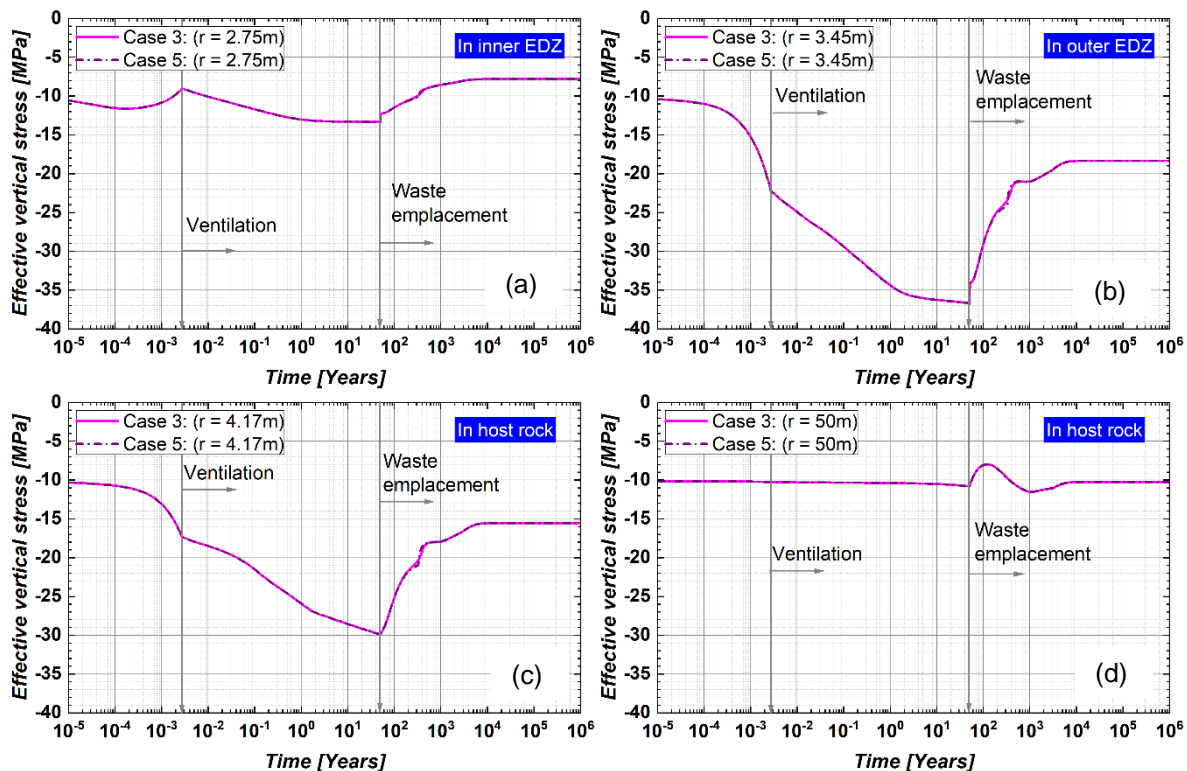


Figure 9-44 Effective vertical stress in Zone B (THMG v/s THM-coupling scenarios).

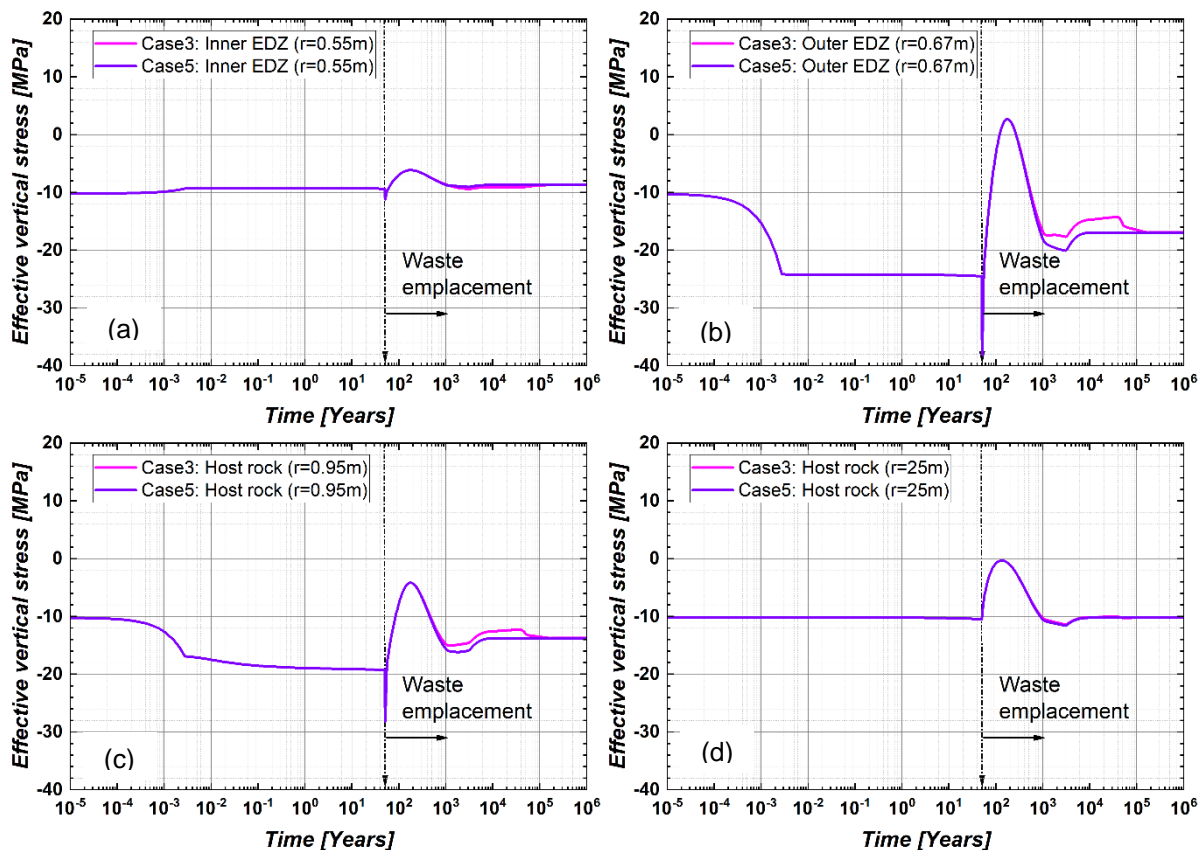


Figure 9-45 Effective vertical stress in Zone C (THMG v/s THM-coupling scenario).

9.6 Conclusion

Within the framework of WP GAS: Task 4.2, a two-dimensional (2D) plane strain finite element simulation campaign was performed to enhance the mechanistic understanding of gas (hydrogen) transport in a generic repository case. The simulation was performed using the in-house softwares LAGAMINE for two different disposal strategies i.e., Zone B and Zone C. The main objective was to identify the state variables which govern the gas pressure evolution, and also to highlight the role of far-field boundary conditions and the coupling scenarios on the gas pressure evolution. The key observations and results are summarized as a forerunner of a full-scale three-dimensional (3D) simulation. In the given task, the effect of water retention curve (SWRC) formulation, effect of geometric features, consequences of temperature rise during waste emplacement, and the role of gas pressure in stress distribution in the host rock were investigated.

In both Zone B and C, no significant effect of SWRC is observed on the simulation results. It is worth mentioning here that in Zone B, some numerical issues were observed while adopting the given SWRC formulation considering the gas entry pressure. The consideration of overlaying and underlying geological formations significantly affect the thermal response, a much shorter thermal period (3000 years) was observed without the top/bottom aquifers as compared to the opposite case (30,000 years). A change in the thermal response induces cascading effect on the PWP and gas (hydrogen) pressure evolution. Comparing a fully coupled THMG versus HMG case, rise in the temperature induces excess PWP, thus affecting the gas pressure (hydrogen) evolution. As a result, higher PWP and Gas pressure are observed in THMG case as compared to HMG coupling case, while comparing the fully coupled THMG case versus HMG case, it was found that the gas pressure does not affect the temperature or PWP evolution.

The above observations provide an insight of gas transport mechanism under repository-relevant boundary conditions, and also highlight the key parameters which affect the simulation results. Such as, the specified formulations for gas and water relative permeability are important to feature the role of gas entry pressure in water retention behaviour. Also, the temperature induced PWP has a cascading effect on the other locations, whereas the gas pressure evolution or distribution depends upon the spatial/local parameters along with the features of introduced source. Considering the geometric features i.e., Top and Bottom aquifers primarily effects thermal response, which leads to a different PWP and gas pressure evolution. The above fact helps to comment on the results from a full 3D analysis. With the observed trends, the rate of increase in temperature should be expected to be lower in a 3D analysis as compared to a 2D analysis. This is because of the flow perpendicular to the plane (inward/outward) which is only possible in a 3D analysis.

9.7 References

1. Collin, F., Li, X.-L., Radu, J.-P., & Charlier, R. (2002). Thermo-hydro-mechanical coupling in clay barriers. *Engineering Geology*, 64. doi:10.1016/S0013-7952(01)00124-7

9.8 Appendix I

Table A1: Mechanical properties of different elements of reference disposal concept for Zone C

Material	Parameter	Symbol	Value	Unit
Steel liner / Air void	Young's modulus	E	1.00E+05	Pa
	Poisson ratio	ν	0.3	[-]
	Solid specific mass	ρ_s	2875	kg/m ³
Inner EDZ	Young's modulus	E	5.00E+08	Pa
	Poisson ratio	ν	0.3	[-]
	Solid specific mass	ρ_s	2875.0	kg/m ³
Outer EDZ	Young's modulus	E	5.00E+09	Pa
	Poisson ratio	ν	0.3	[-]
	Solid specific mass	ρ_s	2875.0	kg/m ³
Host rock	Young's modulus	E	5.00E+09	Pa
	Poisson ratio	ν	0.3	[-]
	Solid specific mass	ρ_s	2875.0	kg/m ³
Top/Bottom aquifer	Young's modulus	E	5.00E+09	Pa
	Poisson ratio	ν	0.3	[-]
	Solid specific mass	ρ_s	2875.0	kg/m ³

Table A2: Mechanical properties of different elements of reference disposal concept for Zone B

Material	Parameter	Symbol	Value	Unit
Concrete buffer (Same as cement backfill)	Young's modulus	E	5.00E+08	Pa
	Poisson ratio	ν	0.3	[-]
	Solid specific mass	ρ_s	3500.0	kg/m ³
Cement backfills	Young's modulus	E	5.00E+08	Pa

Material	Parameter	Symbol	Value	Unit
	Poisson ratio	ν	0.3	[-]
	Solid specific mass	ρ_s	3500.0	kg/m ³
	Concrete liner	Young's modulus	E	4.00E+10
	Poisson ratio	ν	0.25	[-]
	Solid specific mass	ρ_s	2764.70	kg/m ³
	Inner EDZ	Young's modulus	E	5.00E+08
	Poisson ratio	ν	0.3	[-]
	Solid specific mass	ρ_s	2875.0	kg/m ³
	Outer EDZ	Young's modulus	E	5.00E+09
	Poisson ratio	ν	0.3	[-]
	Solid specific mass	ρ_s	2875.0	kg/m ³
	Host rock	Young's modulus	E	5.00E+09
	Poisson ratio	ν	0.3	[-]
	Solid specific mass	ρ_s	2875.0	kg/m ³
	Top/Bottom aquifer	Young's modulus	E	5.00E+09
	Poisson ratio	ν	0.3	[-]
	Solid specific mass	ρ_s	2875.0	kg/m ³

Table A3: Hydraulic and thermal parameters for different elements for Zone C

Material	Parameter	Symbol	Value	Unit
Air void or steel liner (Steel liner is replaced with the air void in zone C)	Porosity	n	0.99	[-]
	Intrinsic permeability (water)	K_{water}	1E-13	m ²
	Intrinsic permeability (gas)	K_{gas}	1.00E-16	m ²
	Parameter related to SWCC	n	0.33	[-]
	Air-entry pressure	P_r	0.1	MPa
	Gas-entry pressure	P_e	0	MPa
	Residual degree of <i>water saturation</i>	S_{res}	0	[-]
	Field saturation	$S_{r,field}$	1	[-]
	Henry coefficient	H	0.0193	[-]
	Thermal conductivity (Assumed constant with saturation)	λ	1.3	W.m ⁻¹ .K ⁻¹
	Thermal dilation of solid matrix	β^T_s	2x10 ⁻⁵	K ⁻¹
	Dry material specific heat	C_{ps}	500	J.kg ⁻¹ .K ⁻¹
	$\rho \cdot C_p = \rho_s \cdot C_{ps} \cdot (1 - n) + \rho_w \cdot C_{pw} \cdot n$ (Kept constant during simulation)	-	4.14E+06	J. m ⁻³ .K ⁻¹
	Parameter related to M-Q equation	a	1	[-]
	Parameter related to M-Q equation	b	15	[-]
Inner EDZ	Porosity	n	0.2	[-]
	Intrinsic permeability (water)	K_{water}	1.00E-16	m ²
	Intrinsic permeability (gas)	K_{gas}	1.00E-16	m ²
	Parameter related to SWCC	n	0.33	[-]
	Air-entry pressure	P_r	16	MPa
	Gas-entry pressure	P_e	0	MPa
	Residual degree of <i>water saturation</i>	S_{res}	0	[-]
	Field saturation	$S_{r,field}$	1	[-]
	Henry coefficient	H	0.0193	[-]

Material	Parameter	Symbol	Value	Unit
	Thermal conductivity (Assumed constant with saturation)	λ	1.70	$W.m^{-1}.K^{-1}$
	Thermal expansion coefficient	β_s^T	4.00E-05	K^{-1}
	Dry material specific heat	c_{ps}	720	$J.kg^{-1}.K^{-1}$
	$\rho.C_p = \rho_s.C_{ps}.(1-n) + \rho_w.C_{pw}.n$ (Kept constant during simulation)	-	2.492E+06	$J.m^{-3}.K^{-1}$
	Parameter related to M-Q equation	a	1.5	[-]
	Parameter related to M-Q equation	b	10	[-]
Outer EDZ	Porosity	n	0.2	[-]
	Intrinsic permeability (water)	K_{water}	1.00E-18	m^2
	Intrinsic permeability (gas)	K_{gas}	1.00E-17	m^2
	Parameter related to SWCC	n	0.33	[-]
	Air-entry pressure	P_r	16	MPa
	Gas-entry pressure	P_e	2	MPa
	Residual degree of <i>water saturation</i>	S_{res}	0	[-]
	Field saturation	$S_{r.field}$	1	[-]
	Henry coefficient	H	0.0193	[-]
	Thermal conductivity (Assumed constant with saturation)	λ	1.70	$W.m^{-1}.K^{-1}$
	Thermal expansion coefficient	β_s^T	4.00E-05	K^{-1}
	Dry material specific heat	c_{ps}	720	$J.kg^{-1}.K^{-1}$
	$\rho.C_p = \rho_s.C_{ps}.(1-n) + \rho_w.C_{pw}.n$ (Kept constant during simulation)	-	2.492E+06	$J.m^{-3}.K^{-1}$
	Parameter related to M-Q equation	a	1.5	[-]
	Parameter related to M-Q equation	b	10	[-]
Host rock and Top/bottom aquifer (As the properties of top/bottom aquifers were considered same as host rock.)	Porosity	n	0.2	[-]
	Intrinsic permeability (water)	K_{water}	1.00E-20	m^2
	Intrinsic permeability (gas)	K_{gas}	1.00E-18	m^2
	Parameter related to SWCC	n	0.33	[-]
	Air-entry pressure	P_r	16	MPa
	Gas-entry pressure	P_e	6	MPa
	Residual degree of <i>water saturation</i>	S_{res}	0	[-]
	Field saturation	$S_{r.field}$	1	[-]
	Henry coefficient	H	0.0193	[-]
	Thermal conductivity (Assumed constant with saturation)	λ	1.70	$W.m^{-1}.K^{-1}$
	Thermal expansion coefficient	β_s^T	4.00E-05	K^{-1}
	Dry material specific heat	c_{ps}	720	$J.kg^{-1}.K^{-1}$
	$\rho.C_p = \rho_s.C_{ps}.(1-n) + \rho_w.C_{pw}.n$ (Kept constant during simulation)	-	2.492E+06	$J.m^{-3}.K^{-1}$
	Parameter related to M-Q equation	a	1.5	[-]
	Parameter related to M-Q equation	b	10	[-]

Table A4: Hydraulic and thermal parameters for different elements in Zone B.

(Note: properties concerning inner EDZ, outer EDZ, host rock, and top/bottom aquifers were similar to Zone C.)

Material	Parameter	Symbol	Value	Unit
Concrete buffer and cement backfill	Porosity	n	0.40	[-]
	Intrinsic permeability (water)	K_{water}	1.00E-16	m^2
	Intrinsic permeability (gas)	K_{gas}	1.00E-16	m^2
	Parameter related to SWCC	n	0.33	[-]
	Air-entry pressure	P_r	1	MPa
	Gas-entry pressure	P_e	0	MPa
	Residual degree of <i>water saturation</i>	S_{res}	0	[-]
	Field saturation	$S_{r,field}$	1	[-]
	Henry coefficient	H	0.0193	[-]
	Thermal conductivity (Assumed constant with saturation)	λ	1.3	$W.m^{-1}.K^{-1}$
	Thermal expansion coefficient	β_s^T	2.00E-05	K^{-1}
	Dry material specific heat	c_{ps}	500	$J.kg^{-1}.K^{-1}$
	$\rho \cdot C_p = \rho_s \cdot C_{ps} \cdot (1 - n) + \rho_w \cdot C_{pw} \cdot n$ (Kept constant during simulation)	-	2.7236E+06	$J.m^{-3}.K^{-1}$
	Parameter related to M-Q equation	a	1	[-]
	Parameter related to M-Q equation	b	15	[-]
Concrete liner	Porosity	n	0.15	[-]
	Intrinsic permeability (water)	K_{water}	1.00E-16	m^2
	Intrinsic permeability (gas)	K_{gas}	1.00E-16	m^2
	Parameter related to SWCC	n	0.33	[-]
	Air-entry pressure	P_r	10	MPa
	Gas-entry pressure	P_e	0	MPa
	Residual degree of <i>water saturation</i>	S_{res}	0	[-]
	Field saturation	$S_{r,field}$	1	[-]
	Henry coefficient	H	0.0193	[-]
	Thermal conductivity (Assumed constant with saturation)	λ	2.3	$W.m^{-1}.K^{-1}$
	Thermal expansion coefficient	β_s^T	2.00E-05	K^{-1}
	Dry material specific heat	c_{ps}	900	$J.kg^{-1}.K^{-1}$
	$\rho \cdot C_p = \rho_s \cdot C_{ps} \cdot (1 - n) + \rho_w \cdot C_{pw} \cdot n$ (Kept constant during simulation)	-	2.7426E+06	$J.m^{-3}.K^{-1}$
	Parameter related to M-Q equation	a	2	[-]
	Parameter related to M-Q equation	b	4	[-]

Table 5: Properties of liquid water, air, and hydrogen

Material	Parameter	Symbol	Value	Unit
Liquid water	Dynamic viscosity	$\mu_{w,0}$	0.001	<i>Pa.s</i>
	Density	$\rho_{w,0}$	1000	<i>kg.m³</i>
	Compressibility coefficient	$1/\chi_w$	5.00E-10	<i>Pa⁻¹</i>
	Thermal expansion coefficient	β_w^T	3.80E-04	<i>K⁻¹</i>
	Thermal conductivity	$\Gamma_{w,0}$	0.528	<i>W.m⁻¹. K⁻¹</i>
	Specific heat	$c_{p,w0}$	4180	<i>J.kg⁻¹. K⁻¹</i>
Gas (Air)	Dynamic viscosity	$\mu_{a,0}$	1.80E-05	<i>Pa.s</i>
	Density	$\rho_{a,0}$	1,205	<i>kg.m³</i>
	Thermal conductivity	$\Gamma_{a,0}$	0.025	<i>W.m⁻¹. K⁻¹</i>
	Specific heat	$c_{p,a0}$	1000	<i>J.kg⁻¹. K⁻¹</i>
Gas (Hydrogen)	Dynamic viscosity	$\mu_{H,0}$	9.00E-06	<i>Pa.s</i>
	Density	$\rho_{H,0}$	0.0794	<i>kg.m³</i>
	Thermal conductivity	$\Gamma_{H,0}$	0.18	<i>W.m⁻¹. K⁻¹</i>
	Specific heat	$c_{p,H0}$	1430	<i>J.kg⁻¹. K⁻¹</i>

10. Discussion

The above chapters describe the work carried out by each team in the sub-task 4.2 of EURAD-GAS. Although some general discussions have been proposed by some of them, the aim of this chapter is to draw from all of these results added values and good practices for a phenomenologically representative assessment of maximum gas pressures in a repository and their possible impacts on the host rock integrity and/or radionuclide transfers.

10.1 Mechanical coupling

10.1.1 General comments

Models proposed by EURAD-GAS Task 4 participants and discussions among them suggest that **exhaustive hydromechanical coupling models on the scale of the entire repository is not foreseeable in the coming years.**

Up to now, even at cell scale (2D slice, EDF, chapter 6, SCK CEN, chapter 8, ULiège, chapter 9 or 3D, EDF, chapter 6, SCK CEN, chapter 8) the hydromechanical process models proposed are mainly based on elastic approaches. The main reason is that it is easier to compare the participant responses from elastic hydromechanical models, compared to process models with plasticity or explicitly integrated fracture initiation. This is also partly due to the complexity to estimate parameters of these models and their inherent complexity.

Knowing that the gas pressure build-up appears well after the excavation (inducing plasticity and fracturation), from a theoretical point of view, as long as the maximum gas pressure generates only elastic deformations of the materials (host rock but also EBS), no irreversible behaviour is foreseen and so the mechanical integrity of materials is maintained. In those conditions, elastic models are sufficient to represent the phenomenological behaviour associate to the transport of gas. From a practical view, this is right only if the gas pressure stays under the minimum in-situ mechanical stress.

In two-phase flow models, a compressibility sub-process is integrated under the form of the specific storage coefficient. In that way, two-phase flow approach can be seen as equivalent to an elastic hydromechanical model assuming no porosity change. The correspondence between the elastic parameters and the specific storage coefficient is however not straightforward. In theory, the specific storage corresponds to the inverse of the elastic modulus; however, in practice, specific storage coefficient is generally deduced from non-steady-state hydraulic tests whereas the Biot Modulus is deduced from porosity and Young modulus. Both approaches can lead to uncertainties in parameter estimation, especially considering the anisotropic behaviour of the materials.

As the two-phase formulation does not include damage, the gas pressure evaluations carried out with this approach are generally conservative compared to evaluations considering coupling with mechanics. Indeed, damage implies an increase in permeability which has the effect of a tendency for pressure to decrease, effect that the two-phase formulation does not consider.

Finally, as long as maximum gas pressure remains below the minimum in-situ stress, the representativeness of two-phase flow models is similar (and even conservative) to that of an elastic hydromechanical model, assuming that the value of the specific storage coefficient is consistent with that of the Biot Modulus. Under these conditions, two-phase flow models can be used to assess the mechanical integrity of the host rock. This approach is however not able to account for the time-dependent behaviour of the clay rock (creep).

10.1.2 Dilatancy versus two-phase flow

Most of the experiments done in the framework of EURAD-GAS on clay host rock show that, under gas pressure fracturing, migration of an expressed gas phase is mainly controlled by dilatancy processes (D6.8, “advection” part). Said otherwise, two-phase flow is a second order process if it exists.

As at the disposal scale numerical gas migration models are built on two-phase flow, their representativity can be questioned. However, by broadening the knowledge beyond that acquired within the framework of EURAD-GAS different elements can be provided to demonstrate that this is not the case:

- For tested clay host rocks, dilatancy is the main gas migration process at laboratory scale (centimetric scale) (EURAD-GAS D6.8), but for some in-situ experiments, on more larger scales (decametric to metric scale) two-phase flow modelling can reproduce the complex gas pressure evolution imposed by the experimental procedure (PGZ at Bure URL⁵)
 - Local behaviours are dilatancy controlled but at larger scale, once the REV (Representative Elementary Volume) for two-phase flow is reached, this representation can give sufficiently accurate estimates for global (large scale bulk estimates) assessment of gas flow and pressure.
- The clay host rocks gas entry pressures are so high that they hardly desaturate during gas phase transient after disposal closure. More than this, their retention curves are so high that even if a desaturation initiates, the desaturation level will be very low:
 - The EBS (backfill and seal core) gas entry pressure and retention curves are lower than the one of the host rock; if a desaturation occurs in a disposal, it will develop essentially in these material;
 - In the intact host rock only dissolved gas will migrate on metric or more important special scales.
- There is no evidence that in the EBS dilatancy is the main gas transport process. On the contrary, most of the EBS (backfill and seal cores) include a portion of granular material (sand) and two-phase flow characterization of these materials are well matching the experimental results.

For disposal scale evaluations, two-phase formulations are thus sufficient to estimate global gas migration and pressures even if very local assessment are out of reach with this type of representation.

10.2 Model extension

The sensitivity analysis done on model extension (total repository, stand-alone zones, with or without shaft) has shown that the size of the model can result in over- or underestimations of the maximum gas pressure:

- If the model does not include the zone producing the most hydrogen, the estimation can be underestimated;
- If the model does not include important gas escape pathways (e.g. toward the shaft or ramp), the estimation can be overestimated.

⁵ De La Vaissière R., Talandier J., Armand G., Vu M.-N., and Cornet F. H. (2019). From Two-Phase Flow to Gas Fracturing into Callovo-Oxfordian Claystone. Presented at the 53rd U.S. Rock Mechanics/Geomechanics Symposium.

Even if on specific evaluations 1D or 2D models can be seen as similar to 3D models (SCK CEN, chapter 8), this cannot be considered as a global conclusion valid for all the disposal concepts. For instance, the evaluations made by SCK CEN are dedicated to zone B of the generic model and whatever the model dimension (1D, 2D or 3D) they miss the high pressure that builds up in the zone A of this generic repository (Andra, chapter 3).

The only model that can give a reasonable estimation of the maximum gas pressure is a model integrating the totality of the designed architecture of the repository.

10.3 Mesh refinement

The sensitivity analysis on mesh discretisation have shown that even if the extension of the model covers the total extension of the repository, it is important that all the zones of gas pathways are well discretised (from production zones of hydrogen, i.e. all the cavern and/or access and disposal galleries, towards the upper aquifer via the shafts/ramps, e.g. the EDZ, the backfill and the lining). If not, this can lead to an overestimation of the estimated maximum gas pressure (Andra, chapter 3, BGR, chapter 4).

A reasonable estimation of the maximum gas pressure can only be achieved if all the materials representing a potential gas pathway are explicitly represented in the model and well discretised by a sufficiently fine mesh.

10.4 Uncertainty on the gas pressure results

The comparison of the results from all the teams involved shows that depending on how the repository is modelled, **uncertainties on the estimated maximum gas pressures can be very significant**. The differences have been established on all the available results from a single generic repository problem, irrespective of the mechanical coupling considered, the extension of the model and/or the representativity of the escape pathways for the gas.

Some teams succeeded to reduce the difference between their results at the same modelled scale (2D vertical slice of a deposition cell).

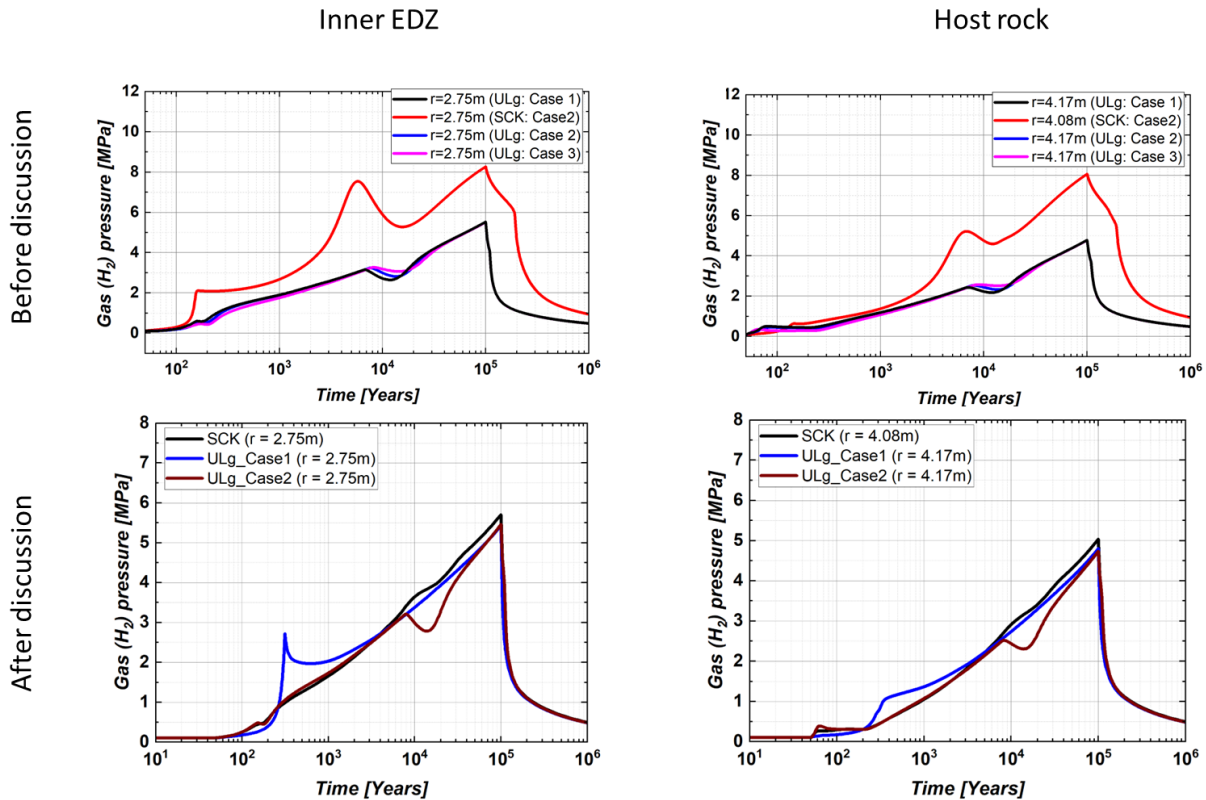


Figure 10-1: Example for zone B of reduction of differences between two models after discussions between ULiège and SCK CEN modelling teams; initial differences were mainly linked to different compressibility formulations

Nevertheless, even by considering **the same extension, the same representation of gas pathways toward the exit, and the same set of parameters, a remaining uncertainty on maximum gas pressure still persist. The two main causes for discrepancies between the codes come from the way the hydro-mechanical coupling is considered (i.e. specific storage versus inverse of Biot Modulus, see more explanations in chapter 10.1.1) and the integration of the retention curve formulation.**

This conclusion has to be taken with caution (i) as the number of independent simulations on which this work was performed during EURAD-GAS is very limited and (ii) as it is derived from a generic model and has to be verified on specific national repository concepts.

However, this type of global numerical uncertainty, including the human aspect, has to be evaluated on each national concept in order to assess the gas transport regimes that can be active at the scale of a geological disposal system and their potential impact on barrier integrity and repository performance. However, it must be kept in mind that by increasing the ease of gas migration at the disposal scale this also includes radioactive gases such as ¹⁴C and that these effects must be taken into account in safety assessments.

10.5 Optimized design for maximum gas pressure reduction

The sensitivity analysis has shown that assuming a certain architecture for a repository, there exist some ways to reduce the maximum gas pressure by optimizing the EBS two-phase flow characteristics. Increasing the permeability of the backfill is one of these (Andra, chapter 3). More generally **designing the EBS (backfill, concrete lining, seals...) to increase as much as possible the ease of gas flow can help to significantly reduce the maximum gas pressure estimated in a specific architecture for a given repository.**

Another way to reduce the gas pressure in a repository is to minimize, as much as possible, the amount of metal present in post-closure in the repository (Andra, chapter 3). One way to do this could be to optimize the reinforcement of the concrete lining or even to replace it by non-metallic elements.

10.6 Gaseous radionuclides transfer

In the generic repository, the characteristic time for gaseous radionuclides to reach the shaft from the deposition zones is of several hundred years at least (Andra, chapter 3).

This means that even under gaseous form all the radionuclides having a $\frac{1}{2}$ life of less than at least several tens of years will never reach the shaft with a significant flux (could be repository design dependant).

Another element is that gaseous radionuclides move much more rapidly toward the shaft than soluble one (Andra, chapter 3). Thus, **to have a good evaluation of the potential impact of radionuclides that can migrate at least partially under gaseous form, an evaluation considering two-phase flow at repository level is necessary.**

10.7 Solute radionuclides transfer

The sensitivity analysis made on gas source terms (Andra, chapter 3) has shown that when these terms are limited:

- the time of first arrival is reduced
- the maximum flux at shaft is increased.

However, from the evaluations made, the order of magnitude of first arrival time and of maximum flux at shaft should not change.

Nether the less, the less gas in the repository, the faster the migration and the higher the flux of soluble radionuclides towards the shaft via the galleries network.

This conclusion is derived from evaluations on the “generic repository” architectural concept developed for EURAD-GAS; it must stay qualitative, but it should be valid for all types of disposals, the quantitative evaluations being concept dependant.

Based on this conclusion, making soluble radionuclides migration evaluations under saturated conditions is conservative in term of arrival time and fluxes at shafts/ramps via the galleries network.

11. Synthesis

Task 4 aims at fulfilling the second high-level objective of the WP GAS of EURAD, which is to evaluate the gas transport regimes that can be active at the scale of a geological disposal system and their potential impact on repository performance. It is dedicated in particular to end-users questions concerning:

- the effects of the presence of gas and its transport on the transfer of soluble and volatile radionuclides;
- the consequences of gas-induced hydro-mechanical perturbations on barrier integrity and long-term performance.

It is known that gas generated by corrosion and/or radiolysis in large quantities may result in the development of a gas phase within the existing porosity of the engineered barrier system (EBS), within the Excavation Damaged Zone (EDZ) and, to some extent, within the host rock. Experimental evidence suggests that discrete, transient, gas-specific pathways may also form through (or between) EBS materials, the EDZ and the host rock in the form of dilatant pathway or cracks. Desaturation can also have a significant effect on soluble radionuclide migration: it may limit the extent of diffusion of soluble radionuclides but may also result in advective transport of radionuclides, if groundwater is displaced one way or another by gas as a consequence of pressurization or suction. High levels of desaturation may even affect the gas source term by decreasing the availability of water for gas production processes. Continuous gas pathways, possibly evolving and unstable, may form from the deposition zones to the repository access. These would affect the migration of volatile radionuclides. Finally, high gas pressures may possibly result in mechanical damage to the engineered and natural barriers, including the host rock, and could affect the global functioning of the repository. It is important to assess if this could occur in practice and if such damage would be transient only or would have a lasting effect and how this would affect (or not) the outcome of a safety case.

Built on the basis of the EC project FORGE, which ran from 2008-2013, Task 4 was driven from an end-user perspective of gas induced effects in order to improve repository scale modelling by:

- including in the analysis hydro-mechanical couplings;
- including in the analysis the transfer of soluble and volatile radionuclides;
- promoting the use of multiple assessment approaches, supported by different numerical modelling tools.

This task benefited from recent advances in phenomenological understanding from the CAST (CARbon-14 source term and fate) and BEACON (bentonite mechanical evolution) EC projects allowing respectively (i) a better understanding of potential release mechanisms of carbon-14 (in the form of methane for instance) from radioactive waste materials under conditions relevant to geological disposal facilities and (ii) a better characterisation of hydro-mechanical coupling in swelling clayey materials (from the installation of materials to their evolution over the long term).

Task 4 was broken down into two complementary subtasks:

- Subtask 4.1, the objective of which is to assemble phenomenological descriptions of gas transport at repository scale and of its consequences on the mechanical integrity of the host rock as well as on the transport of radionuclides, soluble or gaseous. At the start of the work package, this sub-task participated in the writing of SOTA-1 for which it collected and compared storyboards of gas transport and related processes. From these, it proposed a generic storyboard for reference (see Section 1.1). It also provided a generic repository model inspired by broad features of the concepts currently studied by national programmes taking part to EURAD GAS, for use in subtask 4.2 (See section 1.2). Throughout the duration of EURAD GAS,

the WMOs and TSO involved in subtask 4.1 challenged and stimulated the scientific programme from an end-users perspective. This was achieved through active participation of Subtask 4.1 participants to all meetings of Tasks 2&3 and involvement in the reviewing of milestone documents and of the deliverables of these tasks.

- The main work of Subtask 4.2 was to compare modelling approaches at repository scale and to assess the capabilities of numerical simulation tools. An additional purpose of this was to consolidate the phenomenological knowledge describe in the 1st state-of-the-art of EURAD-GAS (Levasseur et al., 2021) and to assess the need to integrate (or not) new results and data acquired by Tasks 2&3 in repository-scale models, based on the results of calculations and parameter sensitivity analyses carried out (see for example discussion on representativity of dilatancy versus two-phase flow at repository scale, chapter 10.1.2). Numerical aspects were also discussed (for example, is it better to base the evaluation on 2D models faster allowing more sensitivity or on 3D models more representative of disposal concepts as a whole but allowing less sensitivity analyses).

This chapter brings together outcomes from subtask 4.1 (detailed in the 1st state-of-the-art of EURAD-GAS, Levasseur et al. 2021) and from subtask 4.2 (detailed in this report). These outcomes are generic in nature, being based on the generic storyboard and repository model proposed by subtask 4.1. These cover:

- Uncertainties associated to the complexity of the problem to be treated and the inherent limitations of modelling tools (see Section 11.3)
- Assessment of the mechanical integrity of the host rock (see Section 11.4)
- Assessment of the impact of gas on the migration of radionuclides (see Section 11.5)
- Recommendations for a treatment of gas at the repository design stage (see Section 11.6)

11.1 Proposal of a generic storyboard at repository scale

It should be noted that because of the composition of the work package, the generic storyboard developed in EURAD GAS is somehow biased towards GDFs in clay host rocks. The main drivers and controls of the development of a gas transient phase in a radioactive waste repository in a clayey rock could be as follows (see Figure 11-1):

1. Rapid saturation (a few decades) of the access shafts and ramps up to the access seals by water from overlying aquifers. Because of these seals, there is little or no flow of water into the rest of the repository from that path at this stage.
2. A slow and radial saturation of the engineered barrier system (EBS) in the repository galleries and drifts by the waters of the host rock, limited by its low permeability. Inflow through the now saturated access seals is also very limited.
3. During the saturation of the EBS, no significant desaturation of the host rock is expected beyond the excavation damaged zone because of the high suction prevailing in the intact rock. Air initially present in the porosity of the EBS materials and the technological voids is expected to dissolve in porewater (in the case of oxygen, part of it will be consumed by oxidation processes).
4. Gas, mainly hydrogen, is continuously produced by anaerobic corrosion of metals (mostly) and by radiolysis (in particular from organic waste). Metals are present in waste packages, but can also be present in other EBS components, depending on the repository design (e.g. metal lining of disposal cells, reinforcement of concrete gallery lining) and in some waste forms (e.g. claddings). It is to be noted that full saturation is not necessary for corrosion to take place, the presence of humidity in a gas phase is sufficient. Hence gas production is already active during the EBS saturation phase.

5. Gas will dissolve into the pore water and diffuse away, radially from the disposal drifts and galleries. If the gas production exceeds the system capacity for dissolution and diffusive removal, it can prevent the engineered barriers (and possibly the EDZ) attaining full saturation for a very long time, or will induce and maintain partial desaturation if full saturation was achieved before.
6. The intact host rock remains almost saturated with water due to its very high gas entry pressure. Hence, if a gas phase persists or reappears in the system due to gas production, it will be confined to the near field and only dissolved gas will migrate into the far field. Desaturation, if it is considered to happen, would be restricted to the immediate vicinity of the galleries (metre scale), and saturation degree would not decrease by more than a few percent from full saturation in that zone.
7. The fraction of the produced gas that does not dissolve in the surrounding groundwater can expand through the galleries towards the repository access structures, also increasing the contact surface between the gas and liquid phase, favouring further dissolution. An expanding gas phase is not expected to displace large quantities of water along the galleries mainly because water is more easily pushed into the immediate, saturated surroundings than displaced along the galleries. Because a limited desaturation of the EBS/EDZ is sufficient to obtain high enough transmissivities for gas, the gas phase can extend over long distances within the system. The progress of the gas phase through the underground infrastructures can be hindered as it encounters seals.
8. Once the gas phase encounters a seal, its pressure will increase further. This will at first result in more desaturation of the underground infrastructures (in particular, the backfill of galleries). At some point the pressure can attain a value at which gas pathways can develop either through the seal or through the EDZ around it and the progression of the gas phase will resume. Depending on the repository concept and the expected quantities of gas to be managed, design requirements could be defined (e.g. properties of the seal such as its gas entry pressure or swelling pressure) to limit the pressurization of the gas phase.
9. Pathways through the EDZ would take advantage of planes of weakness created during the excavation phase. Seals can also be made of a controlled mix of bentonite and sand that favours transport of gas above a (low) threshold pressure while retaining a low hydraulic conductivity. Whichever the pathways, through the seal or through the EDZ, these will close once gas pressures decrease because of the self-sealing capacity of clay materials.
10. Depending on the concept and the gas production, a significant fraction of the gas may reach the geological layers above the host rock through the access shafts and ramps and/or along their EDZ depending on the performance of the seals. Simulations performed in FORGE and confirmed in subtask indicate that the time scales for the onset of these releases, and their duration, can be of the order of several tens to several hundred thousand of years.

From the above, we can identify salient elements in a repository performance perspective. If a gas phase develops through the repository and even though most of it will be composed of inactive gas (hydrogen), the presence of this phase could affect the transport of water-soluble and/or volatile radionuclides through the system:

- Dissolved radionuclide transport is not expected to be enhanced because the water displacement associated to the evacuation of gas is limited and would occur only over short distances. In fact, total system performance assessment models in most national programmes considering clayey barriers and/or host formations do not currently represent directly the effects of gases on dissolved radionuclide transport. Indeed, it is assumed that the transport rate of solutes, among which soluble radionuclides, is higher in a system that would remain saturated with water, because a gas phase is an obstacle for solute diffusion. It is thus deemed conservative in estimating the transport of radionuclides in water-saturated conditions.
- Volatile radionuclides that would not completely dissolve into the pore water upon release from the waste form can be carried toward the shafts and/or ramps along with the inactive

gas (generated in much larger quantities). However, the duration of the transport from the gas source to the shafts and/or ramps may take several hundreds to several thousand years (order of magnitude, concept dependent) and only radionuclides with half-lives around this duration or higher will present a significant concentration in the gas phase when arriving in the upper formations. In addition, all along the gas pathways, part of the gaseous radionuclides will also dissolve (as inactive gas also do) into the porewater present in the surrounding materials.

Upon total saturation of the repository when the gas source term reduces to zero, typically after several tens to hundreds of thousands of years after closure (concept dependant), and closure of gas pathways, if any, self-sealing will maintain the very low hydraulic conductivity of clay barriers.

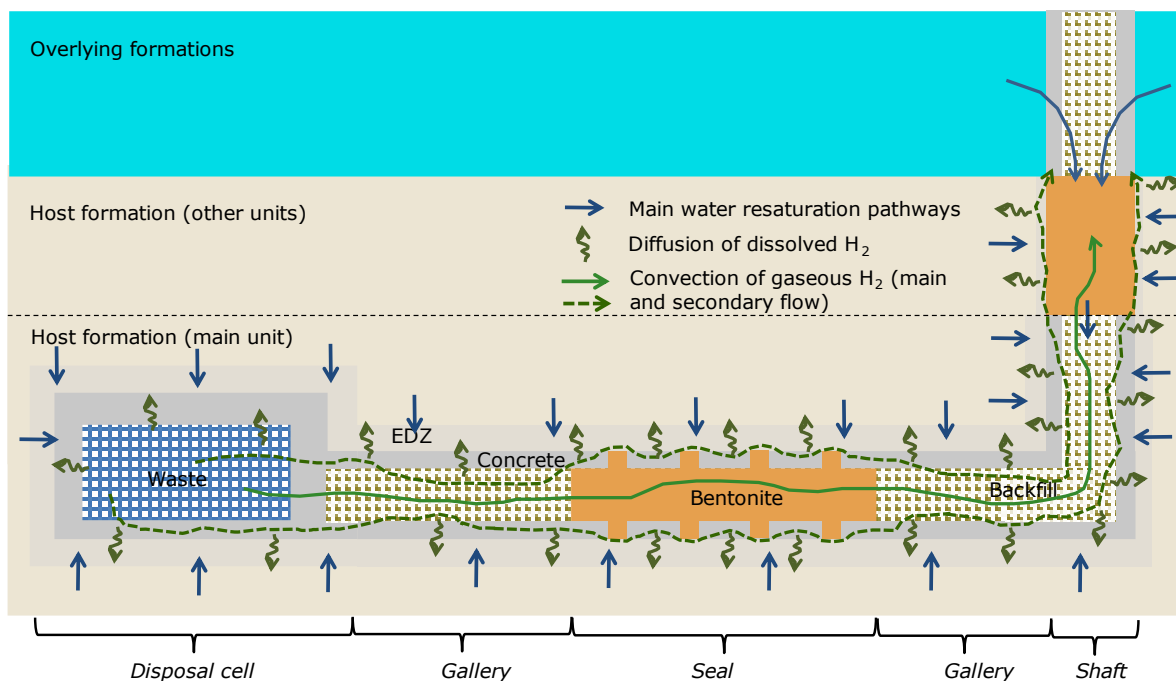


Figure 11-1: schematic representation of the main elements driving the storyboard at repository scale

11.2 Generic repository model

A generic repository model is proposed, to provide a practical support for a comparison of modelling approaches at repository scale and of the use of different numerical simulation tools. The proposed model (Figure 11-2) borrows traits from various repository configurations considered in national programmes in Europe. Salient characteristics and simplifications of this generic repository include: disposal on a single level, separation of zone for high activity, heat-emitting wastes (zones B and C) from a zone for long-lived medium activity waste, backfilling of access galleries at once at zone closure, positioning of intermediate seals in the accesses to the disposal area in addition to the sealing of the (single) access shaft. As for the storyboard, this generic model is biased towards disposal in clays but it can support the testing of approaches and tools that can be of use in other host rocks too (e.g. treatment of seals).

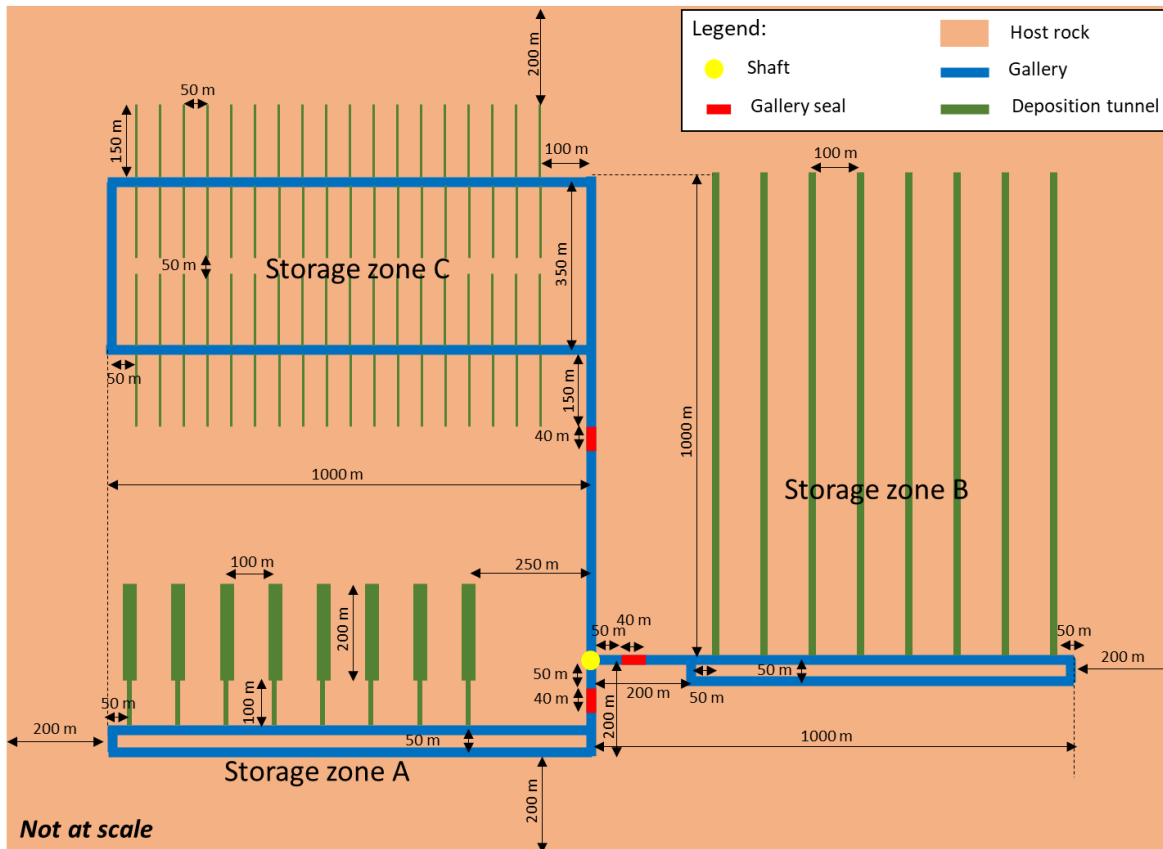


Figure 11-2: Generic repository: schematic representation at main repository depth

11.3 Uncertainties associated to the complexity of the problem to be treated and inherent limitations of modelling tools

With respect to modelling of gas transport at repository scale, gas dissolution and diffusion is well-understood, process-level models show good predictive capacity and upscaling to repository scale in a continuum framework is simple.

When it comes to an expressed gas phase, the current knowledge allows to estimate the threshold under which gas pressure is not affecting the host-rock integrity.

When gas pressure stays under this limit, although at small scale dilatancy may represent the main migration process in rich clay media (the host rock) (D6.8 of EURAD-GAS), two-phase flow formulation is able to account for a representative assessment of gas flow and pressure at disposal scale (see chapter 10.1.2).

In line with the conclusions of the FORGE EC project, modelling approaches and tools that have been compared in EURAD-GAS confirm that repository scale modelling of gas transport explicitly representing all couplings with the mechanical behaviour of the barriers and for the development of individual pathways through clayey materials is currently out of reach and will probably remain so in the foreseeable future, because of the local and instable nature of gas pathway initiation and propagation which cannot be represented by continuous models.

The conceptual complexity of the problem to be addressed implies that the modellers carrying out simulations at repository scale have to introduce simplified representations of phenomena, for example two-phase flow and linear elastic mechanical behaviour. Even with these simplified representations of phenomena, carrying out a hydromechanical numerical simulation on the scale of a repository is beyond the reach of all the teams who participated in EURAD-GAS task 4.2, in the current state of computing power. However, it is possible to carry out two-phase flow simulations on the scale of a complete repository, but this requires specific numerical approaches such as the use of "macro-elements", non-conforming meshes and homogenization of materials. For example, in Task 4.2 simulations integrate:

- a mechanical coupling through the use of a single, bulk compressibility coefficient considering the compressibility of the grains of the host rock, the compressibility of water and porosity;
- simplifications of the geometry taken into account component-scale and repository-scale models;
- homogenization of the different materials present in and around the repository, for example the use of a single material on the extrados of the backfill in the galleries homogenizing a concrete lining and the EDZ;
- simplification of initial and boundary conditions and/or their temporal evolution, for example by not considering the ventilated exploitation phase of the repository.

All hydromechanical numerical simulations were carried out on the scale of a 2D section of a gallery or at best of a complete 3D gallery. Limited scale models can also be built for the different components of the system that are expected to be passed through (e.g. seals, backfilled galleries, EDZ,...). These component models can explicitly describe the mechanical couplings. Gas pressure-flux relationships estimated from these smaller scales models under specific pressure conditions can then be integrated into repository scale model as complement to the more conceptual storyboard approaches. In turn, repository-scale model results can be compared to the assumed pressure conditions in the component-scale models, that can be adjusted if necessary.

It has to be noted, however, that except for what concerns diffusion of dissolved gas, the predictive capabilities of repository-scale models is expected to remain limited in the foreseeable future due to inherent uncertainties in the development of gas pathways that are unstable by nature and the uncertainties associated to the simplifications above, that cannot be avoided. Moreover, differences in the sets of parameters in the broad sense (mesh, homogenization, physical process, temporal management, boundary/initial conditions, etc.) produced by different teams to represent the same physical evolution on the same real object was found to lead to very significant differences in terms of maximum gas pressure.

These differences integrate all the results independently of the model extension (2D, 3D at cell/zone scale, with and without exit to the shaft, total repository) and the numerical implementation of the process models (especially formulations on the way how compressibility is taken into account) in the used codes. A complementary work initiated in the framework of EURAD-GAS task 4.2 has shown that for models having the same extension, the same representation of gas route toward the exit and the same set of parameters, uncertainty can be reduced to much lower values (chapter 10.4).

No quantitative assessment of this uncertainty is given (i) as the number of independent simulations on which this work was performed during EURAD-GAS is very limited and (ii) as it is derived from a generic model and has to be verified on specific national repository concept.

However, whatever the national concept defined, such uncertainty has to be evaluated and taken into account in the global assessment of gas transport regimes that can be active at the scale of a geological disposal system and their potential impact on barrier integrity and repository performance.

11.4 Assessment of the mechanical integrity of the host rock

In the evaluations carried out within Task 4.2, the mechanical integrity of the host rock is assessed through the evaluation of a single indicator which is the maximum gas pressures in the repository, from which the change in stress in the different components of that repository can be estimated.

For this, it is essential to represent the repository as a whole. If this is not the case:

- The assessment may overestimate the maximum gas pressure when the simulated area does not include the gallery system up to the accesses which represent an escape path for gases;
- The assessment may underestimate the maximum gas pressure when the simulated zone does not include the repository portion in which the gas source term is maximum regarding the local possibilities for evacuating this gas (difficult to quantify a priori).

The tools available today (computer codes, in particular the solvers, and the hardware) make it possible to carry out two-phase simulations on the scale of a complete repository. These simulations integrate the mechanical couplings through a (constant) storage coefficient (assuming linear elasticity). It is essential to match the value of this coefficient to the available data. This coefficient can be estimated directly from hydraulic experiments in transient conditions. It can also be evaluated based on its mathematical formulation, which can be different from one code to another, from the porosity, the compressibility of water and the compressibility of the porous matrix (i.e. the Young's modulus), potentially anisotropic.

This type of simulation gives a representative estimate of the maximum gas pressure in the repository if this value remains in the linear part of the mechanical behaviour of materials important for long-term safety, typically the seals and the host rock, but other materials may be included in this list depending on repository concepts and national requirements. It is therefore important to experimentally determine the mechanical behaviour of each of these materials, considering all the associated uncertainties, in order to know the stress limit beyond which linear elastic behaviour is no longer representative and to be able to compare this value to the stresses resulting from the maximum gas pressure estimated in the repository, taking also into account all the uncertainties inherent in its estimation.

11.5 Assessment of the impact of gas on the migration of radionuclides

As for the evaluation of the maximum gas pressure, to correctly assess the migration of radionuclides in the repository, it is essential to represent it as a whole and thus to integrate in the simulation the exit paths towards the upper aquifer, therefore the system of galleries and accesses.

For a good estimate of the transfer of volatile radionuclides, considering the hydraulic-gas transient phase is essential as these radionuclides can migrate quickly through a gas phase essentially composed of (inactive) hydrogen and be carried along with it, if this gas phase is expanding through the system. Without taking this transient phase into account, volatile radionuclides are supposed to dissolve and therefore migrate by diffusion in the pore water, which is a very slow process. In terms of the volatile radionuclides fluxes through the top of the host rock and out from the shafts for the generic repository depicted in Figure 11-2, these two types of evaluations (with and without considering a gas phase) give estimates which can differ by several orders of magnitude, with the evaluation taking into account the presence of hydrogen as a carrier gas resulting in the largest quantity.

Regarding soluble, non-volatile radionuclides, the presence of gas implies a partially saturated near field, with pores filled with gas being unavailable for solute diffusion. Thus, calculations performed in Task 4.2 accounting for this result in computed radionuclide fluxes through the host rock that are slightly lower than those obtained assuming a completely saturated environment, but of the same order of

magnitude. If an expanding gas phase displaces pore water, radionuclides dissolved in that water are displaced with it. However, results from the calculations performed in task 4.2 for a generic repository show that water is principally displaced radially, over a short distance, around the galleries and drifts, not axially along the galleries. In general, this will depend on hydraulic properties and the state of saturation of the EBS materials (in particular on the composition of the backfill and seals but also of the structural elements) and is therefore concept dependant.

Overall, regarding the impact of gas on radionuclide transport, the results in Task 4.2 are consistent with the generic storyboard assembled at the beginning of the work package (section 11.1).

11.6 Recommendations for a treatment of gas at the repository design stage

Beyond the conclusions and recommendations presented above, the results of EURAD-GAS task 4 make it possible to propose some elements that should be integrated by end-users, as early as the repository design phase, to manage the impacts of gas on the barriers:

- Estimate the gas source term and carry out simulations of gas transport by dissolution and diffusion and by two-phase flow at the scale of the repository.
 - These simulations require at least the provision of the following elements:
 - ✓ A repository architecture which in addition to the geometry of the excavations (galleries, cells, ramps, wells, etc.) integrates the location of the metals which will be present in the different zones of the repository after closure (reinforcement of concrete liners, repository packages, primary packages, waste, etc.) in terms of mass and surface area, because the corrosion of these metals can be a significant or even the main part of the gas source term.
 - ✓ An estimate of the other components of the gas source term (e.g. radiolysis of organics).
 - ✓ An estimation of the corrosion rate for each type of metal present in the disposal and in relation with the material in contact (lower corrosion rate in concrete for instance)
 - ✓ A two-phase flow characterization (water and gas permeability, relative permeability curves, retention curve, gas entry pressure, porosity, storage coefficient, diffusion coefficient of hydrogen in water and variation depending on saturation, etc.) for all materials present in the repository, including the host rock and the damaged zone. The two-phase flow parameters for each material should be derived from lab and in-situ experiments (e.g. in this Work Package, from Tasks 2 and 3) through a dialogue between modellers and experimentalists.
 - ✓ A characterization of the mechanical behaviour of the materials present in the repository and the geological environment (engineered barriers and the host rock), which are concept dependant, and in particular the stress range corresponding to linear elastic behaviour.
 - If the maximum gas pressure in the repository evaluated by numerical simulation, considering all the associated uncertainties, is lower than the value of the stress corresponding to the top of the linear part of the mechanical behaviour of the materials important for long-term safety, considering all the associated uncertainties, the numerical evaluations can be considered representative. Otherwise, at least one of the materials important for long-term safety could incur mechanical damage at least during the hydraulic-gas transient phase (self-sealing after resaturation).

- Two phases flow numerical simulations of radionuclide transfer can be carried out, both on gaseous radionuclides and on soluble radionuclides.
- If it is believed that the mechanical integrity of a component that has no self-sealing capacity, or if even a temporary loss of integrity is unacceptable, an evolution of the repository concept might be necessary to reduce the maximum gas pressure. Such a reduction may be possible by focusing concept evolutions on one or another of the following elements:
 - Reduce the gas source term, by reducing the mass and external surface area of metal components present in post-closure inside the repository. For example, replacing metal reinforcements of structural elements made of concrete with non-metallic reinforcements.
 - Modify the composition of the repository closure system, in particular the backfill(s) and/or the seal(s), to facilitate gas evacuation. For example, by the addition of sand to a swelling clay for the mixture constituting a seal.

In any case a design approach, that considers gas from the start is required. The general knowledge about gas transport mechanisms through a repository and its components, as presented in the generic storyboard (Section 11.1) is readily available for that purpose. However, uncertainty on the values of key properties that control gas transport can be large at the start of a programme. Also, the determination of parameter values that can be used for repository-scale evaluations is not direct but the outcome of a dialogue between experimentalist and modellers. In addition, repository designers need to be involved with respect to EBS material selection and host rock conditions at the time of repository closure because the parameter values need to be determined for these specific conditions and materials. Hence, also for gas, the design approach will be iterative by nature.

12. ANNEX: milestone MS 61

12.1 Aim of the exercise

In the framework of EURAD-GAS, Task 4 is dedicated to conceptualisation and evaluation at the scale of a repository. This implies space scale of several kilometres and time scale of several hundreds of thousands of years.

To do such an evaluation the only available tool is numerical modelling. As the results should be useful for all participants, it has been decided to define a “generic repository” including elements of disposal concepts of the different national programmes involved.

It has also been decided that the aim of the « generic repository » exercise would be mainly to compare different calculation methods (full 3D model, 2D approximations, lumping techniques and network models, ...) to illustrate how these can be used to obtain relevant indicators such as pressure or flow at key locations in the system and to check that different methods return consistent values of these indicators (taking into account evaluation uncertainties).

So this exercise is not a benchmark of codes, even if different types of codes will be used, but rather a benchmark of numerical methods in order to evaluate the fitness of each method for the purpose of the evaluation of the impact of gas generation on the repository hydro-mechanical transient.

12.2 Geometry of the generic repository

The “generic repository” includes, in part, highly simplified and generic elements of disposal concepts from several European countries for a repository in clay host rock; three of them have been selected for three different disposal zones (A, B, and C on Figure 12-2). However, in order to ease the meshing and to reduce the calculation time, geometrical representations have been simplified compared to the original complexity of these concepts.

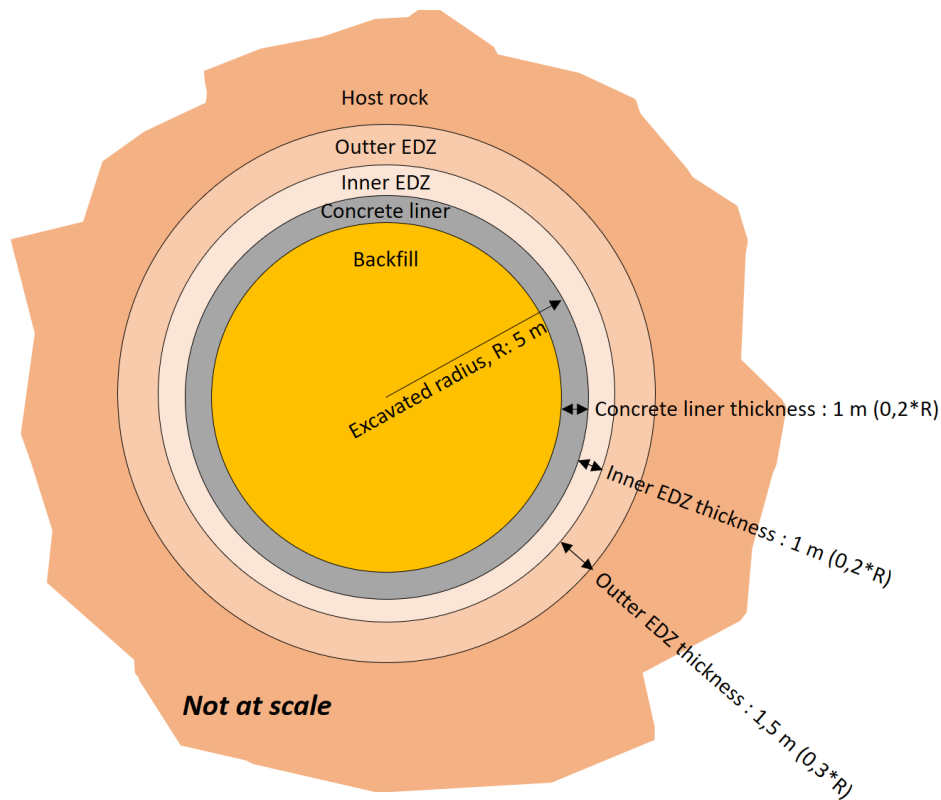


Figure 12-3 - Schematic vertical slice of a gallery

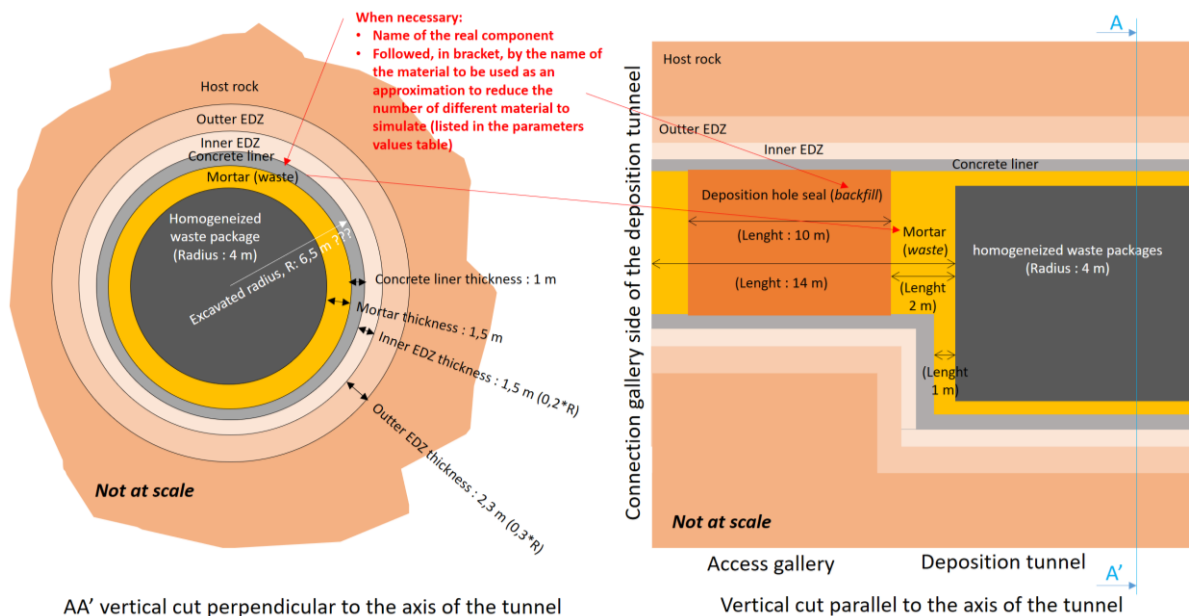


Figure 12-4 - Schematic representation of deposition tunnel in disposal zone A

Note that, as described in Figure 12-4, in order to reduce the number of material to represent in the mesh, some components have been represented by an approximation listed in the parameters list table (Section 12.6). For instance, the mortar, present only in the disposal Zone A, is represented by the

material “waste” listed in Section 12.6. In the following figures, each time a component name is followed by a material name in bracket, the latter is to be used in the mesh.

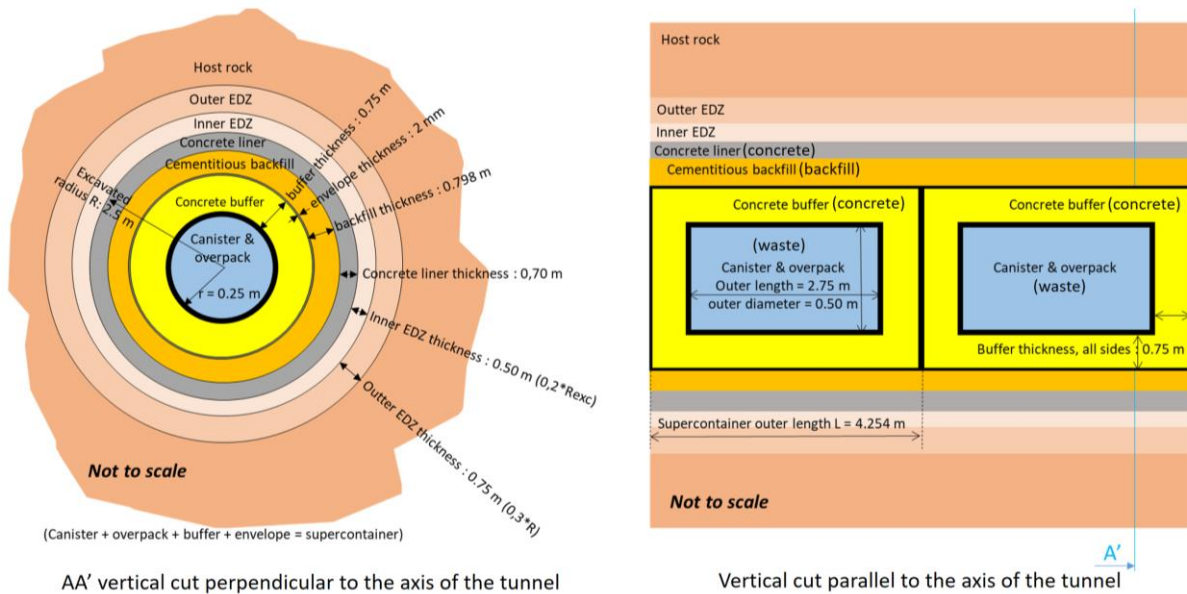


Figure 12-5 - Schematic representation of a deposition tunnel in disposal zone B

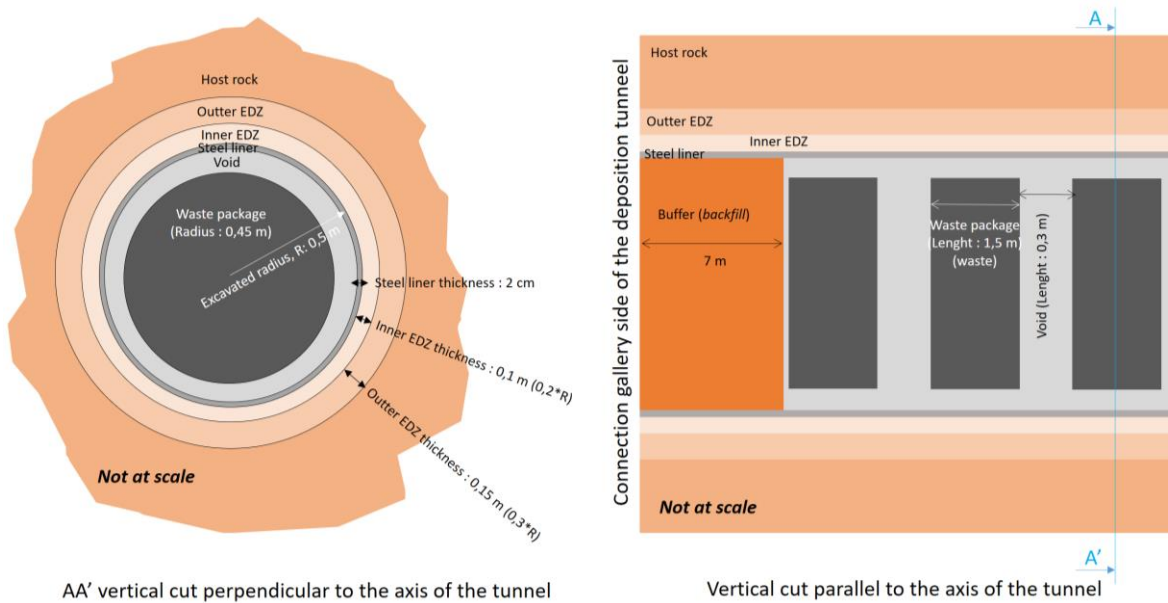


Figure 12-6 - Schematic representation of a deposition tunnel in disposal zone C

Connection gallery seals (horizontal)

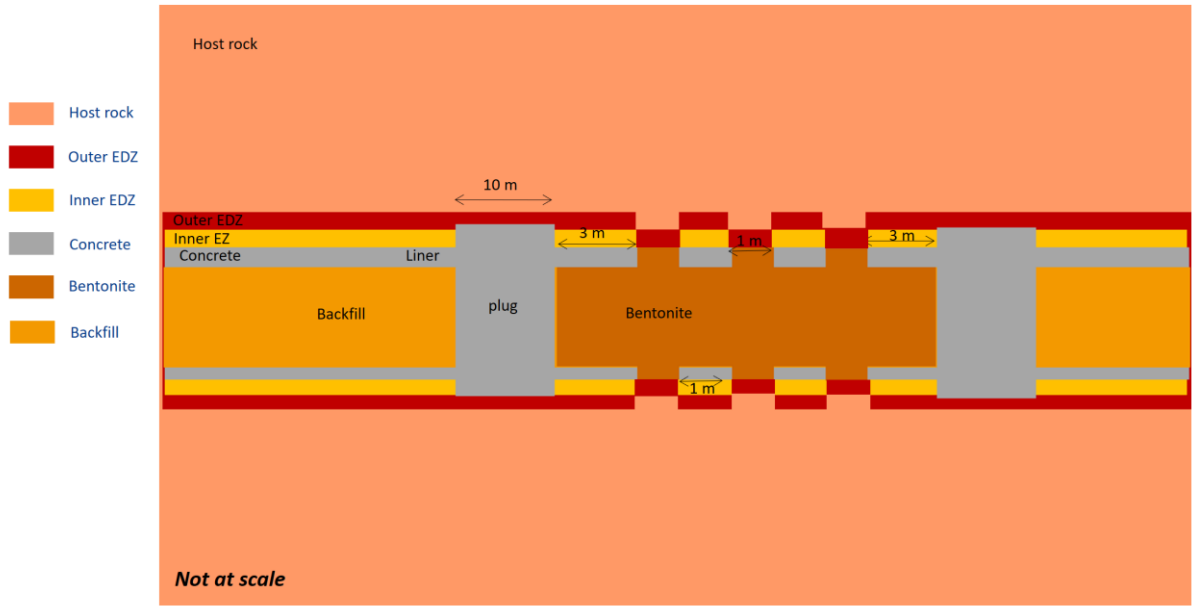


Figure 12-7 - Schematic representation of a connection gallery seal

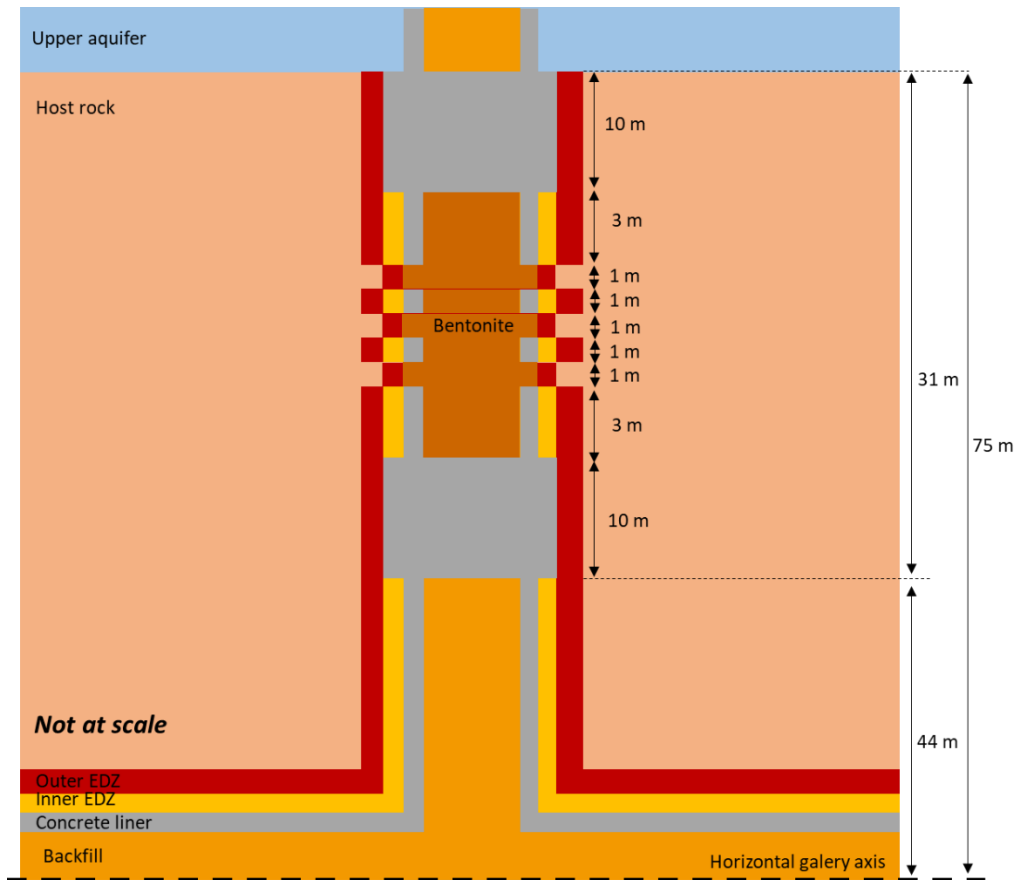


Figure 12-8 - Schematic representation of the shaft seal

12.3 Initial boundary conditions

Initial and boundary conditions are given at surface and “bottom” of the model but also for the host rock layer in case some teams would like to limit the mesh to the host rock layer (Figure 12-9). Boundary and initial conditions are given in terms of pressure, temperature and mechanical constraints.

Note that hydraulic head is assumed constant in the upper aquifer as well as in the bottom aquifer and that the difference in hydraulic head between both implies a vertical gradient inside the host rock allowing vertical water flux from the bottom toward the top under natural hydraulic conditions and explaining the difference in terms of water pressure from a hydraulic equilibrium at hydrostatic pressure.

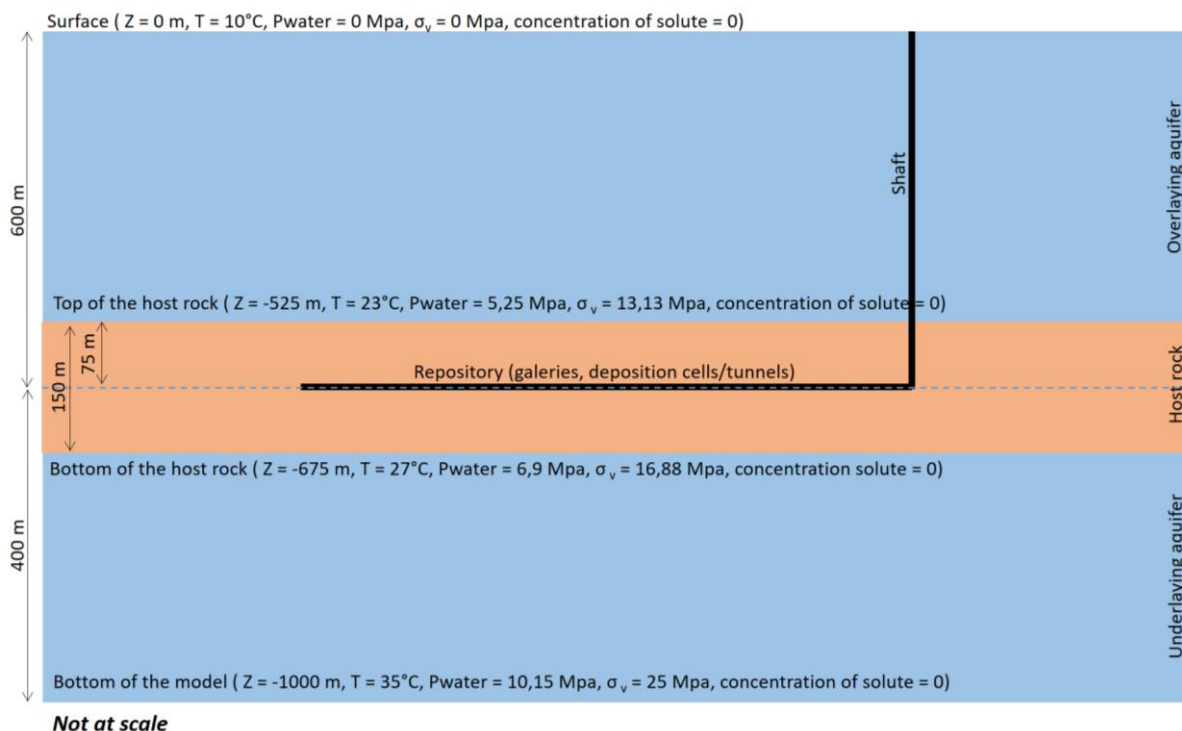


Figure 12-9 - Schematic vertical slice of the generic repository with boundary and initial conditions

12.4 Time varying conditions

Initially, the repository is not present in the model. The time varying elements are as follows:

- T < 0: hydrostatic pressure (and mechanical and/or thermal equilibrium if pertinent) assuming the repository is not present in the model.
- T = 0: instantaneous excavation of the whole repository. Ventilation of all the excavation with an air at 80% of relative humidity except for the HLW cells of the disposal zone C which are not ventilated.
- T = 50 years: instantaneous emplacement of the waste and closure of the whole repository. All emplaced materials are assumed to have an initial water saturation of 80%.

For the purpose of sensitivity analysis, some parameters may change at larger timescale. For instance it could be decided that around the bentonite core of the seals, the EDZ characteristics could evolve once the bentonite is resaturated and develops its swelling pressure.

12.5 Source terms

The aim of the « generic repository » exercise is mainly to compare different calculation methods (complete 3D model, lumping technics, 2D approximations, ...) in order to analyse if whether or not they give, for the same indicator (i.e., pressure or flow at a certain location), evaluations that can be considered identical (taking into account evaluation uncertainties).

Thus, it is not needed for the source terms to be “realistic” (i.e., corresponding to existing wastes/component): they just have to be of the right order of magnitude concerning the values and the duration.

12.5.1 Thermal source terms

Only for HLW canisters (for ILLW canisters, thermal load is supposed to be zero).

The Figure 12-10 and the associated table of values is given per meter of canister/overpack [one canister per section for disposal zone C (length of canister 1.5 m) and B (length of overpack 2.75 m)].

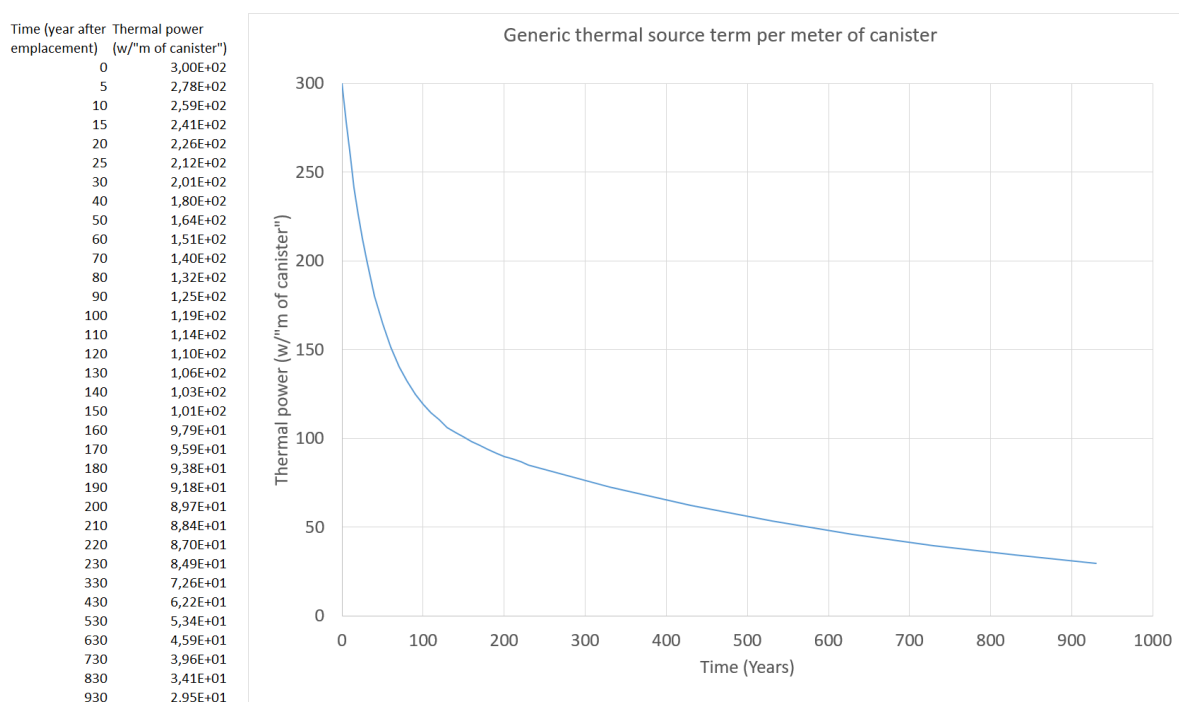


Figure 12-10 - Thermal source term per meter of canister/overpack

12.5.2 Gas source terms

The generic gas source term is supposed to be composed solely by hydrogen generated by anoxic corrosion of only non-allied steel (i.e., no other metallic component, no radiolysis, no bacterial activity, no radionuclides decay).

The generation rate is approximated as follows

$$F = S \cdot CR \cdot C$$

With:

F: hydrogen generation flux (mol/y)

S: available surface of metallic component (m²)

CR: Corrosion Rate (m/y)

C: constant coefficient to pass from m³/y to mol/y (mol/m³). For hydrogen and non-allied steel, C can be approximated by 215 000 mol/m³.

Some schematic representation of the emplacement of the different gas source terms described below can be found in Figure 12-11.

For all galleries (including the 100 m long access galleries of the ILLW cells present in disposal zone A)

Per meter of galleries: surface of metallic component (concrete rebars): 1000 m², thickness of metallic component: 0.5 cm, corrosion rate: 10⁻⁷ m/y (low value because of the alkaline environment). This leads to a gas source term of 21.5 mol/y (per meter of gallery) from T=0 to T=50 000 y (time needed to corrode 0.5 cm of thickness)

For ILLW waste cells in disposal zone A

Per meter of cell:

Due to the reinforced concrete liner: surface of metallic component (concrete bars): 1500 m², thickness of metallic component: 1 cm, corrosion rate: 10⁻⁷ m/y (low value because of the alkaline environment). This leads to a gas source term of around 32 mol/y (per meter of ILLW waste cell) from T=0 to T=100 000 y (time needed to corrode 1 cm of thickness)

Due to the metallic component of the wastes: surface of metallic component: 2000 m², thickness of metallic component: 1 mm, rate 10⁻⁷ m/y (low value because of the alkaline environment). This leads to a gas source term of 43 mol/y (per meter of ILLW waste cell) during 10 000 years.

Mortar is considered to have no reinforcement and thus no gas source term.

For HLW waste cells in disposal zone B

Per meter of cell:

Due to the reinforced concrete liner: surface of all metallic components: 12 m², average thickness of metallic components: 1 cm, rate 10⁻⁷ m/y (low value because of the alkaline environment). This

leads to a gas source term of around 0.25 mol/y (per meter of zone B HLW cell) during 100 000 years.

Concrete buffer is considered to have no reinforcement and thus no gas source term.

No metallic component in the waste: assumed to be made of nuclear glass

For HLW waste cells in disposal zone C

Due to the metallic liner and waste container: average per meter of cell not including the buffer part: surface of metallic component: 9 m², thickness of metallic component: 4 cm, rate 10⁻⁶ m/y (no passivation linked to an alkaline environment). This leads to a gas source term of around 1.9 mol/y (per meter of zone C HLW cell) during 40 000 years.

No metallic component in the waste: assumed to be made of nuclear glass.

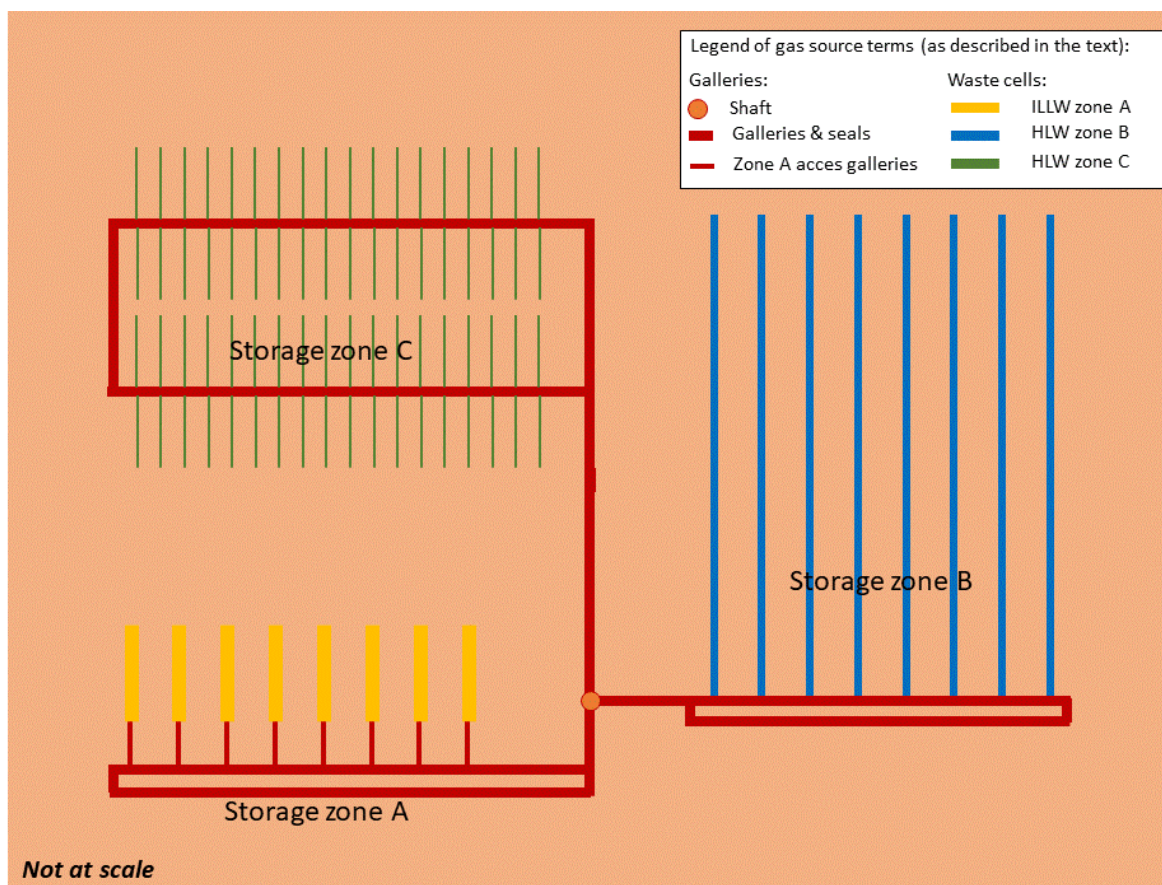


Figure 12-11 - Schematic representation of the gas source terms emplacements in the repository

12.5.3 Radionuclides source terms

The radionuclides sources terms are not affecting the hydraulic transient: nonphysical values can be used:

14C source terms:

Only for ILLW cells (disposal zone A): flux of 1 mol/y/m³ inside “waste” material, from T=0 to T=10000 years

129I source term:

For cells in ILLW disposal zone A: flux of 1 mol/y/ m³ inside “waste” material, from T=0 (no tightness of ILLW canisters) to T=100000 years (low degradation of the wastes)

For cells in HLW disposal zone C: flux of 1 mol/y/ m³ inside “waste” material, from T=10 000 (loss of tightness of the canisters) to T=110 000 years (low degradation of the nuclear glass)

For cells in HLW disposal zone B: flux of 10 mol/y/ m³ inside “waste” material, from T=100 000 (loss of tightness of the canister) to T=110 000 years (rapid degradation of the nuclear glass)

It shall be stressed that these source terms are per cubic meter of the waste components and that no boundary between the waste and outside should be considered.

12.6 Parameters values

The table below gives value for all relevant hydro-thermo-mechanical parameters for the main materials present in the repository or its near surrounding. The values in the table are meant for the base calculation case. For sensitivity analysis, extreme values for some parameters could be chosen (to be defined sensitivity by sensitivity, not present in this table).

Some assumed simplifications for the simulations:

- When a component (see Section 12.2) is not present in all concepts, its representation may be approximated by a material present in the following table (component name followed by a material name in brackets in Section 12.2 figures).
- Linked to the very long time scales, all metallic parts (liners, waste canisters) are assumed to be water “transparent” in the simulation as, due to corrosion, their water tightness will disappear after some time; Figures of Section 12.2 may represent these elements, but for the sake of simplicity, they are not explicitly represented in the meshes.
- Some models may use more parameters than the one provided in the table above. In this case these parameters have to be explicated by the teams using them.
- Water properties are assumed standard ones of the pure water.
- The backfill can be considered as “looser” bentonite if needed for some reason

Some parameters are linked to specific mathematical formulations. These formulations are given below the table

Table 12-1 – Parameters values

Parameter	Host rock			Bentonite	Concrete	Backfill	waste	voids
	Undisturbed	Outer EDZ*	Inner EDZ**					
Porosity « ω » (-)	0,2			0,35	0,15	0,4	0,4	1
Water permeability (m ²)	10 ⁻²⁰	10 ⁻¹⁸	10 ⁻¹⁶	10 ⁻¹⁹	10 ⁻¹⁶	10 ⁻¹⁶	10 ⁻¹³	10 ⁻¹³
Gas permeability (m ²)	10 ⁻¹⁸	10 ⁻¹⁷	10 ⁻¹⁶	10 ⁻¹⁹	10 ⁻¹⁶	10 ⁻¹⁶	10 ⁻¹³	10 ⁻¹³
Van Genuchten « n » (-)	1,5			1,6	1,5	1,5	1,5	1,5
Van-Genuchten « Pr » (MPa)	16			17	10	1	0.1	0.1
Gas entry pressure « Pe » (MPa)	6	2	0	4	0	0	0	0
Residual water saturation "Slr" (-)	0							
Dissolved H ₂ « a » and « b » for Millington-Quirk (-)	a = 1,5 b = 10			a = 2,5 b = 15	a = 2 b = 4	a = 1 b = 15	a = 1 b = 15	a = 1 b = 15
Gaseous H ₂ « a » and « b » for Millington-Quirk (-)	a = 2,5 b = 2,5			a = 3 b = 3	a = 0 b = 5	a = 3 b = 3	a = 3 b = 3	a = 3 b = 3
Dissolved ¹⁴ C « a » and « b » for Millington-Quirk (-)	a = 1,5 b = 10			a = 2,5 b = 15	a = 2 b = 4	a = 1 b = 15	a = 1 b = 15	a = 1 b = 15
Gaseous ¹⁴ C « a » and « b » for Millington-Quirk (-)	a = 2,5 b = 2,5			a = 3 b = 3	a = 0 b = 5	a = 3 b = 3	a = 3 b = 3	a = 3 b = 3

Parameter	Host rock			Bentonite	Concrete	Backfill	waste	voids
	Undisturbed	Outer EDZ*	Inner EDZ**					
Dissolved ¹²⁹ I « a » and « b » for Millington-Quirk (-)	a = 2,5 b = 15			a = 5 b = 20	a = 2 b = 4	a = 1 b = 20	a = 1 b = 20	a = 1 b = 20
Gaseous ¹²⁹ I « a » and « b » for Millington-Quirk (-)	No gas phase for ¹²⁹ I							
Dissolved H ₂ « D ₀ » (m ² /s)	5 · 10 ⁻⁹							
Gaseous H ₂ « D ₀ » (m ² /s)	9 · 10 ⁻⁵							
Dissolved ¹⁴ C « D ₀ » (m ² /s)	2 · 10 ⁻⁹							
Gaseous ¹⁴ C « D ₀ » (m ² /s)	2 · 10 ⁻⁵							
Dissolved ¹²⁹ I « D ₀ » (m ² /s)	2 · 10 ⁻⁹							
Gaseous ¹²⁹ I « D ₀ » (m ² /s)	No gas phase for ¹²⁹ I							
Henry's coefficient "H" for H ₂ (Pa ⁻¹)	1.4 · 10 ⁻¹⁰							
Henry's coefficient "H" for ¹⁴ C (Pa ⁻¹)	3 · 10 ⁻¹⁰							
Henry's coefficient "H" for ¹²⁹ I (Pa ⁻¹)	No gas phase for ¹²⁹ I							
Heat conductivity (w/m/°C) (assumed constant with saturation)	1,7			1,5	2,3	1,3	1,3	1,3
Dry material specific heat (J/Kg/°C)	720			700	900	500	500	500
Pore compressibility (1/Pa)	7 · 10 ⁻¹⁰			2 · 10 ⁻⁹	10 ⁻⁹	10 ⁻⁹	10 ⁻⁹	10 ⁻⁹

Parameter	Host rock			Bentonite	Concrete	Backfill	waste	voids
	Undisturbed	Outer EDZ*	Inner EDZ**					
Pore expansivity (thermal dilatation of solid matrix) (1/°C)	4 10 ⁻⁵			2 10 ⁻⁵	2 10 ⁻⁵	2 10 ⁻⁵	2 10 ⁻⁵	2 10 ⁻⁵
Young modulus (MPa)***	5 000	5 000	500	$\kappa_{i0} = 0.05$ $\alpha_i = -0.003$ $\kappa_{s0} = 0.18$ $\alpha_{sp} = -0.16$ $p_{ref} = 0.01$	40 000	$\kappa_{i0} = 0.01$ $\kappa_{s0} = 0.002$ (κ_i and κ_s are constant)	500	0
Poisson ratio (-)	0,3			0,3	0,25	0,3	0,3	0,3
Biot coefficient (-)	0,8			1	1	1	1	1

*: in the seal, radially of a direct contact between bentonite and host rock, the EDZ is recompressed: the Outer EDZ parameters are similar to those of undisturbed rock

** : in the seal, radially of a direct contact between bentonite and host rock, the EDZ is recompressed: the Inner EDZ parameters are similar to those of Outer EDZ

***: for bentonite and backfill,
$$d\varepsilon_v^e = \frac{\kappa_i(s) dp'}{1 + e p'} + \frac{\kappa_i(p') ds}{1 + e s + 0.1}$$

With:

$$\kappa_i(s) = \kappa_{i0}(1 + \alpha_i s)$$

$$\kappa_s(p') = \kappa_{so} \left(1 + \alpha_{sp} \ln \left(\frac{p'}{p_{ref}} \right) \right)$$

(s = suction, p' = net mean stress, e = void ratio)

Bentonite mechanical parameters are fitted to get a swelling pressure of 4 MPa at fully saturated state (0 MPa for backfill)

Van-Genuchten retention curves formulations taking into account explicit gas entry pressure (with linearization near $S_e=1$)

$$S_e = \frac{S_l - S_{lr}}{1 - S_{lr}}$$

$$p_c = \begin{cases} -\frac{1}{\alpha} \left((S_e^* S_e)^{-\frac{1}{m}} - 1 \right)^{\frac{1}{n}}, & \text{if } S_e \leq 1 - \varepsilon \\ -\frac{1}{\alpha} \left((S_e^* S_e)^{-\frac{1}{m}} - 1 \right)^{\frac{1}{n}} \cdot \frac{1 - S_e}{\varepsilon}, & \text{if } (1 - \varepsilon) < S_e < 1 \\ 0, & \text{if } S_e = 1 \end{cases}$$

With: $S_e^* = (1 + (\alpha p_e)^n)^{-m}$

$m = 1 - 1/n$, and $\alpha = 1/P_r$

ε is a numerical parameter that should be small, in the order of 0.01 or 0.001 at least.

Van-Genuchten relative permeability curves (modified to account for an explicit gas entry pressure)

$$S_e = \frac{S_l - S_{lr}}{1 - S_{lr}}$$

$$k_{rw} = \begin{cases} \sqrt{S_e} \cdot \left[\frac{1 - (1 - (S_e^* S_e)^{1/m})^m}{1 - (1 - S_e^{*1/m})^m} \right]^2, & \text{if } S_e < 1 \\ 1, & \text{if } S_e = 1 \end{cases}$$

$$k_{rg} = \begin{cases} f_g \cdot \sqrt{1 - S_e} \cdot \left[\frac{(1 - S_e^{*1/m})^m - (1 - (S_e^* S_e)^{1/m})^m}{(1 - S_e^{*1/m})^m - 1} \right]^2, & \text{if } S_e < 1 \\ 0, & \text{if } S_e = 1 \end{cases}$$

With: $S_e^* = (1 + (\alpha p_e)^n)^{-m}$

$m = 1 - 1/n$, and $\alpha = 1/P_r$

fg: ratio between gaz permeability (m2) and water permeability (m2) in the table above

Millington-Quirk relative diffusion coefficient formulation

$$S_e = \frac{S_l - S_{lr}}{1 - S_{lr}}$$

$$D_e = D_0 \omega^{1+a} S_e^b$$

Henry formulation

$$Pp g_x = \frac{MF_x}{H_x}$$

With:

Ppgx: Partial gas pressure of x (Pa)

MFx: Molar fraction of x in the liquid phase (-)

Hx: Henry's coefficient for x (Pa-1)

X: element (H2, 14C, 129i)

12.7 Indicators

Indicators for the evaluation of the impact of gas on the hydro-thermo-mechanical transient of the repository will mainly be:

- Maximum gas pressure evaluated over the whole repository (or disposal zone per disposal zone) and over the whole duration of the two-phase flow period (scalar, in [MPa]);
- Time of the maximum of gas pressure [year] evaluated over the whole repository (or disposal zone per disposal zone) and over the whole duration of the two-phase flow period (scalar, in [year]);
- Evolution with time of pressures at certain points within the excavation of the repository (time table [year, MPa]);
- Evolution with time of water saturations at certain points within the excavation of the repository ([year, %]);
- Evolution with time of water and/or gas and/or solutes flow rates through certain surfaces within the excavation of the repository ([year, m3/year] for water; [year, mol/year] for gas & solutes);

In addition to these hard indicators of predictive type, the participating teams are invited to propose sensitivity analysis to demonstrate the capacity of their models to reproduce trends which are of interest for the SA/PA analysis (for instance, the order of magnitude of response of maximal gas pressure to the increase of the source term). Some common sensitivity test cases shall be defined on the basis of the simulation results obtained for the reference test case.

12.8 Position of output points and surfaces

Points at which output will be requested are presented in Figure 12-12 below

Control sections for flow rate outputs are positioned in Figure 12-13 and include all materials inside the excavations and the entire EDZ (inner and outer) around.

For computational models that provide individual fluxes through various component, each team is free to also provide more details if he/she thinks that it is relevant, e.g. for a control section located at a seal, the fraction of the total gas flow through the seal itself vs the fraction that flows around the seal (i.e. inside the EDZ)

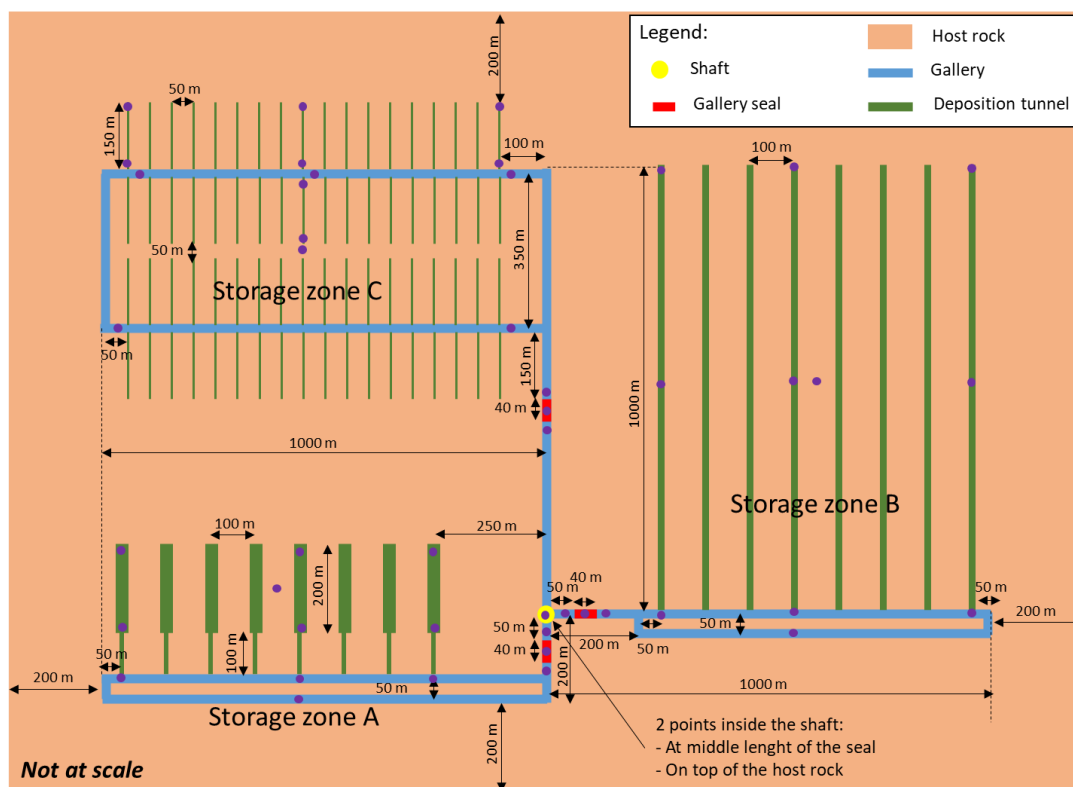


Figure 12-12 - Schematic horizontal slice at repository depth positioning the 47 points (purple circles) for output values

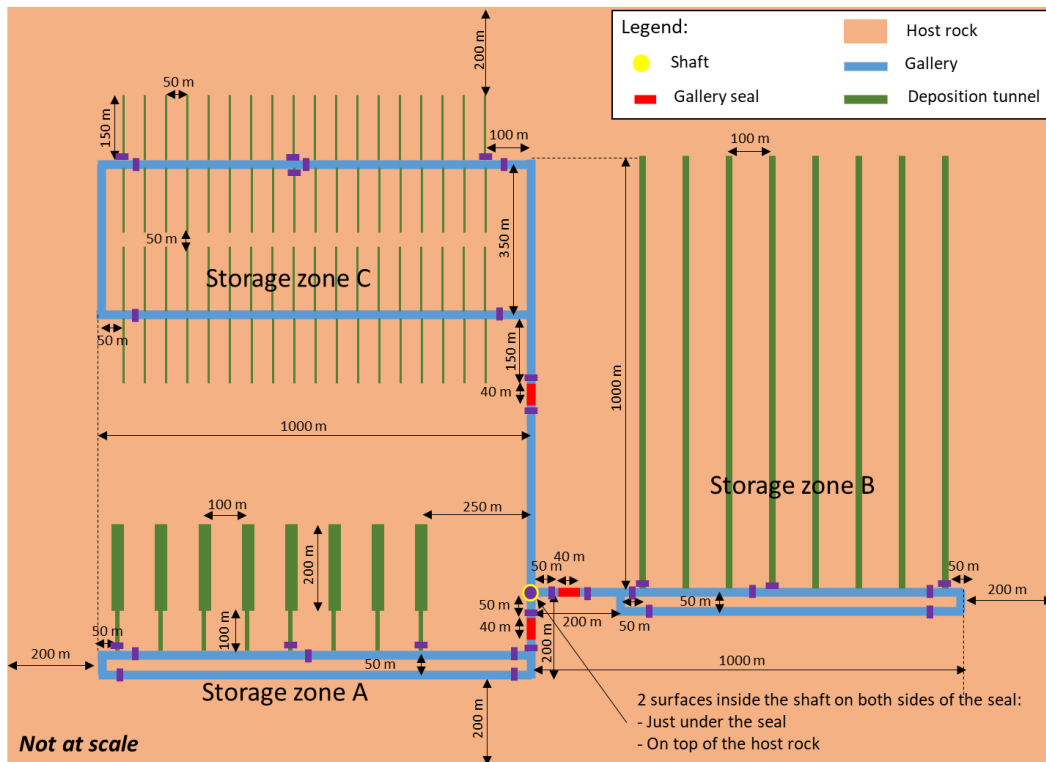


Figure 12-13 - Schematic horizontal slice at repository depth positioning the 33 surfaces (purple segments) for output values